Imperial College London
Department of Earth Sciences and Engineering

Shaping an Island Arc: The Influence of Tectonic History and Slab Hydration at the Lesser Antilles Subduction Zone

Robert W. Allen

Submitted in fulfilment of the requirements for the degree of
Doctor of Philosophy
September 2020

Abstract

Island arc volcanism is driven by the release of water from the subducting slab. Over time variations in the distribution of chemically bound water in the down-going lithosphere may influence an array of arc processes from rates of seismicity to arc structure. In slow spreading oceanic crust such as the Atlantic strong variations in crustal structure can lead to a pattern of hydration which changes across relatively short wavelengths along the slab front. As one of only two subduction zones to consume slow spreading lithosphere the Lesser Antilles is a key location for understanding the influence that the distribution of subducting fluids may have on potentially hazardous arc processes. However, the tectonics of the Caribbean plate are complex, with a history of arc volcanism which extends over 100 My. As a result it is unclear to what degree along arc variations are result of the influence of recent subduction, and how much is the result of inherited compositional and structural variations in the over-riding plate.

The VoiLA (Volatile Recycling in the Lesser Antilles) project collected an array of geophysical and geochemical data across the Lesser Antilles arc system in 2016 and 2017 in order to test the role that subducted volatiles have played in shaping the Lesser Antilles. In this thesis I present marine geophysical data including wide-angle and multichannel seismics, bathymetry and potential field data, collected as part of two research cruises by the R.R.S. James Cook. These data are used to constrain the relative contributions of 1) the Tertiary history of the eastern Caribbean and 2) the degree of alteration in the down-going slab to shaping the modern arc. Results are combined with other key project findings to explain along strike variability in the Lesser Antilles arc.

Copyright Declaration

The copyright of this thesis rests with the author. Unless otherwise indicated, its contents are licensed under a Creative Commons Attribution-Non Commercial 4.0 International Licence (CC BY-NC). Under this licence, you may copy and redistribute the material in any medium or format. You may also create and distribute modified versions of the work. This is on the condition that: you credit the author and do not use it, or any derivative works, for a commercial purpose. When reusing or sharing this work, ensure you make the licence terms clear to others by naming the licence and linking to the licence text. Where a work has been adapted, you should indicate that the work has been changed and describe those changes. Please seek permission from the copyright holder for uses of this work that are not included in this licence or permitted under UK Copyright Law

Declaration of Originality

I declare that this thesis, titled *Shaping an Island Arc: The Influence of Tectonic History and Slab Hydration at the Lesser Antilles Subduction Zone* and the work presented within is my own work. This research was conducted between October 2016 and September 2020 at the Department of Earth Science and Engineering, Imperial College under the supervision of Prof. Jenny S. Collier. All published and unpublished material contributing to this thesis has been referenced and given full acknowledgement. No portion of this thesis has been submitted elsewhere for any additional qualifications or in support of any other degree.

Robert W. Allen

Department of Earth Sciences and Engineering
Imperial College London
Sept 2020

'*On Ilkley Moor Baht'at (where's that?)*'

For Aunty Terry

Acknowledgements

First of all thanks go to my main supervisor Jenny Collier, for her help and advice over the last 4 years, and for giving me the opportunity to work on this amazing project. During the course of my PhD I have been given the opportunity to do fieldwork on remote Caribbean islands, attend my first scientific conferences, publish my first papers, experiences that I will never forget and that would not have been possible without her coaching and support. Furthermore, the last 6 months of this PhD were carried out under the shadow of lockdowns and coronavirus, and I will never not be grateful for the patience shown me as I staggered towards the finish line.

Thanks also to my second supervisor Tim Henstock for his support. His recommendations on seismic data processing and interpretation in particular were invaluable, and his willingness to provide detailed and helpful feedback, often at short notice, on both this manuscript and others was hugely appreciated.

Thanks also to everyone I've had the opportunity to collaborate with during the course of this PhD. Not limited to Saskia Goes, Richard Davy, Alex Stewart, Cameron Berry, Ben Maunder, George Cooper, Lidong Bie, Andreas Rietbrock and Ben Chichester, who helped much of this work reach it's potential. And to the rest of the VoiLA family, for always being willing with comments, improvements and suggestions, and for keeping things interesting along the way! In particular thanks go to our partners at the University of the West Indies Seismic Research Center, for their assistance and advice.

Thanks to Mel Gray, Sian Evans, Sophie Butcher, Dan Possee, Laura Petrescu, and many others, including the rest of the cast and crew of R.R.S. James Cook, who kept me going during fieldwork and 3 months at sea, and often closer to home as well. Not least to Chris Ogden, who for some reason has been willing to eat lunch with me almost every day for the last 4 years, but those hours spent chewing over the intricacies of Championship football were a much-needed distraction and really kept me going.

Finally, thanks go to my family who have never shown me anything other than total encouragement and support throughout this entire process. To my mum Jane, sister Mary and young Andy, who helped me every step of the way, and to the grandparents, aunts and uncles on whose support I knew I could always rely.

Last but not least thanks go to my fiancée, Charlotte, who has seen this whole process through with me from the very first time I opened my laptop and googled the words "Geophysics PhD". You have kept me going through every high and low since and I truly wouldn't have done this without you. I suppose we'll have to plan that wedding now.

Contents

Thesis Abstract **2**

Copyright Declaration **3**

Declaration of Originality **4**

Acknowledgements **5**

1 Introduction **21**

1.1 Island Arc Volcanism 21

1.2 The Lesser Antilles 22

1.3 Project VoiLA 24

1.4 Thesis Outline 24

2 Background: the Lesser Antilles Arc **30**

2.1 Introduction 30

2.2 Arc Structure and Processes 32

2.2.1 Crustal Structure 32

2.2.2 Seismicity 36

2.2.3 Arc Geochemistry 39

2.3 Sources of Slab Hydration 43

2.3.1 Slow Spreading Lithosphere 46

2.4 Correlating Arc Properties and Slab Structure 47

3 Background: Tectonic Setting 52

3.1 Introduction 52

3.2 The Caribbean Plate 53

3.3 A Tectonic Framework for the Greater Caribbean Region 55

3.3.1 Caribbean Plate Formation 55

3.3.2 Proto-Caribbean Spreading 58

3.3.3 Mechanisms for Subduction Reversal 58

3.3.4 The Great Arc of the Caribbean 60

3.3.5 Closure of the Great Arc 61

3.4 The Cenozoic History of the Eastern Caribbean 63

3.4.1 The Grenada Basin 63

3.4.2 The Limestone Caribbees 67

3.5 Learnings from G-Plates Reconstructions 70

3.5.1 Changes in Slab Structure 72

3.6 Key Uncertainties 73

4 Results: Tertiary History of the Lesser Antilles 75

4.1 Abstract 75

4.2 Introduction 76

4.3 New Model for the Evolution of the Lesser Antilles 79

4.4 Implications 83

5 Results: Structure of the Tiburon Basin 87

5.1 Abstract 87

5.2 Introduction 88

5.3 Sedimentation on the Incoming Plate 90

5.4 The Barbados Accretionary Prism 91

5.5 The VoiLA experiment: Data Acquisition 93

5.5.1 Bathymetry Data 94

5.5.2 Multichannel Seismic Data 94

5.5.3 Wide-Angle Seismic Data 97

5.6 Interpretation 104

5.6.1 Local Well Data 104

5.6.2 Incoming Plate Lithology 105

5.6.3 Structural Divisions 110

5.7 Velocity Model 118

5.8 Discussion 120

5.8.1 Controls on the Geometry of the Accretionary Prism 120

5.8.2 Relating the Subduction Channel to Seismic Activity 123

5.9 Conclusions 125

6 Results: Outer Rise Hydration 128

6.1 Abstract 128

6.2 Introduction 129

6.2.1 Regional Setting: The Lesser Antilles . . . 131

6.3 Data . . . 132

6.3.1 Phase Identification . . . 133

6.4 Tomography . . . 138

6.4.1 Inversion Scheme . . . 139

6.4.2 Initial Inversion Tests . . . 140

6.4.3 Optimizing the Starting Model . . . 141

6.4.4 Final Tomographic Inversion . . . 145

6.4.5 Resolution Testing . . . 147

6.4.6 Monte Carlo Analysis . . . 149

6.5 Modelling the Low Velocity Layer . . . 152

6.6 Results . . . 156

6.7 Discussion . . . 157

6.7.1 Structure of the Incoming Plate . . . 158

6.7.2 Hydration Beneath the Outer Rise . . . 161

6.7.3 The Nature of the Low Velocity Layer . . . 163

6.7.4 Constraining Water Storage in the Crust and Mantle . . . 166

6.7.5 Global Context . . . 168

6.7.6 Implications for Lesser Antilles Arc Behaviour . . . 172

6.8 Conclusions . . . 174

7 Results: Monitoring the Kick-'em-Jenny Volcano, Lesser Antilles 176

7.1 Abstract . . . 177

7.2 Introduction . . . 177

7.3 Kick-'em-Jenny . . . 179

7.3.1 Eruption History and Hazard . . . 179

7.3.2 Morphology . . . 183

7.4 Data . . . 185

7.5 Results . . . 192

7.5.1 1985-2003 . . . 192

7.5.2 2003-2013 . . . 194

7.5.3 2013-2016 . . . 195

7.5.4 2016-2017 . . . 196

7.6 Discussion . . . 197

7.6.1 T-Phase Episodes, Morphological Change and Eruption History . . . 197

7.6.2 Implications for Hazard and Monitoring . . . 200

7.7 Conclusions . . . 201

8 Discussion and Future Work 204

8.1 Introduction . . . 204

8.2 Water Release Beneath the Arc . . . 204

8.3 Controls over Arc Structure . . . 205

8.4 Controls over Seismicity . . . 210

8.5 Controls over Arc Geochemistry . . . 211

8.6 Potential Future Work . . . 213

8.6.1 The Grenada Basin . . . 213

8.6.2 Outer Rise Hydration 214

9 Summary of Thesis Achievements **216**

Bibliography **216**

A Appendix: Tracing Water Release Beneath the Lesser Antilles **256**

A.1 Introduction 256

A.2 Modelling Fracture Zone Locations 257

A.3 Calculating Water Release from Serpentine 259

B Appendix: Chapter 4, Data Processing and Supporting Data **261**

B.1 Magnetics 262

B.2 Seismic 268

B.2.1 Introduction 268

B.2.2 MCS Processing 268

B.2.3 Wide-Angle Modelling 270

B.3 Timing of Igneous Activity in the Lesser Antilles Region 274

B.3.1 Late Cretaceous to mid-Paleocene: GAC and Aves Ridge 274

B.3.2 Eocene to Early Miocene: Outer Arc 275

B.3.3 Neogene: Lesser Antilles Arc 281

C Appendix: Chapter 5, OBS Record Section Plots **282**

D Appendix: Chapter 6, OBS Record Section and Ray Trace Plots **329**

List of Tables

5.1 Sediment Model: Travel Time Misfit by Phase 98

6.1 Starting Model Tests: Travel Time Misfit by Phase 141

6.2 Lithosphere Model: Travel Time Misfit by Phase 145

6.3 Previous Outer Rise Studies: Survey Parameters 166

6.4 Previous Outer Rise Studies: Hydration Parameters 170

7.1 KeJ Bathymetric Survey Statistics 186

7.2 KeJ Volume Changes Between Surveys 193

B.1 Geochemical Studies: Reference Compilation 279

List of Figures

1.1 Classic Subduction Zone Structure 22

1.2 Project VoiLA Data Acquisition 25

2.1 Lesser Antilles Arc Map 31

2.2 Summary of Moho Depth Estimates 33

2.3 Arc Velocity Profile (Kopp et al. 2011) 35

2.4 Along Arc Seismicity (Bengoubou-Valerius et al. 2008) 38

2.5 Along Arc B-Value (Schlaphorst et al. 2016) 39

2.6 Along Arc Sr-Nd Variations (Bezard 2014) 41

2.7 Subduction Zone Fluid Contributions (Hacker 2008) 44

2.8 The Subduction Water Cycle 45

2.9 Hydration in Slow Spreading Lithosphere 47

2.10 Summary: Along Arc Behavioural Trends 48

3.1 Tectonics of the Caribbean Plate 54

3.2 Models for the Origin of the Caribbean Plate 56

3.3 Tectonics of the Proto-Caribbean 57

3.4 Aves Ridge Velocity Profile (Christeson et al. 2008) 62

3.5 Models of Grenada Basin Spreading (Aitken et al. 2011) 64

3.6 Grenada Basin Opening: Fan Model 65

3.7 Grenada Basin Opening: Forearc Model (Aitken et al. 2011) 66

3.8 Regional Plate Reconstruction 1: 90-70 Ma 68

3.9 Regional Plate Reconstruction 2: 50-30 Ma 69

3.10 Proto-Caribbean Spreading Velocity 71

4.1 Lesser Antilles Map and Timeline of Volcanism 78

4.2 Marine Magnetic Data for the Caribbean Region 80

4.3 Crustal Structure of the Grenada Basin 82

4.4 A New Tectonic Model for the Eastern Caribbean 84

5.1 Barbados Accretionary Prism Local Data 89

5.2 Seismic Profiles across the Barbados Accretionary Prism 92

5.3 JC149 Profile 1: Local Bathymetry 95

5.4 Final PSTM MCS Profile 96

5.5 Record Section OBS7: Sediment Model Picks 100

5.6 Record Section OBS36: Sediment Model Picks 101

5.7 Final Sediment Column Vp Model 102

5.8 Comparison of Wide-Angle and Semblance Velocities 103

5.9 Local Stratigraphic Timeline (Pichot et al. 2012) 106

5.10 MCS Interpretation: The Incoming Plate 109

5.11 MCS Interpretation: The Outer Rise 112

5.12 MCS Interpretation: The Accretionary Prism 114

5.13 MCS Profile: Accretionary Prism Toe 115

5.14 Variations in Décollement Reflectivity 116

5.15 Accretionary Prism Taper Geometry (Fagereng 2011) 121

6.1 Chile Outer Rise Hydration Example (Contreras-Reyes et al. 2007) 129

6.2 Study Location: The Tiburon Basin 132

6.3 Record Section Examples: Lithosphere Model Picks 134

6.4 Record Section Examples: Lithosphere Model Picks 2 135

6.5 Record Section Examples: Shadow Zone Geometry 137

6.6 Velocity Profile: Initial Test Model 142

6.7 Velocity Profile: Constant Gradient Test Model 143

6.8 Velocity Profile: Preferred Model 146

6.9 Final Model: Ray Coverage (DWS) 147

6.10 Final Model: Resolution Tests 148

6.11 Final Model: Monte Carlo Analysis 150

6.12 Final Model: Ray Tracing 151

6.13 Synthetic Record Section: Incoming Plate Structure 153

6.14 Synthetic Record Section: Low Velocity Layer 154

6.15 Synthetic Record Section: Upper Mantle Test 155

6.16 Central Atlantic Lithosphere Structure (Davy et al. 2020) 159

6.17 Final Model: Interpretation 160

6.18 Lithology vs Serpentinization: Vp Trends 162

6.19 Final Vp Model: Lithosphere Structure Cartoons 164

7.1 KeJ Survey Location 180

7.2 KeJ Eruption Timeline 181

7.3 KeJ Bathymetry: 3D Projection 183

7.4 Bathymetry Processing: Sounding Standard Deviation 187

7.5 Bathymetry Processing: Sounding Density 188

7.6 Final Bathymetry Grids 189

7.7 Final Bathymetry Grids: Depth Changes 191

7.8 Final Bathymetry Grids: Depth Profiles 194

7.9 KeJ 2017 Eruption: Bathymetry and Water Column Anomalies 198

8.1 Controls over Arc Structure 206

8.2 Controls over Arc Seismicity 209

8.3 Controls over Arc Geochemisty 212

A.1 Atlantic Fracture Zone Modelling 257

A.2 Fracture Zone Slab Projection (Cooper et al., 2020) 258

A.3 Excess Water Release Beneath the Antilles 260

B.1 Marine Magnetics: Ship-track Dataset 263

B.2 Magnetic Observatories: Diurnal Variation Curves 264

B.3 Marine Magnetic Dataset Xover Analysis 266

B.4 Comparison of Regional Magnetic Grids 267

B.5 Grenada Basin: Regional Seismic Profiles 269

B.6 Grenada Basin Wide-Angle Survey: OBS Record Section Examples 271

B.7 Grenada Basin Final Wide-Angle Models 272

B.8 Age Distribution of Regional Igneous Activity 276

B.9 Map of Island Locations: Geochemical Studies 277

Chapter 1

Introduction

1.1 Island Arc Volcanism

Subduction zones occur at convergent plate boundaries where the denser of two colliding plates descends into the mantle beneath the other (White et al., 1970; Stern, 2002). This process is the main mechanism by which volatiles and many other key chemical elements are transferred between the Earth's surface and mantle, and forms a fundamental component of the Earth's water cycle. As the slab sinks into the mantle increasing heat and pressure drives a series of pro-grade metamorphic reactions, resulting in the release of chemically-bound water from hydrous mineral phases in the slab (Schmidt and Poli, 1998; Hacker, 2008). This influx of water into the sub-arc mantle wedge reduces the solidus temperature and triggers melting. This melt is buoyant, ascends, and results in volcanism on the surface of the over-riding plate. In the case of intra-oceanic subduction systems this leads to the formation of an island arc (Figure 1.1), a linear system of volcanic centres set back from the subduction trench (Syracuse and Abers, 2006). Such systems represent ∼40% of global subduction (Leat and Larter, 2003) and are the location of some of the planet's most significant volcanic and seismic hazards.

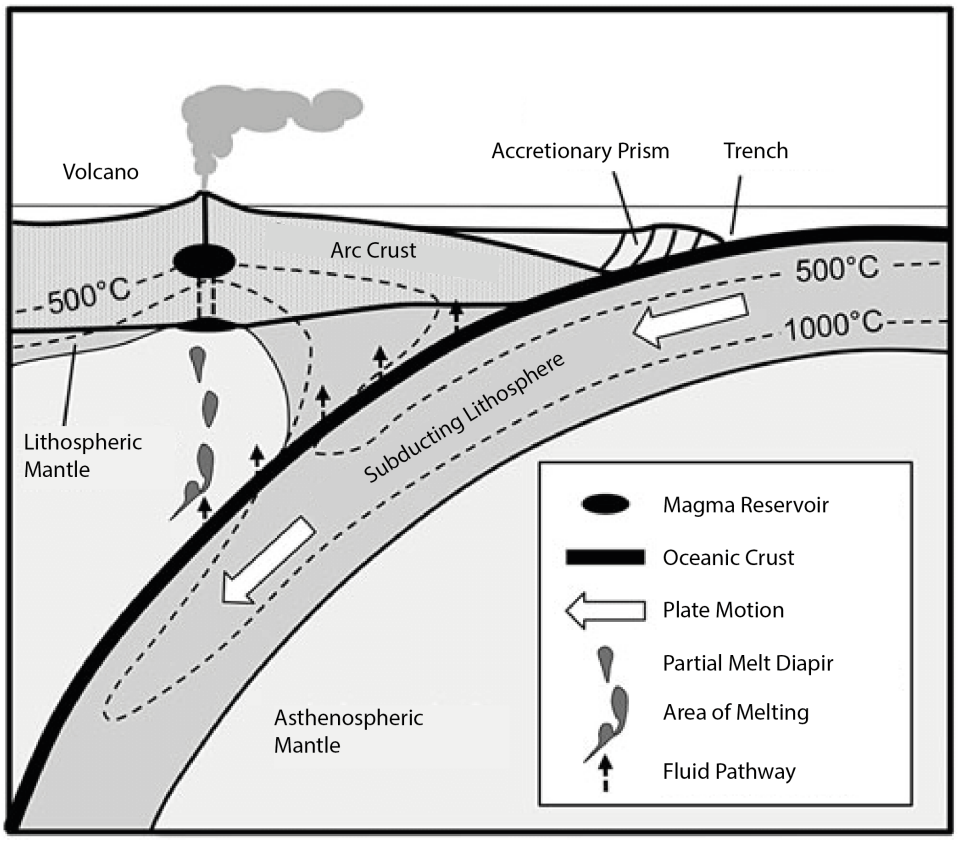


Figure 1.1: Schematic diagram through a generic subduction system, demonstrating structural features common to most subduction. The release of water from the subducted lithosphere is the primary driver of subduction volcanism. Figure from Nakada (2018).

1.2 The Lesser Antilles

The Lesser Antilles arc forms the eastern boundary of the Caribbean plate, and is the result of the slow westward subduction of Atlantic oceanic crust. As one of only two subduction zones which subducts slow spreading lithosphere formed at the Mid-Atlantic Ridge, the Lesser Antilles is an important global subduction zone end member when it comes to understanding the role that variations in the structure and composition of the slab might play in both long-term arc structural development and hazard.

Compared to many intra-oceanic island arc systems the down-going plate is relatively uniform in terms of age, convergence velocity and slab dip (Stein et al., 1982; Syracuse and Abers, 2006; Bengoubou-Valerius et al., 2008; Müller et al., 2019), key factors in determining the thermal structure of the slab and distribution of melting in the mantle wedge. Despite this the

Lesser Antilles still shows major along strike variations in arc structure, crustal thickness and composition (Boynton et al., 1979; Gonzalez et al., 2018; Schlaphorst et al., 2018), geochemistry (Brown et al., 1977; Davidson, 1985; Bezard et al., 2015) and seismicity (Schnur et al., 2017; Stein et al., 1982). This has led to the suggestion that much of the along arc heterogeneity observed at the Lesser Antilles may ultimately derive from spatial variations in the hydration state of the slab (Goes et al., 2019).

Tectonic processes at transform faults can introduce water into the oceanic lithosphere. Deep faulting at transform faults exposes mantle rocks at relatively shallow crustal depths, making them vulnerable to water inundation. This leads to the storage of large volumes of chemically bound water within the slab as the mineral serpentine, an alteration product of olivine in peridotite. A number of recent studies have suggested that this focused hydration may be the primary control over many arc processes at the Lesser Antilles, linking variations in the distribution and style of seismicity (Schlaphorst et al., 2016; Paulatto et al., 2017), and crustal structure (Schlaphorst et al., 2018; Melekhova et al., 2019) to deserpentinization and the release of water from fracture zones distributed every 150-200 km along the arc front.

However, the tectonic development of the over-riding Caribbean plate is complex, with a history of almost continuous arc volcanism stretching over more than 100 My as the leading edge of the Caribbean plate migrated from the Pacific, where it was formed, into the Atlantic domain (Pindell and Kennan, 2009; Boschman et al., 2014). Within this framework there are a number of major uncertainties, including the influence that multiple periods of arc migration and backarc spreading have had on the nature of the basement crust upon which the modern arc was built (Speed and Walker, 1991; Bird et al., 1993; Aitken et al., 2011). Away from the major fracture zones, the storage of water in the oceanic lithosphere is also poorly understood. The process of outer rise hydration is well documented at Pacific subduction systems, where it is shown to deliver significant quantities of water to sub-arc depths, however no equivalent study exists for a subduction system in the Atlantic. These crucial uncertainties make it difficult to conclusively determine whether the majority of the variation observed at the Lesser Antilles is derived directly from patterns of slab hydration, or inherited from the pre-existing structure of the Caribbean Plate.

1.3 Project VoiLA

This PhD was conducted under the umbrella of the VoiLA (Volatile Recycling in the Lesser Antilles) consortium. This provided many opportunities for fieldwork and to contribute to research outside the immediate PhD plan. The VoiLA project, a multi-disciplinary collaborative project between several UK universities and the University of the West Indies, ran from 2016-2020 (Goes et al., 2019). The project objective was to understand the influence that along strike variations in the level of hydration within the subducting slab has had on various arc processes along the Lesser Antilles, and by extension what this can tell us about the behaviour of other global subduction systems. This work was divided into a series of distinct work packages, covering aspects of subduction from constraining the hydration in the down-going Atlantic slab to seismic and volcanic hazard.

As part of the project a diverse set of geological and geophysical data was acquired in the region, including geochemical samples, a year long landstation and 18 month OBS station deployment (Figure 1.2). The research presented in this thesis uses new marine geophysical datasets acquired in the Lesser Antilles by the R.R.S. James Cook as part of two research cruises, JC133 and JC149 conducted in 2016 and 2017 respectively (Collier, 2017). Survey data includes towed streamer and wide-angle seismic profiles, both in the Lesser Antilles backarc and across the outer rise on the incoming plate, as well as magnetic data and targeted bathymetric surveys of the submarine volcano Kick-'em-Jenny. The processing and interpretation of these data will contribute to an improved understanding of the structure and tectonic history of the over-riding Caribbean plate, as well as poorly defined processes such as outer rise bending in slow spreading lithosphere. From these results it will be possible to identify the most significant influences on the long-term evolution of the arc, providing a better understanding of the links between slab hydration and arc behaviour, not just at the Lesser Antilles but globally.

1.4 Thesis Outline

This research is presented in Chapters 4-7 of this thesis.

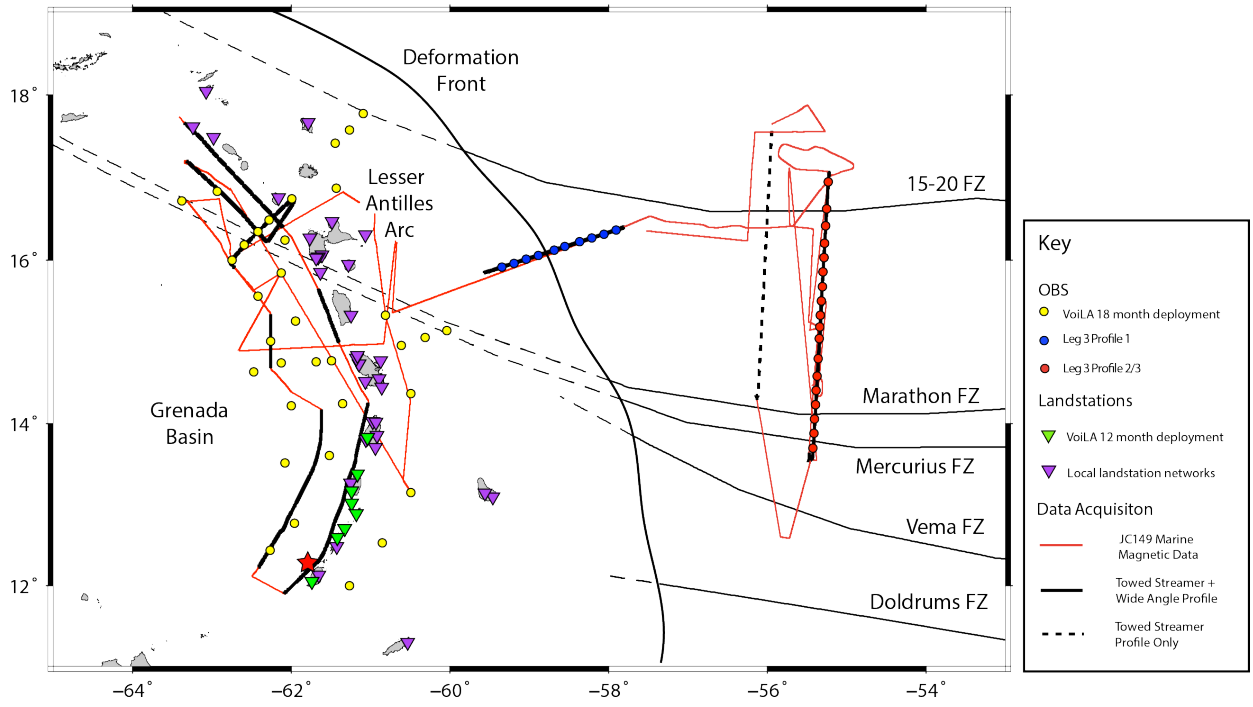


Figure 1.2: Summary of geophysical data acquired as part of the VoiLA project In April-June 2017. Marine magnetic data, along with seismic profiles acquired in the Grenada Basin are discussed in Chapter 4. Processing of results from Profile 1 on the incoming plate is discussed in Chapters 5 and 6. Red star denotes the location of the Kick-'em-Jenny submarine volcano. Kick-'em-Jenny was the subject of detailed bathymetric studies as part of both JC133 and JC149. The results of these surveys are discussed in Chapter 7.

Chapter 2 presents a review of the current literature concerning the Lesser Antilles subduction zone. In particular along-strike variation in arc traits such as seismicity, volcanism and crustal structure, as well as the possible distribution of hydration along the incoming plate are discussed in detail.

In Chapter 3 I review the current understanding of the tectonics of the greater Caribbean region in order to identify how this may have influenced the current structure of the island arc. Key uncertainties in the region's recent tectonic history are also identified.

Chapter 4 presents a new marine magnetic anomaly compilation, along with wide-angle and towed streamer seismic profiles in order to generate a new tectonic framework for the study area. A clear transition in the crustal structure of the backarc is identified from oceanic crust in the south to older, thick, island arc crust in the north. This transition, which is likely also

representative of the crust beneath the island arc itself prior to volcanism, implies that some major structural and geochemical variations along the arc are likely derived from pre-existing structures of the over-riding plate, rather than variations along the slab. The analysis also suggests that rather than a partial migration of the northern half of the arc in the early Miocene this migration took place along the arc's full length, with the evidence for the southern, extinct arc segment now buried beneath the thick sediments of the Barbados Accretionary Prism. **A version of this chapter is published in Geology (Allen et al., 2019)**.

Chapter 5 presents a newly acquired 2D PSTM reflection profile and a corresponding wide-angle velocity study of the sediments of the Tiburon Basin region of the incoming plate. This profile provides a continuous transect over a significant length of the incoming plate and accretionary prism, including one of three aseismic ridges currently entering the Lesser Antilles subduction zone. Sedimentary structure within the region is shown to be in keeping with previous seismic and borehole data in the region, with the structure of the accretionary prism primarily the result of a very thin accreted sediment package. A low critical taper angle, combined with low sediment velocities from within the prism are indicative of fluid overpressuring along a weak subduction interface. A significant increase in the rate of shallow seismicity along the northern arc may be the result of changes in the thickness of the underthrust sediment package. This contrasts with the south of the arc, where thick terrestrial sediments on the incoming plate mean that the shallowest part of the plate interface is almost totally aseismic.

Chapter 6 uses the same wide-angle profile discussed in Chapter 5, this time with the aim of determining the degree of serpentinization of the mantle beneath the Lesser Antilles outer rise. The observation of a shadow zone on OBS data beneath the outer rise is consistent with the presence of a velocity inversion within the upper mantle. This inversion likely results from a very high degree of serpentinization, reducing Vp to less than 7 km s^{-1} below the Moho. A reflection identified from an alteration front constrains the maximum depth of this alteration to the upper 5 km of the mantle. High levels of outer rise hydration are likely to contribute to the thick crust and greater rates of seismicity observed beneath the central and northern parts of the arc.

Chapter 7 looks at the processes currently shaping one of the arcs youngest volcanic centres. The Kick-'em-Jenny volcano, offshore Grenada is the only known active submarine volcano within the Lesser Antilles. It has undergone 13 recorded eruptions since its discovery in 1939, however these eruptions are largely only known from seismic recordings. Time-lapse bathymetry from 5 separate surveys encompassing 30 years and several eruption cycles are used to analyse how these eruptions have affected the morphology of the volcanic dome, and the implications for future local hazard in the region. **A version of this chapter is published in Geochemistry, Geophysics, Geosystems (Allen et al., 2018)**.

Work presented in this thesis has also contributed to the following publications:

My contribution to these studies is described in italics.

Cooper, G. F., Macpherson, C. G., Blundy, J. D., Maunder, B., **Allen, R. W.**, et al. (2020). Variable water input controls evolution of the Lesser Antilles volcanic arc. Nature 582, 525–529.

> *Refined regional plate reconstruction for the Greater Caribbean area, building upon the model of Müller et al. (2019). This model is used to determine the timing of subduction of fracture zones and rifted boundaries along the Antilles, and the current location of said features on the slab. This geometry is used to estimate predicted levels of mantle hydration along the arc. See Appendix A for further details.*

Bie, L. D., Rietbrock, A., Hicks, S., **Allen, R.**, et al. (2020). Along-arc heterogeneity in local seismicity across the lesser antilles subduction zone from a dense ocean-bottom seismometer network. Seismological Research Letters, 91(1):237–247.

> *Contributed to the instillation of broadband seismometers on St. Lucia, St. Vincent and Grenada and BBOBS recovery as part of JC149. Picked travel times for arrivals from the crust and upper mantle on backarc OBS network to help constrain shallow structure for the inversion of along arc velocity structure. See Chapter 4 for further discussion of this wide-angle experiment.*

Braszus, B., Goes, S., **Allen, R.**, et al. (2020). Subduction history of the Caribbean from upper mantle seismic imaging and plate reconstruction. Nature Communications, *Under Revision.*

> *Refined regional plate reconstruction for the Greater Caribbean area, building upon the model of Müller et al. (2019). Updated in order to better constrain the boundary between the proto-Caribbean and Atlantic, and the internal structure of spreading within the proto-Caribbean ocean. The updated model was used to determine the probable location of the Caribbean slab in the mantle and timing of subduction of major structural features such as fracture zones. See Section 3.5 and Appendix A for further details.*

Chichester, B., Rychert, C., Harmon, N., **Allen, R.**, et al. (2020). Seafloor sediment thickness beneath the VoiLA broadband ocean-bottom seismometer deployment in the Lesser Antilles from P-to-S delay times. Geophysical Journal International, *In press.*

> *Provided estimates of sediment thickness in the Grenada Basin determined by wide-angle modelling of the BBOBS profiles published in Allen et al. (2019). Estimates were used to compare and contrast with predictions from receiver function analysis. See Chapter 4 for further discussion of this wide-angle experiment.*

Chapter 2

Background: the Lesser Antilles Arc

2.1 Introduction

The Lesser Antilles arc is the surface expression of volcanism associated with the westward subduction of Atlantic oceanic crust at rates of less than 2 mm yr^{-1} (Stern, 2002) beneath the Caribbean plate. The current ∼800 km arc consists of up to 21 active volcanoes, spread across 11 islands (Lindsay and Robertson, 2018) and trends approximately north-south from the islands of the Greater Antilles, to the northeastern South American continental margin. The earliest volcanism associated with the current Lesser Antilles arc occurred ∼40 Ma on the (now extinct) islands of the Limestone Caribbees (Briden et al., 1979; Davidson et al., 1993; Weiss, 1994). These islands form an abandoned easterly limb of the Lesser Antilles arc north of Guadeloupe (Figure 2.1). The Lesser Antilles shows clear N-S variations in a range of arc characteristics, including crustal structure and potentially hazardous processes such as seismicity and the productivity and geochemistry of volcanic centres, which may correlate with hydration anomalies along the incoming plate. The structure of the incoming plate is highly variable with several high-offset fracture zones and basement ridges currently subducting beneath the arc front.

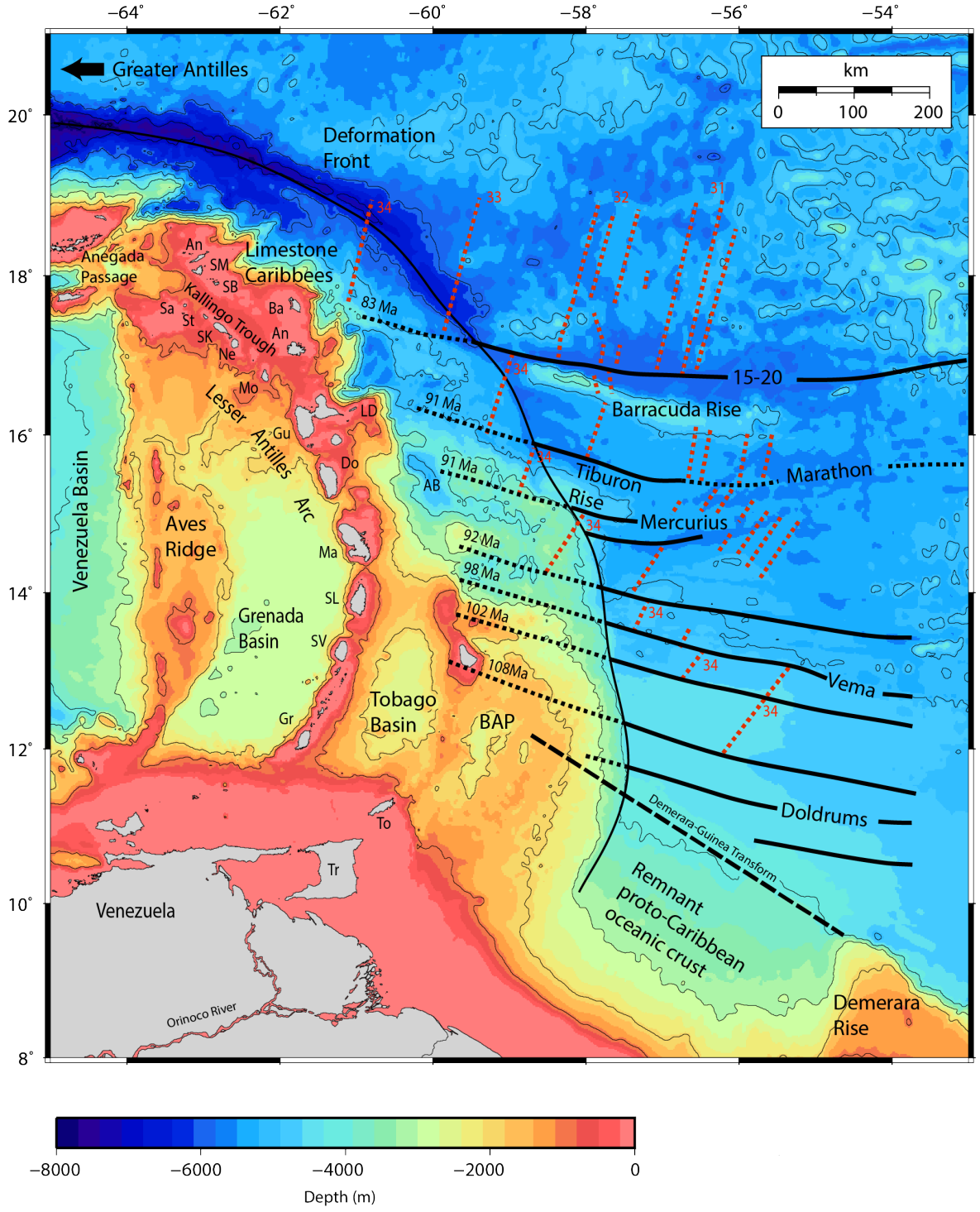


Figure 2.1: Bathymetric Map of the Lesser Antilles. Map shows islands of the Lesser Antilles as well as major structural features, subducting fracture zones and seafloor spreading anomalies. Fracture zones and seafloor spreading anomalies are adapted from Carpentier et al. (2008), with seafloor age at the point of subduction beneath the arc calculated assuming a spreading Cretaceous half spreading rate of 2.2 cm yr^{-1} from anomaly 34 (Cogné and Humler, 2004). Abbreviations are as follows Tr: Trinidad, To: Tobago, Gr: Grenada, SV: St. Vincent, SL: St. Lucia, Ma: Martinique, Do: Dominica, LD: La Désirade, Gu: Guadeloupe, Mo: Montserrat, Ne: Nevis, SK: St. Kitts, SE: St. Eustatius, Sa: Saba, An: Antigua, Ba: Barbuda, SB: St. Barthelemy, SM: St. Martin, An: Anguilla, Bb: Barbados, BAP: Barbados Accretionary Prism, AB: Arawak Basin.

2.2 Arc Structure and Processes

2.2.1 Crustal Structure

Boynton et al. (1979) was the first to suggest the presence of major along strike variations in crustal structure in the Lesser Antilles. As part of the LASP (Lesser Antilles Seismic Project) they acquired a series of wide-angle seismic lines both along arc (ranging from Guadeloupe to Grenada), and arc perpendicular across the Grenada and Tobago Basins. Using depth charges as the seismic source they identified a highly variable two-layer crustal structure within which the upper layer varied in thickness from 2 km to 20 km with an average velocity of 6.2 km s^{-1}, attributed to plutonic rocks of intermediate composition. A more mafic lower crustal layer with velocities in excess of 6.9 km s^{-1} was interpreted as gabbros and basic cumulates associated with arc volcanism, though the boundary between the two layers is likely to be highly gradational in places. Although the sub-arc Moho was not imaged directly, from combined analysis of gravity and seismic data they estimate the crustal thickness beneath Martinique to be on the order of 30 km, and around 35 km beneath St. Vincent (Figure 2.2).

Constraints from Passive Seismology

Most modern attempts to constrain variations in the whole arc crustal structure have come from passive seismology (Figure 2.2). Schlaphorst et al. (2018) analysed the crustal structure at 10 islands (ranging from Grenada in the south to Saba in the north) using receiver function inversions, combining seismological data with Vp/Vs ratio estimates based upon crustal lithology. Their results, which produced a best fitting 1D velocity profile for each island, observed evidence for an unusual strong, and highly variable, mid-crustal discontinuity, which in many cases proved a good fit to that proposed by Boynton et al. (1979). Similar to the mid-crustal discontinuity the Moho beneath the arc showed considerable lateral variation, with the shallowest Moho, at 24 km occurring under Dominica, and the deepest under the adjacent island of Guadeloupe at 37 km. Variations in both the depth and nature of these seismic discontinuities are attributed to lateral changes in the mechanisms of melt generation and differentiation along the arc, driven by the fluid content of the down-going slab.

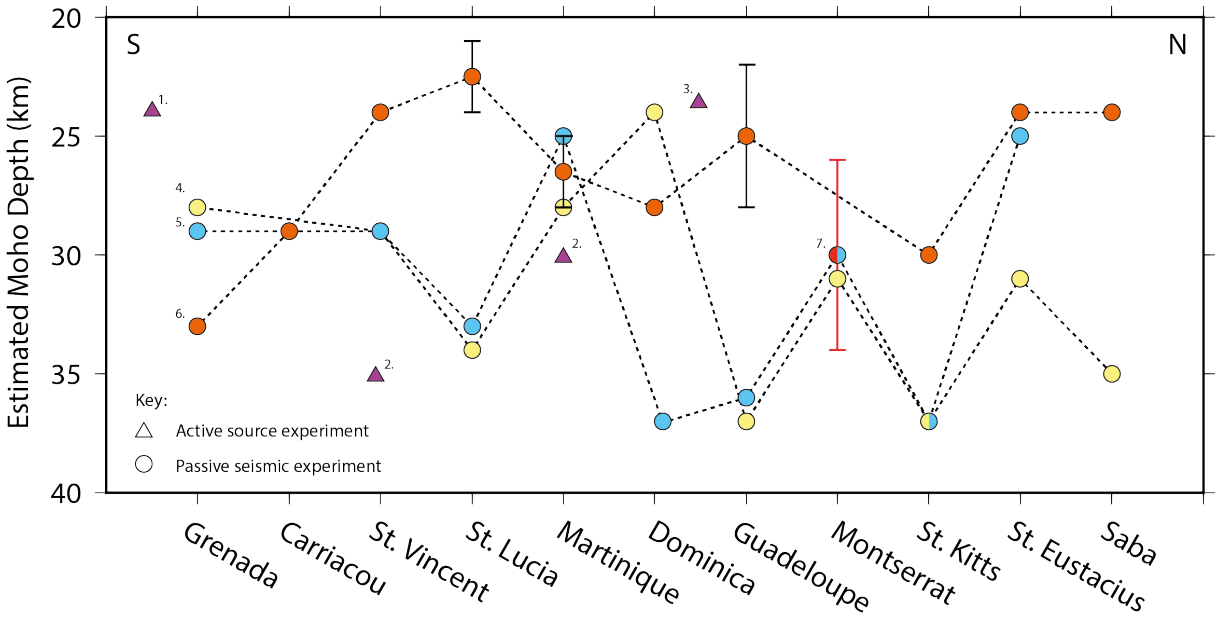


Figure 2.2: Compilation of estimated crustal thickness from active source and passive seismic experiments along the Lesser Antilles arc. Numbered studies are as follows: 1) Christeson et al. (2008), wide-angle profile, 2) Boynton et al. (1979), wide-angle profile with supporting gravity measurements, 3) Kopp et al. (2011), wide-angle profile, 4) Schlaphorst et al. (2018), receiver function analysis, 5) Melekhova et al. (2019), receiver function analysis with additional petrological constraints, 6) Gonzalez et al. (2018), joint inversion of surface wave dispersion and receiver function analysis, 7) Sevilla et al. (2010), receiver function analysis. In the case that a study provides multiple crustal thicknesses for a given island the full range of proposed crustal thickness estimates is denoted by error bars. The estimated Moho depth is generally greater beneath the islands of the northern section of the arc.

Melekhova et al. (2019) used a similar seismic dataset and methodology to the Schlaphorst et al. (2018) study, introducing constraints on Vp, Vs and density within the receiver function inversions derived from the estimated equilibrium depths of crustal xenoliths collected from along the arc. Unsurprisingly their results matched closely with the Schlaphorst et al. (2018) study (Figure 2.2), particularly in terms of Moho depth, again attributing abrupt variations in crustal thickness and along arc crustal Vp to the influence of slab hydration on the rate of magma production.

The result of these studies varies quite significantly from those of Gonzalez et al. (2018) who used the joint inversion of receiver functions and surface wave dispersion to produce a layered S-wave model under a large number of the islands. Their results showed less along arc variation in terms of crustal thickness than the previous studies, assuming that a Vs of 4 km s^{-1} was representative of the crust-mantle transition, with crustal thicknesses averaging ~25 km along the length of the arc. An exception to this is seen at the far southern end of the arc, where

Moho depths beneath Grenada reached 33 km.

Although these studies are well-matched in the centre of the arc (Figure 2.2), consistently estimating crustal thicknesses on the order of 23-27 km, on some islands the differences in crustal thicknesses estimated via these methods exceeds 10 km (e.g. Guadeloupe and St. Lucia). Some of the variation observed between these studies may arise from the fact that crustal structure varies much more rapidly than can be accurately constrained with a single seismometer location, or 1D solution for each island. Sevilla et al. (2010) used receiver function analysis to estimate crustal thicknesses at a number of locations under the island of Montserrat, identifying a transition from a Moho at 26 km depth in the north, to 34 km in the south. They also postulate that due to a lack of sharpness the crust-mantle transition may be transitional and as much as 4 km in thickness, which would again add to the uncertainty in Moho depth estimates. Given that Montserrat is only ∼16 km across, it is easy to understand why 1D estimates of crustal structure from other, larger, islands (e.g. Guadeloupe which is ∼70 km across) might vary dependent on the methodology used.

Active Source Studies

The southernmost constraint on Antilles arc structure comes from the wide-angle TRIN profile of Christeson et al. (2008), which intersects the arc south of Grenada. The seismic velocity structure here shows crustal velocities rapidly increasing from the seafloor to 6-6.3 km s^{-1} at 6-7 km depth before a more gradual increase to 7.3 km s^{-1} at the base of the crust, which is 24 km thick.

Similar to Christeson, Kopp et al. (2011) observed a crustal thickness on the order of 23-24 km beneath the arc between Guadeloupe and Martinique, with a maximum lower crustal velocity of 7.3 km s^{-1} (Figure 2.3). Like several of the other studies mentioned, they also identified a clear mid-crustal discontinuity at ∼15 km depth (Boynton et al., 1979; Schlaphorst et al., 2018; Melekhova et al., 2019). One of the most significant consequences of the Kopp et al. (2011) line is the surprising consistency of the crustal structure along the arc and into the forearc, with the thickest crust beneath the Karukéra Spur, rather than beneath the arc itself. This would support an argument that much of the crustal thickness along the Antilles may have been present prior to the modern phase of arc volcanism, with the authors suggesting that

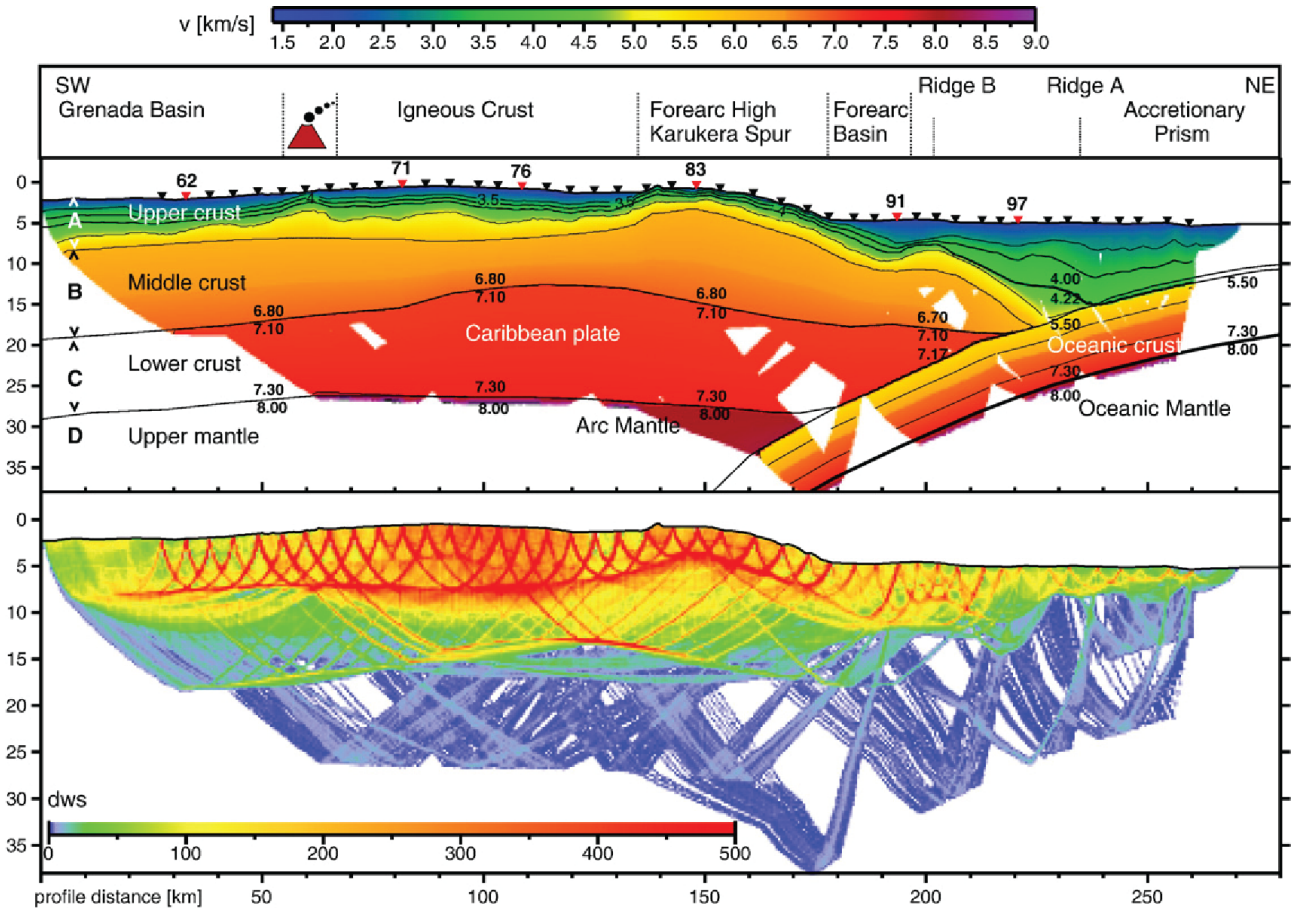


Figure 2.3: Arc perpendicular wide-angle Vp profile from Kopp et al. (2011). Profile shows ∼23 km thick crust beneath the active arc between Guadeloupe and Dominica. Similar to previous results this study also identifies distinct middle and lower crustal layers. Note the extremely uniform crustal thickness and structure both under the arc and over 100 km into the forearc, well away from the volcanic axis. This uniformity supports the suggestion that much of the crustal thickness observed at the Lesser Antilles is likely to be inherited from the pre-existing basement crustal structure. Figure from Kopp et al. (2011).

an oceanic plateau may underlie much of the modern arc. This thick inner forearc crust has also been imaged in several wide-angle profiles covering the arc front between Dominica and Antigua as part of the Sismantilles II experiment (Evain et al., 2013).

Although there are major differences between many of these estimates of crustal thickness and composition based on the techniques used, there are a number of clear consistencies. All studies consistently find little evidence for lower crustal velocities in excess of 7.3 km s^{-1} (Boynton et al., 1979; Christeson et al., 2008; Sevilla et al., 2010; Kopp et al., 2011; Melekhova et al., 2019), as have been observed previously in the Aleutian (7.3-7.7 km s^{-1}) and Izu-Bonin arcs (7.2-7.6 km s^{-1}) and is generally interpreted as the presence of mafic and ultra-mafic cumulates at the base of the crust. The absence of such a layer at the Lesser Antilles is consistent with low magma

production rates (Figure 2.10) compared to other similar arc systems.

Crustal thickness estimates define a fairly wide envelope between 22 km and 37 km, though clearly crustal thicknesses vary rapidly over fairly short length scales. In trying to resolve a single best fitting 1-D velocity model for the whole arc, Bie et al. (2020) found a Moho at 27 km depth to be the best fitting solution, in keeping with many of the individual estimates of crustal thickness along the arc (Figure 2.2). Many studies also consistently find evidence for a strong mid-crustal discontinuity (Boynton et al., 1979; Kopp et al., 2011; Schlaphorst et al., 2018), which may be representative of the transition from the pre-existing basement below to overlying arc volcanics. It has been suggested by Gailler et al. (2017) that the lower crustal layer may not be representative of the arc crust at all, but instead some kind of front within the mantle e.g. a hydrated/serpentinized upper mantle section, based upon their modelling of the Curie point depth with the Moho as shallow as 13 km beneath the central arc. Although not impossible, such a result would mean that the crust at the Lesser Antilles was verging on one of the thinnest examples of intra-oceanic island arc crust on the planet, akin to the Bonin arc, where crust as thin as 10 km is observed (Kodaira et al., 2007). This seems unlikely given the potential age, and extensive history of arc volcanism within the basement upon which the modern Lesser Antilles arc has been constructed (see Chapter 3).

Despite the short wavelength variations observed, many of these studies suggest the existence of an overarching long wavelength binary trend in the distribution of the crustal structure beneath the arc, with a particularly thick section of crust beneath the northern arc under the group of islands from Dominica to St. Kitts, and generally thinner crust to the south from Martinique to Grenada (Figure 2.2).

2.2.2 Seismicity

The hydration pattern of the subducting slab may also be key in determining patterns of seismicity at many subduction systems. There are several mechanisms via which slab fluids can influence the distribution of seismic activity. For example, at the Hikurangi margin, the presence of a pressurized, fluid rich underthrust sediment column promotes failure through stable, aseismic sliding, whilst relatively sediment and fluid poor regions increase coupling and the likelihood of earthquake nucleation along the plate interface (Heise et al., 2013, 2017). Deeper

in the subduction system, the release of fluids from serpentine and other hydrous minerals in the slab can increase local fluid pressures or lead to increased intermediate depth seismicity and intra-slab failure through processes such as dehydration embrittlement (Peacock, 2001; Shillington et al., 2015).

In general rates of seismicity along the Lesser Antilles are very low given the length of the arc (Dorel, 1981; Stein et al., 1982; Bengoubou-Valerius et al., 2008). A disproportionate amount of seismicity also occurs along the slab as intraplate earthquakes, rather than at the plate interface, with a particular concentration of intra-slab seismicity beneath the islands of Guadeloupe, Dominica and Martinique. This has led to the suggestion that a significant proportion of the strain along the arc is not being accounted for seismically, with only 26 earthquakes M 6 or greater since 1900 and none larger than M 8 in that time (Hayes et al., 2014). Unfortunately, the region lacks a consistent seismometer/GPS network of the quality required to seriously interrogate whether this strain is being released via slow slip processes.

One of the key features of seismicity along the Lesser Antilles is a striking difference in the rates of seismicity in the northern and southern segments of the arc with a sharp drop off south of Martinique (Figure 2.4). Historically, variations in the thickness and composition of subducting sediments, and the presence of topographic features on the slab such as the Barracuda and Tiburon ridges (aseismic ridges of uplifted crust on the incoming plate formed as a result of N-S deformation, Figure 2.1) in the northern arc have also been cited as possible causes of this disparity (McCann and Sykes, 1984; Mccann and Sykes, 1986).

There is evidence, however, that the hydration of the down-going slab is strongly influencing the pattern of seismicity. Paulatto et al. (2017) identified two clear clusters of intra-slab earthquakes beneath the central arc. The first of these, at 50-80 km depth is attributed to dehydration reactions amongst hydrous crustal mineral phases, combined with the stresses induced by densification and slab bending. The second concentration of seismicity at 135-155 km is attributed to dehydration reactions in the mantle, namely the breakdown of the hydrous mineral serpentine. From tomography, linear Vp/Vs anomalies coincident with the down-slab projection of the major subducting fracture zones in the centre of the arc are consistent with a greater concentration of hydrated ultramafic rocks in the slab.

Schlaphorst et al. (2016) also identified variations in the style of along arc seismicity coincident with subducting fracture zones (Figure 2.5). High b-value anomalies correlate with the location

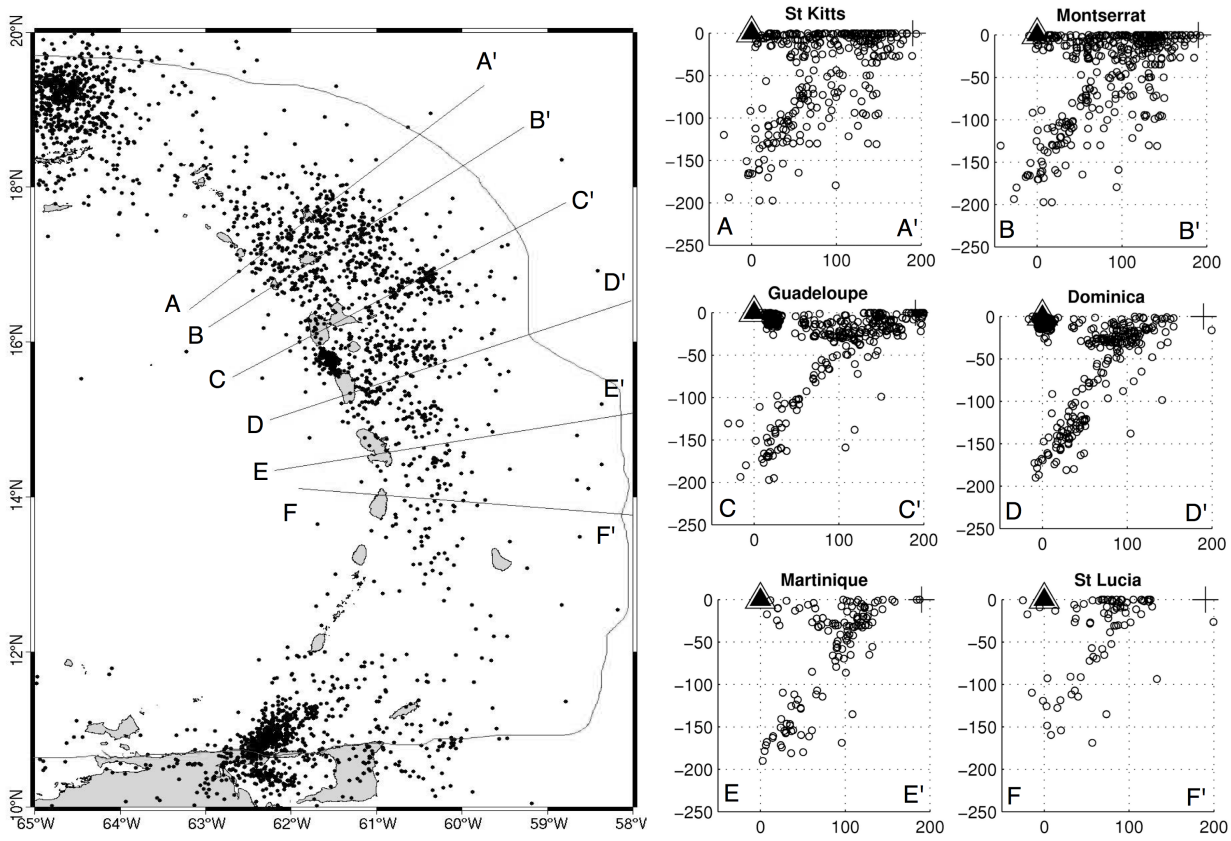


Figure 2.4: Map of seismicity recorded by the French Antilles Seismological Data Base since the 1950s. Figure adapted from Bengoubou-Valerius et al. (2008). Map shows the clear imbalance in seismicity rates between the northern and southern sections of the arc. Depth profiles show local; earthquakes from within 75 km of the mapped lines.

of subducting fracture zones. The "bulls-eye" geometry of these anomalies would seem to rule out factors such as the thickness of sediment (which increases significantly from north to south) or subduction obliquity as being the primary control over the observed style of seismicity. These anomalies are instead explained as the result of increased fluid release, with lubrication of faults along the slab reducing the minimum stress required for failure and resulting in a higher rate of smaller earthquakes adjacent to subducting fracture zones.

Historically, the low rates of seismicity have led to major differences in the estimated slab geometry beneath the arc between different studies (Bengoubou-Valerius et al., 2008). Studies based on different catalogues have led to up to 30 degree differences in slab dip at the same location along the arc, with no consistent variation observed in slab dip along strike (Dorel, 1981; Wadge and Shepherd, 1984; Bengoubou-Valerius et al., 2008). Several studies however have argued for the presence of a kink, or tear in the structure of the slab beneath central arc, often thought to be associated with the N-S American plate boundary (e.g. Wadge and

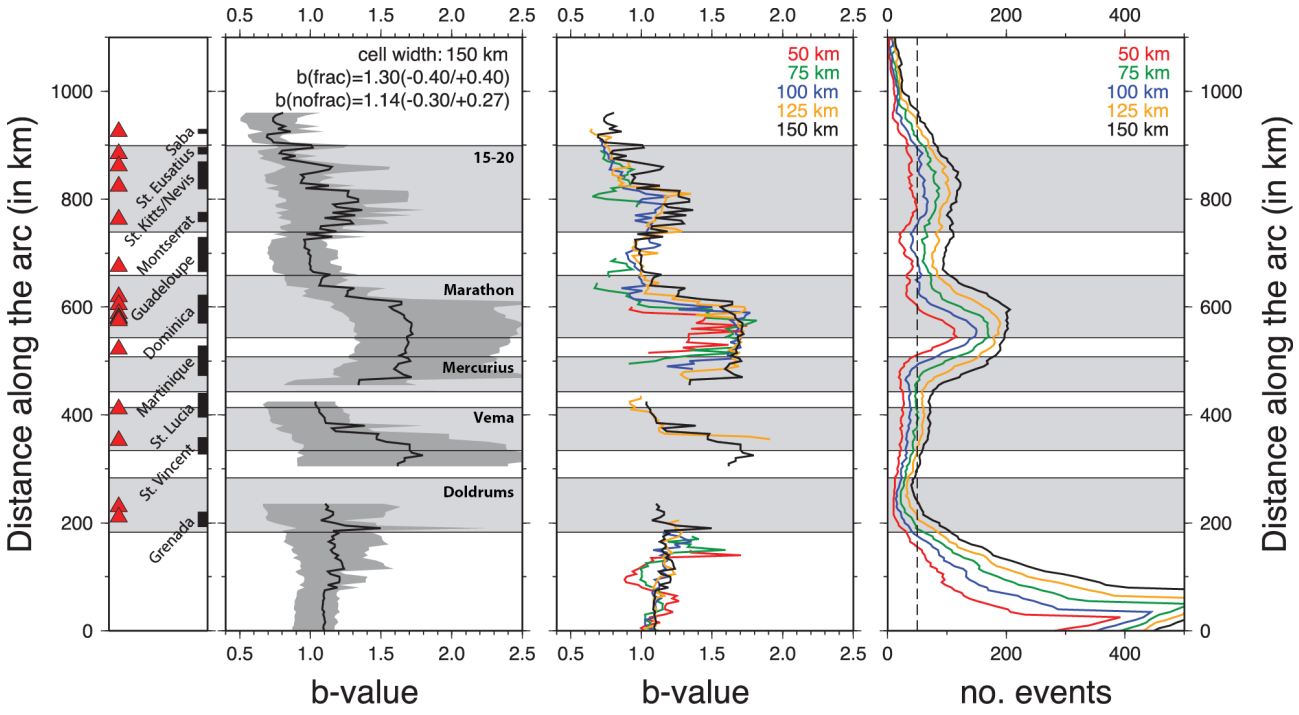


Figure 2.5: Variations in along arc b-value from Schlaphorst et al. (2016). B-value calculation uses the catalogue of the Seismic Research Centre of The University of the West Indies from the years 2008 to 2013. Column 1: Positions of volcanoes (red triangles) and islands (black rectangles) along the arc. The horizontal areas in grey represent the areas around the subducting fracture zones. Column 2: Calculated b-values for cells of 150 km along the arc with uncertainties. Column 3: Results without uncertainties for a range of different cell widths. Column 4: Number of events per cell for a range of different cell widths.

Shepherd 1984).

2.2.3 Arc Geochemistry

As well as influencing rates of volcanism, both the volume and source of water released from the down-going slab can effect the chemical composition of arc lavas. At the Aleutian Arc Singer et al. (2007) has suggested that various geochemical anomalies, including Sr, Nd, and Pb isotope ratios and Th/Nd and B/La ratios derive from a prolonged metasomatism of the sub-arc mantle derived from the subduction of the Amila fracture zone. Spikes in B/Zr ratios at the Andean subduction zone have also been tied to the increased release of fluids from serpentinized fracture zones in the Pacific (Manea et al., 2014). Logically therefore, if the concentrated release of water from subducting fracture zones is a key driving force behind arc processes at the Lesser Antilles we might expect to see a clear correlation between similar geochemical indicators of hydration and seismic activity and crustal structure.

Antilles arc lavas show clear compositional differences along strike, with volcanics encompassing the full global array of arc rocks. The northern and central segments of the Lesser Antilles show a dominantly andesitic composition, whilst volcanism in the southern arc is primarily basaltic/basaltic-andesites (Melekhova et al., 2019). Although igneous differentiation processes are responsible for a large part of this, further isotopic variations arise from both the contribution and composition of subducted sediments, and the origin and concentration of fluids in the down-going slab. Wadge (1984) suggested that over the last 100,000 years there has been a concentration of volcanic activity beneath the central part of the arc, and the island of Dominica in particular, with magma produced at a rate more than 4x higher than is seen anywhere else along the arc. This could again be the result of the concentrated release of fluids from the slab beneath the central arc.

Several studies observe variations in the along arc Nd, Sr and Pb isotopic compositions of arc lavas (Hawkesworth and Powell, 1980; Davidson, 1983; Thirlwall and Graham, 1984). This trend divides the arc into two sections, a northern arc from Saba to Dominica, and a southern/central arc (Figure 2.6). This north-south transition is associated with increases in $^{87}Sr/^{86}Sr$ and decreases in $^{143}Nd/^{144}Nd$, interpreted as contamination of these lavas by a continental component. Where many studies disagree however, is on the origin of this contamination, with two schools of thought, that these geochemical variations can be explained entirely by variations in the composition and degree of incorporation of sediments on the down-going plate, or by variations in the degree of assimilation of sediments from the over-riding plate.

The Role of Sediment

The Barbados Accretionary Prism (BAP) is one of the thickest accumulations of sediment on the planet and in places it may exceed 20 km in thickness (Gomez et al., 2018). In addition to the normal accretion of sediments from the incoming plate, this extreme thickness of sediment is due to the high sediment flux from continental South America and in particular the outflow of sediments associated with the Orinoco river. The thickening of the prism is further exaggerated by the presence of the Tiburon Rise (Figure 2.1), which acts as a barrier to the northward transport of sediments (Patriat et al., 2011; Pichot et al., 2012). Similarly, a very large thickness of South America derived sediments, exceeding 10 km (Aitken et al., 2011), has also accumulated in the Grenada Basin backarc basin during the Cenozoic.

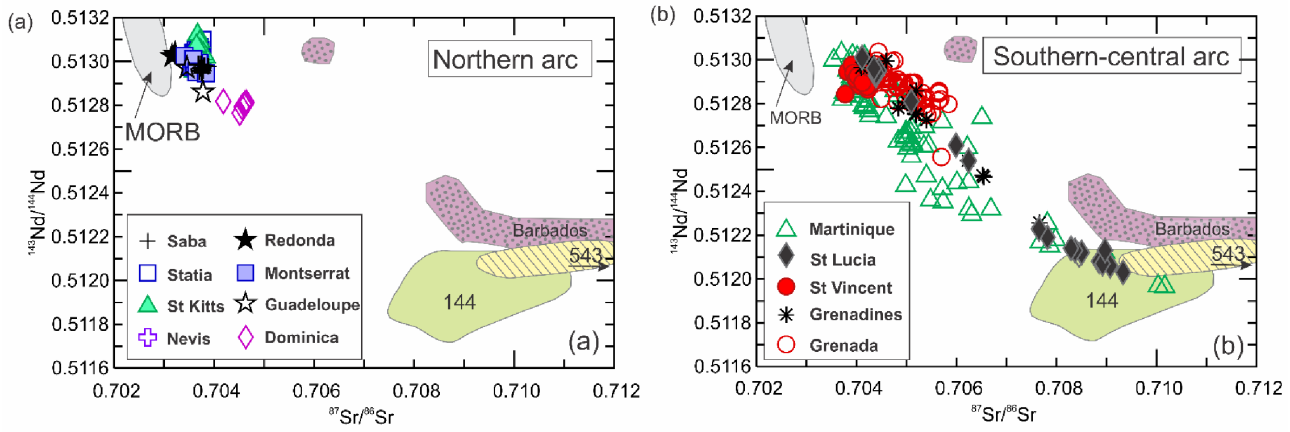


Figure 2.6: Sr and Nd compositional variations along the Lesser Antilles arc. Figure from Bezard (2014). 144 and 153 correspond to Atlantic sediments cored outboard of the trench at DSDP sites 144 and 543. Barbados corresponds to sediment outcrops on Barbados from Carpentier et al. (2008). Some researchers argue that these Nd, Sr isotopic compositions can be explained via direct mixing of incoming plate sediments similar to those sampled at 543 and 144 in the northern and southern arc respectively. Others argue that assimilation of continental material from the over-riding plate is required to explain this distribution.

The sediment column on the incoming plate has been sampled at several key locations, thought to be representative of the sediment composition on the slab. At the toe of the accretionary prism in the Tiburon Basin, DSDP 78A site 543 found the sedimentary sequence beneath the décollement largely to consist of pelagic and radiolarian clays (Biju-Duval et al., 1982), with the full sedimentary succession showing relatively uniform Sr, Nd and Pb isotopic signatures (Carpentier et al., 2008). In the south of the arc, the only real constraint on sediment composition comes from DSDP site 144 on the edge of the Demerara plateau, several hundred kilometres from the current trench. Here the sediment column is much more variable with the oldest, early Cretaceous, sediments consisting of synrift clay, silt and sandstones (Carpentier et al., 2008). At this well site, the Late Cretaceous unit 3 (96-84 Ma) is dominated by a 60 m organic rich black shale layer. The presence of highly radiogenic Pb signatures (Carpentier et al., 2008), as well as other isotopic anomalies such as a high Mo anomaly in southern arc lavas (Freymuth et al., 2016) are thought to derive from this black shale layer. This is considered evidence that not only is this sediment column representative of the sediments currently subducting beneath the southern arc, but that the geochemical composition of such sediments exerts a strong control over arc magma compositions.

Some studies argue that these isotopic variations are entirely derived from the differences in the degree of incorporation of these two sediment types (White and Dupre, 1986; Vidal et al.,

1991; Carpentier et al., 2008). Although estimates in the north of the arc are fairly consistent, with incorporation of approximately 1% of subducted sediment in arc magmas capable of reproducing the observed isotopic composition, in the south estimates are more varied and suggest anywhere between a 1% and 10% sediment contribution. These higher estimates would require a significant increase in slab temperature along the southern section of the arc in order to explain the increased sediment derived melt.

Crustal Contamination and the Role of Fluids

Davidson (1985) proposed that such variations are the result of contamination of arc lavas by an older crustal component with a continental signature. Systematic increases in $\delta^{18}O$ with increasing $^{87}Sr/^{86}Sr$ and decreasing $^{143}Nd/^{144}Nd$ are interpreted as contamination of mantle-derived magmas by variable amounts of an ancient crustal component, largely within the crust of the arc. Given the lack of evidence for any crust of continental composition in the basement of the Lesser Antilles (Chapter 3) the most likely origin of such a contaminant comes from sediments deposited on the over-riding plate, influencing the isotopic composition of magmas in the southern/central portion of the arc.

This hypothesis has subsequently been supported by various further studies. Bezard et al. (2014) suggested that crustal assimilation was the most likely cause of arc isotopic compositions based on a lack of correlation between subducting black shales and highly radiogenic Os isotopes in arc lavas. Rojas-Agramonte et al. (2017) identified ancient xenocrystic zircons (some as old as Paleoarchean) in arc lavas providing strong evidence for assimilation of detrital sediments in a proto-Grenada/Tobago Basin. Van Soest et al. (2002) performed $^{4}He/^{3}He$ analysis on olivines and pyroxenes derived from lavas throughout the arc, observing a pattern of contamination explained by assimilation of terrigenous sediments in the south. The thick sediments of the Grenada and Tobago basins are obvious candidates for this contaminant (Bezard et al., 2014). In the north they proposed that assimilation was relatively minor, and likely consisted of an older arc crust.

The origin of fluids contributing to arc lavas have also been traced via variations in along arc geochemistry. Davidson (1985) identified the presence of highly radiogenic Sr compositions in arc lavas from Martinique and St. Lucia indicative of a major influx of slab derived fluid into

the mantle wedge. Davidson and Wilson (2011) also observed in a comparison of magmatic suites from the northern (the Quill) and central (Mt Pelee) arc that differences in magma compositions were derived from differences in source compositions along the arc. Although some of these variations could be explained by sediment mixing as discussed above, some LILE concentrations and radiogenic Sr and Pb ratios could only be explained by the varying addition of water from the slab. In the latter case isotopic constraints could only be satisfied by the addition of fluids from the oceanic crust.

2.3 Sources of Slab Hydration

The Lesser Antilles shows clear along arc variations in seismicity, magmatic productivity, geochemistry and arc structure. Many studies of the region (Section 2.2) cite the hydration level of the subducting slab as the likely driving force behind much of this variation.

In the oceans, large volumes of water are held in fractures and pore space of the upper crust and overlying sediments (Jarrard, 2003; Hacker, 2008). Additionally, oceanic lithosphere accrues structurally-bound water as it migrates from the ridge to the trench (Figure 2.8). On the ridge flanks hydrothermal circulation through the hot, highly fractured upper crust leads to extensive hydrous alteration (Anderson, 1972). This hydration likely drops off considerably with age as the crust cools, and with the increasing thickness of the overlying sediment blanket, with limited alteration after ∼15 Ma (Hart and Staudigel, 1986).

Water can also be added to the oceanic lithosphere shortly before it subducts as outer rise bend faulting creates pathways via which seawater can access the rocks of the lower crust and upper mantle (Ranero et al., 2003; Grevemeyer et al., 2018). The specifics of the mechanism by which this hydration occurs are still highly debated, with proposals ranging from seismic pumping to pressure-driven flow through high permeability fault zones (Faccenda et al., 2009; Hatakeyama et al., 2017). However, the resulting alteration can be clearly observed in wide-angle seismic studies as a result of the decrease in Vp associated with the hydration of mafic crustal material, and in particular, the serpentinization of mantle olivine (hydrous alteration to serpentine group minerals, which can contain up to 13 wt% H_2O). Upper mantle p-wave velocities as low as 6.8 km s^{-1} observed beneath the outer rise at the Mariana trench could be the result of as much as 38% serpentinization (Grevemeyer et al., 2018; Wan et al., 2019). In the case of relatively

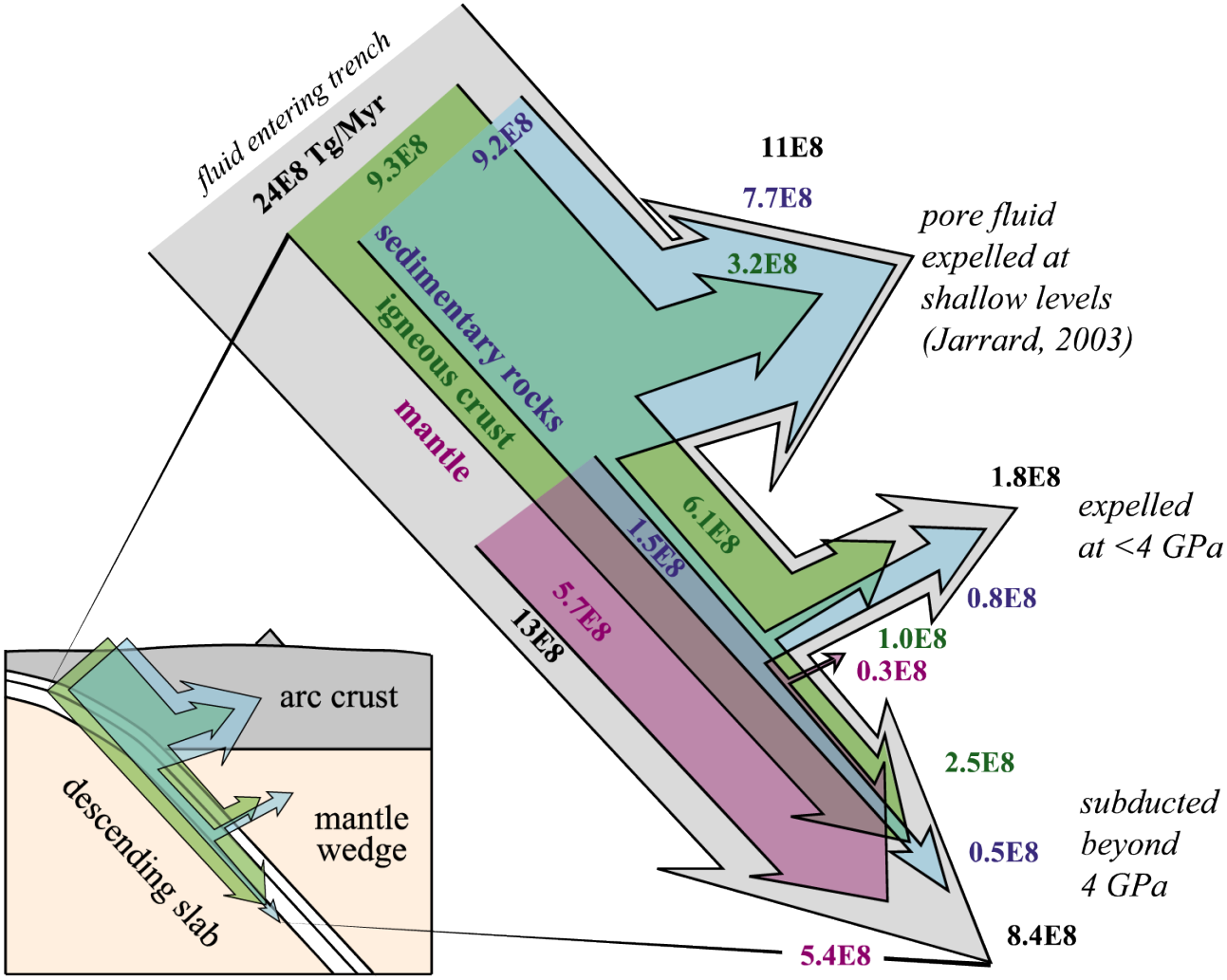


Figure 2.7: Global H_2O flux from trench to post-arc depths for oceanic lithosphere from Hacker (2008). Arrow width corresponds to the magnitude of the H_2O flux from each of the sources. Serpentine in the upper mantle of the subducting slab (red arrow) is responsible for transporting a large volume of water to sub-arc depths.

warm subduction systems such as the Mariana trench where the subducting slab undergoes almost complete dehydration prior to 230 km depth, dehydrating mantle peridotites may be the largest single contributor of water to the sub-arc mantle wedge (Schmidt and Poli, 1998; van Keken et al., 2011).

Previous studies of outer rise hydration have suggested that the thickness of the overlying sediment blanket (Grevemeyer et al., 2005, 2018), style of faulting (Fujie et al., 2018) and degree of slab bending (Faccenda, 2014) may influence the resulting levels of alteration. This stage of hydration is well studied from the Pacific and Indian oceans (Faccenda, 2014; Grevemeyer et al., 2018), where the subducting crust is intermediate-fast spreading. Currently, it is unclear what contribution this process may make to arc volcanism in slow spreading lithosphere such

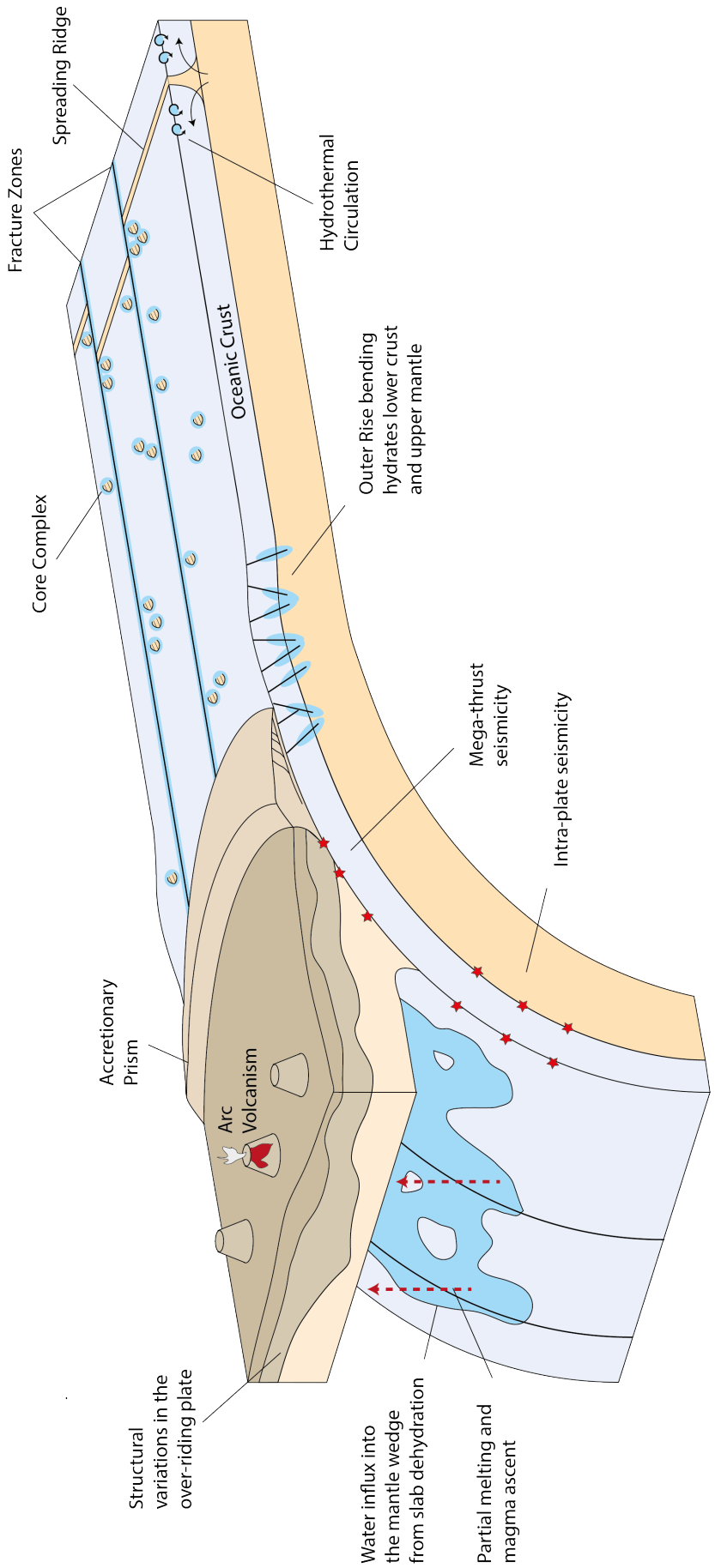


Figure 2.8: The subduction water cycle. In slow spreading oceanic lithosphere hydration may be concentrated at structural features such as fracture zones and core complexes. A second phase of hydration occurs as a result of bend faulting in the outer rise. The resulting variations in the release of water from the slab into the sub-arc mantle may strongly influence long-term arc development, as well as the distribution of seismicity and volcanic centres.

as that of the Atlantic, where the slab is highly structurally variable along strike.

2.3.1 Slow Spreading Lithosphere

Tectonic processes at transform faults can also introduce water into the lower oceanic lithosphere. Deep faulting at transform faults exposes mantle rocks at relatively shallow crustal depths, making them vulnerable to water inundation. In the Atlantic serpentinized mantle peridotites have been dredged directly from the seafloor at the Vema (Lagabrielle et al., 1992) and Oceanographer fracture zones (Fox et al., 1976). Samples from the ultra-slow spreading fracture zones along the Southwest Indian Ridge suggests that serpentinization of the upper mantle could extend to depths of 13 km (Prigent et al., 2020) and hydration may even extend to depths beyond the serpentine stability field (Figure 2.9).

In slow spreading oceanic crust the discovery of detachment faulting and core complex formation, leading to the exposure of lower crustal and mantle rocks at the seafloor of the Mid Atlantic Ridge (Cann et al., 1997), gave a second mechanism to acquire structurally bound water at the ridge axis (Figure 2.9). Core complexes are the result of the exhumation of mantle peridotites along detachment faults, which accommodate slow, asymmetric seafloor spreading, and can greatly increase the amount of water stored as serpentine in the shallow lithosphere (Smith et al., 2008; Planert et al., 2010a; Escartin et al., 2017). These processes preferentially occur at the relatively magma-poor ends of seafloor spreading segments. The presence of such features in addition to the already variable thickness and composition (Escartin et al., 2008) of slow spreading crust leads to a pattern of hydration which shows considerable variation across the slab front when compared to fast-spreading lithosphere.

Much of the water stored in the subducted sediment column and the upper crust is expelled as a result of compression close to the plate interface at depths too shallow to greatly influence arc magmatism (Figure 2.7). The resulting variations in pore pressure, however, may affect plate coupling and seismicity along the subduction mega-thrust (Kodaira et al., 2004; Kitajima and Saffer, 2012). Water release from the slab is dominated by two reactions, the eclogitization of basalts and gabbros generally occurs at intermediate depths and, at greater depths, the deserpentinization of hydrated mantle rocks (Kirby et al., 1996; Faccenda, 2014). As well as driving melting, both reactions also directly influence the distribution of intra-slab seismicity

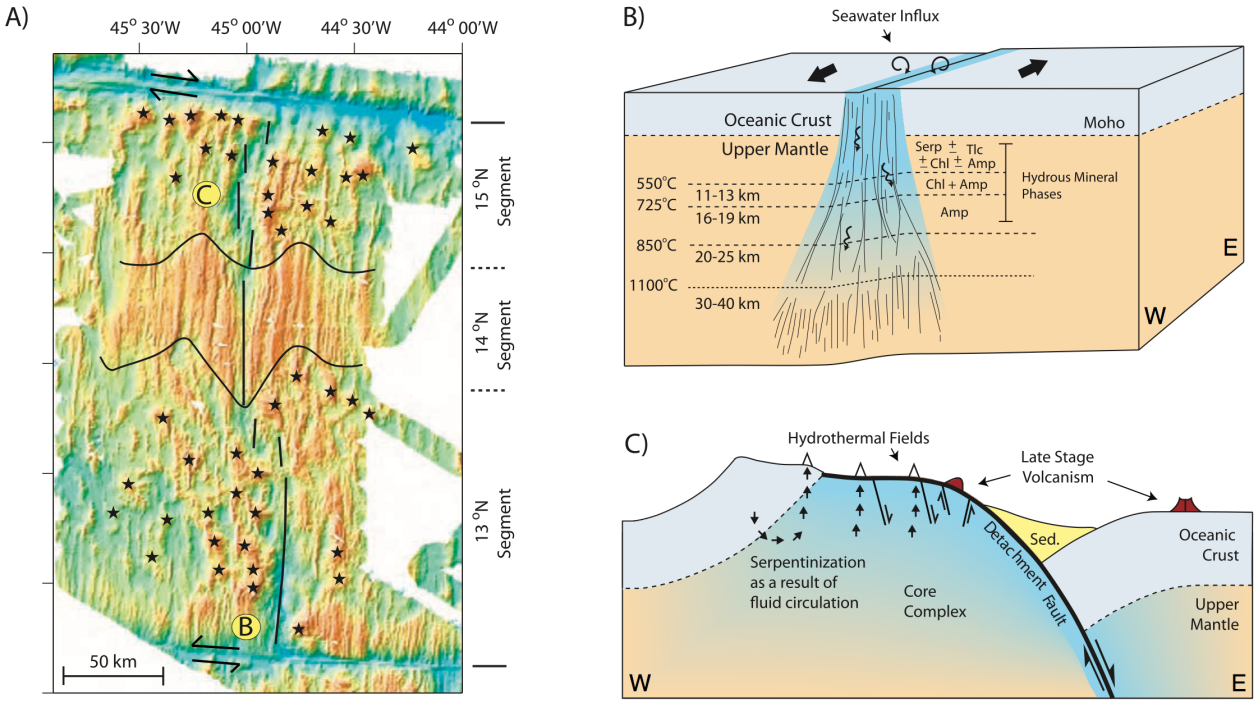


Figure 2.9: The hydration of slow spreading lithosphere. A) Bathymetric map of the MAR between two large-offset transform faults. Two modes of seafloor spreading are seen: conventional abyssal hill fabric (central segment) and core-complex dominated fabric (stars). The structure of slow spreading Atlantic lithosphere is observed to vary rapidly across short-distance as a result of decreased magma supply at segment ends. Serpentinization of mantle peridotites, exposed by fracture zones (B) and large detachment faults (C/stars) can lead to a spatially varying pattern of hydration throughout the oceanic lithosphere. Adapted from Smith et al. (2008). B) Schematic of hydration of the upper mantle at a transform fault. Faulting may facilitate hydration to depths in excess of 25 km within the shear zone. Adapted from Prigent et al. (2020). C) Schematic of hydration of mantle peridotites at a core complex. Large detachment faults accommodate seafloor spreading in magma-poor regions and expose mantle rocks to seawater inundation, resulting in serpentinization. Adapted from Escartin et al. (2017).

(Peacock, 2001; Paulatto et al., 2017).

2.4 Correlating Arc Properties and Slab Structure

Many studies of the Lesser Antilles assume that hydration of the slab beneath the arc is concentrated at a series of major fracture zones subducting along the arc front (Figure 2.1). These features have been implicated as a cause of much of the along arc variability observed, including trends in crustal structure (Section 2.2.1), seismicity (Section 2.2.2) and geochemical

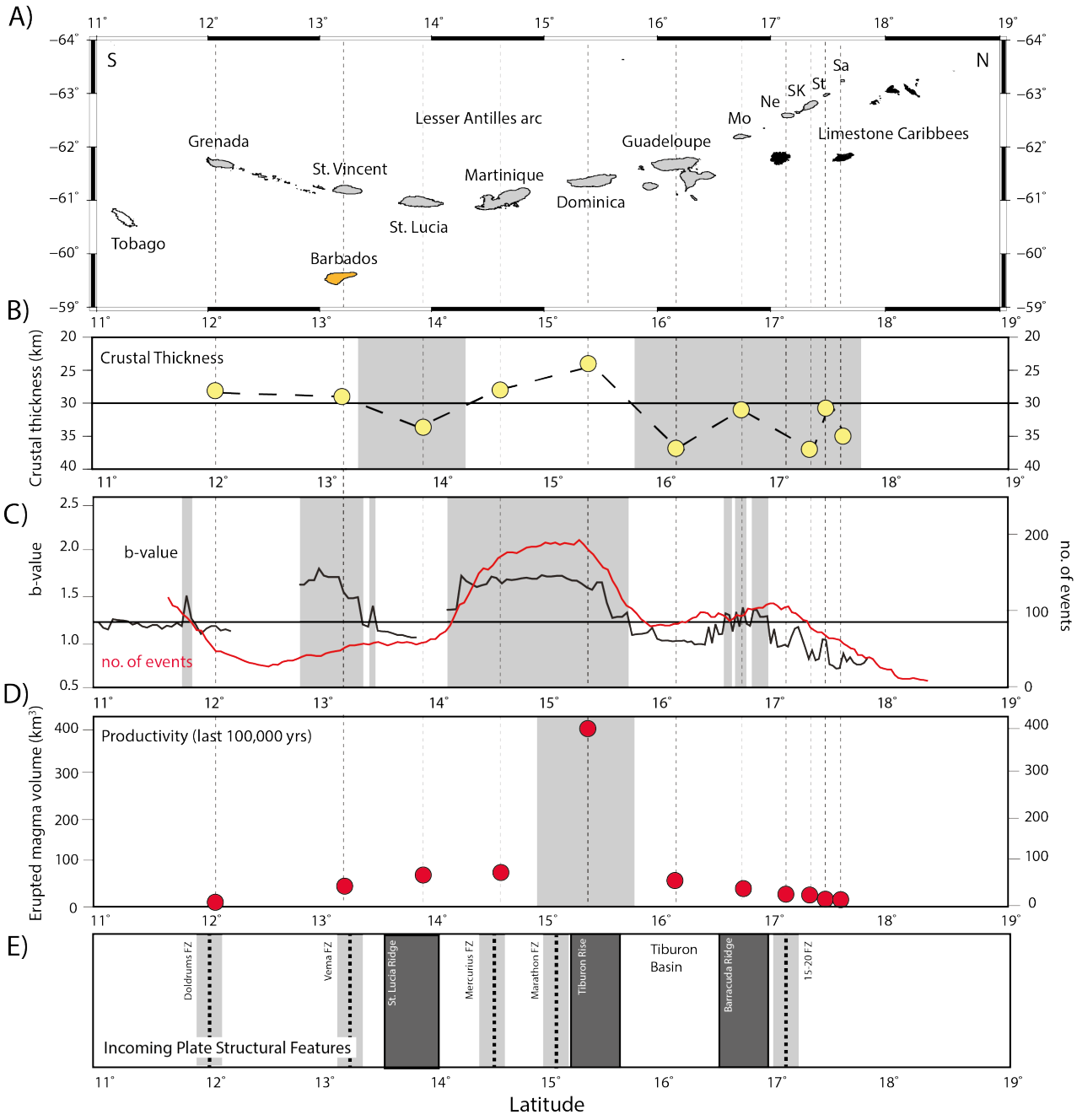


Figure 2.10: A summary of key along arc trends at the Lesser Antilles. A) Geometry of the modern Lesser Antilles arc. B) Crustal thickness variations along the Lesser Antilles arc from Schlaphorst et al. (2018). Regions of the thickest crust are highlighted in grey. C) Along arc variations in b-value and cumulative seismicity from Schlaphorst et al. (2016). Number of events incorporates all events occurring perpendicular to the arc, within a shifting window of 150 km length. Regions of high b-value (thought to correlate with increased hydration of the down-going slab) are highlighted in grey. D) Magmatic productivity along the arc from the last 100,000 years from Wadge and Shepherd (1984). Note the much higher rates of magmatism beneath the central section of the arc. E) Key structural features on the incoming Atlantic plate, major fracture zones (dashed lines) and basement ridges (dark grey) are plotted at the point at which they enter the trench from Schlaphorst et al. (2016).

anomalies (Section 2.2.3). The most significant fracture zones, possessing of the largest offset, are (from north to south), the 15-20, Marathon, Mercurius, Vema and Doldrums (Figure 2.1). In slow spreading lithosphere such as in the Atlantic we might expect hydration to be further concentrated at the end of ridge segments as a result of the additional hydration of the crust at core complexes (Figure 2.9). The position at which these features enter the trench is compared to some of the key along arc trends discussed previously in Figure 2.10.

There are clearly along-arc trends which do correlate well with the proposed location of these fracture zones. In particular highs observed in b-value, with an apparent wavelength of 150-200 km along the arc front (Figure 2.10C) could be the result of concentrated hydration along these features (Schlaphorst et al., 2016). In other cases this relationship is far less obvious. It is much more difficult to explain the more binary N-S divisions in seismicity rate and crustal structure given the apparent fracture zone distribution (Sections 2.2.1, 2.2.2).

The extent to which focused hydration along fracture zones may be driving these arc processes is uncertain. The degree of hydration in the subducting slab away from the main fracture zones is poorly constrained; outer rise hydration, whilst well studied in the Pacific (Grevemeyer et al., 2018) has never been studied in detail at an Atlantic subduction system. The structure of the slow spreading oceanic lithosphere and distribution of sediments on the down-going slab may also influence patterns of seismicity and geochemical trends.

As a result of the thick sediments and unclear magnetic anomalies on the incoming plate, many studies also disagree on the location at which these fracture zones enter the trench, and how they then project beneath the arc. For instance, Carpentier et al. (2008) have the Marathon fracture zone entering the trench north of the Tiburon Rise at $\sim$16°N, in contrast Schlaphorst et al. (2016) have the same fracture zone entering the subduction zone south of the Tiburon Rise. A difference of more than 100 km. This has clear implications for where we might expect water to be released beneath the arc.

Spatial variations in the crustal affinity and volcanic history of the crust of the over-riding plate are highly uncertain and before any correlation can be made with the features of the incoming plate these processes must be properly understood. Whilst individual seismic profiles such as those of Kopp et al. (2011) have suggested the presence of a thick basement crust prior to the current period of volcanic activity along the arc, little is known about the composition, or distribution of the basement along the majority of the arc. The structure of this basement will

directly affect arc crustal thickness in particular, but could also influence other geochemical and seismic trends.

In the following chapters I will seek to constrain some of the most significant uncertainties associated with observed variations in arc processes at the Lesser Antilles arc. This will be done in two stages.

1) First I will explore the history and structure of the over-riding Caribbean plate and the likely structure of the region prior to the current period of volcanism. Key outstanding questions here include: What is the nature of the basement below the modern arc? How are the Limestone Caribbees related to the modern arc, and what drove this recent arc migration? I will answer these questions by first presenting a literature review of the current understanding of the tectonic history of the region in Chapter 3, outlining the key uncertainties in the arc's history. In Chapter 4 I will analyse new seismic and magnetic data in the backarc to devise a new tectonic model for the region.

2) Secondly I explore the structure, and distribution of hydration in the down-going slab. Key questions include: Is the incoming Atlantic plate fully saturated (via water influx near the ridge axis) or is additional hydration gained through plate bending? If plate bending hydration is present, then what is the true distribution of water in the slab at the point of subduction, and what influence might this have over arc processes. Chapter 5 will examine the structure of the subducting basement and sediments through processing of newly acquired seismic data in the Tiburon Basin region of the incoming plate. In Chapter 6 I will use the same dataset to assess the hydration of subducting Atlantic lithosphere in the region, and in particular the role played by outer rise hydration along the Lesser Antilles.

Chapter 3

Background: Tectonic Setting

3.1 Introduction

A key question for isolating the influence of the slab and over-riding plate structure on arc processes is the nature of the crust below the Lesser Antilles. This uncertainty exists due to the very limited exposure of basement rock along the current arc. A rare outcropping of Late Jurassic (c. 153 Ma) basement is found on the island of La Désirade, which sits 10 km east of Guadeloupe (Cordey and Cornee, 2009; Neill et al., 2010). These rocks possess geochemical indicators indicative of formation in a supra-subduction setting (enrichment in Th relative to high field strength elements and negative Ce, Nb–Ta and Ti anomalies), whilst retaining many of the characteristic of mid-ocean ridge basalt (Th/Yb and Ta/Yb ratios), and likely originated in the backarc of a much older subduction system (Neill et al., 2010). In contrast, on the island of Mayreaux in the southern arc the geochemistry of pillow basalts, uplifted by subsequent arc volcanism, are indicative of oceanic spreading beneath the arc as recently as the Eocene (Speed and Walker, 1991; White et al., 2017).

Before we can understand subduction processes at the Lesser Antilles in detail it is clear that we must first understand the origin of such complexities in the over-riding plate, and what influence they may still have over the structure and behaviour of the modern arc.

3.2 The Caribbean Plate

The Caribbean plate is a small oceanic plate, constrained to the north and south by the much larger continental American Plates. The northern and southern plate boundaries are predominantly transform in nature to facilitate the westward motion of the North and South American plates. It is this westward motion that is the primary driver of Antilles subduction, with the Caribbean plate having been largely static in a mantle reference frame throughout the majority of the Cenozoic (Muller et al., 1993; Pindell and Kennan, 2009) and Atlantic subduction essentially "forced" along the eastern plate boundary in the wake of the American plates. The western boundary of the Caribbean plate is also defined by subduction, where the Nazca and Cocos plates subduct along the Middle America Trench. Paleomagnetic data from the sediments of the Nicoya Peninsula, Costa Rica provide evidence for arc volcanism along the western Caribbean plate boundary from *c.* 100 Ma (Boschman et al., 2019).

The crust of the Caribbean plate interior is inherently oceanic, although large areas of it have been thickened by the eruption of the Caribbean Large Igneous Province (CLIP). The CLIP has been sampled by several ODP/DSDP drill sites (Sinton et al., 1998), and although the majority of dating places the eruption of this flood basalt between 91-88 Ma some studies suggest secondary phases of volcanism which may cover a time period as broad as 139-69 Ma (Sinton et al., 1998; Hoernle et al., 2004; Loewen et al., 2013). The boundary beneath the older oceanic crust below and the overlying flood basalts is clearly visible in seismic reflection images, with total crustal thicknesses in some areas exceeding 15 km (Mauffret and Leroy, 1997). However, the region is relatively data poor, and as a result the exact distribution of this flood basalt is relatively poorly constrained. The observation of 5 km thick oceanic crust in the eastern region of the Venezuela Basin (Diebold et al., 1981), and the absence of CLIP volcanics amongst material sampled from the Aves Ridges (Neill et al., 2011), would suggest it is limited to a region comfortably west of the Lesser Antilles (Figure 3.1). Thus, it is thought unlikely that CLIP material is present amongst the basement of the modern arc, though several studies still suggest that a thickened oceanic basement plateau is required to explain the >24 km thick crust beneath the northern arc and forearc (Kopp et al., 2011; Evain et al., 2013).

Along the northern plate boundary the islands of the Greater Antilles are punctuated by a complex 250 km wide zone of deformation, accommodating oblique convergence between the

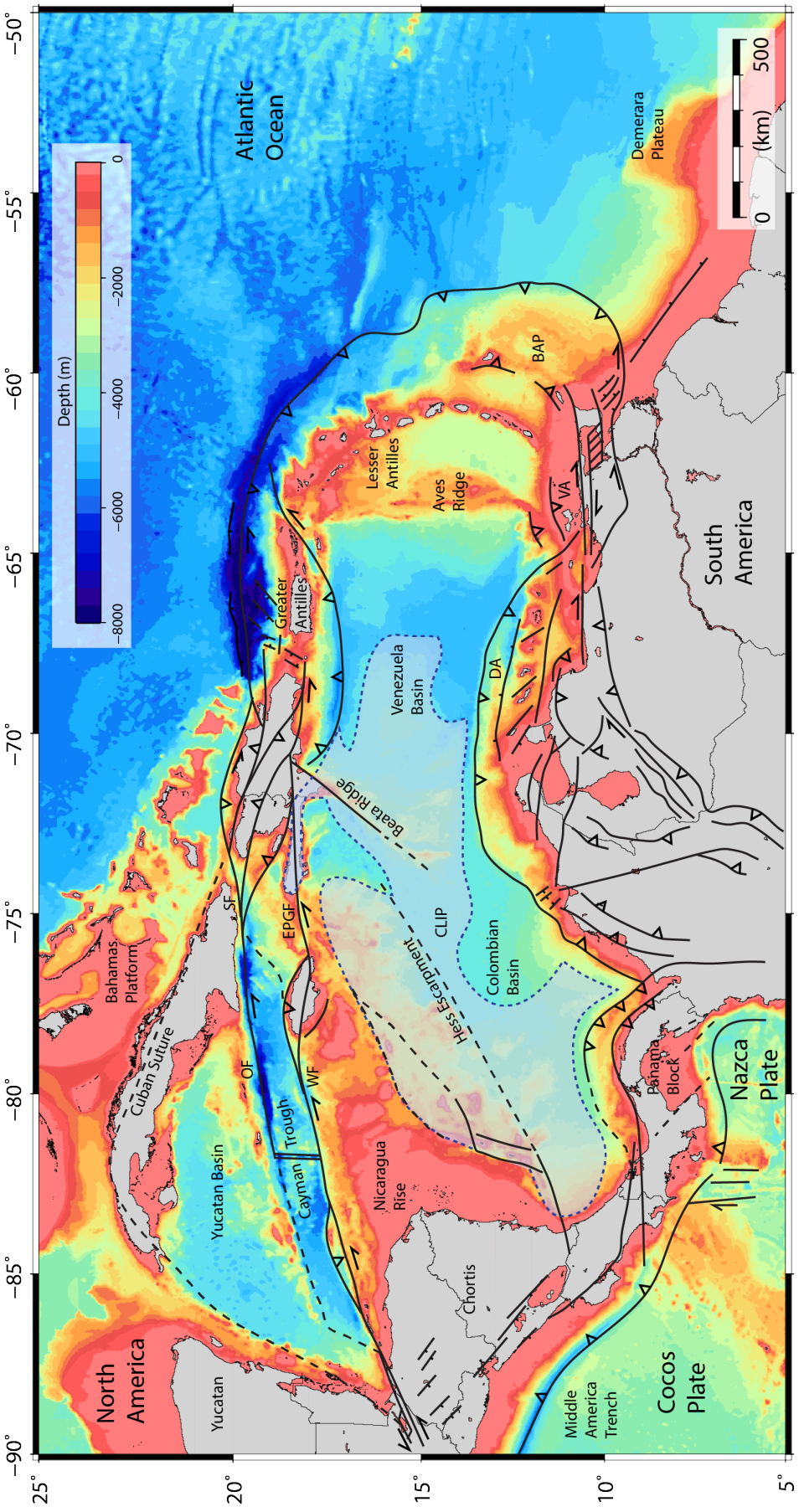


Figure 3.1: Bathymetric map of the Greater Caribbean region. Map shows main regional terranes as well as island groups and structural features. Structural interpretation adapted from Pindell and Kennan (2009), Boundary of CLIP (Caribbean Large Igneous Province) adapted from Serrano et al. (2011). Additional abbreviations are as follows, BAP: Barbados Accretionary Prism, DA: Dutch Antilles, VA: Venezuelan Antilles, OF: Oriente Fault, WF: Walton Fault, SF: Septentrional Fault, EPGF: Enriquillo-Plantain Garden Fault.

Caribbean plate interior, the Greater Antilles, and the Bahamas Bank on the North American plate (Figure 3.1). Large left-lateral strike slip systems such as the Enriquillo–Plantain Garden Fault Zone and Septentrional–Oriente Fault Zone take up much of this motion (Mann et al., 1984; Bruna et al., 2014). The Puerto Rico trench is oblique to the prevailing subduction direction, and is not currently under-going active subduction. Further west, the system becomes increasingly transtensional. Ultra-slow seafloor spreading along the Cayman trough (<10 mm yr^{-1}) is responsible for ∼1100 km of relative motion between the North American and Caribbean plates since its inception *c.* 45 My ago (Rosencrantz et al., 1988; Leroy et al., 2000).

To the south of the Lesser Antilles, relative motion between the Caribbean plate and South America occurs on a series of large offset transform faults along the South American margin, including the El Pilar fault, which has accumulated a total 200 km of offset in northern Venezuela over the previous 10 My (Pindell and Kennan, 2009) and the Central Range fault, which bisects the island of Trinidad (Soto et al., 2011). Further west this system becomes increasingly convergent. The Caribbean plate subducts obliquely beneath the northwestern corner of South America, whilst the South Caribbean deformed belt accommodates further deformation within the Caribbean plate interior (Pindell and Kennan, 2009; Boschman et al., 2014).

3.3 A Tectonic Framework for the Greater Caribbean Region

3.3.1 Caribbean Plate Formation

The eruption of the CLIP has largely over-printed the original seafloor spreading magnetic fabric in the Caribbean Sea, making the age and origin of the oceanic crust difficult to determine (Ghosh et al., 1984). Magneto-stratigraphic data from within the CLIP itself is also of limited use as its eruption coincided with the Cretaceous magnetic quiet zone (Sinton et al., 1998). Plate reconstructions of the region are therefore unable to rely on such data to constrain the motions of the plate through time (e.g. Boschman et al. 2014) as they generally would in oceanic settings. Current understanding of the history of the greater Caribbean region is heavily reliant on the structural relationships of the various terranes that comprise the Caribbean plate and

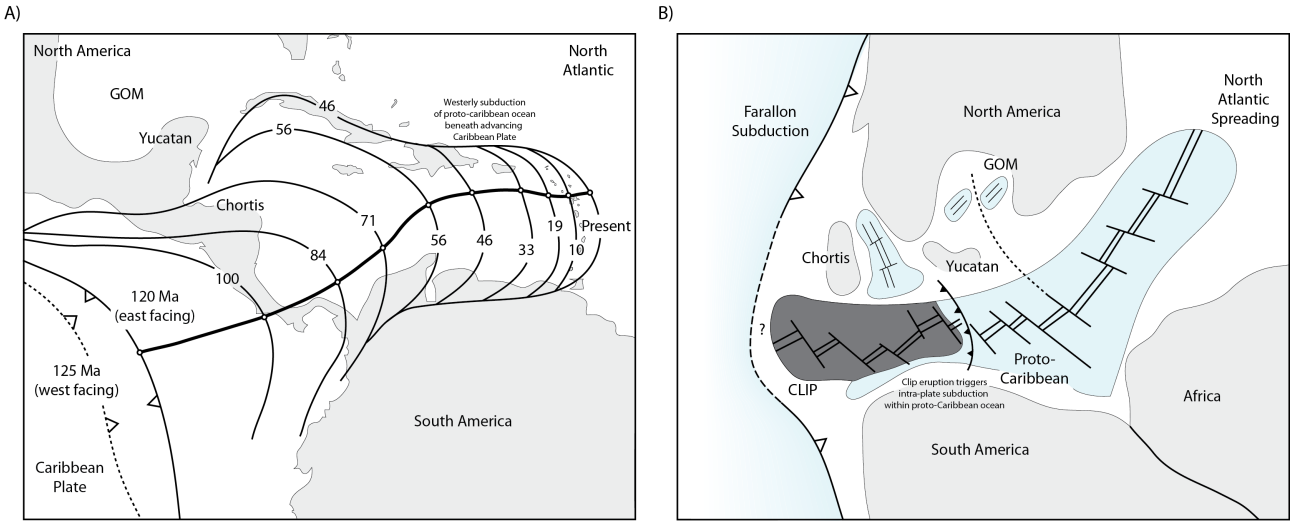


Figure 3.2: Models of Caribbean Plate Origin A) Pacific origin model. The Caribbean plate is a former segment of Farallon oceanic crust. Following a subduction inversion along the Middle America Trench, the plate migrates into its current location between the Americas. This motion is facilitated by subduction of the proto-Caribbean ocean along a large regional subduction zone called the Great Arc of the Caribbean. Figure adapted from Pindell and Kennan (2009) and assumes an Aptian date for subduction reversal. B) In situ origin Model. The Caribbean plate is a fragment of the proto-Caribbean ocean which forms between North and South America during the break-up of Pangea. Following CLIP volcanism, subduction initiates within the proto-Caribbean ocean, forming the Caribbean plate. Adapted from Giunta et al. (2006)

.

border regions, as well as a thorough understanding of the chronology and tectonic affinity of the rocks exposed along the islands which mark the plate boundaries (Pindell and Kennan, 2009; Boschman et al., 2014).

Historically, models of the Caribbean plate's history have essentially fallen into one of two categories. In the Pacific origin model, the Caribbean plate formed through seafloor spreading in the Pacific before migrating into its current location between the American plates (Pindell and Kennan, 2009; Boschman et al., 2014). In the in situ origin model, the Caribbean plate formed as a result of seafloor spreading in its current location as North America broke away from Pangea (James, 2005; Giunta et al., 2006; James, 2009), with subduction initiating entirely within the proto-Caribbean ocean (Figure 3.2). There is now an over-whelming weight of scientific evidence against the in situ model, which in particular fails to account for extension along the Cayman Trough, the extensive regional history or Albian-Eocene arc volcanism, or the presence of a proto-Caribbean slab observed in seismic tomography (Pindell et al., 2006). As such the in situ model will not be discussed further here.

The lack of datable Caribbean seafloor spreading anomalies means that even within the frame-

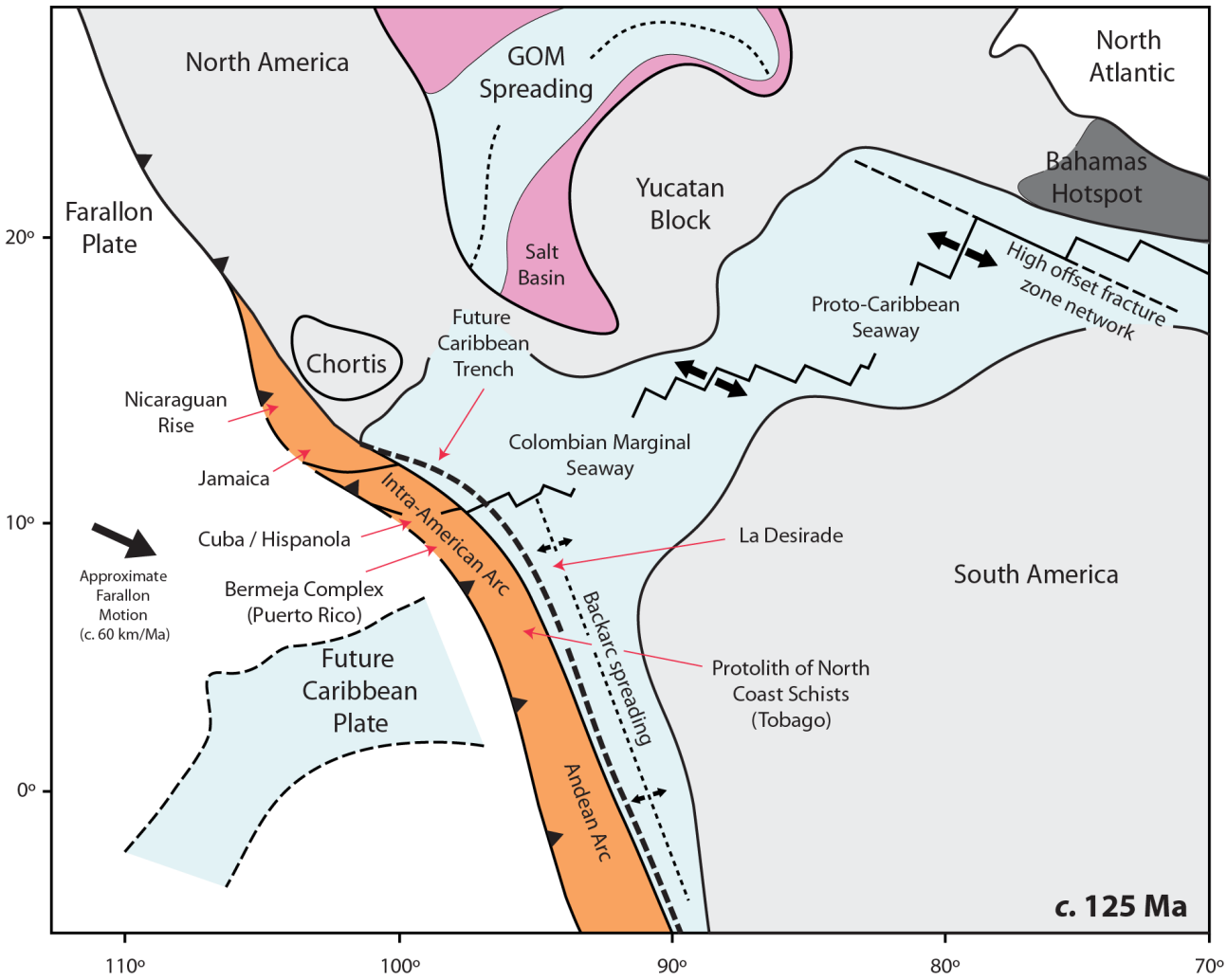


Figure 3.3: Map of Caribbean region during the Cretaceous. Figure demonstrates key tectonic features prior to Intra-American subduction reversal and the onset of Great Arc of the Caribbean volcanism including spreading in the proto-Caribbean and GOM (Gulf of Mexico). Adapted from Pindell and Kennan (2009).

work of the Pacific origin model its formation is poorly constrained (Ghosh et al., 1984; Boschman et al., 2019). Almost all regional reconstructions however agree that the plate likely formed relatively south and west of its current location in what was then the Panthalassa ocean. Boschman et al. (2019) suggest that it may have formed at a spreading centre between the Phoenix and Farallon Plates prior to 170 Ma. Both the Phoenix and Farallon plates have subsequently fragmented into a series of smaller plates (e.g. the Cocos and Juan de Fuca plates in the latter case), and been largely subducted beneath the American continents.

3.3.2 Proto-Caribbean Spreading

Rifting of the North American plate from Pangea from *c.* 190 Ma triggered a major restructuring of the region. In the central Atlantic seafloor spreading accommodated the separation of North America and Eurasia. By the Late Jurassic this phase of spreading extended as far south as the Marathon and Mercurius fracture zones, which subduct beneath the northern Lesser Antilles today (Figure 2.1). Similarly, the north-westerly drift of North America has to be taken up by spreading in a new ocean forming between the North and South American continents (Figure 3.3). Following an initial stage of continental rifting, this extension leads to full oceanic spreading in the Gulf of Mexico from *c.* 158 Ma and NW-SE orientated spreading in what would become the proto-Caribbean ocean shortly after (Pindell and Kennan, 2009).

Initially spreading occurred within several discrete basins (Pindell and Kennan, 2009), including the proto-Caribbean seaway and Colombian marginal seaway (Figure 3.3). The easternmost segment of proto-Caribbean spreading may have been initially influenced by hot-spot volcanism associated with the Bahamas Bank and Demerara Rise, leading to the formation of seaward dipping reflectors associated with synrift volcanism as observed in 2D seismic profiles (Reuber et al., 2016). By the Early Cretaceous the proto-Caribbean ridge formed one continuous spreading system from the boundary with the Pacific in the west (Figure 3.3) through to the North Atlantic (Pindell and Kennan, 2009; Reuber et al., 2016). Connectivity between the proto-Caribbean ocean and the central Atlantic would have required a high-offset system of fracture zones (Figure 3.3) in order to circumnavigate the thickened crust of the Bahamas platform (Pindell and Kennan, 2009; Reuber et al., 2016).

3.3.3 Mechanisms for Subduction Reversal

In the early Cretaceous the western boundary of the proto-Caribbean was marked by a triple junction between the proto-Caribbean spreading ridge and an eastward dipping subduction zone known as the Intra-American arc (Pindell and Kennan, 2009). This arc subducted the oceanic lithosphere of the Farallon plate, forming a continuous band of arc volcanism from southern Mexico through to north-west South America, where it transitions into the Andean subduction system (Figure 3.3).

The mechanism that led to transition from this eastward dipping subduction zone to the westward dipping subduction of proto-Caribbean lithosphere beneath the Caribbean plate (thus facilitating the migration of the Caribbean plate into its modern day location), is perhaps the most contentious stage in the tectonic history of the region (Burke, 1988; Pindell et al., 2006). In particular the timing of this reversal and what role the eruption of the CLIP might have played remains highly controversial.

Two fundamental models exist, in the first the CLIP was erupted prior to subduction reversal, this thickened crust effectively jamming the Intra-American trench, and triggering the formation of a new subduction zone to the east (Burke, 1988). As discussed previously, the majority of drilled rocks from the CLIP are dated to 91-88 Ma (Sinton et al., 1998), meaning that subduction reversal would have to post-date this, likely occurring in the Campanian (83.6 - 72.1 Ma). In the second model the reversal occurs prior to CLIP eruption, likely within the backarc of the Intra-American arc (Pindell et al., 2006; Pindell and Kennan, 2009). An analogue for this exists today in the Scotia sea where subduction of Antarctic oceanic lithosphere along the Scotia arc initiated in the backarc of an older South American - Antarctic subduction system. Half of that former backarc is now preserved in the forearc of the South Sandwich Islands (Neill et al., 2010). In this model the subduction reversal occurs much earlier, during the Aptian at ∼125-112 Ma, possibly triggered by an increase in the velocity of the South American plate relative to the Caribbean (Barker, 2001; Pindell and Kennan, 2009).

For the purposes of understanding the influences over the structure of the Lesser Antilles arc which model is correct isn't overly essential. The most important outcome of the reversal from eastward to westward facing subduction is that as the Caribbean plate advances eastward, terranes associated with arc magmatism along the Intra-American arc are accreted across its leading edge. Examples of pre-Aptian arc material, throughout the region include the 133 Ma arc derived Mabujina Amphibolite Complex on Cuba (Rojas-Agramonte et al., 2011), the 136 Ma island arc tholeiites of the Lower Devil's Racecourse formation on Jamaica (Hastie et al., 2009) and the Tithonian (152.1-145 Ma) Bermeja complex of Puerto Rico (Schellekens, 1998). Given the age of many of these deposits most major regional plate reconstructions generally tend towards the Aptian model of subduction reversal (e.g. Boschman et al. 2014).

In the vicinity of the Lesser Antilles there are two clear outcroppings of such material. The first, as previously discussed is the island of La Désirade (Section 3.1). Neill et al. (2010)

suggest that this basaltic crust most likely formed in the backarc of the Intra-American arc system close to the equator within the Colombian marginal seaway (Figure 3.3). An ∼10 km basaltic section is exposed on the island as a result of uplift along a fault scarp in the Lesser Antilles forearc. It is the only known exposure of Mesozoic basement material along the arc. It is unclear exactly how widespread Intra-American arc derived material could be within the basement of the Lesser Antilles, where it may make a substantial contribution to the observed along arc heterogeneities in crustal structure.

The protoliths of the north coast meta-sediments and meta-igneous rocks of Tobago are also thought to have formed in the Colombian marginal seaway (Figure 3.3), before undergoing metamorphism at 129-110 Ma, in keeping with Aptian models of subduction reversal (Neill et al., 2012). Like La Désirade, these rocks were accreted to the advancing Caribbean plate, and now reside to the south-east of the Lesser Antilles forearc. In the Late Cretaceous, the Tobago Volcano-Plutonic suite formed as a result of a second phase of arc volcanism (Neill et al., 2012). This volcanism occurred along the Great Arc of the Caribbean (GAC), the large regional subduction zone that formed as the Caribbean plate advanced into the proto-Caribbean seaway.

3.3.4 The Great Arc of the Caribbean

Following subduction reversal, the Caribbean plate advanced north-north-easterly relative to South America (Figure 3.2A). Arc volcanism, driven by the subduction of proto-Caribbean lithosphere would have been widespread along the northern boundary, and is recorded in the rock record of Jamaica (Mitchell, 2006; Hastie et al., 2010), the northern Nicaraguan Rise (Lewis et al., 2011), Cuba (Lázaro et al., 2009; Rojas-Agramonte et al., 2011; Lázaro et al., 2013), Hispanola (Torro et al., 2017) and Puerto Rico (Jolly et al., 1998; Schellekens, 1998). On Puerto Rico, the record of island arc volcanism spans the period from 120 - 48 Ma, making it one of the longest-lived sites of arc volcanism anywhere in the world and leading to crustal thicknesses in excess of 30 km (Jolly et al., 1998). From the global plate reconstruction of Müller et al. (2019) subduction would have occurred at rates on the order of 4 cm yr^{-1}. Subduction was likely accompanied by backarc spreading between 80-75 Ma, with this backarc crust now forming the metamorphic sole of the Moa–Baracoa ophiolite on Cuba (Lázaro et al., 2013; Boschman et al., 2014).

The southern Caribbean plate boundary underwent oblique collision with the north-west South American margin from 120 - 110 Ma, marked by the presence of Lower Cretaceous island arc rocks and high-pressure metamorphism of continental material in the Northern Andes (Pindell and Kennan, 2009). This ongoing collision accommodated as much as 1300 km of strike slip motion and 200 km of convergence in the period 100 - 70 Ma alone (Boschman et al., 2014). Oblique convergence continued until the early Cenozoic, when intrusive rocks throughout the northern Andes (Cardona et al., 2011; Bayona et al., 2012; Boschman et al., 2014) mark the collision of the GAC with the South American continent, resulting in another subduction reversal and CLIP subduction beneath South America.

It is a somewhat novel feature of the Aptian model of subduction reversal, that the proto-Caribbean ocean being consumed by the advancing Caribbean Great Arc would have still been under-going active spreading (at least until ∼70 Ma when extension stopped between the North and South American plates, see Section 3.5). The slab-gap that resulted from the subduction of this active ridge, may have been sufficient to allow mantle upwelling to occur through the subducted plate, facilitating the eruption of the CLIP between 91 - 88 Ma (Pindell et al., 2006; Pindell and Kennan, 2009). The lack of geochemical indicators typical of supra-subduction volcanism in studied CLIP rocks is one of the main arguments against such a scenario, however given the uniqueness of the proposed setting and a lack of geodynamic modelling to truly examine its viability, it is hard to assess whether this is particularly significant.

3.3.5 Closure of the Great Arc

The modern eastern Caribbean plate boundary would have been oblique to much of GAC subduction. Despite that the Aves Ridge (which now sits west of the Grenada Basin in the Lesser Antilles backarc, Figure 3.1), and the islands of the Dutch Antilles record active arc volcanism between 88-59 Ma constrained by zircon U-Pb dating (Neill et al., 2011). Although sampling from the ridge itself is relatively poor, dredged basaltic and andesitic material support this island arc origin, despite the presence of unusual trace element signatures, thought to be derived from a plume-like mantle source as a result of adjacent CLIP magmatism (Neill et al., 2011). The interpretation of the Aves Ridge as an arc segment is also supported by wide-angle seismics. The TRIN profile of Christeson et al. (2008) encompasses the southern Aves Ridge, as well as the Grenada and Tobago Basins and Lesser Antilles arc south of Grenada (Figure

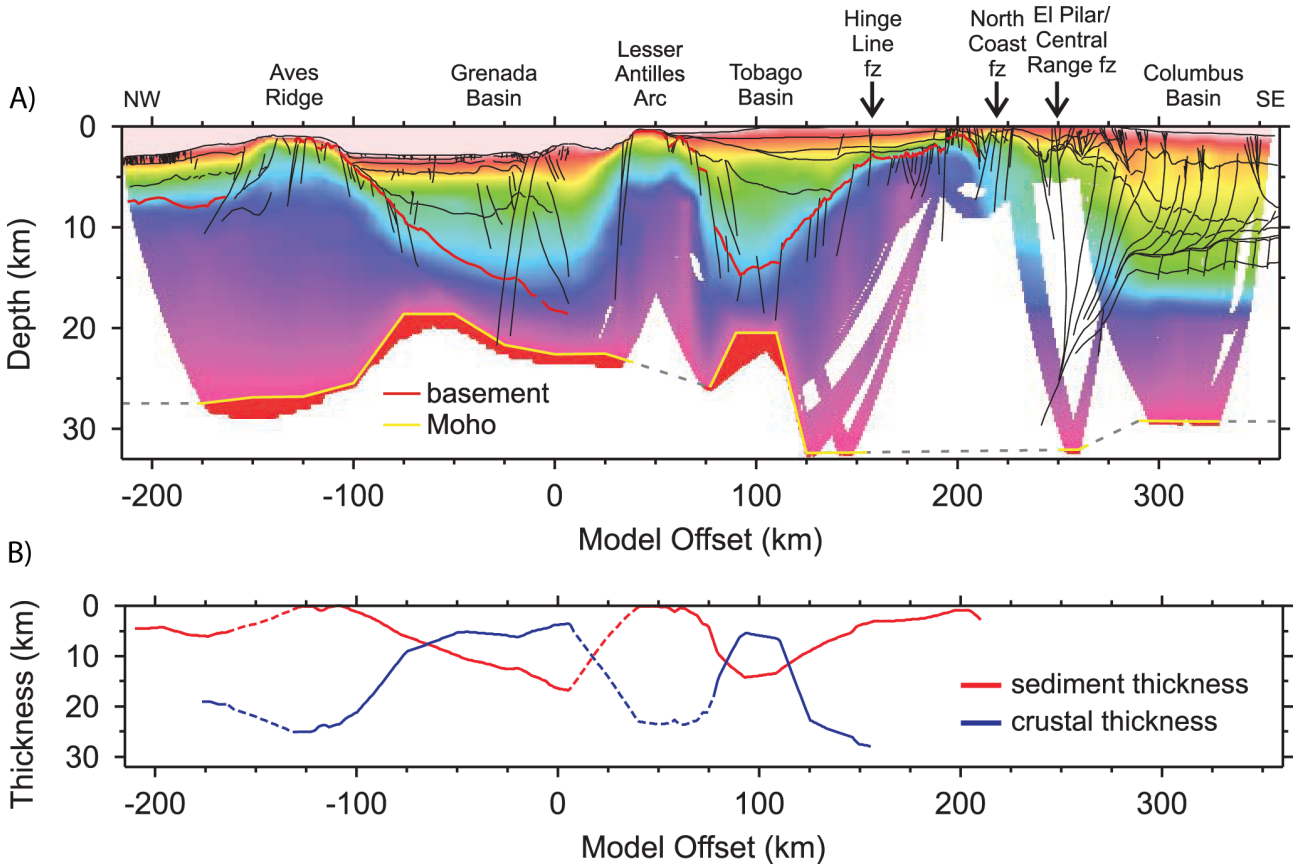


Figure 3.4: wide-angle Vp model across the southern Aves Ridge, Grenada Basin and Lesser Antilles arc, from Christeson et al. (2008). Model shows thick crust of 24-26 km thickness beneath the Aves Ridge and Lesser Antilles and similar velocity profiles in keeping with crust formed as a result of arc volcanism. In the Grenada and Tobago Basins the crust is thinner and may be oceanic in nature. Sediment thickness in the Grenada Basin is in excess of 12 km.

3.4). Beneath the Aves ridge they identify ∼26 km thick crust, with a lower crust Vp of 7.3 km s^{-1}, similar to that of the adjacent Lesser Antilles. Clark et al. (2008) also demonstrated a similar Vp structure over a wide-angle profile across the far southern portion of the ridge, near the South American margin.

During the Paleocene, subduction beneath the Aves Ridge became increasingly direct as relative motion between the Caribbean plate and the American plates rotated to a more east-west orientation in order to accommodate the now dominantly westward motion of the Americas (Pindell and Kennan, 2009; Boschman et al., 2014). Plate reconstructions place this reorganization at *c.* 64 Ma as a direct result of slowing divergence between North and South America (Figure 3.10), leading to the complete shut-down of proto-Caribbean spreading (Boschman et al., 2014; Müller et al., 2019). This coincided with the closure of the final northern segment of the GAC, following sequential collisions with the Chortis block at *c.* 85 Ma, the Yucatan block during

the Late Cretaceous (Campanian–Maastrichtian) and finally the hot-spot thickened crust of the Bahamas platform at in the Early Paleogene (Venable, 1994; Pindell and Kennan, 2009; Ratschbacher et al., 2009). In the latter event the accretion of Cuba to the Barbados Bank led to the northern Caribbean plate boundary migrating up to 450 km south to the Oriente fault (Figure 3.1) in order to accommodate the continued westward motion of the North American plate (Boschman et al., 2014). Ultra-slow seafloor spreading along the Cayman trough, responsible for much of the ongoing motion along the northern Caribbean plate boundary, began at *c.* 49 Ma (Leroy et al., 2000; Boschman et al., 2014).

Given the lack of basement exposure it is difficult to know precisely what influence this phase of subduction had over the future basement rocks of the Lesser Antilles. Given the geometry of the region, the basement crust of the Lesser Antilles must at the very least have sat in the forearc of the Aves Ridge system, making it susceptible to high levels of deformation and alteration. It is highly likely that much of the crust that would come to underlie the Lesser Antilles following the opening of the Grenada Basin, would have experienced direct arc magmatism during this period, especially in the north of the arc, where subduction would have been less oblique. Drill core from the Saba Bank and Anegada Passage (the structural boundary between the Lesser and Greater Antilles) recovered Paleocene igneous rocks dated *c.* 66-64 Ma (Warner, 1989).

3.4 The Cenozoic History of the Eastern Caribbean

3.4.1 The Grenada Basin

U-Pb dating indicates that the arc volcanism along the Aves Ridge and the islands of the Dutch Antilles ended at *c.* 59 Ma (Neill et al., 2011), with arc volcanism along the eastern Caribbean plate boundary re-establishing itself along the islands of the Limestone Caribbees from the Upper Eocene (Andreieff et al., 1988b; Weiss, 1994). The exact cause of this migration is unclear, and could derive from the changes in the relative plate motion between North and South America, slab rollback, or just the result of the reduced obliquity of subduction following closure of the northern Great Arc. Although there is a seeming hiatus in eastern plate boundary arc volcanism from ∼58 - 40 Ma arc migration is well recorded in the eastern trending arc volcanism of the Greater Antilles and Virgin Islands (Jolly et al., 1998; Lidiak and Jolly, 1998).

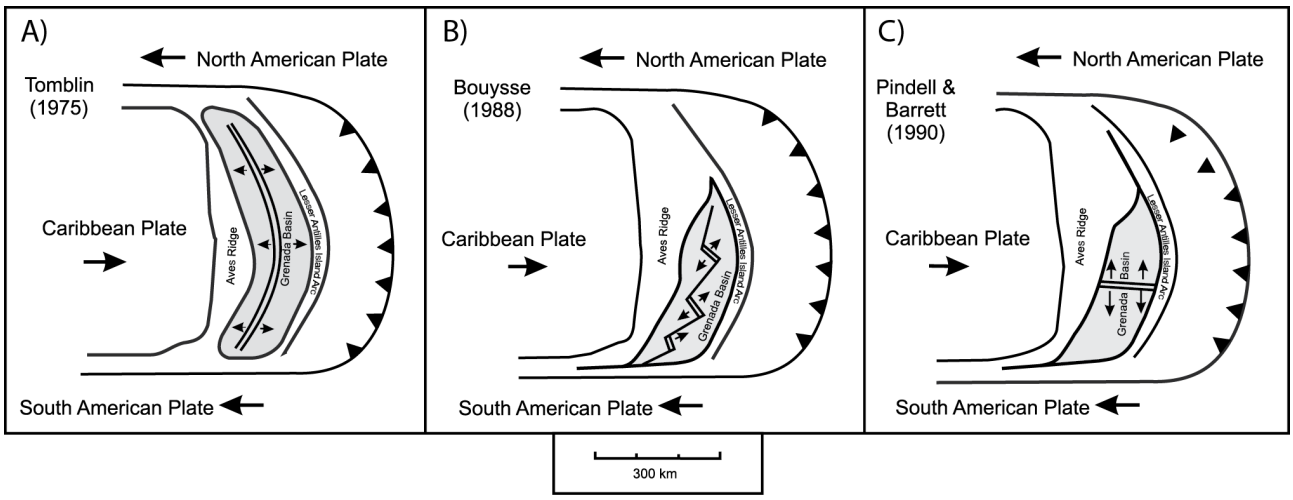


Figure 3.5: Models of Grenada Basin backarc spreading from A) Tomblin (1975), whole arc E-W orientated spreading; B) Bouysse (1988), southern arc NE-SW orientated spreading; C) Pindell and Barrett (1990), southern arc N-S orientated spreading. Adapted from Aitken et al. (2011).

Along the southern plate boundary this coincides with collision between the southernmost Great Arc and South America, and subsequent subduction reversal and CLIP subduction (Cardona et al., 2011; Bayona et al., 2012; Boschman et al., 2014).

The transition from Aves Ridge volcanism to that of the Lesser Antilles likely drove the opening of the Grenada (backarc) Basin. Eocene basalts exposed on the island of Mayreau show a distinctly MORB like composition. Elevated TiO_2 and Zr concentrations and Ce/Zr ratios (Speed and Walker, 1991; White et al., 2017) have led to the interpretation that these rocks formed during Grenada Basin backarc spreading, and have subsequently been uplifted by Antilles volcanism. The lack of clear organized magnetic anomalies in the Grenada Basin again mean that the mechanism by which this basin formed is highly disputed (Bird et al., 1993, 1999; Aitken et al., 2011). In addition, apart from the wide-angle profile of Christeson et al. (2008), which is in the far south of the basin, and observed crust with a thickness and velocity structure typical of oceanic material, little is known about the crustal structure of the basin. This is in part due to the extreme thickness of South America derived sediment in the south of the basin, which in places exceeds 12 km (Christeson et al., 2008; Aitken et al., 2011).

This ambiguity has led to a range of models being proposed for the opening of the backarc basin. Initial models such as those of Tomblin (1975), proposed a simple N-S orientated spreading system throughout the entirety of the basin (Figure 3.5). The observation of highly deformed basement in the northern basin means that most models are in agreement that backarc spreading

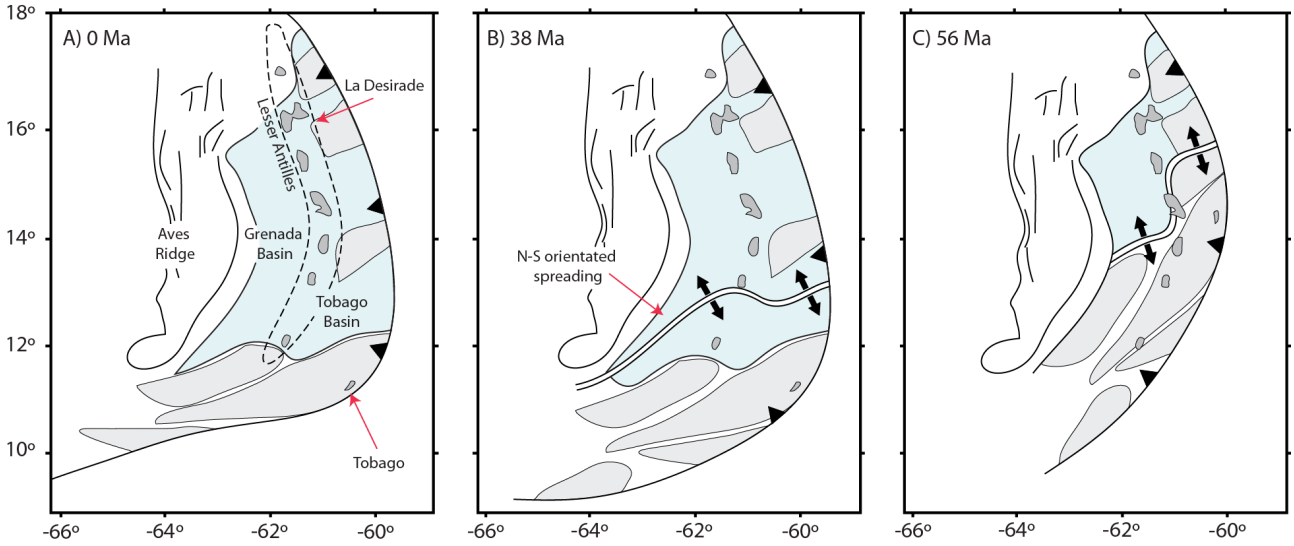


Figure 3.6: Pindell and Kennan (2009) model of complex fan-like opening of the Grenada Basin during the Cenozoic. This model leaves blocks of old crust derived from the arc and forearc of the Aves Ridge interspersed with regions of new oceanic crust formed as a result of backarc spreading along an E-W orientated spreading center in the basement of the Lesser Antilles prior to arc volcanism. Adapted from Pindell and Kennan (2009).

was likely limited to the south. However, the orientation and limits of this spreading is still highly debated (Bouysse, 1988; Bird et al., 1999; Pindell and Kennan, 2009; Aitken et al., 2011), largely due to the presence of the thick sediments in the southern basin (Christeson et al., 2008; Aitken et al., 2011), which prevent detailed basement mapping, magnetic anomaly measurements, or direct sampling, and the general lack of seismic data within the region. More recently, a number of more complex models have arisen for the formation of both the Grenada and Tobago basins, with significant differences in the proposed nature of the crust underlying the modern day arc.

Pindell and Kennan (2009) proposed a model of distributed intra-arc rifting and seafloor spreading predominantly along NW-SE orientated spreading centres, forming both the Grenada and Tobago basins (Figure 3.6). They argue that this spreading was the result of the gravitational collapse of the Aves Ridge arc crust during slab rollback in the Paleocene-Eocene. According to their reconstruction, such a mechanism accurately reproduces arc basement structures, whilst continuing to accommodate the eastward motion of the Caribbean plate relative to South America, and explaining the location of the Tobago terrane. From such a model we would expect a highly heterogeneous crustal structure prior to the initiation of arc volcanism along the southern and central Antilles, with isolated enclaves of stretched Aves Ridge arc and forearc crust, and newly formed oceanic crust, distributed throughout the southern arc.

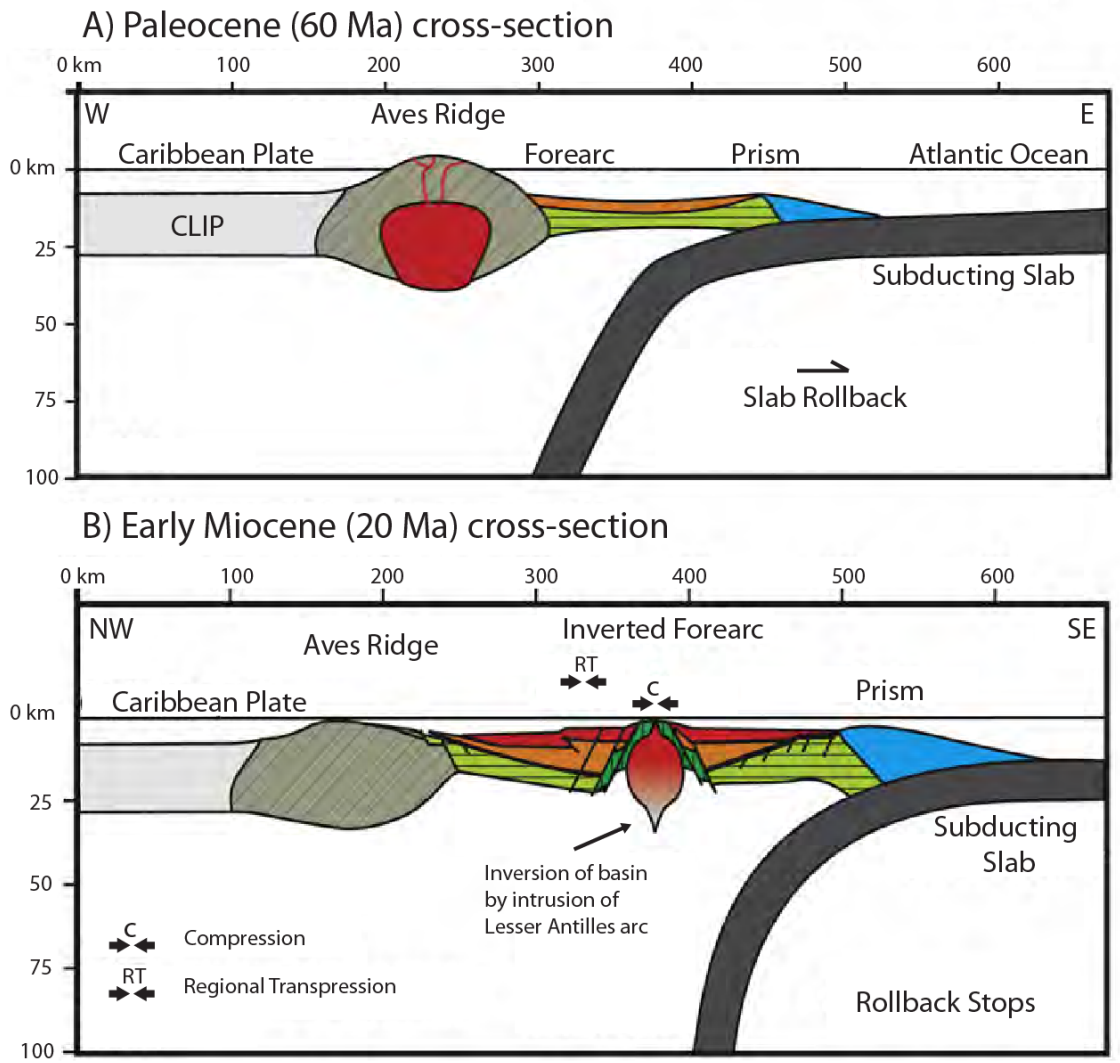


Figure 3.7: Cross-sections through the southeastern Caribbean region at A) 60 Ma and B) 20 Ma demonstrating the Aitken et al. (2011) model for Grenada Basin opening. In this model the pre-existing forearc crust of the Aves Ridge undergoes lateral extension of ∼70 km without any need for the formation of new crust through backarc spreading. This basin is later subdivided by Antilles volcanism forming the Grenada and Tobago Basins. In this case the Antilles basement would be entirely formed from GAC/Aves Ridge arc and forearc material. Adapted from Aitken et al. (2011).

Aitken et al. (2011) have argued that the Grenada Basin formed as a forearc basin, ahead of the Aves Ridge segment of the Great Arc of the Caribbean, before undergoing further extension of up to 70 km as a result of slab rollback in the Eocene (Figure 3.7). They interpret three major sedimentary mega-sequences in the seismic stratigraphy of both the Grenada and Tobago Basins, dated early Paleogene to present. From this observed about-arc symmetry they argue that the two were one continuous basin during the Eocene, prior to the initiation of arc volcanism along the centre of this basin during the Oligocene. In this model the pre-existing

crustal structure of the full length of the Lesser Antilles would therefore be extended Aves Ridge arc and forearc crust.

3.4.2 The Limestone Caribbees

Arc volcanism along the islands of the Limestone Caribbees (Figure 2.1) extended from the Upper Eocene to Oligocene, and is well recorded on the islands of St. Barthelemy, Antigua and St. Martin (Andreieff et al., 1988b; Davidson et al., 1993; Weiss, 1994). On the latter this period of volcanism consists of a typical subduction suite of mildly tholeiitic to calc-alkaline basalts and andesites (Davidson et al., 1993). Following the extinction of these islands, and a second apparent short volcanic hiatus in the region, arc activity is re-established along the islands of the modern Lesser Antilles. The Late Oligocene rocks of the Basal Complex of Martinique, another series of tholeiitic to calc-alkaline lavas, are some of the oldest arc material associated with the current island arc (Andreieff et al., 1988a; Westercamp and Andreieff, 1989; Germa et al., 2011). Although few reliable radiometric ages exist for these rocks, their age is well constrained by overlying Late Oligocene limestones. In the north of the arc the modern volcanic centres, including islands such as Montserrat and St. Kitts and Nevis, are situated ∼75 km west of the pre-existing islands of the Limestone Caribbees (Figure 2.1). These are separated by the Kallinago trough, a Late Miocene, intra-arc rift basin, which formed as a result of the westward migration from the Limestone Caribbees to the modern arc position (Mann, 1999).

This second phase of arc migration has generally been linked to the subduction of aseismic ridges on the incoming plate, similar to the Barracuda and Tiburon ridges which are subducting beneath the central/northern forearc today (Figure 2.1). These ridges mark a ∼200 km zone of deformation, centred about the Tiburon Basin represents distributed convergence across the N-S American plate boundary, with uplift beginning in the Mid-Late Miocene (Patriat et al., 2011; Pichot et al., 2012). It has been suggested that such features may also lead to a shallowing of the subducting slab (McCann and Sykes, 1984; Mccann and Sykes, 1986), either as a result of buoyancy, or increased coupling with the over-riding plate, thereby controlling the location of seismic activity along the plate interface and volcanism on the over-riding plate.

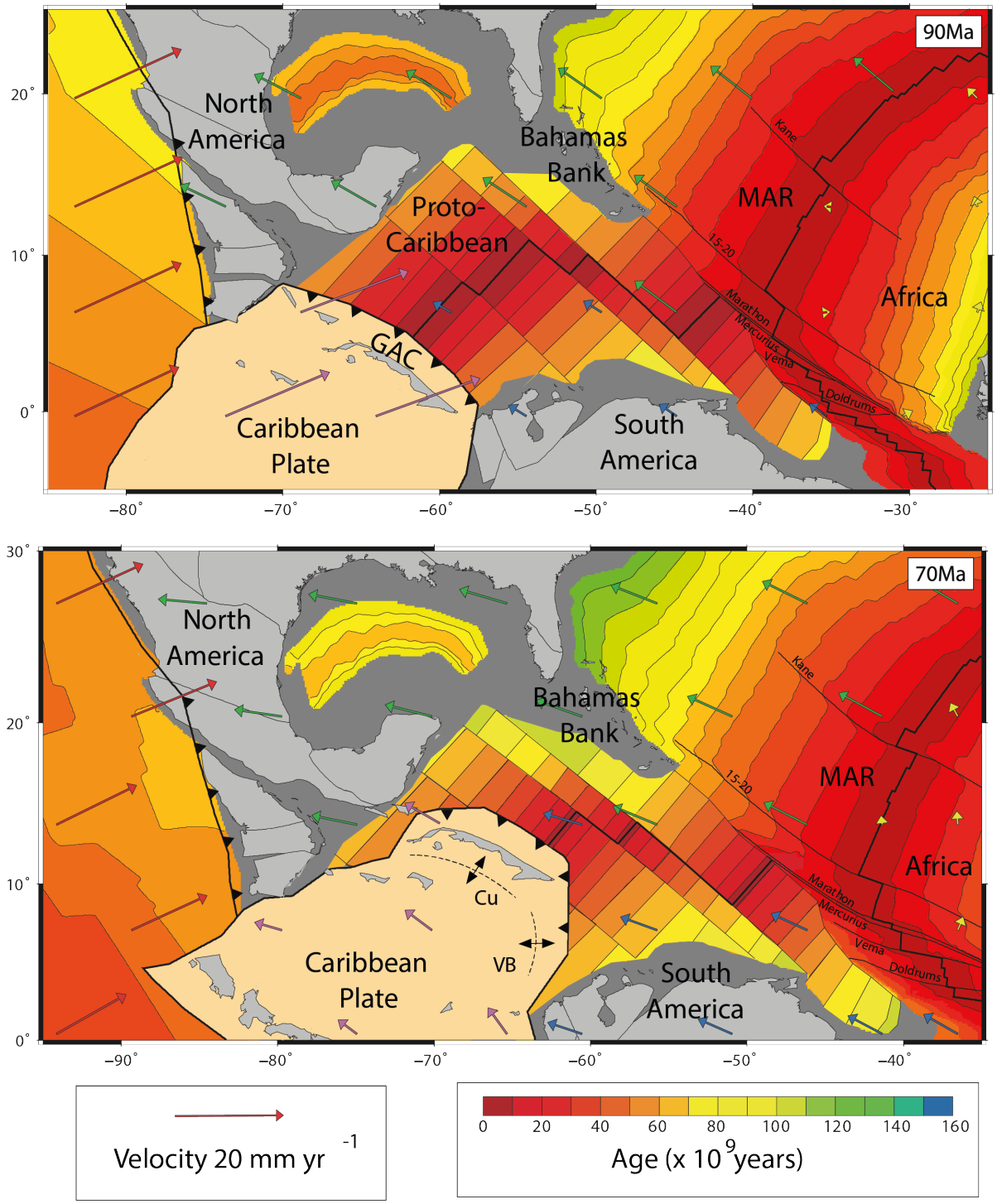


Figure 3.8: Plate reconstruction for the Caribbean region at 90 Ma and 70 Ma showing the advance of the Caribbean plate into the proto-Caribbean domain behind the Great Arc of the Caribbean. Reconstruction generated using the model of Müller et al. (2019). Arrows show velocity relative to the mantle reference frame for the Pacific (red), North American (green), South American (blue), Caribbean (pink) and African (yellow) plates. Seafloor age data in the Atlantic, Pacific and Gulf of Mexico is from the age grid accompanying the Müller et al. (2019) model. Age of seafloor in the proto-Caribbean ocean calculated assuming a simple network of fracture zones modelled as flowlines in the software G-Plates between the North and South American plates and symmetrical seafloor spreading initiating *c.* 150 Ma. Some minor edits have been made to simplify the boundaries between the Atlantic and proto-Caribbean in the model, however all model poles have been left unchanged. MAR = Mid-Atlantic Ridge. Cu = Cuban backarc spreading. VB = Venezuela Basin backarc spreading (see Chapter 4).

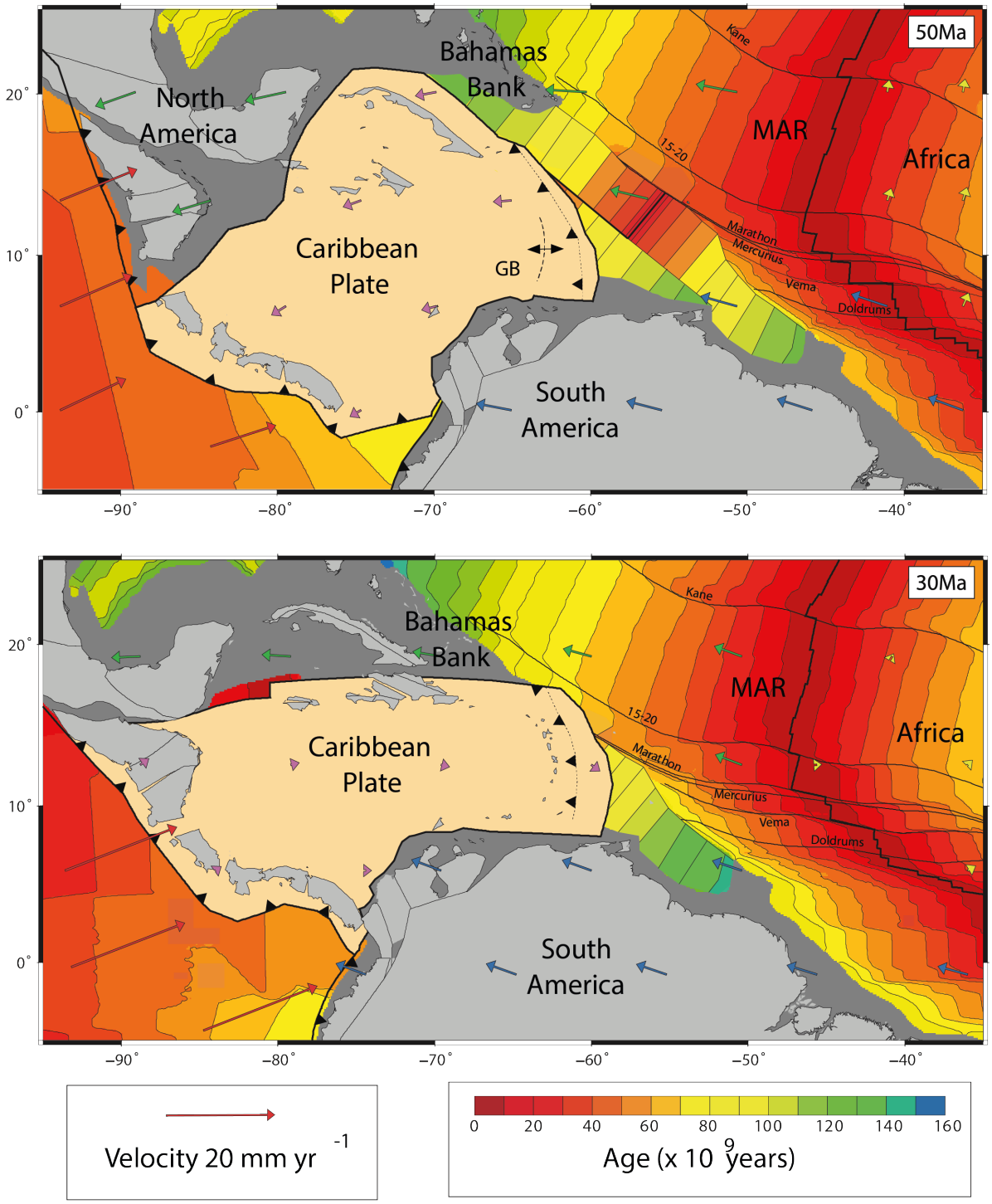


Figure 3.9: Plate reconstruction for the Caribbean region at 50 Ma and 30 Ma. During this time period the down-going slab under the eastern Caribbean transitions from the proto-Caribbean to Atlantic lithosphere. During this period a number of major structural features are subducted on the down-going slab, including the final segments of the proto-Caribbean spreading ridge and the large-offset fracture zone system in the eastern proto-Caribbean. Reconstruction generated as per Figure 3.8. GB = Grenada Basin backarc spreading (see Chapter 4).

3.5 Learnings from G-Plates Reconstructions

Given the importance of the various tectonic boundaries through time for the development of the Lesser Antilles their geometries were investigated within the framework of the recent Müller et al. (2019) global plate reconstruction (Figures 3.8, 3.9). In the Caribbean region this model is heavily based upon the work of Boschman et al. (2014), with the addition of deformable plate boundaries. Following refinements to the Atlantic - proto-Caribbean boundary, and modelling of the position of the various Atlantic fracture zones through time, these models were used by Cooper et al. (2020) to constrain the location of fracture zones along the slab, and resulting water delivery to the arc (see Appendix A for details).

By modelling these fracture zones as flowlines within the Müller et al. (2019) model in G-Plates (Appendix A) it is demonstrable that prior to the initiation of equatorial Atlantic spreading, the Marathon and Mercurius fracture zones are the most likely location of the mechanical boundary between central Atlantic spreading controlled by North American-African relative motion, and that of the proto-Caribbean dictated by North American-South American motion (Figure 3.8).

The opening of the Equatorial Atlantic from *c.* 120 Ma formed a short-lived triple junction between the northern/central Atlantic, proto-Caribbean and Equatorial Atlantic spreading systems, although as the separation of North and South America slowed through the Cretaceous, the proto-Caribbean ridge was progressively abandoned along the line of the Mercurius fracture zone (Figure 3.8). Initial central-Atlantic spreading would have occurred along a rift between the eastern extension of the Mercurius fracture zone (to the north) and proto-Caribbean oceanic crust (to the south). This is clear from the geometry of the Vema and Doldrums fracture zones (the northernmost major fracture zones formed during Equatorial Atlantic spreading), which terminate against the older Mercurius fracture zone off Africa (Figures 3.8A, A.1). The equivalent contact between these fracture zones and the crust of the proto-Caribbean in the western Atlantic has since subducted beneath the Lesser Antilles forearc, but is required in order to restore the Demerara rise against the Guinea plateau (Reuber et al., 2016).

Although almost the entirety of the proto-Caribbean ocean has now subducted beneath the Caribbean plate, a fragment still exists along the northeastern South American coast, between the Demerara Rise and the Antilles subduction zone (Reuber et al. 2016, Figure 2.1). The boundary between this proto-Caribbean material and the Equatorial Atlantic (the Demerara-

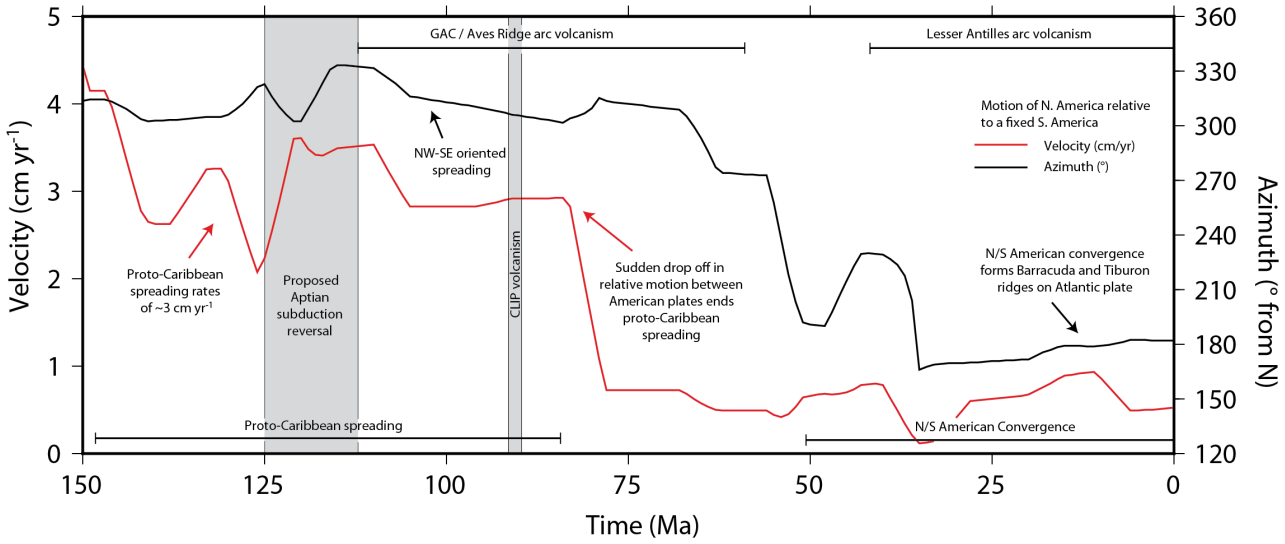


Figure 3.10: Velocity and velocity azimuth of the North American Plate relative to a stable South America from the model of Müller et al. (2019) at 16°N, -73°W, extracted using the software G-Plates. Model clearly demonstrates NW-SE orientated spreading in the proto-Caribbean region at rates of ~3 cm yr^{-1} from 150 Ma through to the Late Cretaceous, after which time North and South America begin to converge.

Guinea transform) trends north-west beneath the thick sediments of the Barbados Accretionary Prism (Pindell and Kennan, 2009; Reuber et al., 2016). Thus crust formed as a result of spreading in the proto-Caribbean likely represents a large portion of the slab beneath the south of the modern arc (for further details see Appendix A).

While it cannot be studied directly these plate reconstructions can also tell us something about the conditions under which this proto-Caribbean crust was formed. This is important as spreading rate is likely to be a key parameter when it comes to determining the concentration of structurally bound water within the down-going crust (see Section 2.3). From the initiation of seafloor spreading at ~150 Ma through to the late Cretaceous when spreading abruptly ends, the proto-Caribbean ocean is spreading at a full-rate of ~30 mm yr^{-1} (Figure 3.10). This is well below the 55 mm yr^{-1} upper cut-off for what is considered slow spreading crust (Dick et al., 2003). It is also of a similar magnitude to spreading rates in the central Atlantic today (Cande and Kent, 1992; Cogné and Humler, 2004; Müller et al., 2008). During the Early Cretaceous, when much of the Atlantic oceanic crust which is sitting at depth beneath the northern arc today would have formed, spreading rates were slightly higher at ~40 mm yr^{-1} (Cande and Kent, 1992; Cogné and Humler, 2004; Müller et al., 2008), though still well within the boundaries of what would be considered slow spreading crust (Dick et al., 2003).

Given the similar spreading rates between the modelled proto-Caribbean ocean and the modern Atlantic, the latter can likely be considered a good proxy for water distribution in that now subducted proto-Caribbean crust. We might expect asymmetric spreading, facilitated by detachment faults and the formation of core complexes to be common-place, just as it is in the Atlantic today. Furthermore, we should not expect any major difference in the levels of hydration in the slab at depth tied purely to changes in the spreading rates across the transition in the slab from subducted Atlantic to proto-Caribbean lithosphere.

3.5.1 Changes in Slab Structure

Several major structural features are subducted on the down-going plate during the Cenozoic (Figure 3.9). This includes the subduction of the large proto-Caribbean transform network around the Bahamas Platform (Figure 3.3), the final section of the proto-Caribbean spreading ridge, and the transition from the NE-SW orientated structural fabric of the proto-Caribbean crust, to the E-W orientated fabric of the central Atlantic (Figure 3.9). Each of these structures could affect the distribution of water in the subducting lithosphere. It should be noted that by the point of subduction, the final segments of the proto-Caribbean ridge would likely have been extinct for 30+ My, and as a result may not have shown any real structural differences with the rest of the subducted proto-Caribbean crust (Figure 3.9). During this time the proto-Caribbean region would also have experienced N-S shortening at rates of $\sim$1 cm yr^{-1} (Figure 3.10) as a result of convergence between the North and South American plates (Müller et al., 2019).

During the Great Arc of the Caribbean phase, subducting NW-SE orientated fracture zones would have been orientated much closer to arc parallel, likely leading to a highly episodic delivery of water into the Great Arc of the Caribbean. With the transition to the Atlantic domain, fracture zones (particularly the 15-20, Marathon and Mecurius fractures) are subducting at an angle closer to trench perpendicular, and coupled with the slower rates of subduction, are likely to result in a more spatially varying water supply along the arc over long time-periods. The rifted boundary between the crust of the proto-Caribbean and the equatorial Atlantic may also represent a hydration anomaly on the slab (Figure 3.9, Appendix A).

3.6 Key Uncertainties

The eastern Caribbean region provides a record of arc volcanism which may extend as far back as 150 My. Despite this, a combination of poor exposure, and limited regional geophysical data means that there are still major unknowns even in the relatively recent history of the Lesser Antilles arc. Amongst the most important of these uncertainties are the distribution of water within a structurally complex slab, which consists of oceanic crust formed during three distinct phases of seafloor spreading. On the Caribbean Plate, there is also limited understanding of the forces that shaped the opening of the Grenada Basin, and caused multiple stages of arc migration during the Cenozoic, first from the Aves Ridge (GAC) to the Limestone Caribbees, and then from the Limestone Caribbees to the modern arc. Understanding these processes is vital if we are to interpret the key drivers behind the distribution of crustal structure and composition beneath the modern arc. In the next chapter I use new seismic and magnetic datasets acquired in the Grenada Basin to better determine the structure of the over-riding plate, and constrain some of these major unknowns.

Chapter 4

Results: Tertiary History of the Lesser Antilles

This chapter appears as Allen et al. (2019).

Allen, R., Collier, J., Stewart, A., Henstock, T., Goes, S., Rietbrock, A., and the VoiLA Team (2019). The role of arc migration in the development of the lesser antilles: A new tectonic model for the cenozoic evolution of the eastern caribbean. *Geology*, 47(9):891–895.

Key contributions of other named authors:

Collier, J. S., Henstock, T.: Project supervisors, planned R.R.S. James Cook geophysical surveys and performed initial data processing at sea.

Stewart, A. (MSci Student, University of Bristol): Assisted understanding of regional geochemical and geochronological constraints. Wrote Section B.3 of the supplement (Appendix B) in order to expand on these arguments.

4.1 Abstract

Continental arc systems often show evidence of large-scale migration both toward and away from the incoming plate. In oceanic arc systems, however, while slab roll-back and the associated

processes of backarc spreading and arc migration toward the incoming plate are commonplace, arc migration away from the incoming plate is rarely observed. We present a new compilation of marine magnetic anomaly and seismic data in order to propose a new tectonic model for the eastern Caribbean region that includes arc migration in both directions. We synthesized new evidence to show two phases of backarc spreading and eastward arc migration toward the incoming Atlantic. A third and final phase of arc migration to the west subdivided the earlier backarc basin on either side of the present-day Lesser Antilles arc. This is the first example of regional multi-directional arc migration in an intra-oceanic setting, and it has implications for along-arc structural and geochemical variations. The back and forth arc migrations were probably due to the constraints imposed by the neighboring American plates on this isolated subduction system, rather than variations in subducting slab buoyancy.

4.2 Introduction

Arc migration is a common feature of oceanic subduction systems. When upper-plate extension results in backarc spreading, generally due to slab roll-back, arcs often split into extinct and active arc segments (Karig, 1974). This results in the movement of both the trench and active magmatic front toward the incoming plate. Arc migration in the opposite direction, however, is very unusual and rarely impacts the whole arc front (e.g., Yang et al. 1996). In contrast, in continent-ocean systems, arc migration in both directions is common. Migration away from the incoming plate of many hundreds of kilometers is often accompanied by (temporary) arc shutdown (e.g., Gerya et al. 2009). Such events are commonly attributed to the subduction of large buoyant features, such as extinct mid-ocean ridges or plateaus, which results in a flattening of the slab (Gerya et al., 2009; Martinod et al., 2013).

The eastern Caribbean is a complex region with a history of island-arc migration (Figure 4.1). Three separate subduction systems have been active at different times, although the mechanisms that relate them are disputed. The oldest volcanic system is known as the Great Arc of the Caribbean (GAC). This Cretaceous–Paleocene arc, of which the Aves Ridge is the clearest remaining expression, is identified from remnants throughout the Dutch, Venezuelan, and Greater Antilles and became extinct at ca. 59 Ma (Neill et al., 2011). Arc magmatism from 40 Ma is found on the islands of the Limestone Caribbees along the northeastern Caribbean

plate boundary. Despite a record of various early Paleocene to Eocene subduction-related rocks tracking migration eastward through the Greater Antilles toward the Virgin Islands (Cox et al., 1977; Jolly et al., 1998), convincing evidence for backarc spreading in the Grenada Basin (GB) to accompany this arc migration has yet to be found. Scarce regional seismic and well data mean that the geometry of any spreading, and the nature of the crust underlying the basin are highly debated (Bird et al., 1999). It has even been suggested that the GB is an extended forearc, leaving its role in arc migration in the Paleogene highly uncertain (Aitken et al., 2011). A further unknown is the location of the southern arc during this time. Speed et al. (1993) recognized the need for a source of volcanic sediment here during the Eocene and Oligocene, yet they found no magmatic evidence for an arc at the site of the southern modern Lesser Antilles.

The final arc migration occurred in the early Miocene, when the Limestone Caribbees became extinct and the 750-km-long modern Lesser Antilles Arc (LAA) was established to the west. It has been proposed that this event was triggered by the subduction of an oceanic ridge, causing the migration of the northern arc segment (McCann and Sykes, 1984). The southern portion of the LAA is assumed to have formed in its current location with no intermediate phase of arc magmatism between extinction of the GAC (ca. 59 Ma) and the initiation of LAA volcanism at ca. 25 Ma (Bird et al., 1999; Aitken et al., 2011).

In this study, we combined new magnetic (Figure 4.2) and seismic (Figure 4.3) datasets acquired in the GB in C.E. 2016–2017 with existing geophysical, geological, and geochronological data to test current models for the development of the LAA. We propose a new model for the tectonic evolution of the region in which the Eocene magmatism (of which the Limestone Caribbees are the only clear expression) was present to the east of the entire length of the current arc. A Miocene westward migration, again along the entire arc front, then divided the previous backarc into the GB and Tobago Basin (TB). The model explains several of the disputed aspects of the region's development and is more consistent with current geodynamical models of subduction behavior. It has significant implications for our understanding of both the structural variations along the LAA and the geochemistry of its magmatic products. We consider it a unique example of a retreating and advancing magmatic front in an oceanic arc setting.

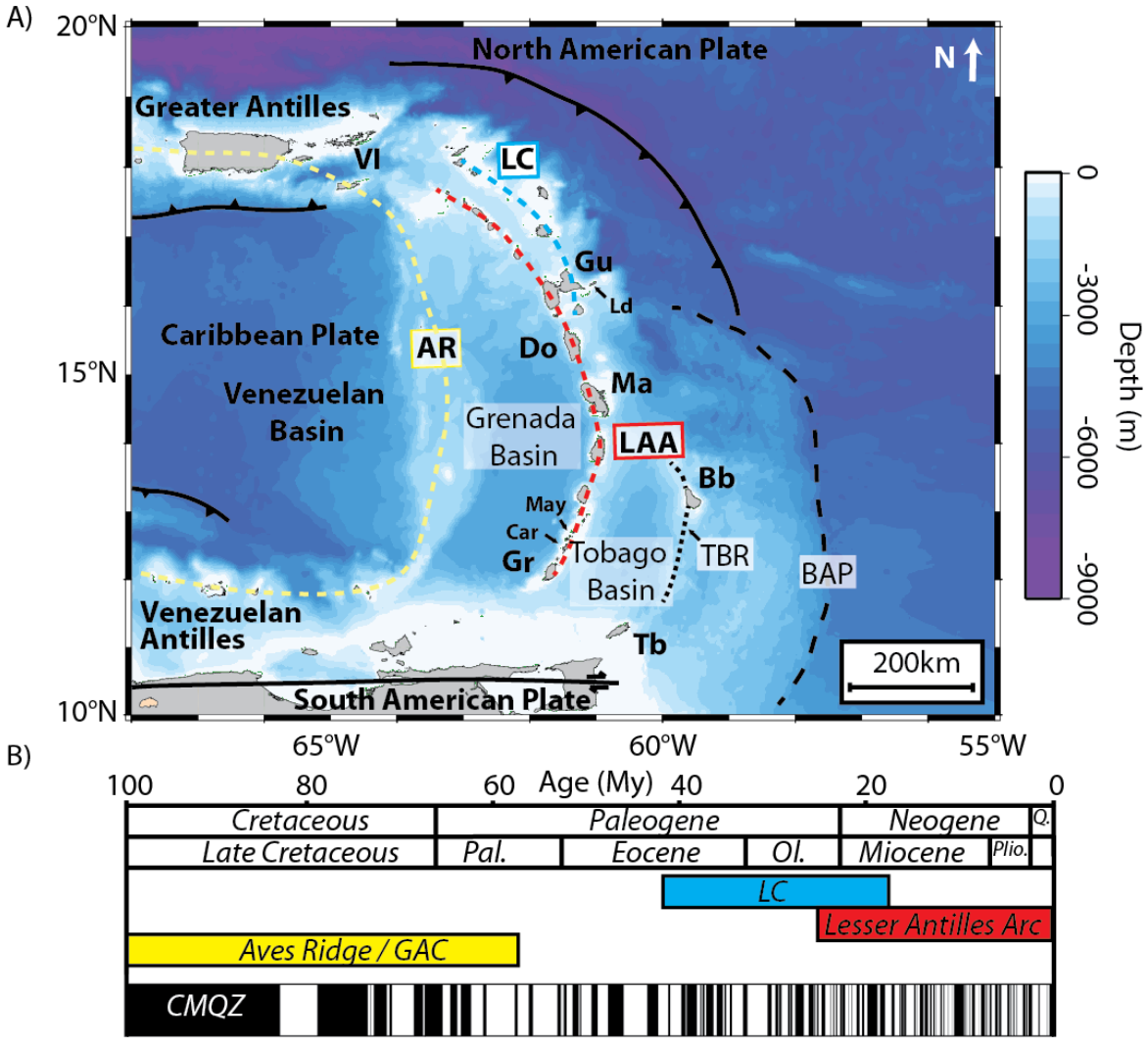


Figure 4.1: A) Map of the Lesser Antilles region highlighting the major tectonic features. Abbreviations: LAA—Lesser Antilles arc (red dashed line), LC—Limestone Caribbees (blue dashed line), AR—Aves Ridge (yellow dashed line), VI—Virgin Islands, BAP—Barbados accretionary prism, TBR—Tobago-Barbados Ridge. Individual islands: Gu—Guadeloupe, Ma—Martinique, Gr—Grenada, Bb—Barbados, Tb—Tobago, May—Mayreau, Car—Carriacou; Ld—La Désirade; Do—Dominica. B) Temporal framework of arc magmatism in the eastern Caribbean. A full breakdown of tectono-magmatic affinities and geochronology is provided in Appendix B, Section B.3. GAC—Great Arc of the Caribbean; LC—Limestone Caribbees; CMQZ—Cretaceous magnetic quiet zone. The geomagnetic polarity time scale is shown for reference (Cande and Kent, 1995). Q—Quaternary; Pal—Paleocene; Ol—Oligocene; Plio—Pliocene.

4.3 New Model for the Evolution of the Lesser Antilles

Figure 4.2A shows our new reduced-to-pole magnetic anomaly chart for the study area. It is a levelled compilation of over 320 scientific cruises from 1950 to 2017 (full processing details are provided in Appendix B, Section B.2) and is a significant improvement on existing charts for the region (Ghosh et al., 1984). Two of these cruises, JC133 and JC149 on the R.R.S. James Cook (Collier, 2017), conducted as part of the VoiLA project, also acquired north-south–oriented multichannel seismic reflection and wide-angle refraction profiles in the GB (Figure 4.3). Wide-angle profiles (full processing details are provided in Appendix B, Section B.2) were modeled using the software RAYINVR (Zelt and Smith, 1992), and together these datasets allow us to offer new insights into the structure and evolution of this historically data-poor region.

The LAA is clear in our magnetic grid as a strong positive anomaly (Figure 4.2). A parallel anomaly of similar character is visible to the east beneath the older Limestone Caribbees. However, rather than merging with the modern arc around Martinique, as in current tectonic models, it extends southward as an unbroken arc, buried beneath the thick sediment of the Barbados Accretionary Prism. This "outer arc" magnetic anomaly passes ∼15 km west of the island of Barbados and the so-called Tobago-Barbados Ridge (Figure 4.1), both of which are thought to be uplifted sections of prism sediments (Gomez et al., 2018). Given its depth of burial (in excess of 10 km, making gravity modeling and seismic imaging of the basement crust difficult), it is the magnetic signature that makes it stand out. The outer arc anomaly terminates against a similar positive anomaly of the Tobago terrane to the south (a Late Cretaceous GAC fragment trapped on the leading edge of the Caribbean plate; Boschman et al. 2014). We interpret the anomaly as evidence for the southward extension of Limestone Caribbees arc magmatism along the whole front of the eastern Caribbean plate boundary during the late Paleogene.

A region of dominantly reverse polarity is visible on either side of the LAA within the southern GB and TB, extending as far north as Dominica and Martinique (Figure 4.2). This regional reverse polarity is consistent with slow backarc opening in the over-riding plate during the dominantly reverse magnetic polarity chrons C26 to C18 (60–40 Ma; Figure 4.1) as arc volcanism migrated from the Aves Ridge to its easternmost location during the Eocene. We propose that a final westward (away from the incoming plate) arc migration in the late Oligocene and

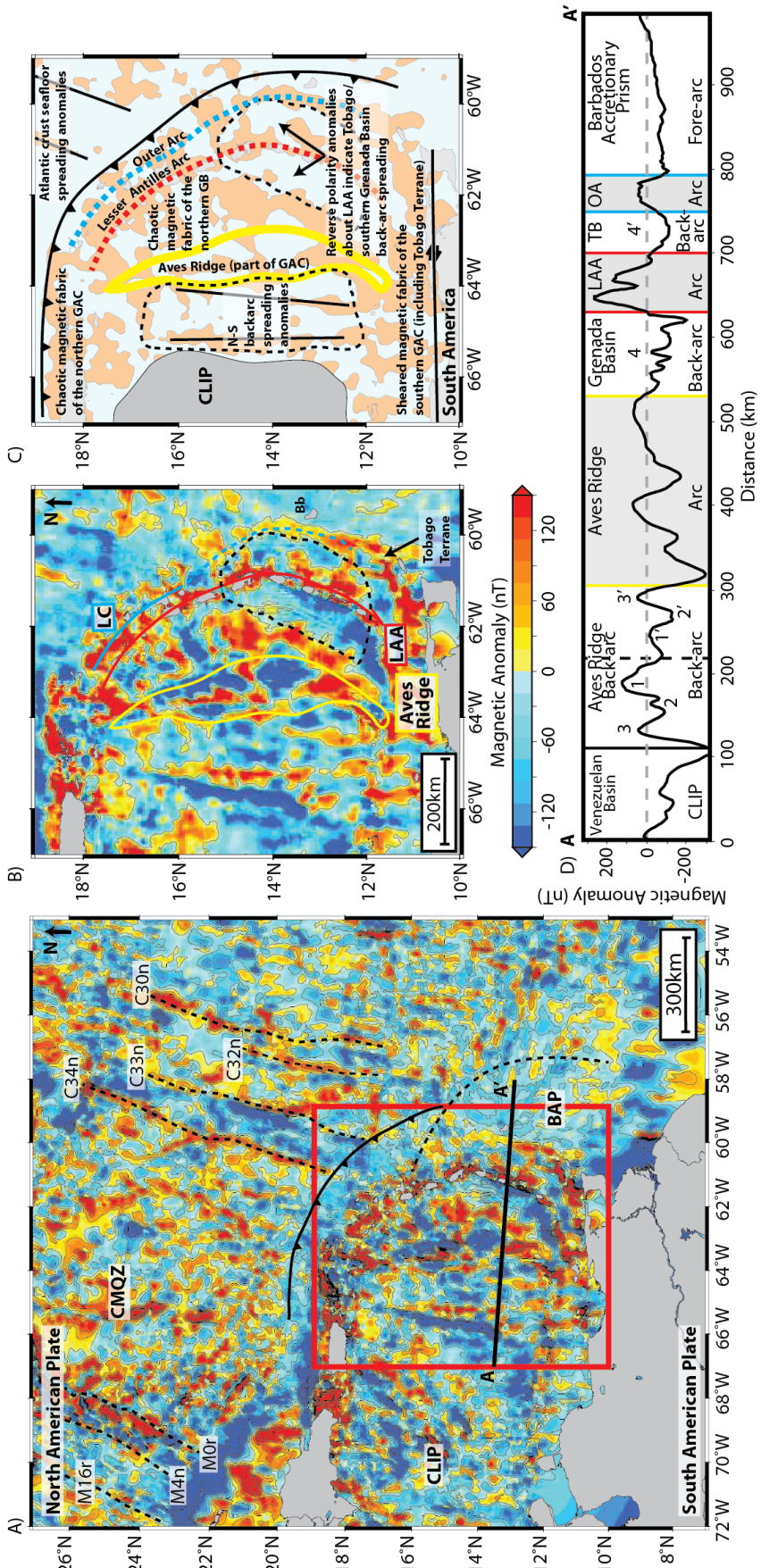


Figure 4.2: A) New regional magnetic anomaly grid. CLIP—Caribbean large igneous province; BAP—Barbados accretionary prism; CMQZ—Cretaceous magnetic quiet zone. (B) Detail of new magnetic anomaly grid over the Aves Ridge (outlined in yellow), Lesser Antilles arc (LAA, red line), and Outer arc (blue line marked with LC [Limestone Caribbees]). Black dashed line denotes potential extent of backarc spreading. Bb—Barbados. (C) Cartoon of key features in the anomaly grid over the LAA. Regions of normal magnetic anomaly polarity are shown in orange, with reverse in blue. (D) Cross section through magnetic grid along the profile shown in A. Magnetic highs are associated with Aves Ridge, LAA, and outer arc magmatism. Note symmetrical spreading anomalies in the Aves Ridge backarc and Grenada Basin (labeled 1–1', etc.). GB—Grenada Basin; TB—Tobago Basin; OA—outer arc.

establishment of the LAA divided the Paleogene backarc basin into the GB and TB. A common origin for these two basins has been proposed previously (Aitken et al., 2011). In our model, the geometry of these basins and their magnetic anomalies implies that the islands of the southern LAA now occupy the axis of the previous backarc spreading.

Backarc spreading in the southern GB and TB is supported by uplifted Paleocene–mid-Eocene submarine basalts and volcanogenic sediments on many of the southernmost islands of the LAA (e.g., the Mayreau Basalt and Anse Bandeau formation of Mayreau, ca. 50–46 Ma; Speed et al. 1993; see the Data Repository for further details). The chemical and isotopic compositions of these rocks are consistent with a depleted backarc source (Speed and Walker, 1991; White et al., 2017). Paleocene to mid-Eocene xenocrystic and detrital zircons found throughout the Grenadines possess a rare earth element composition that suggests they crystallized from magma produced from a much less oxidized mantle than the sources of the modern arc, again consistent with a backarc origin (Rojas-Agramonte et al., 2017).

Wide-angle seismic data (profile 4; Figure 4.3F) further support our interpretation of backarc spreading in the southern GB. Here, thick (up to 11 km), flat-lying sediments overlie a structurally homogeneous 6–7-km-thick crust with a typical oceanic velocity structure (Figure 4.3D). Oceanic crust was also interpreted by Christeson et al. (2008) in the far south of the basin and is likely to extend as far north as southern Martinique. Our new seismic reflection data show a smoothly undulating basement surface (Figure 4.3), with no evidence for an east-west–striking spreading center as previously suggested (e.g., Pindell and Kennan 2009).

In the northern GB, the crust thickens northward from 15 to ∼27 km (Figure 4.3E). Wide-angle modeling requires a high velocity gradient upper crust (4.5-6.6 km s^{-1}) and thick (>10 km) lower crust (6.8-7.2 km s^{-1}), similar to that observed beneath the arc by Kopp et al. (2011) near Guadeloupe. This crustal thickness rules out backarc spreading, and we interpret it as resulting from older arc magmatism in the over-riding plate. Structural heterogeneities displayed in the rough seafloor/basement topography (Figure 4.3B) and the chaotic magnetic fabric of the northern GB are the result of the complex tectonic history of the over-riding plate and GAC magmatism. In contrast to the southern LAA, the islands of the northern LAA developed upon this older arc crust. Support for this comes from the island of La Désirade, where basement volcanic rocks give radiometric ages as old as the Late Jurassic (Neill et al., 2010).

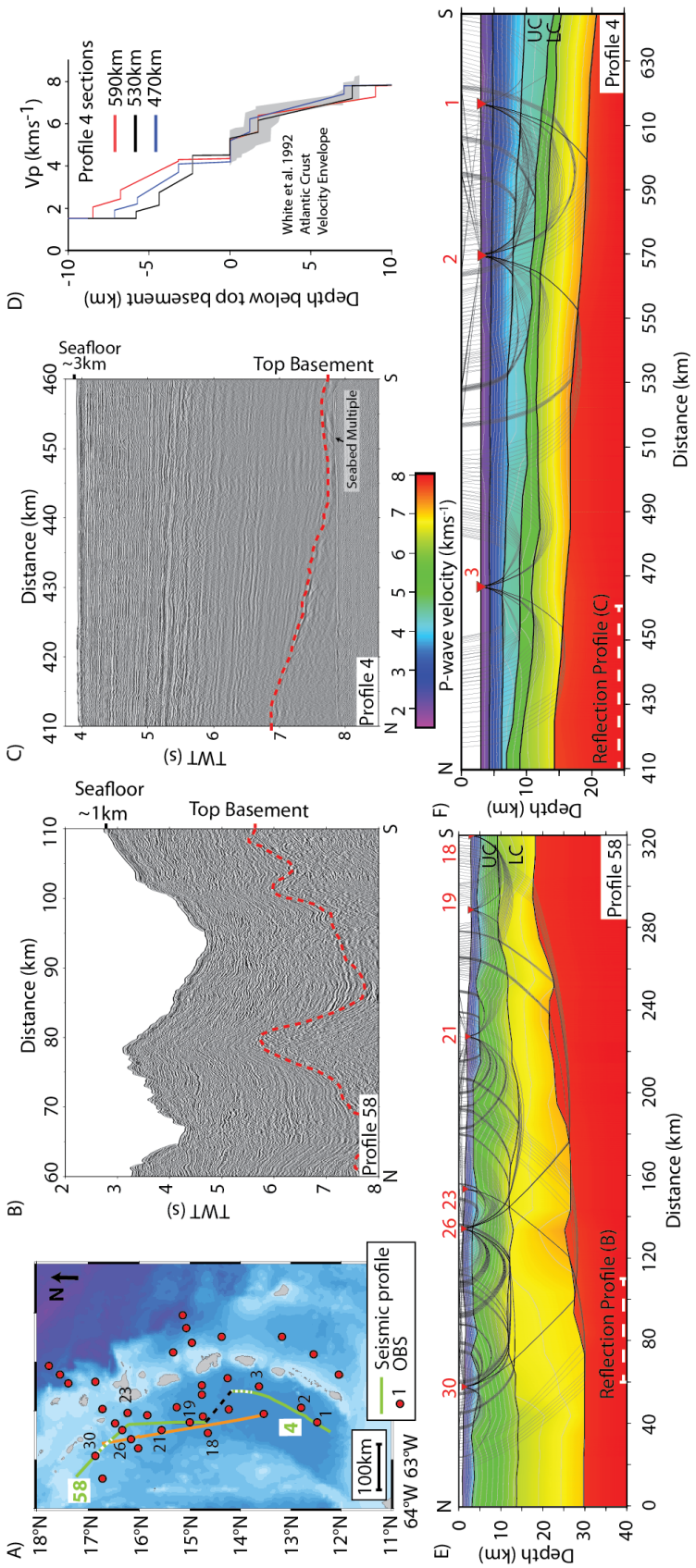


Figure 4.3: Crustal structure of Grenada Basin (GB). (A) Location of seismic reflection/refraction profiles (green) shot by the Volatile Recycling in the Lesser Antilles (VoiLA) project as part of R.R.S. James Cook cruise JC149. Dashed white sections show subset of reflection profiles plotted in B and C. Orange profile gar1 is from the GARANTI 2017 experiment in the GB (R/V L'Atalante; Lebrun, 2017, personal commun.). Travel times from this experiment supplemented our own dataset for wide-angle modeling at long offsets along profile 58. OBS—ocean-bottom seismometer. (B) Section of two-dimensional seismic profile 58 in the northern GB. (C) Section of two-dimensional seismic profile 4 in the southern GB. (D) One-dimensional velocity profiles at three points along refraction profile 4 (Figure 4.3F), corrected to top basement and compared to the Atlantic crust oceanic velocity envelope from White et al. (1992). (E) P-wave velocity model for VoiLA project profile 58 in the northern GB; 1 in 10 of modeled rays are shown. UC—upper crust; LC—lower crust. (F) P-wave velocity model for VoiLA project profile 4 in the southern GB.

The transition between oceanic crust formed through backarc spreading and the thicker arc-like basement of the northern GB must occur in the region between our seismic profiles in the backarc off Martinique. This is coherent with the boundary of the region of oceanic crust identified in magnetic datasets (Figure 4.2C).

4.4 Implications

From our synthesis of magnetic and seismic data in the eastern Caribbean, together with a consideration of regional magmatic ages and tectono-magmatic affinities, we propose a new model for the development of the Lesser Antilles Arc (Figure 4.4).

Slab roll-back from ca. 59 Ma triggered extinction of the Aves Ridge and the eastward migration of the arc front. Thick crust, likely formed along the GAC, which underlies the northern GB, implies that upper-plate extension here was insufficient to trigger backarc spreading. South of the modern day location of the island of Dominica, a north-south–striking spreading ridge created a new backarc basin up to 250 km across. This opening was probably facilitated by the large strike-slip fault systems of the South American margin (e.g., the San Sebastian [offshore Venezuela] and El Pilar [northern Venezuela] faults; Pindell and Kennan 2009), in marked contrast to the collisional boundary between the northern Caribbean and the Bahamas Bank. Between ca. 40 and 25 Ma, the outer arc was formed, although only the northern part is exposed today as the islands of the Limestone Caribbees.

Post–25 Ma, the arc migrated westward into its own backarc, obscuring the southern spreading center and separating the TB from the southern GB. This resulted in a notable difference in the late Miocene sedimentary succession of the two basins (Aitken et al., 2011). The presence of thick backarc sediments in the south provides a possible explanation for some of the isotopic systematics of the southern LAA magmas, which cannot be explained by sediment contributions from the down-going plate alone, and which require sediment assimilation during differentiation within the crust (Davidson and Harmon, 1989; Bezard et al., 2014).

We interpret the Cenozoic history of back-and-forth arc jumps as externally driven by the interaction between the Caribbean and adjacent North and South American plates. The western Atlantic lacks the large-scale, down-going plate buoyant topography that is held responsible

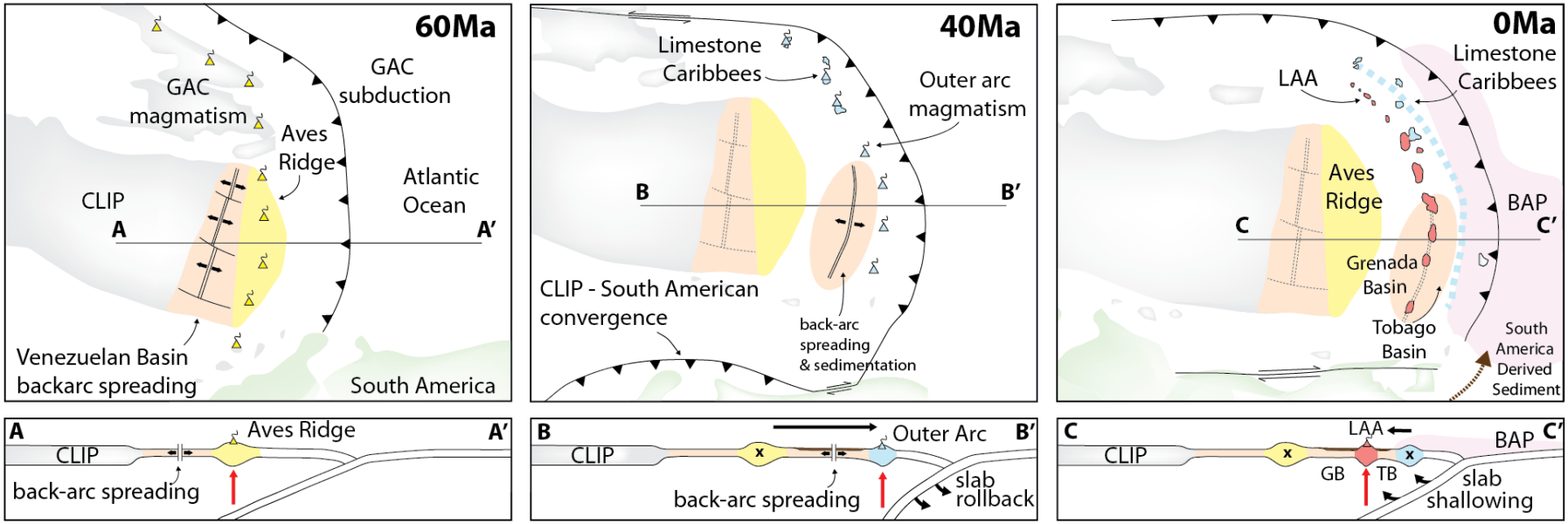


Figure 4.4: Cartoon of new tectonic model for the eastern Caribbean region. Locations of key tectonic blocks are based upon the reconstruction of Boschman et al. (2014). 60 Ma: Regional arc magmatism associated with the late stages of the Great Arc of the Caribbean (GAC). Evidence for this arc is found in the rock record of several island groups, including the Dutch, Venezuelan, and Greater Antilles, as well as in dredged samples from Aves Ridge. CLIP—Caribbean large igneous province. 40 Ma: Slab rollback has led to abandonment of the Aves Ridge and eastward migration of arc volcanism. New Outer arc includes the islands of the Limestone Caribbees to the north. Backarc spreading is limited to the south, with a north-south–oriented spreading axis. 0 Ma: Slab shallowing forces the abandonment of the Outer arc and establishment of the modern Lesser Antilles arc (LAA) to west. Arc volcanism has divided the former backarc basin into Tobago (TB) and Grenada (GB) Basins in the south. Direct evidence for southern extension of the Outer arc is buried beneath the Barbados accretionary prism (BAP).

for regionally flattening the slab and arc migration in continental arcs such as South America (Martinod et al., 2013). Small features such as the Barracuda and Tiburon Ridges, which are being subducted beneath the LAA today, are likely insufficient to cause whole arc migration (Gerya et al., 2009), particularly if the subduction system is driven by far-field forcing (Martinod et al., 2013) from the westward motion of North and South America past the Caribbean. Instead, changes in the motions of the Americas could have driven slab shallowing, thus triggering westward advancement of the arc. An increase in North American–South American convergence and the eastward motion of the arc beyond the large boundary faults of the South American continent (Boschman et al., 2014) might have contributed to readjustment of the arc position.

We believe that this is the first observed case of the regional-scale migration of an intra-oceanic magmatic arc away from the incoming plate. As well as shedding new light on the tectonic history of the eastern Caribbean region, these results have significant implications for our understanding of the behavior of intra-oceanic subduction zones, and in particular highly constrained subduction systems such as the LAA.

Chapter 5

Results: Structure of the Tiburon Basin

5.1 Abstract

In the previous chapter it was demonstrated how the inherited structures of the over-riding Caribbean plate are likely to have an ongoing influence over the modern Lesser Antilles arc. In the following chapters we examine the role played by variations in the incoming plate. The oceanic lithosphere seaboard of the Antilles is highly heterogeneous. Seafloor ridges, such as the Barracuda Ridge and fracture zones, along with the rifted boundary between portions of the slab produced by Atlantic and Proto-Caribbean spreading are all currently subducting beneath the arc. Such features influence local sedimentary processes, lithospheric hydration and slab buoyancy, all of which are likely to be reflected in arc processes. The Tiburon Basin is situated in the centre of the down-going plate, outboard of the islands of Guadeloupe and Dominica in the central portion of the arc. These islands play host to some of the arc's thickest crust and highest rates of volcanism and seismicity. As such the Tiburon Basin is a prime location for understanding the relationships between the incoming plate and potentially hazardous arc behaviours.

In this chapter we present a new 2D multichannel profile, and corresponding wide-angle and bathymetric surveys across the incoming sediments and accretionary prism at the Tiburon

Basin. We compare these data with existing well and regional seismic data in order to better understand variations in basement structure and sedimentation across the incoming plate. The overall make-up of the sediments on the incoming plate is shown to be consistent with other recent studies of the region. Reduced seismic velocities within the accretionary prism are indicative of an over-pressured subduction interface, while a low taper angle may reflect an erosive subduction margin along the northern part of the arc. Variations in basement topography are likely to be heavily influencing patterns of seismicity along the shallowest part of the plate boundary.

5.2 Introduction

The Lesser Antilles arc shows major north-south variations in both the thickness and composition of the subducting sediments. In the north of the arc the sediment column is dominated by clay rich pelagic and hemi-pelagic sediments accrued in the Atlantic (Benson et al., 1970; Pichot et al., 2012). In the south terrestrial sediments from the South American continent are deposited onto the incoming plate, including a several kilometers thick contribution of distal turbidites from the outflow of the Orinoco River. Northward these turbiditic flows are obstructed by a series of basement ridges (Figure 5.1), such as the Tiburon Rise at $\sim$15° N (Westbrook, 1982). This change in sediment make-up is observed not only in local well and seismic data but also in the structural trends of the Barbados Accretionary Prism, which becomes both thicker and broader southward as it incorporates increasingly large volumes of sediment. In the southernmost forearc the resulting total thickness of accreted sediments may reach 20 km (Gomez et al., 2018). North-south variations in seismicity and arc lava geochemistry have been tied to these changes in the pattern of sedimentation on the incoming plate (Section 2.2).

As much as 46 % of the water stored within the oceanic lithosphere is found in the pore space of subducting sediments and the shallow crust (Hacker, 2008). A complex feedback relationship between factors such as the lithology and diagenetic processes within subducting sediments, convergence rate, stress regime and temperature dictates the behaviour and movement of fluids along the plate interface (Saffer and Bekins, 2002; Heise et al., 2013). One of the most important links between sedimentary processes on the incoming plate (and within the accretionary prism) and arc behaviours is seen in their influence over seismicity. In the simplest cases high fluid

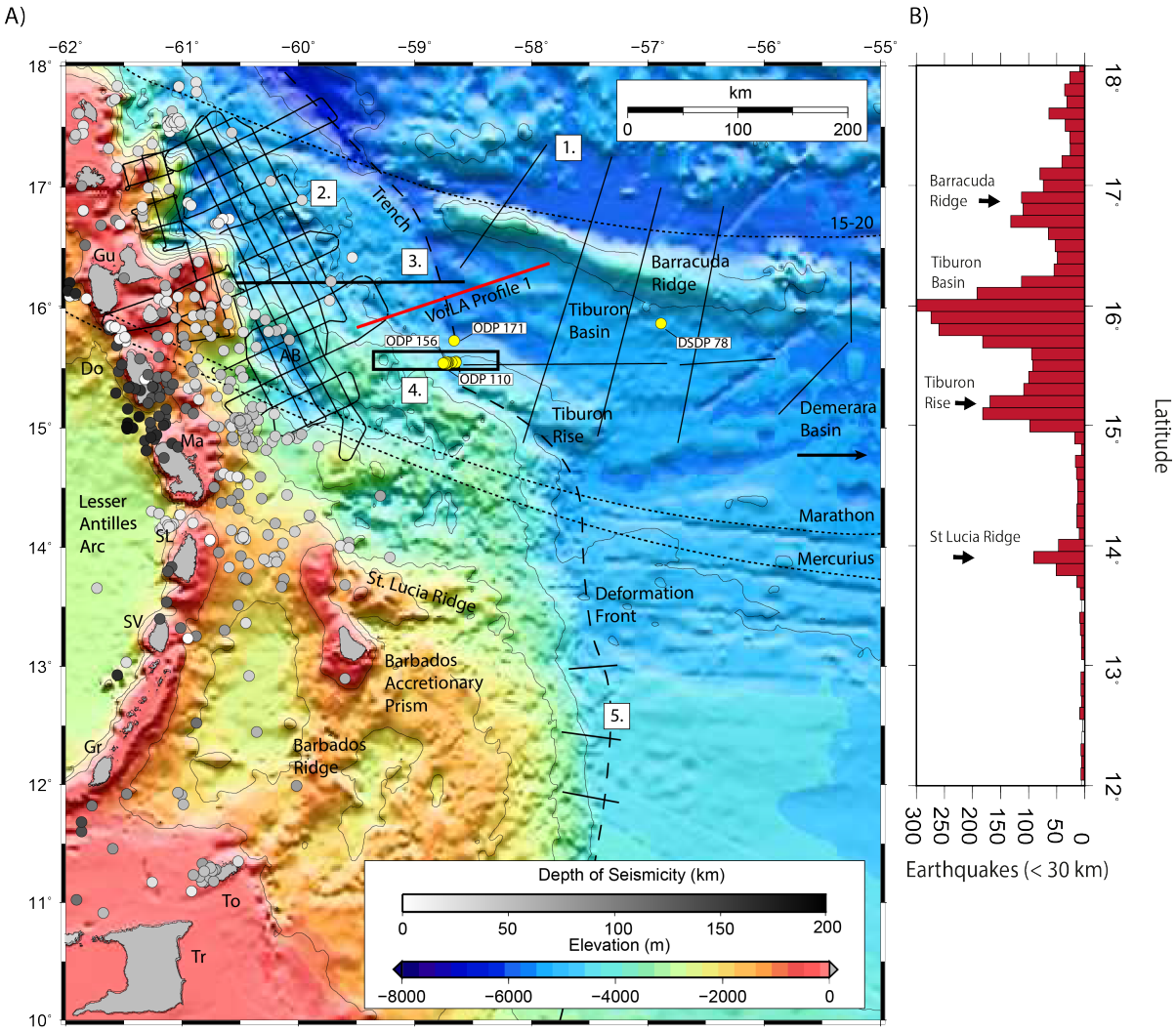


Figure 5.1: VoiLA experiment Profile 1 regional setting. A) VoiLA Profile 1 consisting of corresponding wide-angle and multichannel surveys is shown in red. Other seismic surveys are shown in black. 1: 2D reflection profiles from Pichot et al. (2012), 2: reflection and wide-angle profiles from Evain et al. (2013); Laigle et al. (2013), 3: Regional 2D reflection profile from Westbrook et al. (1988), 4: 5x25 km 3D reflection survey and regional 2D profile from Moore et al. (1996), 5: 2D reflection profiles from Biju-Duval et al. (1982). Yellow circles denote location of ODP and DODP drill sites on the incoming plate and accretionary prism. Grey circles show the location of earthquakes recorded by the VoiLA OBS and landstation deployment in 2016-2017 (Bie et al., 2020). Note the relatively low rates of seismicity in the south of the arc. Abbreviations are as follows Gu: Guadeloupe, Do: Dominica, Ma:Martinique, SL: St. Lucia, SV: St. Vincent, Gr: Grenada, To: Tobago, Tr: Trinidad, AB: Arawak Basin. Dashed black lines show projected location of major fracture zones, modelled as flow lines in the plate reconstruction of Müller et al. (2019), see Appendix A. B) Histogram of seismicity in the Lesser Antilles forearc between 1964-2020, extracted from the ISC seismic catalog. All events shown occur at 30 km depth or shallower (between -58° and -61° W). Note the large increase in the rate of seismicity north of the Tiburon Rise, as well as localized highs associated with the Barracuda Ridge, Tiburon Rise and St. Lucia Ridge. Some of these events are likely to be within the forearc crust of the over-riding plate.

pressures along the décollement (the interface between subducted and accreted sediments), often in combination with a thick subduction channel, can reduce effective stresses across the plate interface and promote stable aseismic sliding (Heise et al., 2017; Saffer, 2017). High fluid pressures may also be a requirement for the generation of slow slip events (Kodaira et al., 2004). Conversely, reduced fluid pressures increase interplate coupling and promote seismic failure.

In the Antilles, Bie et al. (2020) observed two distinct trends in the shallowest interplate seismicity. South of Martinique interplate earthquakes do not occur until depths of ∼30 km. This is as much as 20 km deeper than in the north. Overall rates of interplate seismicity are also much lower in the south than in the north (Figure 5.1). Although previous studies have suggested a link between hydration of the crust and mantle at fracture zones and varying rates of seismicity along the arc, such chemically-bound fluids are not released prior to depths of 50-80 km and are unlikely to explain these trends on the very shallowest part of the plate interface (Schlaphorst et al., 2016; Paulatto et al., 2017).

Given the stark north-south changes observed in the composition and structure of subducting sediments along the Lesser Antilles it is likely that they play a role in dictating seismic processes along the arc. The Tiburon Basin currently subducts beneath a central section of the arc that boasts the thickest crust (Schlaphorst et al., 2018; Melekhova et al., 2019) and highest rates of seismicity (Bengoubou-Valerius et al., 2008; Schlaphorst et al., 2016) and volcanism (Wadge and Shepherd, 1984). In this chapter I present a new 2D seismic profile and coincident bathymetry data from the Tiburon Basin. Multichannel seismic imaging of the structure of the sediments on the incoming plate and geometry of the accretionary prism, coupled with a new Vp velocity model are used to examine the nature of the subduction channel, and the influence that the structure of the Tiburon Basin has over potentially hazardous arc activity.

5.3 Sedimentation on the Incoming Plate

The Tiburon Basin is constrained by the Tiburon Rise to the south, and the Barracuda Ridge to the north. These features formed as a result of deformation along the diffuse North American - South American plate boundary within the Atlantic (Roest and Collette, 1986; Shipley et al., 1997; Patriat et al., 2011; Pichot et al., 2012). The relative pole of rotation for the North and South American plates currently lies at approximately 160.6° N, 53.5°W resulting

in compression to the west (Roest and Collette, 1986). On the basis of local stratigraphic relationships Pichot et al. (2012) concluded that the main phase of uplift at the Tiburon Rise occurred in the Mid-Late Miocene. This timing is constrained by Neogene sediments onlapping on to Miocene deposits in a trough south of the ridge (based on seismic correlation with dated intervals within the Tiburon Basin itself). A series of mass transport deposits which derive from the Tiburon Rise also post-date uplift. The Tiburon Rise has largely subducted beneath the Lesser Antilles forearc, uplifting the accretionary prism and the northern boundary of the Arawak basin (Evain et al., 2013; Laigle et al., 2013). The Barracuda Ridge is younger, the result of deformation across the buried trace of the Fifteen-Twenty fracture zone, as recently as the Pleistocene (Patriat et al., 2011; Pichot et al., 2012). The lag between uplift on the two ridges is the result of the northward migration of the North - South American rotation pole during this period (Muller et al., 1993).

The uplift of the Tiburon Rise and Barracuda Ridge led to abrupt changes in the nature of the subducting sediment column along the arc. These ridges act as a barrier to the northward transport of distal turbidites from South America which comprise much of the thickness of the post-Miocene sedimentary sequence to the south and east (Pichot et al., 2012). To the south of the Tiburon Rise, sediment thicknesses on the incoming plate exceed 4 km (Biju-Duval et al., 1982), increasing to as much as 7 km south of 11° N (Moore et al., 1988). North of the Rise a dense 5 x 25 km 3D seismic experiment (acquired by the R.V. Maurice Ewing, see Figure 5.1) observed a full sediment package of less than 1 km at the toe of the accretionary prism (Shipley et al., 1994, 1997). Quaternary deposits in the Tiburon Basin are as much as 1 sTWT thinner than in the Demerara basin (to the east), where terrigenous sediment flows are not disrupted by the two ridges (Embley et al., 1970; Pichot et al., 2012).

5.4 The Barbados Accretionary Prism

Variations in the thickness and composition of sediments along the incoming plate lead to corresponding changes in the along-strike structure of the Barbados Accretionary Prism. This is clear in the sheer volume of accreted sediments, particularly south of the St. Lucia Ridge (a compressional feature, similar to the Tiburon Rise and Barracuda Ridge, which has now been fully subducted beneath the forearc at ∼13.5° N, Figure 5.1). In the south as much as

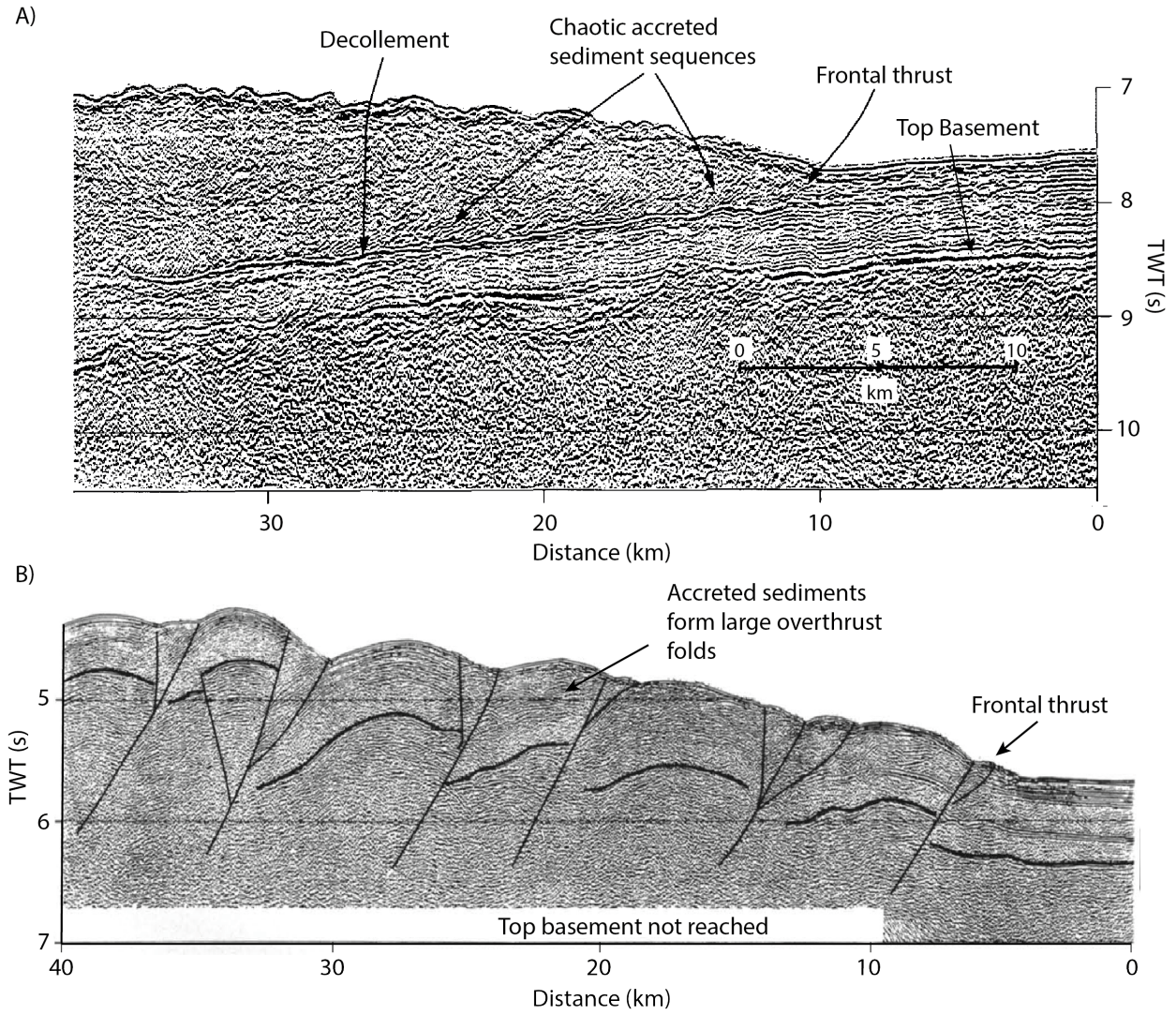


Figure 5.2: North-south variations in structure of the Barbados Accretionary Prism. A) Reflection profile over the toe of the accretionary prism from Westbrook et al. (1988) at ∼16.5° N. A thin accreted sediment package leads to chaotic, short wavelength sedimentary structures within the prism which are difficult to resolve. B) Southernmost reflection profile over toe of the accretionary prism from Biju-Duval et al. (1982), situated at ∼12° N. Here the much thicker overthrust sediment package forms distinct, coherent folds.

1.5 km of sediment is currently incorporated into the accretionary prism above the décollement (Westbrook, 1982). As a result the accretionary prism completely fills the trench, spilling out onto the incoming plate and blanketing the outer rise high (Westbrook, 1982). North of the Tiburon Rise the thickness of the currently accreting sediment package falls to as little as 200 m (Moore et al., 1996).

The overthrust sediments of the accretionary prism are largely structureless to the north of

the Tiburon Rise (Westbrook 1982, Figure 5.2). In the southern arc accreted sediments form packages of large over-thrust folds several kilometres across (Biju-Duval et al. 1982, see Figure 5.2), a product of both the thicker accreted section, and a lower clay content in the southern, terrestrial dominated sediments leading to more competent deformation (Westbrook, 1982) and abundant mud volcanism (Brown and Westbrook, 1988; Lance et al., 1998).

Modelling of the seismic response of the décollement from the Ewing 3D survey over the Tiburon Rise (Figure 5.1), in combination with rock property data from local ODP boreholes have shown that the décollement predominantly forms along a thin, anomalously porous, Miocene radiolarian mudstone bed (Moore et al., 1988; Shipley et al., 1994; Zhao et al., 2000). This interval may be as thin as 14 m in places yet consistently forms the décollement within the 125 km^2 Ewing survey area due to an ability to maintain very high fluid pressures under shear stress, often resulting in a strong negative impedance reflection in seismic data. Pore fluid over-pressure results in decoupling of the highly deformed sediments above the décollement from those below (Housen et al., 1996), and channelized trenchward fluid migration within the décollement (Shipley et al., 1994; Bangs et al., 1996, 1999). This demonstrates how sensitive fluid, and by extension seismic processes might be to even minor changes in the structure of the subducting sediment package. Yet prior to this study, most recent detailed seismic studies in the basin comes from either directly on, or adjacent to the Tiburon Rise (Shipley et al., 1994; Bangs et al., 1996), or Barracuda Ridge (Pichot et al., 2012; Evain et al., 2013; Laigle et al., 2013). In these locations the post-Miocene succession is clearly thinner as a result of basement uplift and focused north-south compressional deformation. Such studies may therefore not be representative of the subduction channel across the majority of the arc front.

5.5 The VoiLA experiment: Data Acquisition

The VoiLA experiment acquired 2D seismic (multichannel and wide-angle profiles) and local bathymetry data across a 174 km profile in the Tiburon Basin. This data was acquired from the research vessel, the R.R.S. James Cook in May 2017 as part of the VoiLA (Volatile recycling in the Lesser Antilles) experiment (Collier, 2017). The coincident wide-angle and multichannel profiles cover ∼74 km of the accretionary prism and ∼100 km of the incoming plate (Figure 5.1). This is the first profile within the basin to provide such a continuous transect, giving

a direct comparison between sedimentary processes on the incoming plate, and corresponding structures within the accretionary prism.

5.5.1 Bathymetry Data

Swath bathymetry data was collected using a Kongsberg EM120 multibeam echosounder, with an operating frequency of 12 kHz, angular coverage of 150 degrees, and 191 beams per ping. Data was then processed in the software CARIS Hips in order to remove spurious depth points (Figure 5.3). The data shows a relatively flat seafloor (∼5.5 km depth) on the incoming plate, with a slight shallowing across the outer rise. An increase in faulting at the seabed is also visible in this region from the bathymetry gradient data (Figure 5.3C), starting ∼60 km seaward of the accretionary prism. The frontal thrust at the toe of the accretionary prism is coincident with the location of OBS28. The accretionary prism shallows across the first ∼25 km before flattening at a depth of ∼5 km across the remainder of the profile. The structure of the seafloor is consistent perpendicular to the OBS profile, thus the results from Profile 1 are likely representative of the structure of the majority of the central Tiburon Basin.

5.5.2 Multichannel Seismic Data

Multichannel data was acquired sailing east to west using a 13 gun, 3750 cu in. array towed at a depth of 9 m, with shots every 20 s giving an approximate 50 m shot separation. Shots were recorded by a 3 km streamer consisting of 240 hydrophones and towed at a depth of 8 m, resulting in a fold of 30 traces per CDP gather. Whilst shooting in the vicinity of OBS28 (i.e. ∼100 km into the profile, near the foot of the accretionary prism), the total array volume was reduced to 3350 cu in. due to an air leak in one of the guns which was shut out to enable firing to continue. Some anomalous noise bursts (potentially from one of the small 200 cu in. guns double firing) were also detected episodically on streamer channel 1. Sea-state was calm throughout profile acquisition (Beaufort scale, Force 2). The 2D multichannel profile was processed in the software SeisSpace 3D. Following initial geometry assignment and CDP binning (traces assigned to 6.25 m bins), processing consisted of an Ormsby Bandpass Filter (3-8-40-70 Hz), predictive deconvolution (200 ms operator, 100 ms operator prediction distance) and

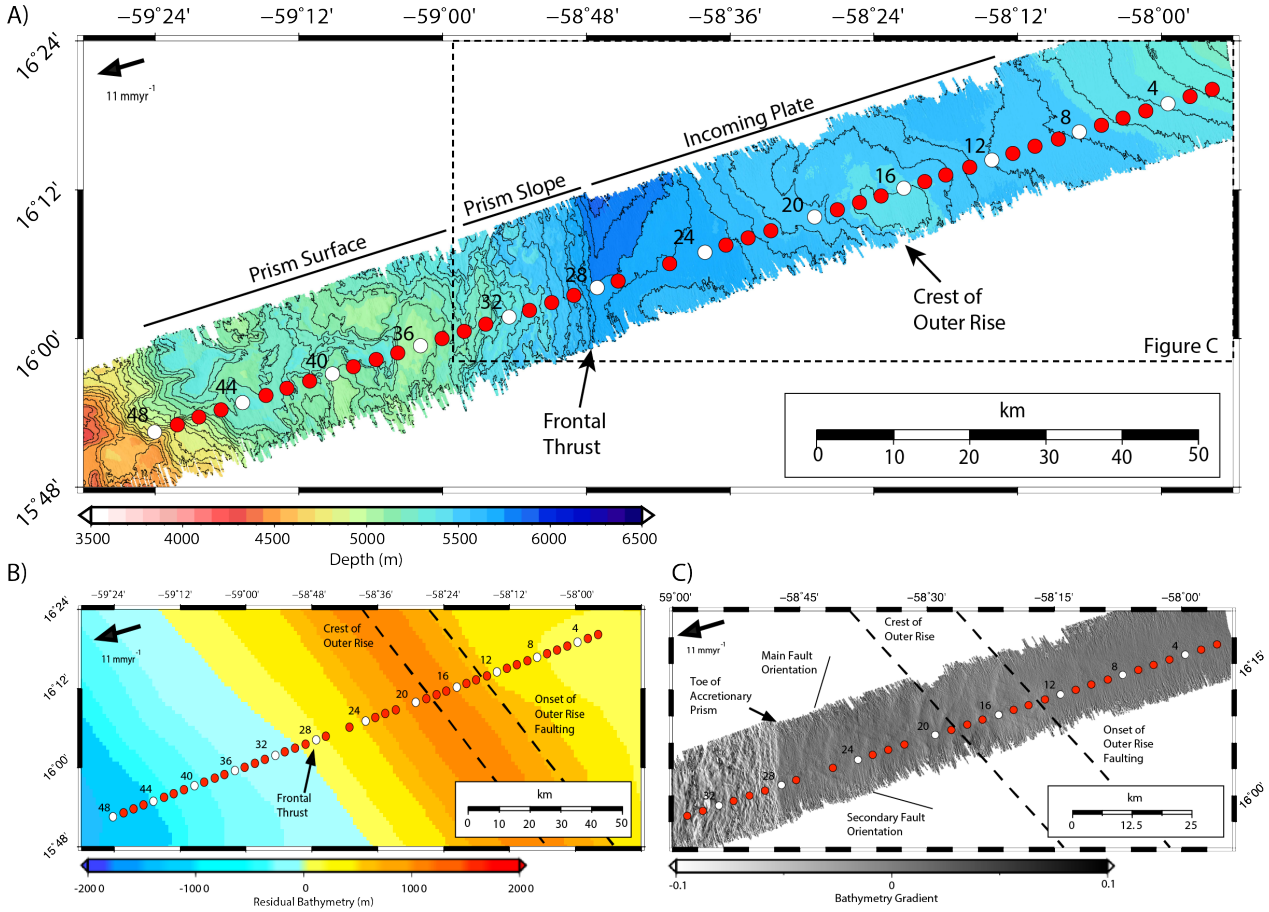


Figure 5.3: Bathymetry data acquired across Profile 1 survey area. A) Full EM120 bathymetry survey across Profile 1 showing location of 46 OBS receivers and key structural features. Contoured at 50 m intervals Dashed line denotes the area covered in Figure C. Note the clear increase in seafloor gradient coincident with the base of the accretionary prism (adjacent to OBS28). This largely flattens off west of OBS35. The crest of the outer rise is clearly visible as a shallow section of seafloor by OBS16,17. B) Residual bathymetry data from Bassett and Watts (2015) across the same area, highlighting the expected location of the outer rise high. C) Bathymetry gradient across outer rise portion of the incoming plate. A clear increase in faulting is observed at the seafloor ∼60 km from the deformation front, coincident with the residual bathymetry high. Faults are dominantly orientated NNE-SSW. Note that OBS stations are coloured purely to aid with identification. Convergence vector taken from Submap 4.2 online database (http://submap.gm.univ-montp2.fr/index.php, Heuret and Lallemand 2005).

time-dependant amplitude correction (time raised to power correction, time-power constant of 2.3).

Data was migrated using a Kirchoff Pre-Stack Time Migration (PSTM) using a velocity structure determined via semblance analysis prior to stacking. For semblance analysis CDP supergathers were created every 500 traces, each consisting of 95 consecutive CDPs. Velocity picking was straightforward on the incoming plate, where the flat-lying laterally continuous bedding would produce clear peaks in the velocity spectra. In the thicker parts of the accretionary

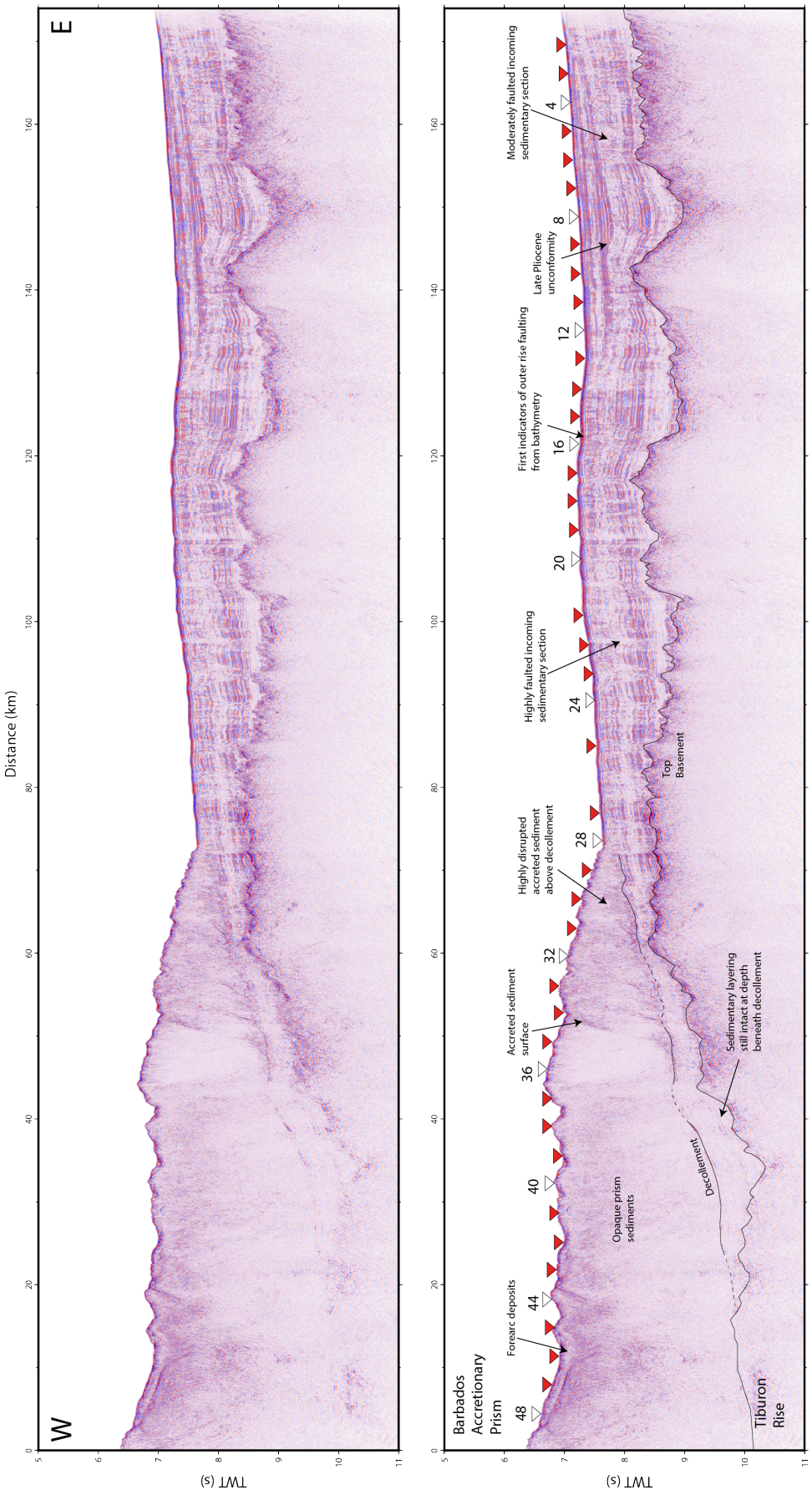


Figure 5.4: Multichannel seismic profile. A) Final 2D PSTM section across survey area. B) As above with key structural features highlighted and OBS locations. Note that OBS stations are coloured purely to aid with identification. Interpreted horizons for the décollement and top basement were used to calculate expected arrival times for reflected phases on the OBS stations to aid in picking. See Figures 5.10-5.12 for detailed interpretation. Plotted with ~5x vertical exaggeration.

prism the lack of reflectivity (besides the décollement surface and some weak reflectivity in the underthrust sediment package, both of which are dipping), makes the velocity picks more uncertain, and the velocity structure is generally smoother here as a result. The PSTM resulted in a significant improvement in imaging compared to a simpler NMO correction, particularly at top basement, where the PSTM does a good job of imaging the rough topography (Figure 5.4). A detailed interpretation of the final MCS profile is given in Section 5.6.

5.5.3 Wide-Angle Seismic Data

Wide-angle data was acquired using a 13 gun, 5000 cu in. array, with shots every 60 seconds, resulting in a spacing of ∼150 m. Shooting occurred from east to west across a network of 4-component OBS, spaced every ∼4 km of which 46 were recovered (Note: OBS1 and OBS25 not recovered). OBS came from two pools, 23 from the German DEPAS OBS pool (broadband instruments), and 25 from the UK OBIC OBS pool, deployed alternately along the profile. Approximately half of these (OBS1-OBS27) were deployed seaward of the front thrust of the accretionary prism, with the remainder (OBS28-48) deployed on the accretionary prism itself. Instruments were previously corrected for internal clock drift, and relocated to account for water column drift using a grid search methodology across local bathymetry, minimizing the misfit with the expected travel time of the water wave arrival (note that this initial correction was carried out by R. Davy alongside the initial data processing for VoiLA profile 2/3, presented in Davy et al. 2020). The maximum resulting correction was ∼1 km, with the average correction ∼460 m. In this chapter we will focus on wide-angle modelling of the velocities in the sediment column across the incoming plate and accretionary prism. The following chapter will focus on the modelling of seismic velocities in the crust and upper mantle, and implications for hydration processes across the outer rise.

Phase Identification

In general arrivals were picked from the vertical component of the seismometer which showed the highest data quality. On a couple of poor quality stations on the slope of the accretionary prism, where the seismometer may have struggled to effectively couple with the seabed, the hydrophone component was preferred for picking. All picks used in generating the final velocity

Phase	Phase Description	No. of picks	RMS Misfit (s)	χ^2
Incoming Plate				
PbP	Reflected phase from top basement	3131	0.061	1.467
Accretionary Prism				
PbP	Reflected phase from top basement	1669	0.052	1.066
PdP	Reflected phase from décollement	739	0.055	1.229
Psed	Turning ray in accretionary prism	2161	0.099	0.983
Pd	A refraction at the décollement interface	408	0.110	1.222
Zero offset predictions				
PbP	Travel time to top basement vertically below each OBS picked from MCS	46	0.087	0.777
PdP	Travel time to decollement vertically below each OBS picked from MCS	15	0.069	0.513

Table 5.1: Travel time misfits in final Vp model listed by phase. For the purpose of calculating χ^2, uncertainties of 0.1 s are assigned to the vertical travel time picks from the MCS profile.

model are summarized in Table 5.1. A complete set of record section plots for the 46 OBS with picked arrivals and forward modelled travel times through the final velocity profile is given in Appendix C.

Picked horizons for the top basement and décollement surfaces from the multichannel profile were used to determine expected zero-offset travel times for reflected phases on each of the OBS. These estimated travel times were used to guide picking of these phases with offset (stars in record section plots, Figures 5.5, 5.6). On the incoming plate this helped to differentiate reflections from the top basement (PbP) from shallower reflections from within the sediment column (which were not used in the model, see Figure 5.5) and to differentiate between reflections from the décollement (PdP) and top basement beneath the accretionary prism (Figure 5.6).

On the incoming plate the top basement reflection (PbP) was generally very clear and identifiable at offsets often exceeding 15 km. Turning rays in the sediments of the incoming plate were only present as secondary arrivals and were generally difficult to differentiate from the PbP reflections (see forward modelling of predicted Psed travel times in Figure 5.5) and water wave. As such only top basement reflections (PbP) are used for constraining sediment velocities on

the incoming plate. On some instruments high amplitude shear phases are shown by forward modelling (assuming a typical oceanic layer 2 crustal structure) as the likely result of a phase conversion at the top basement (Figure 5.5).

Above the deepest part of the accretionary prism, reflected phases were more difficult to identify at short offsets due to the large amount of scattering resulting from the thick (and largely structureless) sediment pile. Beneath the most westerly stations, the underthrust sediment package becomes increasingly thin, eventually pinching out completely against the Tiburon Rise at depth (Figures 5.4). As a result no décollement reflections (PdP) are picked west of OBS43 where they become inseparable from the basement.

Secondary arrivals from within the sediments of the accretionary wedge are clear as the sediment column thickens from OBS30 westwards (located ∼8 km onto the accretionary prism) and typically show apparent velocities of less than 2.5 km s^{-1}. These consist of two distinct phases, turning rays within the upper, accreted part of the accretionary prism (Psed) and refractions at the décollement interface (Pd). There was often no clear change in either amplitude or apparent velocity that could be used to differentiate between these two groups of arrivals. These different arrival types were instead differentiated during the velocity modelling stage where it was found that the travel times of the longest offset arrivals could only be matched if modelled as refractions at the décollement. The décollement refraction can often be picked to very long travel times. On OBS36 sediment arrivals are identifiable to travel times exceeding 21 seconds and offsets of up to 40 km (Figure 5.6). Over the thickest part of the accretionary prism there are identifiable Psed first arrivals (e.g. OBS38-48 see full set of record section plots in Appendix C). Turning rays within the prism show an increase in velocity from east to west. This is very clear on OBS36 (Figure 5.6) where the gradient of the negative offset arrivals (from the west) is much steeper than those with positive offset (from the east).

The final sediment model is determined using a dataset of 8108 travel time picks (including 4800 basement reflection picks, 739 décollement reflection picks). As PbP and PdP were generally straightforward to identify, and were further constrained by the interpreted travel times from the MCS profile uncertainties of 0.05 s were assigned for the purposes of velocity modelling. Psed and Pd were given higher uncertainties of 0.1 s in order to counter the lack of internal structure within the accreted sediments, and comparatively poor quality of several of the instruments on the accretionary prism.

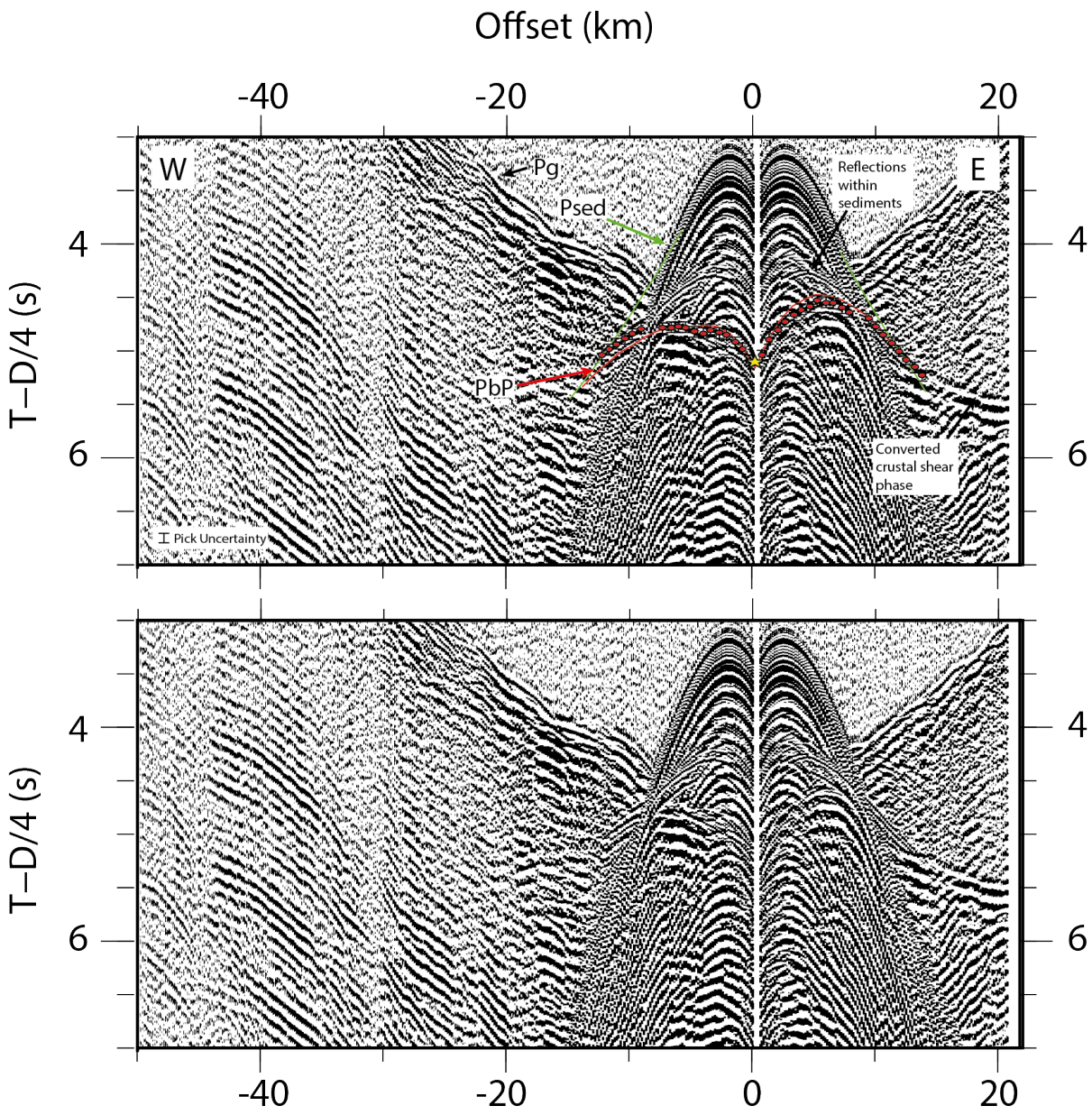


Figure 5.5: Receiver gather from OBS7, typical of stations on the incoming plate. Water depth here is ∼5.5 km. A) Gather with labelled phases. Circles denote picked phases with 0.05 s error envelopes. Coloured lines are forward modelled travel times through final sediment model (Figure 5.7). Phases are as follows, PbP (red): a P-wave reflection off the top basement, Psed (green): a refraction turning through the sediment column. On the incoming plate Psed is generally difficult to differentiate from the PbP reflection and water wave. As a result only PbP arrivals were used to constrain velocities on the incoming plate. Yellow star marks zero offset travel time to top basement interpreted from PSTM profile. B) As above without annotations.

RAYINVR Modelling

Sediment travel times were modelled in the software RAYINVR (Zelt and Smith, 1992). RAYINVR models consist of a series of layers with a velocity assigned at regular intervals to the

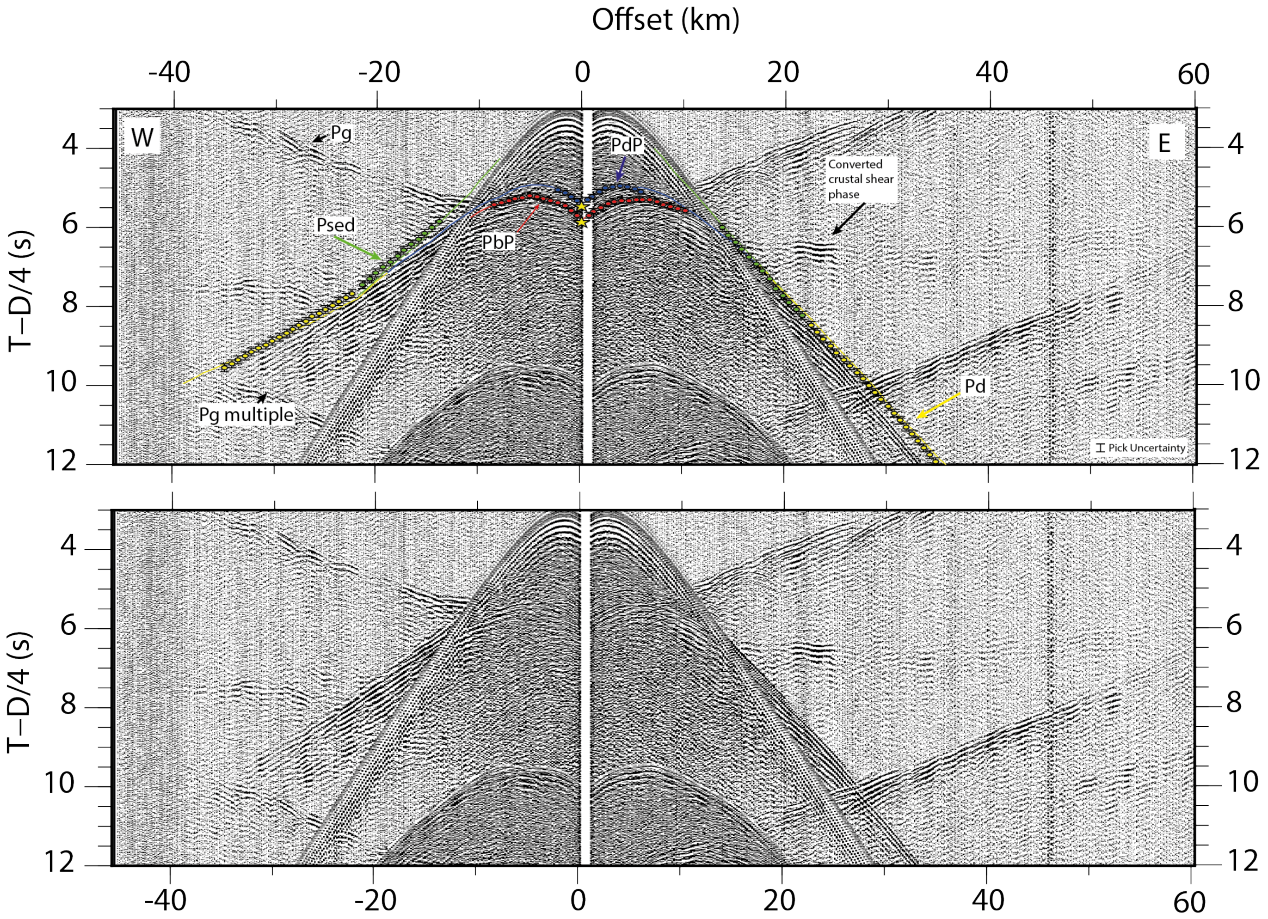


Figure 5.6: Receiver gather from OBS36, typical of stations on the accretionary prism. Water depth here is ∼5.2 km. A) Gather with labelled phases. Circles denote picked phases with error envelopes (0.05 s for PdP and PgP, 0.1 s for Psed and Pd). Coloured lines are forward modelled travel times through final sediment model (Figure 5.7). Phases are as Figure 5.5, with the addition of Blue (PdP): a P-wave reflection off the décollement, Yellow, (Pd) a refraction at the décollement interface. Yellow star marks zero offset travel times to décollement (upper), and top basement (lower) interpreted from PSTM profile. B) As above without annotations. Note the decrease in the amplitude of Pg compared to Figure 5.5 as a result of the attenuating effect of the thick sediments of the accretionary prism.

upper and lower surface of each layer. The velocity gradient in each layer is then assumed to be linear.

A simple 3 layer model was used (Figure 5.7). Layer 1 is the water layer, with a constant velocity of 1.5 km s^{-1}. The seabed is at ∼5 km depth across most of the profile. The second layer is limited to the accreted wedge of sediments above the décollement within the accretionary prism (pinching out to 0 km thickness east of the 74 km point along the profile), with the sediments of the incoming plate and underthrust sediments beneath the accretionary prism modelled as one continuous third layer. An initial sediment model was generated by interpreting the top

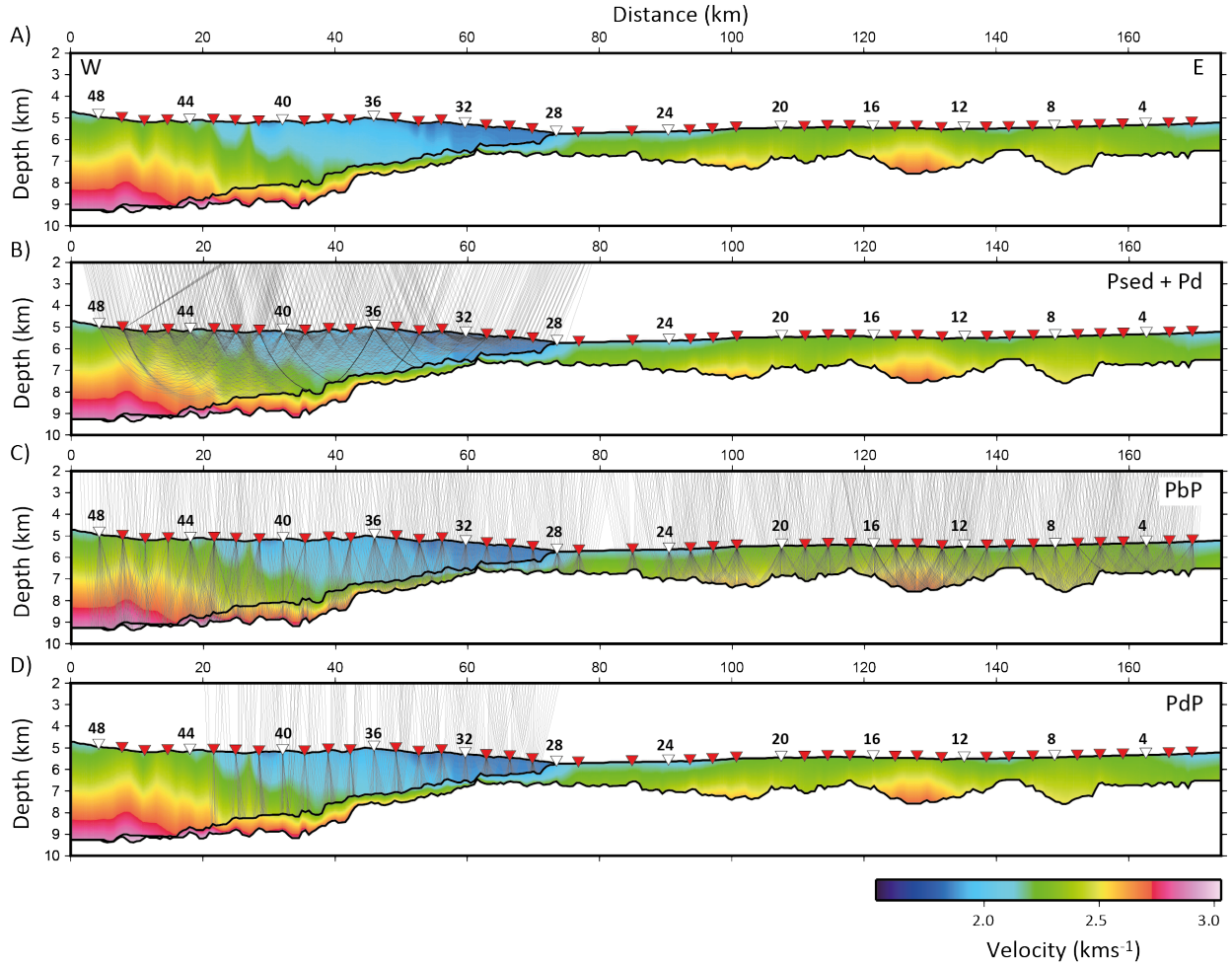


Figure 5.7: Final RAYINVR sediment model. A) Final 2D velocity model for sediments of the incoming plate and accretionary prism. B) As above, with ray paths for refractions through the sediment of the accretionary prism (Psed), and décollement refractions (Pd) plotted. B) As above, with ray paths for basement reflections (PbP) plotted. C) As above, with ray paths for décollement reflections (PdP) plotted. In all cases one in five of rays are plotted. Note that while velocities beneath the westernmost part of the accretionary prism are relatively unconstrained by turning rays, they are consistent with velocities from semblance analysis (Figure 5.8).

basement from the reflection data and converting to depth assuming a velocity of 1.8 km s^{-1} at the seabed. An estimate for the velocity at the base of the sediment column was extracted from the semblance velocity analysis of the multichannel data (Figure 5.8). This initial model tended to overestimate the velocities in the deep sediments, and underestimate the velocity of the shallowest sediments. The layers in the model consist of positional nodes every 0.5 km, with velocity nodes every 4 km on the incoming plate and 2 km within the accretionary prism. The final model was then generated via a process of iterative forward modelling guided where necessary by targeted minor inversions (Figures 5.7, 5.8).

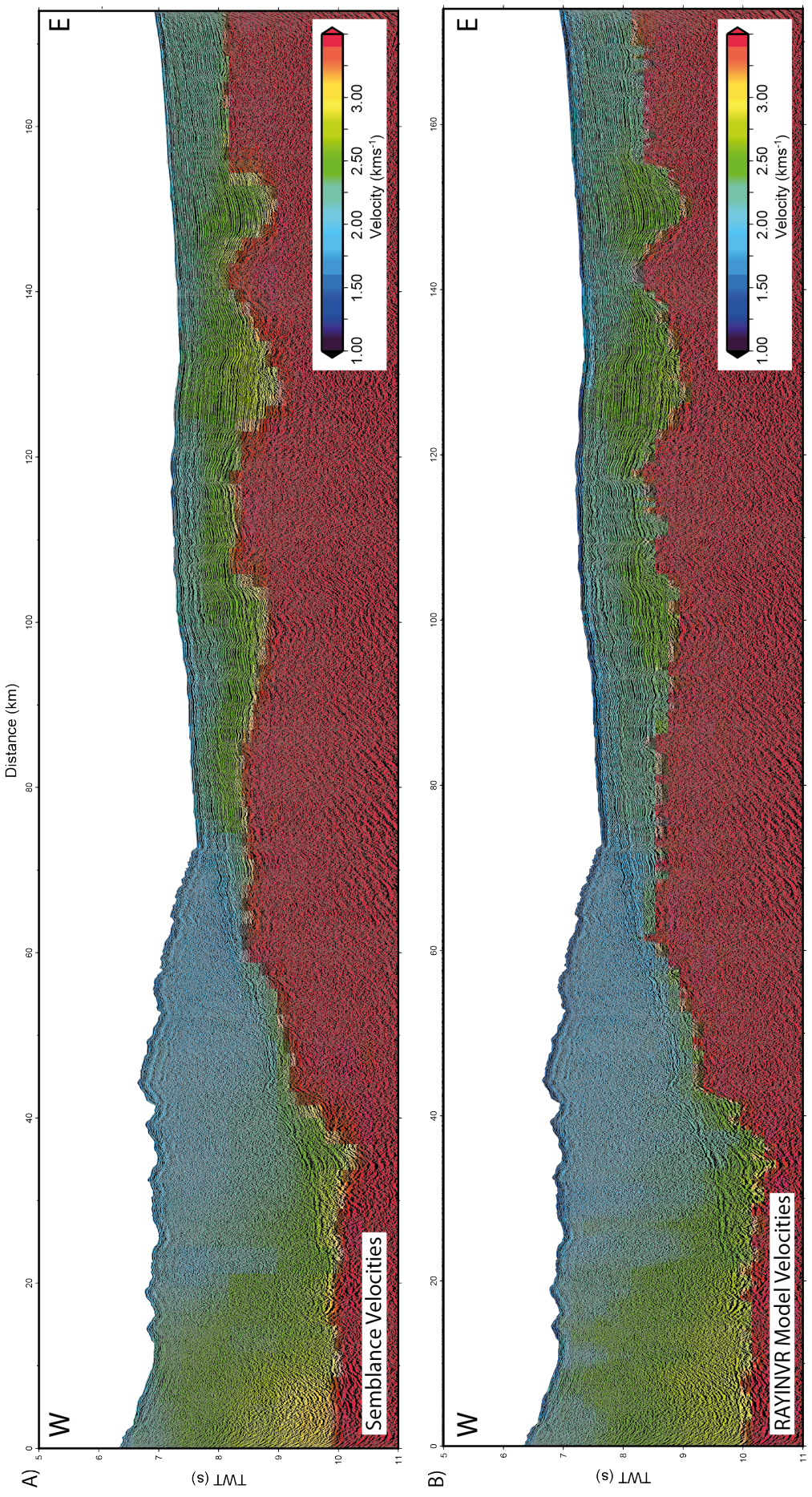


Figure 5.8: PSTM section with velocity overlays. A) Final PSTM section overlain with semblance velocities determined via velocity analysis. B) Final PSTM section overlain with RAYINVR model velocities determined from wide-angle data and converted to time. A major velocity drop is clearly visible in both profiles associated with deformation as sediments enter the accretionary prism. Overall velocity structure between the two profiles is consistent, despite the different methods used, giving confidence in the accuracy of the final RAYINVR model. Note that for the purpose of both plots, velocities below the top basement have been arbitrarily set to 5 km s^{-1}. Plotted at ~5x vertical exaggeration.

The final model generated is shown in Figure 5.7 and possesses an RMS travel time misfit of 0.061 s (chi^2: 1.467) on the incoming plate (constrained by OBS2-OBS27) and 0.081 s (chi^2: 1.066) within the accretionary prism (constrained by OBS28-OBS48). The travel times misfit for all phases are summarized in Table 5.1. The greater RMS misfit over the accretionary prism comes from the large number of crossing rays within the sediment (rays turning in the accretionary prism, Psed, are fitted with an RMS of 0.099s, refractions at the décollement interface, Pd, with RMS of 0.110 s). This misfit may represent the chaotic internal structure of the accretionary prism (Figure 5.4), where the assumption of a single linear velocity gradient is too simple to represent the geological complexity. Pd in particular was very sensitive to even minor changes in the topography of the décollement horizon. Basement reflections (PbP) are well-matched throughout the models with RMS misfit values of 0.061 s on the incoming plate and 0.052 s beneath the accretionary prism. Décollement reflections (PdP) are fitted with an RMS misfit of 0.055 s.

The initial zero-offset travel time predictions for the top basement determined from the multichannel profile are matched with an RMS misfit of 0.087 s. The zero offset travel time predictions for the décollement reflector were similarly fitted with an RMS misfit of 0.069 s. The final sediment model shows clear agreement with the finalized semblance velocities used in the migration of the PSTM section (Figure 5.8). The similarity between these two velocity profiles, derived using different methodologies gives us greater confidence in the final overall velocity structure.

5.6 Interpretation

5.6.1 Local Well Data

The sediments immediately to the north of the Tiburon Rise are well sampled in a series of ODP and DSDP drilling campaigns (ODP 110, 156, 171; DSDP 78, totalling 14 boreholes, Figure 5.1). Many of these wells were drilled in order to better understand the nature of the décollement interface in the region in association with the 3D seismic survey conducted by the R.V. Ewing in 1992 (Moore et al., 1982; Mascle and Moore, 1990; Moore et al., 1996; Moore, 2000). Of particular importance are ODP sites 543 (Moore et al., 1982) and 672 (Moore et al.,

1988), which sit just prior to the toe of the accretionary prism and sample the undisturbed sedimentary succession of the incoming plate prior to accretion. DSDP 4 also drilled a single penetration (Site 27) on the southern flank of the Barracuda Ridge (Benson et al., 1970). These wells encompass the full succession of sediments on the incoming plate, from the oldest Campanian (Cretaceous 83.6-72.1 Ma) deposits (Moore et al., 1982). The sediment column dominantly consists of pelagic clays, marls and, in some cases, calcareous mudstone interbedded with some distal terrigenous turbidites (Moore et al., 1982, 1988). From the Miocene onwards the hemipelagic sediments also contain a major volcanic component, the result of ash-fall from the nearby Lesser Antilles arc.

5.6.2 Incoming Plate Lithology

The multichannel profile is interpreted according to the same stratigraphic regime used by Pichot et al. (2012). This scheme breaks sedimentation in the basin down into three broad packages, Cretaceous-Oligocene (Unit 1, Blue), Miocene-Pliocene (Unit 2, Brown) and Pliestocene-Holocene (Unit 3, Yellow). These are summarized in Figure 5.9, with a detailed interpretation of the multichannel profile given in Figures 5.10 - 5.12. Whilst more detailed sedimentary classifications have been proposed for the basin (e.g. Moore et al. 1988 broke the sediments of the incoming plate down into 5 distinct packages based upon the results of ODP leg 110, site 672), the Pichot et al. (2012) study is the only one to incorporate well data from disparate ends of the Tiburon Basin and to trace the relevant horizons across several large regional seismic lines. Due to the absence of a well penetration adjacent to our profile which can be used to directly constrain the stratigraphy, matching the seismic facies descriptions from those profiles is the most straightforward way of gaining a reasonable understanding of the sedimentary processes within the basin.

The lowermost sedimentary interval in the region is a thin layer of high acoustic impedance Campanian-Maastrichtian sediments, which lie directly over the Cretaceous basement. Previously, Pichot et al. (2012) made no attempt to interpret these sediments separately from the top basement surface due to a lack of acoustic contrast between the two. However, the new MCS profile presented here does a good job of imaging this division. A clear image of the top basement surface was also important for interpreting zero offset travel times beneath the OBS to the top basement and the décollement for the purposes of wide-angle modelling. These oldest

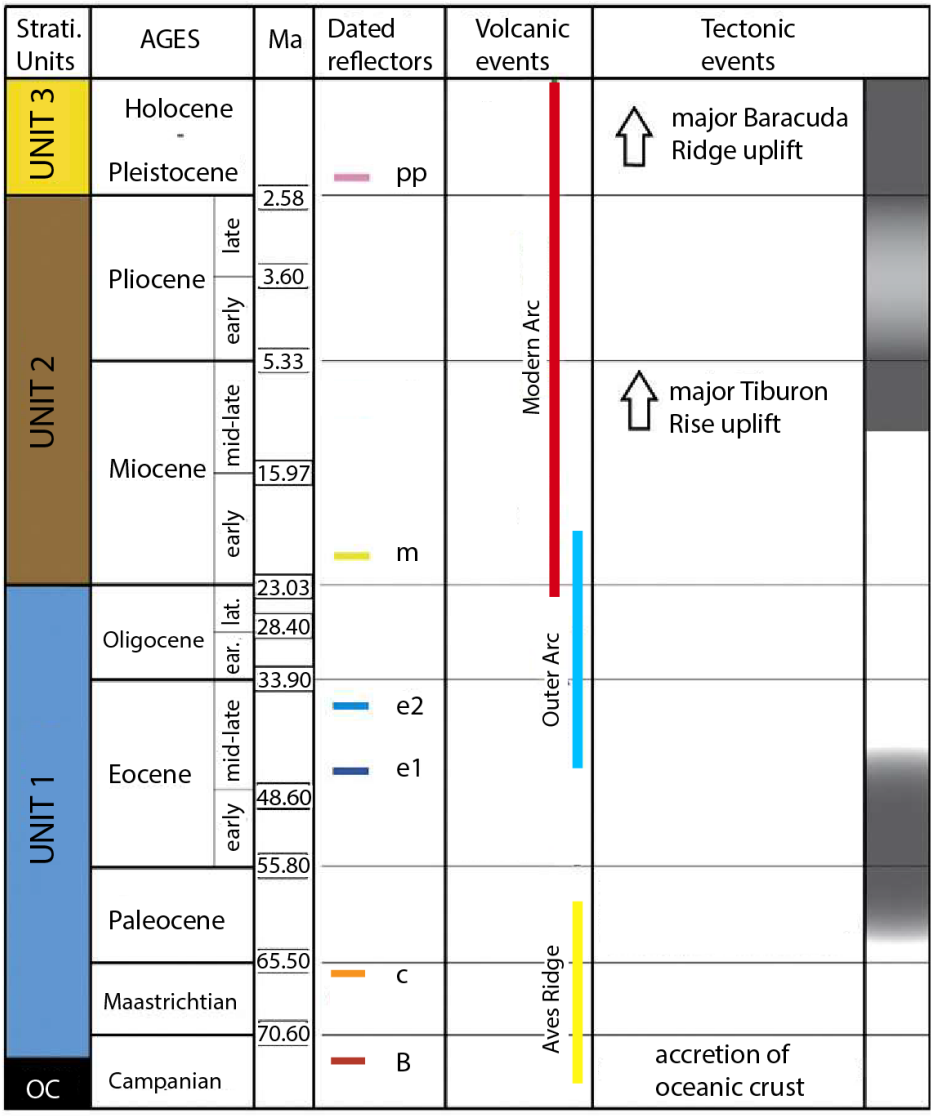


Figure 5.9: Regional timeline for major stratigraphic intervals and tectonic events in the Tiburon Basin region. Adapted from Pichot et al. (2012). Dated reflectors correspond to those used in the interpretation of VoiLA profile (see Figures 5.10-5.12). These key horizons were dated using data from the local well penetrations shown in Figure 5.1 and then mapped to regional reflection profiles by Pichot et al. (2012). Note that reflector "c" was not part of the original Pichot et al. (2012) stratigraphy (Section 5.6.2). Timeline of volcanic events has been updated to be consistent with the new tectonic model for the eastern Caribbean presented in Chapter 4.

sediments are separated from the rest of unit 1 by the horizon "c" (Figure 5.9). Sediments of this age have been sampled at ODP site 543, consisting of calcareous and ferruginous claystone, directly above the pillow basalts of the upper oceanic crust (Moore et al., 1982).

The rest of unit 1 is composed of a thick Eocene-Oligocene succession. Within this package two stratigraphic horizons "e1" and "e2" are interpreted. Between horizons "c" and "e1", the

sediments are acoustically-transparent siliceous pelagic deposits, which correlate with sediments sampled at ODP sites 543 and 672. Between "e1" and "e2" is a package of much stronger impedance, continuous reflectors. At site 672, this change in seismic character reflects cyclic alternating bands of claystones, laminated calcareous mudstones and marls (Moore et al., 1988). Note that both sites 672 and 543 are in shallower water depths than this profile, and therefore the lithologies sampled at these drill sites may contain a much higher carbonate content as a result of the shallower water depth. Locally the carbonate compensation depth occurs relatively deep, at ∼5300 m in the region of DSDP leg 78A (Moore et al., 1982), though this is still shallower than the seabed across much of the profile. At both sites 672 and 543, discrete terrigenous sand and silt beds have also been cored throughout the mid-Eocene to Oligocene section. These are probable distal turbidites deposited in the region prior to the uplift of the Tiburon Rise in the Miocene (Patriat et al., 2011; Pichot et al., 2012).

The Oligocene interval (between reflectors "e2" and the base Miocene reflector "m"), is relatively acoustically transparent, though the impedance of layers within this interval is quite variable laterally. This reduction in impedance contrast reflects a reduction in the terrigenous sand content compared to the layers below, with more acoustically homogeneous claystones, calcareous claystones, mudstones, marls and silts the dominant lithologies. Unit 1 is well dated from core recovered at site 672, with well-preserved foraminifera and nanofossils in the Oligocene section, calcareous fossils in the mid-Eocene and radiolarians in the lowest Eocene sediments respectively (Moore et al., 1988). The upper part of unit 1 was deposited during a time period coincident with volcanic activity along the Limestone Caribbees and Outer Arc (Allen et al., 2019), however at this time the currently subducting section of the incoming plate was still situated too far east to have captured ash fall from this period. Ash deposits from this time are however known from sediments uplifted on the islands of Grenada and the Grenadines (Speed et al., 1993).

Unit 2 consists of Miocene-Pliocene deposits. The "m" horizon marks the base of this Miocene interval, and is generally a high amplitude reflector compared to the sediments both above and below. The Miocene-Pliocene section consists of discontinuous parallel strong to weak reflectors, dominated by hemi-pelagic mudstones and a consistent overall thickness throughout the basin of ∼0.2 sTWT (Pichot et al., 2012). Several changes in local sedimentary processes are observed in the Miocene as a result of the uplift of the Tiburon Rise, and the increasing

proximity to the arc. The Miocene interval is the first to show evidence of ash fall from the adjacent Lesser Antilles, with isolated ash beds observed throughout unit 2 (Moore et al., 1982, 1988). There is also an absence of terrestrial sediments, as is observed in unit 1, as a result of the main phase of Tiburon Rise uplift, creating a barrier to the northward transport of turbidites.

Within this section we also interpret a horizon "pd", which appears to correlate with the décollement forming layer beneath much of the accretionary prism (note that this horizon was not part of the stratigraphic description of Pichot et al. 2012). This horizon generally separates a relatively high impedance upper Miocene section from a comparatively transparent section in the lower Miocene. Note that Pichot et al. (2012) interpreted an additional horizon "m2" within this second unit. This surface however was largely defined by the presence of a mid-Miocene unconformity in the vicinity of the Barracuda Ridge. A distinct change in seismic character is observed to high impedance contrast, laterally continuous beds between reflectors "pd" and "pp" in the upper section of Unit 2 (Figure 5.10, see Miocene sediments at 148 km). However, there is no clear corresponding unconformity in the mid-Miocene that can be used to definitively label this horizon.

Unit 3 consists of Quaternary Pleistocene-Holocene sediments. The base of this package (horizon "pp") is often observed to form a characteristic unconformity with the Pliocene sediments below (e.g. at 135 km and 168 km in Figure 5.10). Sediments in this unit consist of muds, marls and calcareous clays with frequent ash layers, forming strong, laterally continuous reflectors (Moore et al., 1982, 1988). Pichot et al. (2012) observed a number of thick mass transport deposits within this interval, the result of flows of sediments from the recently uplifted Tiburon and Barracuda ridges. These deposits are characterized as thick, lens like packages of sediment, with chaotic internal structure, and often erosional contact with sediments below, and are not observed on our profile. This may be a result of the fact that Profile 1 is located further from the Tiburon Rise and Barracuda Ridge in the central part of the basin, compared to the Pichot et al. (2012) profiles (Figure 5.1). Moore et al. (1982) observed an order of magnitude increase in the sedimentation rate of this youngest sediment package, which as a result is poorly consolidated. This increase in the sedimentation rate is a function of both increasing proximity to the arc (leading to an increase in both eroded sedimentary run-off and ash fall) and erosion from the recently formed Tiburon and Barracuda Ridges.

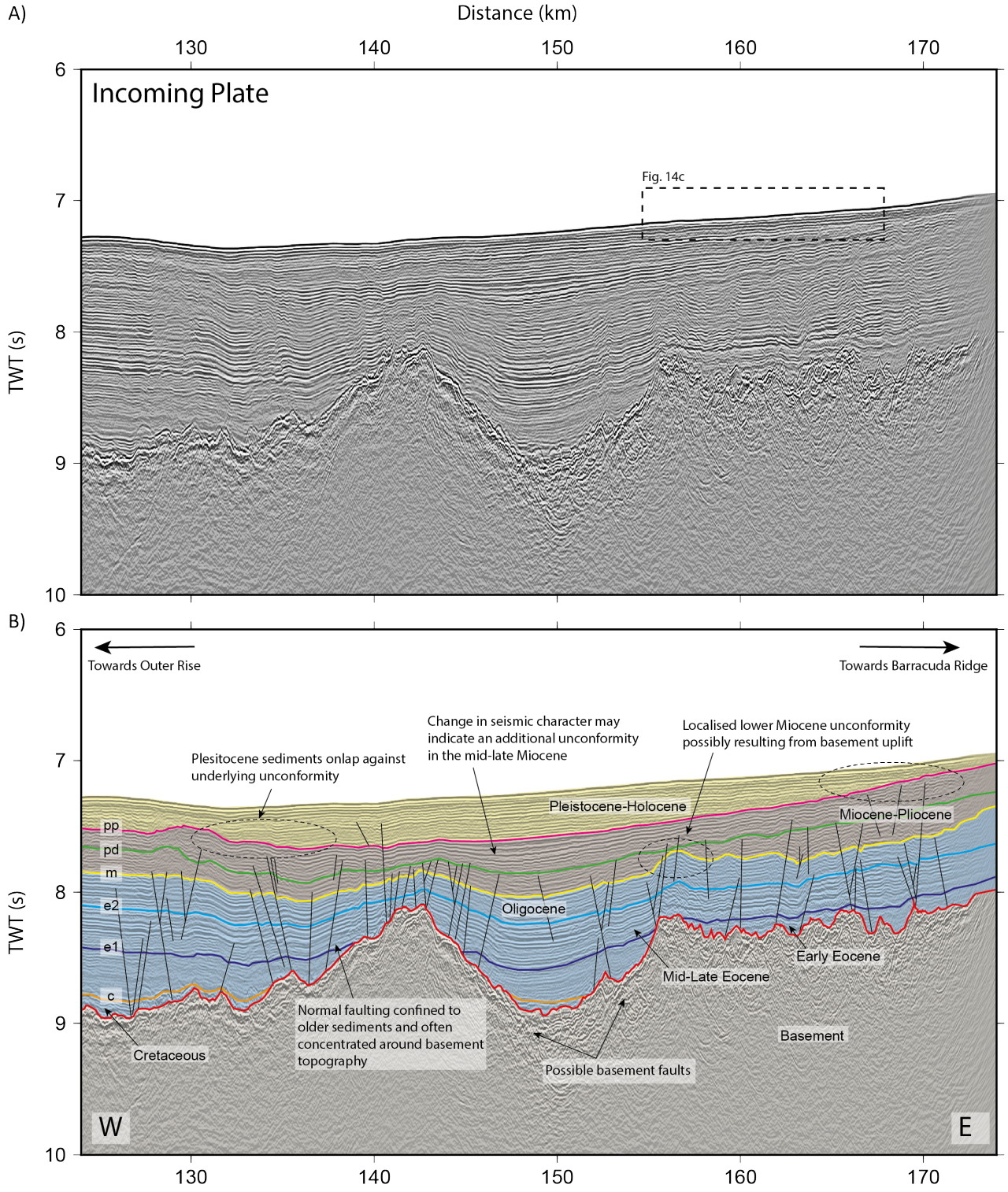


Figure 5.10: Detailed interpretation of the incoming plate. A) Incoming plate section of PSTM profile. B) As above with interpretation overlaid. Stratigraphic intervals match those shown in Figure 5.9. Note the addition of horizon "pd" (proto-décollement), a mid-Miocene surface which forms the décollement beneath the majority of the accretionary prism. Despite the proximity to the Barracuda Rise there is little indication of compressional faulting in this region, though the base Pleistocene unconformity may the result of localized deformation associated with uplift of the Barracuda Ridge.

5.6.3 Structural Divisions

To simplify the interpretation the multichannel profile is broken down into 3 distinct structural sections, the incoming plate, the outer rise and the accretionary prism (Figures 5.10-5.12). The structure across the deformation front at the toe of the accretionary prism is shown in Figure 5.13.

1. The Incoming Plate

The incoming plate refers to the easternmost 50 km of the profile (full profile 124 - 174 km, Figure 5.10). This section sits closest to the Barracuda Ridge, and is yet to be affected by bend faulting across the outer rise, as is observed in bathymetry (Figure 5.3). The stratigraphy in this section clearly corresponds to the seismic facies descriptions of Pichot et al. (2012). The consistency of these intervals across our entire profile is a good indication that the make-up of sediments is relatively continuous throughout the basin.

Unit 1 shows major variations in thickness which correlate with the basement topography. Both the oldest Cretaceous, and Eocene sediments clearly onlap onto the top basement, indicating that much of this basement structure is likely to have been created during crustal formation (i.e. rather than occurring more recently during a phase of uplift similar to that which created the Tiburon and Barracuda ridges). The Eocene section in particular shows major changes in thickness across relatively short distances as a result of basement topography (from 0.2 - 1 sTWT), with the entire section deeper than the "e2" reflector absent across the most significant basement high (at ∼142 km).

In comparison, unit 2 (Miocene-Pliocene) shows relatively uniform thickness of 0.2-0.3 sTWT across the profile. Generally, unit 2 overlies unit 1 conformably, though there is a minor unconformity located at ∼157 km. Here the basal Miocene strata onlap onto the Oligocene sediments below. This unconformity is one of the few possible indicators of compressional deformation despite the proximity of this easternmost part of the profile to the Barracuda Ridge. This base Miocene unconformity must pre-date Barracuda Ridge uplift, which doesn't occur until the end of the Pliocene (Figure 5.9) though it is probable that it is still the result of distributed convergence of the North and South American plates.

A second unconformity is observed at the boundary between units 2 and 3 in keeping with the observations of Pichot et al. (2012). They attributed this unconformity to deformation associated with uplift of the Barracuda Ridge. Unlike that study, however, we observe no clear indications of ongoing faulting associated with this phase of deformation, though it is possible that our profile is too oblique to the primary north-south shortening direction to image such faulting effectively. It is also possible that this unconformity is a function of the change in sedimentation rates associated with the increasing proximity to the trench. Across much of the profile unit 3 is of an equivalent thickness with unit 2, despite being deposited in ∼10 % of the time. This clearly highlights the differences in deposition rate within this interval observed at ODP Sites 543 and 672 (Moore et al., 1982, 1988). There is also a thinning of this youngest interval eastward towards the Barracuda Ridge, away from the main depocenter in the central part of the basin (Pichot et al., 2012).

Faulting in this part of the profile is dominantly extensional, and almost entirely constrained to the Lower Miocene and older sediments. The largest faults are spaced every 3-5 km and generally correlate with major pieces of basement topography. A particular cluster of minor faults is visible across the crest of the basement high at ∼ 142 km, and may be the result of variable compaction. Even the largest faults in this section show only very minor offsets, at most a few 10s of meters. Some possible faults are identified within the basement (Figure 5.10), though imaging beneath the basement surface is generally relatively poor (the Moho is not imaged anywhere along the profile).

2. The Outer Rise

The outer rise section of the profile extends between 74-124 km (Figure 5.11). This encompasses the area from the crest of the outer rise observed in bathymetry (Figure 5.3), to the toe of the accretionary prism (outer rise crest occurs at ∼113 km along profile). The sediment package in this region shows little variation compared to that already described across the incoming plate. The thickness of the younger Miocene-Present sediments is uniform across this section of the profile, with both units 2 and 3 consistently ∼0.2 sTWT thick. The thickness of unit 1 continues to be highly dependent on basement topography. Notably, the section of sediment immediately prior to the toe of the accretionary prism is particularly thin, with “e2” the oldest of the interpreted horizons present. Unit 1 is again observed to onlap onto the basement

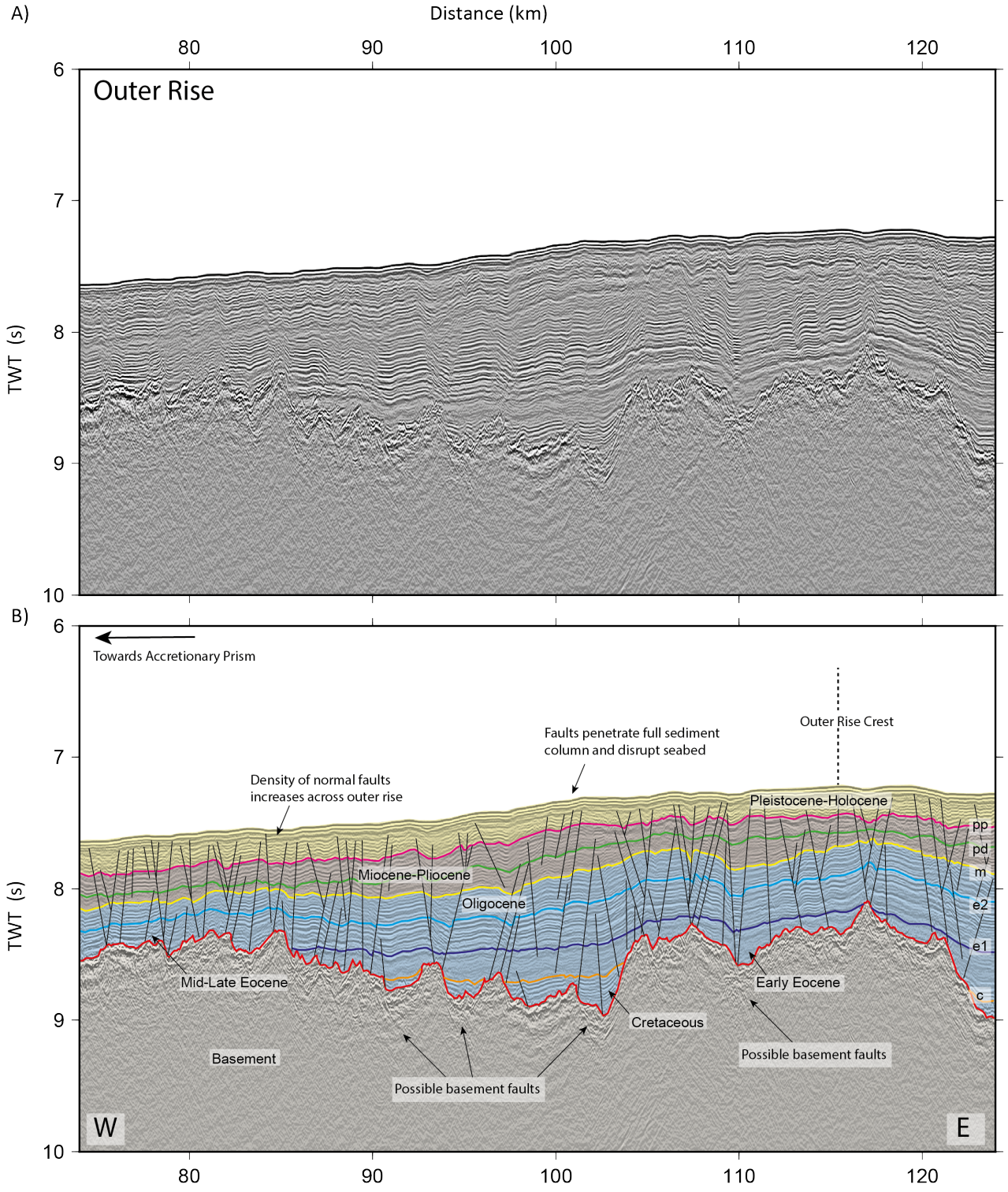


Figure 5.11: Detailed interpretation of the outer rise section of the incoming plate. A) Outer rise section of PSTM profile. B) As above with interpretation overlaid. Stratigraphic regime is the same as described in Figures 5.9 and 5.10. Note the increase in the length, and decrease in spacing between normal faults compared to Figure 5.10 as a result of bending across the outer rise.

topography, confirming that the majority of the basement structure pre-dates this oldest phase of sedimentation.

There is a significant increase in both the density and length of faults in this section of the profile. A majority of faults now penetrate the full thickness of the sediment column, and are spaced as tightly as 1-1.5 km (as opposed to 3-5 km on the incoming plate). The offset on these steeply dipping surfaces is still relatively small (on the order of 10s of meters at most). However, a number of faults clearly disrupt the seabed, and these faults are also visible in bathymetry (Figure 5.3C). From the bathymetry, these faults are predominantly striking NNE ($\sim$20°), as a result the profile cuts them quite obliquely, and may not be imaging the true dip. A secondary weaker fault fabric is also cutting approximately WNW ($\sim$290°).

In this region the trench strikes NNW, and given that the convergence vector here is approximately WSW, neither of these fault orientations is particularly optimal in order to accommodate bending (particularly the dominant NNE orientation). Hence, we might assume that rather than being fresh bend faults, these features instead represent a reactivation of a pre-existing basement fault fabric. In the new marine magnetic grid for the region, developed in the previous Chapter (Figure 4.2), this NNE trend is seen in spreading anomalies on the incoming plate including very clear magnetic reversals such as C34n and C33n, just north of our survey area. It has been suggested from previous studies of the Middle America, Central Chile and Sumatran subduction zones that for bending to reactivate a pre-existing fault fabric in this manner faults must be oriented at an angle of less than 30° to the trench axis (Ranero et al., 2005; Graindorge et al., 2008). In this location we are probably right at the limit of this 30° cut-off (the trench strikes NNW, while the dominant fault fabric is orientated $\sim$20°N, Figure 5.3), hence this style of bend faulting might not be consistent along the entirety of the arc.

Although these faults have low offsets, they offer a possible pathway for the flow of water into the deeper lithosphere, which may result in the hydration of the lower crust and mantle beneath the outer rise. I will explore such processes in greater depth in the following chapter.

3. The Accretionary Prism

The accretionary prism constitutes the westernmost 74 km of the multichannel profile (0-74 km, see Figure 5.12). At the toe of the prism, the total thickness of the incoming sediment

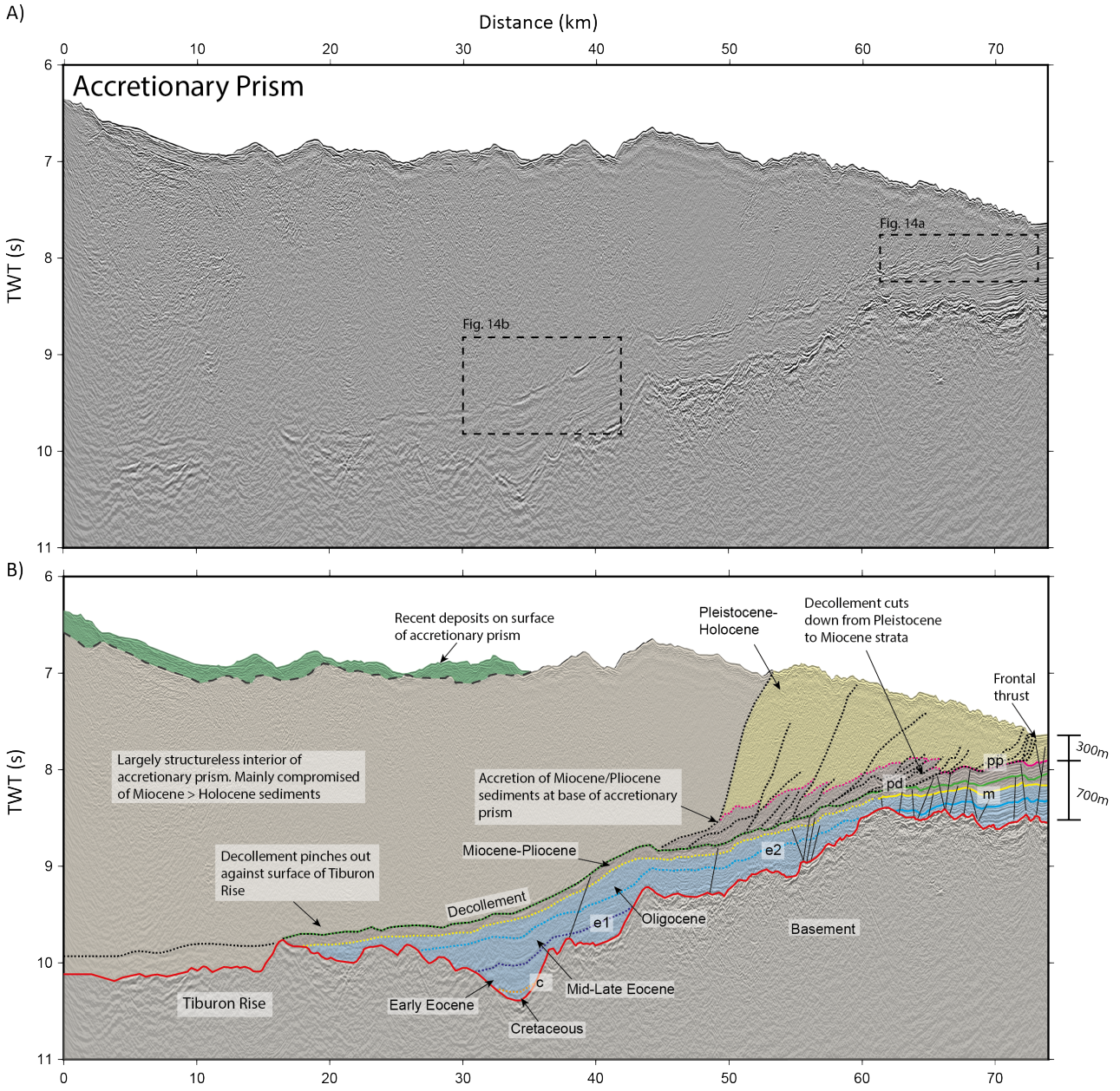


Figure 5.12: Detailed interpretation of the accretionary prism section of the profile. A) Accretionary prism section of PSTM profile. B) As above with interpretation overlaid. Stratigraphic regime is the same as described in Figures 5.9 and 5.10. décollement initially forms along base Pleistocene "pp" horizon, before cutting down through Miocene section to "pd" ∼15 km from the toe of the prism. Thickness of the underthrust section is heavily influenced by basement topography. Although some large sediment packages are visible between faults within the accretionary prism, the thin accreted section means that sediments are generally highly deformed.

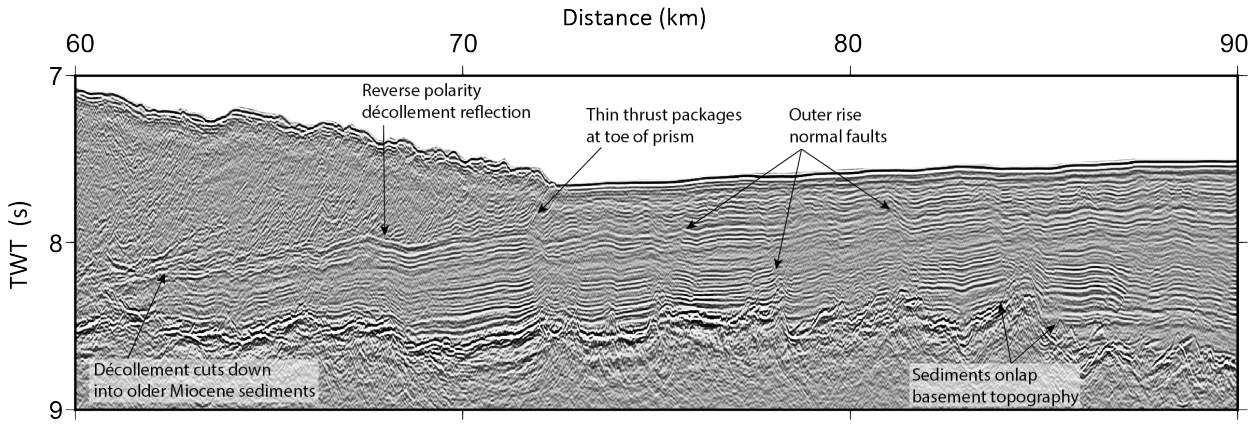


Figure 5.13: Close up of multichannel section across the toe of the accretionary prism showing the accretion of the youngest sediments. Décollement initially forms at the "pp" horizon at the base of the Pleistocene, and is expressed as a reverse polarity reflection, possibly indicating high fluid pressures at the shallowest part of the subduction interface.

column is relatively thin compared to parts of the profile further east, totalling ∼1 km. Of this incoming sediment section ∼300 m are incorporated into the accretionary prism, with the remaining 700 m forming the underthrust sediment package beneath the décollement. Initially the décollement forms along horizon "pp" at the base of unit 3 (i.e. the Quaternary sediments).

The total incoming sediment column is thicker than that observed in the region of the Ewing 3D survey (Figure 5.1), where the incoming sediment thickness varied from 490-850 m (Moore et al., 1996). The difference in the total thickness of the incoming sediment package between VoiLA Profile 1 and the Ewing survey (situated just ∼60 km further south) appears to be largely the result of differences in the thickness of the youngest sediments deposited following Tiburon Rise uplift in the Mid-Late Miocene. At DSDP site 543, the Quaternary section is on the order of ∼50 m thick, as opposed to ∼300 m along this profile.

However, the 300 m accreted section is still thin compared to the arc front south of the Tiburon Rise, and as a result we see the same largely structureless, thin-skinned deformation observed by Westbrook (1982), aside from a few thin thrust packages at the very forefront of the accreted section. Due to a lack of structure in the accretionary wedge, it is difficult to know whether thrust faults spaced every ∼5 km within the accreted sediments represent distinct packages of sediment from the incoming plate, or are later, out of sequence thrusts.

In the frontal 10 km of the accretionary prism, where the décollement is still coincident with the Pliocene-Pleistocene surface, the décollement reflector is reverse polarity (Figures 5.12, 5.13, 5.14). This character is similar to the reverse polarity reflector observed beneath much of the

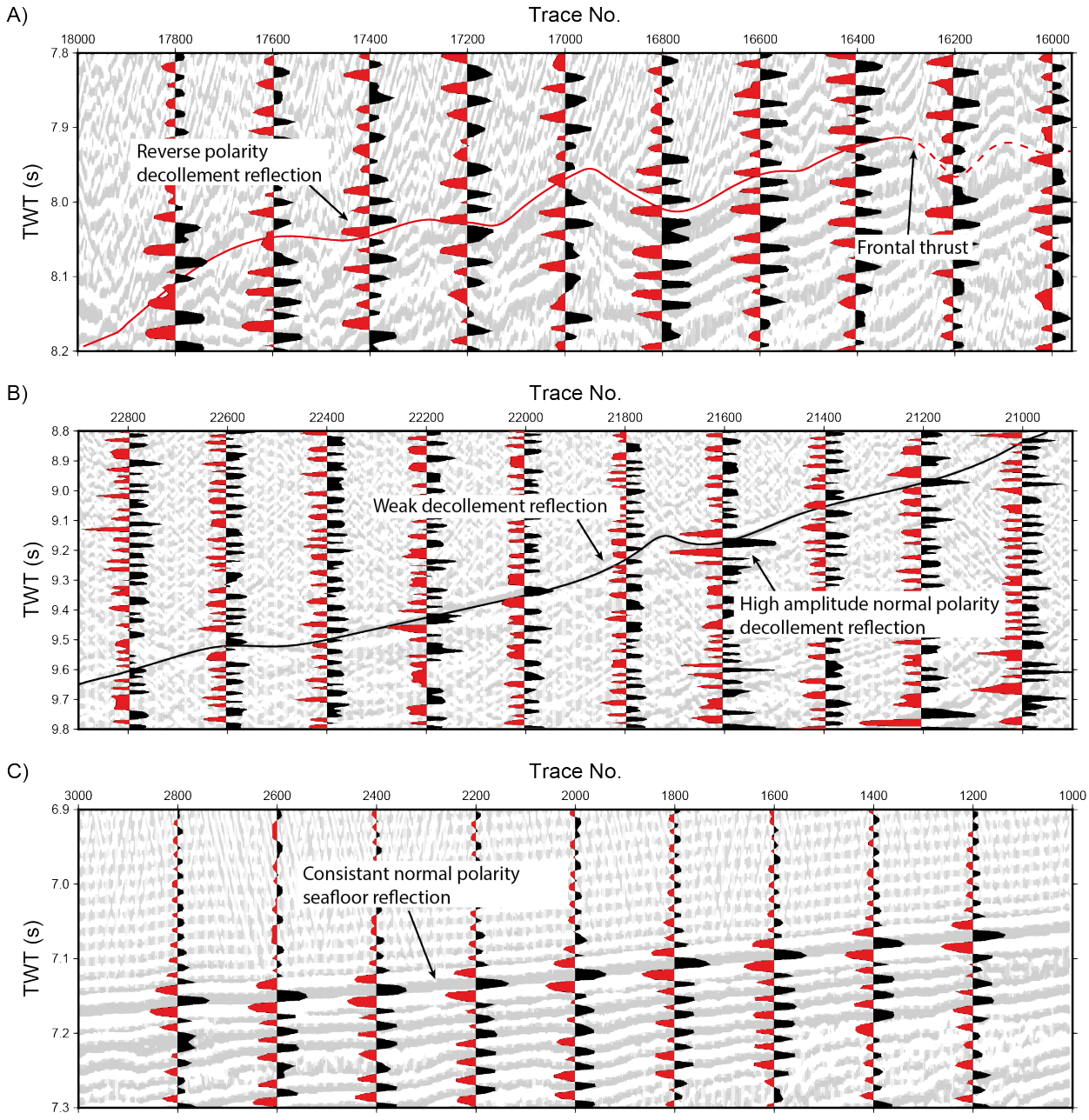


Figure 5.14: The décollement reflector. A) Close up on décollement reflection at toe of accretionary prism. Décollement here is consistently reverse polarity, potentially indicative of fluid over-pressuring at the décollement interface. In all cases wiggle traces come from a trace mixed version of the final PSTM section, averaged across 5 adjacent traces. B) Deeper in the accretionary prism the nature of the décollement interface reflector is much more variable, transitioning between little impedance contrast, to a clear high amplitude normal polarity reflection. This may indicate a reduction in fluid pressures within the deeper sediments of the accretionary prism. See Figure 5.12a for location of two sections of décollement shown. C) Wiggle trace plot across the seabed at the easternmost end of the profile, shows a consistent normal polarity seafloor reflection.

frontal portion of the accretionary prism by the 3D Ewing survey (Shipley et al., 1994; Bangs et al., 1996). In that study it was shown that lithological contrasts across the décollement alone were insufficient to produce this seismic response, which is likely the result of high fluid over-pressure in a thin, 14-40 m thick, high porosity, mudstone interval (Shipley et al., 1997; Bangs et al., 1999). In this case however the décollement forming interval was within the Lower Miocene, at a deeper stratigraphic level than the initial décollement imaged here.

It is possible that in this central part of the basin, the décollement initially forms at the Pliocene-Pleistocene boundary due to the relative weakness of the quickly deposited, poorly consolidated Quaternary sediments. Beyond the first 10-15 km the décollement surface abruptly cuts down onto the Lower Miocene reflector "pd", with the intervening upper Miocene-Pliocene section subcreted onto the base of the accretionary prism. "pd" sits at a very similar stratigraphic level to the thin Lower-Miocene interval observed by the Ewing survey, though without direct well control it is impossible to know whether they correspond to the same mudstone interval (Shipley et al., 1997; Bangs et al., 1999). Following the cut-down, the seismic response of the décollement reflection is far more chaotic, alternating between a normal polarity reflection and little/no impedance contrast (Figure 5.14). Often the nature of this reflection is seen to vary with basement topography (e.g. the very weak reflection from the décollement above the basement high at ∼42 km). Zhao et al. (1998) previously attributed similar character changes in the nature of the décollement to variable compaction of the sediments overlying major pieces of basement topography. Even if "pd" does represent the same thin mudstone interval observed previously by Shipley et al. (1997), Bangs et al. (1999) and others, in this part of the basin it does not seem able to maintain the very high porosities, and fluid pressures which led to the extensive reverse polarity reflection observed by those studies. The loss of fluid into the overlying accretionary wedge may be accelerated by thrust faulting associated with the change in stratigraphic level of the décollement (Figure 5.12).

Bangs et al. (1990) observed that approximately two thirds of pore fluid is expelled from the Barbados décollement in the first few kilometres. However, substantial changes in the nature of the décollement reflection are documented across relatively small length scale of 1-2 km as a result of channelized fluid flow, differential compaction and variations in fracture permeability (Zhao et al., 1998; Bangs et al., 1999). As such we must be cautious not to over-interpret the nature of the décollement interval based on a single 2D profile.

Similar to the sediments on the incoming plate the underthrust sedimentary section shows thickness variations with the basement topography, pinching out entirely against the eastern face of the Tiburon Rise (at ∼17 km). At 62 km (Figure 5.12) the basement also comes very close to completely closing against the décollement. Bedding is well imaged in the underthrust sediments even beneath the deepest parts of the accretionary prism, giving confidence that the lack of structure in the main accreted section is a true reflection of the nature of the sediments there, rather than the result of poor imaging.

5.7 Velocity Model

Sediment velocities across the outer rise and incoming plate are relatively consistent, with no obvious reduction in velocity as a result of the increased faulting seaward of the accretionary prism (Figure 5.7, 5.8). Velocities at the base of the incoming sediments appear to be purely a function of the degree of compaction, with the highest sediment velocities (of up to 2.7 km s^{-1}) correlating with the thickest deposits (particularly at 130 km, 150 km). The velocity gradient in the sediments of the incoming plate is ∼0.2 s^{-1}. This is in keeping with velocity-depth functions which have been proposed for the undeformed sediments of the region previously (Bangs et al., 1990). A clear westward increase is seen in the internal velocities of the accretionary prism. Particularly west of OBS37 where the accretionary prism slope has levelled off. This likely reflects compaction, dewatering and a reduction in pore space with the increasing thickness of the sediments in the prism.

Velocities in the shallowest sediments on the incoming plate (1.9-2 km s^{-1}) are relatively high for poorly compacted marine sediments, whilst this may be the result of a volcanic sediment component, these velocities exceed P-wave measurements made in the shallow sediments at DSDP drill sites 572 and 673 (Moore et al., 1982, 1988). This is likely to be a function of the relative simplicity of this section of the model, with a 1D velocity gradient not accurately capturing differences in the rate of deposition and compaction between Unit 3 and the older sediments. The unconformity at the boundary between Units 2 and 3 is likely a good candidate for the additional reflected phases observed from within the sediments on the incoming plate (Figure 5.5).

At the toe of the accretionary prism there is a distinct reduction in the velocity of sediments

as they are incorporated into the wedge, with velocities of less than 2 km s^{-1} at the seabed within the first 25 km of the prism. The velocity gradient within the accreted sediments is also reduced to $\sim$0.1 s^{-1}. This is likely due to some combination of lithology (only the poorly compacted Quaternary sediments are initially accreted onto the prism), deformation, and fluid over-pressure. Ray coverage is relatively low through the toe of the accretionary prism compared to some other sections of the model, so it is possible that this is an artefact of the initial parameterization, however, this velocity decrease is clearly observed in both the RAYINVR model and original semblance velocity model (Figure 5.8).

Sediments in the underthrust sediment package also show a distinct initial decrease in velocity at the foot of the accretionary prism. Again this may be due to fluid over-pressure, as the over-burden pressure from the thickening accretionary wedge increases more rapidly than the low permeability sediments can dewater.

Beneath the accretionary prism, the underthrust sediments reach thicknesses of up to 1.2 km. This is much thicker than at sites such as ODP 543 (Moore et al., 1982) where the total incoming sediment package (encompassing the full Cretaceous-Quaternary succession) is only 400 m. The high clay content of the pelagic and hemi-pelagic sediments that constitute a significant portion of the incoming sediment package are expected to provide a barrier to the vertical escape of fluids from within the underthrust section, with the potential to maintain very high fluid pressures at depth. In keeping with the results of (Bangs et al., 1990), and direct sampling of the décollement at drill sites such as ODP 671 (Moore et al., 1988) there is no indication of inverted velocities beneath the décollement. Beyond the initial 10-15 km the normal polarity décollement reflection observed in the multichannel profile, coupled with the apparent velocity of the Pd refraction, support a positive impedance contrast across the plate interface.

Distal terrestrial turbidites in the older Eocene-Oligocene section may provide a route for the eastward, lateral transport of water within those underthrust sediments, limiting the degree of fluid over-pressure that can be sustained at depth. Even within the thickest parts of the accretionary prism however, Vp in both the accreted wedge, and subduction channel is lower than would be expected for an equivalent thickness of sediment under normal compaction conditions (maximum velocities of 3 km s^{-1} vs predicted velocities of 3.5 km s^{-1} or greater given the thickness of sediment present, Bangs et al. 1990), and the velocity gradient is $\sim$50% that observed

on the incoming plate. This supports some degree of sustained high pore fluid throughout even the innermost accretionary prism. Bangs et al. (1990) observed similarly reduced semblance velocities in the prism which were attributed to ongoing, slow dewatering of even the oldest sediments within the accretionary wedge as much as 100 km from the deformation front.

5.8 Discussion

5.8.1 Controls on the Geometry of the Accretionary Prism

Of the along arc trends discussed in Chapter 2, there are two areas in which the nature of the sediments on the incoming plate may be expected to play a key role, these are the geochemistry of arc lavas (see Section 2.2.3) and seismicity (see Section 2.2.2). Given that this study does not provide any new information regarding the chemical composition of sediments within the Tiburon Basin, and that the broad sediment make-up seems to be largely in keeping with that observed in previous seismic studies and well penetrations there seems to be little that can be added to the geochemical story discussed previously. What this profile does offer however is one of the few modern seismic profiles imaging the structure of the shallow subduction channel away from the deformation associated with the Tiburon (Shipley et al., 1994) or Barracuda (Pichot et al., 2012) Ridges.

At accretionary margins, the taper of the accretionary prism is often considered to be a good indication of the degree of coupling across the plate interface, assuming that the prism has reached critical taper (and will therefore slide as new material is accreted, rather than deforming internally; Davis et al. 1983). Low levels of coupling generally result from elevated pore fluid pressures (which in turn is the result of a combination of factors such as lithology and convergence rate, Saffer and Bekins 2002) and generally promote stable, relatively aseismic sliding. This relationship between pore fluid pressures and coupling has been observed explicitly along the northern Hikurangi subduction zone using resistivity data, with the locked portions of the interface associated with high resistivity measurements (i.e. fluid poor regions of the subduction interface, Heise et al. 2013, 2017).

The accretionary prism, as imaged by Profile 1 has a very low angle frontal taper in a global

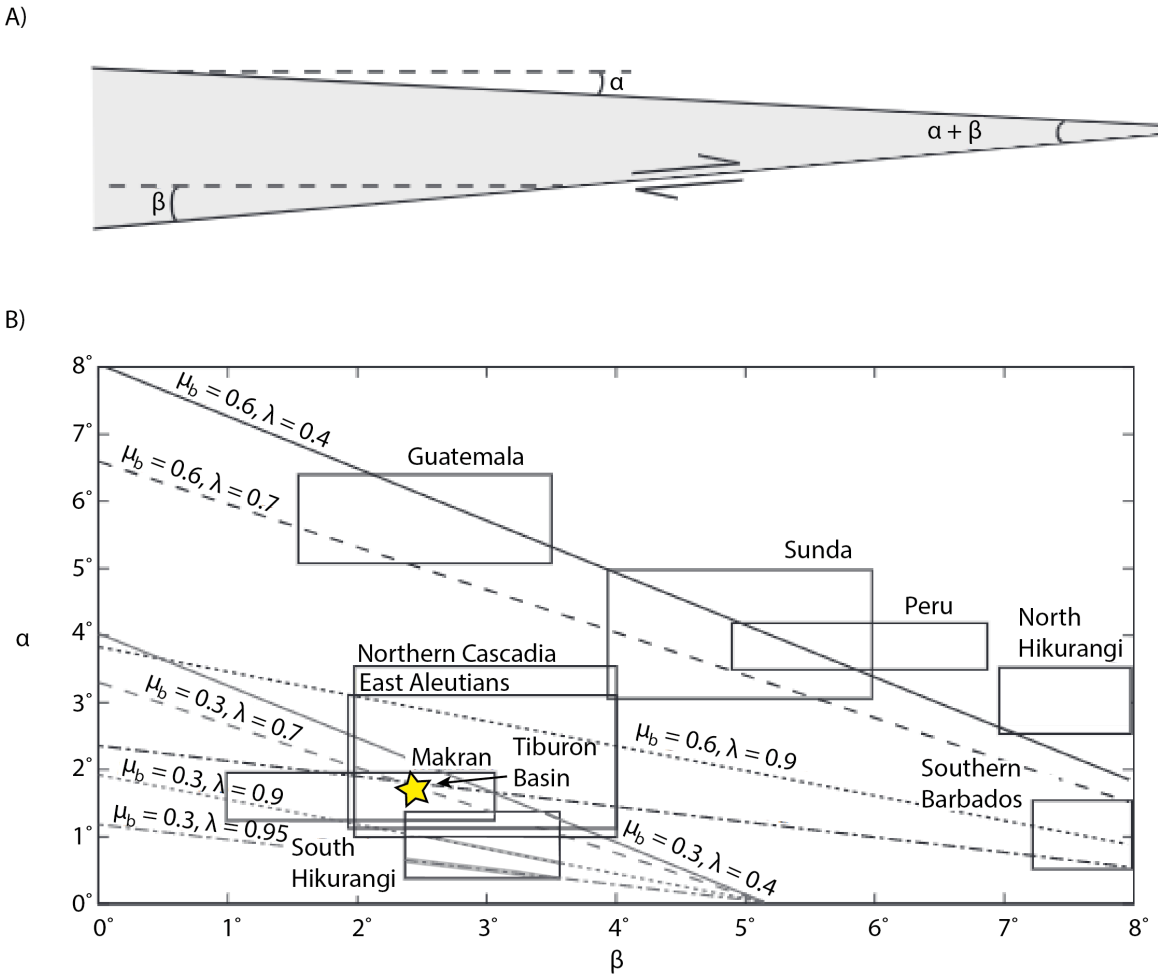


Figure 5.15: Accretionary prism geometry, from Fagereng (2011). A) Geometry of an accretionary prism. α denotes the prism slope. β denotes the basement/décollement slope. $\alpha + \beta$ is the prism taper. B) Summary plot of α (prism slope) vs β (basement/décollement slope) for an array of global subduction systems. Yellow star denotes the location of our Tiburon Basin profile within the plot. Dashed lines denote modelled trends for values of static coefficient of friction along the décollement (μ_b) and pore fluid factors (the ratio of fluid pressure over vertical stress, λ). The Tiburon Basin plots in a similar space to Makran, and South Hikurangi, where the low taper angle indicates weak interplate coupling. This is in keeping with the dominantly clay-like lithologies observed in the Tiburon Basin. Southern Barbados has a steeper basement slope, but is still expected to be exceedingly weakly coupled (in keeping with the low rates of seismicity).

sense (Figure 5.15). This value, the sum of the surface slope of the prism (α, $\sim$1.7° across the first 25 km of the prism slope) and the décollement dip (β, $\sim$2.5° between the frontal thrust and the point at which it pinches out against the Tiburon Basin) totals 4.2° along this profile. This agrees well with other studies of the prism geometry with a 0.6° surface slope previously observed north of the Tiburon Rise, versus 1.7° slope south of it (Biju-Duval et al., 1982; Westbrook, 1982). These values are similar to other global subduction systems such

as northern Cascadia (Figure 5.15B), which are proposed to have weakly coupled subduction interfaces (Fagereng, 2011). This is seemingly in keeping with the overall low rates of seismicity observed along the Lesser Antilles and the weak interplate coupling predicted across the arc front from GPS measurements (Symithe et al., 2015).

The presence of elevated fluid pressures within the accreted sediments is further supported by the Vp model within the accretionary prism. Velocities within the prism are lower than would be predicted from traditional compaction relationships with depth (Bangs et al., 1990). These elevated pore fluid pressures are likely to be sustained by the relatively clay rich composition, particularly within the post-Miocene sedimentary section, leading to water retention throughout the prism. The reverse polarity of the décollement reflection along the first 10-15 km of the subduction interface may also derive from focused high fluid pressures directly at the subduction interface. Whether these pressures are sustained at depth is unclear given the westward changes in the polarity of this décollement reflector (Figure 5.14).

Given these indicators of a seemingly weak subduction interface, not just within the Tiburon Basin, but across the whole arc front why then do we observe both a shallowing, and an increase in the rate of seismicity on the shallow part of the interface north of the Tiburon Rise (Bie et al. 2020, Figure 5.1)? The assumption that taper angle is entirely a function of coupling at the plate interface may be overly simplistic. A low taper angle can also be the result of erosion as a result of topography on the down-going plate. High levels of subduction erosion however are generally associated with strong interplate coupling (e.g. along parts of the Chile margin; von Huene and Ranero 2003). Subduction zones which show the highest rates of subduction erosion also tend to possess high convergence rates, unlike the Lesser Antilles (Clift and Vannucchi, 2004). Clift and Vannucchi (2004), proposed a transition from accretionary to erosional behaviour where sediments on the incoming plate at subducting margins fell below 1-1.5 km thickness. Although there are patches within the Tiburon Basin where this sediment thickness is exceeded (e.g. at 130 km, where sediment thickness is 2 km), the majority of sediments on the incoming plate north of the Tiburon Rise fall below this cut-off. Therefore, although the taper of the accretionary prism is consistently low across the entire arc front, there may obscure a transition across the Tiburon Rise from a weakly coupled accretionary margin where very thick sediments are subducting in the south, to an erosive margin, subducting a much thinner incoming sediment column in the Tiburon Basin.

5.8.2 Relating the Subduction Channel to Seismic Activity

As shown in Figure 5.1B, there are notable spikes in shallow interplate seismicity associated with the subduction of the Barracuda Ridge, Tiburon Rise and, to a lesser extent the St. Lucia Ridge beneath the south of the arc. These spikes are indicative of patches of localized coupling at the plate interface. Some degree of coupling is fairly indisputable, given the clear deformation of the forearc along the projection of the three ridges, giving rise to features such as the Arawak Basin (Laigle et al., 2013), and several studies have previously related the subduction of these features to local increases in the rate of seismicity (Stein et al., 1982; Christeson et al., 2003; Bie et al., 2020). The fact that the subduction channel is observed to be greatly reduced, if not entirely absent across the Tiburon Rise would only further increase the strength of this local coupling between the subducting ridges and the over-riding plate.

A similar process may also explain the increase in the rate of seismicity beneath the sections of the arc where the central part of the Tiburon Basin is currently subducting. Whilst the three ridges (Barracuda, Tiburon and St. Lucia) are the largest pieces of basement topography entering the arc, they are by no means the only basement topography observed on the incoming plate. In slow spreading crust, the crust is highly tectonized, the result of magma-poor volcanism and faulting to accommodate spreading (Section 2.3). Along this profile, the onlap of the oldest Cretaceous-Eocene sediments onto these basement features confirms that they are old structures, formed at the ridge. As a result of this topography, the thickness of the sediment column across the Tiburon Basin varies from just a few hundred meters (Moore et al., 1996) to as much as 2.5 km along the VoiLA profile. This variation is replicated in the thickness of the underthrust sediments. On this profile alone the offset between the décollement and top basement is seen to vary anywhere from less than 100 m to as much as 1.2 km, and it is inconceivable that there would not be several places within the central Tiburon Basin where this thickness reduces to zero, putting the basement of the incoming plate directly into contact with the base of the accretionary prism and crust of the forearc (which is particularly thick along this section of the arc, Section 2.2.1), leading to increased coupling and erosion of the over-riding plate.

The increase in the rate of interplate seismicity with subduction of the central Tiburon Basin is likely to be the result of this variability in the thickness of sediment, tied to substantial basement topography in the subduction channel. In the Pacific Ocean, the subduction of seamounts in

otherwise poorly coupled subduction systems has been seen to increase local coupling (Scholz and Small, 1997; Watts et al., 2010). The basement highs observed in the crust of the Atlantic, although formed through a different process may behave similarly. Localized variations in sediment thickness and basement topography both create frictional asperities and lead to spatial variations in fluid pressures within the décollement and underthrust sediments (Zhao et al., 1998). Despite elevated fluid pressures throughout the accretionary wedge sediments, as indicated by the velocities observed in the wide-angle profile, short-lived zones of increased coupling can form across the subduction interface and fail seismically, even at depths as shallow as 10 km (Bie et al., 2020). The over-riding plate is also likely to have experienced damage as a result of the subducting topography, and the southward sweeping of the Tiburon Rise in particular, leading to further heterogeneities along the megathrust (Evain et al., 2013; Laigle et al., 2013). That is not to say that very large strain buildups, and major earthquakes in this region are impossible, as the earthquake of 8^{th} February 1843 (one of only two earthquakes in the recorded history of the Antilles to exceed a magnitude of 8), likely occurred north of Guadeloupe, within the confines of the subducting Tiburon Basin (Feuillet et al., 2011). Large megathrust earthquakes may be aided by the relatively cold nose of the mantle wedge at the Lesser Antilles, which extends the seismically active portion of the plate interface to depths of as much as 65 km (Bie et al., 2020).

In contrast, in the south of the arc, the extreme thickness of terrestrial derived sediments totally blanket the topography of the incoming plate, this creates a much smoother interface along the subduction channel, and a transition to more accretionary margin behaviours, with little/no seismicity along the plate interface at depths of less than 30 km. However, other subduction systems with a thick subduction channel, and seemingly weak interface still host large seismic events (Ruff, 1989). Indeed, the earthquake of 11^{th} January 1839 (the second earthquake of magnitude greater than 8 known from the Antilles) occurred south of the Tiburon Rise near Martinique (Feuillet et al., 2011). At depth, the loss of water from a thick sediment channel such as that in the southern Lesser Antilles may provide an almost ideal surface for a large regional failure of the plate interface (Ruff, 1989; Scherwath et al., 2009; Contreras-Reyes et al., 2010). Similar correlations between the largest megathrust events and the thickest parts of the subduction channel are known from the Chile subduction zone (Scherwath et al., 2009; Contreras-Reyes et al., 2010). It is therefore possible that the plate interface in the south of the arc could be capable of hosting earthquakes as large, if not larger, than those recorded from

the more seismically active north of the arc. As a result regions such as east of Grenada, which from recorded seismicity are almost totally aseismic (Section 2.2.2), may be purely a function of the very low convergence rates at the Lesser Antilles. Despite the seeming lack of seismic activity in these regions they should be considered a considerable earthquake risk.

5.9 Conclusions

In this chapter I have presented the interpretation of a new high resolution PSTM multichannel profile, along with corresponding bathymetry data, and a wide-angle P-wave velocity model for the sediments across the central part of the Tiburon Basin.

- Interpretation of the profile, and comparison to previous seismic studies and well data within the region suggests that sediment composition is relatively consistent throughout the basin. Sediment thicknesses on the incoming plate vary from as little as 400 m to more than 2 km. This variation is principally controlled by variable basement topography across the slow-spreading, tectonized Atlantic oceanic crust.

- Within the accretionary prism, a new wide-angle profile indicates low sediment velocities as a result of elevated fluid pressures throughout the sediment wedge. A low taper on the accretionary prism may also indicate weak interplate coupling. Alternatively, the low taper angle in the north may be the result of a transition to an erosive margin as a result of thinning of the sediments on the incoming plate.

- A stark increase in shallow interplate seismicity is observed coincident with the subducting Tiburon Basin. This is proposed to be the result of a heterogeneous subduction channel creating considerable spatial variations in the degree of coupling within the basin. These variations are primarily driven by the basement topography of the slow-spreading Atlantic oceanic lithosphere.

- The Lesser Antilles is likely still capable of producing large subduction interface earthquakes exacerbated by the extended cold nose. In the south, which is typically considered "aseismic" the thick subduction interface may create optimum conditions for large megathrust events once the underthrust sediments dewater at $\sim$30 km.

- An increase in faulting observed in bathymetry and multichannel data across the outer rise may provide pathways via which water is able to infiltrate the upper oceanic lithosphere. Understanding the role played by outer rise hydration along the Lesser Antilles arc will be the subject of the next chapter.

Chapter 6

Results: Outer Rise Hydration

The following chapter is presented in the form of a manuscript draft in preparation for submission to JGR.

6.1 Abstract

Island arc volcanism is driven by the release of H_2O from subducting slabs. Constraining the water content of the slab is therefore vital if we are to understand patterns of arc behaviour including hazardous processes such as volcanism and seismicity. A significant volume of the water contained in the subducting lithosphere and released at depth during subduction is stored within the mineral serpentine, the product of the hydrous alteration of olivine. In studies of subduction zones in the Pacific and Indian oceans, the majority of mantle hydration occurs as a result of bend faulting in the outer rise. This process can be imaged in wide-angle seismic surveys due to the reduced Vp of serpentinite compared to unhydrated peridotite velocities. This chapter presents the first wide-angle experiment across the outer rise of the Lesser Antilles arc, one of only two subduction zones globally to subduct slow spreading oceanic crust. As the incoming plate passes the outer rise the lower oceanic crust velocity is reduced by 0.3-0.4 km s^{-1} due to hydrous alteration. Most strikingly a shadow zone consistently observed on instruments between 30-45 km offset is indicative of an abrupt velocity inversion near the Moho. A wide-angle reflection from ∼3-5 km beneath the top of the velocity inversion is interpreted

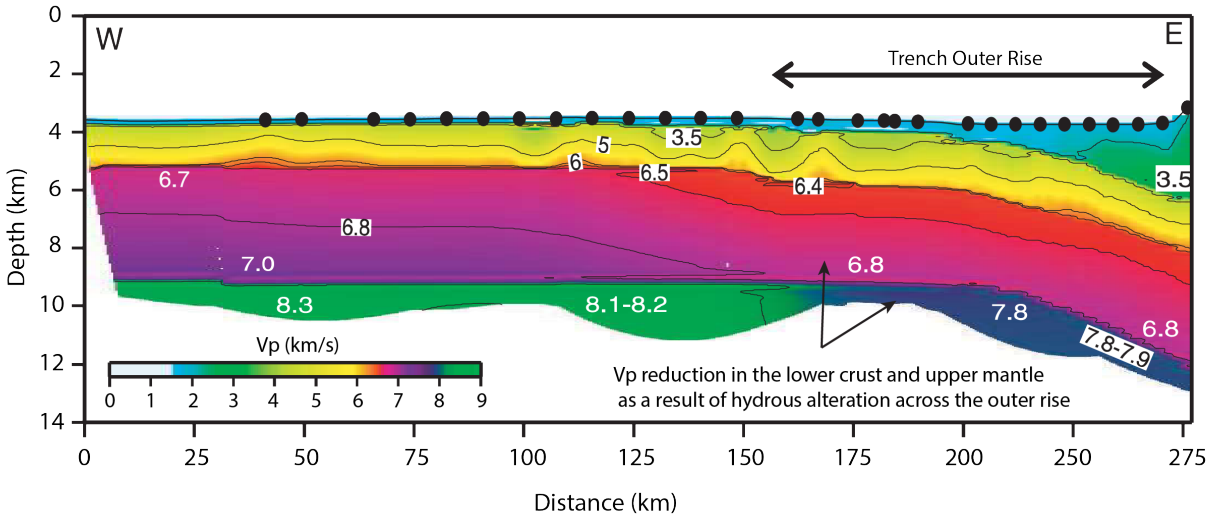


Figure 6.1: Example of outer rise hydration, captured in a wide-angle study from the Chile trench. Note the reduction in the velocities of the lower oceanic crust and upper mantle as a result of alteration, starting ∼50 km seaward of the trench. Figure from Contreras-Reyes et al. (2007).

as a hydration front, constraining the maximum depth of serpentinization. Velocities in the upper mantle are observed as low as 6.2 km s^{-1} indicating a high degree of hydrous alteration. The observed structure is explained by low convergence rates across the Lesser Antilles trench, combined with the highly tectonised structure of slow spreading crust, establishing a high degree of serpentinization across the outer rise.

6.2 Introduction

The release of water through breakdown of hydrous minerals in the slab is the main driver of subduction volcanism, depressing the solidus of the over-riding mantle wedge and producing melt (White et al., 1970; Stern, 2002). The mineral serpentine, formed via the hydrous alteration of olivine, contains up to 13 wt% H_2O and, is volumetrically one of the largest contributors of water to the deep mantle wedge during subduction (Schmidt and Poli, 1998; Hacker, 2008; van Keken et al., 2011). In slow spreading crust, serpentine is concentrated at the end of ridge spreading segments at transform faults, second order non-transform offsets, and core complexes (Section 2.3).

Oceanic crust formed by slow seafloor spreading is thought to be inherently more hydrated than that generated by fast spreading (Section 2.3). At many subduction zones, a second

phase of hydration is observed across the outer rise as the down-going plate enters the trench (Grevemeyer et al., 2018). Bend faults create pathways via which water can access the lower crust and upper mantle. These fault systems have been observed using a range of methodologies including seismic imaging (Ranero et al., 2003), bathymetric surveys (Boston et al., 2014; Fujie et al., 2018), and mapping of extensional earthquakes within the crust of the incoming plate (Lefeldt et al., 2009; Craig et al., 2014). At the Middle America trench these faults are imaged in seismic data to sub-Moho depths (Ranero et al., 2003). Along the Middle America Trench Naif et al. (2015) observe a clear correlation between resistivity anomalies and bending faults, supporting the hypothesis that permeable fault zones are acting as conduits to transport water into the lower crust and mantle.

The reaction to form serpentinite from dry peridotite alters the mechanical properties of the upper mantle, resulting in volumetric expansion, and a density reduction of up to 20% (3.3 g cm^{-3} to 2.65 g cm^{-3}, O'Hanley 1992). This alteration leads to a decrease in Vp, which allows it to be imaged in wide-angle seismic surveys (Figure 6.1). The degree of serpentinization observed varies widely between different subduction systems. Particularly large velocity anomalies have been observed at the outer rise of the Nicaragua subduction zone (Van Avendonk et al., 2011) and Mariana (Wan et al., 2019). In the latter case upper mantle P-wave velocities are reduced to as little as 6.8 km s^{-1} (versus 7.8 - 8 km s^{-1} for dry peridotite). This equates to as much as 38% serpentinization of the upper mantle (Wan et al., 2019). This contrasts with Cascadia, where there is no detectable velocity reduction (Horning et al., 2016). The degree of alteration may be influenced by factors including sediment thickness on the incoming plate (Contreras-Reyes et al., 2007), the age of the slab (Horning et al., 2016; Grevemeyer et al., 2018) and the orientation of convergence at the trench compared to the seafloor spreading fabric (which may dictate the style of bend faulting, Fujie et al. 2018).

As one of only two subduction zones to consume slow spreading Atlantic crust, the Lesser Antilles arc is an important case-study if we are to understand the relationships between the hydration of the subducting slab and potentially hazardous arc processes (Section 2.2). The incoming Atlantic lithosphere is likely to possess a heterogeneous hydration pattern (Section 2.3) which may be dictating along strike variations in crustal structure (Schlaphorst et al., 2018; Melekhova et al., 2019), seismicity (Schlaphorst et al., 2016; Paulatto et al., 2017) and arc geochemistry (Davidson, 1985). The degree to which further hydration of the lithosphere as

a result of bend faulting in the outer rise may contribute to arc processes is essentially unknown. Previous wide-angle studies of outer rise hydration come exclusively from the Pacific and Indian oceans (Grevemeyer et al. 2018, and references therein), where the crust is universally faster spreading and structurally uniform. In the most well studied subduction systems such as the Chile trench and Central America the subducting crust is also considerably younger (and therefore warmer) than the 90 Ma lithosphere subducting at the Lesser Antilles today (e.g. Contreras-Reyes et al. 2007; Van Avendonk et al. 2011). The arc is thus also a key end-member in understanding the processes which govern serpentinization beneath the outer rise.

6.2.1 Regional Setting: The Lesser Antilles

The Lesser Antilles is the surface expression of the slow westerly subduction of Atlantic oceanic lithosphere at rates of less than 2 mm yr^{-1}. The structure of the incoming plates is complex, with several fracture zones, non-transform offsets (NTOs), and aseismic ridges currently undergoing subduction (Figure 6.2). The Tiburon Basin is located in the centre of the 800 km arc, outboard of Dominica. The basin lies between the Barracuda and Tiburon Ridges, which formed as a result of convergence across the diffuse North and South American plate boundary since the Cenozoic (Chapter 5). This central portion of the arc is home to some of the highest rates of magmatic and seismic activity (Section 2.4). The basin is the optimal location to assess outer rise hydration along the arc. Further north subduction becomes increasingly oblique, leading to a flattening of the slab, as the Lesser Antilles transitions into the Puerto Rico Trough. To the south, the sediments on the incoming plate may exceed 7 km thickness (Moore et al., 1988). This accumulation is the result of the obstruction of the northward transport of large volumes of terrestrial sediment from South America by basement topography such as the Tiburon Rise on the incoming plate (Chapter 5). Aside from any influence this may have over the degree of outer rise hydration, such thick deposits would likely limit the resolution of any wide-angle study of the area.

Bathymetry data and coincident multichannel seismic data from the Tiburon Basin show that there is an increase in both the density and length of faults in the sediments of the incoming plate as it approaches the trench (see Chapter 5). There is no evidence for the formation of new, high offset bend faults in the multi-channel profile as has been previously identified across the outer rise of subduction systems such as Middle America (Ranero et al., 2003) and Japan

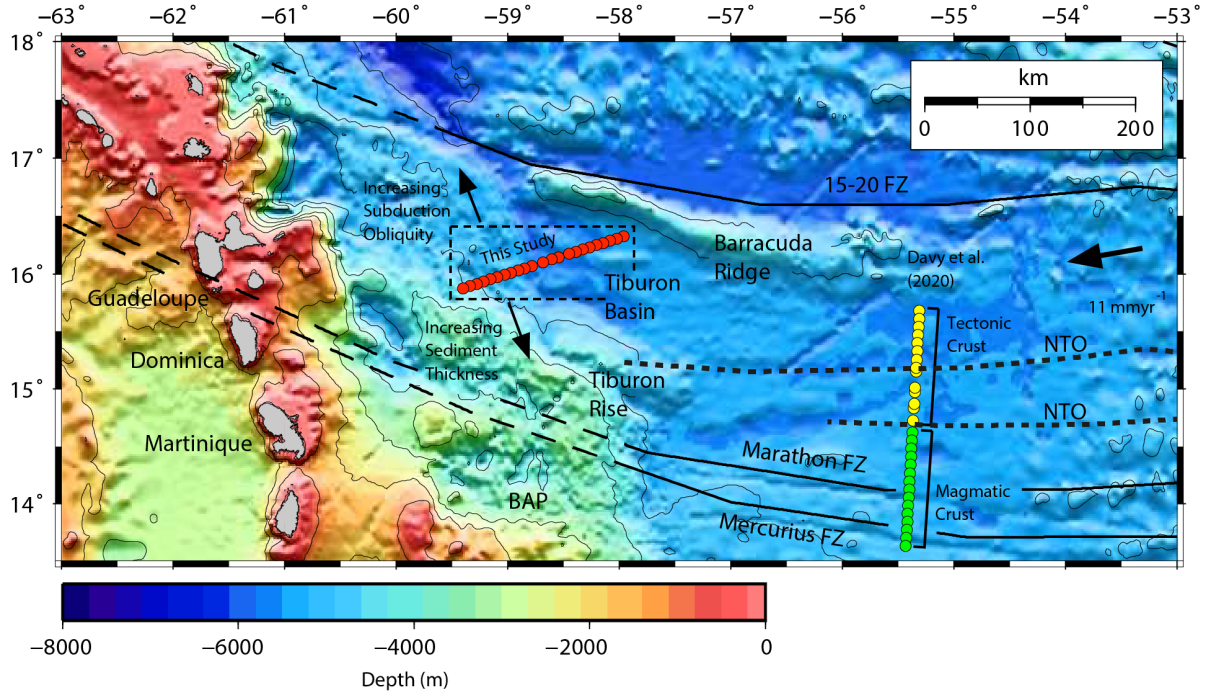


Figure 6.2: Location of wide-angle study conducted across Lesser Antilles outer rise. OBS stations used in the acquisition of VoiLA profile 1 are shown in red. To the east the location of the wide-angle study of VoiLA profile 2/3 presented in Davy et al. (2020) is shown with OBS above tectonically controlled crust in yellow, and magmatic crust in green. The final Vp model along profile 2/3 is shown in Figure 6.16. In the case of both profiles every second OBS station is shown. Geometry of subducting fracture zones shown were modelled as flow lines in G-Plates (see Appendix D for details), using the model of Müller et al. (2019). Geometry of secondary discontinuities (Non Transform Offsets, NTOs) from Davy et al. (2020). Convergence vector taken from Submap 4.2 online database (http://submap.gm.univ-montp2.fr/index.php, Heuret and Lallemand 2005). BAP = Barbados Accretionary Prism.

(Fujie et al., 2018). Instead, outer rise bending seems to be largely reactivating the pre-existing seafloor spreading fabric (which is primarily orientated NNE-SSW, ∼30° offset from the trench axis, Figure 5.3). This network of normal faults is first visible at the seabed ∼60 km from the toe of the accretionary prism, with faults spaced approximately every 1-1.5 km (Figure 5.11) and provides a possible pathway for hydration of the subducting slab.

6.3 Data

The data discussed here comes from the same wide-angle experiment described in the previous chapter (see Section 5.5 for survey acquisition and geometry, and preliminary processing steps), acquired by the R.R.S. James Cook in May 2017 as part of leg JC149 of the VoiLA (Volatile

Recycling in the Lesser Antilles) experiment (Collier, 2017). This chapter focuses exclusively on the 174 km wide-angle profile, and the generation of a velocity model in order to assess hydration processes beneath the Lesser Antilles outer rise.

6.3.1 Phase Identification

As discussed in Chapter 5, VoiLA profile 1 was instrumented with 48 OBS numbered from OBS1 at the eastern end (incoming oceanic crust), to OBS48 at the western end (accretionary prism). See Appendix D, for a full set of summary record section and corresponding ray-trace plots through the final velocity profile.

The apparent velocities of all first arrivals were influenced by the basement topography of the incoming plate to some degree, particularly at short offsets. The precise transition from Pg (turning rays within the crust) to Pn (turning rays within the mantle) was often difficult to determine as a result. The amplitude of first arrivals was also reduced on the instruments above the accretionary prism, particularly at long offsets. This is likely a product of increased attenuation as a result of scattering within the sediments of the accretionary prism, which possess little coherent internal structure (Figure 5.12) and poorer coupling between the seismometer and the seabed. On instruments 34, 36 and 41, the hydrophone was preferred for picking due to the poor quality of arrivals on the broadband seismometer. On instruments such as OBS19 (Figure 6.3), Pn arrivals show a clear reduction in apparent velocity as a result of the dipping basement beneath the first 25 km of the accretionary prism.

On instruments on the easternmost section of the profile (OBS2-OBS14) the pattern of arrivals is typical for oceanic crust (Figure 6.3). Pg first arrivals, with apparent velocities of 4.5-7 km s^{-1}, give way to Pn first arrivals with apparent velocities of $\sim$8 km s^{-1} at offsets of 30-40 km (Figures 6.3, 6.4 6.5). A reflection, most likely PmP (a reflected P-wave from the Moho) forms a triplication with Pg and Pn arrivals (Figures 6.3, 6.4, 6.5), and was picked at offsets between 20-40 km.

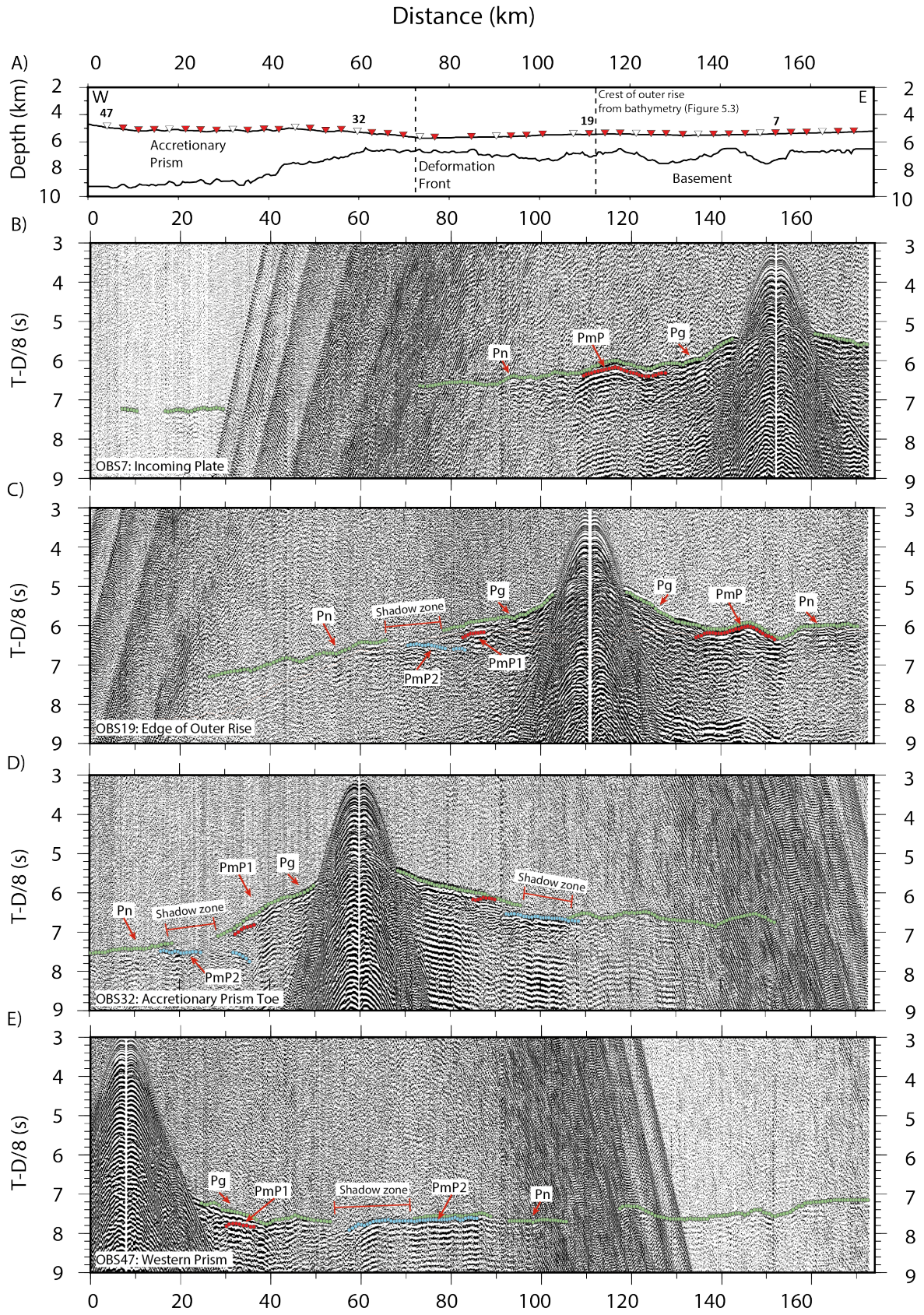


Figure 6.3: Examples of OBS record sections with key phases labelled. First arrival picks (Pg + Pn) are shown in green, PmP/PmP1 in red and PmP2 in blue. B) Record section from OBS7 typical of the incoming plate on the easternmost part of the profile. Moving westward (from OBS14), we observe a clear shadow zone and PmP1 and PmP2 reflections. OBS19 bridges this transition, leading to the clear asymmetry between shots from the east (positive offsets) and west (negative offsets) even before the topography of the accretionary prism has an affect. Plots repeated without overlying interpretation in Figure 6.4. See Appendix D, for a full set of record sections, and corresponding ray-trace plots

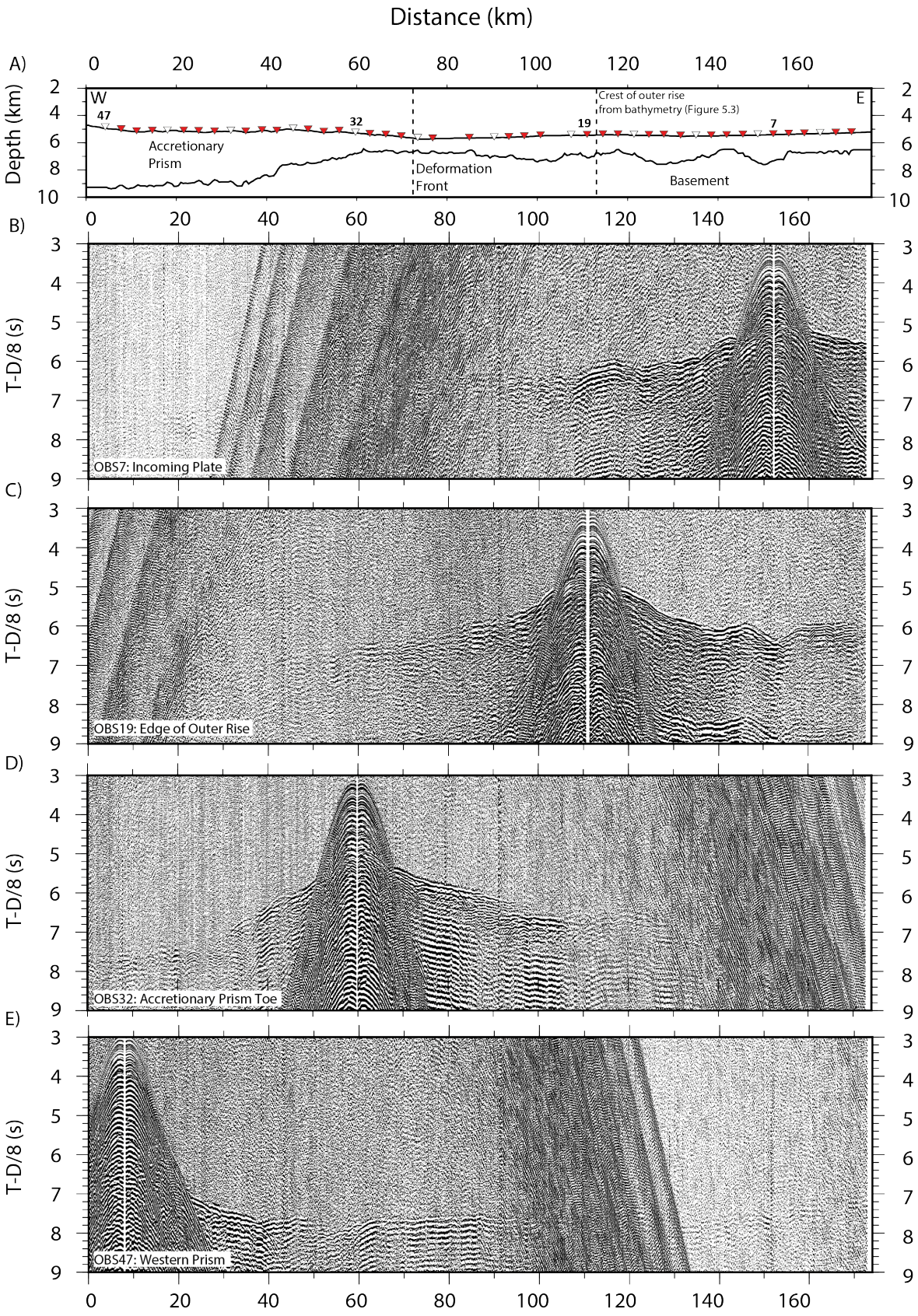


Figure 6.4: Uninterpreted versions of the OBS record sections shown in Figure 6.3. See Appendix D, for a full set of record sections, and corresponding ray-trace plots.

On instruments west of OBS14, one of the most striking features of the data is the presence of a shadow zone (Figures 6.3, 6.4, 6.5). On wide-angle data, shadow zones are caused by negative velocity gradients, most commonly as a result of the presence of magma chambers in surveys at mid-ocean ridges (e.g. Singh et al. 1998). The shadow zone was present on shots to the west (negative offsets) of all instruments west of OBS14, and was present on both the positive and negative offsets of all instruments west of OBS24 (Figure 6.5). Across these stations, the shadow zone appeared at a mean offset of 32 km, extending to 45 km (i.e. 13 km across). On OBS39 the shadow zone is observed at offsets as short as 25 km. Conversely, on OBS47 it does not occur until an offset of 45 km. The breadth of the shadow zone varies from as little as 5 km (OBS16) to as much as 31 km (OBS48, though here it may reflect image quality, no other station shows a shadow zone more than 23 km wide).

The shadow zone coincides with the transition from crustal Pg first arrivals (with apparent velocities between 4.5-6.5 km s^{-1}), to upper mantle Pn arrivals (with apparent velocities of 7.5+ km s^{-1}) suggesting that it is the result of a low velocity layer either at, or across, the oceanic Moho. On instruments where there is a shadow zone, two reflected phases were visible, rather than a simple PmP reflection. The first of these, PmP1, was a weak reflected phase coincident with the top of the shadow zone. PmP1 was clearest at offsets of 20-25 km (Figure 6.5). PmP2 was coincident with the base of the shadow zone. It was higher amplitude than PmP1 and appeared at longer offsets between ∼30-50 km (Figure 6.5).

The change in the pattern of arrivals is coincident with the onset of the influence of outer rise bending identified in Chapter 5. The first clear observations of PmP2, on OBS14 and OBS15, would suggest a bounce point at ∼110-115 km along the profile, ∼15 km within the region influenced by outer rise bending. On instruments such as OBS19 (Figure 6.3C), located near this transition from the crust of the incoming plate to the region affected by outer rise bending, this results in a clear asymmetry between positive and negative offset arrivals.

On almost all stations Pn travel times were picked to offsets in excess of 100 km, often encompassing the full range of offsets outside of regions of previous shot multiple (which particularly obscured the first arrival from offsets of 80-120 km, Figure 6.3) and the shadow zone. On some stations picking within this noise was aided by the use of trace mixing (across a window of 5 adjacent traces) and/or F-K filtering (using a fan shaped filter, removing velocities of 1.5-2.5 km s^{-1}, and frequencies of 3-40 Hz) which suppressed the wrap-around noise.

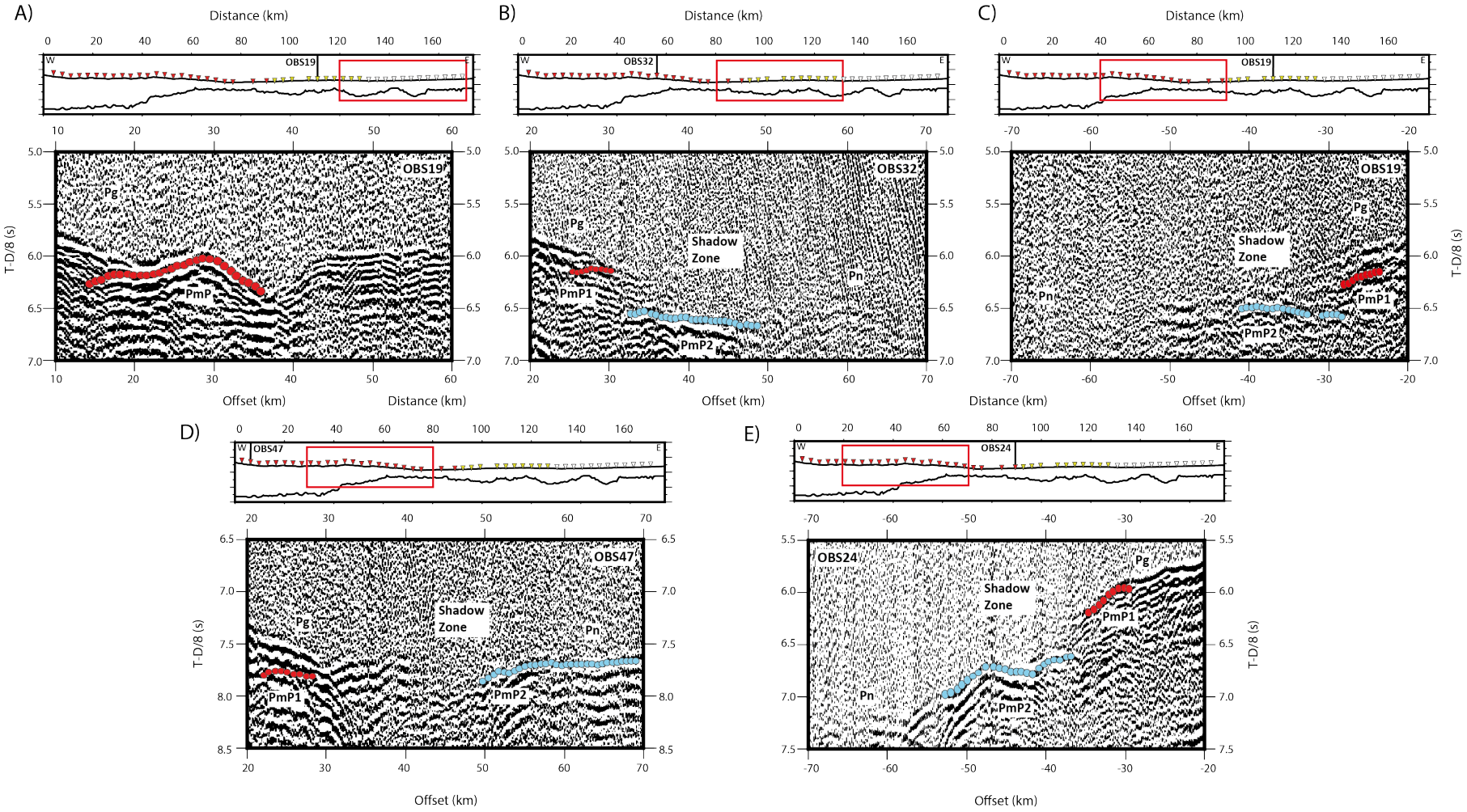


Figure 6.5: Examples of OBS record sections focused across the transition from Pg to Pn. On upper profiles OBS where no shadow zone is observed shown in white (OBS2-OBS13). OBS where shadow zone is only observed in negative offsets shown in yellow (OBS14-OBS23). OBS where shadow zone is observed on both positive and negative offsets shown in red (OBS24-OBS48). PmP/PmP1 picks shown in red, PmP2 picks in blue. 1 in 5 picks shown. Red box denotes the window of offsets shown in the record section below. Note that on the easternmost part of the profile (OBS19, A), there is clear continuity between Pg and Pn despite basement topography. PmP forms a triplication between Pg and Pn and is observed between 20-40 km offset. West of OBS14 a shadow zone of ∼13 km offset is observed disrupting first arrivals. Two distinct reflections are observed. PmP1 is generally picked between 20-25 km offset, though is relatively weak and inconsistent. PmP2 is a clearer arrival (See B and E in particular) observed within the shadow zone at offsets of 30-50 km. See Appendix D, for a full set of record section and corresponding ray-trace plots.

For the purposes of tomographic inversion, well imaged first arrivals (Pg + Pn), with an offset of less than 50 km were assigned a pick uncertainty of 0.05 s. As offsets increased, and the wrap-around noise affected the clarity of arrivals, uncertainties were increased linearly to 0.1 s over a window of 50-75 km offset. All arrivals from more than 75 km offset were assigned an uncertainty of 0.1 s. Uncertainties of 0.1 s were assigned to all reflected phases, which were more susceptible to misinterpretation than the first arrivals (particularly the weak PmP1 reflection). The uncertainty of 0.1 s is approximately equivalent to a maximum picking error of one full wave cycle.

6.4 Tomography

Inversion of picked travel times to produce a final P-wave model was done using the joint reflection/refraction travel time tomography code Tomo2d (Korenaga et al., 2000). This code simultaneously inverts for reflected and refracted phases in order to find a best fitting 2d velocity model. The sediment velocity structure discussed in the previous chapter (Section 5.7) was reformatted for Tomo2d and is used to define the sedimentary section of the model. The Tomo2d model consists of a velocity mesh constructed of nodes every 0.5 km laterally. Vertically the node spacing starts at 0.1 km to a depth of 5 km (fully encompassing the maximum thickness of the accretionary prism) and is then linearly increased to a spacing of 0.5 km at the base of the model (25 km below the seafloor). Reflected phases within Tomo2d are modelled as floating reflectors, and do not necessarily correspond to a velocity discontinuity within the mesh.

Similar to the RAYINVR software (Zelt and Smith, 1992) utilized in the previous chapter Tomo2d makes use of seismic ray theory, in which the 3 dimensional displacement field is simplified to a series of individual rays travelling normal to the wave-front between the source and receiver. This approach allows the behaviour of individual phases such as direct P and S wave arrivals and reflected phases to be considered independently, but ignores wave behaviours such as diffraction and scattering. As such these travel-time inversion schemes do not take into account observations such as the amplitude reduction observed on instruments on the accretionary prism. In order to solve for these ray paths and associated travel times Tomo2d uses a hybrid method (Korenaga et al., 2000), first calculating the shortest path between source and receiver (the graph method), before minimizing the travel time along the calculated ray

path (the ray bending method). The graph method alone can often lead to over-estimates of the travel time between two points as rays will tend to zigzag between adjacent velocity nodes.

6.4.1 Inversion Scheme

As the sediment Vp structure was already well-defined by the RAYINVR modelling discussed previously (Section 5.5.3) and Tomo2d is unable to model secondary arrivals (such as the majority of the turning rays within the accretionary prism), no full inversion is performed for the sediment structure. Instead, a lightly damped inversion was run using just the picked top basement (PbP) reflections (Section 5.5.3) along the whole profile to ensure that no major velocity anomalies had been introduced during the conversion from the layered RAYINVR format to the Tomo2d mesh. This inversion used a horizontal and vertical correlation length of 3 km and 0.5 km respectively. The depth of the top basement reflector was not allowed to vary. After 10 inversion steps no velocity changes greater than 0.07 km s^{-1} were introduced into the sediment column, and the full set of PbP arrivals were fitted with an RMS of 0.091 s. As a result, the sediment column was left fully damped for all subsequent inversion stages.

Inversions were performed using a top-down methodology in three stages following initial tests to optimize the parameterization for the weighting and smoothing of the model at each stage. Unless otherwise specified this inversion scheme is used in all inversion tests discussed in the following sections. The first stage of the inversion focused on the crust. Where no shadow zone was present this used Pg arrivals with an offset of less than 50 km. Where a shadow zone was present only arrivals from prior (i.e. shorter offsets) to the shadow zone were used (totalling 13,028 picks). PmP (OBS2-24) and PmP1 (OBS14-48) were modelled as a single continuous floating reflector (total 4,502 picks) with a node every 4 km. All inversion steps use a velocity smoothing weighting factor of 70, horizontal correlation lengths that increased from 3 km to 15 km with depth and vertical correlation lengths that increased from 0.5 km to 2 km with depth. For the reflectors a correlation length of 10 km and depth smoothing weighting factor of 50 was used. A depth kernel weighting factor of 1 meant that reflected and refracted phases were weighted equally.

The output model from stage 1 was then used as an input to invert for the velocity structure of the lower crust and upper mantle. This inversion contained Pg and Pn arrivals from all offsets

(28,657 picks), and the same set of PmP + PmP1 reflections from the previous stage (4,502). The final stage of the inversion determines the velocities within the upper mantle and position of the PmP2 reflector. As Tomo2d only allows for one floating reflector to be used at a time the model was fully damped down to the depth of the best fitting PmP/PmP1 reflector from the previous inversion steps (damping weight of 10000) such that the velocity structure above it would remain essentially unchanged. The step contained the same set of refracted arrivals as in the previous step (28,657 picks), plus PmP2 reflections (4,163 picks).

6.4.2 Initial Inversion Tests

It is well known that the result of tomographic inversions such as these can be heavily influenced by the structure of the starting model. Hence, it was important to first optimize the structure of the starting velocity mesh. Key assessment criteria of the resulting velocity models includes 1) the overall travel-time misfit of picked arrivals, 2) χ^2 (targeting a value of 1), 3) the final model should be geologically reasonable (in particular offering an explanation for the shadow zone and paired PmP1 and PmP2 reflections seen on OBS).

An initial inversion test was done using a starting model (starting model 1) with an initial crustal structure taken from the global oceanic compilation of White et al. (1992), consisting of a "typical" 2-layer igneous crustal structure (starting model 1). Velocities in the upper crust (oceanic layer 2) increase linearly from 4.5 km s^{-1} to 6.6 km s^{-1} over a depth of 2.11 km. In the lower crust "layer 3" the velocity gradient is reduced, increasing from 6.6 km s^{-1} to 7.6 km s^{-1} over a depth of 4.97 km. Figure 6.6 shows the result when this model is inverted according to the scheme described previously. The result of this inversion, along with the other trial starting models discussed in the following section, are summarized in Table 6.1.

Following inversion of starting model 1, the output velocity profile (Figure 6.6B) had a good overall RMS travel time misfit of 0.062 s (Table 6.1). The resulting model also showed clear changes in the velocity structure of the upper lithosphere moving east to west towards the trench. As a result of the lack of first arrivals through the shadow zone, the inversion near the crust-mantle boundary is poorly constrained west of OBS14. Regardless of the inversion scheme or parameterization used the code was unable to generate a low velocity layer capable of explaining the shadow zone observed on OBS. Beneath the western part of the profile, the

Model	Phase	RMS Misfit (s)	Chi^2
1) White et al. (1992) structure (Figure 6.6)	Pg + Pn	0.059	0.82
	PmP + PmP1	0.061	0.38
	PmP2	0.083	0.69
2) Constant gradient velocity structure (Figure 6.7)	Pg + Pn	0.071	0.20
	PmP + PmP1	0.074	0.55
	PmP2	0.088	0.77
3) Low Velocity Layer (0.3 km s^{-1} contrast)	Pg + Pn	0.063	0.88
	PmP + PmP1	0.060	0.36
	PmP2	0.088	0.79
4) Low Velocity Layer (0.4 km s^{-1} contrast)	Pg + Pn	0.058	0.79
	PmP + PmP1	0.060	0.37
	PmP2	0.083	0.69
5) Low Velocity Layer (0.5 km s^{-1} contrast, Figure 6.8)	Pg + Pn	0.058	0.80
	PmP + PmP1	0.061	0.37
	PmP2	0.084	0.72
6) Low Velocity Layer (0.6 km s^{-1} contrast)	Pg + Pn	0.063	0.89
	PmP + PmP1	0.060	0.36
	PmP2	0.092	0.84

Table 6.1: Travel time misfit listed by phase for key starting model tests. Starting model 5 (Figure 6.8) was preferred for the final model as it produced both a good travel time misfit and correlation between the top of the low velocity layer and PmP1 floating reflector.

velocity gradient of the lower crust is reduced to <0.2 s^{-1}. However, this is not atypical for oceanic crust (White et al., 1992; Christeson et al., 2019). This indicated that a generic starting model such as this was insufficient to explain key initial observations from the data.

6.4.3 Optimizing the Starting Model

A fresh inversion of all the picked data was run using a starting model with a simplified, constant gradient throughout the whole lithosphere (starting model 2). The velocity structure within the crust and mantle, increased linearly from 4.5 to 8 km s^{-1} at a depth of 12 km beneath top basement. This very simple structure was tested in order to remove any pre-existing conceptions regarding the structure of the lithosphere, such as the depth of the oceanic layer 2/3 boundary, or depth of the Moho (Figure 6.7), thus avoiding concentrations of ray coverage due to boundaries in the starting model. This used a simplified version of the inversion scheme described above with velocity smoothing weighting factors reduced to 50. Whilst this led to a less smooth final model, it made it easier to identify regions where the inversion had made significant changes to the starting velocity structure.

This test produced a velocity model which was broadly the same as that shown previously

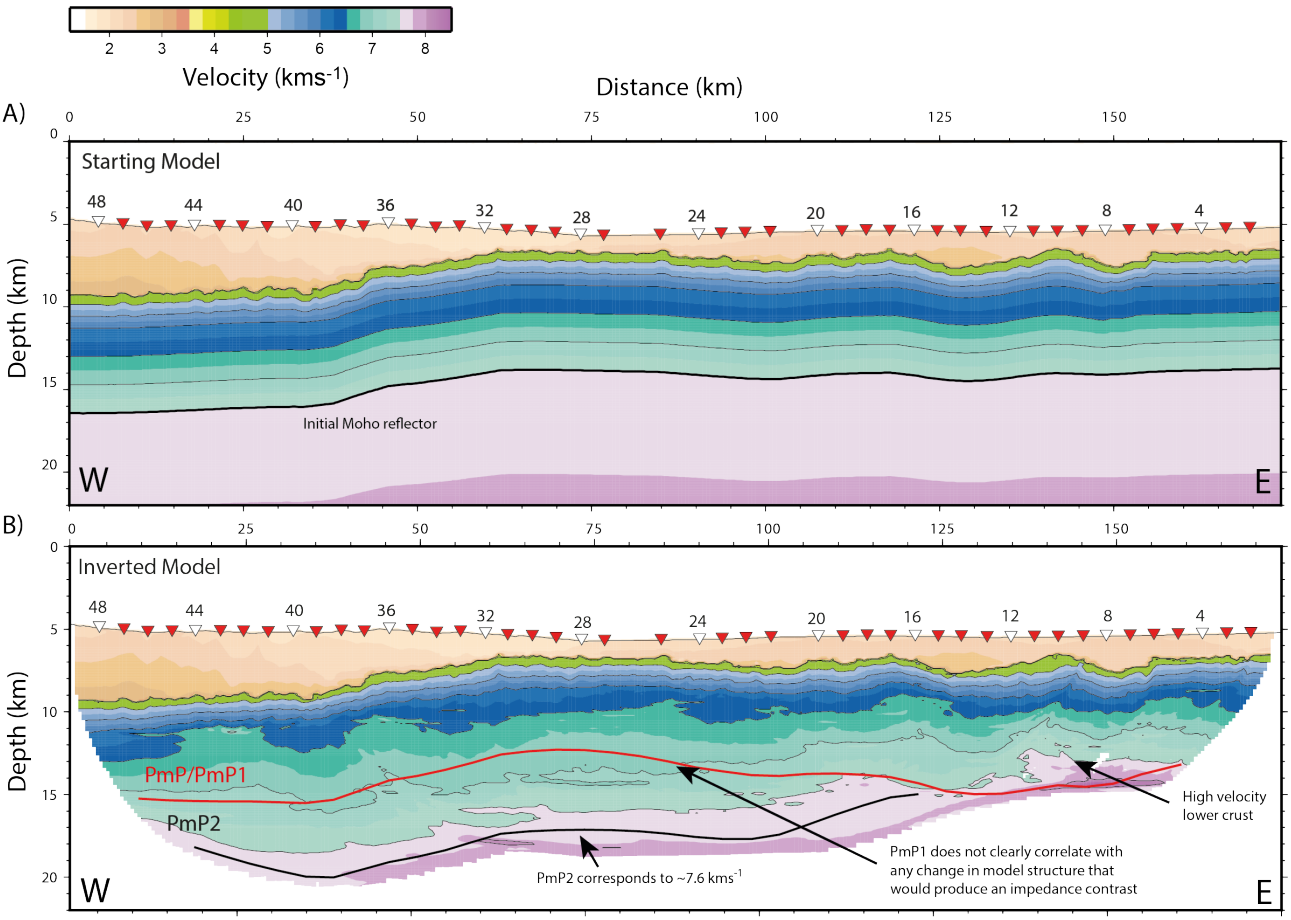


Figure 6.6: Result of initial inversion test, using a starting model based on the average global oceanic crustal structure from White et al. (1992). A) Starting model 1. Sediment velocities are converted from the sediment velocity model described in the previous chapter (Section 5.7). B) Final model following 3 stage top down inversion. Along the easternmost part of the velocity profile (125 - 174 km), prior to the influence of the shadow zone, model shows 7 km thick crust. High velocities (>7.4 km s^{-1}) in the lower crust may be indicative of a transitional Moho. To the west PmP2 seems to correlate with "dry" peridotite velocities of >7.6 km s^{-1} in the upper mantle (15 - 120 km). This model does not provide any clear explanation for the PmP1 reflector, or the shadow zone observed on OBS and so was rejected.

(Figure 6.7B vs 6.6B), again failing to generate a low velocity layer. However, the difference plot (Figure 6.7C) clearly identified a region under the western part of the model (35-90 km, ~5 km below top basement) in which the inversion was unable to make any changes to the initial velocity structure. The upper surface of this layer coincided with the floating reflector fitting the PmP1 arrivals (Figure 6.7C). This seemingly poorly constrained region is the most likely location for a low velocity layer responsible for the shadow zones observed on OBS.

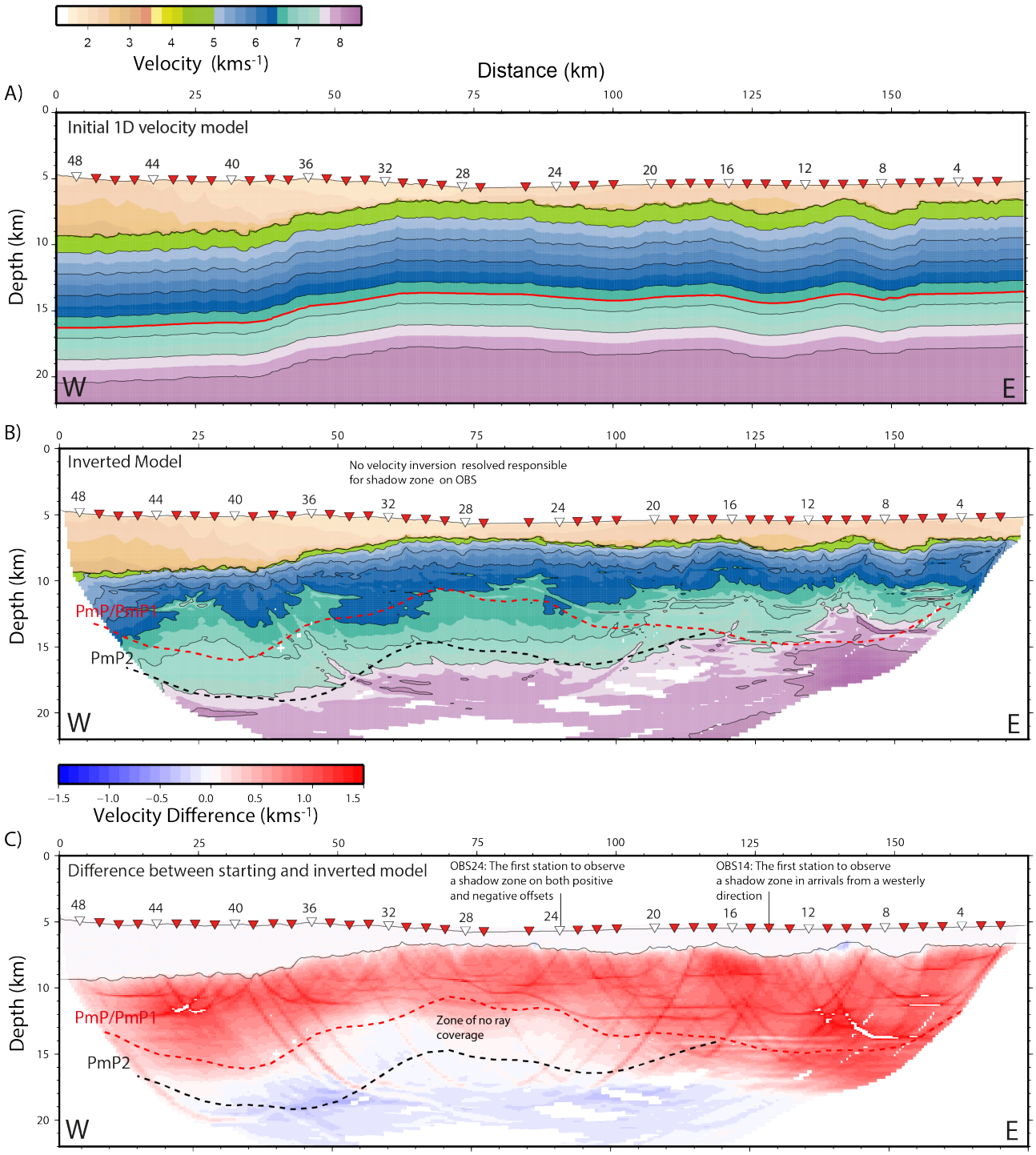


Figure 6.7: Results of a trial inversion using a simple starting model consisting of a constant velocity gradient. A) Starting model 2. Sediment velocities are converted from the sediment velocity model described in the previous chapter (Section 5.7). Velocities beneath basement consist of a simple linear gradient increasing from 4.5 km s^{-1} at top basement to 8 km s^{-1} at depth. Red line represents the starting depth of the PmP1/PmP and PmP2 reflections B) Results of a 2 stage inversion using all picked phases. Note the absence of a low velocity layer required to explain the shadow zone observed on OBS. C) Difference plot between the starting and inverted models. Note the region under the western part of the model (35-90 km, beneath the PmP1 reflection) where the inversion has been unable to make any real changes to the initial, simplistic, 1D structure. This region is the most likely location of the low velocity layer responsible for the shadow zone observed on the OBS and so was rejected.

The outcome of starting model 2 was used to define a new starting model (Figure 6.8A). Away from the low velocity layer (which is placed between 35-90 km) the starting model is based upon the velocity structure observed along the eastern parts of the profile in Figures 6.6B and 6.7B, with velocities of 7.6 km s^{-1} at the Moho at a depth of 7 km below top basement. In the unconstrained region from 35-90 km, a velocity inversion is inserted beneath the PmP1 reflector. Whilst the shadow zone could be the result of a region of very low / zero velocity gradient (i.e. constant velocity), some velocity contrast is required at the top of the low velocity layer in order to explain the PmP1 reflection (Figure 6.3, 6.4, 6.5). Such a velocity inversion prevents turning rays, generating the shadow zone observed on OBS.

A series of trial inversions were performed on starting models containing low velocity layers of varying velocity contrast with the overlying crust. The velocity gradient within the low velocity layer was set such that the layer would return to velocities of 7.6 km s^{-1} at depths of 7 km beneath top basement in keeping with the starting Moho across the rest of the profile (Figure 6.8A). At relatively low velocity contrasts (i.e. less than 0.2 km s^{-1}) the inversion would generally converge towards an output model similar to that in Figure 6.6, reducing the velocity inversion, often with anomalous focused ray paths in the middle crust, where some fragment of the initial velocity inversion remained. When the imposed velocity inversion exceeded ~0.2 km s^{-1}, the low velocity layer became more stable. A series of models were tested, each increasing the size of the velocity contrast across PmP1 in steps of 0.1 km s^{-1} (Table 6.1). Initially this increased the total travel time misfit through the final model. However, when the velocity contrast at the top of the low velocity layer was on the order of 0.4-0.5 km s^{-1} the misfit of first arrivals through the final model fell to 0.057-0.058 s, equivalent to the fit of the model with no artificial low velocity layer.

Trial starting models were also varied by shifting the depth of the low velocity layer. This had a relatively minor impact on the travel time misfit. However, if placed at the wrong depth, the floating PmP1 reflector would quickly become divorced from the upper surface of the low velocity layer in the final velocity model. The low velocity layer in the preferred starting model used in the final inversion (Figure 6.8A) is situated 500 m deeper than the PmP1 reflector initially generated by the inversion in Figure 6.7. Note that the impact of further variations in the starting model on the final result are examined in Section 6.4.6.

Inversion Stage	Phase	No. of picks	RMS Misfit (s)	Chi^2
Final Model				
Step 1: Upper Crust	All picks	17,530	0.058	0.97
	Pg	13,028	0.053	1.13
	PmP + PmP1	4,502	0.071	0.50
Step 2: Lower Crust	All picks	33,159	0.061	0.79
	Pg + Pn	28,657	0.060	0.85
	PmP + PmP1	4,502	0.061	0.37
Step 3: Mantle	All picks	32,820	0.062	0.80
	Pg + Pn	28,657	0.058	0.80
	PmP2	4,163	0.084	0.72

Table 6.2: Travel time misfit listed by inversion step and phase during inversion of final Vp profile. Model shown in Figure 6.8.

6.4.4 Final Tomographic Inversion

The preferred starting model is shown in Figure 6.8A. The low velocity layer extends from 35-95 km. Based on the trials discussed previously, the velocity at the top of the low velocity layer is set to 6.3 km s^{-1}, a reduction of 0.5 km s^{-1} compared to the crust above. Upper mantle velocities are set at 7.6 km s^{-1} at a depth of 7 km below top basement. The inversion for the final Vp structure was done using the same three stage, top-down scheme discussed previously. In the starting model the PmP/PmP1 floating reflector corresponds to the upper surface of the low velocity layer (Figure 6.8A). The initial PmP2 reflector was placed 7 km beneath top basement. The travel time misfits through the final model produced are 0.058 s for Pg + Pn (χ^2 0.81), 0.061 for PmP/PmP1 (χ^2 0.36) and 0.085 s for PmP2 (χ^2 0.72). The very low χ^2 values for PmP/PmP1 may suggest that the current pick uncertainty of 0.1 s is an over-estimation for that phase, this was initially assigned such a high uncertainty to reflect possible errors in picking this often weak reflection. These misfits are broken down by phase and inversion stage in Table 6.2.

Ray coverage through the final model is expressed as the derivative weight sum, a function of the total ray length through each grid cell (Figure 6.9). In the western part of the model (0-100 km), there is a distinct absence of rays turning at lower crust/upper mantle depths as a result of the low velocity layer. In this region almost all rays pass vertically downwards, only turning at, or below the PmP2 reflector. This drop-off in ray coverage occurs west of 110 km, ∼20 km past the first observations of outer rise faulting from bathymetry (Figure 6.8B). The final DWS grid is used as a mask for all further plots of the velocity grid in order to conceal unconstrained

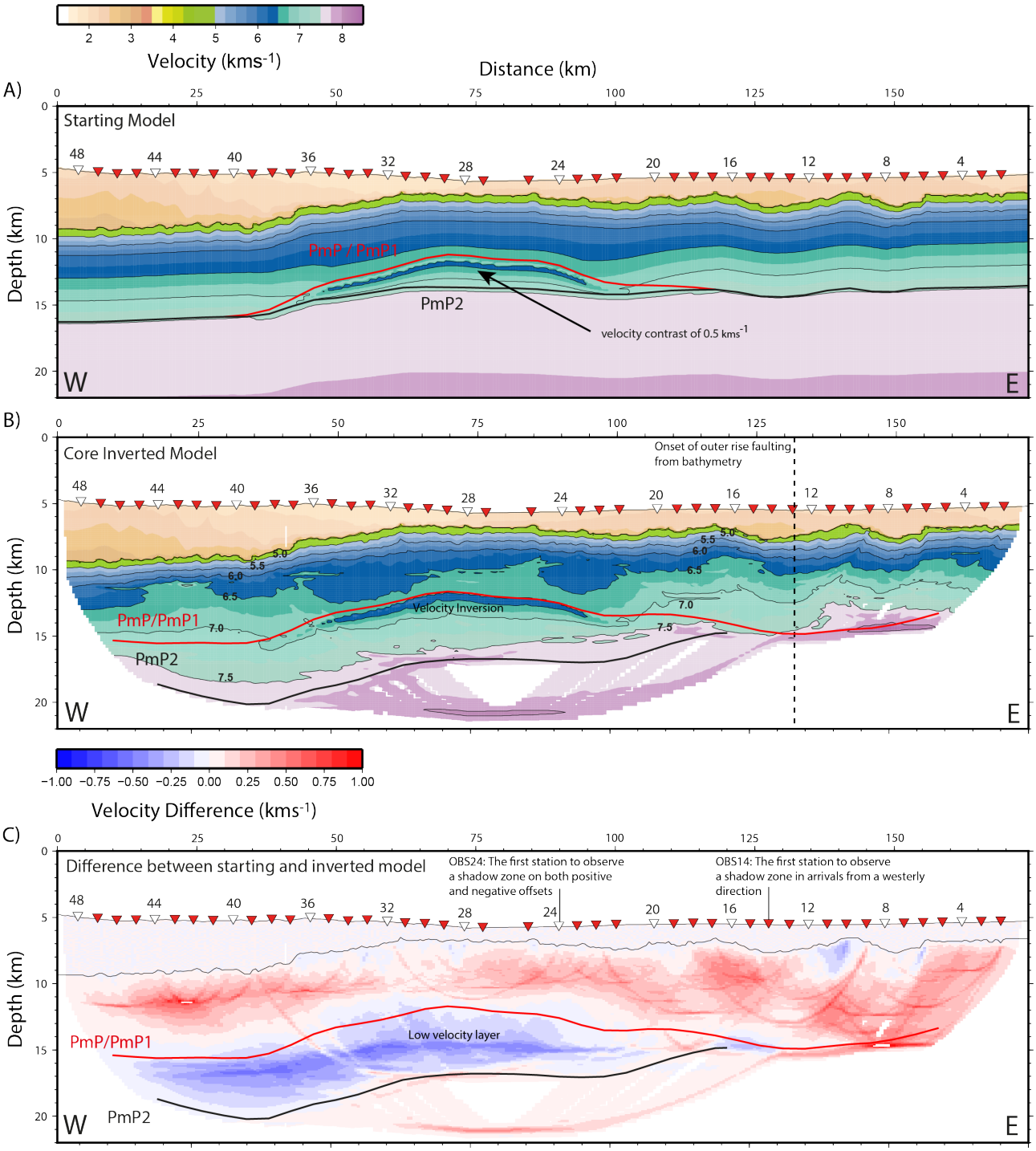


Figure 6.8: Output velocity model from inversion of preferred starting model 5. A) Starting model for crustal inversion. Initial inverted velocity layer with a contrast of 0.5 km s^{-1} based on previous testing is included under the western part of the model beneath the outer rise. B) Final velocity model following 3 stage inversion. PmP/PmP1 reflector shown in red. PmP2 reflector shown in black. The low velocity layer under the western part of the model satisfies the geometry required to generate the shadow zone seen on OBS. C) Difference plot between the starting and inverted models. Note how the changes in velocity outline the low velocity wedge between PmP1 and PmP2. Velocities at the top of the low velocity layer are relatively unchanged.

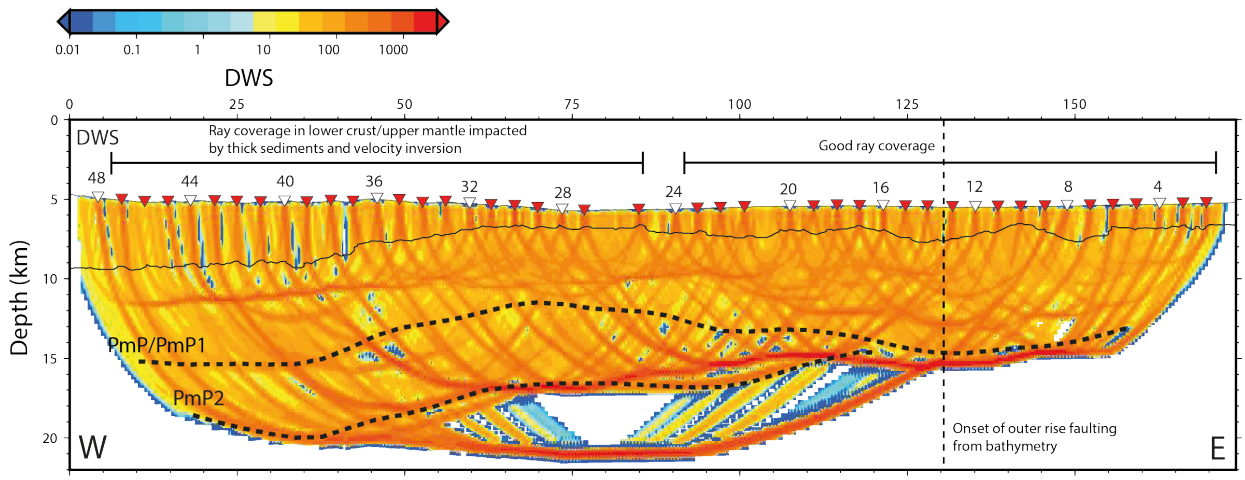


Figure 6.9: DWS (ray coverage) through final model (Figure 6.8). Note the distinct drop-off in rays turning in the lower crust and upper mantle between 0-100 km (depths greater than 10 km) as a result of the shadow zone.

regions of the final model (i.e. DWS = 0).

6.4.5 Resolution Testing

The resolution of the final model was analysed using checkerboard testing (Figure 6.10). A sinusoidal velocity perturbation of +/-5% was added to the final model and a set of travel times forward modelled through the perturbed model. Random noise, up to the maximum uncertainty assigned to each pick, was then added to each of these travel times in order to replicate potential picking error in the travel time dataset.

The initial inversion scheme was then re-run using these synthetic travel times as input in order to recover a new velocity model and compare against the known input. Note that as a full inversion was not conducted for the sediment section, the velocity anomalies were artificially inserted into this section of the final checkerboard. Figure 6.10 shows the recovery of anomalies of 12 x 5 km. Recovery is reasonable under the easternmost section of the model (100-174 km). There is a drop off in quality over the region of the low velocity layer (40-100 km) where the resolution is clearly impacted by the absence of rays turning at lower crustal/upper mantle depths. However, anomalies are still recovered, even across the PmP1 reflector at the top of the low velocity layer. Velocities at the base of the model along the interface of PmP2 are also well recovered. In the westernmost part of the model however (0-35 km) resolution is

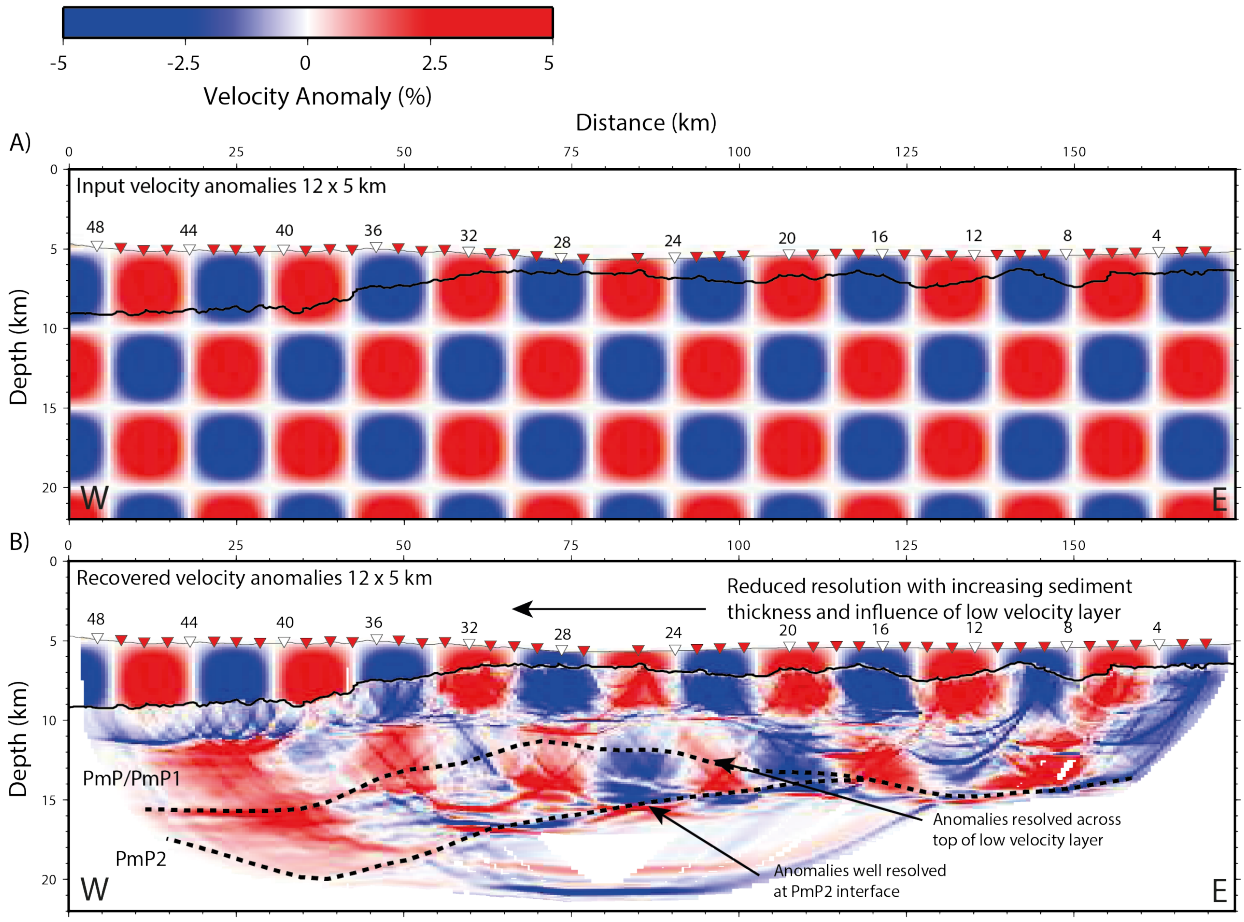


Figure 6.10: Checkerboard tests show resolution of final velocity model. A) Initial starting checkerboard consisting of 5% 12 x 5 km velocity anomalies from final model. B) Recovery of 5% 12 x 5 km velocity anomalies from final model. Recovery is reasonably good under the easternmost section of the model. Note the drop off in resolution west of 100 km as both the shadow zone, and thick sediments of the accretionary prism impact imaging.

exceedingly poor. This is the combined result of an absence of rays turning in the middle/lower crust due to the low velocity layer, the poorer data quality of some stations on the accretionary prism, and a relative lack of rays turning in the shallowest part of the crust as a result of the thick sediments. Velocity anomalies are also smeared at the far extents of the profile due to an absence of crossing rays. Tests with a checkerboard of half this size (6 x 2.5 km), showed almost no recovery west of 100 km as a result of the poor ray coverage.

6.4.6 Monte Carlo Analysis

Due to the relatively poor resolution under the western end of the section, and the fact that the inverted velocity layer has been inserted into the starting model *a priori*, it is important to fully understand how much of an influence the starting model has over the final model produced. In order to understand the possible errors involved in the inversion, Monte Carlo analysis was performed by analysing the results of 100 inversion runs with randomized starting models (Figure 6.11). The inversion scheme was left unchanged from that outlined previously. The preferred starting model was used as a baseline with velocity anomalies of up to 5% randomly introduced at the top basement (+/- 0.22 km s^{-1}), layer 2/3 boundary (+/- 0.33 km s^{-1}) and Moho (+/- 0.38 km s^{-1}). The low velocity layer was incorporated in all 100 trial models, however, the velocity contrast across the initial PmP1 reflector compared to the crust above was allowed to vary between 0.35 km s^{-1} and 0.65 km s^{-1} (i.e. +/-15%, in the final model this contrast was 0.5 km s^{-1}). A depth shift of up to 5% was also applied to the layer 2/3 boundary (+/- 200 m). The starting location of both floating reflectors was also shifted randomly by up to +/- 1km (note that it is only the depth of the floating reflector that is varied, not the depth of the low velocity layer within the mesh).

The inversions converge to a consistent solution, with the mean model and standard deviation of all 100 models shown in Figure 6.11. The standard deviation plot shows that the model is in general well constrained, with much less variation than was introduced into the array of starting models, and standard deviations of the velocity mostly less than 0.1 km s^{-1}. The main exception to this at the top of the low velocity layer where as expected, there is an increase in the uncertainty in the model, with the standard deviation of velocities in this region of all the grids produced as high as 0.15-0.2 km s^{-1}. This is unsurprising given the absence of turning rays in order to constrain the velocities in this part of the model. Other patches of relatively high uncertainty, where the standard deviation exceeds 0.1 km s^{-1}, are also found at the far extents of the model, and to a lesser extent in the shallowest igneous crust, where there are few turning rays. The maximum standard deviation of any depth node along PmP/PmP1 is 390 m. Away from the inverted velocity layer this falls as low as 66 m. The maximum standard deviation along PmP2 is as high as 1 km, though this is principally due to the uncertainty in the velocity at the top of the overlying low velocity layer. This fit shows that apart from the velocities directly at the low velocity layer interface the final velocity structure is exceedingly

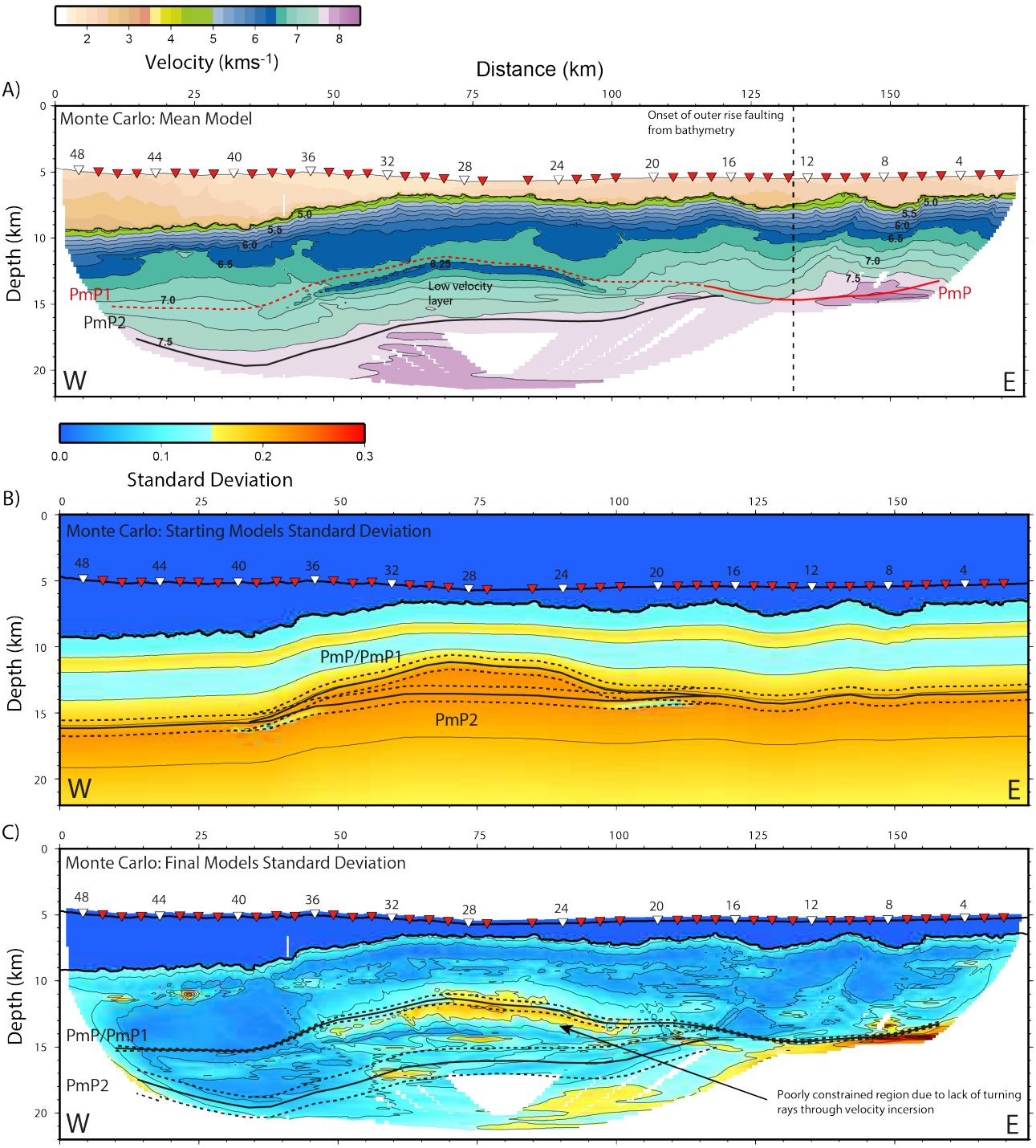


Figure 6.11: Monte Carlo analysis. a) Final Monte Carlo averaged velocity model. This model is the result of 100 inversions of randomly varying velocity models, with variations of up to 5%. PmP/PmP1 reflector shown in red. Section of reflector constrained by normal polarity PmP reflections shown as solid red line. Section constrained by reverse polarity PmP1 reflections shown as dashed red line. PmP2 reflector shown in black. b) Standard deviation of velocity in 100 starting models used for Monte Carlo analysis. c) Standard deviation of velocity in 100 velocity models resulting from Monte Carlo inversions. Uncertainty is significantly less than was introduced into the starting models, with the largest uncertainties coincident with the top of the low velocity layer.

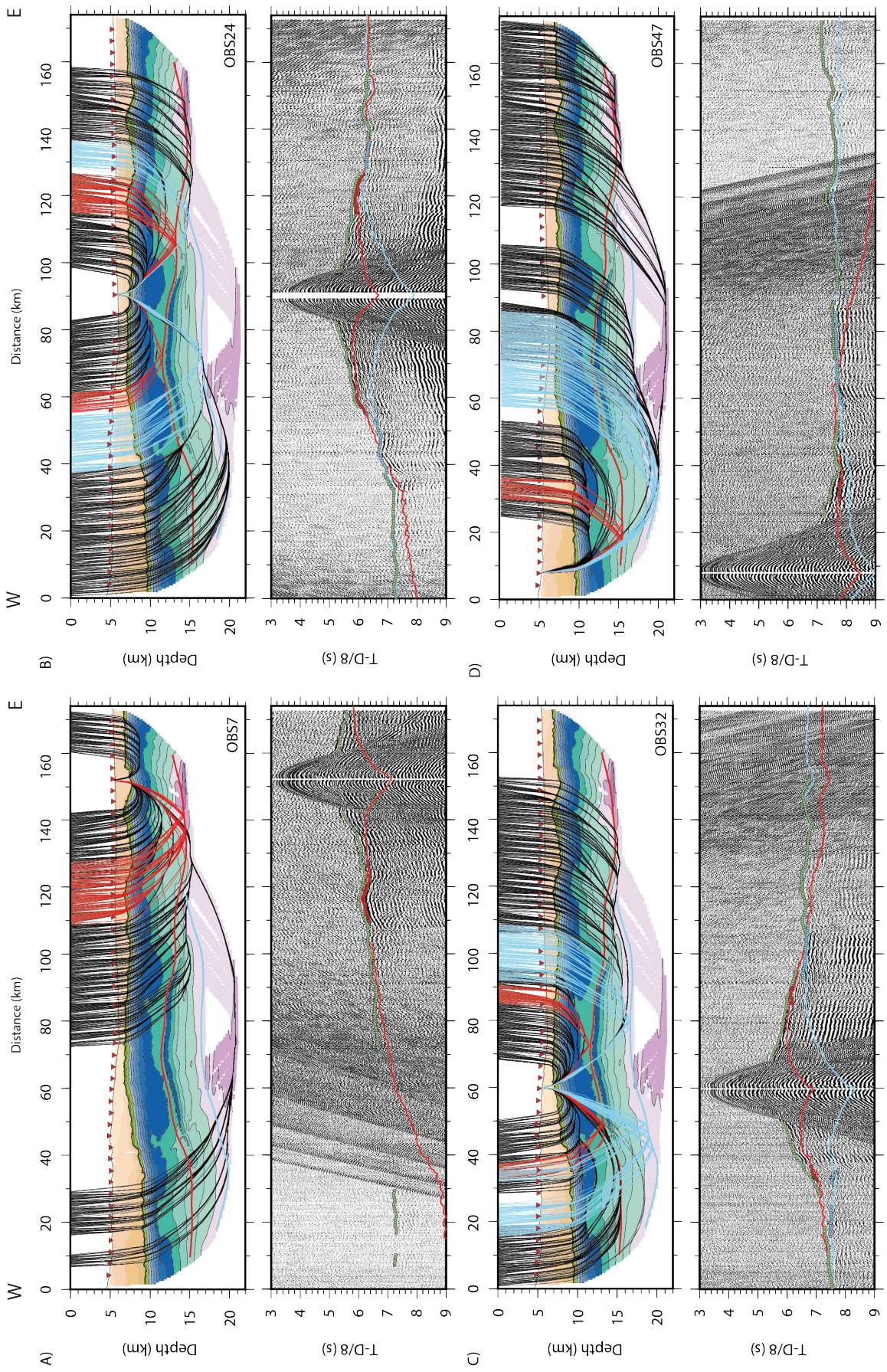


Figure 6.12: Examples of rays traced through final velocity model from 4 OBS stations evenly spaced along the profile. A) OBS7, typical of an OBS situated on the easternmost part of the profile prior to the influence of hydrous alteration. Turning rays (Pg + Pn) are shown in black on the final Monte Carlo averaged velocity model and the PmP reflection in red. On the OBS receiver gather turning ray picks (Pg + Pn) are shown in green, and PmP in red. One in ten picks shown. Red line corresponds to forward modelled travel times for the PmP/PmP1 reflector through the final model. B) As above for OBS24, with the addition of PmP2, shown in blue. Note how the rays missing as a result of the shadow zone correspond to those that would turn through the shallowest part of the low velocity layer. C) As above for OBS32. D) As above for OBS47.

robust to the starting conditions.

6.5 Modelling the Low Velocity Layer

From the checkerboards and Monte Carlo analysis it is clear that velocity structure at the top of the low velocity layer is poorly constrained. Given the limitations of the travel time tomography some simple forward models, representative of the velocity structure in the final Tomo2d profile, were used to generate synthetic seismograms in order to sense-check the final velocity structure. These models were used to confirm that the structure of the final model could feasibly reproduce the shadow zone and geometry of the PmP1 and PmP2 reflected phases observed on the OBS. A series of simple, 100 km, layered velocity models are created in the program RAYINVR (Zelt and Smith, 1992). These tests use simplified 4/5 layer models to replicate the velocity structure along the profile. A 5.5 km water column replicates the depth to the seabed observed along the incoming plate portion of the profile. A 1 km thick sediment package is defined with velocities increasing from 2-2.5 km s^{-1}, an approximation of the sediments on the incoming plate from the previous chapter (Section 5.7). A simplified version of the crustal structure from Figure 6.8B is used to confirm that this final model can replicate the observed phases recorded on OBS (Figures 6.13-6.15).

Travel times for key phases, including reflections off of the top and base of the low velocity layer are forward modelled and the amplitudes of the various arrivals are calculated using the program TRAMP (Zelt and Smith, 1992), and used to plot synthetic record sections for each model (Figures 6.13-6.15). The absolute amplitudes of the various phases calculated in these synthetics should not be over-interpreted. While the assumptions of ray theory are generally sufficient for accurate travel time tomography, they ignore a number of fundamental aspects of wave behaviour. In this case the influence of attenuation as a result of scattering through the structureless sediments of the accretionary prism, and highly faulted sediments and upper basement of the incoming plate are not accurately accounted for. In future, finite-difference modelling may be used to improve the accuracy of these synthetics. However, for now this modelling can only be considered to replicate the travel times and offsets of the various phases with any accuracy. For the purpose of these models, attenuation was set 1/3 higher in the mantle compared to the overlying crust.

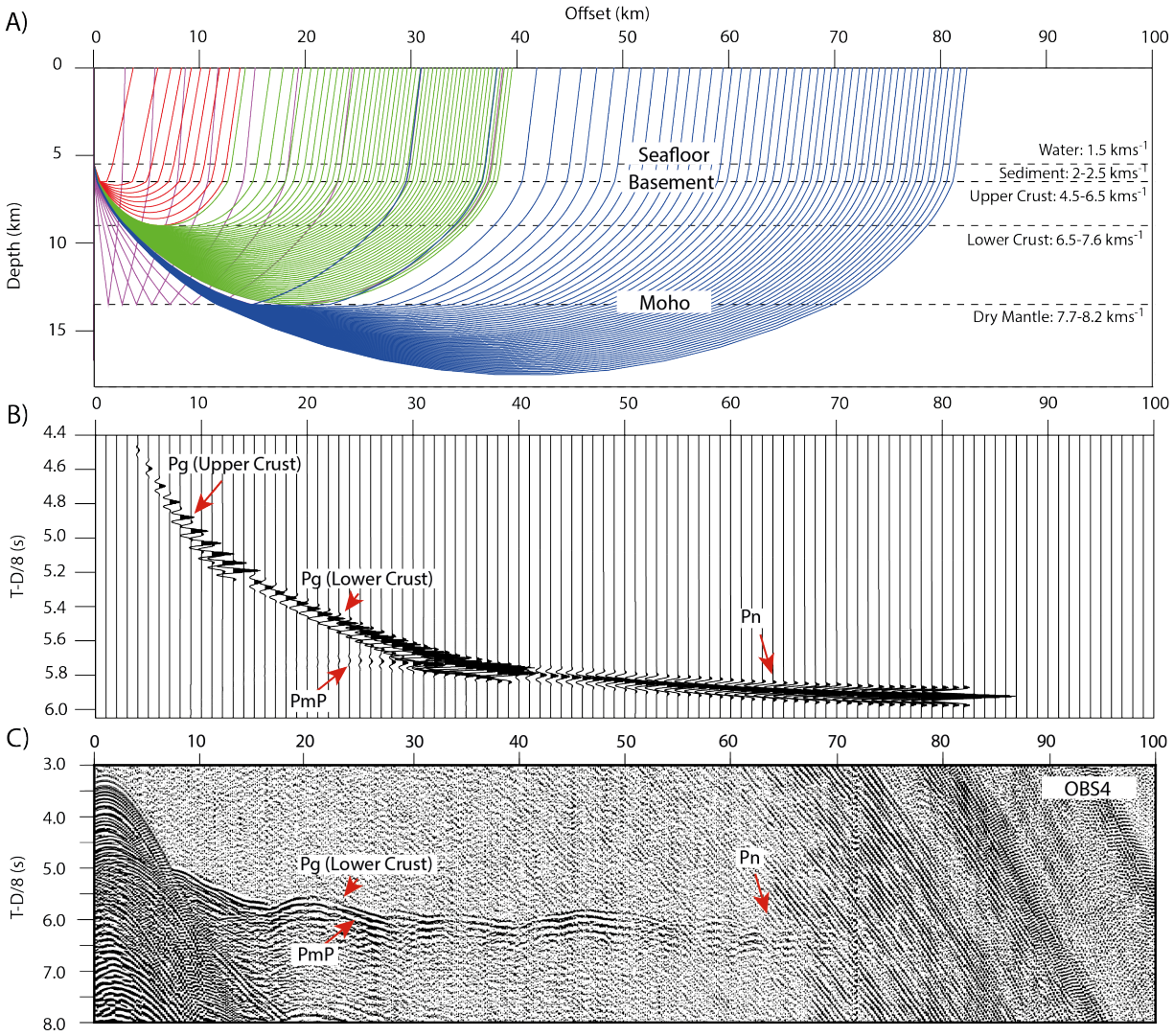


Figure 6.13: RAYINVR model to simulate travel times and amplitudes of key phases through a "typical" oceanic crustal structure based on the global average from White et al. (1992). Thickness of water and sediment layers are based on the velocity structure for the sediments of the incoming plate determined in the previous chapter. OBS receiver is located at 0 km. A) Velocity model structure and ray paths of key phases, Pg upper crust (red), Pg lower crust (green), Pn (dark blue), PmP (purple). B) Synthetic receiver gather calculated for the given geometry. C) Example of a comparable record section from OBS4 (Note that the offset has been flipped to match the geometry of the model.)

Figure 6.13 demonstrates this methodology applied to an oceanic crustal structure typical of the eastern portion of the profile beyond the outer rise and the influence of the low velocity layer (ignoring the influence of topography on the OBS travel times), this model does a good job of replicating the arrivals observed on OBS along this part of the profile (Figure 6.13). PmP is predicted at offsets of 20-30 km, with the transition from Pg to Pn at ∼40 km offset.

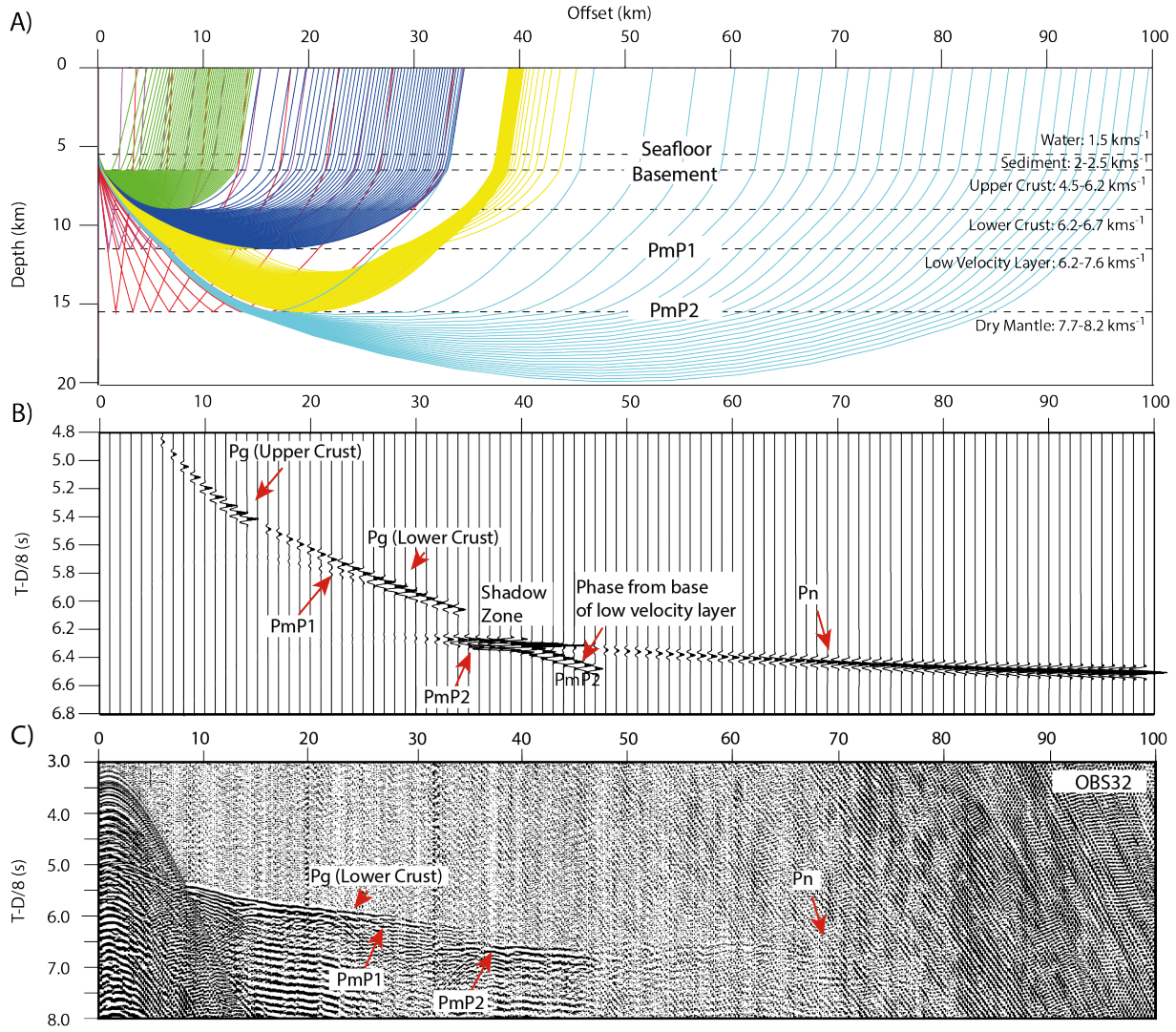


Figure 6.14: RAYINVR model to simulate travel times and amplitudes of key phases through a low velocity layer geometry similar to that shown in Figure 6.8, beneath a relatively thin crustal section of 5 km. Thickness of water and sediment layers are based on the velocity structure for the sediments of the incoming plate determined in the previous chapter. OBS receiver is located at 0 km. A) Velocity model structure and ray paths of key phases, Pg upper crust (green), Pg lower crust (dark blue), Pn (light blue), PmP1 (purple), PmP2 (red), rays turning through base of low velocity layer (yellow). B) Synthetic receiver gather calculated for the given geometry. C) Example of a comparable record section from OBS32, note the excellent correlation with the geometry of the shadow zone and PmP2 reflection shown in B. PmP1 and PmP2 are the result of reflections from the top and bottom of this low velocity zone respectively.

Figure 6.14 shows a case representative of the structure beneath the western part of the profile (from 35-90 km) incorporating the low velocity layer. The low velocity layer is modelled at a depth of 5 km below top basement, (in keeping with the final depth of the PmP1 reflector), with a velocity of 6.2 km s^{-1} at the top of the layer (a reduction of 0.5 km s^{-1} compared to

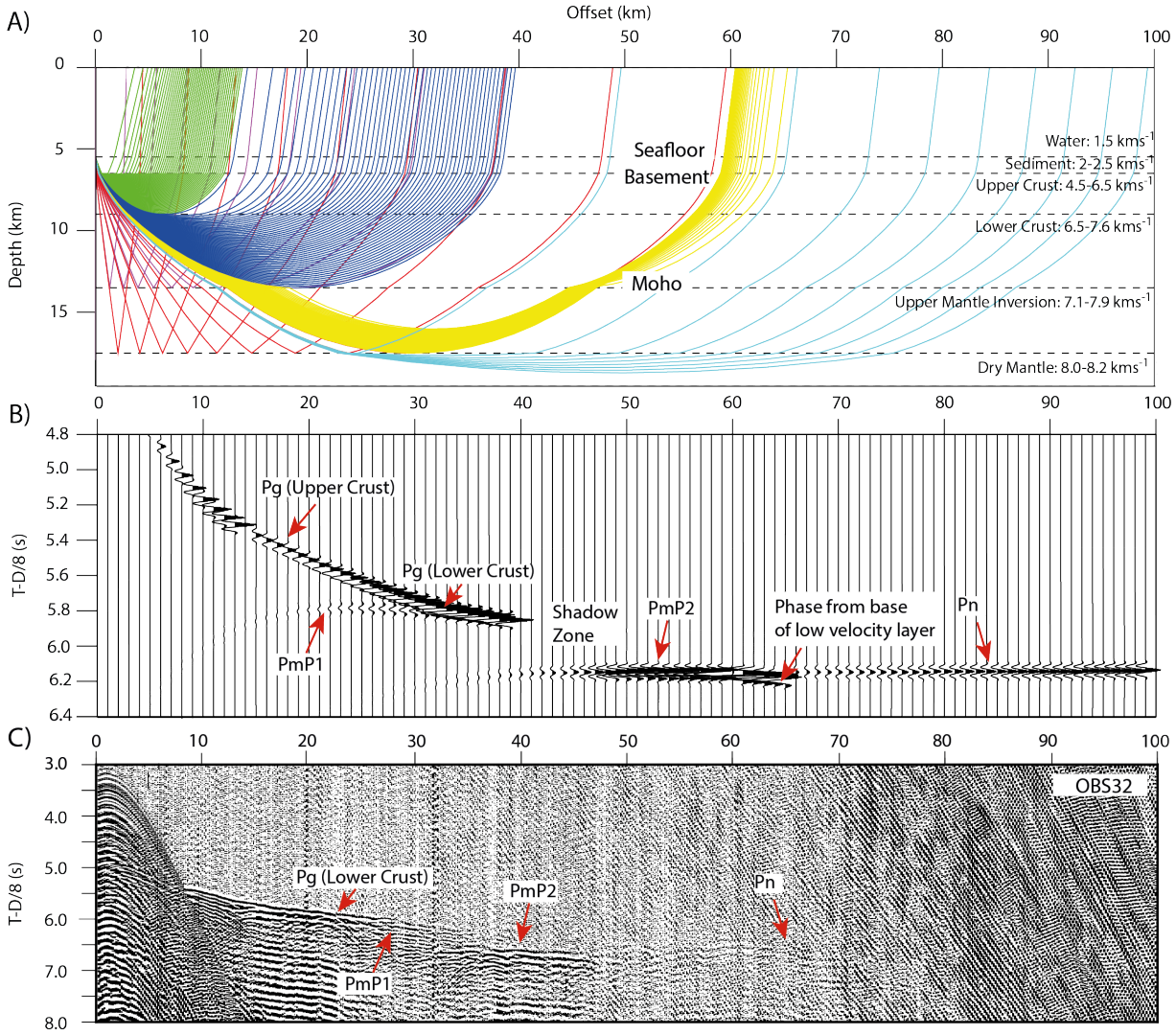


Figure 6.15: RAYINVR model to simulate travel times and amplitudes of key phases through an oceanic crustal structure with a low velocity layer in the upper mantle. Thickness of water and sediment layers are based on the velocity structure for the sediments of the incoming plate determined in the previous chapter. OBS receiver is located at 0 km. A) Velocity model structure and ray paths of key phases, Pg upper crust (green), Pg lower crust (dark blue), Pn (light blue), PmP1 (purple), PmP2 (red), rays turning through base of low velocity layer (yellow). B) Synthetic receiver gather calculated for the given geometry. B) Synthetic receiver gather calculated for the given geometry. C) Example of a comparable record section from OBS32. Note that compared to the synthetic, both the shadow zone and PmP2 appear at much shorter offset.

the overlying crust, in keeping with the final velocity model in Figure 6.8). This layer is 4 km thick, with a velocity of 7.6 km s^{-1} at its base. This boundary generates the PmP2 reflection. As shown in Figure 6.14 the synthetic record section produced is an excellent match to the geometry of the arrivals observed on the OBS and increases confidence in the final velocity

profile. The offsets of arrivals from the PmP1 reflector (20-25 km) and PmP2 reflector (30-45 km) are both matched by this model, as is the shadow zone, which extends from 35-50 km offset. The maximum offset of the Pg phase is controlled by the depth to the top of the low velocity layer. The asymptotic velocity of PmP2 is controlled by the velocity at the base of the low velocity layer, and is again well-matched.

In the Pacific, some of the clearest influences of outer rise hydration are seen below the oceanic crust-mantle boundary (as in Figure 6.1). Figure 6.15 shows an example of what would happen if the low velocity layer was placed much deeper in the model, at the crust-mantle transition, assuming that the crustal structure is consistent with that observed along the easternmost part of the profile (i.e. 7 km thick), and that the low velocity layer again extends 4 km into the upper mantle. A velocity reduction of 0.5 km s^{-1} is again placed at the top of the low velocity layer. The resulting synthetic generated by this model shows major differences compared to the OBS data, the clearest of which is that PmP2 does not occur until much longer offsets in excess of $\sim$45 km. There were only two instances along the profile where the onset of the shadow zone occurred at offsets >35 km, OBS45 and OBS47 (where it is likely a reflection of the dipping basement beneath the accretionary prism) and clearly rules out such a geometry for the low velocity layer.

6.6 Results

The final averaged Monte Carlo velocity model for VoiLA profile 1 is shown in Figure 6.17A. From east to west the final model shows clear changes in velocity structure.

In the east of the profile (105-174 km) the p-wave model shows a "typical" oceanic structure with a clear division between oceanic layers 2 and 3. In the upper 2 km of the crust, velocities increase from 4.5 km s^{-1} to 6.2 km s^{-1}, a velocity gradient of 0.85 s^{-1}. Lower crustal velocities increase from 6.2 km s^{-1} to 7.5 km s^{-1} at a depth of 7 km, coincident with the PmP reflection. This corresponds to a decrease in the velocity gradient to 0.25 s^{-1}. Beneath PmP velocities rapidly increase to 8.0 km s^{-1}. Between 110-130 km there is a slight reduction in the velocity gradient in the lower crust to 0.2 s^{-1}

West of 105 km, the model contains a low velocity layer at a depth of $\sim$5 km below top basement.

The upper and lower surface of this low velocity layer are defined by the PmP1 (which is reverse polarity) and PmP2 reflections respectively which diverge westward. PmP1 and PmP2 are first observed on OBS14. When traced through the final Vp model, the easternmost bounce point for these reflected phases occurs at ∼115 km (Figure 6.12), 18 km west of the first observations of increased faulting from bathymetry (Figure 5.3), and almost directly beneath the crest of the outer rise at 113 km. The PmP1 and PmP2 reflectors diverge westward, forming the upper and lower boundary of a low velocity layer. The absence of rays turning through the shallowest part of this low velocity layer is responsible for the shadow zone observed on OBS (Figure 6.5, 6.12). The maximum thickness of the low velocity layer is 5 km between 45-70 km. In the upper crust (oceanic layer 2), velocities show little variation compared to the eastern section of the profile. In the lower crust velocities directly above the velocity layer are ∼6.7 km s^{-1}. This represents a decrease of 0.3-0.4 km s^{-1}, compared to the crust at the same depth (i.e. 5 km below top basement) on the incoming plate, and a reduction in velocity gradient to 0.17-0.2 s^{-1}. This velocity reduction happens rapidly across a window of ∼10 km between 95-105 km. Velocities at the top of the low velocity layer are between 6.2-6.3 km s^{-1}, a reduction of 0.5 km s^{-1} compared to the overlying crust. The depth of the PmP2 reflector consistently corresponds to velocities of 7.6 km s^{-1}, largely at depths of 9-11 km beneath top basement. The velocity gradient within the low velocity layer is higher than in the overlying crust at ∼0.3 s^{-1}.

Monte Carlo analysis shows that the velocity at the top of the low velocity layer is highly dependent on the starting model (Figure 6.11). However, the fact that the final travel time misfit is equivalent to models without a low velocity layer inserted *a priori* (Table 6.1), and that calculated synthetic record sections accurately replicate the geometry of the shadow zone and reflected phases observed on OBS (Figures 6.13, 6.14), gives confidence in this final model structure.

Beneath the Tiburon Rise (0-35 km), model resolution is exceedingly poor, as such we cannot read too much into the velocity structure here (Figure 6.10).

6.7 Discussion

The final model satisfies criteria required to explain key observations from the OBS data including a shadow zone, and a pair of reflections (PmP1, PmP2) along the western part of the

profile. The most significant aspects of the final model are as follows:

1) When rays are traced through the final model, the shadow zone coincides with first arrivals which should have turned through the upper part of the low velocity layer (Figure 6.12). 2) The PmP1 reflector aligns with the top of the low velocity layer (Figure 6.11). 3) The PmP2 reflector is coincident with the base of the low velocity layer and a transition back to velocities of 7.6 km s^{-1}, more typical of the upper mantle.

6.7.1 Structure of the Incoming Plate

Whilst ideally changes in the velocity structure across the profile would be interpreted purely as the influence of outer rise hydration, in slow spreading lithosphere such as the Atlantic this is far from straightforward. As a result of variations in the rate of magma delivery at the ridge, both spatially and with time, crustal structure in the Atlantic can vary abruptly both within and between adjacent spreading segments (White et al., 1992; Christeson et al., 2019; Davy et al., 2020). Along relatively magma poor sections of the ridge the oceanic crust can show major deviations from what is thought of as the typical 3-layer "Penrose" model, with spreading often accommodated through detachment faulting (Escartin et al., 2008, 2017).

Along VoiLA Profile 2/3 situated ∼300 km W of this profile (Figure 6.2), Davy et al. (2020) described two distinct crustal types with clear differences in structure, separated by transform faults and NTOs. This profile is shown in Figure 6.16. In regions of crust formed via magmatically robust spreading, crustal thicknesses were on the order of 6.8 +/- 0.8 km, consistent with the traditional "Penrose" model, and most major compilations of oceanic crustal structure (White et al., 1992; Christeson et al., 2019). The upper crust was ∼1.9 km thick, with a gradient of ∼0.9 s^{-1}, while the lower crust had an average thickness of 5.0 +/- 0.8 km, and a velocity gradient of ∼0.2 s^{-1}. In contrast, regions of tectonically controlled (i.e. highly tectonized sections of crust formed by magma poor spreading) showed reduced crustal thicknesses, in some places less than 5 km (though it was often unclear whether the interpreted PmP reflection was representative of the true crust-mantle transition, or a hydration front within the lower crust). The structure of the crustal section (including the upper oceanic layer 2) was also much more variable as a result of disruption by detachment faulting, and the emplacement of core complexes.

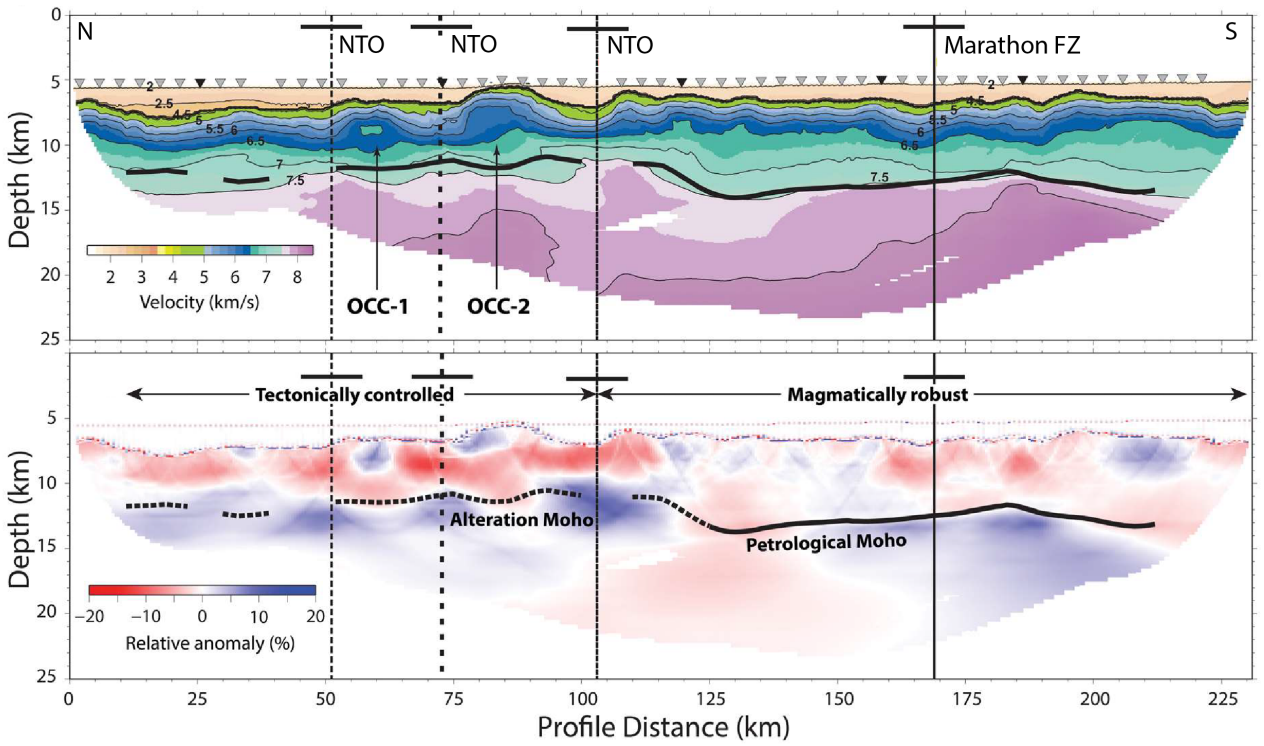


Figure 6.16: Results of wide-angle survey along VoiLA profile 2/3 from Davy et al. (2020). Profile shows the highly variable nature of crustal structure possible within the Atlantic. In the south of the profile, the crust was formed through relatively magma rich spreading and crustal thicknesses reach up to 7.6 km. In the north the crust was formed under magma poor spreading conditions and is as thin as 4-5 km. The structure is also locally disrupted by the presence of core complexes (OCC). The relatively shallow Moho reflector in the northern tectonically controlled segment is interpreted as an alteration front indicating some pre-existing serpentinization of peridotites in the lower crust/upper mantle, and may not represent the true petrological Moho.

In Figure 6.17C 1D velocity profiles through the final Monte Carlo averaged model are compared to that obtained by Davy et al. (2020) to the east along VoiLA profile 2/3 (Figures 6.2, 6.16). Between 105-174 km, VoiLA Profile 1 shows many of the features that would be expected of "typical" oceanic crust. On OBS data, a clear triplication between Pg, Pn and the normal polarity PmP reflection is observed consistently throughout this section (Figures 6.3, 6.4, 6.5). There is clearly a strong similarity between the "magmatically robust" velocity structure described by Davy et al. (2020) and the velocity structure within this section of the profile, including a total crustal thickness of 7 km, and velocity gradients of $\sim$0.8 s^{-1}, and $\sim$0.25 s^{-1} in the upper and lower crust respectively. The crustal structure is laterally consistent and shows little indication of disruption by detachment faulting or the formation of core complexes. Note that this crustal structure differs to that observed by Davy et al. (2020) in younger crust formed along the same ridge segment (between the 15-20 and Marathon fracture zones, the

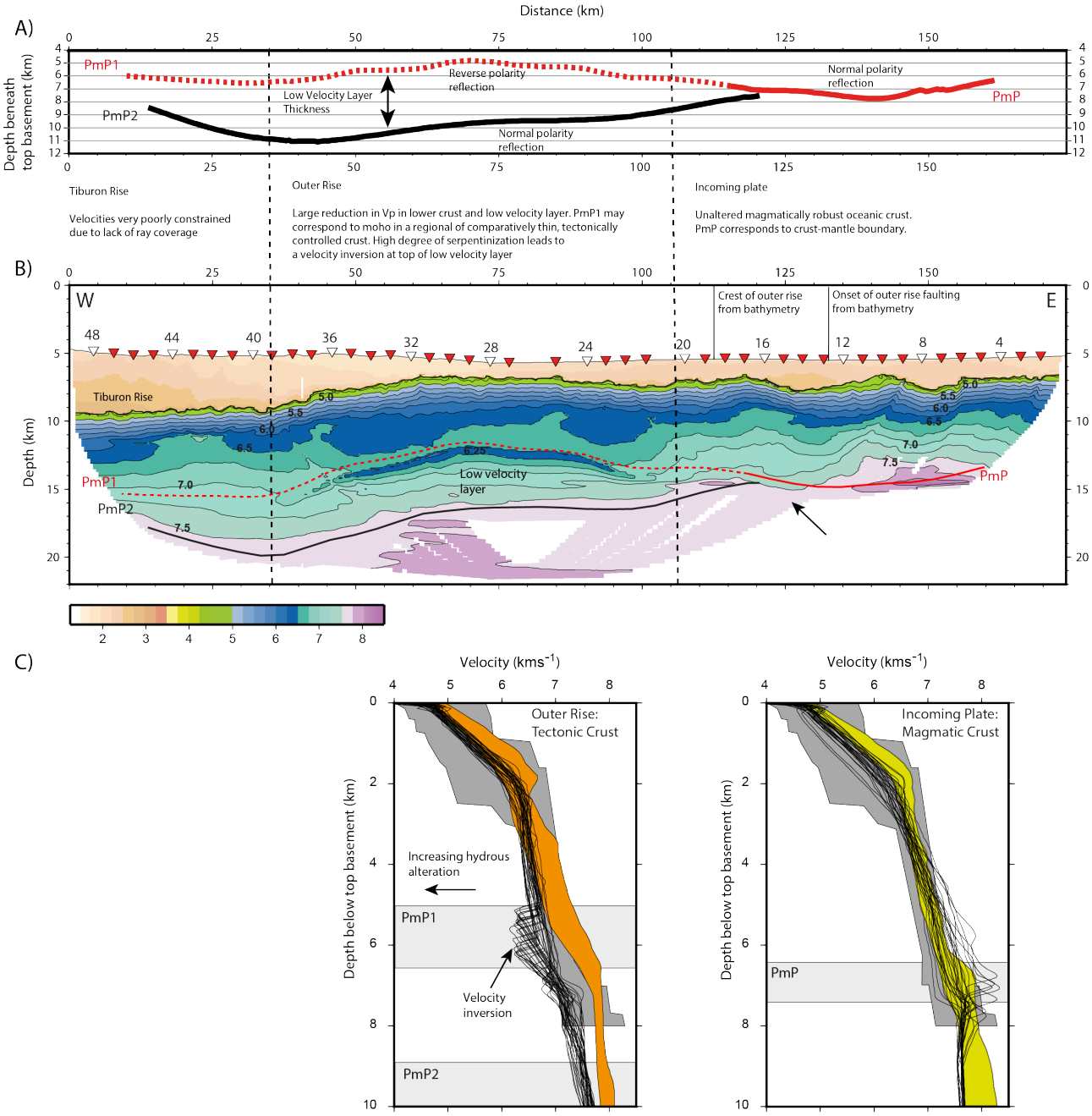


Figure 6.17: Final Monte Carlo average velocity model A) Offset between PmP/PmP1 and PmP2 reflectors and top basement. Note how the depth of PmP2 increases westward with increasing serpentinization. PmP1 also shallows across the inverted velocity layer. Section of the upper reflector constrained by normal polarity PmP reflections shown as solid red line. Section constrained by reverse polarity PmP1 reflections shown as dashed red line. B) Final Monte Carlo model divided into 3 key sections. The majority of the alteration appears to occur in a relatively small window of ∼10 km between 100-110 km. C) Comparison of 1D velocity profiles through final model (sampled every 2 km). Beneath the incoming plate, the velocity structure is a good match to the magmatically robust crust velocity envelope (yellow) of Davy et al. (2020), see also Figure 6.16. Moving west the shallower PmP1 reflector is more in keeping with a magma poor tectonic crustal structure (Orange velocity envelope, also from Davy et al. 2020). Global velocity envelope of White et al. (1992) is also shown in dark grey.

northernmost part of the profile in Figure 6.16), indicating a change to more tectonically controlled (magma poor) spreading in the Central Atlantic during the late Cretaceous, between the survey locations of VoiLA profiles 1 and 2/3.

East of ∼105 km the PmP reflector occurs at a depth of ∼7 km beneath top basement, coincident with velocities of between 7.5-7.75 km s^{-1}, below which velocities rapidly increase to 8 km s^{-1}. This reflector is interpreted as the crust-mantle boundary, separating mafic crustal rocks above from mantle peridotites below. Velocities of greater than 7.2 km s^{-1} within the lower crust may indicate a gradational Moho, with a large peridotite component (or very olivine rich gabbroic composition) above the PmP reflection (Figure 6.18). These high lower crustal velocities may also be an artefact of the increasing correlation lengths with depth used in the Tomo2d inversion. The increase to velocities of 8 km s^{-1} below the Moho is however comparatively abrupt, giving some confidence that this is a true representation of the lower crustal velocity structure.

6.7.2 Hydration Beneath the Outer Rise

The first indicators of bend faulting occur at 131 km in bathymetry (Figure 5.3), with the crest of the outer rise at ∼113 km. Increased faulting is also clear in multi-channel data from 50 km prior to the toe of the accretionary prism (Figure 5.11). The most significant changes in the deep velocity structure along this profile also coincide with this transition, with the first appearance of the shadow zone, PmP1 and PmP2 reflectors on OBS14 in shots from west of ∼120 km (Figure 6.5).

Compared to the incoming plate, the structure of the upper oceanic crust (layer 2) across the outer rise is consistent, again showing velocities increase from 4.5 km s^{-1} to 6.2 km s^{-1} with a velocity gradient of 0.85 s^{-1}. The consistent velocity structure of the upper 2 km of the crust across the entire profile would seem to suggest that the upper crust is fully saturated with respect to water due to hydrothermal circulation at or close to the ridge.

Clear changes in velocity structure are however observed in layer 3 and the upper mantle. Within layer 3 velocities at a depth of 5 km beneath top basement are reduced from ∼6.7 km to as little as 6.3 km. This decrease in the velocity of layer 3 occurs rapidly in a ∼10 km window between 100-110 km, immediately to the west of the crest of the outer rise (at 113

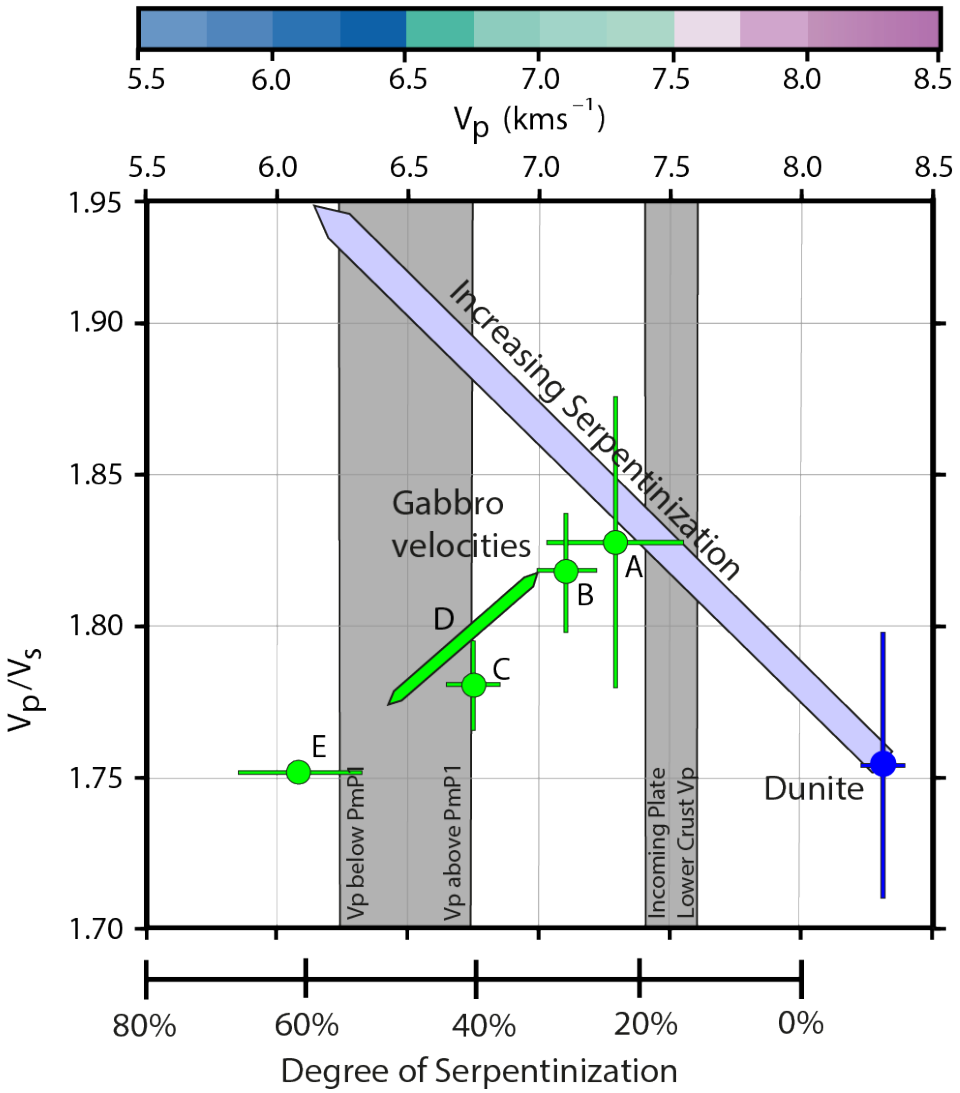


Figure 6.18: Variations in Vp and Vp/Vs with lithology and serpentinization. Dunite (olivine rich peridotite) velocities, and corresponding serpentinization trend from White et al. (2010). Gabbro velocities A) from White et al. (2010) based on laboratory experiments of Christensen (1996). B) Velocities measured from ODP Hole 735B cored olivine rich gabbros at the Atlantis II Fracture Zone (Iturrino et al., 1991). C) Velocities measured from ODP Hole 735B cored Fe-Ti gabbros at the Atlantis II Fracture Zone (Iturrino et al., 1991). D) Gabbro Vp, Vs velocity trend from Carlson and Miller (1997). Based on 98 gabbro/diabase samples of varying composition from ophiolites and ocean drilling. E) Vp of altered olivine rich gabbros cored from the Atlantis Massif (Collins et al., 2009). Plotted calculating Vp/Vs assuming the same trend from Carlson and Miller (1997). Degree of serpentinization axis based on Grevemeyer et al. (2018) and refers to a pure peridotite lithology. Note how velocities in the lower crust along the final VoiLA 1 profile overlap with both gabbro and peridotite lithologies, depending on the degree of alteration.

km). While this velocity decrease could be explained by a change in composition of the mafic lower crust, the fact that this change coincides with observations of outer rise faulting, and there is also a corresponding drop in velocity gradient to 1.7-2 s^{-1} would support that this is

the result of hydrous alteration of the lower crust (Figure 6.18). This velocity reduction is of a similar magnitude (∼0.3 km s^{-1}) to that shown in Figure 6.1, observed by Contreras-Reyes et al. (2007) as a result of hydrous alteration of the lower crust at the Chile trench. While increased faulting may also contribute to this velocity reduction, no corresponding decrease in Vp is observed in the upper crust.

The correlation between outer rise bending and the reduction in velocities within layer 3 suggests that the reactivated spreading faults observed along the MCS profile (Figure 5.11) are facilitating the infiltration of water into the lithosphere. Similar reactivated, abyssal hill fault systems have been seen to lead to serpentinization of the upper mantle at the Middle America (Van Avendonk et al., 2011) and Kuril trench (Fujie et al., 2013). Given the same spatial correlation exists between the onset of the low velocity layer (west of 100 km) and PmP1 and PmP2 reflections in the final velocity model, it also seems likely that hydrous alteration is key to forming the low velocity layer.

6.7.3 The Nature of the Low Velocity Layer

The low velocity layer is defined as the region of the model between the PmP1 and PmP2 reflectors, and increases in thickness westward from 100 km, reaching a maximum thickness of ∼5 km at 70 km along the profile. The velocities at the top of the low velocity layer are as low as 6.2 km s^{-1}, a drop of 0.5 km s^{-1} compared to the overlying mafic crust. Fully serpentinized peridotite can hold up to 13 wt% water, versus just ∼2 wt% water in hydrated gabbroic crust (Ulmer and Trommsdorff, 1995). At 100% serpentinization, this can reduce the velocity of peridotite to as little as 4.5 km s^{-1}. The presence of a highly serpentinized peridotite layer is thus the simplest explanation for the abrupt decrease in velocity at the top of the low velocity layer.

At approximately 20-30% serpentinization however, the Vp of altered peridotite becomes indistinguishable from that of typical gabbros in the lower crust (Figure 6.18). Samples from the Atlantis Massif (Collins et al., 2009), have demonstrated considerable overlap between altered oceanic gabbros with a high olivine composition and the Vp of even very highly serpentinized peridotites. Thus, in the current absence of a shear velocity model for the profile, which would greatly increase our ability to differentiate changes in the level of alteration from changes in

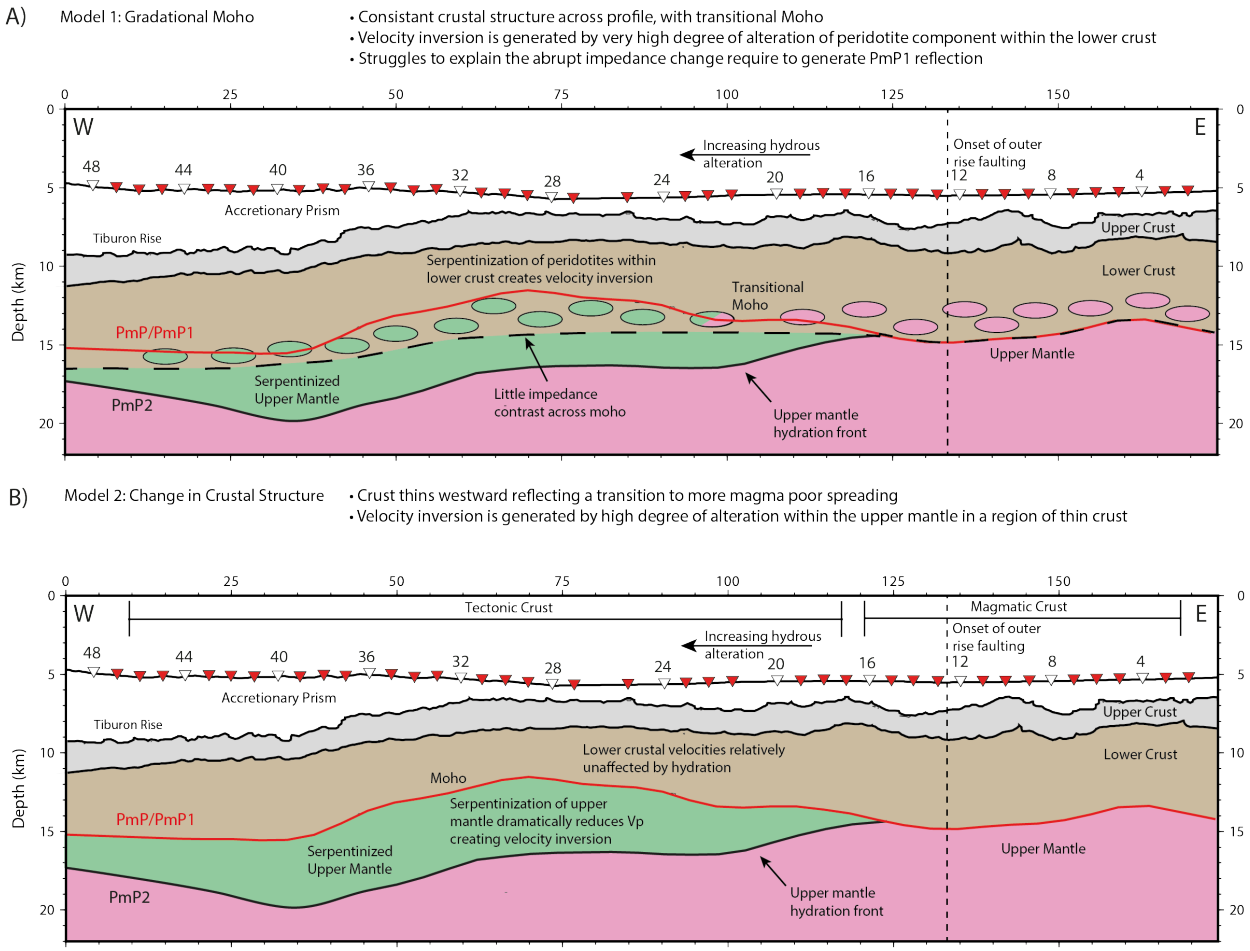


Figure 6.19: Possible end-member interpretations of final velocity structure along VoiLA profile 1. A) Crustal thickness is consistent at ∼7 km across the profile. Transitional Moho means that there is no clear reflection from the crust-mantle boundary. Low velocity layer results from highly altered peridotites / olivine rich gabbros within the lower crust. Struggles to explain the abrupt velocity contrast required to generate the PmP1 reflection. B) Crust thins westward coincident with increasing alteration beneath the outer rise. PmP1 represents the petrological Moho, with the low velocity layer generated by high levels of alteration in the upper mantle. Thinner crust in the west results from relatively magma poor "tectonic" seafloor spreading.

lithology (Figure 6.18), it cannot be ruled out that compositional and structural changes also contribute to the observed variations in Vp. As a result of the overlapping velocities of the possible lithologies, and the potential changes in crustal structure within the Atlantic there are essentially two end-member scenarios that must be considered to explain the velocity structure of the low velocity layer (Figure 6.19).

In the first case the magmatically robust crustal structure observed between 105-174 km is assumed to be consistent across the whole profile (Figure 6.19A). High velocities (>7.4 km s^{-1}) in the lower crust are the result of a transitional Moho, with a significant peridotite component,

or olivine rich gabbroic composition within the lower crust. In this case, the westward shallowing of PmP1 would represent a compositional front within the lower crust, below which an olivine bearing component is subject to very high levels of alteration. In this model there would be little to no impedance contrast across the true crust-mantle transition, which doesn't generate any clear reflection as a result. The PmP2 reflection at depth marks the boundary between hydrously altered upper mantle rocks above, back to dry peridotite below. This model however, struggles to explain the velocity drop at the top of the low velocity layer required to generate the PmP1 reflection.

In a second preferred scenario, as well as the influence of outer rise bending and hydration, variations in Vp are also the result of a fundamental east to west change in crustal structure along the profile (Figure 6.19B). Beneath the outer rise, PmP1 is situated 5 km beneath the top basement in keeping with many previous wide-angle observations of crustal thickness in regions of magma poor spreading within the Atlantic (Dannowski et al., 2010; Dunn et al., 2017; Davy et al., 2020). This westward shallowing of PmP1 is therefore potentially diagnostic of a transition to crust formed through more magma poor, tectonically controlled spreading west of $\sim$ 105 km. In addition to the increasing levels of hydration, this change contributes to the differences in the structure of the final model between the incoming plate and outer rise. In this case, PmP1 is representative of an abrupt crust-mantle transition. The velocity inversion at the top of the low velocity layer is thus the result of the juxtaposition of gabbro in the lower oceanic crust (where even high levels of alteration have a comparatively limited impact on Vp) above and highly serpentinized peridotites below. PmP2 again marks the boundary between hydrously altered upper mantle rocks above to dry peridotite below.

In this scenario, the increase in the density of faulting observed across the outer rise region in Chapter 5 (Figure 5.11), may not be purely the result of outer rise bending, but also derive from a much more heavily faulted, tectonized basement. As there is no clear evidence (either from seismic or gravity and magnetic data) for a fracture zone or other discontinuity in this central area of the Tiburon Basin this change in structure would instead represent a transition to more magmatic spreading during the Late Cretaceous. It should be noted however that there is no indication of the emplacement of core complexes, or similar disruption to the structure of the oceanic layer 2 as a result of detachment faulting, as has been documented previously by wide-angle studies of magma poor tectonically controlled crust (Dannowski et al., 2010; Dunn

Study	Location	Receiver Spacing (km)	Source Size (cu. in.)	Shot Spacing (m)
This Study	Lesser Antilles	4	5000	170
Ranero and Sallares (2004)	Chile	8	ns	ns
Contreras-Reyes et al. (2007)	Chile	5	3900	150
Contreras-Reyes et al. (2008)	Chile	5	3900	150
Contreras-Reyes et al. (2014)	Chile	5	3124	150
Contreras-Reyes et al. (2015)	Chile	5	3100	150
Moscoso and Grevemeyer (2015)	Chile	5	11200	150
Grevemeyer et al. (2007)	Nicaragua / Costa Rica	4	5850	110
Ivandic et al. (2008)	Nicaragua	6	5850	110
Ivandic et al. (2010)	Nicaragua	10	3900	130
Van Avendonk et al. (2011)	Nicaragua / Costa Rica	17	6600	500
Horning et al. (2016)	Cascadia	16	6600	500
Shillington et al. (2015)	Alaska	15	ns	ns
Fujie et al. (2016)	Japan	6	7800	200
Fujie et al. (2013)	Kuril	6	7200	200
Wan et al. (2019)	Mariana	15	1500	ns
Contreras-Reyes et al. (2011)	Tonga	8	4900	150
Planert et al. (2010b)	Sunda-Banda	7.5	3900	130

Table 6.3: Compilation of survey parameters for previous wide-angle outer rise experiments. Data taken from individual publications. ns = data not stated.

et al., 2017; Davy et al., 2020).

6.7.4 Constraining Water Storage in the Crust and Mantle

The depth extent of mantle serpentinization is a major uncertainty, and remains a barrier to properly understanding the amount of hydrous alteration which occurs beneath the outer rise at many subduction systems. Estimates from wide-angle studies are generally on the order of a few kilometres (e.g. Contreras-Reyes et al. 2008; Ivandic et al. 2008; Van Avendonk et al. 2011), although often the deepest extent of mantle serpentinization is not imaged or is poorly resolved. Ranero and Sallares (2004) suggested that a layer of 20% serpentinization could extend to as much as 20 km beneath the Moho through gravity modelling at the Chile trench.

Emry and Wiens (2015) proposed that most outer rise hydration was limited to the upper 5 km of the mantle through accurate mapping of earthquake sources in the northern and

western pacific. At the Middle America trench Lefeldt et al. (2012) observed reduced upper mantle velocities to depths of 10 km beneath the Moho from a joint 3D inversion of active-source data, local micro-seismicity and regional earthquakes. They observed a good correlation between local micro-seismicity and the maximum proposed depth of hydration, suggesting that depth penetration of faults into the upper mantle is key in controlling the depth extent of serpentinization at the outer rise.

Along profile 1, PmP2 coincides with velocities of 7.6-7.7 km s^{-1} and is interpreted as a reflection from the base of the serpentinized wedge in the upper mantle. Between PmP1 and PmP2 the velocity gradient is approximately 0.3 s^{-1}. The relatively steep velocity gradient between PmP1 and PmP2 ($\sim$0.3 s^{-1} compared to $\sim$0.2 s^{-1} in the overlying crust) is interpreted as decreasing hydrous alteration with depth.

As far as we are aware, this is the first time that a reflection of this type has been documented in wide-angle data. Comparing key acquisition parameters of the VoiLA survey, such as receiver spacing and source size, to that used in previous studies (Table 6.3), there is no obvious experimental reason why this study should pick up this reflection where previous studies have not. A number of studies including Van Avendonk et al. (2011); Fujie et al. (2013); Moscoso and Grevemeyer (2015); Fujie et al. (2016) all boast larger source sizes, often in areas of thinner sediments, and should have had sufficient resolution at depth. It may be that the presence of the shadow zone aids identification of this phase.

The offset between the final PmP1 and PmP2 reflectors suggests that serpentinization affects a layer of up to 5 km thickness into the upper mantle (Figure 6.17). Given that the Lesser Antilles slab is $\sim$60 My older than the crust subducting at the Middle America, the $\sim$500° cut-off below which serpentine is stable (Ulmer and Trommsdorff, 1995) should occur at greater depth, and we might reasonably therefore have expected to observe hydration to greater depth than has been proposed by Lefeldt et al. (2012) and others. The length of bend faults may therefore be limiting the depth of water circulation.

Grevemeyer et al. (2018) describe a simple linear relationship between Vp and the degree of serpentinization (ϕ) assuming a pure peridotite lithology: $Vp = 8 - 3.1\phi$. If beneath the outer rise the PmP1 reflector does indeed represent the Moho transition in a region of highly tectonized crust, then the velocities in the top of the low velocity layer are entirely the result of the serpentinization of peridotite in the upper mantle. Velocities of $\sim$6.3 km s^{-1} would

thus correspond to 55% serpentinite at the top of the low velocity layer, equivalent to 6.5 wt% water (Carlson and Miller, 2003). Assuming a linear drop off in the degree of serpentinization with depth between PmP1 and PmP2 this is therefore equivalent to an average of ∼3.25 wt% water in the upper 5 km of the mantle. Even assuming a much more conservative case, with a highly gradational crust-mantle boundary, and a transition to a pure peridotite composition at a depth of 7 km beneath top basement (in keeping with crustal model A, Figure 6.19), this would correspond to velocities of ∼7 km s^{-1} or ∼32% serpentinization of the upper mantle (equivalent to 1.86 wt% H_20).

Anisotropy can also influence velocities in the upper mantle. Lizarralde et al. (2004) observed up to 3% anisotropy in the upper mantle of the North Atlantic near Bermuda, with fast velocities orientated in the spreading direction as a result of alignment of olivine crystals. VoiLA Profile 1 is offset from this preferred fast orientation by as much as 30°, thus the influence of anisotropy is likely to be comparatively minor. A difference of 3% at the top of the low velocity layer would correspond to an error of ∼0.19 km s^{-1}, or ∼6% serpentinization, and thus has little bearing on the interpretation of these results.

6.7.5 Global Context

Along Profile 1 we observe clear reductions in the velocity of the lower crust and upper mantle. While a velocity reduction of ∼0.3-0.4 s^{-1} in the mafic crust of oceanic layer 3 is in-keeping with many other studies of outer rise hydration (Contreras-Reyes et al., 2007; Grevemeyer et al., 2018), the degree of upper mantle serpentinization observed here is potentially very much higher, reducing upper mantle velocities to as little as 6.2 km s^{-1} (Table 6.4). Although the potential for very extreme reductions in Vp of peridotite with serpentinization are well established, this is the first documented example of alteration of the upper mantle beneath an outer rise extensive enough to produce a velocity inversion.

Upper mantle velocities below 7 km s^{-1} have only been observed previously at the Mariana trench (Wan et al., 2019), and Nicaragua (Van Avendonk et al., 2011). Compared to previous outer rise studies the Lesser Antilles incoming plate shows a comparatively thick sediment blanket (from 1-2.5 km thickness). Such a thick sediment cover has been previously considered a hindrance to outer rise hydration (Contreras-Reyes et al., 2008), though few studies have

put this to the test in sediment thicknesses greater than 0.6 km (Table 6.4). Furthermore, this hydration appears to be enabled by fluid flow along reactivated abyssal hill faults formed during spreading at the Mid Atlantic ridge. The multichannel profile in the previous chapter demonstrated that the offset across these faults (following reactivation) is relatively minor (Figure 5.11), yet they seem able to convey large volumes of water into the lower lithosphere. This would again appear to conflict with studies that have previously suggested that, fresh, crustal scale bend faults are required in order to facilitate the very highest levels of mantle serpentinization (Fujie et al., 2018; Boneh et al., 2019)

Table 6.4 presents a compilation of key subduction parameters in order to try and explain these apparent contradictions. Using the slab radius of curvature (a measure of the bending dissipation in slabs) calculated by Buffett and Heuret (2011) as a proxy for the degree of bending in the outer rise (as an alternative to slab dip, which is often highly variable or poorly constrained in slab models), the Lesser Antilles is not an extreme case. The slab age is also younger than that studied by Planert et al. (2010b) along the Sunda-Banda arc (134 Ma +), where mantle velocities were not observed lower than 7.4 km s^{-1}. Iyer et al. (2012) did however demonstrate that the temperature gradient in older lithosphere is more favourable for greater serpentinization at mantle depths, so age may play some role. There are two parameters however, where the Lesser Antilles is a very clear end-member, the rate of seafloor spreading of the subducting lithosphere (21 mm yr^{-1}, half spreading rate), and the subduction convergence rate (11 mm yr^{-1}).

The precise mechanism by which water enters the lower crust along bend faults is still debated. One of the most widely accepted mechanisms, described by Faccenda et al. (2009) is a model in which bending and extension within the subducting crust creates a negative pressure gradient that encourages localized pumping along faults. They posited that this may be locally aided by the presence of pre-existing cracks and fractures, and therefore may be aided by a highly tectonized, slow spreading oceanic crustal structure. Fault propagation in the lower crust and upper mantle is assisted by the gradual serpentinization process, which can lead to rheological weakening, and further localized deformation. Hatakeyama et al. (2017) modelled that the potential extent of serpentinization could be between 120-1390 m from a given fault zone. Both the extent and degree of serpentinization were heavily dependent on the permeability of the serpentine present (which in this case is unknown), and the timescale over which peridotites

Study	Location	Fault Style	Sediment Thickness (km)	Upper Mantle Vp (km s^{-1})	Radius of Curvature (km)	Slab Age (My)	Half Spreading Rate (mm yr^{-1})	Subduction Rate (mm yr^{-1})
This Study	Lesser Antilles	1	1-2.5	7.0	230	91	21	11
Ranero and Sallares (2004)	Chile	2	0.2	7.6	300	53	ns	74
Contreras-Reyes et al. (2007)	Chile	2	0.6-2.4	7.8	356	15	44	79
Contreras-Reyes et al. (2008)	Chile	1	0.4-2.4	7.8	105	30	59	80
Contreras-Reyes et al. (2014)	Chile	2	0.2	7.6	298	42	59	75
Contreras-Reyes et al. (2015)	Chile	2	0.2	7.8	298	41	58	75
Moscoso and Grevemeyer (2015)	Chile	2	0.2-0.4	7.5	399	35	55	80
Grevemeyer et al. (2007)	Nicaragua / Costa Rica	1	0.4-0.6	7.4	132	24	45	83
Ivandic et al. (2008)	Nicaragua	1	0.4-0.6	7.6	132	24	50	83
Ivandic et al. (2010)	Nicaragua	1	0.4-0.5	7.4	132	24	49	78
Van Avendonk et al. (2011)	Nicaragua / Costa Rica	1	0.3-0.6	7.0	132	24	49	78
Horning et al. (2016)	Cascadia	1	0.1-0.3	8.1	ns	9	41	32
Shillington et al. (2015)	Alaska	1	0.4-0.6	7.7	341	53	42	63
Fujie et al. (2016)	Japan	2	ns	7.0	286	134	60	92
Fujie et al. (2013)	Kuril	1	ns	7.8	169	126	55	82
Wan et al. (2019)	Mariana	2	0.2	6.8	106	150	50	30
Contreras-Reyes et al. (2011)	Tonga	2	0.1-0.4	7.3	249	80	55	108
Planert et al. (2010b)	Sunda-Banda	1	0.3-0.6	7.4	261	134/157	84	65

Table 6.4: Compilation of results and key subduction parameters for previous outer rise wide-angle experiments. Where available data was taken from the pre-existing compilation of Grevemeyer et al. (2018), otherwise was lifted from the individual studies. Fault style 1 indicates that bending across the outer rise is seen to reactivate a pre-existing oceanic basement fault structure. Fault style 2 indicates the formation of fresh bend faults across the outer rise, usually parallel to the trench. Radius of curvature from Buffett and Heuret (2011), Slab Age and Half Spreading Rates from Müller et al. (2008), Subduction Rate from Heuret and Lallemand (2005). ns = data not stated.

were exposed to water. The lateral extent of serpentinization was up to 3x greater over a period of 1 Myr versus 0.2 Myr.

At ∼11 mm yr^{-1} (Heuret and Lallemand, 2005) the convergence rates at the Lesser Antilles trench are extremely slow compared to the vast majority of global subduction systems. At that rate material will take ∼5 My to traverse the ∼50 km of the outer rise. The idea that longer timescales of exposure within the outer rise might significantly increase the resulting levels of serpentinization is supported by the results of Wan et al. (2019) at the Mariana trench. The southern Mariana possesses the next slowest convergence rates from the available studies (∼32 mm yr^{-1}) leading to modelled serpentinized mantle velocities as low as 6.8 km s^{-1} (Table 6.4). At Cascadia (∼30 mm yr^{-1}) the crust is too young and hot for stable serpentine formation (Horning et al., 2016; Grevemeyer et al., 2018). The next slowest examples, at locations along the Alaskan (upper mantle Vp 7.7 km s^{-1}) and Sunda-Banda (upper mantle Vp 7.4 km s^{-1}) subduction zones (Table 6.4), have convergence rates up to 6x faster than that observed at the Lesser Antilles, taking ∼0.8 My to traverse the same distance. Given the almost uniquely long residence time that Atlantic lithosphere spends within the extensional regime of the Lesser Antilles outer rise, this may explain how such high levels of alteration are achieved in spite of apparent drawbacks such as the thick sediment blanket.

If the crust currently beneath the outer rise did indeed form under magma poor spreading conditions it can be expected to be highly faulted and tectonized. In bathymetry and 2D reflection data, this fault network appears to be tightly spaced (faults 1-1.5 km apart), with at least two overlapping fault orientations (Figure 5.3). This fault fabric may represent a much higher total fault surface area within the shallow lithosphere and therefore may lead to more pervasive serpentinization than at systems such as Chile or Japan, where convergence rates are much higher, and bending is accommodated by newly formed, and widely spaced, outer rise normal faults (Table 6.4). Compared to cases such as Kuril (Fujie et al., 2013), where hydration also results from reactivation of abyssal hill faults, the high offset, potentially crustal scale detachment faults which can form in tectonized, slow spreading Atlantic crust may convey water to much greater depths than their equivalents in the Pacific. Several studies of Atlantic crust close to the ridge have shown that such fault systems are capable of facilitating geothermal circulation, and hydrous alteration all the way to the Moho (Canales et al., 2000; Hooft et al., 2000; Planert et al., 2009).

Given that our profile is relatively central within a ridge spreading segment, these process may be even more significant at the more heavily tectonized segment ends, where large detachment faults exhume core complexes all the way to the seabed (Smith et al., 2008; Planert et al., 2010a; Escartin et al., 2017). While water storage in the mafic crust seems to be equivalent to previous examples from the Pacific, leading to a velocity reduction of ∼0.3 km s^{-1} (e.g. Contreras-Reyes et al. 2007, Figure 6.1), the total volume of serpentine being subducted beneath the Lesser Antilles may be very much greater than any of those previous Pacific or Indian Ocean examples. If the presence of highly tectonized crust is a key variable in the development of these very high levels of alteration, this may lead to further spatial and temporal variations in water storage across the Antilles slab between magmatically robust and tectonically controlled regions of spreading.

6.7.6 Implications for Lesser Antilles Arc Behaviour

The high levels of hydrous alteration observed beneath the Lesser Antilles outer rise do not directly result in increased H_20 flux compared to other subduction zones. Whilst slow convergence may facilitate the very high levels of mantle serpentinization observed, they also greatly reduce the rate at which the hydrated slab is delivered into the sub-arc mantle. For example, subduction systems such as Chile where estimates of the degree of upper mantle serpentinization do not exceed ∼16% (Moscoso and Grevemeyer, 2015; Grevemeyer et al., 2018) are likely to deliver equivalent volumes of water to sub-arc depths as a result of the much greater convergence rate (Table 6.4). This feedback mechanism may limit the amount of variation which is possible globally today in terms of the rate at which water is delivered into different subduction systems, and explain the relatively low seismicity and volcanism along the Lesser Antilles arc despite the high degree of hydrous alteration observed (Sections 2.2.2, 2.2.3).

There are also likely to be variations in the degree of outer rise hydration along-strike within the Lesser Antilles system. This is particularly true to the south, where the sediment thickness in the accretionary prism increases with proximity to the South American margin, actively building out onto the incoming plate (Westbrook, 1982). Although the high levels of alteration observed within the Tiburon Basin occur despite the presence of a 1+ km thick incoming sediment column, the much thicker sediment pile south of the Tiburon Rise (which may reach 7 km on the incoming plate, Moore et al. 1988) is unlikely to be circumnavigated so easily,

especially where the accretionary prism spills out onto the outer rise. To the north the increasing obliquity of subduction with the transition from the Lesser Antilles to the Puerto Rico trench (where there is effectively no active convergence, with motion almost entirely strike-slip) may lead to a similar reduction due to a flattening of the slab (Bie et al., 2020) and reduction in bend faulting. The Tiburon Basin thus represents a high point of outer rise hydration along the Lesser Antilles slab.

There is a well established connection between the presence of serpentine and increased intra-slab seismicity. This may arise either from dehydration embrittlement (Peacock, 2001; Jung et al., 2004), or ductile deformation as a result of increased fluid pore pressure following deserpentinization (Proctor and Hirth, 2015). The style and distribution of bend faulting may itself exert some control over the distribution of intra-slab seismicity. Boneh et al. (2019) identified a global correlation between the throw on outer rise faults and seismicity rates, thought to reflect the depth and degree of fluid circulation. At the Middle America and Chile trenches Ranero et al. (2005) observed that not only did intra-slab seismicity increase in regions of increased bend faulting, but that failure occurred through reactivation of these bend faults, rather than correlating with the maximum shear stresses.

The peak in hydration within the Tiburon Basin correlates well with an increase in intra-slab seismicity observed beneath the central and northern Antilles arc (Section 2.2.2), as well as the thicker crust of the northern arc (Section 2.2.1). Fault plane solutions for these earthquakes are approximately trench parallel and correlate well with the orientation of faults which accommodate bending in the outer rise (Bie et al., 2020). These intra-slab normal faulting earthquakes, are also much rarer from the northern and southernmost sections of the arc (Bie et al., 2020). Previously this increased seismicity had been linked to subducting fracture zones (Schlaphorst et al., 2016; Paulatto et al., 2017), however, the high degree of additional hydration beneath the outer rise must also contribute.

Previous studies of fracture zones in the Atlantic have suggested that close to the ridge-transform intersection, a region of as much as 14 km deep by 20 km wide may be susceptible to serpentinization (Boschi et al., 2013). Porphyroclastic peridotites collected from the Vema ridge show 80-90% serpentinization which pre-dates uplift and exposure on the seabed (Boschi et al., 2013). Such rocks are concentrated on the inside corner of the ridge intersection where the crust is thinnest (Escartin and Cannat, 1999). Despite the high levels of serpentinization

observed by this study the concentration of water bound within the subducting crust will still be higher, and extend to greater depths, along fracture zones than in the surrounding crust. Hence, these results do not disagree with those studies which have previously observed correlations between along strike seismicity (Schlaphorst et al., 2016; Paulatto et al., 2017) and crustal structure (Schlaphorst et al., 2018; Melekhova et al., 2019) with subducting fracture zones (Section 2.2.2). However, the high degree of serpentinization observed here must also contribute to the thicker crust and higher rates of seismicity in the central portion of the arc.

6.8 Conclusions

Using a new high resolution wide-angle dataset across the Lesser Antilles outer rise we observe a high degree of hydrous alteration in the subducting lithosphere as a result of bend faulting. Velocities as low as 6.3 km s^{-1}, may indicate as much as 55% serpentinization of the uppermost mantle. This very high degree of alteration creates a velocity inversion, compared to the overlying gabbroic crust, creating a shadow zone observed on OBS. This is the first time that such a high degree of mantle serpentinization has been observed in a outer rise setting. The maximum depth of alteration is constrained by a reflected phase (PmP2) off the base of this low velocity layer in the upper mantle. This alteration seemingly results from the very slow convergence rates at the Lesser Antilles trench, and a dense network of reactivated normal faults, the results of slow seafloor spreading in a region of tectonized crust, which provide myriad pathways via which water can access the lower crust and mantle. This high degree of alteration is possible in spite of a relatively thick sediment layer on the incoming plate. The resulting large volumes of water stored in the upper mantle are likely to contribute to the increased rates of intra-slab seismicity and crustal thickness observed in the central arc, in addition to concentrated serpentinization at fracture zones.

Chapter 7

Results: Monitoring the Kick-'em-Jenny Volcano, Lesser Antilles

This chapter appears as Allen et al. (2018).

Allen, R. W., Berry, C., Henstock, T. J., Collier, J. S., Dondin, F. J. Y., Rietbrock, A., Latchman, J. L., and Robertson, R. E. A. (2018). 30 years in the life of an active submarine volcano:A time-lapse bathymetry study of the kick-'em-jenny volcano, lesser antilles. *Geochemistry Geophysics Geosystems*, 19(3):715–731.

Key contributions of other named authors:

Berry, C. (MSci Student, Imperial College, London: Performed initial editing on bathymetry surveys from R/V Ronald H. Brown (2003), R/V Nautilus (2013/2014) and R.R.S. James Cook Survey in contribution to MSci project (Berry, 2017).

Collier, J. S., Henstock, T.: Project supervisors, planned R.R.S. James Cook surveys and performed initial data processing at sea.

7.1 Abstract

Effective monitoring is an essential part of identifying and mitigating volcanic hazards. In the submarine environment this is more difficult than onshore because observations are typically limited to land-based seismic networks and infrequent shipboard surveys. Since the first recorded eruption in 1939, the Kick-'em-Jenny (KeJ) volcano, located 8 km off northern Grenada, has been the source of 13 episodes of T-phase signals. These distinctive seismic signals, often coincident with heightened body-wave seismicity, are interpreted as extrusive eruptions. They have occurred with a recurrence interval of around a decade, yet direct confirmation of volcanism has been rare. By conducting new bathymetric surveys in 2016 and 2017 and reprocessing 4 legacy datasets spanning 30 years we present a clearer picture of the development of KeJ through time. Processed grids with a cell size of 5 m and vertical precision on the order of 1–4 m allow us to correlate T-phase episodes with morphological changes at the volcano's edifice. In the time-period of observation 7.09 x 10^6 m^3 of material has been added through constructive volcanism – yet 5 times this amount has been lost through landslides. Limited recent magma production suggests that KeJ may be susceptible to larger eruptions with longer repeat times than have occurred during the study interval, behavior more similar to sub-aerial volcanism in the arc than previously thought. T-phase signals at KeJ have a varied origin and are unlikely to be solely the result of extrusive submarine eruptions. Our results confirm the value of repeat swath bathymetry surveys in assessing submarine volcanic hazards.

7.2 Introduction

Accurately quantifying the risk associated with volcanic hazards requires detailed monitoring and where possible a thorough understanding of the scale and impact of historic events. Technological improvements have made it possible to monitor terrestrial volcanoes to increasingly high degrees of accuracy. Geodetic measurements such as GPS (Puglisi et al., 2001; Puglisi and Bonforte, 2004; Paris et al., 2014), tilt meters (Fiske and Shepherd, 1990; Bonaccorso et al., 2002; Ricco et al., 2013), strain meters (Voight et al., 2010; Bonaccorso et al., 2012) and electronic distance meters (Jackson et al., 1998) create a detailed record of morphological changes through time. When combined with satellite imaging technologies such as Synthetic Aperture

Radar (SAR), which has the capacity to measure deformation to centimetre scale accuracy (Massonnet et al., 1995; Massonnet and Feigl, 1998; Parks et al., 2012), and other monitoring techniques including volcanic gas emission (Duffell et al., 2003; Edmonds et al., 2003), seismicity (Aki and Ferrazzini, 2000; Chiarabba et al., 2000; Brenguier et al., 2008), magnetics (Del Negro et al., 2002, 2004), microgravity (Rymer, 1994; Budetta et al., 1999), and photogrammetry (Baldi et al., 2000; Diefenbach et al., 2012), these datasets are powerful resources in attempts to assess volcanic risk (Dzurisin, 2003; Sparks, 2003; Cashman and Sparks, 2013).

In the submarine realm the work of monitoring volcanoes is made much more difficult. Events at NW Rota-1 in the Mariana arc (Embley et al., 2006) and West Mata in the NE Lau Basin (Resing et al., 2011) are the only direct visual observations of deep-sea submarine eruptions. Shallow water island-forming eruptions, such as the creation of Surtsey (near Iceland) between 1963 and 1967 (Moore, 1985), Myojinsho between 1952 and 1953 (Fiske et al., 1998) and Nishinoshima (both Japan) between 2013 and 2015 (Maeno et al., 2016), are not uncommon. Yet until fairly recently we had exceedingly limited understanding of the behavior of deeper submarine volcanoes throughout the eruption cycle despite associated hazards including potentially tsunamigenic landslides and eruptions.

Many more submarine eruptions, both from seamounts and ocean ridges, are now being recorded and surveyed both before and after volcanic activity (Rubin et al., 2012). Although shipboard surveys are unable to match modern satellite techniques for precision or repeat interval, recent time-lapse bathymetry studies from volcanoes such as Monowai (Chadwick et al., 2008b; Wright et al., 2008; Watts et al., 2012), Santorini (Watts et al., 2015), NW Rota-1 (Chadwick et al., 2008a; Schnur et al., 2017) and West Mata (Embley et al., 2006; Clague et al., 2011) have greatly improved our understanding of the evolution of submarine volcanoes. On both Monowai and NW Rota-1 the authors were able to identify multiple episodes of both positive and negative depth changes in the form of landslides tied to volcanic and seismic activity. However, despite their obvious value studies of this nature over submarine volcanoes are still uncommon. Although new technologies for remote sensing of submarine eruptions are emerging e.g. the 2014 instillation of a permanent cabled underwater observatory monitoring Axial Seamount on the Juan de Fuca ridge (Kelley et al., 2014), these methods are still a long way from matching the amount of detailed information which can be gathered during terrestrial volcanic eruptions.

Today, remote detection of submarine eruptions is largely reliant on identifying T-phase arrivals

on regional hydrophones and seismometers, e.g., Dziak and Fox (1999) and Bohnenstiehl et al. (2013). These distinctive hydro-acoustic signals can be produced by submarine earthquakes or by the interaction between water and fresh magma and are capable of travelling long distances through the minimum velocity SOFAR (Sound fixing and Ranging) channel (Lindsay et al., 2005; Ito et al., 2012; Metz et al., 2016). At KeJ volcanic T-phase arrivals (which are thought to indicate submarine eruptions) are differentiated from signals with a purely seismic origin by their low frequency content, impulsive onset and duration (often several 10 s of seconds), regularly running together into a sustained tremor-like signal during periods of high activity (Lindsay et al., 2005). They are also lacking associated P and S wave arrivals as would be expected from a signal with an earthquake source.

In this paper we present new and reprocessed multibeam bathymetry data covering a period of more than 30 years over the volcano Kick-'em-Jenny (KeJ) in the southern Lesser Antilles. New bathymetric surveys conducted from the R.R.S. James Cook in 2016 and 2017 combined with legacy datasets from 1985, 2003, 2013, and 2014 allow us to view morphological changes at the volcano through top the present day. The surveys span several episodes of recorded volcanic T-phases in 1988, 1995, 2001 (Lindsay et al., 2005), 2015 (Robertson et al., 2015) and 2017 (Latchman et al., 2017). By combining these datasets we are able to describe the changes to the edifice through time and offer insight into the processes controlling the evolution of submarine volcanoes.

7.3 Kick-'em-Jenny

7.3.1 Eruption History and Hazard

KeJ sits near the southern end of the Lesser Antilles island arc with a current summit depth of 197 m below sea level (bsl) Located 8 km north of the island of Grenada it is the only known active submarine volcano in the region (Figure 7.1). The arc, active since the Cretaceous (Bouysse, 1988; Bouysse and Westercamp, 1990), is located above the site where Atlantic oceanic crust is slowly subducting beneath the Caribbean plate at rates of $\sim$2 cm yr^{-1} (Symithe et al., 2015). Of the arc's terrestrial volcanoes Soufrière Hills on Montserrat has seen the most activity in recent years having been in a constant state of eruption since 1995 (Druitt and

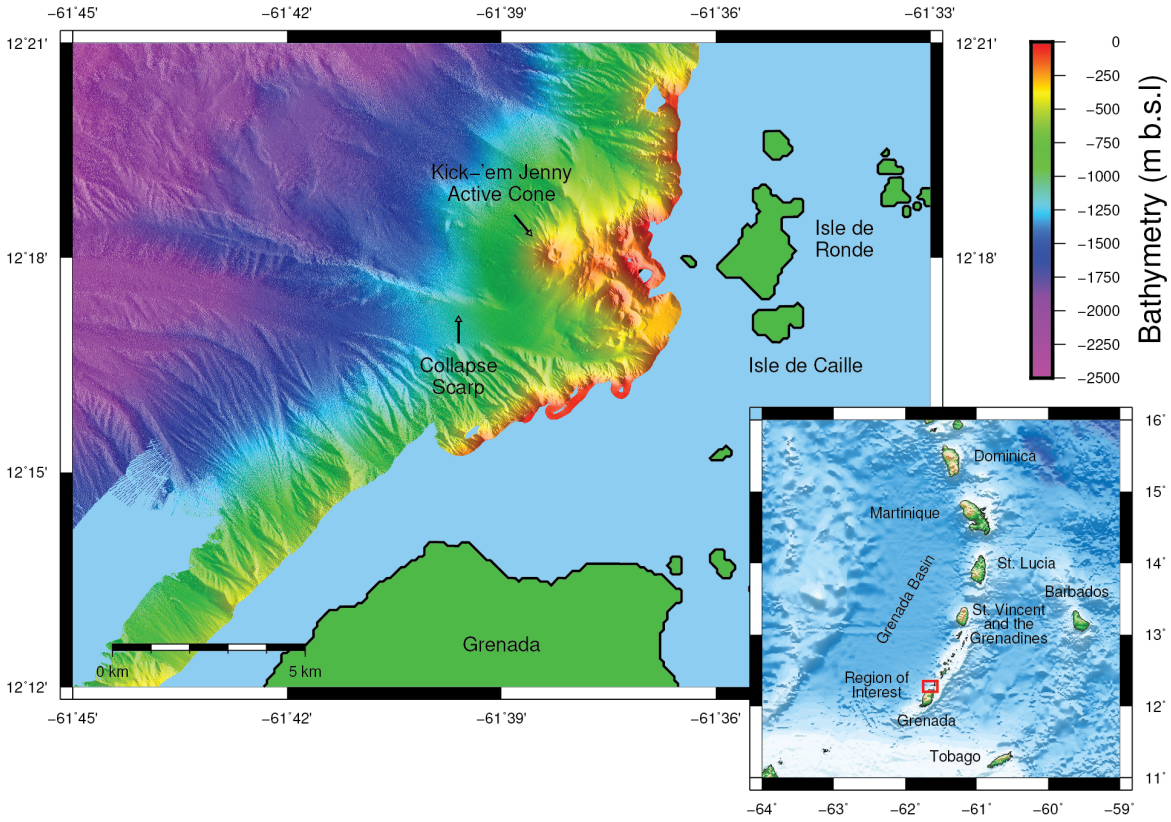


Figure 7.1: Map showing location of Kick-'em-Jenny in the southern Lesser Antilles. Bathymetry comes from the 2013 R/V Nautilus dataset in the main map and GEBCO in the inset. The cone of KeJ can be clearly observed within the large horseshoe shaped collapse scarp, located on the western flank of the arc.

Kokelaar, 2002; Wadge et al., 2014).

KeJ lavas are commonly olivine basalts and basaltic andesites (Sigurdsson and Shepherd, 1974; Devine and Sigurdsson, 1995). Similar compositions are common throughout Grenada and much of the southern Grenadines (Sigurdsson and Shepherd, 1974). It has been proposed that KeJ is the active vent of a larger volcanic system (Lindsay et al., 2005) which also encompasses nearby islands such as Isle de Ronde and Isle de Caille (Figure 7.1). There is evidence for both explosive and effusive eruptions at KeJ, though the former seems to be by far the more common. ROV observations have documented extensive explosive breccias and pyroclastic deposits (McClelland et al., 1989; Carey et al., 2016), but little to no evidence of lava flows (Sigurdsson and Shepherd, 1974), though there was an episode of dome building tied to volcanic activity in 1977 (Devine and Sigurdsson, 1995).

KeJ was unknown until 1939, when a large eruption occurred which was observed from northern Grenada. Local reports describe an ash cloud extending ∼300 m above sea level and ground

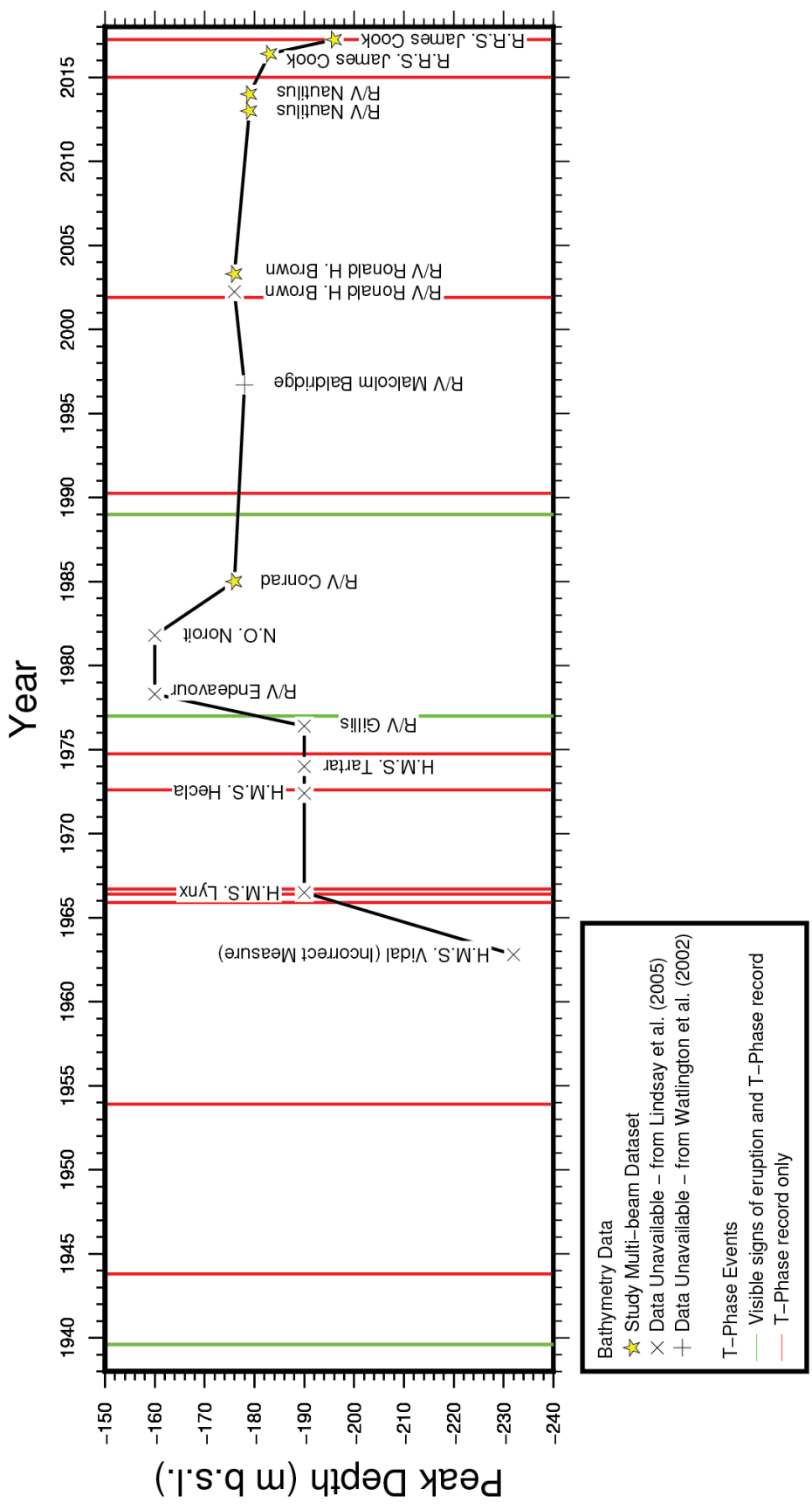


Figure 7.2: Timeline of bathymetric surveys and recorded T-phase episodes at KeJ. Depth values for the peak of KeJ are taken from the compilation of Lindsay et al. (2005) where original data sources were unavailable. Stars indicate multibeam bathymetry datasets used in this study. Note that depth measurements refer to the single shallowest point on KeJ from that survey, in most cases this is the rim of the crater, but for the R/V Endeavour (1978), N.O. Noroit (1981) and R/V Conrad (1985) it is the peak of a volcanic dome on the northern side of the crater.

shaking in the north of the island (Devas, 1974). Since then there have been 13 notable episodes of T-phase signals attributed to KeJ (Figure 7.2) interpreted as submarine eruptions (Lindsay et al., 2005), the most recent of these occurred in April 2017 (Latchman et al., 2017). T-phases have been recorded in association with KeJ as far back as 1943 despite the presence of only a couple of seismometers in the Caribbean at this time (Lindsay et al., 2005). Repeat times between periods of activity, on the order of a decade, mean that KeJ is considered one of the Antilles arc's most active volcanoes. Based purely on visual observations the 1939 eruption was by far the largest, with only two further events (1974 and 1988) showing low-level signs of activity at the sea surface, limited to water discoloration and small volumes of ejecta (Bouysse et al., 1988; McClelland et al., 1989; Lindsay et al., 2005).

In 2001, 2015 and 2017 T-phase activity was preceded by several days of heightened seismicity around the volcano (Lindsay et al., 2005; Robertson et al., 2015; Latchman et al., 2017). However, reports of shaking from northern Grenada (and on occasion as far away as Martinique) coincide with the majority of instrumental T-phase recordings (Shepherd and Robson, 1967; McClelland et al., 1988; Lindsay et al., 2005; Robertson et al., 2015; Latchman et al., 2017), so this correlation with seismic activity is not an entirely new phenomenon.

A near-shore location and history of regular activity means that KeJ is a major concern for inhabitants of the southern Caribbean islands. The shallow water and complex topography between the islands makes the specifics of any tsunami in this region hard to model (Smith and Shepherd, 1996; Harbitz et al., 2012) though due to the volume of material required, the risk of a tsunami triggered by eruption alone, and without some additional major mass-movement is considered minimal (Gisler et al., 2006). Recent modelling of such an event has shown that a collapse at the edifice in the region of 0.7 km^3 could trigger large enough waves to cause hazardous run-up on local islands (Dondin et al., 2017). Lindsay et al. (2005) concluded that the risk posed to shipping by gas release and ejecta during eruptions was the more pressing and likely hazard concern posed by KeJ. Such gas releases are possible outside of periods of volcanic activity.

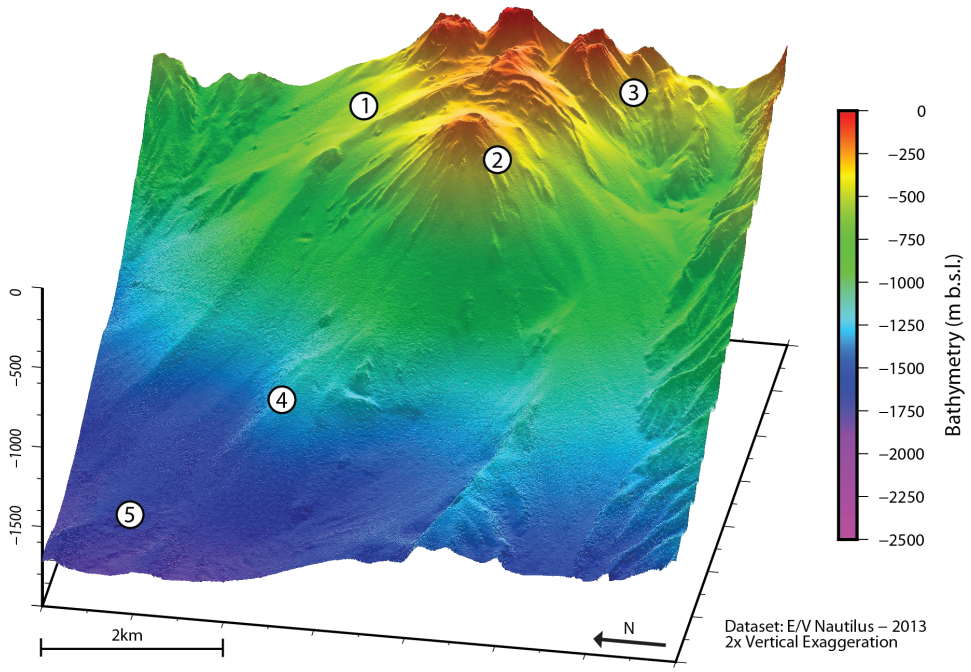


Figure 7.3: 3-D projection of KeJ bathymetry using R/V Nautilus (2013) bathymetric dataset. Viewpoint is from an azimuth of 205°. (1) Horseshoe shaped scarp surrounding KeJ, the result of the collapse of a larger "Proto-Jenny" at 43 ka (Dondin et al., 2017). (2) Active cone of KeJ. (3) Kick-'em-Jack, the largest of the volcanic cones in the back-wall above KeJ. (4) Deposit from the 43 ka collapse of "Proto-Jenny". Kick-'em-Jenny has subsequently grown through this debris flow. (5) Run out of the debris flow extends for up to 14 km into the deep water of the Grenada Basin.

7.3.2 Morphology

The perceived risk associated with KeJ has motivated 15 bathymetric surveys starting with the H.M.S. Vidal in 1962 (Figure 7.2). This wealth of data means that the general morphology of KeJ is well known. The volcano consists of an asymmetric circular cone with a central crater measuring approximately 300 m in diameter. The peak height of the rim, (currently at ∼197 m bsl), has remained fairly constant through time, besides a period of dome building in the 1970s / 1980s when it was observed as shallow as 160 m (Figure 7.2). Recent measurements have disproved the previously erroneous view that KeJ was growing rapidly toward the surface and has the potential to form a new volcanic island (Devine and Sigurdsson, 1995; Watlington et al., 2002). Such conclusions were largely driven by an error in the depth measurement made from the H.M.S. Vidal (1962) which put the summit at 232 m bsl (Lindsay et al., 2005). The current edifice is situated on the flanks of the Lesser Antilles arc ridge and stands 1,300 m

above the Grenada backarc Basin to the west.

The cone sits within a large collapse scarp (Figure 7.3). This horseshoe shaped feature, up to 14 km long and 6 km wide is the result of a near-total collapse of a previous incarnation of KeJ. This "proto-Jenny" is modeled to have stood significantly above sea-level before failure at approximately 43 ka (Dondin et al., 2012, 2017). Evidence for similar high volume sector collapses and slope failures are observed at almost all of the major island volcanoes along the arc (Deplus et al., 2001; Boudon et al., 2007; Watt et al., 2012a,b). Globally such events, as well as submarine volcanic explosions, are frequently tsunamigenic (Paris et al., 2014). The debris flow created by the collapse of proto-Jenny is clearly observable on bathymetry for over 14 km onto the plain of the Grenada Basin with an approximate volume of 4.4 km^3 (Dondin et al., 2012; Carey et al., 2014). The modern cone of KeJ has grown through this older debris flow. A major failure on this scale today would certainly be capable of triggering a regional tsunami. However, given the smaller size of the cone (a total volume of 0.585 km^3 measuring down to the 600 m contour), and greater depth below sea level it is unlikely that a major sector collapse at KeJ today would have such a significant impact.

KeJ is a highly active hydrothermal system, with numerous surveys and ROV studies observing active venting both from within the crater (Wishner et al., 2005; Koschinsky et al., 2007; Graff et al., 2008; Carey et al., 2016) and on the flanks of the edifice (Koschinsky et al., 2007). Emanating fluid temperatures have reached as high as 270–280 °C (Koschinsky et al., 2007; Graff et al., 2008) with volcanic sediment within the crater showing evidence for extensive alteration to clay minerals and surface Fe-oxyhydroxide mineralization (Carey et al., 2016). These harsh conditions, coupled with the regularity of eruptions and gas releases greatly limits macrofaunal activity within the crater (Wishner et al., 2005; Graff et al., 2008).

The heavily faulted back-wall of KeJ hosts a number of smaller volcanic cones, the largest of these, Kick-'em-Jack, sits shallower than KeJ with a peak depth of 112 m bsl. No volcanic activity has been definitively tied to these cones during modern observations of KeJ. In contrast to KeJ, ROV images taken by the R/V Nautilus in 2013/2014 show the edifice of Kick-'em-Jack is home to an array of sub-sea life, and extensive mineralization is further evidence for a cone which has been dormant in recent time.

7.4 Data

Data from 6 swath bathymetry surveys are used for this investigation (Figure 7.2). These surveys from the R/V Robert D. Conrad (1985), R/V Ronald H. Brown (2003), R/V Nautilus (2013 and 2014) and R.R.S. James Cook (2016 and 2017) cover a period of 32 years and 5 seismic episodes (1988, 1990, 2001, 2015, and 2017) at KeJ. The acquisition parameters of each of the surveys can be found in Table 7.1. The survey geometries and further data quality information (grid standard deviation and sounding density) are also shown in Figures 7.4 and 7.5.

The R.R.S. James Cook surveys recorded the bathymetry on both EM710 (∼70 to 100 Hz high frequency system designed for use in shallow water) and an EM120 (12 Hz low frequency deep water system) multibeam echo sounder, with the EM120 covering a much larger spatial extent down-dip to the west of KeJ. In this down-dip region geologically significant differences between the surveys were minimal (Berry, 2017). From here on, discussion of the R.R.S. James Cook surveys will refer to the higher resolution survey done across the edifice of KeJ with the EM710 system. We reprocessed both the 2013 and 2014 Nautilus surveys, but there are no significant morphological changes between them (Berry, 2017). The 2013 survey was of significantly higher quality and so we will not present the 2014 data in the following analysis. Backscatter data were also reviewed for the two R.R.S. James Cook surveys, however the results of these were inconclusive and so will not be shown here.

The surveys from the Brown, Nautilus and Cook were received as raw, unedited swath bathymetry files (xyz format for the Brown dataset and gsf format for the Nautilus datasets) which were processed in the bathymetry editing programme CARIS/HIPS to remove noisy data such as during ROV operations and erroneous depth soundings, particularly from the outer beams. The decision to reprocess this data was taken in order to ensure consistency in editing over all surveys, increasing confidence in our final interpretations. All work was conducted in UTM zone 20N.

Final depth surfaces were gridded at a horizontal resolution of 5 m (Figure 7.6). The edited data from the R.R.S. James Cook and R/V Nautilus were gridded using the CARIS/HIPS Uncertainty Weight algorithm which was found to produce grids with the lowest standard deviation within each cell (Table 7.1). In this algorithm the contribution of an individual

Table 7.1: Survey Statistics of the Bathymetric datasets and Final Grids Used in the Study

Cruise	Vessel	Instrument make	Model	Frequency (kHZ)	Beams per ping	Mean survey speed (knots)	Maximum theoretical swath width (m) (x water depth)	Mean standard deviation of cells in final grid (m)	Depth shift relative to final R/V Nautilus 2013 grid (m)
1985	R/V Robert D. Conrad	General Instrument Corporation	SeaBeam	12	19	5.2	3.0	-	-1.5
2003	R/V Ronald H. Brown	Sea Beam Instruments Inc.	SeaBeam 2112	12	120	6.4	3.4	7.8	-0.35
2013	R/V Nautilus	Kongsberg	EM302	30	432	7.8	5.5	1.1	0
2014	R/V Nautilus	Kongsberg	EM302	30	432	9.2	5.5	1.1	0
2016	R.R.S. James Cook	Kongsberg	EM710	70–100	200	5.0	5.5	2.2	+0.5
2017	R.R.S. James Cook	Kongsberg	EM710	70–100	200	5.0	5.5	3.8	+2.1

Note. Mean survey velocities were calculated from the timing/location data within each dataset. Maximum theoretical swath width is calculated based on the maximum possible beam angle for each system. Following processing the true swath width is likely to be significantly less than this (due to the lower precision of the outer, high angle soundings). Standard deviation values for each grid were calculated as part of the gridding process in CARIS/HIPS. Each grid has a cell size of 5 m, except for the 1985 survey which has a cell size of 30 m. More detailed maps of the standard deviation in each cell and the sounding density for each grid can be found in the supporting information. [a] Positive values correspond to an upward shift i.e. the surface was initially deeper than the R/V Nautilus (2013) grid.

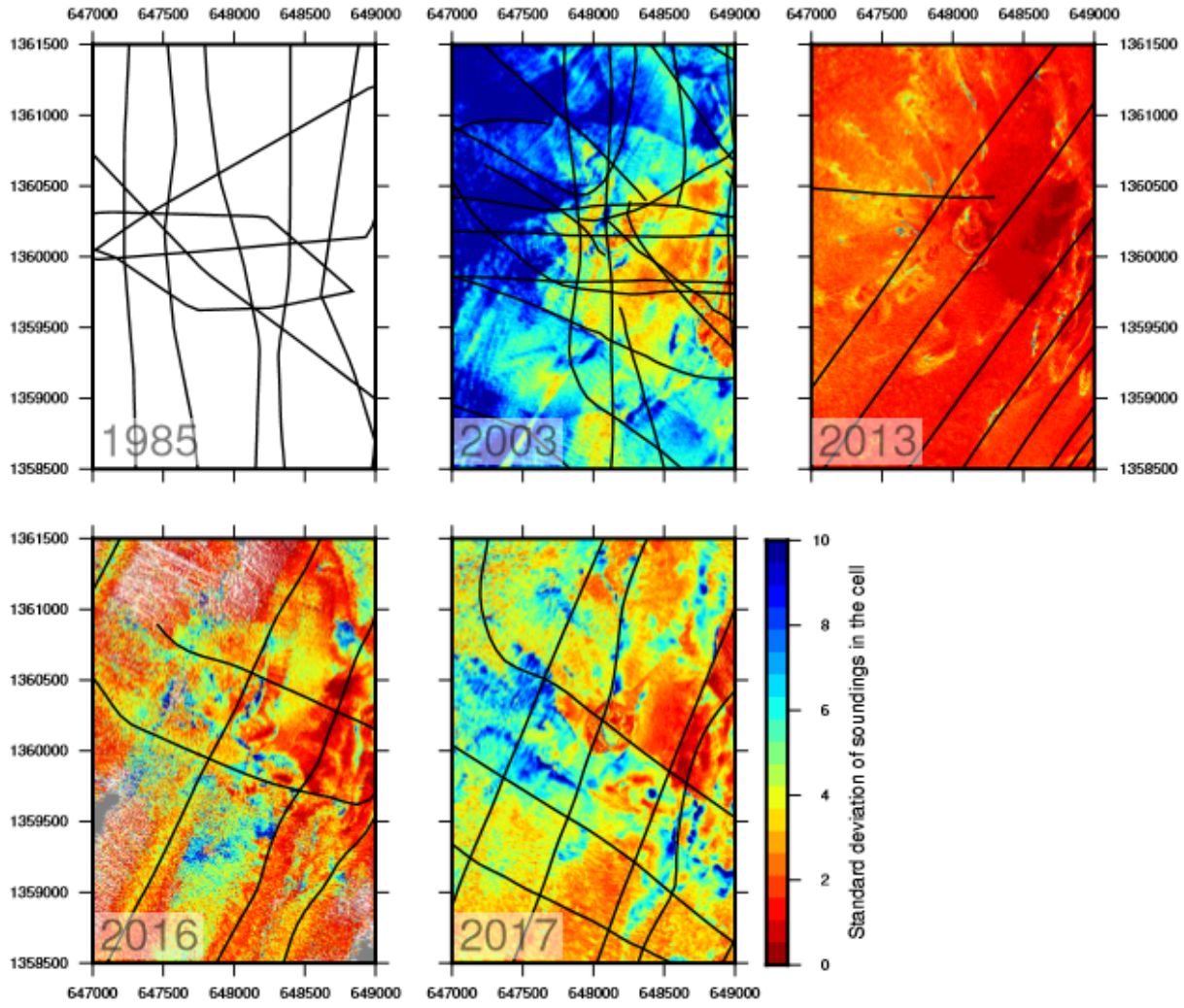


Figure 7.4: Standard deviation of soundings contributing to each cell of the grids presented in Figure 7.6. These values were calculated as part of the gridding process in CARIS/HIPS. In particular these maps highlight the very high quality of data in the region of the crater and upper slopes of the edifice of KeJ. For the 1985 dataset in which the vast majority of cells only contain a single depth sounding we have not calculated these values as they would have little significant meaning. Tracks (black lines) shown are only for the periods during which the vessels were acquiring swath data. Any apparent discontinuities are the result of the mbes system being switched off or data removed by us during activities such as ROV surveying.

sounding is scaled according to its depth uncertainty (this depth uncertainty takes into account both the distance from the node and the sounding's horizontal uncertainty). It was not possible to run this algorithm on the older R/V Ronald H. Brown data, and so a Swath Angle Weight algorithm was used in which the inner beams are weighted more highly due to their higher incidence angle to the seabed.

When tested on the newer datasets it was found that the Swath Angle algorithm generally added between 1 and 2 m to the standard deviation of the cells in the final grid compared to

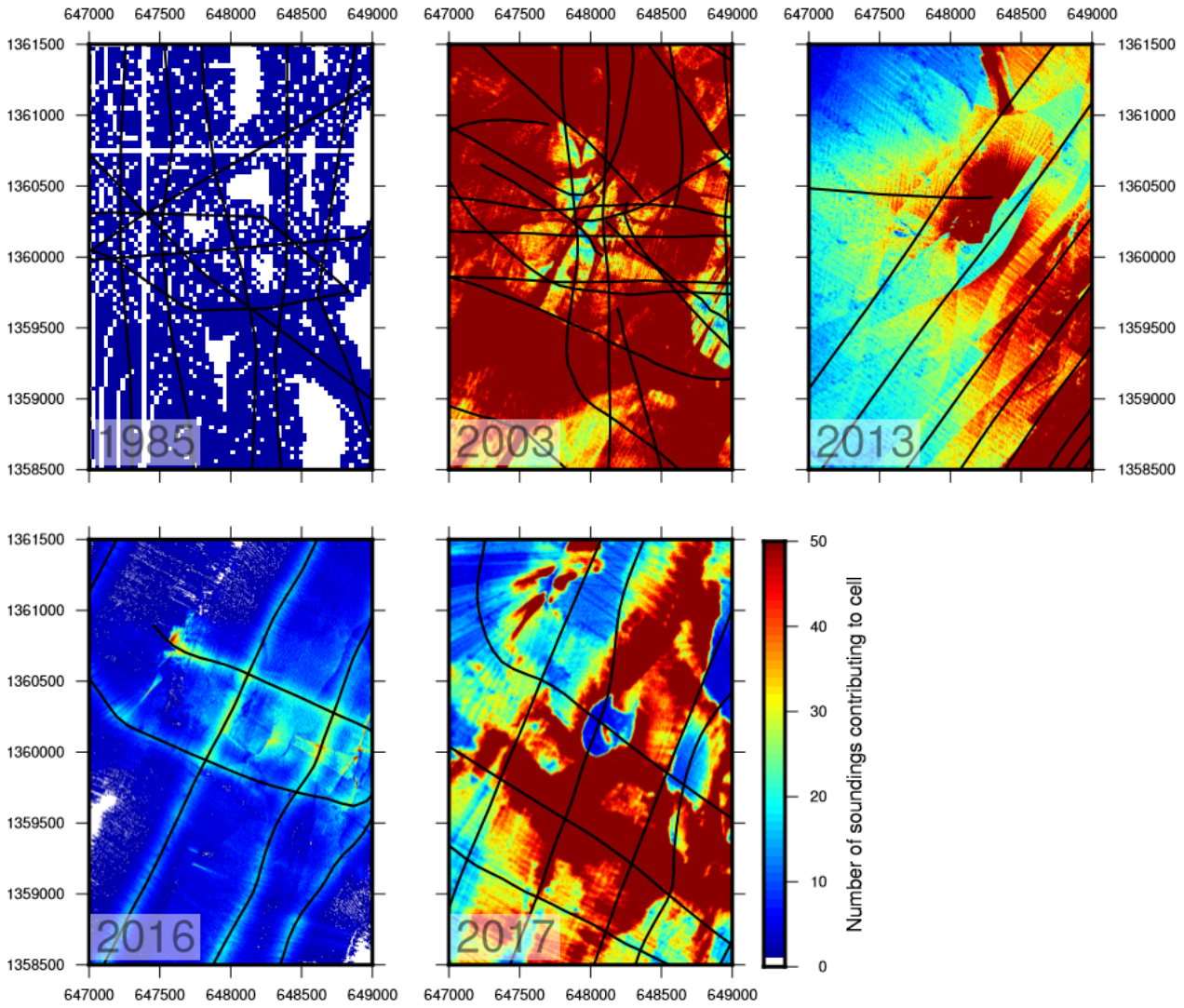


Figure 7.5: Number of soundings contributing to each cell of final grids presented in Figure 7.6. For the 4 most recent surveys these images highlight the high density of data recorded and the large number of depth soundings contributing to each cell. For the surveys from 2003-2017 these images were produced as part of the gridding process in CARIS/HIPS with a cell size of 5m. For the 1985 dataset the values were calculated by comparing the original sounding locations to the final grid in ARC GIS. In general these datasets were continuous and required little to no interpolation in the area of interest around the edifice of KeJ. In the courser 1985 30m grid it shows a number of gaps in the dataset which were interpolated using a continuous curvature surface algorithm. However none of our interpreted depth changes (Figure 7.7) coincide with these areas, giving us confidence that our results are reliable. Tracks (black lines) shown are only for the periods during which the vessels were acquiring swath data. Any apparent discontinuities are the result of the mbes system being switched off or data removed by us during activities such as ROV surveying.

the Uncertainty Weight algorithm. This in part explains the comparatively high mean deviation of 7.8 m for the 2003 grid. In the case of the final 2013 R/V Nautilus grid, the mean standard deviation of depth soundings contributing to each grid cell is just 1.1 m (Table 7.1, Figure

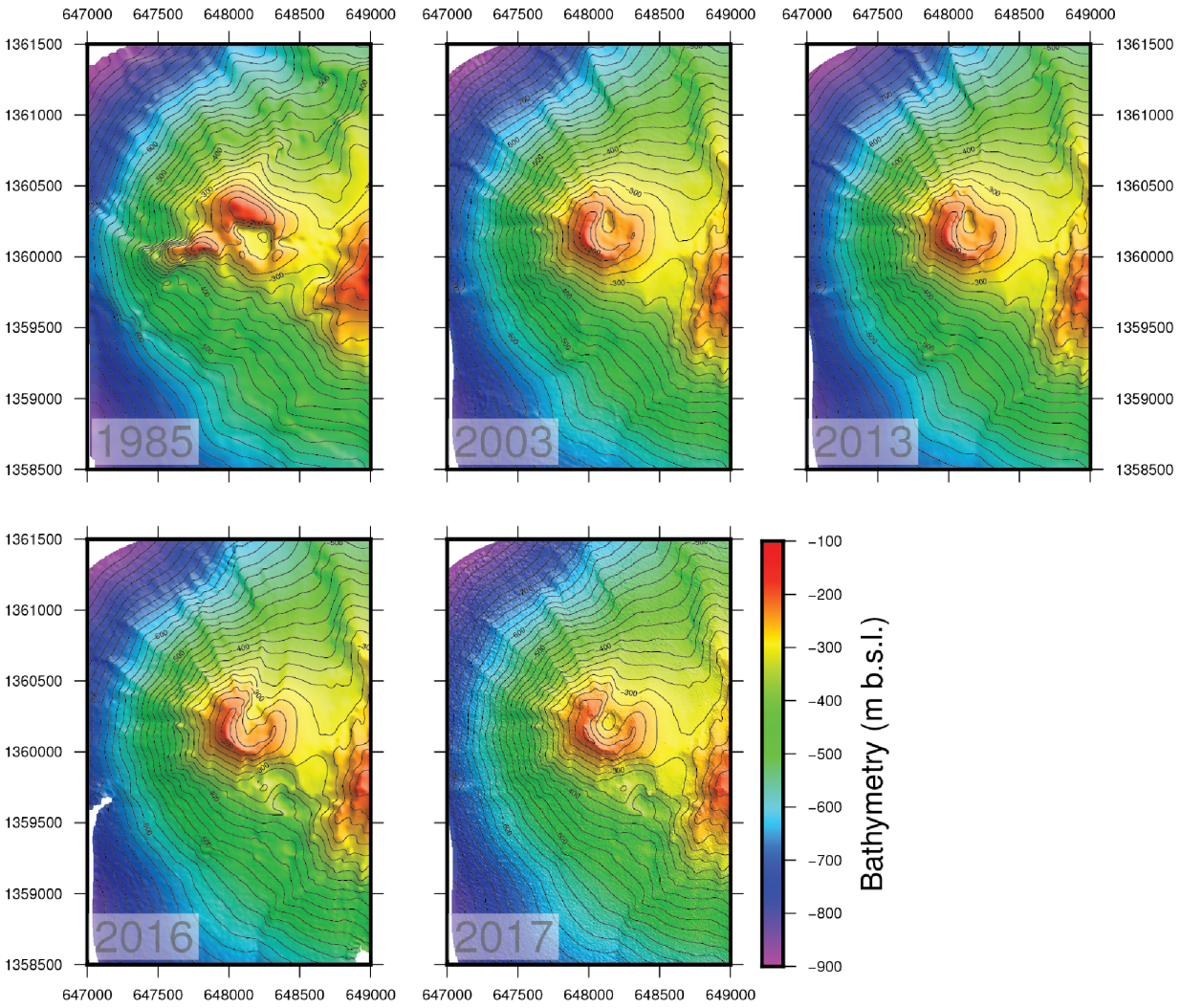


Figure 7.6: Final bathymetric grids produced following reprocessing of legacy bathymetry datasets. Surfaces shown have been smoothed using a 50 m filter for the purposes of display. The unsmoothed 5 m grids are used for all depth change calculations discussed in the paper and differences shown in Figure 7.7. All surfaces are contoured at 25 m intervals. For survey parameters associated with each grid see Table 7.1

7.4). The high precision is likely the result of a relatively oversampled grid (Table 7.1). The 30 Hz EM302 instrument used for the survey is also less susceptible to noise than the high frequency system used on the R.R.S. James Cook. Any small gaps in the data were removed by interpolating values based on an area of 5 x 5 cells around any missing grid squares. Such gaps were largely down-dip from the area of interest around the edifice, and these interpolated values have little impact on our final results (Figure 7.5).

Raw swath files were unavailable for the 1985 dataset which was sourced from the NOAA (National Oceanic and Atmospheric Administration) archive as edited swaths in mbsystem

format. The data were not further edited by us but simply extracted as xyz values and gridded in GMT using a continuous curvature surface algorithm with a tension of 0.35 (recommended for steep topography). Due to the significantly lower sounding density of this dataset (Table 7.1, Figure 7.5) a cell size of 30 m was used.

Prior to calculation of the depth changes between the multibeam surveys, mean depths were calculated for each grid over a presumed stable area of $\sim$10 km^2 down dip to the west of the volcano. There is no evidence for long wavelength inflation or deflation of the study area during the survey interval. Final grids were shifted in depth so as to match the R/V Nautilus (2013) survey, the most precise dataset used in the study (Table 7.1). A similar process was used by Wright et al. (2008) in their study of Monowai. Surveys were processed with the same water column velocity model which had been applied by the collecting organization. Water column velocity measurements made during the surveys by the R.R.S. James Cook reduce from 1,540 ms^{-1} at the surface to 1,490 ms^{-1} at 600 m depth. At such depths you would only need a mean water column velocity error of around 12 ms^{-1} to cause a 5 m depth change. The largest mean-depth offset observed from the other surveys to the Nautilus grid was $\sim$2 m (see Table 7.1) an entirely reasonable amount of error considering the difference in the age and design of the bathymetric systems, and potential errors arising from sea-state. No tidal correction was made during processing due to the very low tidal range in the waters around Grenada (maximum $\sim$0.5 m).

Positioning errors were always expected to be minimal and none of the calculated depth change grids show strong or consistent errors resulting from offsets in topography. As an example the R.R.S. James Cook uses an Applanix POS MV 320 Global Positioning System (GPS) which is expected to be accurate to 0.5–2 m. Any errors on this scale will not be visible once the data are gridded at 5 m. This is of greater concern for the older surveys, particularly the 1985 R/V Robert D. Conrad bathymetry, given its age. However the difference images show none of the artefacts expected from positioning errors so we are confident that the positioning is consistent.

Depth change grids were calculated in ArcGIS (Figure 7.7) by subtracting time-adjacent surveys. To reduce noise, subtractions were clipped at a base value thus retaining only the most significant morphological changes and making them easier to interpret. A value of 5 m was chosen for the most recent time-lapses, while 30 m was used for the 1985–2003 grid, which is heavily influenced by the comparatively low data density of the Conrad survey (Table 7.1, Fig-

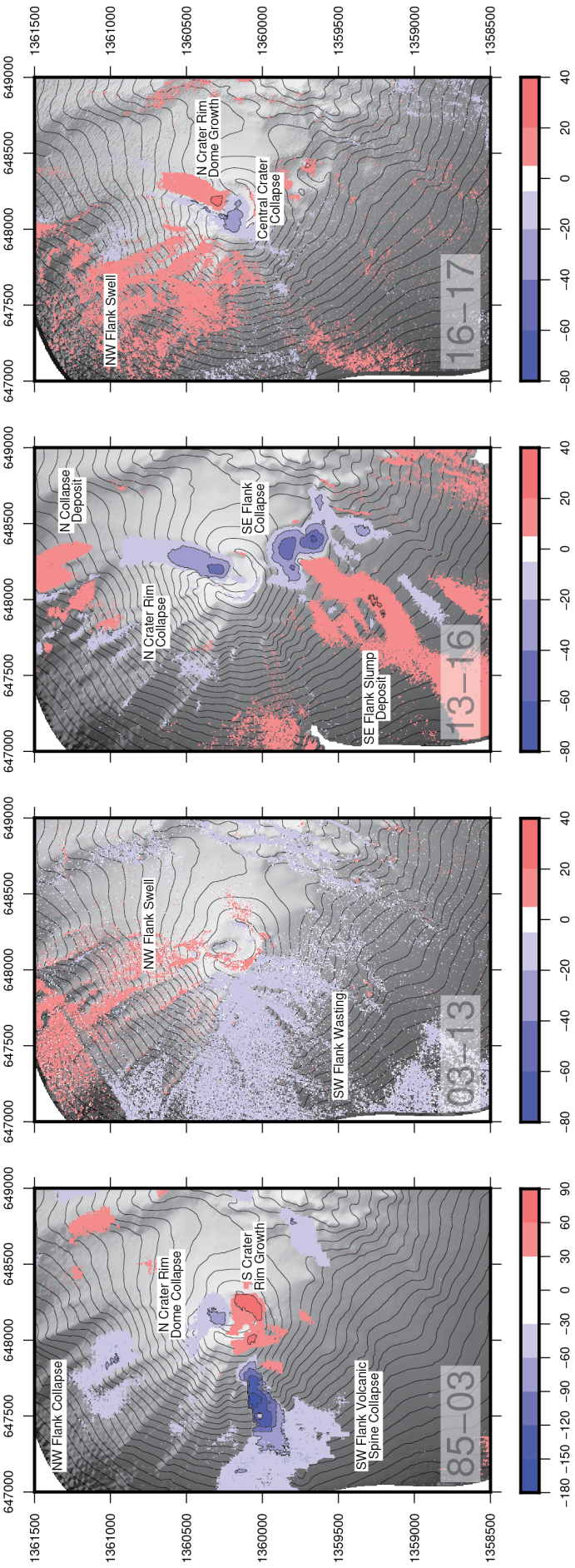


Figure 7.7: Depth-difference images calculated from final bathymetric grids. Cleaned difference grids (red-blue scale) are shown on top of the latter of the two bathymetric grids used in the time-lapse (grey scale). Labeled morphological changes correspond to volumes shown in Table 7.2.

ure 7.5). These values were chosen as they are close to the standard deviation of the difference grids themselves. Changes in volume resulting from the most significant of these depth changes were then calculated from the cleaned difference grids and are shown in Table 7.2.

7.5 Results

The final bathymetric grids show clear variations in the topography of KeJ through time. In all 4 time-lapses we are able to record both positive (growth) and negative (collapse) features. The most significant of these clearly correlate with episodes of T-phase signals.

7.5.1 1985-2003

The 1985–2003 time-lapse is the longest timespan covered in our study. This 18 year period covers 3 T-phase episodes in 1988, 1990, and 2001.

The 1985 survey shows a number of morphological features that do not appear in the later surveys. In 1985 a small (30 m) volcanic dome existed on the northern flank of the crater. Growth of this dome has been tied to the 1977 T-phase episode (the first of the two events post 1939 large enough to be observable from the sea surface), having first been detected in a 1978 bathymetric survey from the R/V Endeavour (Watlington et al., 2002; Lindsay et al., 2005). To the SW of the crater rim is a steep sided volcanic spine. During the period to 2003 both of these structures collapsed (see Figures 7.6, 7.7). The northern dome leaves a deep breach in the crater rim following the removal of 4.62 x 10^6 m^3 of material, a deepening of up to 70 m. This collapse has been tied to the 1988 eruption of KeJ by submersible observations made from the R/V Seward Johnson in 1989 (McClelland et al., 1989; Watlington et al., 2002). The collapse of the spine on the SW flank is the largest morphological change observed in any of our time-lapses with a loss of 2.18 x 10^7 m^3 of material and a depth increase of up to 174 m.

The 1988 episode is the second of the two T-phase events (post 1939) which was observed at the sea surface and is therefore the most likely candidate for the growth of the SE rim of the crater. The destabilizing effect of this relatively large eruption could well be the trigger for the two collapses. However, trying to separate out the timeline of changes associated with the

Table 7.2: Volume Changes Calculated From Cleaned Difference Grids Over KeJ

Description	Time-lapse	Maximum depth change (m)	Mean depth change (m)	Volume change (x 10^6 m^3)
SW Flank Volcanic Spine Collapse	1985-2003	-174.62	-58.47	-21.8
S Crater Rim Growth	1985–2003	+86.95	+48.98	+4.26
N Crater Rim Dome Collapse	1985-2003	-82.90	-44.90	-2.48
NW Flank Collapse	1985-2003	-70.01	-42.20	-4.62
SW Flank Wasting	2003–2013	-26.84	-7.25	-1.88
N Crater Rim Collapse	2013–2016	-59.61	-18.45	-2.29
N Collapse Deposit	2013–2016	+23.50	+11.20	+1.12[a]
SE Flank Collapse	2013–2016	-65.88	-21.36	-4.36
SE Flank Slump Deposit	2013–2016	+27.59	+10.34	+5.74[a]
N Crater Rim Dome Growth and Flow	2016–2017	+35.66	+10.50	+0.59
Central Crater Collapse	2016–2017	-37.11	-13.13	-0.94
NW Flank Swell	2016–2017	+32.95	+8.04	+2.24
			Net Total:	-31.28

Note These grids with labeled morphological changes can be seen in Figure 7.7. The total positive (addition of material) volume gain is 7.09 x 10^6 m^3. The total negative (loss of material) volume decrease is -38.37 x 10^6 m^3. [a] These positive changes are clearly deposits corresponding to up-slope collapses during this time period as such they have not been included in the total volume balance shown.

three events in this time-lapse is made difficult by the lack of high quality bathymetry during the intervening periods.

2001 was the first T-phase episode at KeJ to be associated with several days of sustained seismic activity (Lindsay et al., 2005). We assume that the majority of this seismicity was related to the movement of magma at depth. Latchman et al. (2017), tie precursory VT signals (volcano-

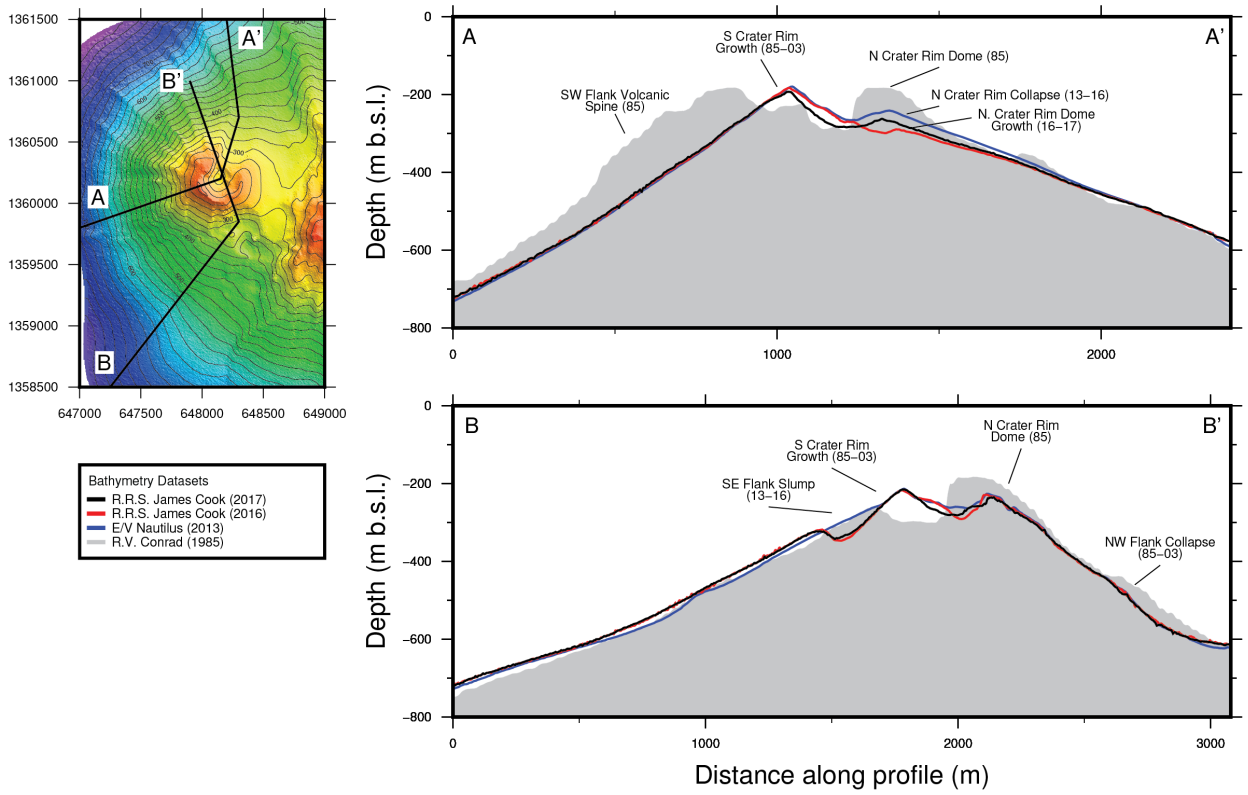


Figure 7.8: Profiles through final bathymetric grids over KeJ. Note that due to the relatively minor changes between 2003 and 2013, the 2003 survey is not shown for the sake of simplicity. Values in brackets refer to the year(s) in which a given feature was present.

tectonic seismic events) to ascending magma opening a new channel (or widening an existing one), suggesting a less open conduit than pre-2001 eruptions. However, Lindsay et al.'s (2005) relocation of these earthquakes places them several kilometers to the north/north-west of the cone of KeJ.

7.5.2 2003-2013

The 2003–2013 time-lapse covers an extended period of quiescence from 2001 to 2015 (Figure 7.2), the longest stretch of time without any recorded activity since monitoring of KeJ began. The absence of recorded T-phases coincides with a period in which morphological changes are on a smaller scale than is observed in the other comparisons (Table 7.2). The only noteworthy change is a small volume of apparent mass wasting from the SW flank of the cone. This area, the location of the volcanic spine collapse in the previous time-lapse, apparently continued to shed material (Figure 7.7). Given that no T-phases were recorded, this is likely to be a long-

term process of erosion of unstable material left behind by the previous collapses rather than an eruption driven collapse. The relatively small volume of -1.88 x 10^6 m^3 is lost in this way, with a mean depth change of 7.2 m.

The NW flank of the cone and much of the crater rim appear to show a weak positive swell during this time period of up to 14 m. This may be due to redistribution of volcaniclastic sediment from higher up the cone or, given the lack of T-phase signals during this period, the result of a slight mismatch between the two surveys in this area.

7.5.3 2013-2016

The 2013–2016 time-lapse covers a period of activity in July 2015 during which two clear T-phases were recorded (Robertson et al., 2015). Two landslides are observed, the first on the northern side of the crater rim is a further failure of the area from which the dome collapsed during the 1988 episode. This highly channelized collapse led to further deepening of the crater breach by up to 60 m removing 2.29 x 10^6 m^3 of material. Down-dip this material was redeposited, covering an area of 9.6 x 10^3 m^2 with an average thickness of ∼10 m (note that some of this deposit likely extends outside the area of our study). The similarity of the 2013 and 2014 Nautilus surveys implies these changes occurred between October 2014 and February 2016.

The second major collapse on the SE flank of the volcano removed 4.36 x 10^6 m^3 of material. The location of this collapse was surprising as the SE flank had previously been one of the most stable parts of the edifice (Dondin et al., 2017). A small volume from the backwall also contributed to this collapse as well as material from the edifice. This collapse is fairly deep (up to 66 m) and steep sided. The steep sides and a sharp up-dip boundary of the associated deposit (see Figure 7.8, profile b), indicate that failure occurred as a fairly coherent slump.

During the 2015 event, seismic stations recorded two occurrences of sustained seismic tremor each of which lasted longer than an hour and were coincident with T-phase signals. At the time these were interpreted as indicators of sustained periods of eruption (Robertson et al., 2015). Given the lack of volcanic growth we suggest that these are more likely to be the real-time recordings of the landslides themselves. Hydroacoustic recordings of submarine landslides on a

scale of several hours, have been previously reported from marine volcanoes such as Kilauea, Hawaii (Caplan-Auerbach et al., 2001).

In the case of the SE flank collapse in particular it is difficult to see how this could be an eruption triggered event, given its location away from the active vents within the KeJ crater (Carey et al., 2016). This collapse is likely the result of instabilities created by over-steepening of the flank of the volcano during the 1988 eruption and triggered by precursory seismic activity. The failure of the northern rim is more likely to have been triggered by eruption and volcanic loading. The morphology of this landslide is similar to those modeled by (Acocella, 2005) for loading of an unconsolidated cone (a good model for the volcanic sediment which forms much of the outer surface of KeJ).

7.5.4 2016-2017

The April 2017 seismic episode at KeJ lasted for 4 days from the 29 April until the 2 May, and was again associated with several days of heightened seismicity, with the main T-phase signal on the morning of the 29^{th}, lasting ∼15 m and consisting of 3 clear pulses (Latchman et al., 2017). The R.R.S. James Cook survey took place a few days later, on the morning of the 8^{th} May, the shortest interval between a seismic signal and the following survey. As a result this should offer the most precise documentation of the effects of one of these events, since there was insufficient time for overprinting by erosion, sediment deposition or later activity.

In this time-lapse we observe what we interpret as the growth of a small lava dome (∼25 m high), a clear circular growth in the mouth of the breach in the northern rim of the crater. This eruption also led to the filling of much of the collapse scar created by the landslide in the previous time period by approximately 11 m. This growth occurs in an identical location to the dome which formed in 1977 and suggests that there may still be an active volcanic conduit there. This interpretation is further supported by the imaging of active venting in the water column over this site detected during the 2017 R.R.S. James Cook survey (Figure 7.9). At the same time there is a drop in the central crater floor of up to 30 m. We attribute this deflation as being caused by the expulsion of magma from the shallow interior of the cone. An alternative interpretation is that much of the central crater floor has collapsed through the breach in the crater rim, with the constructive signal purely the result of the redistribution of this material.

Without ROV observations however it is difficult to know which of these scenarios is most likely.

There is also an extensive distributed swelling of the north-western flank of KeJ during this time interval. With a mean depth change of 8 m this signal is only slightly above the 5 m cut-off used on the data and cannot be easily attributed to any form of eruption given its separation from the active vents in the crater. We speculate that this signal may be the result of intrusion of magma at shallow depths on the flank of KeJ.

7.6 Discussion

7.6.1 T-Phase Episodes, Morphological Change and Eruption History

During the study period we observe both positive and negative changes in the topography of KeJ. The most significant of these can be associated with reported volcanic T-phase signals. However, the bathymetric differences show that T-phase signals should not necessarily be equated to extrusive eruptions. The lack of evidence for significant addition of material, during the 2015 landslides in particular, means that T-phases produced by other processes should be considered. As well as being a direct recording of the landslides themselves these long duration T-phase signals could result from interactions between water and hot material uncovered by these landslides.

Many of the collapses take advantage of pre-existing weaknesses in the edifice of the volcano, with both the northern crater rim and the SW outer rim failing on more than one occasion during the study period. Landslides may be the result of over-steepening by previous eruptions, weakening by hydrothermal alteration, or structural weakening from previous collapses. Further loading during eruptions or shaking from seismic activity are probable triggers. Despite several previous collapses the SW flank of the cone in particular may still be gravitationally unstable (Dondin et al., 2017). The slump on the SE flank of the cone from the 2013–2016 time period may also still be unstable and liable to future failure.

Recent studies of Monowai (Kermadec arc) have observed a similar pattern of collapse structures

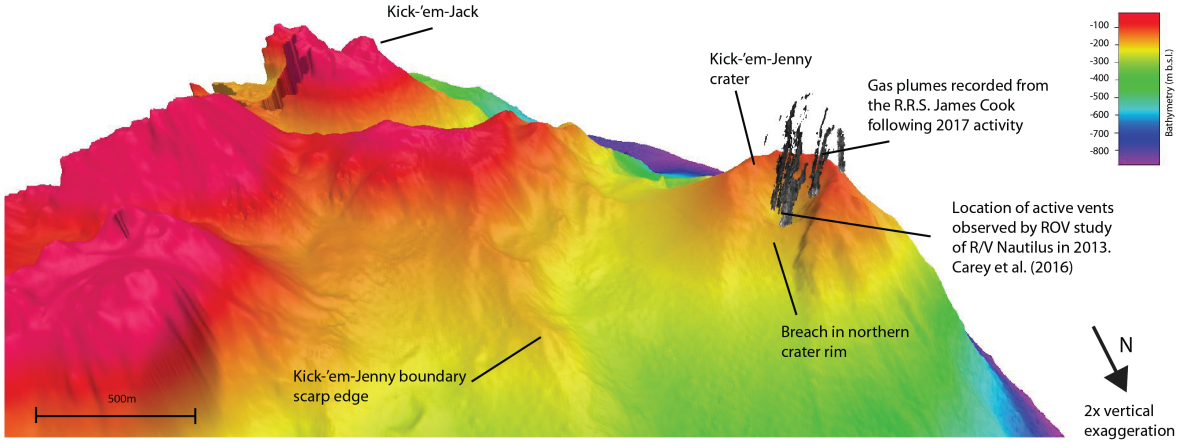


Figure 7.9: 2017 EM710 multibeam bathymetry and water column data. Gas plumes shown were visible as backscatter anomalies in the water column data and were extracted using the software FM Midwater before being rendered in 3-D using IVS Fledermaus. Similar methodology was used by Chadwick et al. (2014) in imaging gas plumes over NW Rota-1. As well as the expected gas plumes from vents in the crater floor, we also observe a plume being emitted from a vent on the outer western crater rim. This Fledermaus scene is available to view via the supporting information.

that could be correlated with volcanic activity (Chadwick et al., 2008b; Wright et al., 2008; Watts et al., 2012). Regular collapses on a similar scale have also been recorded at NW Rota-1 in the Mariana arc (Embley et al., 2006; Chadwick et al., 2008a; Schnur et al., 2017). These small scale landslides (constituting fractions of a percent of the edifice's total volume and commonly 10 s of meters deep) are increasingly being shown to play a key role in the long term evolution of submarine volcanoes, and the similarity in size and morphology of collapses from these three volcanoes, despite their locations in three markedly different island arcs is undeniable.

The volumes of documented collapses at KeJ are significantly smaller than would be considered a tsunami hazard. Taking Harbitz et al.'s (2012) work as a benchmark, (though it should be noted that these models consider an absolute worst case scenario) a collapse volume of 6 x 10^8 m^3 could cause >6 m waves on nearby Grenada and up to 1 m as far away as Puerto Rico. Our biggest recorded collapse is only 2.18 x 10^7 m^3, almost 30 times smaller than this amount. Nor do we see evidence for any large scale motion along the KeJ scarp which could be a precursor to a large sector collapse on the scale of the 43 ka event. The total edifice today (measured down to the 600 m contour) has a volume of 5.85 x 10^8 m^3 (0.585 km^3). In order to create a dangerous tsunami a large proportion of the cone would have to fail. Such a total failure seems highly unlikely without a significant episode of cone building and steepening of KeJ, or an explosive eruption on a scale which is historically unprecedented. Similar to the conclusions

of Lindsay et al. (2005), we conclude that the tsunami risk associated with current KeJ activity is quite low, given the current edifice configuration.

A strong disparity exists between the volumes of material being lost from the volcano in landslides and added to it as fresh deposits. Over the 1985–2017 time period, the calculated volume changes show 3.8 x 10^7 m^3 was lost through collapses yet only around a fifth of this amount (7.09 x 10^6 m^3) was added as fresh volcanic deposits. Note that constructive anomalies which are clearly loose deposits resulting from collapses further up-structure (e.g. the two deposits in the 2013–2016 time period) are not included in these totals (see Table 7.2). Over the period of study, this gives a mean rate of magma output of 2.2 x 10^5 m^3yr^{-1}. This is significantly less than the rate estimates of Devine and Sigurdsson (1995) of $\sim 10^7$ m^3yr^{-1} based on changes in the height of the volcanic cone between 1962 and 1978. These values were known to likely be an overestimate due to being based on the erroneous 1962 H.M.S. Vidal bathymetric measurements (Lindsay et al., 2005).

The slow rate of magma production at KeJ results in a very different eruption style to that of Monowai, which during the period 2004–2007 quickly grew from 128 m bsl to just 49 m bsl (Watts et al., 2012) or NW Rota-1 which emitted 3.4 x 10^7 m^3 of volcaniclastic deposits in just 3 years between 2003 and 2009 (Chadwick et al., 2012). This is a similar volume to the total volume lost through mass wasting in 30 years at KeJ. In these other locations the volumetrics of collapses and eruptions are similar on a timescale of just a few years (Chadwick et al., 2008b; Wright et al., 2008; Watts et al., 2012; Schnur et al., 2017). Given that KeJ and Monowai are of comparable size (KeJ stands 1,300 m above the surrounding seafloor, Monowai 1,000 m) and summit depth (peak of KeJ $\sim$190 m bsl., Monowai 50–150 m bsl) this suggests fundamental differences between the eruption cycles at the two volcanoes. At KeJ this volume deficit is clearly not sustainable and we interpret that it must be capable of larger eruptions (or periods of much more intense activity) than those captured by this study. In order to fully balance out the material lost in the last 32 years would require the equivalent of an eruption depositing a 10 m thick layer of material over the entire edifice all the way down to the 600 m contour.

We conclude that constructive eruptions at KeJ are less frequent than previously thought. Cone construction occurs by infrequent eruptions and shallow emplacement events, rather than being a process which stays largely in step with collapse as observed elsewhere. Growth phases are interspersed with sustained periods of erosion and collapse driven by seismic activity and

predominantly explosive eruptions which contribute little to the growth of the cone. The 1939 eruption is a likely candidate for one of these infrequent constructive episodes. The large ash cloud produced by this eruption that breached the ocean surface is certainly indicative of a much larger eruption than anything observed in recent decades (Devas, 1974). Despite the seeming regularity of eruptions, the majority of the historical events have contributed little in terms of constructive growth.

7.6.2 Implications for Hazard and Monitoring

The cyclical behavior of eruptive episodes, interspersed with extended relatively quiescent periods lasting several decades and dominated by landslides and erosion is a behavior similar to that recorded for many of the Antilles arc's subaerial volcanoes. La Soufrière (Guadeloupe) has experienced 6 major phreatic episodes since 1690 (the most recent in 1976–1977), a repeat time of approximately 63 years (Feuillard et al., 1983; Villemant et al., 2005; Jackson, 2013). Soufrière, St. Vincent has also had a comparable eruption history (five major eruptions since 1718), with both episodes of dome building and phreatic explosions during that time (Heath et al., 1998a,b). The eruption cycle at KeJ may be similar.

A sustained eruption would look very different seismologically to recent recordings. In particular we would expect a much higher number of T-phase events associated with any such prolonged eruption e.g. the May 2011 eruption of Monowai, which produced a total erupted volume of 8.75 x 10^6 m^3 (which would only satisfy about 1/4 of our observed construction deficit) was associated with 5 days of T-phase activity, with as many as 150 detected signals per day (Watts et al., 2012). In comparison, the 2015 episode at KeJ consisted of just two clear T-phase arrivals (Robertson et al., 2015). Activity associated with a larger event is likely to present a much more significant risk to shipping in the vicinity of the volcano. Large volume gas releases and more violent ejecta are likely, and a larger event could trigger higher volume landslides. We would hope that an eruption akin to the 1939 event would be almost immediately recognizable seismically as something of more major concern.

This study confirms the value of time-lapse bathymetry as a tool for monitoring submarine volcanoes. It should be noted this value is dramatically increased with the frequency of surveys. Where possible, if such a volcano is deemed a hazard, it is key that it is surveyed as soon as

possible after any suspected activity. Coupled ROV surveys would also add a lot of additional information to what can be gleaned from bathymetry alone. Although this may be difficult given resources required it is the only way to accurately ground-truth the results of submarine volcanic activity. Even if a survey cannot be done immediately there is significant value to be gained by surveying the edifice before another volcanic episode can take place. As we saw with the 1985–2003 time-lapse, which contained 3 periods of T-phase activity, it can make interpretation of changes, and assigning these changes accurately to recorded events substantially more difficult.

Shallow water and proximity to shore may provide a number of possibilities for future monitoring of KeJ which would not be possible in less accessible locations. Autonomous underwater vehicles (AUVs) are increasingly being used to collect bathymetric data in a range of shallow water settings (Grasmueck et al., 2006; Dupre et al., 2008; Clague et al., 2011). Such a system could easily be launched from the shore near KeJ and would provide a relatively cheap means by which to conduct repeat bathymetric surveys compared to dedicated cruises. This would also have the advantage of being able to exactly repeat pre-programmed survey geometries. Alternatively KeJ would be a prime candidate for an underwater monitoring system, such as the Ocean Observatory Initiative's cabled array at Axial Seamount (Kelley et al., 2014) or the older HUGO system installed on Lo'ihi, Hawai'i in 1998 (Caplan-Auerbach and Duennebier, 2001).

7.7 Conclusions

Through the analysis of six multibeam bathymetric surveys spanning the time period 1985 – 2017, we have identified a number of major morphological changes at the KeJ volcano in the southern Lesser Antilles with important implications for associated hazard. In doing so we have again demonstrated the value of time-lapse bathymetry for the monitoring of submarine volcanism.

1. Morphological changes including dome construction, landslides and slumping can be correlated with T-phase signals at KeJ. This behavior of morphological changes through regular, discrete, low-volume landslides is demonstrably similar to observations at other

submarine arc volcanoes such as Monowai and NW Rota-1.

2. T-phase signals are likely to have a range of sources including landslides rather than being solely the result of extrusive volcanism.

3. During the period of study approximately 5 times more material was shed from the cone then was added to it by constructional volcanism.

4. The repeat time of major eruptions at KeJ is likely to be on a longer timescale than previously thought. This is more similar to the behavior of many of the sub-aerial volcanoes in the arc (e.g. La Soufrière, St. Vincent which erupts on an $\sim$50 year cycle) because the regular decadal activity at KeJ has contributed little to the construction of the cone

5. In agreement with previous studies we conclude that tsunami risk associated with KeJ is minimal. The risk posed to shipping by ejected material and large gas releases during periods of eruption (particularly something on the scale of the 1939 event) should be the key hazard management concern

Chapter 8

Discussion and Future Work

8.1 Introduction

Throughout this thesis I have investigated the key factors which may be driving north-south variations in a range of arc processes along the Lesser Antilles. New marine geophysical datasets across the Lesser Antilles backarc and incoming plate provide new constraints over a number of important inputs into this arc system. These essentially fall into one of two categories, the inherited structure of the over-riding plate (Chapters 3 and 4) and variations in the hydration and structure of the subducting slab (Chapters 5 and 6). Only when all such contributions are taken into account can we begin to explain the observed behaviours of the modern day arc. Here some of the most important along arc trends discussed at the beginning of the thesis (Chapter 2), are revisited, and reinterpreted in light of these results.

8.2 Water Release Beneath the Arc

The modern Lesser Antilles arc shows major along strike variations in the distribution of seismicity, magmatic productivity, geochemical trends and the thickness of arc crust (Section 2.2). In slow-spreading Atlantic crust, transform faults are expected to be more seismically active, and permit the infiltration of water to greater depth than in fast spreading oceanic lithosphere (Section 2.3). Further hydration of the subducting lithosphere may be concentrated at the end

of magma-poor ridge segments where detachment faulting places mantle peridotites at shallow crustal depths, making them vulnerable to hydrous alteration (Section 2.3). The release of water from the breakdown of serpentine, an alteration product of olivine, along these structures has been proposed as a controlling influence over the distribution of potentially hazardous arc processes (Section 2.2).

The best estimate of water release from fracture zones beneath the arc comes from the study of Cooper et al. (2020). Their methodology and my own contribution to modelling of the fracture zones in that study, are explained in Appendix A. Of the 5 major Atlantic fracture zones subducting beneath the arc (Figure A.1), only the Marathon and Mercurius have subducted to sub-arc depths, and are likely to have made any substantial contribution to water release beneath the arc (Figure 8.1C). These two fracture zones have swept southward beneath the arc over the last 25 Ma (i.e. since the first recorded instances of modern arc volcanism; Smith et al. 2013). In the Quaternary, water released from these fracture zones has been strongly concentrated beneath the islands of Guadeloupe and Dominica. South of Dominica, the slab consists of crust formed through spreading in the proto-Caribbean (Chapter 3 / Appendix A). The distribution of fracture zones within this section of the slab is comparatively unconstrained.

However, variations in arc processes are observed on a range of different length scales, from elevated levels of magmatic productivity concentrated beneath the central portion of the arc, to more binary north/south divisions in crustal structure and rates of seismicity (Section 2.2). The influence of fracture zone subduction alone is therefore insufficient to explain many of these along strike trends in arc behaviour (Figure 8.1 - 8.3).

8.3 Controls over Arc Structure

The arc crust of the Lesser Antilles varies over a range of length-scales (see Chapter 2, Section 2.2.1). Whilst substantial variations in crustal thickness are observed between adjacent islands (Schlaphorst et al., 2018; Melekhova et al., 2019), and variations on the order of several kilometres are even recorded within individual islands (Sevilla et al., 2010), the predominant trend is a north-south division, with ∼35 km thick crust beneath the arc north of Dominica, and comparatively thin crust of <30 km thickness in the south (Figure 8.1A).

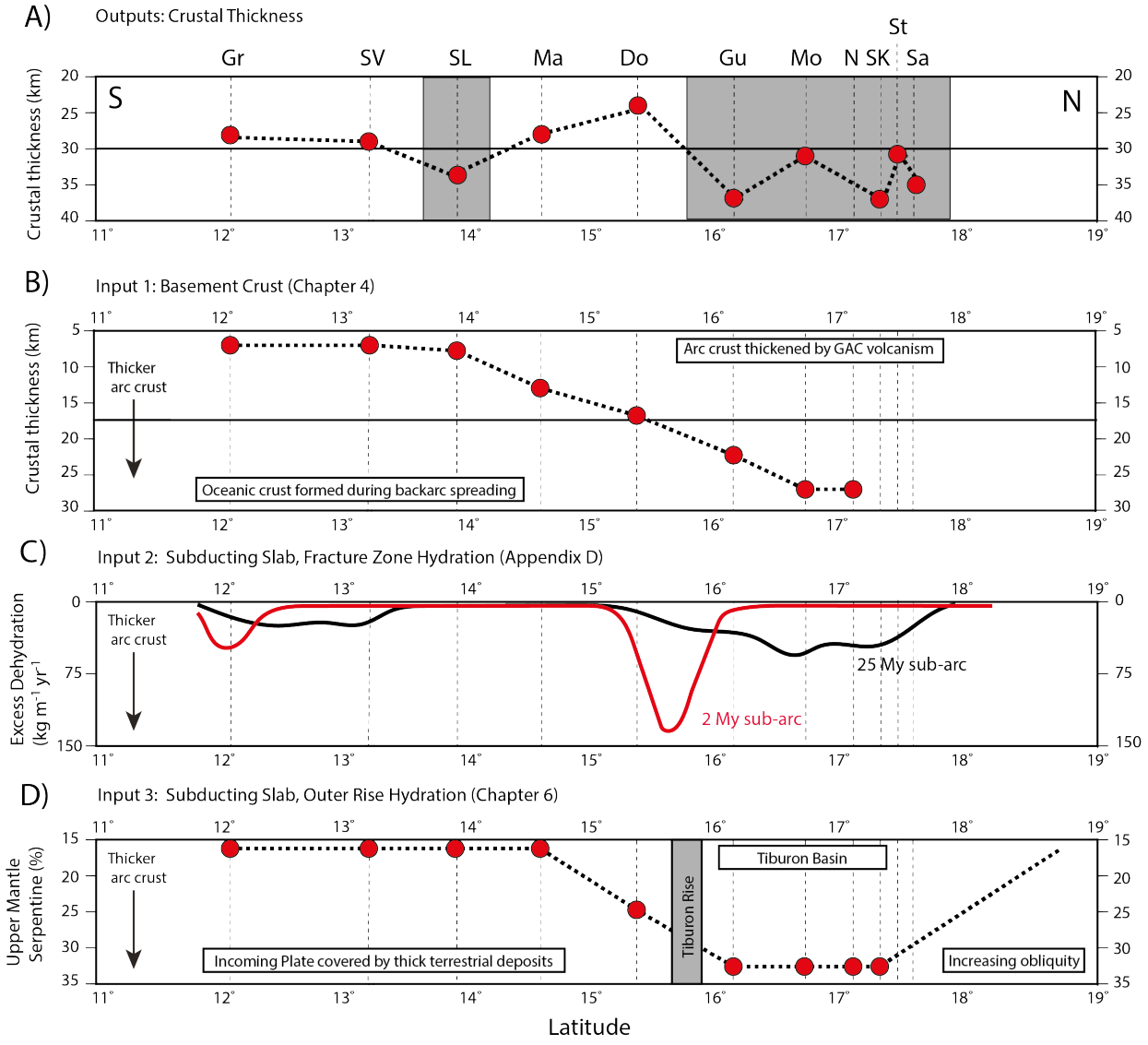


Figure 8.1: Contributions to along arc trends in crustal structure. A) Along arc Moho depths derived by receiver function analysis from Schlaphorst et al. (2018). Regions where arc crust exceeds 30 km shaded grey. B) Thickness of backarc crust from wide-angle profiles presented in Chapter 4. It is proposed that this crust forms the basement of the modern arc, and is a major contributor to the north-south divide in crustal thickness. C) Calculated excess water release at sub-arc depths from subducting fracture zones from Cooper et al. (2020). Red, excess water release over last 2 My, black, excess water release over last 25 My. D) Upper mantle serpentinization as a result of outer rise faulting. The minimum 32% serpentinization calculated from the wide-angle velocities in Chapter 6 is assumed to be consistent throughout the Tiburon Basin, this may however be as high as 55%. The degree of outer rise hydration is assumed to rapidly fall away with increasing sediment thickness on the incoming plate to the south, and obliquity of subduction to the north. A background serpentinization value of 16% corresponds to an upper mantle velocity of 7.5 km s^{-1}, as observed by Davy et al. (2020) in the equatorial Atlantic. Degree of serpentinization calculated using the relationships of Grevemeyer et al. (2018).

Initially, the modelled release of water from fracture zones would seem to correlate well with this pattern, with the thickest crust beneath the northern arc correlating with the location of the majority of water release from fracture zones over the last 25 Ma, promoting increased rates of volcanism and the thickening of the crust (Figure 8.1). However, overall rates of magma production at the Lesser Antilles are known to be particularly low, as a result of the slow convergence rates across the arc (Wadge and Shepherd, 1984). >35 km crust is very thick for an island arc, even compared to much more active systems in the Pacific (e.g. Kodaira et al. 2007). Similar crustal thicknesses are observed beneath areas of Puerto Rico in the Greater Antilles, but here there is an established history of >70 My of arc volcanism associated with the Great Arc of the Caribbean (Chapter 3). Furthermore, beneath most of the northernmost islands of the active arc (e.g. St. Kitts and Nevis, Montserrat), there is little record of arc volcanism prior to ∼5 Ma (Appendix B, Section B.3). Even with the focused release of water from the Marathon and Mercurius fracture zones (which would have largely passed to the south of these islands by 5 Ma) it is exceedingly difficult to see how such a thick crust could be constructed in such a short period of time through arc volcanism alone.

In Chapter 6 wide-angle data across the outer rise on the incoming plate detected as much as 55% serpentinization of the upper mantle as the slab enters the trench. This second stage of lithospheric hydration is likely to be concentrated in the Tiburon Basin, currently subducting beneath the northern arc. Water released as a result of deserpentinization and the breakdown of hydrous minerals within the crust within this region of the slab will make an additional contribution to rates of volcanism, and by extension the thickness of arc crust north of Guadeloupe, in addition to that provided by the fracture zones. The degree of alteration along the slab is proposed to fall away northward with increasing subduction obliquity, and to the south with deposition of thick terrestrial sediments on the incoming plate (Figure 8.1D).

In Chapter 4 (see also Allen et al. 2019) new seismic profiles across the Grenada basin observed major north-south variations in the crustal structure in the Lesser Antilles backarc. The observation of an oceanic crustal structure in wide-angle data, combined with magnetic anomalies support a period of backarc spreading in the Grenada Basin south of Martinique. This spreading most likely occurred during an eastward arc migration from the Aves Ridge to the Outer Arc position identified in magnetic data (Figure 4.2) in the Eocene. In contrast, the northern Grenada Basin was seen to be underlain by crust as thick as 25 km. Following a

second westward phase of arc migration during the Oligocene (Figure 4.4), this backarc basin became the basement crust upon which the modern islands were built, obscuring the backarc spreading centre in the south, separating the Tobago and Grenada Basins, and leading to a fundamental north-south divide in crustal thickness along the arc.

Whilst previous studies have suggested that this thick crust under the northern arc and forearc might be the result of the Lesser Antilles being built upon an oceanic plateau (Kopp et al., 2011; Evain et al., 2013) similar to the Caribbean Large Igneous Province (CLIP), there remains little geochemical evidence for plume type volcanism amongst either the islands of the Lesser Antilles or Aves Ridge (Neill et al., 2011). Instead, the thickened crust of the northern Grenada Basin and Antilles arc is likely to have been inherited from older, extended periods of arc volcanism associated with the Great Arc of the Caribbean (GAC) and Aves Ridge which started as far back as the early Cretaceous (see Chapter 3). During the eastward migration of the great arc of the Caribbean, it is also known to have accreted several terranes from older arc systems (e.g. basaltic crust exposed on the island of La Désirade most likely formed in the backarc of the Mesozoic age Intra-American arc system; Figure 3.3). Such additions may further contribute to both the total thickness of this basement and the shorter wavelength crustal thickness variations observed along the arc. Recent volcanism onto an already thick arc basement may also explain the presence of a seismic mid-crustal discontinuity, observed by several studies of the arc (Section 2.2.2).

The thick crust of the northern arc is therefore likely to be the product of an inherited thick pre-existing basement, the result of regional arc volcanism throughout the late-Cretaceous and Cenozoic. Over the last 25 My this crust has been thickened further by the focused release of water (driving higher rates of arc volcanism), from the serpentinized mantle along the Marathon and Mercurius fracture zones, and high levels of outer rise hydration within the Tiburon Basin. The thinner crust of the southern arc is the result of volcanism through the recently formed oceanic crust of the southern backarc.

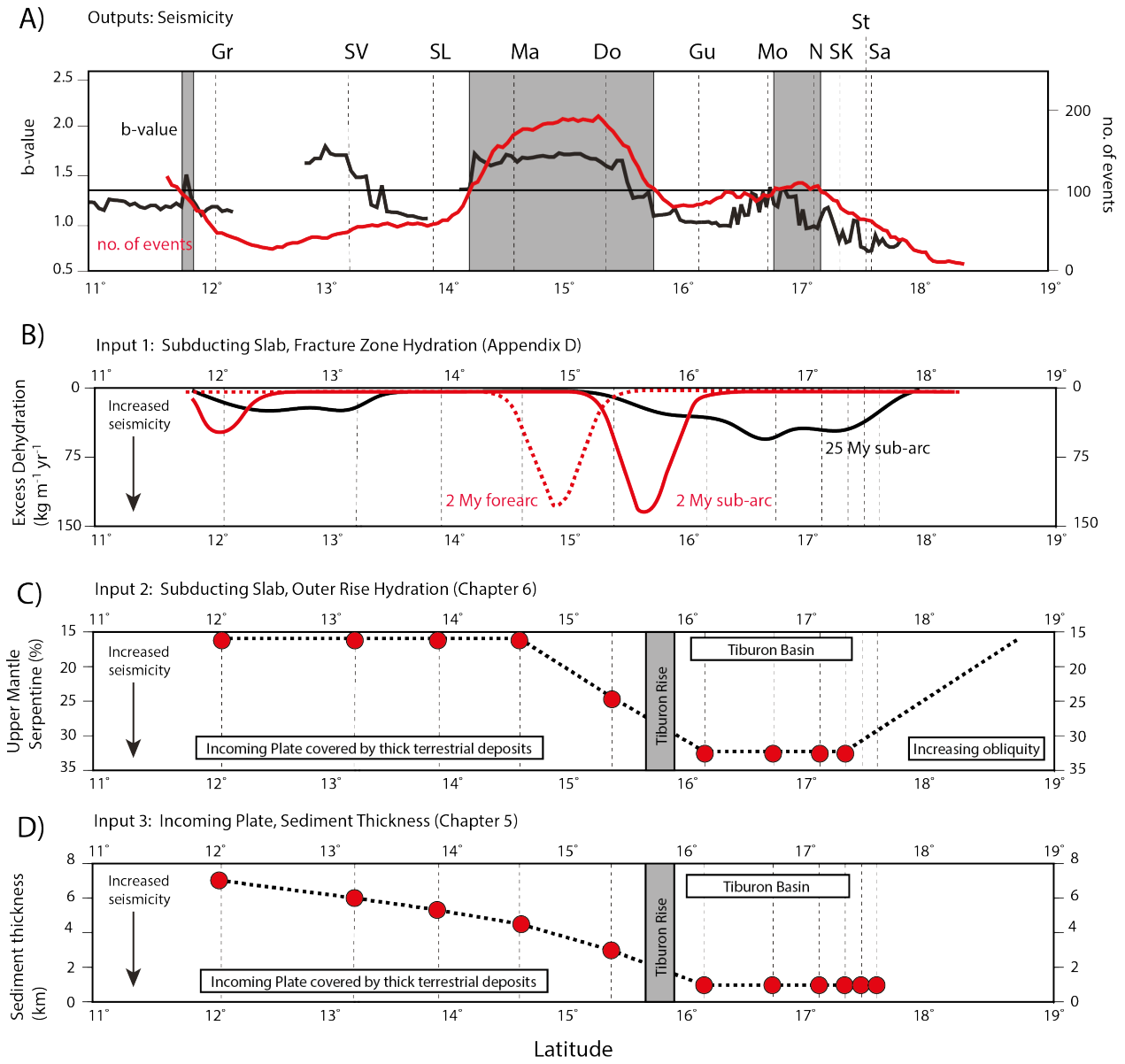


Figure 8.2: Contributions to along seismic trends. A) Along arc variations in b-value and cumulative seismicity from Schlaphorst et al. (2016) for the time period 2008-2013. Number of events incorporates all events occurring perpendicular to the arc, within a shifting window of 150 km length. Regions where no. of events exceeds 100 are highlighted in grey. B) Calculated excess water release at sub-arc depths from subducting fracture zones from Cooper et al. (2020). Red, excess water release over last 2 My, black, excess water release over last 25 My. Dashed red line denotes excess water release beneath the forearc from the same study. C) Upper mantle serpentinization as a result of outer rise faulting. The minimum 32% serpentinization calculated from the wide-angle velocities in Chapter 6 is assumed to be consistent throughout the Tiburon Basin, this may however be as high as 55%. The degree of serpentinization is assumed to rapidly fall away with increasing sediment thickness on the incoming plate to the south, and obliquity of subduction to the north. A background serpentinization value of 16% corresponds to an upper mantle velocity of 7.5 km s^{-1}, as observed by Davy et al. (2020) in the equatorial Atlantic. Degree of serpentinization calculated using the relationships of Grevemeyer et al. (2018). D) Sediment thickness on the incoming plate. Within the Tiburon Basin, sediment thickness is based on the observations from seismic data presented in Chapter 5. South of the Tiburon Rise a linear southward increase is assumed due to increasingly thick terrestrial deposits from South America, reaching a maximum thickness of 7 km in keeping with observations of sediment thickness by Biju-Duval et al. (1982); Moore et al. (1988).

8.4 Controls over Seismicity

There are a number of overlapping trends in seismicity observed along the arc (Section 2.2.2). Total rates of seismicity are low along the arc compared to other similar subduction systems, with a disproportionate amount of the seismicity observed occurring as intra-slab earthquakes, rather than along the subduction interface itself (Bengoubou-Valerius et al., 2008; Bie et al., 2020). A general increase in the total rate of seismicity is recorded in the north of the arc compared to the south, with a particular concentration of seismicity beneath the islands of Guadeloupe and Dominica (Figure 8.2A). Rates of seismicity on the shallowest part of the subduction interface are also higher in the north and occur up to 20 km shallower than in the south of the arc (Bie et al., 2020).

Concentrations of seismicity along the slab correlate well with the subduction of the Marathon and Mercurius fracture zones beneath the centre of the arc (Schlaphorst et al., 2016; Paulatto et al., 2017). The modelling of Cooper et al. (2020) supports this conclusion, with the biggest concentration of recent water release from the subducting fracture zones occurring in this same central part of the arc. This leads to heightened b-value and rates of seismicity (Schlaphorst et al., 2016). Water released through deserpentinization lubricates the plate interface, leading to seismic failure at lower stress thresholds. Dehydration embrittlement as a result of deserpentinization may also contribute to heightened rates of intra-slab seismicity (Peacock, 2001). Paulatto et al. (2017) observed distinct clusters of earthquakes which correlated with both the projected locations of fracture zones along the slab, and the dehydration of mineral phases in the crust (at depths of 60-120 km), and mantle (at depths of 120-150 km).

In their modelling Cooper et al. (2020) assume 50% serpentinization of the upper mantle in the region around the subducting fracture zones (Appendix A). In Chapter 6 levels of serpentinization in the uppermost mantle as a result of outer rise processes were proposed as high as 55% in the Tiburon Basin. Although not as focused as the hydration at fracture zones, and extending over a smaller depth into the upper mantle, this still indicates a substantial volume of serpentine and other hydrous minerals within the subducting lithosphere away from the main fractures. Water release from this portion of the slab must also contribute to increased rates of seismicity along the central arc. Steeply dipping intra-slab earthquakes likely represent failure on the original abyssal hill fault fabric, reactivated and highly serpentinized across the outer

rise (Bie et al., 2020). The fault plane solution for many of these normal faulting events strikes approximately parallel to the trench.

As discussed in Chapter 5, reduced seismic velocities throughout the sediments of the accretionary prism indicates elevated pore pressures in subducting sediments, and by extension a relatively weak subduction interface. This is also supported by very low coupling interpreted from GPS studies along the arc (Feuillet et al., 2011). The increase in seismicity along the shallowest parts of the subduction interface in the north of the arc (see Figure 5.1) is most likely representative of the reduced thickness of sediments on the incoming plate north of the Tiburon Rise, leading to a highly variable subduction channel. Topography on the incoming plate forms short-lived frictional asperities, briefly increasing local coupling with the over-riding plate. This is most obvious across the Barracuda Ridge and Tiburon Rise, but appears to happen throughout the northern arc as a result of the basement topography, on the order of 1 km formed through faulting during magma-poor slow spreading. In the south of the arc, the very thick terrestrial sediments on the incoming plate create a much more homogeneous subduction channel. Although rates of seismicity are historically low, the smooth interface along this part of the arc may still be capable of producing large seismic events.

8.5 Controls over Arc Geochemistry

Cooper et al. (2020) also conducted research into Boron isotopes in melt inclusions from along the Lesser Antilles. As a highly fluid mobile element, Boron is a good indicator of the origin of water in lavas. Serpentine preferentially contains the isotope ^{11}B. Arc lavas generated as a result of mantle melting driven by deserpentinization in the slab therefore possess very high δ^{11}B values. Values of δ^{11}B along the arc encompassed much of the known global range for island arcs, but were highest on the islands of Guadeloupe and Dominica, where more than 60% of water in arc lavas is likely derived from a serpentine source (Figure 8.3A). The percentage of serpentine derived fluid then drops away to the north and south of the arc. This again correlates well with the calculated excess water released at fracture zones (a high on St. Vincent may be the result of an unconstrained fracture zone within the proto-Caribbean portion of the slab). The results presented in Chapter 6 would also suggest that the high degree of alteration observed beneath the outer rise in the Tiburon Basin is a likely contributor to this δ^{11}B anomaly

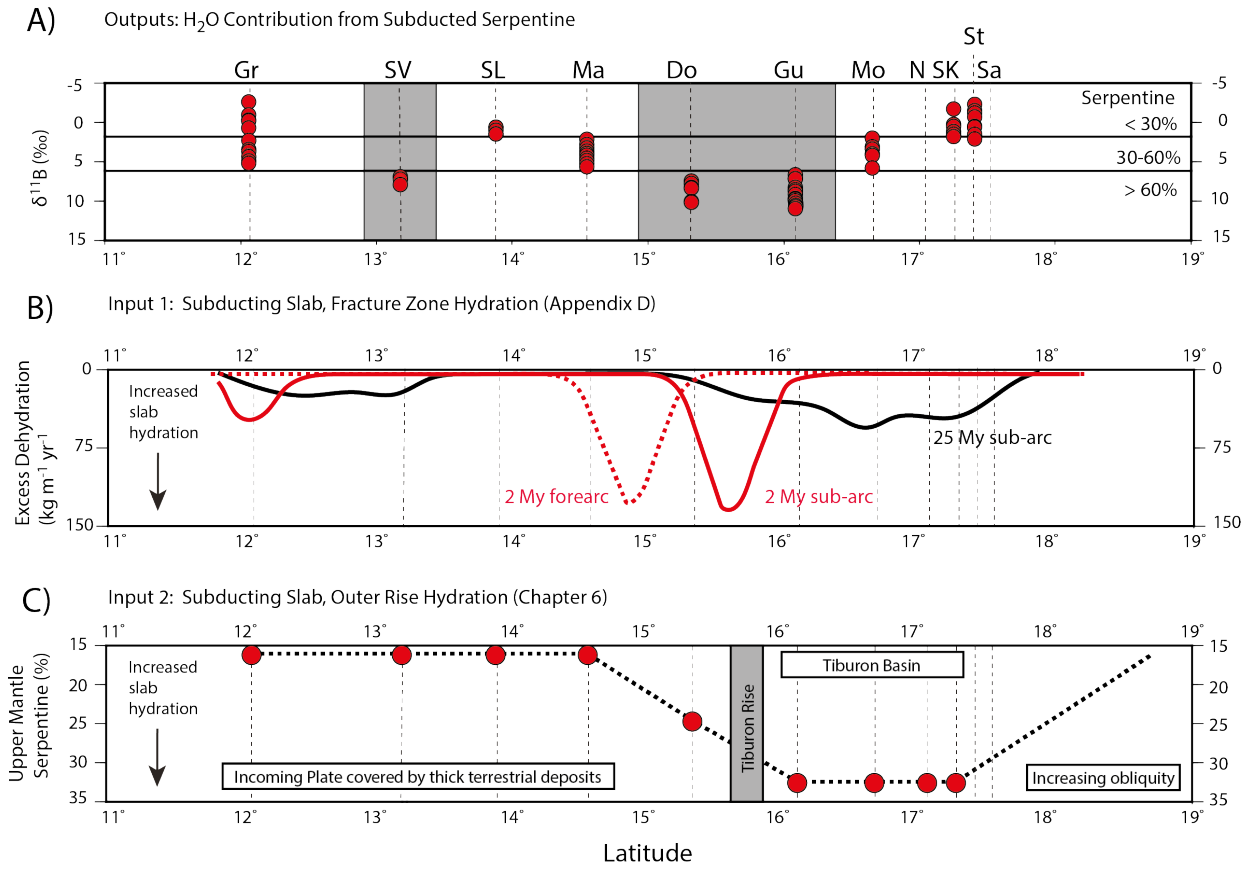


Figure 8.3: Contributions to along geochemical trends. A) Along arc variations in δ^{11}B from Cooper et al. (2020). In regions highlighted in grey Boron isotopes support more than 60% water contribution from subducted serpentine. B) Calculated excess water release at sub-arc depths from subducting fracture zones from Cooper et al. (2020). Red, excess water release over last 2 My, black, excess water release over last 25 My. Dashed red line denotes excess water release beneath the forearc from the same study. C) Upper mantle serpentinization as a result of outer rise faulting. The minimum 32% serpentinization calculated from the wide-angle velocities in Chapter 6 is assumed to be consistent throughout the Tiburon Basin , this may however be as high as 55%. The degree of serpentinization is assumed to rapidly fall away with increasing sediment thickness on the incoming plate to the south, and obliquity of subduction to the north. A background serpentinization value of 16% corresponds to an upper mantle velocity of 7.5 km s^{-1}, as observed by Davy et al. (2020) in the equatorial Atlantic. Degree of serpentinization calculated using the relationships of Grevemeyer et al. (2018).

beneath the northern arc.

As discussed in Chapter 2 (Section 2.2.3), an increase in $^{87}Sr/^{86}Sr$ and decrease in $^{143}Nd/^{144}Nd$ in volcanic samples from the southern arc is interpreted as representative of a high degree of contamination in arc lavas from material with a continental origin. It has been highly debated whether this continental component derives from the thick terrestrial sediments deposited along the incoming plate in the south of the arc (Section 2.2.3) or whether they result from

incorporation of a continental component within the crust of the over-riding plate.

There is no evidence within the history of the Lesser Antilles for incorporation of any significant fragment of continental crust within the arc (Chapters 3 and 4). However, as described in the tectonic model proposed for the western Caribbean region in Chapter 4, backarc spreading in the southern Grenada Basin created a deep sedimentary basin during the early Paleogene. This basin may already have contained as much as 10 km of sediment prior to the initiation of modern Lesser Antilles arc volcanism in the Oligocene (Aitken et al., 2011), due to very high rates of deposition from the South American margin into this newly formed basin. Following the westward migration of the island arc from the Outer Arc position, to the site of modern volcanism (Figure 4.4), a large amount of this sediment would have been incorporated into the crust of the modern arc. Although sediments on the incoming plate cannot be ruled out as the source of this contaminant, this does provide a very clear mechanism for the incorporation of a large quantity of continental derived material into the southern arc, supporting models previously proposed by Bezard et al. (2014) and others.

8.6 Potential Future Work

While the research presented here has allowed us to make clear progress in understanding the most important influences over a number of arc processes at the Lesser Antilles, there are a number of ways in which this research could potentially be advanced in the future.

8.6.1 The Grenada Basin

The OBS deployment and wide-angle survey in the Lesser Antilles backarc were sufficient to identify clear variations in crustal structure between the northern and southern parts of the arc (Chapter 4). However, a lot of the information stored on many of the OBS instruments and landstations deployed as part of project VoiLA remains under-utilized. Despite clearly recording the wide-angle surveys, many of these stations lay too far from the final velocity profiles, or in areas with too much topography to be properly integrated (Figure 4.3). While the 2D profiles generated were able to clearly identify the north-south transition in crustal structure, they were unable to corroborate the 3D distribution of the different crustal types

interpreted from marine magnetic data (Figure 4.2). The unused data might be better utilized in a 3D inversion for the velocity structure of the crust in the arc and backarc. Paulatto et al. (2017) had success using similar methodology across a relatively small segment in the centre of the arc, in combination with travel times from local seismicity. Applying a similar methodology incorporating the VoiLA dataset may allow for a much more detailed 3D structure of the shallow lithosphere, both through the backarc, and across the arc itself.

8.6.2 Outer Rise Hydration

In Chapter 6, we demonstrated that the shallow lithosphere of the incoming plate is highly affected by hydration and the formation of serpentine with bend faulting across the outer rise. Due to the possible variations in crustal thickness and lithology in slow spreading lithosphere it is difficult to tell whether the inverted velocity layer observed along the western portion of the wide-angle profile in Chapter 6 is taking place in the lower crust, or the upper mantle. In the upper mantle, where you can assume a homogeneous peridotite composition, it is relatively straight forward to estimate the amount of water that is actually bound up as serpentine (in the case of our profile 1, approximately 3.25 wt% in the upper 5 km of the mantle). In the lower crust however, where the lithology may be a mix of rock types, it is not possible to differentiate between changes in lithology and hydration from a p-wave model alone. The horizontal components of the OBS used on VoiLA Profile 1 record clear shear arrivals. The generation of a corresponding Vs model which is far more sensitive to changes in hydration than lithology (and which by extension would allow for the calculation of Vp/Vs ratios etc.) would go a long way towards separating these two factors. This would then allow for far more accurate estimates of the volume of water stored along the slab.

As a result of the shadow zone observed on OBS stations, the velocities along the upper part of the low velocity layer in the final Vp model described in Chapter 6 are poorly constrained. Whilst we attempted to counter this by trialling a range of starting models, modelling possible low velocity layer geometries in RAYINVR (Zelt and Smith, 1992), and using Monte-Carlo analysis there is more that could be done to better constrain the velocities in this layer (and by extension, the associated levels of serpentinization). Finite difference methods may be used to produce more reliable synthetic record sections for the OBS along the profile. Across many of the OBS instruments, we identified reflections, PmP1, from the surface of the low velocity layer.

The geometry and velocity structure of the low velocity layer in the model is highly dependent on the interpretation of this phase. This reflection from the top of the low velocity layer should result in a very strong converted phase, identifiable on the horizontal components of the OBS. Picking and modelling of these converted arrivals may provide significantly more detail about the nature of this interface, increasing confidence in the proposed velocity structure and better constraining the degree of serpentinization in the upper mantle.

Chapter 9

Summary of Thesis Achievements

The VoiLA project was started with the aim of assessing the role played by subducting volatiles in arc processes along the Lesser Antilles (Goes et al., 2019). The core hypothesis behind the project was that in slow spreading oceanic lithosphere such as the Atlantic, there would be a high concentration of water bound at the end of seafloor spreading segments, as a result of focused lithosphere scale faulting at transform faults and core complexes. Upon subduction these hydration anomalies would drive variations in arc processes such as seismicity and volcanic productivity along the arc. Throughout this thesis I have used new marine geophysical datasets acquired as part of project VoiLA to review tectonic processes in both the over-riding plate (Chapters 3 and 4), and subducting slab (Chapters 5 and 6). Chapter 7 focused on the shorter term processes affecting hazard associated with the submarine volcano Kick-'em-Jenny.

These datasets provide significant new detail to the role played by both the over-riding plate and subducting slab in shaping the modern arc. While concentrated hydration at fracture zones on the incoming plate does appear to play a major role in the distribution of seismicity and magmatic productivity, this process alone is a long way from being able to explain the full suite of arc behaviours. The work presented here provides new constraints on multiple periods of arc migration and backarc spreading on the over-riding plate in the Cenozoic and the distribution of hydration in the subducting lithosphere, making fresh contributions to our understanding of the distribution of volcanism, seismicity, and crustal structure along the arc. Many of these trends can only be properly explained when the influence of several of these inputs to the subduction system are considered in unison.

Bibliography

Acocella, V. (2005). Modes of sector collapse of volcanic cones: Insights from analogue experiments. *Journal of Geophysical Research-Solid Earth*, 110(B2):1–19.

Aitken, T., Mann, P., Escalona, A., and Christeson, G. L. (2011). Evolution of the grenada and tobago basins and implications for arc migration. *Marine and Petroleum Geology*, 28(1):235–258.

Aki, K. and Ferrazzini, V. (2000). Seismic monitoring and modeling of an active volcano for prediction. *Journal of Geophysical Research-Solid Earth*, 105(B7):16617–16640.

Allen, R., Collier, J., Stewart, A., Henstock, T., Goes, S., Rietbrock, A., and the VoiLA Team (2019). The role of arc migration in the development of the lesser antilles: A new tectonic model for the cenozoic evolution of the eastern caribbean. *Geology*, 47(9):891–895.

Allen, R. W., Berry, C., Henstock, T. J., Collier, J. S., Dondin, F. J. Y., Rietbrock, A., Latchman, J. L., and Robertson, R. E. A. (2018). 30 years in the life of an active submarine volcano: A time-lapse bathymetry study of the kick-'em-jenny volcano, lesser antilles. *Geochemistry Geophysics Geosystems*, 19(3):715–731.

Anderson, R. N. (1972). Petrologic significance of low heat flow on the flanks of slow-spreading midocean ridges. *GSA Bulletin*, 83(10):2947–2956.

Andreieff, P., Baubron, J. C., and Westercamp, D. (1988a). Histoire géologique de la martinique (petites antilles): biostratigraphie (foraminifères), radiochronologie (potassium–argon), évolution volcano-structurale. In *Géologie de la France*, volume 2, pages 39–70. Bureau de recherches géologiques et minières, Orleans, B.R.G.M., serv. géol. national, Orléans 45060, France.

Andreieff, P., Westercamp, D., Garrabé, F., Bonneton, J., and Dagain, J. (1988b). Stratigraphie de st martin, petites antilles septentrionales. In *Géologie de la France*, volume 2, pages 71–88. Bureau de recherches géologiques et minières, Orleans, B.R.G.M., serv. géol. national, Orléans 45060, France.

Baker, P. E. (1984). Geochemical evolution of st kitts and montserrat, lesser antilles. *Journal of the Geological Society*, 141:401–411.

Baldi, P., Bonvalot, S., Briole, P., and Marsella, M. (2000). Digital photogrammetry and kinematic gps applied to the monitoring of vulcano island, aeolian arc, italy. *Geophysical Journal International*, 142(3):801–811.

Bangs, N. L., Shipley, T. H., and Moore, G. F. (1996). Elevated fluid pressure and fault zone dilation inferred from seismic models of the northern barbados ridge decollement. *Journal of Geophysical Research-Solid Earth*, 101(B1):627–642.

Bangs, N. L. B., Shipley, T. H., Moore, J. C., and Moore, G. F. (1999). Fluid accumulation and channeling along the northern barbados ridge decollement thrust. *Journal of Geophysical Research-Solid Earth*, 104(B9):20399–20414.

Bangs, N. L. B., Westbrook, G. K., Ladd, J. W., and Buhl, P. (1990). Seismic velocities from the barbados ridge complex - indicators of high pore fluid pressures in an accretionary complex. *Journal of Geophysical Research-Solid Earth*, 95(B6):8767–8782.

Barker, P. F. (2001). Scotia sea regional tectonic evolution: implications for mantle flow and palaeocirculation. *Earth Science Reviews*, 55(1-2):1–39.

Bassett, D. and Watts, A. B. (2015). Gravity anomalies, crustal structure, and seismicity at subduction zones: 1. seafloor roughness and subducting relief. *Geochemistry Geophysics Geosystems*, 16(5):1508–1540.

Bayona, G., Cardona, A., Jaramillo, C., Mora, A., Montes, C., Valencia, V., Ayala, C., Montenegro, O., and Ibañez-Mejia, M. (2012). Early paleogene magmatism in the northern andes: Insights on the effects of oceanic plateau–continent convergence. *Earth and Planetary Science Letters*, 331-332:97–111.

Bengoubou-Valerius, M., Bazin, S., Bertil, D., Beauducel, F., and Bosson, A. (2008). Cdsa: A new seismological data center for the french lesser antilles. *Seismological Research Letters*, 79(1):90–102.

Benson, W. E., Gerard, R. D., and Hay, W. W. (1970). Dsdp volume iv, summary and conclusions, chapter 27. *Initial Reports of the Deep Sea Drilling Project*, 4:659–673.

Berry, C. (2017). *A time lapse study of the Kick 'em Jenny volcano, and an evaluation of its potential hazards*. Thesis, London, UK: Imperial College London.

Bezada, M. J., Levander, A., and Schmandt, B. (2010). Subduction in the southern caribbean: Images from finite-frequency p wave tomography. *Journal of Geophysical Research-Solid Earth*, 115.

Bezard, R. (2014). *Impact of crustal assimilation on the Lesser Antilles arc lava geochemistry*. Thesis, Sydney, Australia: Macquarie University.

Bezard, R., Davidson, J. P., Turner, S., Macpherson, C. G., Lindsay, J. M., and Boyce, A. J. (2014). Assimilation of sediments embedded in the oceanic arc crust: myth or reality? *Earth and Planetary Science Letters*, 395:51–60.

Bezard, R., Schaefer, B. F., Turner, S., Davidson, J. P., and Selby, D. (2015). Lower crustal assimilation in oceanic arcs: Insights from an osmium isotopic study of the lesser antilles. *Geochimica Et Cosmochimica Acta*, 150:330–344.

Bie, L. D., Rietbrock, A., Hicks, S., Allen, R., Blundy, J., Clouard, V., Collier, J., Davidson, J., Garth, T., Goes, S., Harmon, N., Henstock, T., van Hunen, J., Kendall, M., Kruger, F., Lynch, L., Macpherson, C., Robertson, R., Rychert, K., Tait, S., Wilkinson, J., and Wilson, M. (2020). Along-arc heterogeneity in local seismicity across the lesser antilles subduction zone from a dense ocean-bottom seismometer network. *Seismological Research Letters*, 91(1):237–247.

Biju-Duval, B., Le Quellec, P., Mascle, A., Renard, V., and Valery, P. (1982). Multibeam bathymetric survey and high resolution seismic investigations on the barbados ridge complex (eastern caribbean): A key to the knowledge and interpretation of an accretionary wedge. *Tectonophysics*, 86(1-3):275–304.

Bird, D. E., Hall, S. A., Casey, J. F., and Millegan, P. S. (1993). Interpretation of magnetic-anomalies over the grenada basin. *Tectonics*, 12(5):1267–1279.

Bird, D. E., Hall, S. A., Casey, J. F., and Millegan, P. S. (1999). Chapter 15, tectonic evolution of the grenada basin. In Mann, P., editor, *Sedimentary Basins of the World*, volume 4, pages 389–416. Elsevier, Amsterdam.

Bohnenstiehl, D. R., Dziak, R. P., Matsumoto, H., and Lau, T. K. A. (2013). Underwater acoustic records from the march 2009 eruption of hunga ha'apai-hunga tonga volcano in the kingdom of tonga. *Journal of Volcanology and Geothermal Research*, 249:12–24.

Bonaccorso, A., Aloisi, M., and Mattia, M. (2002). Dike emplacement forerunning the etna july 2001 eruption modeled through continuous tilt and gps data. *Geophysical Research Letters*, 29(13):1–4.

Bonaccorso, A., Calvari, S., Linde, A., Sacks, S., and Boschi, E. (2012). Dynamics of the shallow plumbing system investigated from borehole strainmeters and cameras during the 15 march, 2007 vulcanian paroxysm at stromboli volcano. *Earth and Planetary Science Letters*, 357:249–256.

Boneh, Y., Schottenfels, E., Kwong, K., Zelst, I., Tong, X., Eimer, M., Miller, M. S., Moresi, L., Warren, J. M., Wiens, D. A., Billen, M., Naliboff, J., and Zhan, Z. (2019). Intermediate-depth earthquakes controlled by incoming plate hydration along bending-related faults. *Geophysical Research Letters*, 46(7):3688–3697.

Boschi, C., Bonatti, E., Ligi, M., Brunelli, D., Cipriani, A., Dallai, L., D'Orazio, M., Fruh-Green, G. L., Tonarini, S., Barnes, J. D., and Bedini, R. M. (2013). Serpentinization of mantle peridotites along an uplifted lithospheric section, mid atlantic ridge at 11 degrees n. *Lithos*, 178:3–23.

Boschman, L., Van der Wiel, E., Flores, K., Langereis, C., and Van Hinsbergen, D. (2019). The caribbean and farallon plates connected: Constraints from stratigraphy and paleomagnetism of the nicoya peninsula, costa rica. *J. Geophys. Res.*, 124(7):6243– 6266.

Boschman, L., Van Hinsbergen, D., Torsvik, T., and Spakman, W. (2014). Kinematic reconstruction of the caribbean region since the early jurassic. *Earth Sci. Rev.*, 138:102–136.

Boston, B., Moore, G. F., Nakamura, Y., and Kodaira, S. (2014). Outer-rise normal fault development and influence on near-trench décollement propagation along the japan trench, off tohoku. *Earth, Planets and Space*, 66(1):135.

Boudon, G., Le Friant, A., Komorowski, J. C., Deplus, C., and Semet, M. P. (2007). Volcano flank instability in the lesser antilles arc: Diversity of scale, processes, and temporal recurrence. *Journal of Geophysical Research-Solid Earth*, 112(B8):1–28.

Bouysse, P. (1988). Opening of the grenada back-arc basin and evolution of the caribbean plate during the mesozoic and early paleogene. *Tectonophysics*, 149(1-2):121–143.

Bouysse, P., Mascle, A., Mauffret, A., Delepinay, B. M., Jany, I., Leclere-Vanhoeve, A., and Montjaret, M. C. (1988). Submarine tectonic and volcanic structures of the lesser antilles recent arc (kick'em jenny, qualibou, mount pelee, northwest guadeloupe). *Marine Geology*, 81(1-4):261–287.

Bouysse, P. and Westercamp, D. (1990). Subduction of atlantic aseismic ridges and late cenozoic evolution of the lesser antilles island-arc. *Tectonophysics*, 175(4):349–380.

Boynton, C. H., Westbrook, G. K., Bott, M. H. P., and Long, R. E. (1979). Seismic refraction investigation of crustal structure beneath the lesser-antilles island arc. *Geophysical Journal of the Royal Astronomical Society*, 58(2):371–393.

Braszus, B., Goes, S., Allen, R., Rietbrock, A., Collier, J., Harmon, N., Henstock, T., Hicks, S., Rychert, K., Maunder, B., van Hunen, J., Bie, L., Blundy, J., Cooper, G., Davy, R., Kendall, M., Macpherson, C., Wilkinson, J., and Wilson, M. (2020). Subduction history of the caribbean from upper-mantle seismic imaging and plate reconstruction. *Nature Communications*, Under Revision.

Brenguier, F., Shapiro, N. M., Campillo, M., Ferrazzini, V., Duputel, Z., Coutant, O., and Nercessian, A. (2008). Towards forecasting volcanic eruptions using seismic noise. *Nature Geoscience*, 1(2):126–130.

Briden, J. C., Rex, D. C., Faller, A. M., and Tomblin, J. F. (1979). K-ar geochronology and paleomagnetism of volcanic-rocks in the lesser antilles island arc. *Philosophical Transactions of the Royal Society A-Mathematical Physical and Engineering Sciences*, 291(1383):485–528.

Brown, G. M., Holland, J. G., Sigurdsson, H., Tomblin, J. F., and Arculus, R. J. (1977). Geochemistry of lesser antilles volcanic island arc. *Geochimica Et Cosmochimica Acta*, 41(6):785–801.

Brown, K. and Westbrook, G. K. (1988). Mud diapirism and subcretion in the barbados ridge accretionary complex - the role of fluids in accretionary processes. *Tectonics*, 7(3):613–640.

Bruna, J. L. G., Carbo-Gorosabel, A., Estrada, P. L., Munoz-Martin, A., ten Brink, U. S., Ballesteros, M. G., Druet, M., and Pazos, A. (2014). Morphostructure at the junction between the beata ridge and the greater antilles island arc (offshore hispaniola southern slope). *Tectonophysics*, 618:138–163.

Budetta, G., Carbone, D., and Greco, F. (1999). Subsurface mass redistributions at mount etna (italy) during the 1995-1996 explosive activity detected by microgravity studies. *Geophysical Journal International*, 138(1):77–88.

Buffett, B. A. and Heuret, A. (2011). Curvature of subducted lithosphere from earthquake locations in the wadati-benioff zone. *Geochemistry Geophysics Geosystems*, 12.

Burke, K. (1988). Tectonic evolution of the caribbean. *Annual Review of Earth and Planetary Sciences*, 16:201–230.

Caldwell, G., Smith, T. E., Uang, C. H., and Jackson, T. A. (1984). The geochemistry and petrogenesis of the volcanic rocks of carriacou, grenadine islands, west indies. *Bulletin Volcanologique*, 47(3):467–482.

Canales, J. P., Detrick, R. S., Lin, J., Collins, J. A., and Toomey, D. R. (2000). Crustal and upper mantle seismic structure beneath the rift mountains and across a nontransform offset at the mid-atlantic ridge (35°n). *Journal of Geophysical Research: Solid Earth*, 105(B2):2699–2719.

Cande, S. C. and Kent, D. V. (1992). A new geomagnetic polarity time scale for the late cretaceous and cenozoic. *Journal of Geophysical Research*, 97(B10):13917–13951.

Cande, S. C. and Kent, D. V. (1995). Revised calibration of the geomagnetic polarity timescale for the late cretaceous and cenozoic. *Journal of Geophysical Research-Solid Earth*, 100(B4):6093–6095.

Cann, J. R., Blackman, D. K., Smith, D. K., McAllister, E., Janssen, B., Mello, S., Avgerinos, E., Pascoe, A. R., and Escartin, J. (1997). Corrugated slip surfaces formed at ridge–transform intersections on the mid-atlantic ridge. *Nature*, 385(6614):329–332.

Caplan-Auerbach, J. and Duennebier, F. (2001). Seismic and acoustic signals detected at lo'ihi seamount by the hawai'i undersea geo-observatory. *Geochemistry Geophysics Geosystems*, 2.

Caplan-Auerbach, J., Fox, C. G., and Duennebier, F. K. (2001). Hydroacoustic detection of submarine landslides on kilauea volcano. *Geophysical Research Letters*, 28(9):1811–1813.

Cardona, A., Valencia, V. A., Bayona, G., Duque, J., Ducea, M., Gehrels, G., Jaramillo, C., Montes, C., Ojeda, G., and Ruiz, J. (2011). Early-subduction-related orogeny in the northern andes: Turonian to eocene magmatic and provenance record in the santa marta massif and rancheria basin, northern colombia. *Terra Nova*, 23(1):26–34.

Carey, S., Ballard, R., Bell, K. L. C., Bell, R. J., Connally, P., Dondin, F., Fuller, S., Gobin, J., Miloslavich, P., Phillips, B., Roman, C., Seibel, B., Siu, N., and Smart, C. (2014). Cold seeps associated with a submarine debris avalanche deposit at kick'em jenny volcano, grenada (lesser antilles). *Deep-Sea Research Part I-Oceanographic Research Papers*, 93:156–160.

Carey, S., Olsen, R., Bell, K. L. C., Ballard, R., Dondin, F., Roman, C., Smart, C., Lilley, M., Lupton, J., Seibel, B., Cornell, W., and Moyer, C. (2016). Hydrothermal venting and mineralization in the crater of kick'em jenny submarine volcano, grenada (lesser antilles). *Geochemistry Geophysics Geosystems*, 17(3):1000–1019.

Carlson, R. L. and Miller, D. J. (1997). A new assessment of the abundance of serpentinite in the oceanic crust. *Geophysical Research Letters*, 24(4):457–460.

Carlson, R. L. and Miller, D. J. (2003). Mantle wedge water contents estimated from seismic velocities in partially serpentinized peridotites. *Geophysical Research Letters*, 30(5):1250.

Carpentier, M., Chauvel, C., and Mattielli, N. (2008). Pb–nd isotopic constraints on sedimentary input into the lesser antilles arc system. *Earth and Planetary Science Letters*, 272(1-2):199–211.

Cashman, K. V. and Sparks, R. S. J. (2013). How volcanoes work: A 25 year perspective. *Geological Society of America Bulletin*, 125(5-6):664–690.

Castro, M. and Mederos, A. (1985). Litoestratigraffa de la cuenca de carupano. In *Sociedad Venezolana de Geólogos, VI Congreso Geológico*, volume 1, pages 201–224.

Chadwick, W. W., Cashman, K. V., Embley, R. W., Matsumoto, H., Dziak, R. P., de Ronde, C. E. J., Lau, T. K., Deardorff, N. D., and Merle, S. G. (2008a). Direct video and hydrophone observations of submarine explosive eruptions at nw rota-1 volcano, mariana arc. *Journal of Geophysical Research-Solid Earth*, 113(B8):1–23.

Chadwick, W. W., Dziak, R. P., Haxel, J. H., Embley, R. W., and Matsumoto, H. (2012). Submarine landslide triggered by volcanic eruption recorded by in situ hydrophone. *Geology*, 40(1):51–54.

Chadwick, W. W., Merle, S. G., Buck, N. J., Lavelle, J. W., Resing, J. A., and Ferrini, V. (2014). Imaging of co_2 bubble plumes above an erupting submarine volcano, nw rota-1, mariana arc. *Geochemistry Geophysics Geosystems*, 15(11):4325–4342.

Chadwick, W. W., Wright, I. C., Schwarz-Schampera, U., Hyvernaud, O., Reymond, D., and de Ronde, C. E. J. (2008b). Cyclic eruptions and sector collapses at monowai submarine volcano, kermadec arc: 1998-2007. *Geochemistry Geophysics Geosystems*, 9(10):1–17.

Chiarabba, C., Amato, A., Boschi, E., and Barberi, F. (2000). Recent seismicity and tomographic modeling of the mount etna plumbing system. *Journal of Geophysical Research-Solid Earth*, 105(B5):10923–10938.

Chichester, B., Rychert, C., Harmon, N., Allen, R., Collier, J., Henstock, T., and Rietbrock, A. (2020). Seafloor sediment thickness beneath the voila broadband ocean-bottom seismometer deployment in the lesser antilles from p-to-s delay times. *Geophysical Journal International*, In press.

Christensen, N. I. (1996). Poisson's ratio and crustal seismology. *Journal of Geophysical Research: Solid Earth*, 101(B2):3139–3156.

Christeson, G. L., Bangs, N. L., and Shipley, T. H. (2003). Deep structure of an island arc backstop, lesser antilles subduction zone. *Journal of Geophysical Research-Solid Earth*, 108(B7):2327.

Christeson, G. L., Goff, J. A., and Reece, R. S. (2019). Synthesis of oceanic crustal structure from two-dimensional seismic profiles. *Reviews of Geophysics*, 57:504–529.

Christeson, G. L., Mann, P., Escalona, A., and Aitken, T. J. (2008). Crustal structure of the caribbean-northeastern south america arc-continent collision zone. *Journal of Geophysical Research-Solid Earth*, 113(B8):19.

Christman, R. A. (1953). Geology of st. bartholomew, st. martin and anguilla, lesser antilles. *GSA Bulletin*, 64(1):65–96.

Clague, D. A., Paduan, J. B., Caress, D. W., Thomas, H., Chadwick, W. W., and Merle, S. G. (2011). Volcanic morphology of west mata volcano, ne lau basin, based on high-resolution bathymetry and depth changes. *Geochemistry Geophysics Geosystems*, 12(11):1–21.

Clark, S. A., Zelt, C. A., Magnani, M. B., and Levander, A. (2008). Characterizing the caribbean-south american plate boundary at 64 degrees w using wide-angle seismic data. *Journal of Geophysical Research-Solid Earth*, 113(B7):16.

Clift, P. and Vannucchi, P. (2004). Controls on tectonic accretion versus erosion in subduction zones: Implications for the origin and recycling of the continental crust. *Reviews of Geophysics*, 42(2).

Cogné, J.-P. and Humler, E. (2004). Temporal variation of oceanic spreading and crustal production rates during the last 180 my. *Earth and Planetary Science Letters*, 227(3-4):427–439.

Collier, J. S. (2017). Rrs james cook jc149, cruise report. Report, British Oceanographic Data Centre.

Collins, J. A., Blackman, D. K., Harris, A., and Carlson, R. L. (2009). Seismic and drilling constraints on velocity structure and reflectivity near iodp hole u1309d on the central dome of atlantis massif, mid-atlantic ridge 30°n. *Geochemistry Geophysics Geosystems*, 10(1).

Contreras-Reyes, E., Becerra, J., Kopp, H., Reichert, C., and Diaz-Naveas, J. (2014). Seismic structure of the north-central chilean convergent margin: Subduction erosion of a paleomagmatic arc. *Geophysical Research Letters*, 41(5):1523–1529.

Contreras-Reyes, E., Flueh, E. R., and Grevemeyer, I. (2010). Tectonic control on sediment accretion and subduction off south central chile: Implications for coseismic rupture processes of the 1960 and 2010 megathrust earthquakes. *Tectonics*, 29(6).

Contreras-Reyes, E., Grevemeyer, I., Flueh, E. R., and Reichert, C. (2008). Upper lithospheric structure of the subduction zone offshore of southern arauco peninsula, chile, at ∼38 degrees s. *Journal of Geophysical Research-Solid Earth*, 113(B7).

Contreras-Reyes, E., Grevemeyer, I., Flueh, E. R., Scherwath, M., and Heesemann, M. (2007). Alteration of the subducting oceanic lithosphere at the southern central chile trench-outer rise. *Geochemistry Geophysics Geosystems*, 8.

Contreras-Reyes, E., Grevemeyer, I., Watts, A. B., Flueh, E. R., Peirce, C., Moeller, S., and Papenberg, C. (2011). Deep seismic structure of the tonga subduction zone: Implications for mantle hydration, tectonic erosion, and arc magmatism. *Journal of Geophysical Research-Solid Earth*, 116.

Contreras-Reyes, E., Ruiz, J. A., Becerra, J., Kopp, H., Reichert, C., Maksymowicz, A., and Arriagada, C. (2015). Structure and tectonics of the central chilean margin (31 degrees-33 degrees s): implications for subduction erosion and shallow crustal seismicity. *Geophysical Journal International*, 203(2):776–791.

Cooper, G. F., Macpherson, C. G., Blundy, J. D., Maunder, B., Allen, R. W., Goes, S., Collier, J. S., Bie, L., Harmon, N., Hicks, S. P., Iveson, A. A., Prytulak, J., Rietbrock, A., Rychert, C. A., Davidson, J. P., Cooper, G. F., Macpherson, C. G., Blundy, J. D., Maunder, B., Allen, R. W., Goes, S., Collier, J. S., Bie, L., Harmon, N., Hicks, S. P., Rietbrock, A., Rychert, C. A., Davidson, J. P., Davy, R. G., Henstock, T. J., Kendall, M. J., Schlaphorst, D., van Hunen, J., Wilkinson, J. J., Wilson, M., and the Voi, L. A. t. (2020). Variable water input controls evolution of the lesser antilles volcanic arc. *Nature*, 582(7813):525–529.

Cordey, F. and Cornee, J. J. (2009). New radiolarian assemblages from la desirade island basement complex (guadeloupe, lesser antilles arc) and caribbean tectonic implications. *Bulletin De La Societe Geologique De France*, 180(5):399–409.

Corsini, M., Lardeaux, J. M., Verati, C., Voitus, E., and Balagne, M. (2011). Discovery of lower cretaceous synmetamorphic thrust tectonics in french lesser antilles (la desirade island, guadeloupe): Implications for caribbean geodynamics. *Tectonics*, 30:15.

Cox, D. P., Marvin, R. F., Mgonigle, J. W., Mcintyre, D. H., and Rogers, C. L. (1977). Potassium-argon geochronology of some metamorphic, igneous, and hydrothermal events in puerto-rico and virgin-islands. *Journal of Research of the Us Geological Survey*, 5(6):689–703.

Craig, T. J., Copley, A., and Jackson, J. (2014). A reassessment of outer-rise seismicity and its implications for the mechanics of oceanic lithosphere. *Geophysical Journal International*, 197(1):63–89.

Dannowski, A., Grevemeyer, I., Ranero, C. R., Ceuleneer, G., Maia, M., Morgan, J. P., and Gente, P. (2010). Seismic structure of an oceanic core complex at the mid-atlantic ridge, 22°19'n. *Journal of Geophysical Research: Solid Earth*, 115(B7).

Davidson, J. (1985). Mechanisms of contamination in lesser antilles island-arc magmas from radiogenic and oxygen isotope relationships. *Earth and Planetary Science Letters*, 72(2-3):163–174.

Davidson, J. and Wilson, M. (2011). Differentiation and source processes at mt pelee and the quill; active volcanoes in the lesser antilles arc. *Journal of Petrology*, 52(7-8):1493–1531.

Davidson, J. P. (1983). Lesser antilles isotopic evidence of the role of subducted sediment in island arc magma genesis. *Nature*, 306(5940):253–256.

Davidson, J. P., Boghossian, N. D., and Wilson, M. (1993). The geochemistry of the igneous rock suite of st martin, northern lesser antilles. *Journal of Petrology*, 34(5):839–866.

Davidson, J. P. and Harmon, R. S. (1989). Oxygen isotope constraints on the petrogenesis of volcanic arc magmas from martinique, lesser antilles. *Earth and Planetary Science Letters*, 95(3-4):255–270.

Davis, D., Suppe, J., and Dahlen, F. A. (1983). Mechanics of fold-and-thrust belts and accretionary wedges. *Journal of Geophysical Research: Solid Earth*, 88(B2):1153–1172.

Davy, R. G., Collier, J. S., Henstock, T. J., and Consortium, T. V. (2020). Wide-angle seismic imaging of two modes of crustal accretion in mature atlantic ocean crust. *Journal of Geophysical Research: Solid Earth*, 125(6).

Defant, M. J., Sherman, S., Maury, R. C., Bellon, H., de Boer, J., Davidson, J., and Kepezhinskas, P. (2001). The geology, petrology, and petrogenesis of saba island, lesser antilles. *Journal of Volcanology and Geothermal Research*, 107(1-3):87–111.

Del Negro, C., Currenti, G., Napoli, R., and Vicari, A. (2004). Volcanomagnetic changes accompanying the onset of the 2002-2003 eruption of mt. etna (italy). *Earth and Planetary Science Letters*, 229(1-2):1–14.

Del Negro, C., Napoli, R., and Sicali, A. (2002). Automated system for magnetic monitoring of active volcanoes. *Bulletin of Volcanology*, 64(2):94–99.

Deplus, C., Le Friant, A., Boudon, G., Komorowski, J. C., Villemant, B., Harford, C., Segoufin, J., and Cheminee, J. L. (2001). Submarine evidence for large-scale debris avalanches in the lesser antilles arc. *Earth and Planetary Science Letters*, 192(2):145–157.

Devas, R. P. (1974). *A History of the Island of Grenada, 1498-1796, with Some Notes and Comments on Carriacou and Events of Later Years*. Carenage Press, St. George's, Grenada.

Devine, J. D. and Sigurdsson, H. (1995). Petrology and eruption styles of kick'em-jenny submarine volcano, lesser antilles island arc. *Journal of Volcanology and Geothermal Research*, 69(1-2):35–58.

Dick, H. J. B., Lin, J., and Schouten, H. (2003). An ultraslow-spreading class of ocean ridge. *Nature*, 426(6965):405–412.

Diebold, J. B., Stoffa, P. L., Buhl, P., and Truchan, M. (1981). Venezuela basin crustal structure. *Journal of Geophysical Research*, 86(Nb9):7901–7923.

Diefenbach, A. K., Crider, J. G., Schilling, S. P., and Dzurisin, D. (2012). Rapid, low-cost photogrammetry to monitor volcanic eruptions: an example from mount st. helens, washington, usa. *Bulletin of Volcanology*, 74(2):579–587.

Dondin, F., Lebrun, J. F., Kelfoun, K., Fournier, N., and Randrianasolo, A. (2012). Sector collapse at kick 'em jenny submarine volcano (lesser antilles): numerical simulation and landslide behaviour. *Bulletin of Volcanology*, 74(2):595–607.

Dondin, F. J. Y., Heap, M. J., Robertson, R. E. A., Dorville, J. F. M., and Carey, S. (2017). Flank instability assessment at kick-'em-jenny submarine volcano (grenada, lesser antilles): a multidisciplinary approach using experiments and modeling. *Bulletin of Volcanology*, 79(1):1–15.

Dorel, J. (1981). Seismicity and seismic gap in the lesser-antilles arc and earthquake hazard in guadeloupe. *Geophysical Journal of the Royal Astronomical Society*, 67(3):679–695.

Druitt, T. H. and Kokelaar, B. P. (2002). *The Eruption of Soufrière Hills Volcano, Montserrat, from 1995 to 1999*, volume 21 of *Geological Society Memoir*. Geological Society of London, London, UK.

Duffell, H. J., Oppenheimer, C., Pyle, D. M., Galle, B., McGonigle, A. J. S., and Burton, M. R. (2003). Changes in gas composition prior to a minor explosive eruption at masaya volcano, nicaragua. *Journal of Volcanology and Geothermal Research*, 126(3-4):327–339.

Dunn, R. A., Arai, R., Eason, D. E., Canales, J. P., and Sohn, R. A. (2017). Three-dimensional seismic structure of the mid-atlantic ridge: An investigation of tectonic, magmatic, and hydrothermal processes in the rainbow area. *Journal of Geophysical Research: Solid Earth*, 122(12):9580–9602.

Dupre, S., Buffet, G., Mascle, J., Foucher, J. P., Gauger, S., Boetius, A., Marfia, C., Team, A. A., Team, Q. R., and Party, B. S. (2008). High-resolution mapping of large gas emitting mud volcanoes on the egyptian continental margin (nile deep sea fan) by auv surveys. *Marine Geophysical Research*, 29(4):275–290.

Dziak, R. P. and Fox, C. G. (1999). The january 1998 earthquake swarm at axial volcano, juan de fuca ridge: Hydroacoustic evidence of seafloor volcanic activity. *Geophysical Research Letters*, 26(23):3429–3432.

Dzurisin, D. (2003). A comprehensive approach to monitoring volcano deformation as a window on the eruption cycle. *Reviews of Geophysics*, 41(1):1–29.

Edmonds, M., Oppenheimer, C., Pyle, D. M., Herd, R. A., and Thompson, G. (2003). So2 emissions from soufriere hills volcano and their relationship to conduit permeability, hydrothermal interaction and degassing regime. *Journal of Volcanology and Geothermal Research*, 124(1-2):23–43.

Embley, R. W., Chadwick, W. W., Baker, E. T., Butterfield, D. A., Resing, J. A., De Ronde, C. E. J., Tunnicliffe, V., Lupton, J. E., Juniper, S. K., Rubin, K. H., Stern, R. J., Lebon, G. T., Nakamura, K., Merle, S. G., Hein, J. R., Wiens, D. A., and Tamura, Y. (2006). Long-term eruptive activity at a submarine arc volcano. *Nature*, 441(7092):494–497.

Embley, R. W., Ewing, J. I., and Ewing, M. (1970). Vidal-deep-sea-channel and its relationship to demerara and barracuda-abyssal-plains. *Deep-Sea Research*, 17(3):539–552.

Emry, E. L. and Wiens, D. A. (2015). Incoming plate faulting in the northern and western pacific and implications for subduction zone water budgets. *Earth and Planetary Science Letters*, 414:176–186.

Escartin, J. and Cannat, M. (1999). Ultramafic exposures and the gravity signature of the lithosphere near the fifteen-twenty fracture zone (mid-atlantic ridge, 14°-16.5° n). *Earth and Planetary Science Letters*, 171(3):411–424.

Escartin, J., Mevel, C., Petersen, S., Bonnemains, D., Cannat, M., Andreani, M., Augustin, N., Bezos, A., Chavagnac, V., Choi, Y., Godard, M., Haaga, K., Hamelin, C., Ildefonse, B., Jamieson, J., John, B., Leleu, T., MacLeod, C. J., Massot-Campos, M., Nomikou, P., Olive, J. A., Paquet, M., Rommevaux, C., Rothenbeck, M., Steinfuhrer, A., Tominaga, M., Triebe, L., Campos, R., Gracias, N., and Garcia, R. (2017). Tectonic structure, evolution, and the nature of oceanic core complexes and their detachment fault zones (13° 20' n and 13° 30' n, mid atlantic ridge). *Geochemistry Geophysics Geosystems*, 18(4):1451–1482.

Escartin, J., Smith, D. K., Cann, J., Schouten, H., Langmuir, C. H., and Escrig, S. (2008). Central role of detachment faults in accretion of slow-spreading oceanic lithosphere. *Nature*, 455(7214):790–4.

Evain, M., Galve, A., Charvis, P., Laigle, M., Kopp, H., Becel, A., Weinzierl, W., Hirn, A., Flueh, E. R., Gallart, J., and Party, L. A. T. S. (2013). Structure of the lesser antilles subduction forearc and backstop from 3d seismic refraction tomography. *Tectonophysics*, 603:55–67.

Faccenda, M. (2014). Water in the slab: A trilogy. *Tectonophysics*, 614:1–30.

Faccenda, M., Gerya, T. V., and Burlini, L. (2009). Deep slab hydration induced by bending-related variations in tectonic pressure. *Nature Geoscience*, 2(11):790–793.

Fagereng, A. (2011). Wedge geometry, mechanical strength, and interseismic coupling of the hikurangi subduction thrust, new zealand. *Tectonophysics*, 507(1):26–30.

Feuillard, M., Allegre, C. J., Brandeis, G., Gaulon, R., Lemouel, J. L., Mercier, J. C., Pozzi, J. P., and Semet, M. P. (1983). The 1975-1977 crisis of la soufriere de guadeloupe (f.w.i): a still-born magmatic eruption. *Journal of Volcanology and Geothermal Research*, 16(3-4):317–334.

Feuillet, N., Beauducel, F., and Tapponnier, P. (2011). Tectonic context of moderate to large historical earthquakes in the lesser antilles and mechanical coupling with volcanoes. *Journal of Geophysical Research-Solid Earth*, 116:26.

Fiske, R. S., Cashman, K. V., Shibata, A., and Watanabe, K. (1998). Tephra dispersal from myojinsho, japan, during its shallow submarine eruption of 1952-1953. *Bulletin of Volcanology*, 59(4):262–275.

Fiske, R. S. and Shepherd, J. B. (1990). 12 years of ground-tilt measurements on the soufriere of st-vincent, 1977-1989. *Bulletin of Volcanology*, 52(3):227–241.

Fox, P. J., Schreiber, E., Rowlett, H., and McCamy, K. (1976). The geology of the oceanographer fracture zone: A model for fracture zones. *Journal of Geophysical Research*, 81(23):4117–4128.

Freymuth, H., Elliott, T., van Soest, M., and Skora, S. (2016). Tracing subducted black shales in the lesser antilles arc using molybdenum isotope ratios. *Geology*, 44(12):987–990.

Fujie, G., Kodaira, S., Kaiho, Y., Yamamoto, Y., Takahashi, T., Miura, S., and Yamada, T. (2018). Controlling factor of incoming plate hydration at the north-western pacific margin. *Nature Communications*, 9(1).

Fujie, G., Kodaira, S., Sato, T., and Takahashi, T. (2016). Along-trench variations in the seismic structure of the incoming pacific plate at the outer rise of the northern japan trench. *Geophysical Research Letters*, 43(2):666–673.

Fujie, G., Kodaira, S., Yamashita, M., Sato, T., Takahashi, T., and Takahashi, N. (2013). Systematic changes in the incoming plate structure at the kuril trench. *Geophysical Research Letters*, 40(1):88–93.

Gailler, L., Arcay, D., Munch, P., Martelet, G., Thinon, I., and Lebrun, J. F. (2017). Forearc structure in the lesser antilles inferred from depth to the curie temperature and thermomechanical simulations. *Tectonophysics*, 706:71–90.

Germa, A., Quidelleur, X., Labanieh, S., Chauvel, C., and Lahitte, P. (2011). The volcanic evolution of martinique island: Insights from k-ar dating into the lesser antilles arc migration since the oligocene. *Journal of Volcanology and Geothermal Research*, 208(3-4):122–135.

Gerya, T. V., Fossati, D., Cantieni, C., and Seward, D. (2009). Dynamic effects of aseismic ridge subduction: numerical modelling. *European Journal of Mineralogy*, 21(3):649–661.

Ghosh, N., Hall, S. A., and Casey, J. F. (1984). Seafloor spreading magnetic-anomalies in the venezuelan basin. *Geological Society of America Memoirs*, 162:65–80.

Gisler, G., Weaver, R., and Gittings, M. L. (2006). Two-dimensional simulations of explosive eruptions of kick-em jenny and other submarine volcanos. *Science of Tsunami Hazards*, 25(1):34–41.

Giunta, G., Beccaluva, L., and Siena, F. (2006). Caribbean plate margin evolution: constraints and current problems. *Geologica Acta*, 4(1-2):0265–277.

Goes, S., Collier, J., Blundy, J., Davidson, J., Harmon, N., Henstock, T., Kendall, J., Macpherson, C., Rietbrock, A., Rychert, K., Prytulak, J., Van Hunen, J., Wilkinson, J., and Wilson, M. (2019). Project voila: Volatile recycling in the lesser antilles. *Eos*, 100.

Gomez, S., Bird, D., and Mann, P. (2018). Deep crustal structure and tectonic origin of the tobago-barbados ridge. *Interpretation*, 6(2):T471–T484.

Gonzalez, O., Clouard, V., Tait, S., and Panza, G. F. (2018). S-wave velocities of the lithosphere-asthenosphere system in the lesser antilles from the joint inversion of surface wave dispersion and receiver function analysis. *Tectonophysics*, 734:1–15.

Graff, J. R., Blake, J. A., and Wishner, K. F. (2008). A new species of malacoceros (polychaeta : Spionidae) from kick'em jenny, a hydrothermally active submarine volcano in the lesser antilles arc. *Journal of the Marine Biological Association of the United Kingdom*, 88(5):925–930.

Graindorge, D., Klingelhoefer, F., Sibuet, J.-C., McNeill, L., Henstock, T. J., Dean, S., Gutscher, M.-A., Dessa, J. X., Permana, H., Singh, S. C., Leau, H., White, N., Carton, H., Malod, J. A., Rangin, C., Aryawan, K. G., Chaubey, A. K., Chauhan, A., Galih, D. R., Greenroyd, C. J., Laesanpura, A., Prihantono, J., Royle, G., and Shankar, U. (2008). Impact of lower plate structure on upper plate deformation at the nw sumatran convergent margin from seafloor morphology. *Earth and Planetary Science Letters*, 275(3):201–210.

Grasmueck, M., Eberli, G. P., Viggiano, D. A., Correa, T., Rathwell, G., and Luo, J. G. (2006). Autonomous underwater vehicle (auv) mapping reveals coral mound distribution, morphology, and oceanography in deep water of the straits of florida. *Geophysical Research Letters*, 33(23):1–6.

Grevemeyer, I., Kaul, N., Diaz-Naveas, J. L., Villinger, H. W., Ranero, C. R., and Reichert, C. (2005). Heat flow and bending-related faulting at subduction trenches: Case studies offshore of nicaragua and central chile. *Earth and Planetary Science Letters*, 236(1-2):238–248.

Grevemeyer, I., Ranero, C. R., Flueh, E. R., Klaschen, D., and Bialas, J. (2007). Passive and active seismological study of bending-related faulting and mantle serpentinization at the middle america trench. *Earth and Planetary Science Letters*, 258(3-4):528–542.

Grevemeyer, I., Ranero, C. R., and Ivandic, M. (2018). Structure of oceanic crust and serpentinization at subduction trenches. *Geosphere*, 14(2):395–418.

Hacker, B. R. (2008). H_2o subduction beyond arcs. *Geochemistry Geophysics Geosystems*, 9:24.

Harbitz, C. B., Glimsdal, S., Bazin, S., Zamora, N., Lovholt, F., Bungum, H., Smebye, H., Gauer, P., and Kjekstad, O. (2012). Tsunami hazard in the caribbean: Regional exposure derived from credible worst case scenarios. *Continental Shelf Research*, 38:1–23.

Harford, C. L., Pringle, M. S., Sparks, R. S. J., and Young, S. R. (2002). The volcanic evolution of montserrat using $^{40}ar/^{39}ar$ geochronology. *Geological Society, London, Memoirs*, 21(1):93–113.

Hart, S. R. and Staudigel, H. (1986). Ocean crust vein mineral deposition: Rb/sr ages, u-th-pb geochemistry, and duration of circulation at dsdp sites 261, 462 and 516. *Geochimica et Cosmochimica Acta*, 50(12):2751–2761.

Hastie, A. R., Kerr, A. C., McDonald, I., Mitchell, S. F., Pearce, J. A., Millar, I. L., Barfod, D., and Mark, D. F. (2010). Geochronology, geochemistry and petrogenesis of rhyodacite lavas in eastern jamaica: A new adakite subgroup analogous to early archaean continental crust? *Chemical Geology*, 276(3-4):344–359.

Hastie, A. R., Kerr, A. C., Mitchell, S. F., and Millar, I. L. (2009). Geochemistry and tectonomagmatic significance of lower cretaceous island arc lavas from the devils racecourse formation, eastern jamaica. *Geological Society, London, Special Publications*, 328(1):339–360.

Hatakeyama, K., Katayama, I., Hirauchi, K.-i., and Michibayashi, K. (2017). Mantle hydration along outer-rise faults inferred from serpentinite permeability. *Scientific Reports*, 7(1):13870.

Hawkesworth, C. J. and Powell, M. (1980). Magma genesis in the lesser antilles island-arc. *Earth and Planetary Science Letters*, 51(2):297–308.

Hayes, G. P., McNamara, D. E., Seidman, L., and Roger, J. (2014). Quantifying potential earthquake and tsunami hazard in the lesser antilles subduction zone of the caribbean region. *Geophysical Journal International*, 196(1):510–521.

Heath, E., MacDonald, R., Belkin, H., Hawkesworth, C., and Sigurdsson, H. (1998a). Magma-genesis at soufriere volcano, st vincent, lesser antilles arc. *Journal of Petrology*, 39(10):1721–1764.

Heath, E., Turner, S. P., Macdonald, R., Hawkesworth, C. J., and van Calsteren, P. (1998b). Long magma residence times at an island arc volcano (soufriere, st. vincent) in the lesser antilles: evidence from 238u-230th isochron dating. *Earth and Planetary Science Letters*, 163(1-4):413–413.

Heise, W., Caldwell, T. G., Bannister, S., Bertrand, E. A., Ogawa, Y., Bennie, S. L., and Ichihara, H. (2017). Mapping subduction interface coupling using magnetotellurics: Hikurangi margin, new zealand. *Geophysical Research Letters*, 44(18):9261–9266.

Heise, W., Caldwell, T. G., Bertrand, E. A., Hill, G. J., Bennie, S. L., and Ogawa, Y. (2013). Changes in electrical resistivity track changes in tectonic plate coupling. *Geophysical Research Letters*, 40(19):5029–5033.

Heuret, A. and Lallemand, S. (2005). Plate motions, slab dynamics and back-arc deformation. *Physics of the Earth and Planetary Interiors*, 149(1-2):31–51.

Hoernle, K., Hauff, F., and van den Bogaard, P. (2004). 70 m.y. history (139-69 ma) for the caribbean large igneous province. *Geology*, 32(8):697–700.

Hooft, E. E. E., Detrick, R. S., Toomey, D. R., Collins, J. A., and Lin, J. (2000). Crustal thickness and structure along three contrasting spreading segments of the mid-atlantic ridge, 33.5°–35°n. *Journal of Geophysical Research: Solid Earth*, 105(B4):8205–8226.

Horning, G., Canales, J. P., Carbotte, S. M., Han, S., Carton, H., Nedimovic, M. R., and van Keken, P. E. (2016). A 2-d tomographic model of the juan de fuca plate from accretion at axial seamount to subduction at the cascadia margin from an active source ocean bottom seismometer survey. *Journal of Geophysical Research-Solid Earth*, 121(8):5859–5879.

Housen, B. A., Tobin, H. J., Labaume, P., Leitch, E. C., Maltman, A. J., Shipley, T., Ogawa, Y., Ashi, J., Blum, P., Bruckman, W., Felice, F., Fisher, A., Goldberg, D., Henry, P., Jurado, M. J., Kastner, M., Laier, T., Meyer, A., Moore, J. C., Moore, G., Peacock, S., Rabaute, A., Steiger, T., Underwood, M., Xu, Y., Yin, H., Zheng, Y., and Zwart, G. (1996). Strain decoupling across the decollement of the barbados accretionary prism. *Geology*, 24(2):127–130.

Hsu, S. K. (1995). Xcorr - a cross-over technique to adjust track data. *Computers & Geosciences*, 21(2):259–271.

Hutton, C. and Nockolds, S. (1978). The petrology of nevis, leeward islands, west indies. *Overseas Geology and Mineral Resources*, 52:1–31.

Ito, A., Sugioka, H., Suetsugu, D., Shiobara, H., Kanazawa, T., and Fukao, Y. (2012). Detection of small earthquakes along the pacific-antarctic ridge from t-waves recorded by abyssal ocean-bottom observatories. *Marine Geophysical Research*, 33(3):229–238.

Iturrino, G. J., Christensen, N. I., Kirby, S., and Salisbury, M. H. (1991). 11. seismic velocities and elastic properties of oceanic gabbroic rocks from hole 735b. In Von Herzen, R. P., Robinson, P. T., and et al., editors, *Proceedings of the Ocean Drilling Program, Scientific Results, Volume 118*, volume 118, pages 227–244. College Station, Texas (Ocean Drilling Program).

Ivandic, M., Grevemeyer, I., Berhorst, A., Flueh, E. R., and McIntosh, K. (2008). Impact of bending related faulting on the seismic properties of the incoming oceanic plate offshore of nicaragua. *Journal of Geophysical Research-Solid Earth*, 113(B5).

Ivandic, M., Grevemeyer, I., Bialas, J., and Petersen, C. J. (2010). Serpentinization in the trench-outer rise region offshore of nicaragua: constraints from seismic refraction and wide-angle data. *Geophysical Journal International*, 180(3):1253–1264.

Iyer, K., Rüpke, L. H., Phipps Morgan, J., and Grevemeyer, I. (2012). Controls of faulting and reaction kinetics on serpentinization and double benioff zones. *Geochemistry Geophysics Geosystems*, 13(9).

Jackson, P., Shepherd, J. B., Robertson, R. E. A., and Skerritt, G. (1998). Ground deformation

studies at soufriere hills volcano, montserrat i: Electronic distance meter studies. *Geophysical Research Letters*, 25(18):3409–3412.

Jackson, T. A. (2013). A review of volcanic island evolution and magma production rate: an example from a cenozoic island arc in the caribbean. *Journal of the Geological Society*, 170(3):547–556.

James, K. H. (2005). Arguments for and against the pacific origin of the caribbean plate and arguments for an in situ origin. *Caribbean Journal of Earth Sciences*, 39:47–67.

James, K. H. (2009). In situ origin of the caribbean: discussion of data. In James, K. H., Lorente, M. A., and Pindell, J. L., editors, *The Origin and Evolution of the Caribbean Plate*, volume 328, pages 77–125. Geological Society, London, Special Publications, London, UK.

Jarrard, R. D. (2003). Subduction fluxes of water, carbon dioxide, chlorine, and potassium. *Geochemistry Geophysics Geosystems*, 4.

Jolly, W., Lidiak, E., Schellekens, J., and Santos, H. (1998). Volcanism, tectonics, and stratigraphic correlations in puerto rico. In Lidiak, E. G. and Larue, D. K., editors, *Special Paper 322: Tectonics and geochemistry of the Northeastern Caribbean*, pages 1–34. Geological Society of America, Boulder, Colorado.

Jung, H., Green Ii, H. W., and Dobrzhinetskaya, L. F. (2004). Intermediate-depth earthquake faulting by dehydration embrittlement with negative volume change. *Nature*, 428(6982):545–549.

Karig, D. E. (1974). Evolution of arc systems in western pacific. *Annual Review of Earth and Planetary Sciences*, 2:51–75.

Kelley, D. S., Delaney, J. R., and Juniper, S. K. (2014). Establishing a new era of submarine volcanic observatories: Cabling axial seamount and the endeavour segment of the juan de fuca ridge. *Marine Geology*, 352:426–450.

Kirby, S., Engdahl, R. E., and Denlinger, R. (1996). Intermediate-depth intraslab earthquakes and arc volcanism as physical expressions of crustal and uppermost mantle metamorphism in subducting slabs. In Bebout, G. E., Scholl, D. W., Kirby, S. H., and Platt, J. P., editors, *Subduction: Top to Bottom*, volume 96, pages 195–214. American Geophysical Union.

Kitajima, H. and Saffer, D. M. (2012). Elevated pore pressure and anomalously low stress in regions of low frequency earthquakes along the nankai trough subduction megathrust. *Geophysical Research Letters*, 39.

Kodaira, S., Iidaka, T., Kato, A., Park, J. O., Iwasaki, T., and Kaneda, Y. (2004). High pore fluid pressure may cause silent slip in the nankai trough. *Science*, 304(5675):1295–1298.

Kodaira, S., Sato, T., Takahashi, N., Miura, S., Tamura, Y., Tatsumi, Y., and Kaneda, Y. (2007). New seismological constraints on growth of continental crust in the izu-bonin intra-oceanic arc. *Geology*, 35(11):1031.

Kopp, H., Weinzierl, W., Becel, A., Charvis, P., Evain, M., Flueh, E. R., Gailler, A., Galve, A., Hirn, A., Kandilarov, A., Klaeschen, D., Laigle, M., Papenberg, C., Planert, L., Roux, E., Team, T., and Team, T. (2011). Deep structure of the central lesser antilles island arc: Relevance for the formation of continental crust. *Earth and Planetary Science Letters*, 304(1-2):121–134.

Korenaga, J., Holbrook, W. S., Kent, G. M., Kelemen, P. B., Detrick, R. S., Larsen, H. C., Hopper, J. R., and Dahl-Jensen, T. (2000). Crustal structure of the southeast greenland margin from joint refraction and reflection seismic tomography. *Journal of Geophysical Research-Solid Earth*, 105(B9):21591–21614.

Koschinsky, A., Seifert, R., Knappe, A., Schmidt, K., and Halbach, P. (2007). Hydrothermal fluid emanations from the submarine kick'em jenny volcano, lesser antilles island arc. *Marine Geology*, 244(1-4):129–141.

Lagabrielle, Y., Mamaloukas-Frangoulis, V., Cannat, M., Auzende, J.-M., Honnorez, J., Mevel, C., and Bonatti, E. (1992). Vema fracture zone (central atlantic): Tectonic and magmatic evolution of the median ridge and the eastern ridge-transform intersection domain. *Journal of Geophysical Research*, 97(B12):17331.

Laigle, M., Becel, A., de Voogd, B., Sachpazi, M., Bayrakci, G., Lebrun, J. F., Evain, M., and Seismic, T. W. R. (2013). Along-arc segmentation and interaction of subducting ridges with the lesser antilles subduction forearc crust revealed by mcs imaging. *Tectonophysics*, 603:32–54.

Lance, S., Henry, P., Le Pichon, X., Lallemant, S., Chamley, H., Rostek, F., Faugeres, J. C., Gonthier, E., and Olu, K. (1998). Submersible study of mud volcanoes seaward of the barbados accretionary wedge: sedimentology, structure and rheology. *Marine Geology*, 145(3-4):255–292.

Latchman, J. L., Robertson, R. E. A., Lynch, L. L., Dondin, F., Ramsingh, C., Stewart, R., Smith, P., Stinton, A., Edwards, S., Ash, C., Juman, A., Joseph, E. P., Nath, N., Juman, I., Ramsingh, H., and Madoo, F. (2017). 2017/04/29 eruption of kick-'em-jenny submarine volcano. Report, The UWI Seismic Research Centre, St Augustine, Trinidad and Tobago.

Leat, P. T. and Larter, R. D. (2003). Intra-oceanic subduction systems: introduction. *Geological Society, London, Special Publications*, 219(1):1–17.

Lefeldt, M., Grevemeyer, I., Goßler, J., and Bialas, J. (2009). Intraplate seismicity and related mantle hydration at the nicaraguan trench outer rise. *Geophysical Journal International*, 178(2):742–752.

Lefeldt, M., Ranero, C. R., and Grevemeyer, I. (2012). Seismic evidence of tectonic control on the depth of water influx into incoming oceanic plates at subduction trenches. *Geochemistry Geophysics Geosystems*, 13.

Leroy, S., Mauffret, A., Patriat, P., and de Lepinay, B. M. (2000). An alternative interpretation of the cayman trough evolution from a reidentification of magnetic anomalies. *Geophysical Journal International*, 141(3):539–557.

Lewis, J. F., Mattietti, G. K., Perfit, M., and Kamenov, G. (2011). Geochemistry and petrology of three granitoid rock cores from the nicaraguan rise, caribbean sea: implications for its composition, structure and tectonic evolution. *Geologica Acta*, 9(3-4).

Lidiak, E. and Jolly, W. (1998). Geochemistry of intrusive igneous rocks, st. croix, us virgin islands. In Lidiak, E. G. and Larue, D. K., editors, *Special Paper 322: Tectonics and geochemistry of the Northeastern Caribbean*, pages 133–153. Geological Society of America, Boulder, Colorado.

Lindsay, J. M. and Robertson, R. E. A. (2018). Integrating volcanic hazard data in a systematic approach to develop volcanic hazard maps in the lesser antilles. *Frontiers in Earth Science*, 6:42.

Lindsay, J. M., Shepherd, J. B., and Wilson, D. (2005). Volcanic and scientific activity at kick'em jenny submarine volcano 2001-2002: Implications for volcanic hazard in the southern grenadines, lesser antilles. *Natural Hazards*, 34(1):1–24.

Lindsay, J. M., Trumbull, R. B., Schmitt, A. K., Stockli, D. F., Shane, P. A., and Howe, T. M. (2013). Volcanic stratigraphy and geochemistry of the soufriere volcanic centre, saint lucia with implications for volcanic hazards. *Journal of Volcanology and Geothermal Research*, 258:126–142.

Lizarralde, D., Gaherty, J. B., Collins, J. A., Hirth, G., and Kim, S. D. (2004). Spreading-rate dependence of melt extraction at mid-ocean ridges from mantle seismic refraction data. *Nature*, 432(7018):744–747.

Loewen, M. W., Duncan, R. A., Kent, A. J. R., and Krawl, K. (2013). Prolonged plume volcanism in the caribbean large igneous province: New insights from curacao and haiti. *Geochemistry Geophysics Geosystems*, 14(10):4241–4259.

Lázaro, C., Blanco-Quintero, I. F., Rojas-Agramonte, Y., Proenza, J. A., Núñez-Cambra, K., and García-Casco, A. (2013). First description of a metamorphic sole related to ophiolite obduction in the northern caribbean: Geochemistry and petrology of the güira de jauco amphibolite complex (eastern cuba) and tectonic implications. *Lithos*, 179:193–210.

Lázaro, C., García-Casco, A., Rojas Agramonte, Y., Kröner, A., Neubauer, F., and Iturralde-Vinent, M. (2009). Fifty-five-million-year history of oceanic subduction and exhumation at the northern edge of the caribbean plate (sierra del convento mélange, cuba). *Journal of Metamorphic Geology*, 27(1):19–40.

Maeno, F., Nakada, S., and Kaneko, T. (2016). Morphological evolution of a new volcanic islet sustained by compound lava flows. *Geology*, 44(4):259–262.

Manea, V. C., Leeman, W. P., Gerya, T., Manea, M., and Zhu, G. (2014). Subduction of fracture zones controls mantle melting and geochemical signature above slabs. *Nature Communications*, 5(1):5095.

Mann, P. (1999). Caribbean sedimentary basins: Classification and tectonic setting from jurassic to present. In Mann, P., editor, *Sedimentary Basins of the World*, volume 4, pages 3–31. Elsevier, Amsterdam.

Mann, P., Burke, K., and Matumoto, T. (1984). Neotectonics of hispaniola: plate motion, sedimentation, and seismicity at a restraining bend. *Earth and Planetary Science Letters*, 70(2):311–324.

Martinod, J., Guillaume, B., Espurt, N., Faccenna, C., Funiciello, F., and Regard, V. (2013). Effect of aseismic ridge subduction on slab geometry and overriding plate deformation: Insights from analogue modeling. *Tectonophysics*, 588:39–55.

Mascle, A. and Moore, J. C. (1990). Odp leg 110: Tectonic and hydrologic synthesis. *Proceedings of the Ocean Drilling Program, Scientific Results*, 110:409–422.

Massonnet, D., Briole, P., and Arnaud, A. (1995). Deflation of mount etna monitored by spaceborne radar interferometry. *Nature*, 375(6532):567–570.

Massonnet, D. and Feigl, K. L. (1998). Radar interferometry and its application to changes in the earth's surface. *Reviews of Geophysics*, 36(4):441–500.

Mauffret, A. and Leroy, S. (1997). Seismic stratigraphy and structure of the caribbean igneous province. *Tectonophysics*, 283(1-4):61–104.

Maus, S., Barckhausen, U., Berkenbosch, H., Bournas, N., Brozena, J., Childers, V., Dostaler, F., Fairhead, J. D., Finn, C., von Frese, R. R. B., Gaina, C., Golynsky, S., Kucks, R., Luhr, H., Milligan, P., Mogren, S., Muller, R. D., Olesen, O., Pilkington, M., Saltus, R., Schreckenberger, B., Thebault, E., and Tontini, F. C. (2009). Emag2: A 2-arc min resolution earth magnetic anomaly grid compiled from satellite, airborne, and marine magnetic measurements. *Geochemistry Geophysics Geosystems*, 10.

McCann, W. R. and Sykes, L. R. (1984). Subduction of aseismic ridges beneath the caribbean plate - implications for the tectonics and seismic potential of the northeastern caribbean. *Journal of Geophysical Research*, 89(B6):4493–4519.

Mccann, W. R. and Sykes, L. R. (1986). Subduction of aseismic ridges beneath the caribbean plate - implications for the tectonics and seismic potential of the northeastern caribbean - reply. *Journal of Geophysical Research-Solid Earth*, 91(B1):787–791.

McClelland, L., Duncker, K., and Hoppe, K. (1989). Kick-'em-jenny volcano. *Smithsonian Institution, Scientific Event Alert Network Bulletin*, 14(5):12.

McClelland, L., Summers, M., and Duncker, K. (1988). Kick-'em-jenny volcano. *Smithsonian Institution, Scientific Event Alert Network Bulletin*, 13(12):9.

Melekhova, E., Schlaphorst, D., Blundy, J., Kendall, J. M., Connolly, C., McCarthy, A., and Arculus, R. (2019). Lateral variation in crustal structure along the lesser antilles arc from petrology of crustal xenoliths and seismic receiver functions. *Earth and Planetary Science Letters*, 516:12–24.

Metz, D., Watts, A. B., Grevemeyer, I., Rodgers, M., and Paulatto, M. (2016). Ultra-long-range hydroacoustic observations of submarine volcanic activity at monowai, kermadec arc. *Geophysical Research Letters*, 43(4):1529–1536.

Mitchell, S. F. (2006). Timing and implications of late cretaceous tectonic and sedimentary events in jamaica. *Geologica Acta*, 4(1-2).

Moore, G., Zhao, Z., H Shipley, T., Bangs, N., and Moore, J. (1996). Structural setting of the leg 156 area, northern barbados ridge accretionary prism. In Shipley, T., Ogawa, Y., Blum, P., and et al., editors, *Proceedings of the Ocean Drilling Program, Initial Reports, Volume 156 (Pt. 1)*, volume 156. College Station, Texas (Ocean Drilling Program).

Moore, J. C. (2000). Synthesis of results: logging while drilling, northern barbados accretionary prism. In Moore, J. and Klaus, A., editors, *Proceedings of the Ocean Drilling Program, Scientific Results Volume 171A, Proc. ODP, Sci. Results*, volume 171A, pages 1–25. College Station, Texas (Ocean Drilling Program).

Moore, J. C., Biju-Duval, B., Bergen, J. A., Blackington, G., Claypool, G. E., Cowan, D. S., Duennebier, F., Guerra, R. T., Hemleben, C. H. J., Hussong, D., Marlow, M. S., Natland, J. H., Pudsey, C. J., Renz, G. W., Tardy, M., Willis, M. E., Wilson, D., and Wright, A. A. (1982). Offscraping and underthrusting of sediment at the deformation front of the barbados ridge: Deep sea drilling project leg 78a. *GSA Bulletin*, 93(11):1065–1077.

Moore, J. C., Mascle, A., Taylor, E., Andreieff, P., Alvarez, F., Barnes, R., Beck, C., Behrmann, J., Blanc, G., Brown, K., Clark, M., Dolan, J., Fisher, A., Gieskes, J., Hounslow, M., Mclellan, P., Moran, K., Ogawa, Y., Sakai, T., Schoonmaker, J., Vrolijk, P., Wilkens, R., and Williams, C. (1988). Tectonics and hydrogeology of the northern barbados ridge - results from ocean drilling program leg-110. *Geological Society of America Bulletin*, 100(10):1578–1593.

Moore, J. G. (1985). Structure and eruptive mechanisms at surtsey volcano, iceland. *Geological Magazine*, 122(6):649–661.

Moscoso, E. and Grevemeyer, I. (2015). Bending-related faulting of the incoming oceanic plate and its effect on lithospheric hydration and seismicity: A passive and active seismological study offshore maule, chile. *Journal of Geodynamics*, 90:58–70.

Muller, R. D., Royer, J. Y., and Lawver, L. A. (1993). Revised plate motions relative to the hotspots from combined atlantic and indian-ocean hotspot tracks. *Geology*, 21(3):275–278.

Müller, R. D., Sdrolias, M., Gaina, C., and Roest, W. R. (2008). Age, spreading rates, and spreading asymmetry of the world's ocean crust. *Geochemistry Geophysics Geosystems*, 9(4).

Müller, R. D., Zahirovic, S., Williams, S. E., Cannon, J., Seton, M., Bower, D. J., Tetley, M. G., Heine, C., Le Breton, E., Liu, S., Russell, S. H. J., Yang, T., Leonard, J., and Gurnis, M. (2019). A global plate model including lithospheric deformation along major rifts and orogens since the triassic. *Tectonics*, 38(6):1884–1907.

Naif, S., Key, K., Constable, S., and Evans, R. L. (2015). Water-rich bending faults at the middle america trench. *Geochemistry Geophysics Geosystems*, 16(8):2582–2597.

Nakada, S. (2018). Volcanic archipelago: Volcanism as a geoheritage characteristic of japan. In Chakraborty, A., Mokudai, K., Cooper, M., Watanabe, M., and Chakraborty, S., editors, *Natural Heritage of Japan. Geoheritage, Geoparks and Geotourism (Conservation and Management Series)*, pages 19–28. Springer, Cham.

Neill, I., Gibbs, J. A., Hastie, A. R., and Kerr, A. C. (2010). Origin of the volcanic complexes of la desirade, lesser antilles implications for tectonic reconstruction of the late jurassic to cretaceous pacific-proto caribbean margin. *Lithos*, 120(3-4):407–420.

Neill, I., Kerr, A. C., Hastie, A. R., Pindell, J. L., Millar, I. L., and Atkinson, N. (2012). Age and petrogenesis of the lower cretaceous north coast schist of tobago, a fragment of the proto-greater antilles inter-american arc system. *Journal of Geology*, 120(4):367–384.

Neill, I., Kerr, A. C., Hastie, A. R., Stanek, K. P., and Millar, I. L. (2011). Origin of the aves ridge and dutch-venezuelan antilles: interaction of the cretaceous 'great arc' and caribbean-colombian oceanic plateau? *Journal of the Geological Society*, 168(2):333–347.

O'Hanley, D. S. (1992). Solution to the volume problem in serpentinization. *Geology*, 20(8):705–708.

Paris, R., Switzer, A. D., Belousova, M., Belousov, A., Ontowirjo, B., Whelley, P. L., and Ulvrova, M. (2014). Volcanic tsunami: a review of source mechanisms, past events and hazards in southeast asia (indonesia, philippines, papua new guinea). *Natural Hazards*, 70(1):447–470.

Parks, M. M., Biggs, J., England, P., Mather, T. A., Nomikou, P., Palamartchouk, K., Papanikolaou, X., Paradissis, D., Parsons, B., Pyle, D. M., Raptakis, C., and Zacharis, V. (2012). Evolution of santorini volcano dominated by episodic and rapid fluxes of melt from depth. *Nature Geoscience*, 5(10):749–754.

Patriat, M., Pichot, T., Westbrook, G. K., Umber, M., Deville, E., Benard, F., Roest, W. R., Loubrieu, B., and Party, A. C. (2011). Evidence for quaternary convergence across the north america-south america plate boundary zone, east of the lesser antilles. *Geology*, 39(10):979–982.

Paulatto, M., Laigle, M., Galve, A., Charvis, P., Sapin, M., Bayrakci, G., Evain, M., and Kopp, H. (2017). Dehydration of subducting slow-spread oceanic lithosphere in the lesser antilles. *Nature Communications*, 8:15980.

Peacock, S. M. (2001). Are the lower planes of double seismic zones caused by serpentine dehydration in subducting oceanic mantle? *Geology*, 29(4):299–302.

Pearce, J. A. and Parkinson, I. J. (1993). Trace element models for mantle melting: application to volcanic arc petrogenesis. *Geological Society, London, Special Publications*, 76(1):373–403.

Pichot, T., Patriat, M., Westbrook, G. K., Nalpas, T., Gutscher, M. A., Roest, W. R., Deville, E., Moulin, M., Aslanian, D., and Rabineau, M. (2012). The cenozoic tectonostratigraphic evolution of the barracuda ridge and tiburon rise, at the western end of the north america-south america plate boundary zone. *Marine Geology*, 303:154–171.

Pindell, J., Kennan, L., Stanek, K. P., Maresch, W. V., and Draper, G. (2006). Foundations of gulf of mexico and caribbean evolution: eight controversies resolved. *Geologica Acta*, 4(1-2):303–341.

Pindell, J. L. and Barrett, S. (1990). Geologic evolution of the caribbean region; a plate-tectonic perspective. In Dengo, G. and Case, J. E., editors, *The Caribbean Region, the Geology of North America*, page 405–432. Geological Society of America, Boulder, Colorado.

Pindell, J. L. and Kennan, L. (2009). Geologic evolution of the caribbean region; a plate-tectonic perspective. In James, K. H., Lorente, M. A., and Pindell, J. L., editors, *The Origin and Evolution of the Caribbean Plate*, volume 328, pages 1–55. Geological Society, London, Special Publications, London, UK.

Planert, L., Flueh, E. R., and Reston, T. J. (2009). Along- and across-axis variations in crustal thickness and structure at the mid-atlantic ridge at 5°s obtained from wide-angle seismic tomography: Implications for ridge segmentation. *Journal of Geophysical Research: Solid Earth*, 114(B9).

Planert, L., Flueh, E. R., Tilmann, F., Grevemeyer, I., and Reston, T. J. (2010a). Crustal structure of a rifted oceanic core complex and its conjugate side at the mar at 5°s: implications for melt extraction during detachment faulting and core complex formation. *Geophysical Journal International*, 181(1):113–126.

Planert, L., Kopp, H., Lueschen, E., Mueller, C., Flueh, E. R., Shulgin, A., Djajadihardja, Y., and Krabbenhoeft, A. (2010b). Lower plate structure and upper plate deformational segmentation at the sunda-banda arc transition, indonesia. *Journal of Geophysical Research-Solid Earth*, 115.

Prigent, C., Warren, J. M., Kohli, A. H., and Teyssier, C. (2020). Fracture-mediated deep seawater flow and mantle hydration on oceanic transform faults. *Earth and Planetary Science Letters*, 532:115988.

Proctor, B. and Hirth, G. (2015). Role of pore fluid pressure on transient strength changes and fabric development during serpentine dehydration at mantle conditions: Implications for subduction-zone seismicity. *Earth and Planetary Science Letters*, 421:1–12.

Puglisi, G. and Bonforte, A. (2004). Dynamics of mount etna volcano inferred from static and kinematic gps measurements. *Journal of Geophysical Research-Solid Earth*, 109(B11):1–15.

Puglisi, G., Bonforte, A., and Maugeri, S. R. (2001). Ground deformation patterns on mount etna, 1992 to 1994, inferred from gps data. *Bulletin of Volcanology*, 62(6-7):371–384.

Quesnel, Y., Catalan, M., and Ishihara, T. (2009). A new global marine magnetic anomaly data set. *Journal of Geophysical Research-Solid Earth*, 114.

Ranero, C. R., Morgan, J. P., McIntosh, K., and Reichert, C. (2003). Bending-related faulting and mantle serpentinization at the middle america trench. *Nature*, 425(6956):367–373.

Ranero, C. R. and Sallares, V. (2004). Geophysical evidence for hydration of the crust and mantle of the nazca plate during bending at the north chile trench. *Geology*, 32(7):549–552.

Ranero, C. R., Villaseñor, A., Phipps Morgan, J., and Weinrebe, W. (2005). Relationship between bend-faulting at trenches and intermediate-depth seismicity. *Geochemistry Geophysics Geosystems*, 6(12).

Rankin, D. W. (2002). *Geology of St. John, US Virgin Islands*, volume 1631 of *U.S. Geological Survey Professional Paper*. US Geological Survey.

Ratschbacher, L., Franz, L., Min, M., Bachmann, R., Martens, U., Stanek, K., Stubner, K., Nelson, B. K., Herrmann, U., Weber, B., Lopez-Martinez, M., Jonckheere, R., Sperner, B., Tichomirowa, M., McWilliams, M. O., Gordon, M., Meschede, M., and Bock, P. (2009). The north american-caribbean plate boundary in mexico-guatemala-honduras. In James, K. H., Lorente, M. A., and Pindell, J. L., editors, *The Origin and Evolution of the Caribbean Plate*, volume 328, pages 219–293. Geological Society, London, Special Publications, London, UK.

Resing, J. A., Rubin, K. H., Embley, R. W., Lupton, J. E., Baker, E. T., Dziak, R. P., Baumberger, T., Lilley, M. D., Huber, J. A., Shank, T. M., Butterfield, D. A., Clague, D. A., Keller, N. S., Merle, S. G., Buck, N. J., Michael, P. J., Soule, A., Caress, D. W., Walker, S. L., Davis, R., Cowen, J. P., Reysenbach, A. L., and Thomas, H. (2011). Active submarine eruption of boninite in the northeastern lau basin. *Nature Geoscience*, 4(11):799–806.

Reuber, K. R., Pindell, J., and Horn, B. W. (2016). Demerara rise, offshore suriname: Magma-rich segment of the central atlantic ocean, and conjugate to the bahamas hot spot. *Interpretation*, 4(2):T141–T155.

Ricco, C., Aquino, I., Borgstrom, S. E. P., and Del Gaudio, C. (2013). 19 years of tilt data on mt. vesuvius: state of the art and future perspectives. *Annals of Geophysics*, 56(4):1–20.

Robertson, R., Latchman, J. L., Lynch, L., Dondin, F., Ash, C., Camejo, M., Christopher, T., Graham, O., Higgins, M., Jackson, V., Joseph, E., Juman, A., Juman, I., Nath, N.,

Ramsingh, C., Ramsingh, H., Ryan, G., Smith, P., Stewart, R., and Stinton, A. (2015). Report on the 2015 unrest activity at kick-'em-jenny submarine volcano, grenada. Report, The UWI Seismic Research Centre, St Augustine, Trinidad and Tobago.

Roest, W. R. and Collette, B. J. (1986). The 15 20 fracture-zone and the north-american south-american plate boundary. *Journal of the Geological Society*, 143:833–843.

Rojas-Agramonte, Y., Kröner, A., García-Casco, A., Somin, M., Iturralde-Vinent, M., Mattinson, J. M., Millán Trujillo, G., Sukar, K., Pérez Rodríguez, M., Carrasquilla, S., Wingate, M. T. D., and Liu, D. Y. (2011). Timing and evolution of cretaceous island arc magmatism in central cuba: Implications for the history of arc systems in the northwestern caribbean. *The Journal of Geology*, 119(6):619–640.

Rojas-Agramonte, Y., Williams, I. S., Arculus, R., Kroner, A., Garcia-Casco, A., Lazar, C., Buhre, S., Wong, J., Geng, H., Echeverria, C. M., Jeffries, T., Xie, H. Q., and Mertz-Kraus, R. (2017). Ancient xenocrystic zircon in young volcanic rocks of the southern lesser antilles island arc. *Lithos*, 290:228–252.

Rosencrantz, E., Ross, M. I., and Sclater, J. G. (1988). Age and spreading history of the cayman trough as determined from depth, heat-flow, and magnetic-anomalies. *Journal of Geophysical Research-Solid Earth*, 93(B3):2141–2157.

Rubin, K. H., Soule, S. A., Chadwick, W. W., Fornari, D. J., Clague, D. A., Embley, R. W., Baker, E. T., Perfit, M. R., Caress, D. W., and Dziak, R. P. (2012). Volcanic eruptions in the deep sea. *Oceanography*, 25(1):142–157.

Ruff, L. J. (1989). Do trench sediments affect great earthquake occurrence in subduction zones? In Ruff, L. J. and Kanamori, H., editors, *Subduction Zones Part II*, pages 263–282. Birkhäuser Basel, Basel.

Rymer, H. (1994). Microgravity change as a precursor to volcanic activity. *Journal of Volcanology and Geothermal Research*, 61(3-4):311–328.

Saffer, D. M. (2017). Mapping fluids to subduction megathrust locking and slip behavior. *Geophysical Research Letters*, 44(18):9337–9340.

Saffer, D. M. and Bekins, B. A. (2002). Hydrologic controls on the morphology and mechanics of accretionary wedges. *Geology*, 30(3):271–274.

Samper, A., Quidelleur, X., Lahitte, P., and Mollex, D. (2007). Timing of effusive volcanism and collapse events within an oceanic arc island: Basse-terre, guadeloupe archipelago (lesser antilles arc). *Earth and Planetary Science Letters*, 258(1-2):175–191.

Sandwell, D. T., Muller, R. D., Smith, W. H. F., Garcia, E., and Francis, R. (2014). New global marine gravity model from cryosat-2 and jason-1 reveals buried tectonic structure. *Science*, 346(6205):65–67.

Santamaria, F. and Schubert, C. (1974). Geochemistry and geochronology of southern caribbean - northern venezuela plate boundary. *Geological Society of America Bulletin*, 85(7):1085.

Saunders, J. B., Bernoulli, D., Mullermerz, E., Oberhansli, H., Perchnielsen, K., Riedel, W. R., Sanfilippo, A., and Torrini, R. (1984). Stratigraphy of the late middle eocene to early oligocene in the bath cliff section, barbados, west-indies. *Micropaleontology*, 30(4):390–425.

Schellekens, J. H. (1998). Geochemical evolution and tectonic history of puerto rico. In Lidiak, E. G. and Larue, D. K., editors, *Special Paper 322: Tectonics and geochemistry of the Northeastern Caribbean*, pages 35–66. Geological Society of America, Boulder, Colorado.

Scherwath, M., Contreras-Reyes, E., Flueh, E. R., Grevemeyer, I., Krabbenhoeft, A., Papenberg, C., Petersen, C. J., and Weinrebe, R. W. (2009). Deep lithospheric structures along the southern central chile margin from wide-angle p-wave modelling. *Geophysical Journal International*, 179(1):579–600.

Schlaphorst, D., Kendall, J. M., Collier, J. S., Verdon, J. P., Blundy, J., Baptie, B., Latchman, J. L., Massin, F., and Bouin, M. P. (2016). Water, oceanic fracture zones and the lubrication of subducting plate boundaries-insights from seismicity. *Geophysical Journal International*, 204(3):1405–1420.

Schlaphorst, D., Melekhova, E., Kendall, J. M., Blundy, J., and Latchman, J. L. (2018). Probing layered arc crust in the lesser antilles using receiver functions. *Royal Society Open Science*, 5(11).

Schmidt, M. W. and Poli, S. (1998). Experimentally based water budgets for dehydrating slabs and consequences for arc magma generation. *Earth and Planetary Science Letters*, 163(1-4):361–379.

Schnur, S. R., Chadwick, W. W., Embley, R. W., Ferrini, V. L., de Ronde, C. E. J., Cashman, K. V., Deardorff, N. D., Merle, S. G., Dziak, R. P., Haxel, J. H., and Matsumoto, H. (2017). A decade of volcanic construction and destruction at the summit of nw rota-1 seamount: 2004-2014. *Journal of Geophysical Research-Solid Earth*, 122(3):1558–1584.

Scholz, C. H. and Small, C. (1997). The effect of seamount subduction on seismic coupling. *Geology*, 25(6):487–490.

Senn, A. (1940). Paleogene of barbados and its bearing on history and structure of antillean-caribbean region. *AAPG bulletin*, 24(9):1548–1610.

Serrano, L., Ferrari, L., López-Martínez, M., Petrone, C., and Jaramillo, C. (2011). An integrative geologic, geochronologic and geochemical study of gorgona island, colombia: Implications for the formation of the caribbean large igneous province. *Earth and Planetary Science Letters*, 309:324–336.

Sevilla, W. I., Ammon, C. J., Voight, B., and De Angelis, S. (2010). Crustal structure beneath the montserrat region of the lesser antilles island arc. *Geochemistry Geophysics Geosystems*, 11.

Shepherd, J. B. and Robson, R. B. (1967). The source of the t-phase recorded in the eastern caribbean on october 24, 1965. *Bulletin of the Seismological Society of America*, 57(2):227–234.

Shillington, D. J., Becel, A., Nedimovic, M. R., Kuehn, H., Webb, S. C., Abers, G. A., Keranen, K. M., Li, J. Y., Delescluse, M., and Mattei-Salicrup, G. A. (2015). Link between plate fabric, hydration and subduction zone seismicity in alaska. *Nature Geoscience*, 8(12):961–U98.

Shipley, T. H., Moore, G. F., Bangs, N. L., Moore, J. C., and Stoffa, P. L. (1994). Seismically inferred dilatancy distribution, northern barbados ridge decollement - implications for fluid migration and fault strength. *Geology*, 22(5):411–414.

Shipley, T. H., Moore, G. F., Tobin, H. J., and Moore, C. J. (1997). Synthesis of the barbados décollement seismic reflection response from drilling-based geophysical observations and physical properties. *Proceedings of the Ocean Drilling Program, Scientific Results*, 156:293–302.

Sigurdsson, H. and Shepherd, J. B. (1974). Amphibole-bearing basalts from the submarine volcano kick 'em jenny in the lesser antilles island arc. *Bulletin of Volcanology*, 37:891–910.

Singer, B. S., Jicha, B. R., Leeman, W. P., Rogers, N. W., Thirlwall, M. F., Ryan, J., and Nicolaysen, K. E. (2007). Along-strike trace element and isotopic variation in aleutian island arc basalt: Subduction melts sediments and dehydrates serpentine. *Journal of Geophysical Research: Solid Earth*, 112(B6).

Singh, S. C., Kent, G. M., Collier, J. S., Harding, A. J., and Orcutt, J. A. (1998). Melt to mush variations in crustal magma properties along the ridge crest at the southern east pacific rise. *Nature*, 394(6696):874–878.

Sinton, C. W., Duncan, R. A., Storey, M., Lewis, J., and Estrada, J. J. (1998). An oceanic flood basalt province within the caribbean plate. *Earth and Planetary Science Letters*, 155(3-4):221–235.

Smith, A., Roobol, M., Mattioli, G., Fryxell, J., Daly, G., and Fernandez, L. (2013). *The volcanic geology of the mid-arc Island of Dominica, Lesser Antilles, Volume 496 of Geological Society of America Special Paper*, volume 496. Geological Society of America, Boulder, Colorado.

Smith, D. K., Escartin, J., Schouten, H., and Cann, J. R. (2008). Fault rotation and core complex formation: Significant processes in seafloor formation at slow-spreading mid-ocean ridges (mid-atlantic ridge, 13°-15° n). *Geochemistry Geophysics Geosystems*, 9.

Smith, M. S. and Shepherd, J. B. (1996). Tsunami waves generated by volcanic landslides: An assessment of the hazard associated with kick 'em jenny. In McGuire, W. J., Jones, A. P., and Neuberg, J., editors, *Volcano Instability on the Earth and Other Planets*, volume 110, pages 115–123. Geological Society, London, Special Publications, London, UK.

Smith, T. E., Thirlwall, M. F., and Macpherson, C. (1996). Trace element and isotope geochemistry of the volcanic rocks of bequia, grenadine islands, lesser antilles arc: A study of subduction enrichment and intra-crustal contamination. *Journal of Petrology*, 37(1):117–143.

Smith, W. H. F. and Wessel, P. (1990). Gridding with continuous curvature splines in tension. *Geophysics*, 55(3):293–305.

Soto, D., Mann, P., and Escalona, A. (2011). Miocene-to-recent structure and basinal architecture along the central range strike-slip fault zone, eastern offshore trinidad. *Marine and Petroleum Geology*, 28(1):212–234.

Sparks, R. S. J. (2003). Forecasting volcanic eruptions. *Earth and Planetary Science Letters*, 210(1-2):1–15.

Speed, R. C., Smith-Horowitz, P. L., Perch-Nielsen J, K. V. S., Saunders, B., and Sanfilippo, A. B. (1993). *Southern Lesser Antilles Arc Platform: Pre-Late Miocene Stratigraphy, Structure, and Tectonic Evolution, GSA Special Papers*, volume 227. Geological Society of America, Boulder, Colorado.

Speed, R. C. and Walker, J. A. (1991). Oceanic-crust of the grenada basin in the southern lesser antilles arc platform. *Journal of Geophysical Research-Solid Earth*, 96(B3):3835–3851.

Stein, S., Engeln, J. F., Wiens, D. A., Fujita, K., and Speed, R. C. (1982). Subduction seismicity and tectonics in the lesser antilles arc. *Journal of Geophysical Research*, 87(NB10):8642–8664.

Stern, R. J. (2002). Subduction zones. *Reviews of Geophysics*, 40(4).

Symithe, S., Calais, E., de Chabalier, J. B., Robertson, R., and Higgins, M. (2015). Current block motions and strain accumulation on active faults in the caribbean. *Journal of Geophysical Research-Solid Earth*, 120(5):3748–3774.

Syracuse, E. M. and Abers, G. A. (2006). Global compilation of variations in slab depth beneath arc volcanoes and implications. *Geochemistry Geophysics Geosystems*, 7(5).

Thirlwall, M. F. and Graham, A. M. (1984). Evolution of high-ca, high-sr c-series basalts from grenada, lesser antilles - the effects of intra-crustal contamination. *Journal of the Geological Society*, 141:427–445.

Thompson, P. M. E., Kempton, P. D., White, R. V., Saunders, A. D., Kerr, A. C., Tarney, J., and Pringle, M. S. (2004). Elemental, hf-nd isotopic and geochronological constraints on an island arc sequence associated with the cretaceous caribbean plateau: Bonaire, dutch antilles. *Lithos*, 74(1-2):91–116.

Tomblin, J. F. (1975). The lesser antilles and aves ridge. In Nairn, A. E. M. and Stehli, F. G., editors, *The Gulf of Mexico and the Caribbean*, pages 467–500. Springer US, Boston, MA.

Torro, L., Proenza, J. A., Marchesi, C., Garcia-Casco, A., and Lewis, J. F. (2017). Petrogenesis of meta-volcanic rocks from the maimon formation (dominican republic): Geochemical record of the nascent greater antilles paleo-arc. *Lithos*, 278:255–273.

Turner, S. J., Langmuir, C. H., Dungan, M. A., and Escrig, S. (2017). The importance of mantle wedge heterogeneity to subduction zone magmatism and the origin of em1. *Earth and Planetary Science Letters*, 472:216–228.

Ulmer, P. and Trommsdorff, V. (1995). Serpentine stability to mantle depths and subduction-related magmatism. *Science*, 268(5212):858–861.

Van Avendonk, H. J. A., Holbrook, W. S., Lizarralde, D., and Denyer, P. (2011). Structure and serpentinization of the subducting cocos plate offshore nicaragua and costa rica. *Geochemistry Geophysics Geosystems*, 12.

van der Lelij, R., Spikings, R. A., Kerr, A. C., Kounov, A., Cosca, M., Chew, D., and Villagomez, D. (2010). Thermochronology and tectonics of the leeward antilles: Evolution of the southern caribbean plate boundary zone. *Tectonics*, 29.

van Keken, P. E., Hacker, B. R., Syracuse, E. M., and Abers, G. A. (2011). Subduction factory: 4. depth-dependent flux of h2o from subducting slabs worldwide. *Journal of Geophysical Research-Solid Earth*, 116.

Van Soest, M. C., Hilton, D. R., Macpherson, C. G., and Mattey, D. P. (2002). Resolving sediment subduction and crustal contamination in the lesser antilles island arc: A combined he-o-sr isotope approach. *Journal of Petrology*, 43(1):143–170.

Venable, M. E. (1994). *A geologic, tectonic and metallogenic evaluation of the Siuna terrane.* Thesis, The University of Arizona, Arizona.

Vidal, P., Le Guen de Kerneizon, M., Maury, R. C., Dupré, B., and White, W. M. (1991). Large role of sediments in the genesis of some lesser antilles andesites and dacites (soufriere, st. lucia); isotopic constraints. *Bulletin de la Société Géologique de France*, 162(6):993–1002.

Villemant, B., Hammouya, G., Michel, A., Semet, M. P., Komorowski, J. C., Boudon, G., and Cheminee, J. L. (2005). The memory of volcanic waters: Shallow magma degassing revealed by halogen monitoring in thermal springs of la soufriere volcano (guadeloupe, lesser antilles). *Earth and Planetary Science Letters*, 237(3-4):710–728.

Voight, B., Hidayat, D., Sacks, S., Linde, A., Chardot, L., Clarke, A., Elsworth, D., Foroozan, R., Malin, P., Mattioli, G., McWhorter, N., Shalev, E., Sparks, R. S. J., Widiwijayanti, C., and Young, S. R. (2010). Unique strainmeter observations of vulcanian explosions, soufriere hills volcano, montserrat, july 2003. *Geophysical Research Letters*, 37:1–5.

von Huene, R. and Ranero, C. R. (2003). Subduction erosion and basal friction along the sediment-starved convergent margin off antofagasta, chile. *Journal of Geophysical Research: Solid Earth*, 108(B2).

Wadge, G. (1984). Comparison of volcanic production rates and subduction rates in the lesser antilles and central america. *Geology*, 12(9):555–558.

Wadge, G. and Shepherd, J. B. (1984). Segmentation of the lesser antilles subduction zone. *Earth and Planetary Science Letters*, 71(2):297–304.

Wadge, G., Voight, B., Sparks, R. S. J., Cole, P. D., Loughlin, S. C., and Robertson, R. E. A. (2014). An overview of the eruption of soufrière hills volcano, montserrat from 2000 to 2010. In Wadge, G., Robertson, R., and Voight, B., editors, *The Eruption of Soufriere Hills Volcano, Montserrat from 2000 to 2010, Geological Society Memoirs*, volume 39. The Geological Society of London, London, UK.

Wan, K. Y., Lin, J., Xia, S. H., Sun, J. L., Xu, M., Yang, H. F., Zhou, Z. Y., Zeng, X., Cao, J. H., and Xu, H. L. (2019). Deep seismic structure across the southernmost mariana trench: Implications for arc rifting and plate hydration. *Journal of Geophysical Research-Solid Earth*, 124(5):4710–4727.

Warner, A. J. (1989). The cretaceous age sediments of the saba bank and their petroleum potential. In *Transactions of the 12th Caribbean Geological Conference, St. Croix*, pages 341–354.

Watlington, R. A., Wilson, W. D., Johns, W. E., and Nelson, C. (2002). Updated bathymetric survey of kick-'em-jenny submarine volcano. *Marine Geophysical Researches*, 23(3):271–276.

Watt, S. F. L., Talling, P. J., Vardy, M. E., Heller, V., Huhnerbach, V., Urlaub, M., Sarkar, S., Masson, D. G., Henstock, T. J., Minshull, T. A., Paulatto, M., Le Friant, A., Lebas, E., Berndt, C., Crutchley, G. J., Karstens, J., Stinton, A. J., and Maeno, F. (2012a). Combina-

tions of volcanic-flank and seafloor-sediment failure offshore montserrat, and their implications for tsunami generation. *Earth and Planetary Science Letters*, 319:228–240.

Watt, S. F. L., Talling, P. J., Vardy, M. E., Masson, D. G., Henstock, T. J., Huhnerbach, V., Minshull, T. A., Urlaub, M., Lebas, E., Le Friant, A., Berndt, C., Crutchley, G. J., and Karstens, J. (2012b). Widespread and progressive seafloor-sediment failure following volcanic debris avalanche emplacement: Landslide dynamics and timing offshore montserrat, lesser antilles. *Marine Geology*, 323:69–94.

Watts, A. B., Koppers, A. A. P., and Robinson, D. P. (2010). Seamount subduction and earthquakes. *Oceanography*, 23(1):166–173.

Watts, A. B., Nomikou, P., Moore, J. D. P., Parks, M. M., and Alexandri, M. (2015). Historical bathymetric charts and the evolution of santorini submarine volcano, greece. *Geochemistry Geophysics Geosystems*, 16(3):847–869.

Watts, A. B., Peirce, C., Grevemeyer, I., Paulatto, M., Stratford, W., Bassett, D., Hunter, J. A., Kalnins, L. M., and de Ronde, C. E. J. (2012). Rapid rates of growth and collapse of monowai submarine volcano in the kermadec arc. *Nature Geoscience*, 5(7):510–515.

Weiss, M. (1994). Oligocene limestones of antigua, west indies: Neptune succeeds vulcan. *Caribbean Journal of Science*, 30(1-2):1–29.

Wessel, P. (2010). Tools for analyzing intersecting tracks: The x2sys package. *Computers & Geosciences*, 36(3):348–354.

Wessel, P. and Chandler, M. T. (2007). The mgd77 supplement to the generic mapping tools. *Computers & Geosciences*, 33(1):62–75.

Westbrook, G. K. (1982). The barbados ridge complex: tectonics of a mature forearc system. In Leggett, J. K., editor, *Trench-Forearc Geology: Sedimentation and Tectonics on Modern and Ancient Active Plate Margins*, volume 10, pages 275–290. Geological Society, London, Special Publications, London, UK.

Westbrook, G. K., Ladd, J. W., Buhl, P., Bangs, N., and Tiley, G. J. (1988). Cross-section of an accretionary wedge - barbados ridge complex. *Geology*, 16(7):631–636.

Westercamp, D. and Andreieff, P. (1989). *Martinique notice explicative carte geologique a 1/50 000*. BRGM.

Westercamp, D., Andreieff, P., Bouysse, P., Mascle, A., and Baubron, J. (1985). The grenadines, southern lesser antilles. i: Stratigraphy and volcano-structural evolution. In Mascle, A., editor, *Symposium Géodynamique des Caraibes*, pages 109–118, Paris, France. Technip.

White, D. A., Roeder, D. H., Nelson, T. H., and Crowell, J. C. (1970). Subduction. *Geological Society of America Bulletin*, 81(11):3431–3432.

White, R. S., Eccles, J. D., and Roberts, A. W. (2010). Constraints on volcanism, igneous intrusion and stretching on the rockall–faroe continental margin. *Geological Society, London, Petroleum Geology Conference series*, 7(1):831–842.

White, R. S., Mckenzie, D., and Onions, R. K. (1992). Oceanic crustal thickness from seismic measurements and rare-earth element inversions. *Journal of Geophysical Research-Solid Earth*, 97(B13):19683–19715.

White, R. V., Tarney, J., Kerr, A. C., Saunders, A. D., Kempton, P. D., Pringle, M. S., and Klaver, G. T. (1999). Modification of an oceanic plateau, aruba, dutch caribbean: Implications for the generation of continental crust. *Lithos*, 46(1):43–68.

White, W., Copeland, P., Gravatt, D. R., and Devine, J. D. (2017). Geochemistry and geochronology of grenada and union islands, lesser antilles: The case for mixing between two magma series generated from distinct sources. *Geosphere*, 13(5):1359–1391.

White, W. M. and Dupre, B. (1986). Sediment subduction and magma genesis in the lesser antilles - isotopic and trace-element constraints. *Journal of Geophysical Research-Solid Earth*, 91(B6):5927–5941.

Wishner, K. F., Graff, J. R., Martin, J. W., Carey, S., Sigurdsson, H., and Seibel, B. A. (2005). Are midwater shrimp trapped in the craters of submarine volcanoes by hydrothermal venting? *Deep-Sea Research Part I-Oceanographic Research Papers*, 52(8):1528–1535.

Wright, I. C., Chadwick, W. W., de Ronde, C. E. J., Reymond, D., Hyvernaud, O., Gennerich, H. H., Stoffers, P., Mackay, K., Dunkin, M. A., and Bannister, S. C. (2008). Collapse and reconstruction of monowai submarine volcano, kermadec arc, 1998-2004. *Journal of Geophysical Research-Solid Earth*, 113(B8):1–13.

Wright, J. E. and Wyld, S. J. (2011). Late cretaceous subduction initiation on the eastern margin of the caribbean-colombian oceanic plateau: One great arc of the caribbean (?). *Geosphere*, 7(2):468–493.

Yang, T. F., Lee, T., Chen, C. H., Cheng, S. N., Knittel, U., Punongbayan, R. S., and Rasdas, A. R. (1996). A double island arc between taiwan and luzon: Consequence of ridge subduction. *Tectonophysics*, 258(1-4):85–101.

Zami, F., Quidelleur, X., Ricci, J., Lebrun, J. F., and Samper, A. (2014). Initial sub-aerial volcanic activity along the central lesser antilles inner arc: New k-ar ages from les saintes volcanoes. *Journal of Volcanology and Geothermal Research*, 287:12–21.

Zelt, C. A. and Smith, R. B. (1992). Seismic traveltime inversion for 2-d crustal velocity structure. *Geophysical Journal International*, 108(1):16–34.

Zhao, Z., Moore, G. F., Bangs, N. L. B., and Shipley, T. H. (2000). Spatial variations of the décollement/protodécollement zone and their implications: A 3-d seismic inversion study of the northern barbados accretionary prism. *Island Arc*, 9(2):219–236.

Zhao, Z. Y., Moore, G. F., and Shipley, T. H. (1998). Deformation and dewatering of the subducting plate beneath the lower slope of the northern barbados accretionary prism. *Journal of Geophysical Research-Solid Earth*, 103(B12):30431–30449.

Appendix A

Appendix: Tracing Water Release Beneath the Lesser Antilles

A.1 Introduction

The breakdown of serpentine, stored in subducting fracture zones has been proposed as a key factor in controlling the distribution of crustal structure (Schlaphorst et al., 2018; Melekhova et al., 2019) and seismicity (Schlaphorst et al., 2016; Paulatto et al., 2017) along the Lesser Antilles. In order to properly understand the interplay of the various inputs along the arc it is therefore essential to understand where beneath the arc this focused dehydration occurs. However, between different studies there are major differences in the latitude at which these fracture zones are proposed to enter the trench (e.g. Schlaphorst et al. 2016 vs Carpentier et al. 2008), as they become obscured by thick sediments and deformation of the incoming plate.

This is particularly true for the Marathon and Mercurius fracture zones, which are obscured in potential field data by their proximity to the deformation associated with the uplift of the Tiburon Rise (Chapter 5). Further variations then arise in the methodology used to project these fracture zones beneath the island arc. This is complicated by major differences in slab geometry proposed for the arc, as a result of the historically low rates of seismicity (Bengoubou-Valerius et al., 2008; Bie et al., 2020). This leads to obvious inconsistencies in the expected location of water release from these fracture zones beneath the arc.

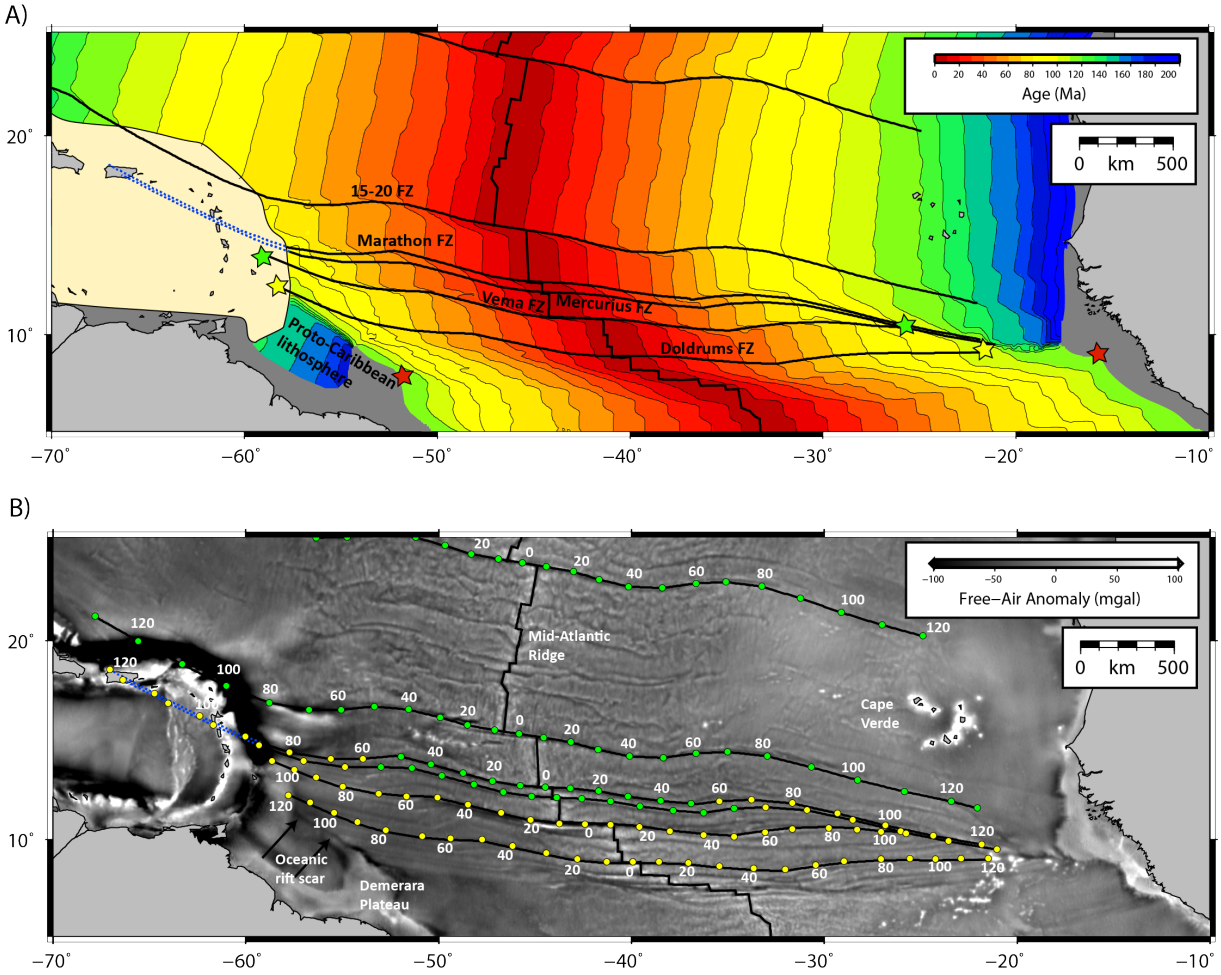


Figure A.1: A) Modelled fracture zones in the central Atlantic, overlain on an oceanic crust age grid from Müller et al. (2019). Coloured stars denote conjugate points associated with opening of the equatorial Atlantic at either end of the Vema (green) and Doldrums (yellow) fracture zones and between the Demerara rise and African continental margin (red). B) Modelled fracture zones overlain on satellite free-air gravity (Sandwell et al., 2014). Coloured dots correspond to age segments along modelled flow lines. Green dots are the result of central Atlantic spreading (NAM-AFR poles). Yellow dots are the result of equatorial Atlantic spreading (SAM-AFR poles). A change in rotation pole along the Marathon and Mercurius fracture zones at 50 Ma is the result of the northward migration of the effective NAM-SAM plate boundary.

A.2 Modelling Fracture Zone Locations

In order to better constrain the position of these fracture zones they are modelled as flow-lines in the recent global plate reconstruction of Müller et al. (2019) using the software G-Plates (in the Caribbean region this model is derived from the reconstruction of Boschman et al. 2014). The 15-20, Marathon, Mercurius, Vema and Doldrums (working north to south) are the highest offset fracture zones currently entering the Lesser Antilles trench (Figure A.1). Modelled flow-

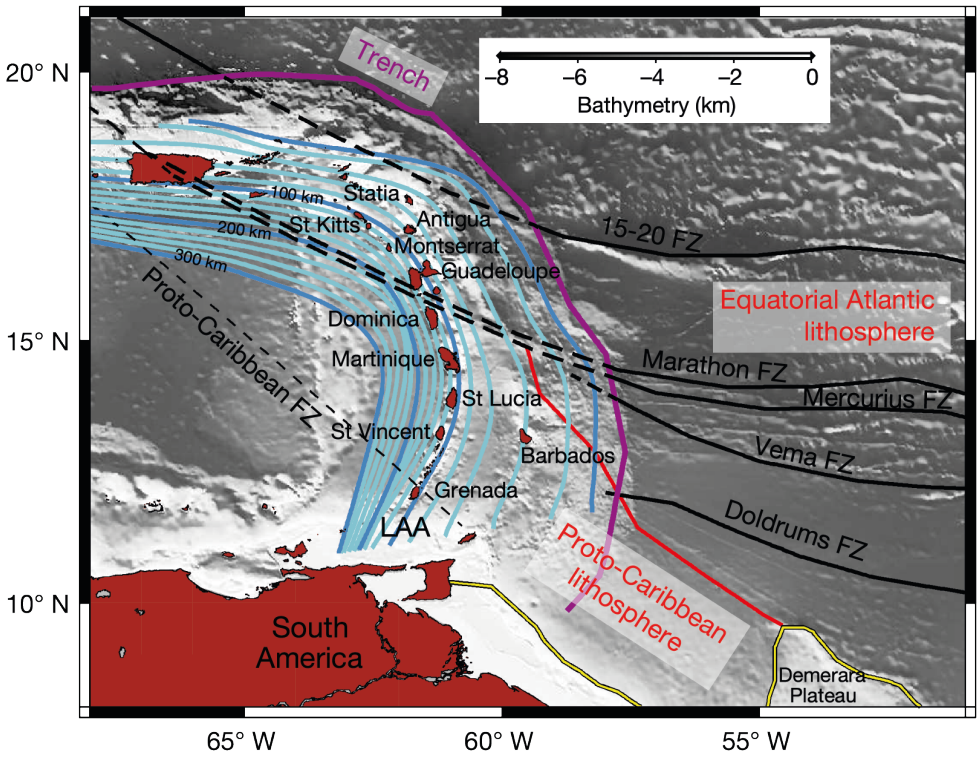


Figure A.2: Antilles slab structure, from Cooper et al. (2020). Projected fracture zone locations overlain on the final slab geometry of Bie et al. (2020). Slab is shown in blue, and is contoured at 20 km intervals. Note that the Marathon and Mercurius Fracture zones are the only features shown to subduct to sub-arc depths. Red line denotes the boundary between oceanic crust of the Proto-Caribbean and Equatorial Atlantic. The structure of the Proto-Caribbean portion of the slab is uncertain, but fracture zones would likely strike NW-SE across the slab.

lines are compared to the geometry of the fracture zones on the African side of the spreading centre, where there is significantly less sedimentary cover, and the fracture zones can be traced all the way to their termination against the African continental margin in satellite free-air gravity (Figure A.1). These flow lines are then assumed to be symmetrical within the western Atlantic. The highest misfit between these projected fracture zones, and the fracture zones observed in the gravity data is 50 km, and gives confidence that the projected locations of the fracture zones on the opposite side of the spreading ridge, as they enter the Antilles trench, are accurate. The best fit to the Marathon and Mercurius fracture zones is found with a transition within the Central Atlantic from spreading controlled by the North American - African rotation pole, to South American - African between 60-50 Ma as a result of the northward migration of the North American - South American plate boundary (Figure A.1).

Another important result of this modelling is that the Vema and Doldrums fracture zones are seen to terminate beneath the Lesser Antilles forearc, well short of sub-arc depths where the

breakdown of serpentine might start to influence arc processes (Figure A.3). These fracture zone terminations allow us to redefine the location of the boundary between crust formed as a result of proto-Caribbean spreading and spreading in the Equatorial Atlantic (see Section 3.3.2), extending it northward from the last remnant of proto-Caribbean material adjacent to the Demerara Rise (Figure A.3).

The geometry of the Mercurius fracture zone (prior to 50 Ma), can be explained entirely by spreading between North America and Africa (after which it is influenced by the northward migration of the North-South American plate boundary). This fracture zone therefore must have formed north of (or itself represents) the boundary between the Atlantic and proto-Caribbean lithosphere (all the fracture zones further south were formed during a later phase of spreading in the central Atlantic, governed by South-American / African relative motion, Figure A.3). The slab at sub-arc beneath the arc south of Dominica was therefore formed as a result of spreading in the proto-Caribbean, not the Atlantic. Although we know that the proto-Caribbean formed at similar spreading rates to the modern Equatorial Atlantic (Section 3.5), the distribution of potentially hydrated features such as fracture zones within this section of the slab is much more poorly constrained. There are also likely to be much larger north-south variations in the age of the slab beneath the Lesser Antilles than has been assumed previously.

Based on these assumptions the boundary between proto-Caribbean and the Central Atlantic spreading domains were updated in the G-Plates model, such that the initial triple junction between the spreading ridges in the Proto-Caribbean, Central, and Equatorial Atlantic spreading ridges formed at the Mercurius fracture zone. This updated geometry is shown in Figures 3.8 and 3.9. The rifted oceanic boundary between the crust of the proto-Caribbean and Equatorial Atlantic may itself represent a major hydration anomaly along the slab, though again it is yet to subduct to a significant depth below the arc, passing east of Barbados beneath the forearc (Figure A.3).

A.3 Calculating Water Release from Serpentine

On the basis of these modelled fracture zone locations Cooper et al. (2020) generated a new quantitative model of the release of water from the subduction of these features. From the catalogue of seismicity recorded using the VoiLA landstation and OBS network (see Section

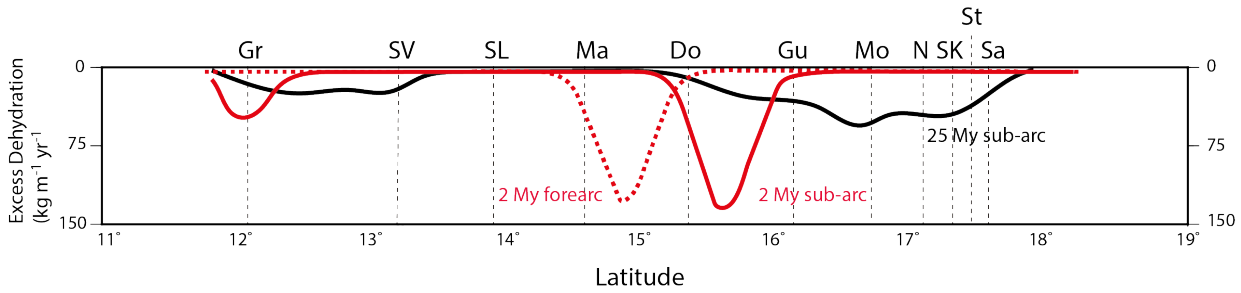


Figure A.3: Excess water release from serpentinized fracture zones beneath the Lesser Antilles Arc from the modelling of Cooper et al. (2020). Note the strong concentration of water released beneath the central part of the arc as a result of the subduction of the Marathon and Mercurius fracture zones. A high in the south of the arc is the result of a theoretical fracture zone within the proto-Caribbean portion of the slab. The location of such a feature is poorly constrained. Red, excess water release over last 2 My (checked: beneath forearc, solid: at sub-arc mantle depths), black, excess water release over last 25 My.

1.3, Figure 1.2), Bie et al. (2020) generated a new updated slab geometry for the region by combining this VoiLA dataset with older global catalogues. Compared to previous estimates of the slab geometry in the region, this new geometry showed a significant reduction in dip between the northern and southern sections of the arc. Assuming this slab geometry was constant through time (besides a small amount of vertical stretching, as the slab sinks into the mantle), and using the same estimated plate motions from the Müller et al. (2019) plate model the location of the key fracture zones, proto-Caribbean-Equatorial Atlantic boundary, and a theoretical, NE-SW striking fracture zone on the proto-Caribbean section of the slab were tracked across the slab through time. Making some basic assumptions about the degree of lithospheric alteration associated with each fracture zone, including a 15 km region of excess hydration about each feature, and 50% mantle serpentinization, these fracture zone positions were then converted into a direct volumetric estimate of water release beneath the arc over the last 25 My (Figure 8.1C).

Appendix B

Appendix: Chapter 4, Data Processing and Supporting Data

This appendix appears as supplementary material to the paper Allen et al. (2019), discussed in Chapter 4 and contains further information on the acquisition and processing of geophysical data well as supporting geochemical/geochronology studies

Allen, R., Collier, J., Stewart, A., Henstock, T., Goes, S., Rietbrock, A., and the VoiLA Team (2019). The role of arc migration in the development of the lesser antilles: A new tectonic model for the cenozoic evolution of the eastern caribbean. *Geology*, 47(9):891–895.

Key contributions of other named authors:

Henstock, T., Collier, J. S.: Project supervisors, planned R.R.S. James Cook geophysical surveys and undertook initial data processing at sea.

Stewart, A. (MSci Student, University of Bristol): Assisted understanding of regional geochemical and geochronological constraints. Wrote Section B.3 in order to expand on these arguments.

B.1 Magnetics

Our new magnetic anomaly grid is created from a dataset of 335 cruises covering the time period from 1960-present (Figure B.1). A region much larger than the target study area of the Lesser Antilles was chosen in order to maximise the treatment of historical cruises which transit across the study area. By including comparatively simple, well studied areas of oceanic crust (e.g. Atlantic crust of the North American plate) with well documented magnetic anomalies we are able to provide a qualitative benchmark for the data quality of the grid as a whole. The accurate capture of seafloor spreading anomalies (Figure B.2) in our grid allows us to interpret similar scale magnetic features in the more tectonically complex Caribbean interior region with confidence.

An initial dataset of 347 cruises was compiled across the region. The bulk of these ship-tracks (327) came from the compilation of Quesnel et al. (2009), a cleaned version of NGDC (National Geophysical Data Centre) magnetic survey data supplemented with a further 18 IFREMER cruises requested from the SeaDataNet database and two cruises (JC133 and JC149) from our own VoiLA (Volatile Recycling in the Lesser Antilles) research project. These additional cruises were independently screened for data spikes and navigational errors. IFREMER cruise data was converted from MGD77 format to useable .gmt files with the MGD77 supplement to the generic mapping tools (Wessel and Chandler, 2007). Data coverage across the study area is generally excellent with the final grid containing more than 1.3 million individual magnetic anomaly points (Figure B.1). Coverage is understandably poor in the very shallow water of the Bahamas Platform, South American passive margin and the Nicaragua Rise. There are also regions of comparatively low data density on the incoming plate to the north and northwest of the study area. However this has not had any great impact on our ability to resolve seafloor spreading anomalies in these areas.

Magnetic anomalies for all cruises were calculated by subtracting the IGRF12 global reference field. Cross-over analysis (Hsu, 1995; Wessel, 2010; Chadwick et al., 2012) was used to provide a quantitative assessment of overall dataset quality by comparing the differences between magnetic anomaly values at intersecting ship-tracks. Initial cross-over analysis of all cruises gave a mean cross-over error of 46.0 nT (from 18207 ship-track interactions).

Diurnal corrections were applied to all cruises based on data from the three nearest permanent

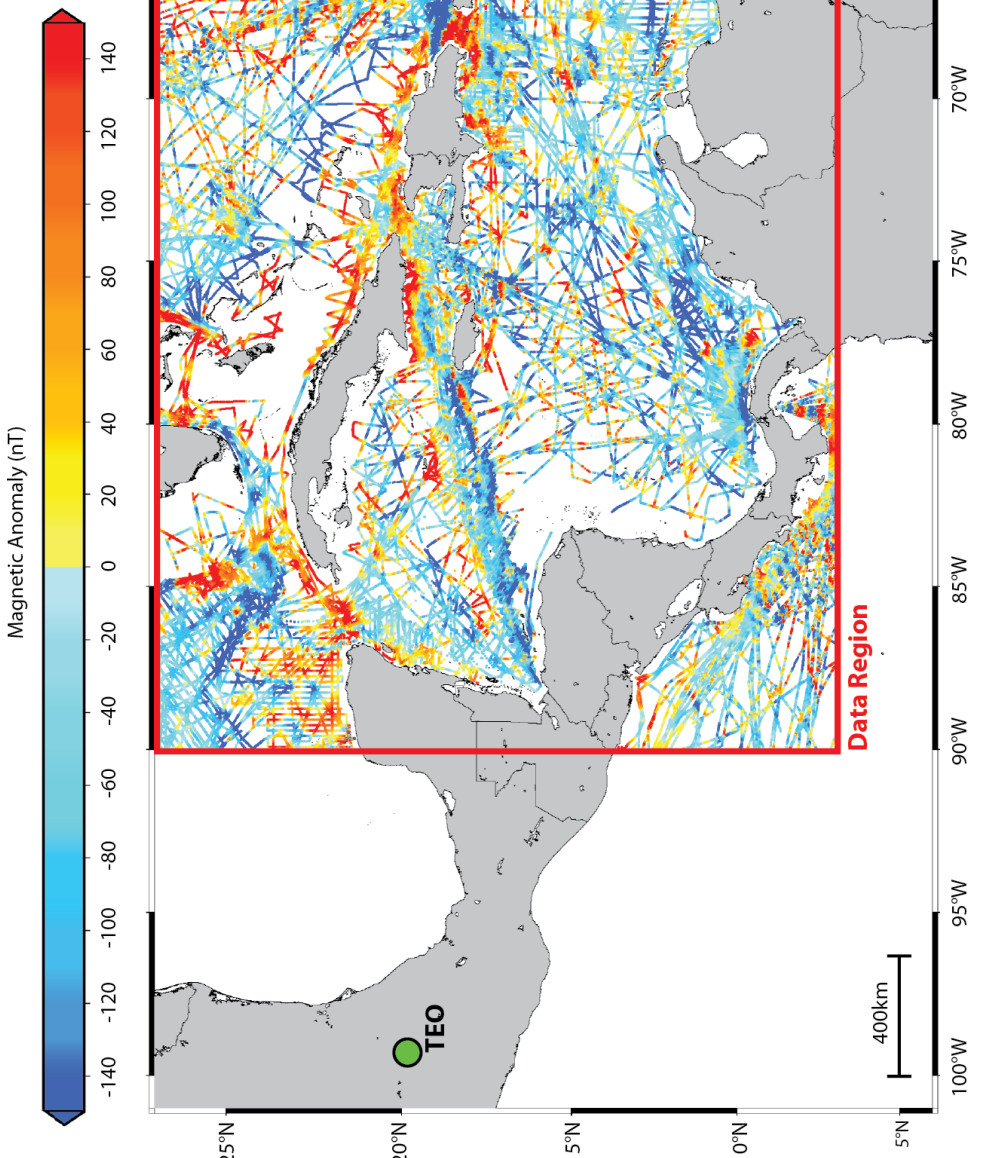


Figure B.1: Map of the ship-track data used in construction of the final magnetic grid across the region. The locations of the three magnetic observatories used in the study are shown as green dots.

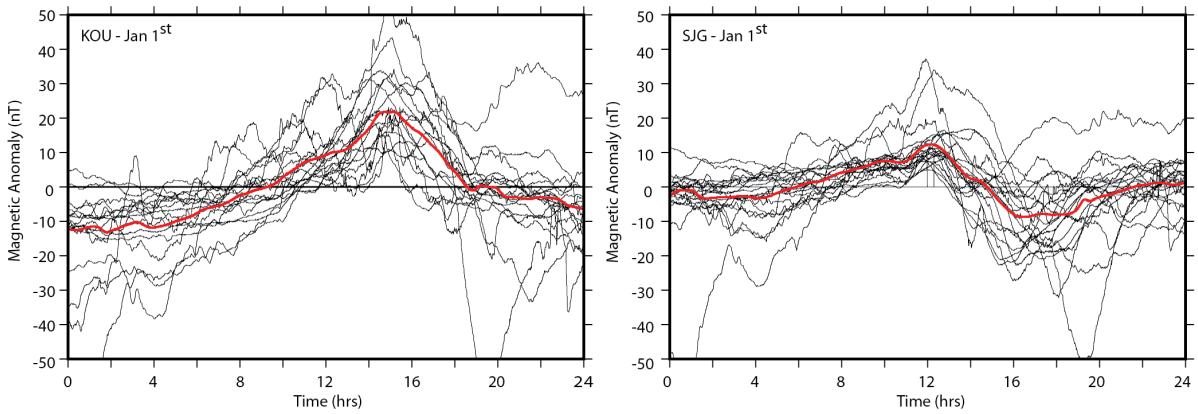


Figure B.2: Diurnal variation curves for two of the magnetic observatories used in the study (SJG and KOU). Fine black lines show measurements made on the 1st January (UTC time) for each year for which data was available. The mean curve is shown in red. The large variation in the magnetic field about this mean, along with the absence of data in the early decades of the study explains the need for levelling of the full dataset.

geomagnetic observatories (TEO: Mexico, SJG: Puerto Rico, KOU: French Guiana, Figure B.1). Data was downloaded from the INTERMAGNET online database. Annual mean diurnal variation curves, sampled at 1 minute intervals, were calculated for each observatory from all available data up to the present day (TEO: 10 years, SJG: 21 years, KOU: 21 years, Figure B.2). These three curves were then used to apply a diurnal adjustment to each individual magnetic anomaly measurement, weighted depending on the linear distance from each of the 3 observatories. This correction only led to a relatively minor reduction in the whole dataset mean xover error to 45.5 nT.

This small improvement was not unexpected given (i) the relatively poor geographical coverage of geomagnetic observatories (ii) the limited recording window (the observatories are only active for about 40% of the time covered by the ship-tracks used and even within that contain extended periods of absent data), (iii) the annual variability of the Earth's magnetic field measurement (curves for individual years regularly deviate from the mean by +/- 20 nT, Figure B.2), and (iv) the accuracy of applying this curve back through time. A regional levelling process was subsequently applied to the whole dataset in order to more accurately reduce the impact of these poorly captured magnetic field variations.

Before further processing the worst quality cruises (12 cruises, those with mean xover errors

of greater than 100 nT) were removed, leaving a final dataset of 335 cruises. This reduced the mean xover error for the dataset to 41.7 (from 17811 interactions) with little impact on the data coverage. The dataset was levelled regionally using the same methodology as Quesnel et al. (2009) to reduce the cross-over error between intersecting tracks. This process corrects the ship-tracks on a regional scale for non-geological variability resulting from factors such as positioning errors as well as outstanding temporal field variations.

In the first step of the levelling process the differences between a given magnetic measurement and all other readings within 10 km (ignoring those along the same ship-track) were calculated. Each of those differences was then given a weight (w) by distance (equation 1, r is distance and r_0 is a constant with a value of 2 km) and summed to calculate an overall regional difference value for each reading, with the closest readings being the most heavily weighted. These difference values were then filtered along each ship-track using a 50 km Gaussian filter. This prevents the applied difference changing too rapidly along a single ship-track, for instance if it enters a region of particularly low data density, or is strongly influenced by a particularly anomalous reading(s) from another ship-track. Filtered differences were then added back on to the original track measurements to give the final levelled magnetic anomaly value.

Equation 1:

$$w = (r_0^2/(r_0^2 + r^2))^2$$

Following this process the absolute mean cross-over error was reduced to 22.5 nT (for the final total of 17811 cross-overs). This improvement in the cross-over error is clearly demonstrated in Figure B.3.

The levelled data were gridded in GMT with a single cruise weighting applied based on the track xover errors such that the highest quality cruises would be counted most strongly in the final grid (Smith and Wessel, 1990). Our final marine magnetic chart for the region is gridded at 2 arc minutes (3.5 km x 3.7 km assuming 15 degrees latitude i.e. $\sim$13 km^2). The final processing step was a Reduction to Pole carried out in GMT using a window of 0.5 degrees and a filter of 25 coefficients (Figure B.4). Inclination and declination were taken from the IGRF12 grid.

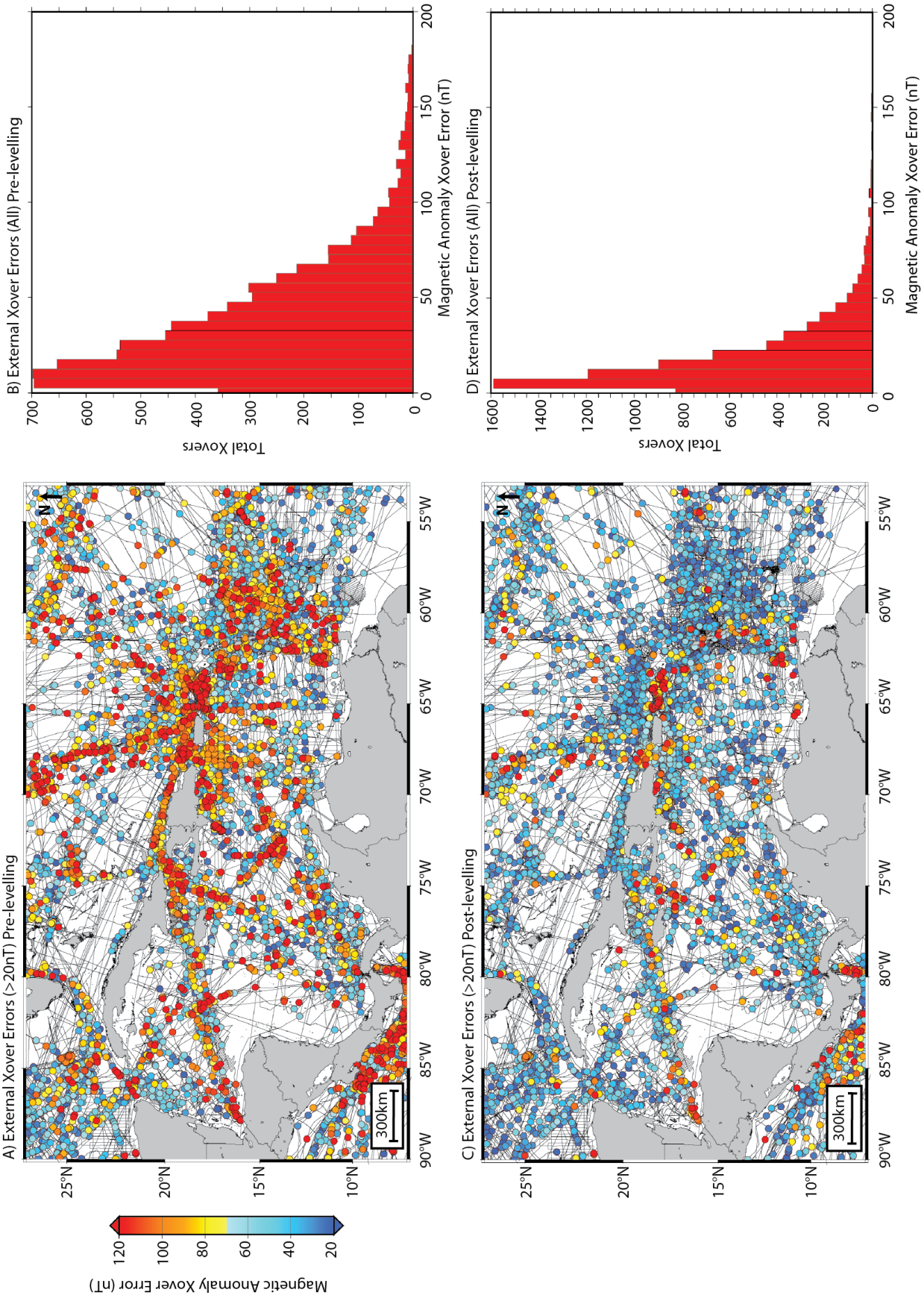


Figure B.3: A) Absolute external Xover errors (difference in magnetic field value) for intersecting ship-tracks prior to levelling. Only errors greater than 20 nT are shown. B) Data shown in A plotted as a histogram. C-D) As A-B following levelling.

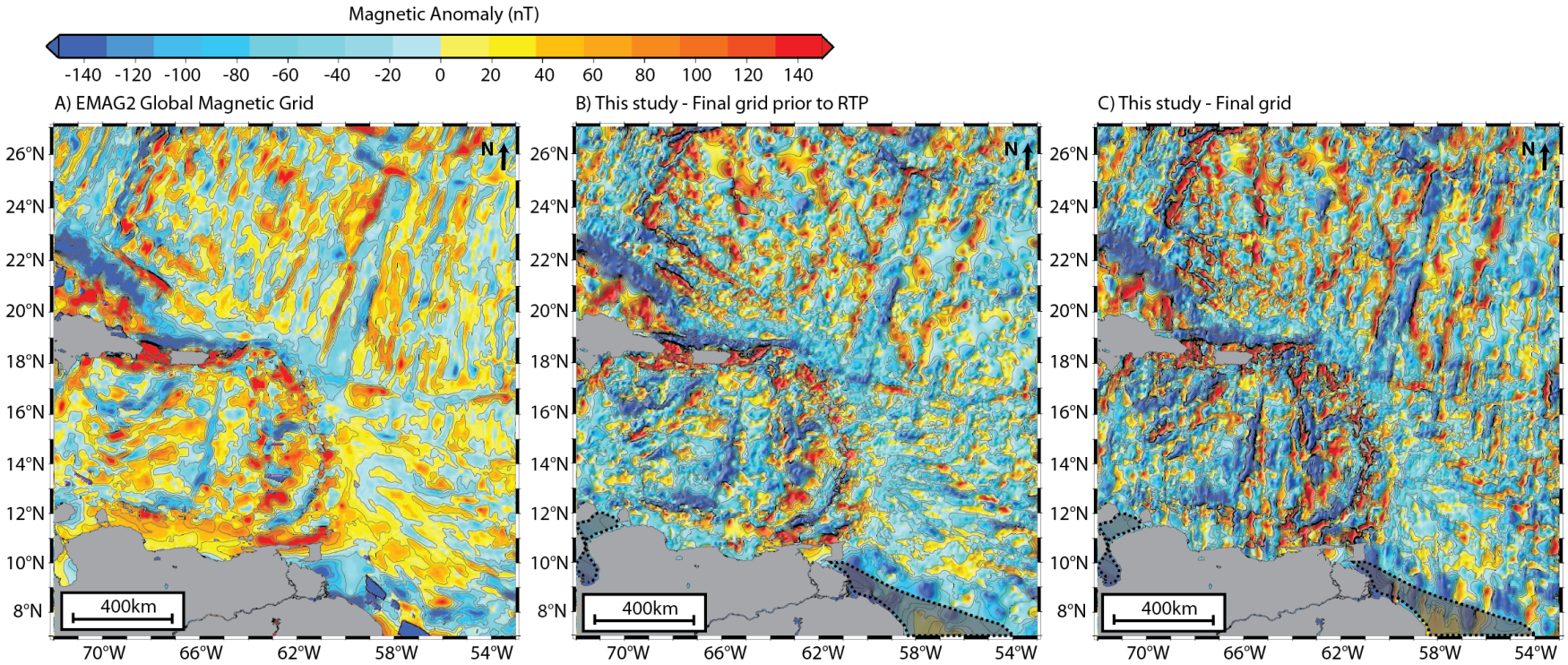


Figure B.4: Comparison of three magnetic anomaly grids. All grids are shown with the same illumination and contouring. A) The EMAG2 global magnetic grid (Maus et al., 2009) B) Magnetic anomaly grid from this study prior to application of reduction-to-pole. C) Final magnetic anomaly grid fro 362 m this study. Figure demonstrates the significantly lower resolution of the dominantly satellite based grid compared to our result based wholly on marine data.

B.2 Seismic

B.2.1 Introduction

The seismic data used for this study was acquired by the R.R.S. James Cook in the period April-May 2017 (Collier, 2017). The survey consisted of a series of 8 MCS and Wide-angle seismic profiles largely orientated (N-S) throughout the Grenada backarc Basin (Figure B.5). The results from profiles 4, 6 and 5+8 are given here. The data were acquired using a 13 gun seismic array of nominal 4800 cu in (79 L) volume and 2000 psi (14 MPa) pressure and towed streamer (3000 m long for profiles 4 and 5, 300 m long for profiles 6 and 8). All data acquisition was done at a speed of 5 knots with a 60 second shot interval leading to an approximate shot spacing of 150m. Shots were recorded by a network of 34 OBS stations (10 Scripps, 24 DEPAS instruments) throughout the Antilles region. Note that there are two breaks in the R.R.S. James Cook shooting tracks due to permitting issues. This was partly compensated by the recording of shots during the GARANTI experiment by our seabed network. These shots (profile gar1 – see Figure B.5) have been used to supplement our own set of picks for the wide-angle modelling along profiles 5 and 8.

The location of the new profiles relative to previous seismic experiments in the area is shown in Figure B.5. Profile 4, in the Southern Grenada Basin, overlaps with previous studies conducted by Christeson et al. (2008) and Boynton et al. (1979) with the more recent study finding oceanic like crust underlying the southern Grenada Basin. In comparison the northern Grenada Basin is much less well studied, with Kopp et al. (2011), off Guadeloupe, the only previous active source seismic experiment close to this region of the backarc.

B.2.2 MCS Processing

Individual profiles were processed using a standardised processing flow. After geometry assignment all traces were first filtered using an Ormsby bandpass filter (3-8-100-200 Hz) for noise reduction. A minimum phase predictive deconvolution with a 200 ms operator was then applied. A spherical divergence correction with a time-power constant of 2.3 (i.e. t*2.3) was applied prior to NMO (Normal Moveout Correction). NMO semblance velocity analysis was

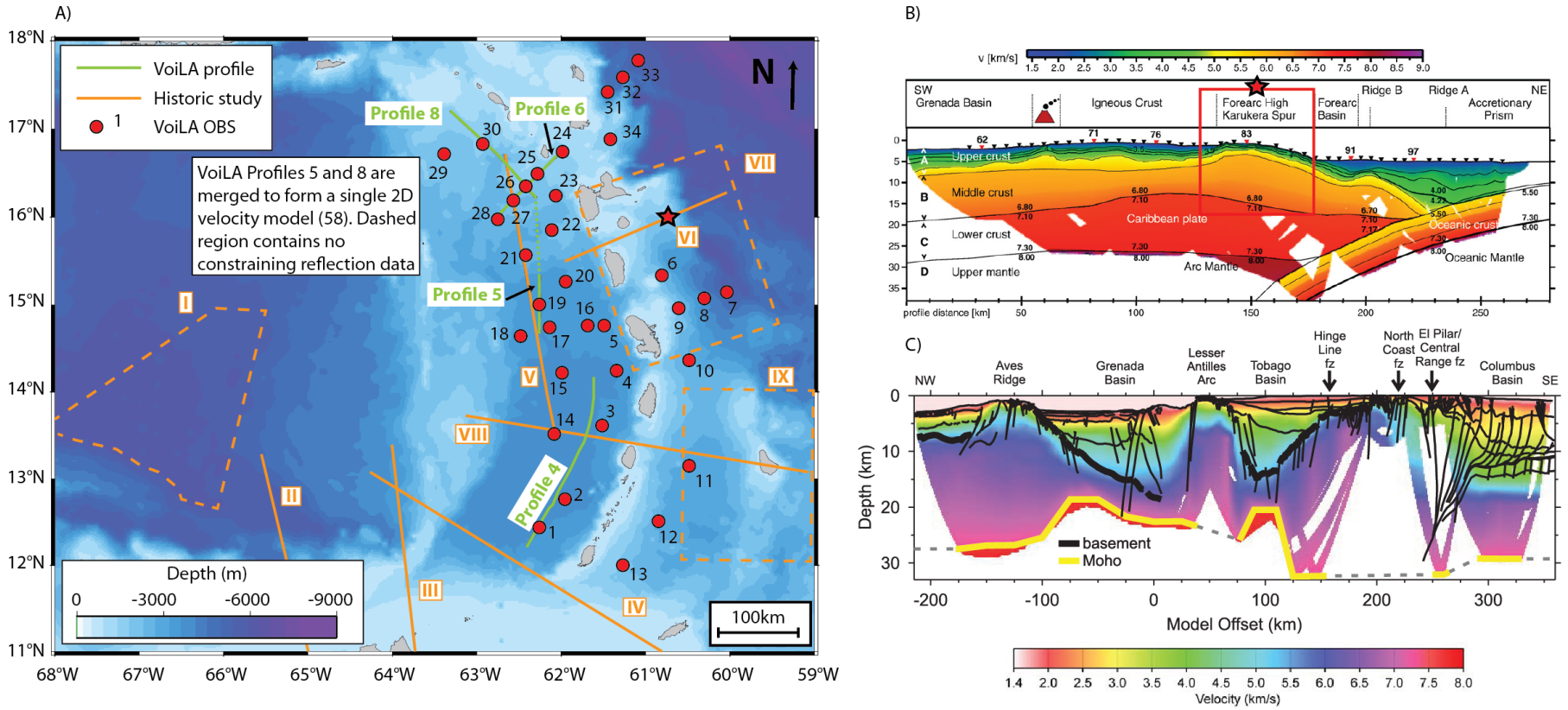


Figure B.5: A) Locations of VoiLA seismic lines (green) and previous seismic studies (orange) in the study area. VoiLA OBS network is shown by red dots. Dashed green line shows the section of profile 58 which is not constrained by reflection data. Seafloor depth over this section was taken directly from regional bathymetry, whilst basement depth was just extended linearly from the end of line 5 to the start of line 8 prior to forward modelling. The key to the historical (orange) profiles is as follows. I = region of oceanic crust identified by Diebold et al. (1981) in the south-eastern Venezuelan Basin, II - IV = wide-angle profiles from the BOLIVAR project described in Bezada et al. (2010), Clark et al. (2008), Christeson et al. (2008) respectively, V = profile gar1 from the GARANTI 2017 experiment (Lebrun, pers. comm.). Shots from this profile were recorded on the VoiLA OBS network and used to supplement wide-angle modelling along profile 58. VI = wide-angle profile described in Kopp et al. (2011). VII = SISMANTILLES experiment (Evain et al., 2013; Laigle et al., 2013). VIII = profile from Boynton et al. (1979). IX = Commercial multi378 channel seismic reflection data shown in Gomez et al. (2018). B) P-wave velocity model for offshore Guadeloupe (historical profile VI) from Kopp et al. (2011). Star highlights forearc high coincident with outer arc identified in magnetics. C) P-wave velocity model for southern arc transect (historical profile IV) from Christeson et al. (2008).

used for the lines which were shot using the long (3000 m) streamer (lines 4 & 5). For processing of the short (300 m) streamer lines (6 and 8) a constant velocity depth function was used (1480 ms^{-1} to 2200 ms, 1500 m^{-1} to 3500 ms, 2000 ms^{-1} to end). Traces were summed using a mean method to produce the final stacks.

B.2.3 Wide-Angle Modelling

Most wide-angle OBS stations recorded arrivals at distances of up to 80 km with the longest picked offsets coming from >180 km.

As the acquisition geometry was not a purpose designed refraction survey the OBS do not lie directly along acquisition lines. For modelling therefore stations were projected onto the nearest point along the shot line. Shots locations were then relocated by the same amount along the line, to maintain the source-receiver offset. The biggest such relocation used in the study was ∼15 km. As a result the models produced are not a perfect representation of the crust along the line, but should instead be thought of as regional "type" lines, representative of an average crustal structure within the vicinity of the line. Occasionally two stations would project onto similar places despite being separated geographically by several 10s of km. In some cases this made it impossible to achieve a working model due to significant changes in crustal structure outside of the plane of the profile (e.g. stations 3 and 14, which are separated by 60 km geographically, but project within 10 km of each other along profile 4). In such an event the closer station was chosen (unless distances were similar and one station possessed notably higher data quality).

All profiles were modelled as a 2D profiles in the ray-tracing software RAYINVR (Zelt and Smith, 1992), which uses a Runge-Kutta method to solve the ray tracing equations in 2D. Lines 5 and 8 were modelled as a continuous combined 2D profile (this combined profile is referred to as line 58 from here onwards) using arrivals from 6 stations (18, 19, 21, 23, 26, 30). Shots from the French R/V L'Atalante cruise line gar-1 were used to further supplement the pick set in this area and contributed greatly to bridging the gap between lines 5 and 8. However, basement depth is poorly constrained in the ∼90 km gap between the two lines where no MCS data was acquired. Lines 4 and 6 were modelled as stand-alone velocity profiles using picked arrivals from 3 OBS (1, 2 and 3) and 5 OBS (24, 25, 26, 27, 28) respectively. For lines

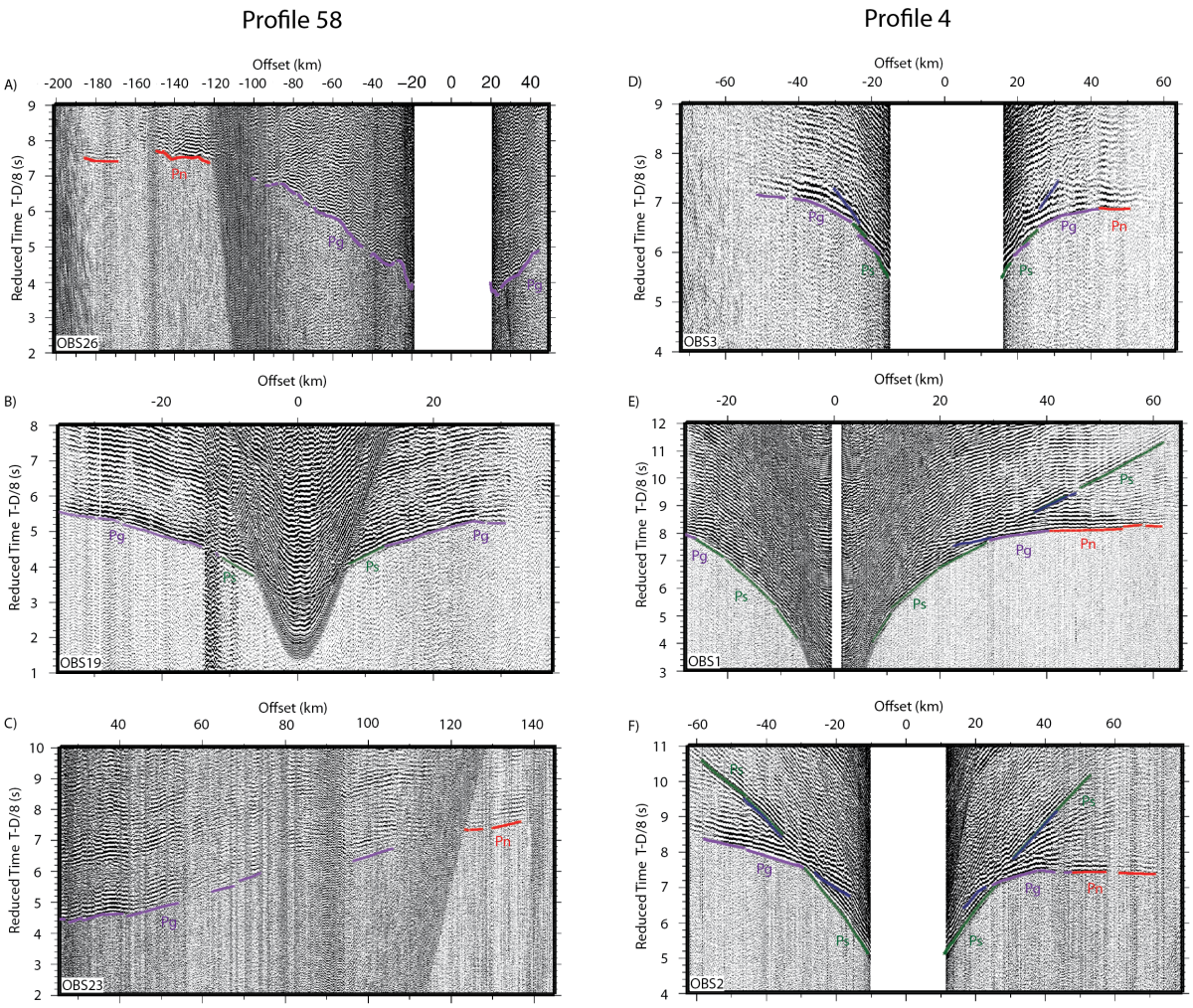


Figure B.6: Examples of six receiver gathers from broadband OBS used in the study. All images show the vertical component (BHZ) of the instrument and have been reduced to 8 kms^{-1} such that mantle arrivals will appear flat. A) OBS26, B) OBS19, C) OBS23, receiver gathers from OBS stations in the northern Grenada Basin. Only sediment (Ps) and crustal arrivals (Pg) are apparent up to offsets of 100 km. Thick crust in the region is indicated by very long offset of the 387 mantle Pn arrivals (>100 km) D) OBS3, E) OBS2, F) OBS1, receiver gathers from stations in the southern Grenada Basin. Clear arrivals are shown from the sediment column, crust and mantle, as are top basement reflections. The first arrivals from the mantle are observed at a relatively short offset (50 km), owing to the thin crust in this region. Secondary sediment arrivals are visible to very long travel times due to the thick sediments of the southern Grenada Basin.

4 (235 km) and 58 (325 km) velocity nodes were 10 km apart. For line 6 which is shorter (135 km) a 5 km spacing was used.

Seafloor and top basement surfaces were picked from the MCS data for each of the profiles. In some regions the presence of a strong seafloor multiple made the top basement hard to

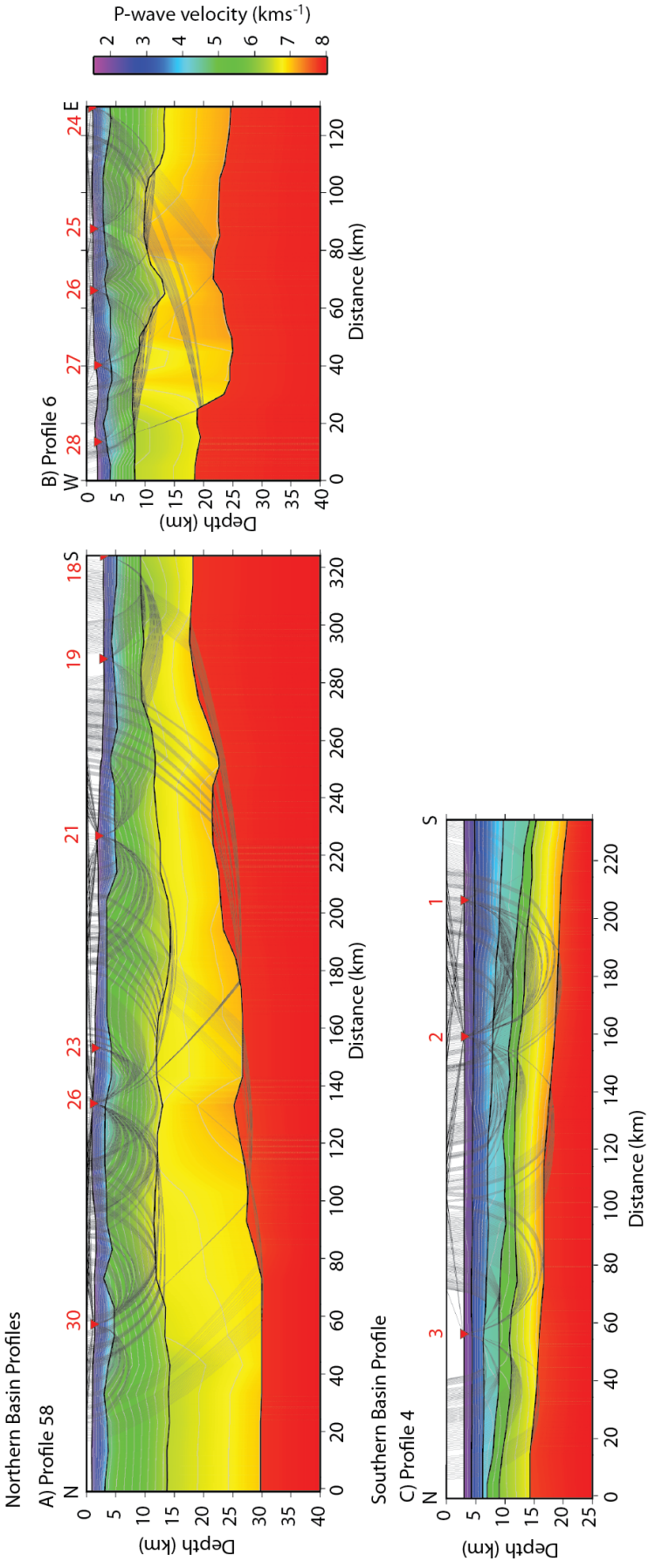


Figure B.7: Final p-wave velocity models. Profile locations are given in Figure B.5 and Figure 4.3 in the main text. All profiles are plotted to the same scale.

interpret. These picks were modelled as reflected phases at 10 km intervals along each of the profiles. A water column velocity of 1.52 km s^{-1} was assumed for all lines, while sediment velocities were determined by modelling of picked arrivals from the sediment column as turning rays and constrained by the top basement travel time picks from the reflection profiles.

In the southern part of the Grenada Basin, there is very little seafloor topography and a relatively flat top-basement surface. Clear Pg and Pn arrivals along with reflected phases from the top basement were identified (Figure B.6 A-C). The thick sedimentary section in the southern basin also meant that turning rays in the deepest sedimentary package were recognisable to exceedingly long travel times (almost 20 s) and offsets (60 km). On all 3 instruments there is a clear $\sim$8 kms^{-1} (Pn) refractor that is clearly the result of the backarc Moho.

In the northern region of the survey, where the seafloor and crustal topography are more heterogeneous it proved difficult to pick consistent reflected phases (Figure B.6A). As a result the velocity models for lines 58 and 6 are entirely built from P-wave first arrival picks separated into distinct upper and lower crustal units. The very thick crustal section (up to 30km in some places) limited the number of recorded arrivals from below the Moho, which is poorly constrained compared to the southern profile, with arrivals from the mantle only appearing at comparatively long offsets of over 100 km.

The final models shown were produced using the software RAYINVR (Zelt and Smith, 1992) through a process of iterative forward modelling until a best overall model fit was achieved, whilst trying to avoid the addition of very extreme lateral velocity variations at depth. Starting models were based on the few existing studies of the Grenada Basin region, with a typical oceanic crustal structure in the southern basin (Christeson et al. 2008, Figure B.5C) and a thick 2 layer crustal structure in the northern arc, based on the outcomes of the studies of Kopp et al. (2011, Figure B.5B) and Sevilla et al. (2010). The thick sediments in the southern Grenada Basin were modelled as 3 layers based on the interpretation of Aitken et al. (2011). The final models shown in Figure B.8 (Main text Figure 5.4) have normalized chi squared values of 0.720 (Line 4 - RMS: 0.085 s), 1.421 (Line58 - RMS: 0.119 s) and 1.427 (Line 6 - RMS: 0.119 s) respectively, with all picks assigned an uncertainty of 0.1 s.

B.3 Timing of Igneous Activity in the Lesser Antilles Region

B.3.1 Late Cretaceous to mid-Paleocene: GAC and Aves Ridge

Records of magmatism associated with the Great Arc of the Caribbean (GAC) can be found across the Aruba-Blanquilla archipelago, extending to the south-eastern part of the Aves Ridge. The volcaniclastic and intrusive rocks of Bonaire (c. 98 - 88 Ma) have long been recognised as an island arc suite related to the progressive obduction of the GAC across the South American continent during the Cretaceous (Thompson et al., 2004; Wright and Wyld, 2011).

During the late Cretaceous and Paleocene, widespread, subduction-related crustal melting resulted in the intrusion of adakitic granitoids throughout the Dutch and Venezuelan Antilles (Neill et al., 2011). On Aruba and Curacao, mafic and volcaniclastic rocks associated with the Caribbean Large Igneous Province (CLIP) are intruded by late Cretaceous (c. 89 – 86 Ma) diorites and quartz-diorite dykes and plutons (Sinton et al., 1998; White et al., 1999). Paleocene quartz-diorites, pegmatites and aplites also intrude CLIP basement on Grand Roque, (c. 68 – 64 Ma) (Thompson et al., 2004). Additional tonalites, trondhjemites and aplites of late Cretaceous to Paleocene age (c. 74 – 59 Ma) are found on the island of La Blanquilla and were also recovered from dredge hauls along the Aves Ridge (Neill et al., 2011; Wright and Wyld, 2011). Similar granitoid complexes intrude the metamorphic basement on the island of La Orchila (60km east of Gran Roque), but are undated. Further eastward; tonalites, trondhjemites, pegmatites and sodic granites are also found on Margarita (c. 76 Ma) and the neighbouring islands of Los Hermanos and Los Testigos. A small, anomalous exposure of undated tholeiitic basalts and gabbros is found on the island of Los Frailes, 5 km to the northeast of Margarita (Santamaria and Schubert, 1974). The emplacement of the igneous rocks on the islands of Gran Roque to Margarita are likely contemporaneous with backarc spreading in the eastern VB, the result of the eastward migration of the GAC/Aves Ridge system.

Currently, there is no record of subduction-related magmatism younger than c. 59 Ma in the Dutch or Venezuelan Antilles. The exact timing of abandonment of the Aves Ridge system is difficult to constrain due to the lack of exposure and more detailed geochronological evidence but is likely represented by the youngest granitoid rocks of Gran Roque, La Blanquilla, Mar-

garita and Los Testigo. It may be no coincidence that this is also the estimated date of the collision of the GAC with the Bahamas Bank. It is clear, however, that a drastic change in the composition of igneous rocks in the mid-Paleogene, from mostly adakitic TTG (tonalite-trondhjemite-granodiorite) suites to dominantly sub-marine basaltic and mafic volcaniclastic rocks (see Section B.3.3), must reflect a fundamental change in the tectono-magmatic environment during this time period (Figure B.8). In our new model we use these lines of evidence, together with the magnetic anomaly results, to infer a >300 km eastward shift of the subduction axis during the Paleogene.

B.3.2 Eocene to Early Miocene: Outer Arc

Subduction magmatism in the north-eastern Caribbean was fairly continuous during the Paleogene. The locus of activity migrated steadily from west to east, from Puerto Rico though to the Virgin Islands and then the Limestone Caribbees, as the obliquity of subduction increased following the collision of the GAC with the Bahamas bank. In our model, the gap in records of subduction magmatism in the southern LAA from c. 59 Ma is attributed to the onset of backarc spreading related to the Outer Arc.

There is direct evidence of renewed subduction-related magmatism in the Lesser Antilles from islands of the Limestone Caribbees, situated to the northeast of the modern LAA (Davidson et al., 1993). On St. Barthelemy, St. Martin and Antigua, Upper Eocene to Oligocene (c. 38 – 22 Ma) sub-marine and sub-aerial volcanic rocks with associated littoral carbonates and hypabyssal plutons are exposed (Westercamp et al., 1985; Andreieff et al., 1988b; Weiss, 1994). An older series of early to mid-Eocene (c. 57-40 Ma) intercalated intermediate to felsic volcanogenic strata and pelagic sediments is exposed beneath the Upper Eocene series on St. Martin (Andreieff et al., 1988b). Given its nearly continuous stratigraphic relationship with the over-riding mid-Eocene arc-related sequence and mineralogical composition, it is also likely to be arc related. To the west, Paleocene igneous rocks (c. 66 – 64 Ma) capped by Eocene limestones were recovered from a drill core off the Saba Bank and Anegada Passage (Warner, 1989), and various early Paleogene to Eocene subduction-related igneous rocks are found throughout the US and British Virgin Islands in the Greater Antilles (Jolly et al., 1998; Lidiak and Jolly, 1998). To the south, there are no ubiquitous exposures of Paleogene igneous rocks along our newly recognised Outer Arc. However, a continuous sequence of regularly

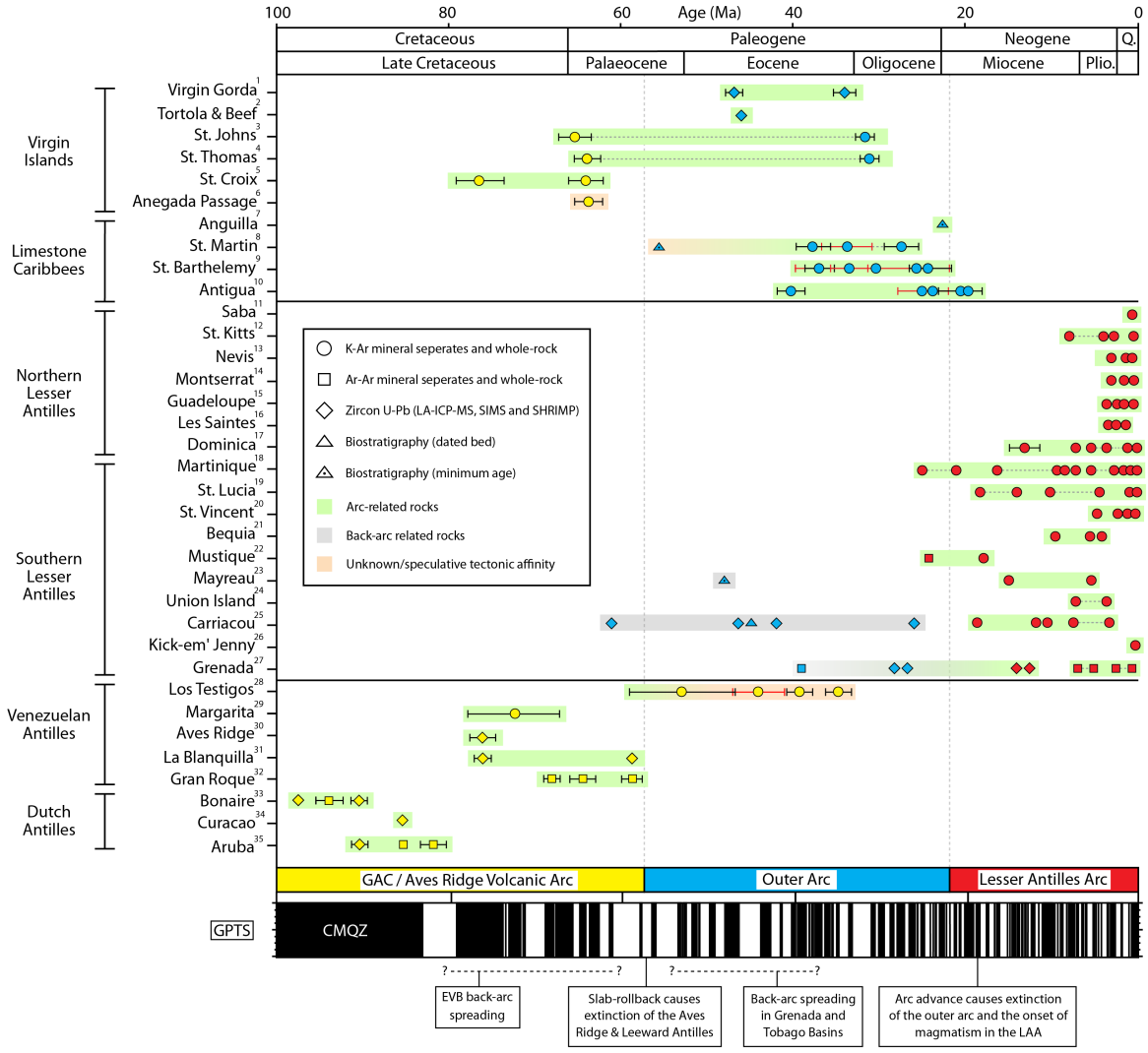


Figure B.8: Age distribution of igneous activity in the eastern Caribbean from the Late Cretaceous to the present. Ages presented in the diagram have been derived from in situ rock samples, dredge hauls, drill cores and xenocrystic and detrital igneous zircons, using radiometric and biostratigraphic constraints. Samples with an arc origin are highlighted in green, those with a backarc origin in grey and disputed tectonic affinity are highlighted in pink. Errors bars for radiometric ages are shown when uncertainties are $\geq$1 Ma. Dashed grey lines connect the lower and upper ages of roughly continuous magmatic activity. Individual data points are coloured yellow, blue or red according to the tectonic stage of our new model (see bar at bottom which is shown together with a magnetic polarity timescale for reference). It should be noted that the variable lower greenschist facies metamorphism of rocks found in the Dutch and Venezuelan Antilles, and common post-magmatic alteration of rocks in the Lesser Antilles means that K-Ar ages may not be an accurate representation of crystallisation age and must be interpreted with caution. For locations see Figure B.9. Data referencing details are given in Table A1.

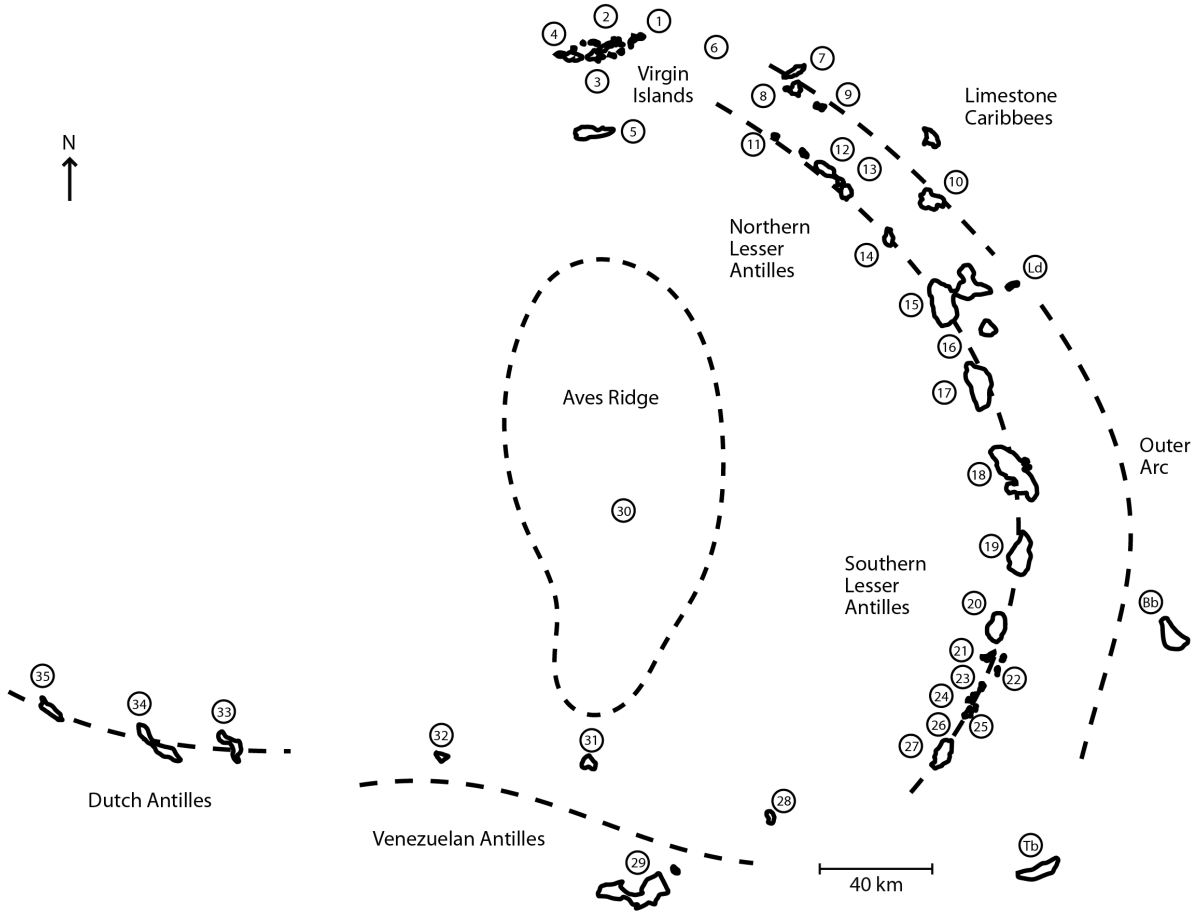


Figure B.9: Map showing location of all islands discussed in section B.3 and featuring in age distribution Figure B.8.

interbedded feldspar-quartz-mica bearing volcaniclastic tuffs and hemipelagic sediments of Upper Eocene to Oligocene age are found within the "Oceanic Formation" of Barbados (Senn, 1940; Saunders et al., 1984). The origin of these volcanic rocks is ambiguous but does provide evidence of magmatic activity in the region of the outer arc during the Paleogene.

Jurassic to Cretaceous (c. 145 Ma) rocks believed to have formed as part of the GAC arc and backarc can also be found much further east, in the Lesser Antilles arc. These exhumed metavolcanics rocks form the basement of La Desirade (Ld) in the central arc segment and on Tobago (Tb) in the south (Neill et al., 2010; Corsini et al., 2011). The new tectonic model presented here, with a previously unrecognised Outer Arc, provides a mechanism for the emplacement of these rocks east of the currently active LAA.

Indicators of Paleogene magmatic activity can also be found throughout the southern Lesser Antilles islands however, it is contested whether any of these are indicative of arc magmatism

at this time, with most samples demonstrating a backarc affinity. In the Grenadines, Paleocene to mid-Eocene xenocrystic and detrital zircons (c. 60 – 40 Ma) have been recovered from young igneous rocks of the Tufton Hall Formation, Belvedere Formation and beach sand samples from Grenada and Carriacou (Rojas-Agramonte et al., 2017). On Mayreau, sub-marine pillow basalts and volcanogenic sediments of the Mayreau Basalt are capped by mid-Eocene pelagic limestones, mafic volcanogenic sediments and minor pillow basalts of the Anse Bandeau Formation (c. 50 – 46 Ma, P10 – P11 zonal range). Similar stratigraphy is observed on the neighbouring island of Carriacou, where mid-Eocene sub-marine pillow basalts, intercalated with minor volcanogenic sediment and pelagic limestones of the Cherry Hill Basalt (c. 46 – 45 Ma, P12 zonal range), are capped by foraminiferal and radiolarian carbonates of the Bogles Limestone. Pillow basalts found on Mayreau and Carriacou have similar morphologies, mineralogical compositions, and stratigraphic relationships, and are suggested to be correlative (Speed et al., 1993). Off the east coast of Mayreau, mid-Eocene volcanogenic strata (c. 43 – 46 Ma, NP16 zonal range) are exposed on the islands of Jamesby and Baradel (Westercamp et al., 1985). Around 180 km to the west of Grenada, an off-shore drill core near Los Testigos intersected mid-Eocene mafic volcanogenic sediments (c. 39 – 35 Ma), that are unconformably overlain by lower Miocene limestones.

There is hence a near continual record of sub-marine basaltic magmatism and contemporaneous pelagic basin sedimentation from the Lower Eocene to the Oligocene in the southern Lesser Antilles, beginning roughly 10 Ma after the cessation of the Aves Ridge system. According to our new tectonic model, these volcanics would have been erupted on the floor of the Grenada-Tobago backarc basin during the formation of the Outer Arc. Later the westward step of this system into its current position in the Oligocene and growth of the LAA through the southern spreading centres bought them to the surface. The restriction of known samples of this phase of volcanism to the Grenadines is likely to be the result of a lack of exposure on the larger volcanic islands (e.g. St. Lucia and St. Vincent) due to almost continuous arc magmatism from the Miocene to the present-day, combined with the inaccessibility of large areas of these islands.

Table B.1: Data Sources for Figure B.8

Island	Number	References
Eastern Greater Antilles and the Virgin Islands	1-6	Cox et al. (1977); Jolly et al. (1998); Lidiak and Jolly (1998); Rankin (2002)
Anguilla	7	Christman (1953)
St. Martin	8	Briden et al. (1979); Davidson et al. (1993)
St. Barthelemy	9	Christman (1953); Briden et al. (1979)
Antigua	10	Briden et al. (1979); Weiss (1994)
Saba	11	Defant et al. (2001)
St. Kitts	12	Baker (1984)
Nevis	13	Hutton and Nockolds (1978)
Montserrat	14	Harford et al. (2002)
Guadeloupe	15	Samper et al. (2007)
Les Saintes	16	Zami et al. (2014)
Dominica	17	Smith et al. (2013)
Martinique	18	Germa et al. (2011)
St. Lucia	19	Lindsay et al. (2013)
St. Vincent	20	Briden et al. (1979); Heath et al. (1998b)
Bequia	21	Briden et al. (1979); Smith et al. (1996)
Mustique	22	Speed et al. (1993)
Mayreau	23	Speed et al. (1993); Rojas-Agramonte et al. (2017)
Union Island	24	Briden et al. (1979)
Carriacou	25	Briden et al. (1979); Caldwell et al. (1984); Rojas-Agramonte et al. (2017)
Kick-'em-Jenny	26	White et al. (2017)
Grenada	27	White et al. (2017)
Los Testigos	28	Santamaria and Schubert (1974); Castro and Mederos (1985)
Margarita	29	Santamaria and Schubert (1974)
Aves Ridge	30	Neill et al. (2011)
La Blanquilla	31	Wright and Wyld (2011)
Gran Roque	32	van der Lelij et al. (2010)
Bonaire	33	Thompson et al. (2004); Wright and Wyld (2011)
Curacao	34	Sinton et al. (1998); Wright and Wyld (2011)
Aruba	35	White et al. (1999); Wright and Wyld (2011)

The Mayreau Basalt and basaltic lavas within overlying Anse de Bandeau Formation (Mayreau) were demonstrated to have elevated whole-rock TiO_2 and Zr concentrations, and Ce/Zr ratios slightly higher than average MORB values (Speed and Walker, 1991). Furthermore, these lavas were also shown to have a clear MORB Nd isotopic compositions, a depletion in LREE elements, concomitant Nb and Tb depletions and elevated radiogenic Sr and Pb isotopic compositions (White et al., 2017). They are also compositionally distinct from Paleogene igneous rocks in the Limestone Caribbees, and recent island arc tholeiites throughout the modern LAA. Such features are characteristic of a depleted, backarc source region for these magmas e.g. Pearce and Parkinson (1993) .

The Tufton Hall Formation (Grenada) and the Belvedere Formation (Carriacou) contain xenocrystic and detrital zircons of mid-Eocene age and are of a similar age to igneous rocks exposed on the proximal islands of Mayreau, Jamesby and Baradel. Furthermore, the rare earth element (REE) composition of the mid-Eocene zircon population suggests that they formed from a magma that was significantly less oxidised than those found in the recently active southern Lesser Antilles arc (Rojas-Agramonte et al., 2017). This corroborates with a backarc origin for the mid-Eocene magmas in the southern LAA, as opposed to a highly oxidised arc source. Moreover, because the constrained biostratigraphic depositional ages of the Tufton Hall Formation and Belvedere Formation agree with detrital U-Pb zircon ages recovered from those same formations, sub-marine igneous activity and pelagic basin sedimentation appear to have occurred coevally during the mid-Eocene. The clear spatial and temporal correlation between sub-marine basalts and mafic volcaniclastic rocks throughout the Grenadines ultimately suggests they were derived from the same tectono-magmatic environment. There are no other igneous rocks of Eocene age found in the Caribbean region that were derived from a depleted, relatively reduced mantle source, and it is difficult to reconcile the geochronological, geochemical and stratigraphic constraints outlined above without invoking the presence of a Paleogene backarc spreading centre where the currently active LAA resides, as has also been suggested by other authors (e.g. Speed and Walker 1991; White et al. 2017). In our model, we suggest that this backarc spreading centre is associated with the Outer Arc, and formed following the migration of the magmatic axis to the east of the Grenada and Tobago basins during the Paleogene.

B.3.3 Neogene: Lesser Antilles Arc

According to our model, during the Upper Oligocene, the arc migrates westward into the backarc region of the Eo-Oligocene Outer Arc. By c. 22 Ma, subduction-related magmatism is underway within the currently active LAA. As a result of activity on the more easterly Outer Arc (∼40 - 25 Ma) the mantle wedge beneath the current southern LAA is likely to have experienced more prolonged metasomatism than would be predicted from its 22 Ma volcanic history. This precursory flushing of fluids and melt through the mantle wedge has the capacity to significantly alter the composition of the ambient mantle below the modern LAA, and impart compositional heterogeneities in both the sub-arc mantle and crust here. This process could be responsible for some of the along arc magmatic compositional variation observed in addition to the crustal contamination of arc magmas arising from the assimilation with Grenada/Tobago Basin sediments and backarc crust in our model.

Studies rarely invoke the possibility of pre-existing compositional heterogeneities in the sub-arc mantle in the LAA, although many of them suggest that some of the isotopic variability must have been inherited from the mantle wedge (Thirlwall and Graham, 1984; Bezard et al., 2015). A new consideration of a previously unpredicted, pre-existing ambient mantle composition may prove essential to fully reconcile the observed trace element and isotopic variability in the LAA (e.g. Turner et al. 2017).

Appendix C

Appendix: Chapter 5, OBS Record Section Plots

This appendix contains a series of record section plots for each of the OBS stations used in the development of the wide-angle velocity model for structure of the sedimentary structure along VoiLA Profile 1 in Chapter 5. See Chapter 5 for details of receiver layout and phase identification. In all cases the vertical component of the seismometer are shown (except for OBS34,36,41 where the hydrophone component is plotted). All sections are reduced at 4 km s^{-1}. A) Record section plots overlain with travel time picks, and forward modelled travel times by phase. In all cases circles represent travel-time picks, and plotted lines show forward modelled travel times for the corresponding phase through the final model. 1 in 5 picks are shown. Phases are as follows PbP: red (all instruments), PdP: blue (instruments 28-48), Ps: Green (forward modelled travel times shown for all instruments, only picked on OBS28-48), Pd: Yellow. Picks plotted with corresponding uncertainty envelopes (0.05 s for PgP and PdP, 0.1 s for Ps and Pd). Yellow stars represent zero offset travel times to top basement (All instruments) and décollement (OBS28-48) for each instrument interpreted from MCS profile (Figure 5.4). B) As above with overlay.

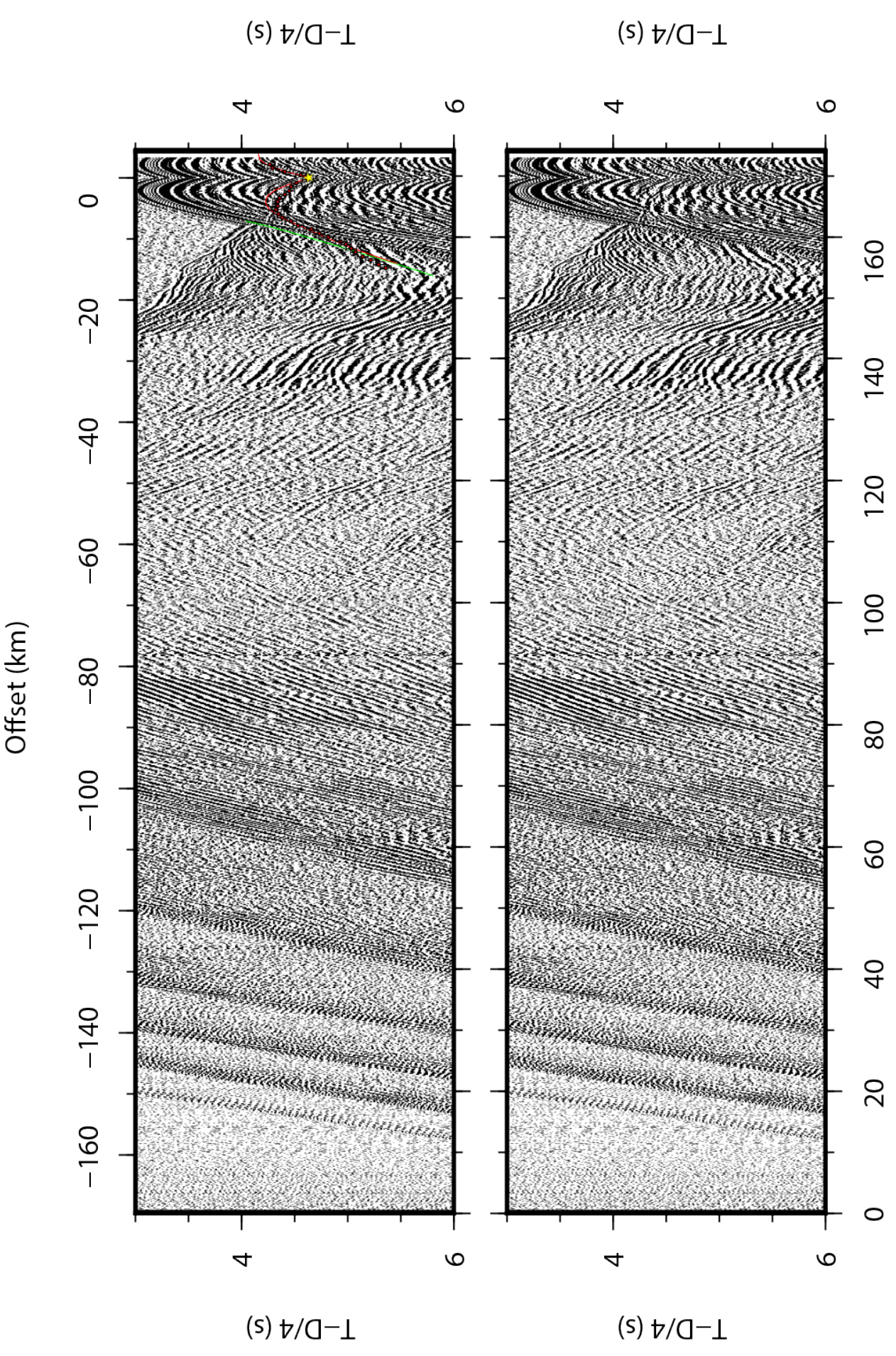


Figure C.1: Record Section: OBS2

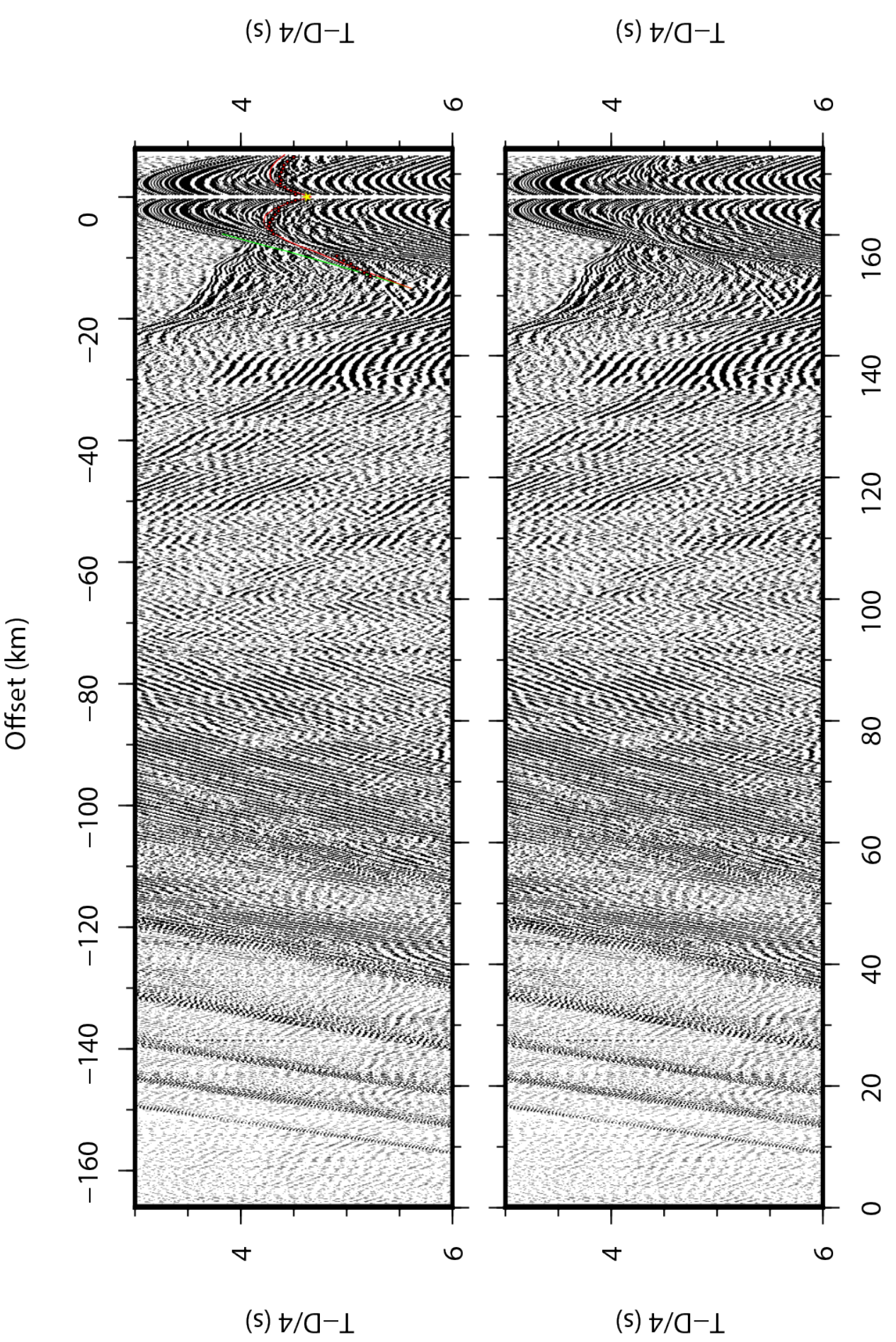


Figure C.2: Record Section: OBS3

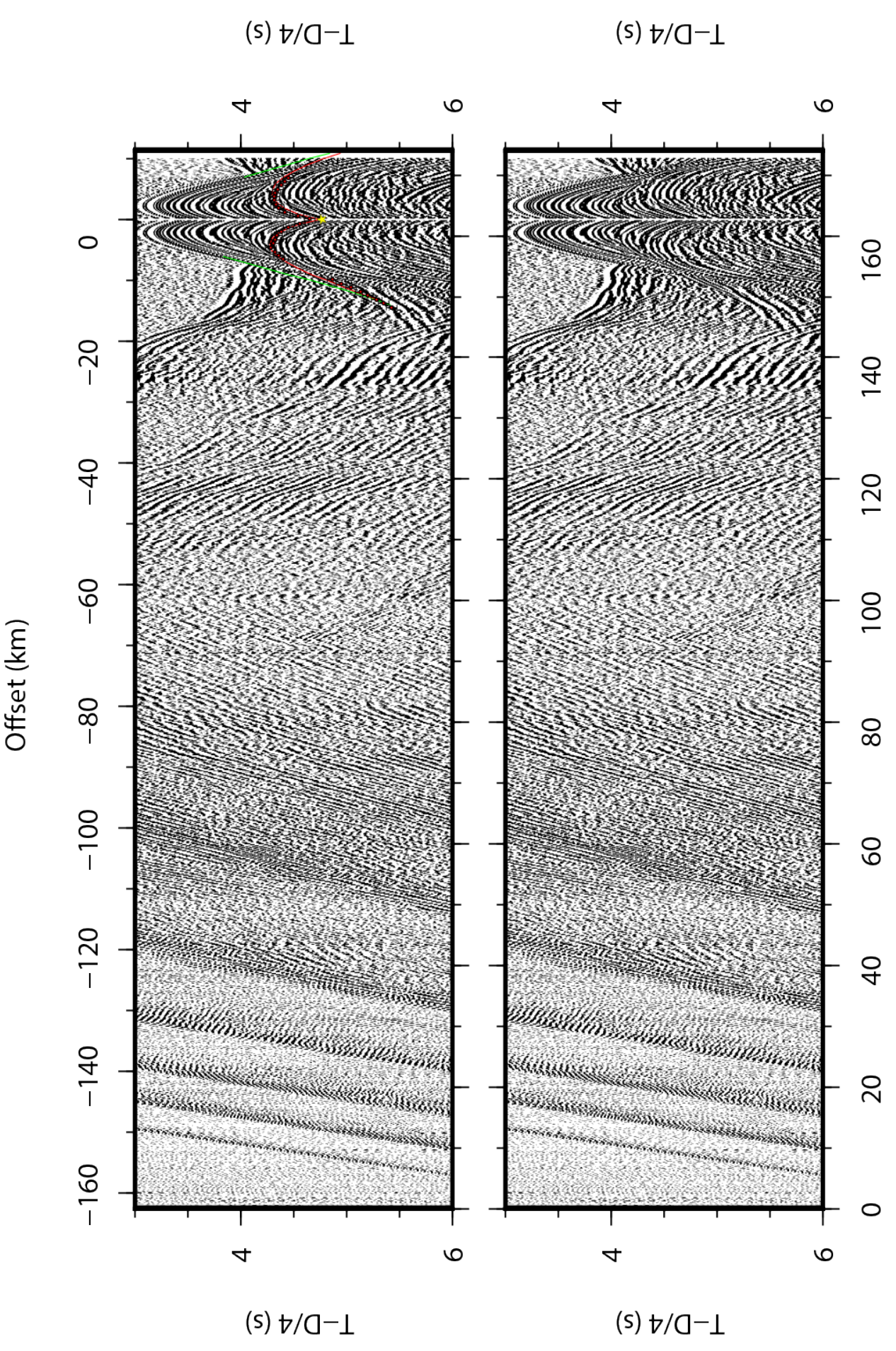


Figure C.3: Record Section: OBS4

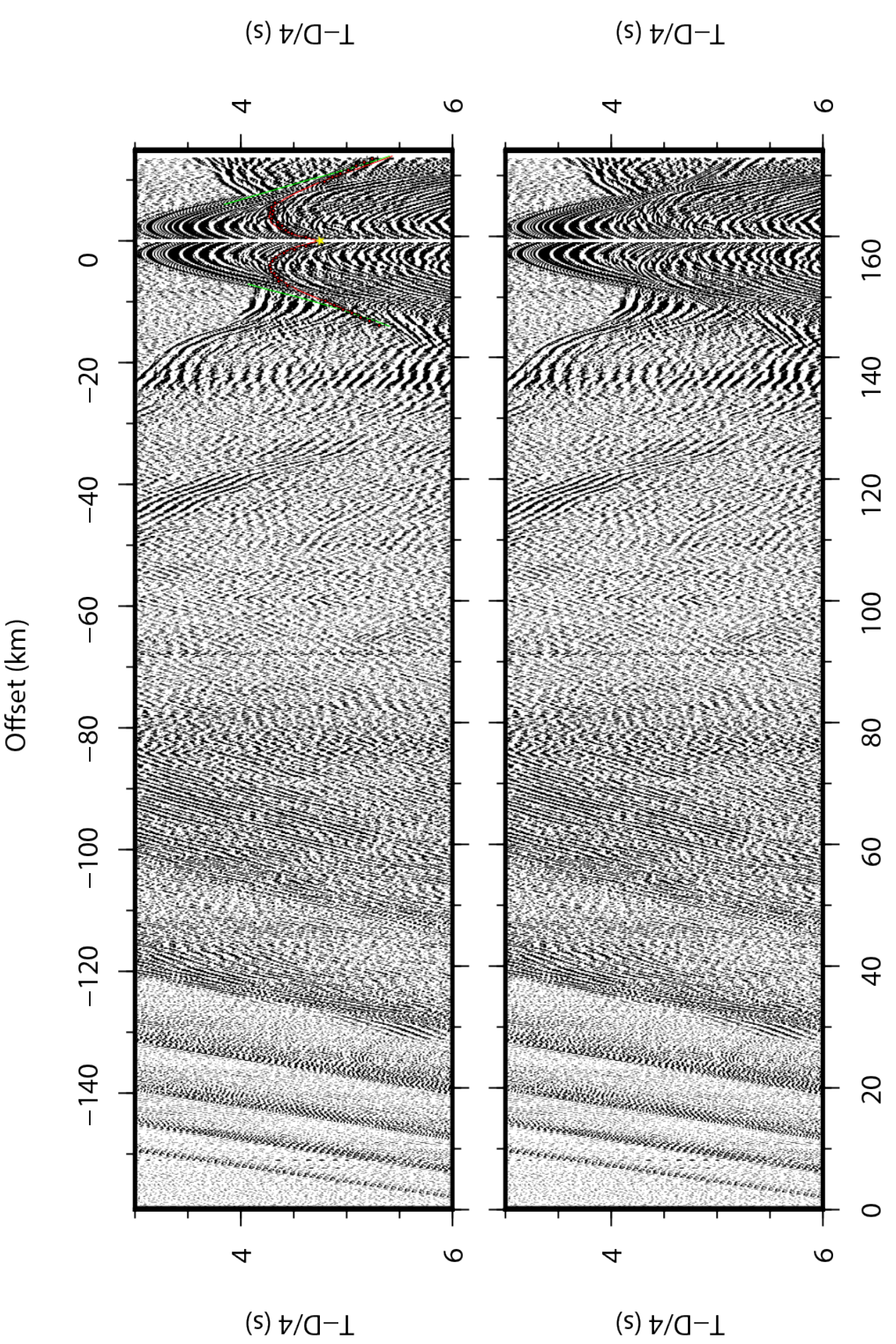


Figure C.4: Record Section: OBS5

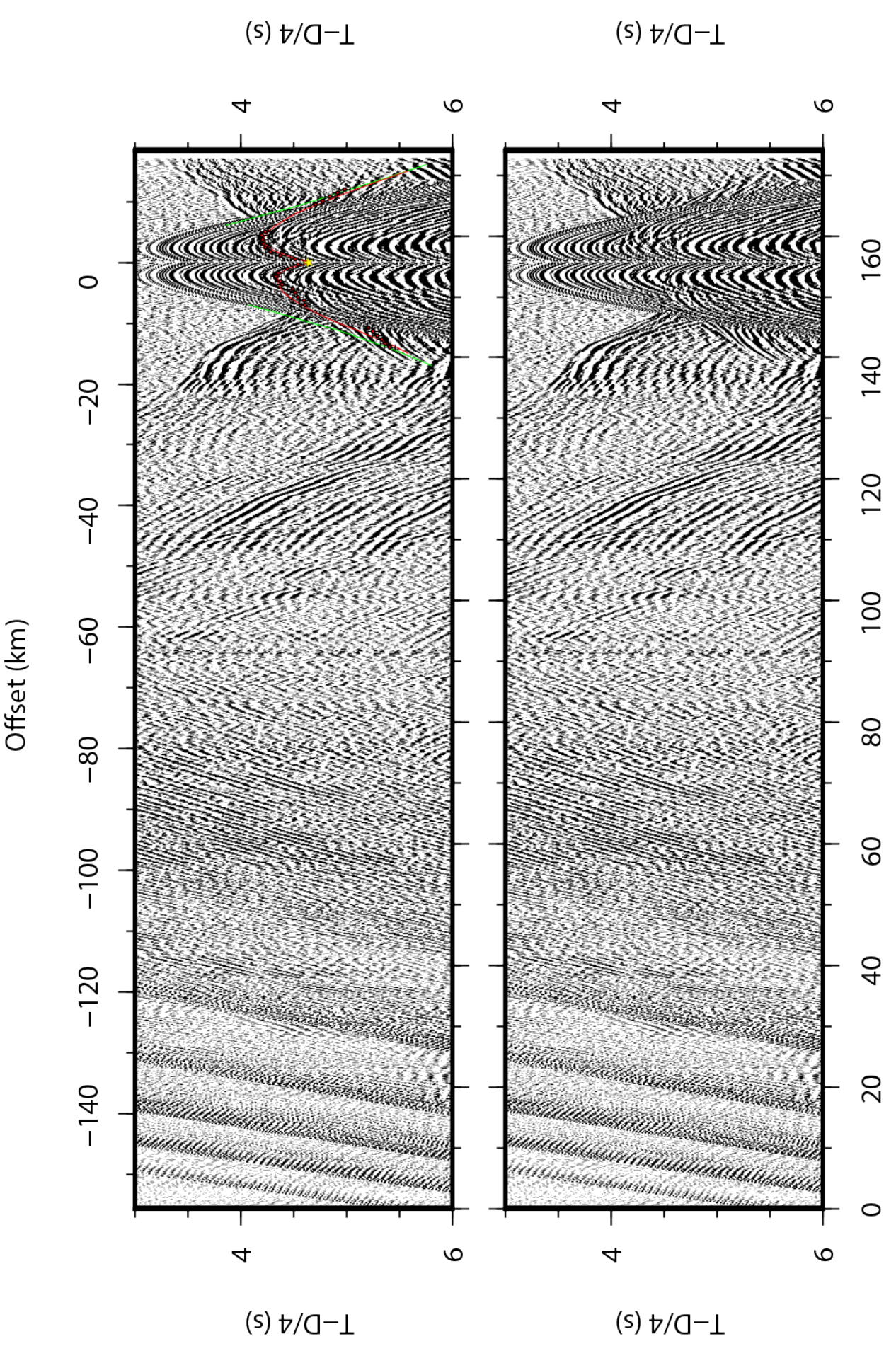


Figure C.5: Record Section: OBS6

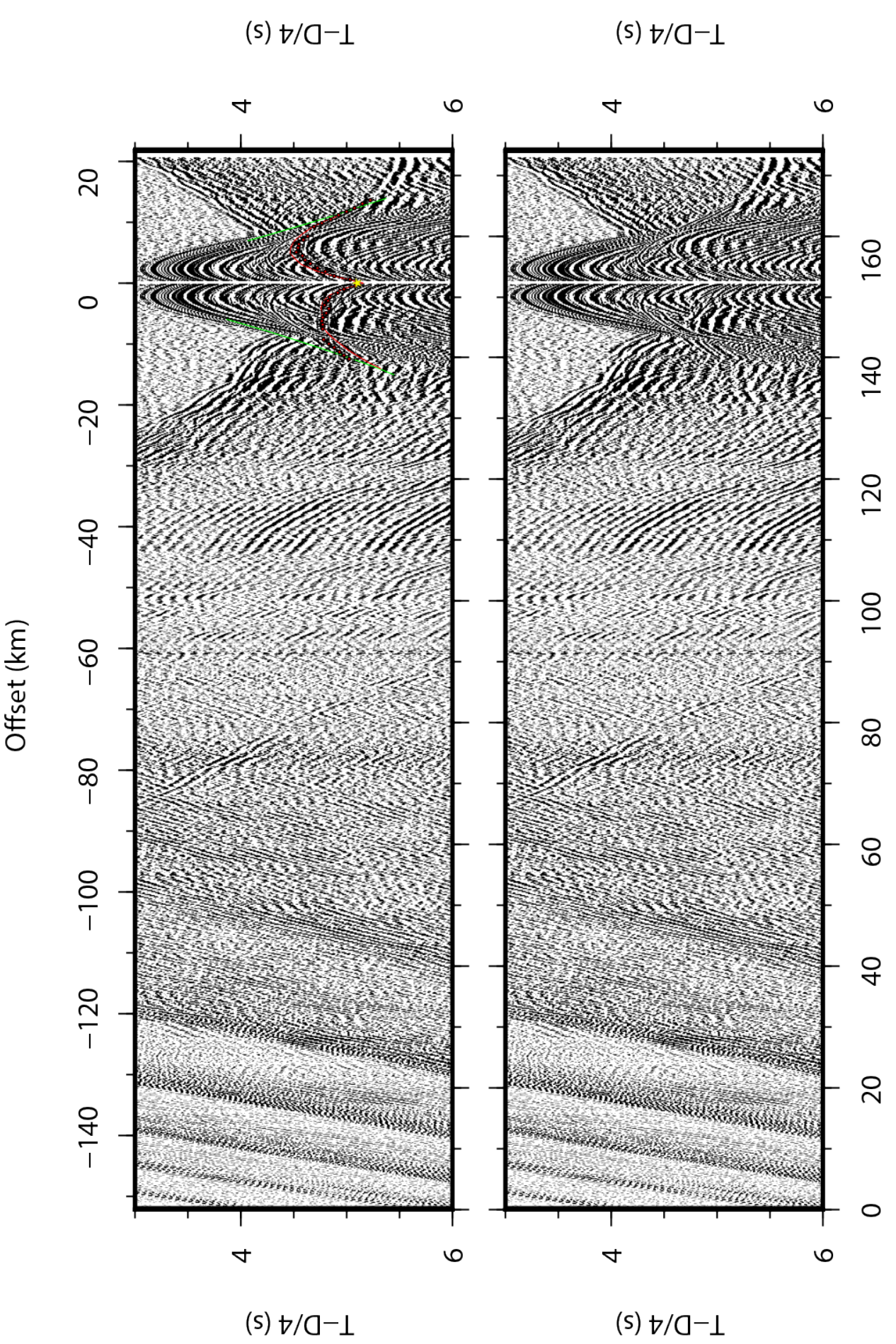


Figure C.6: Record Section: OBS7

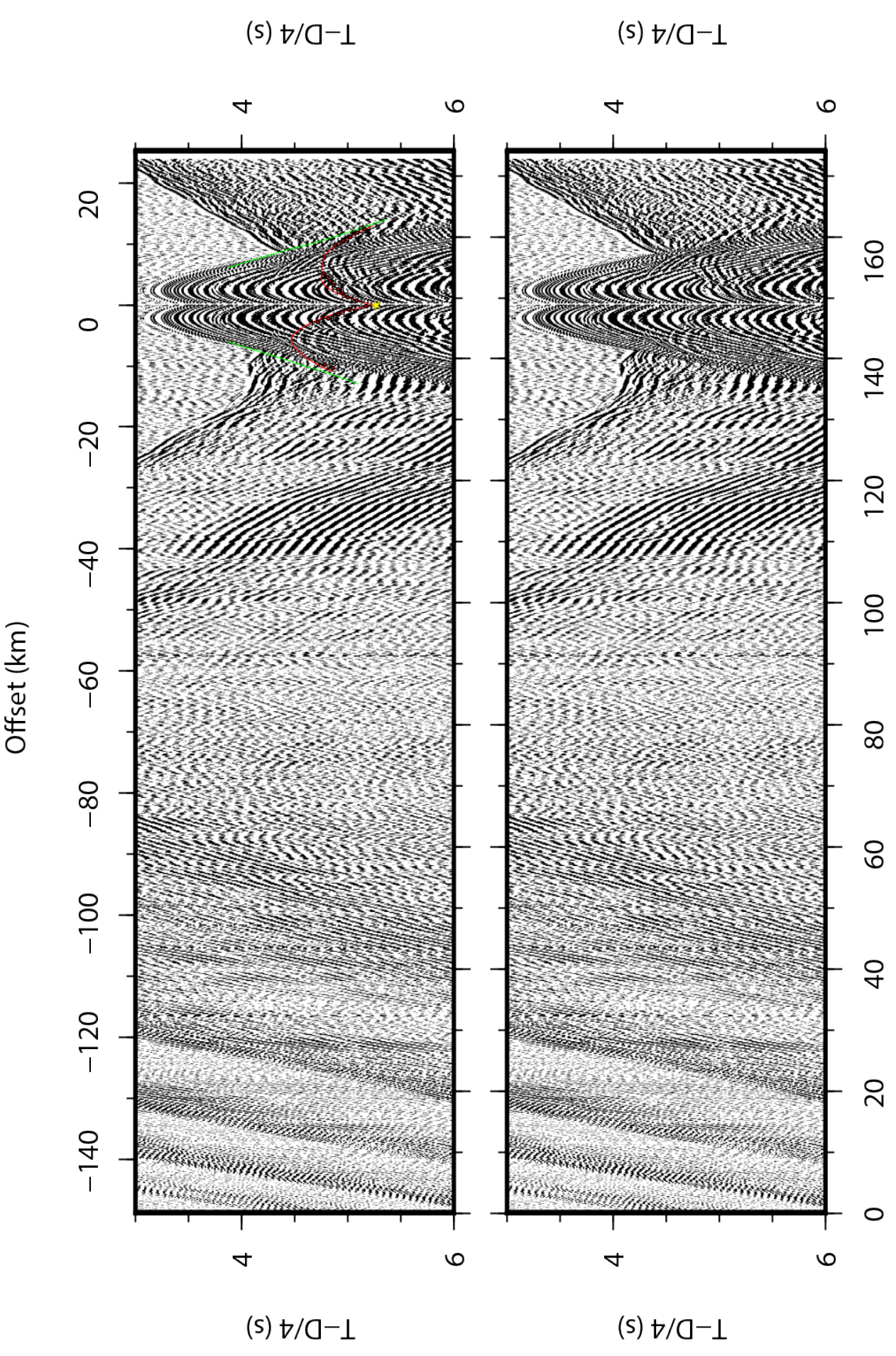


Figure C.7: Record Section: OBS8

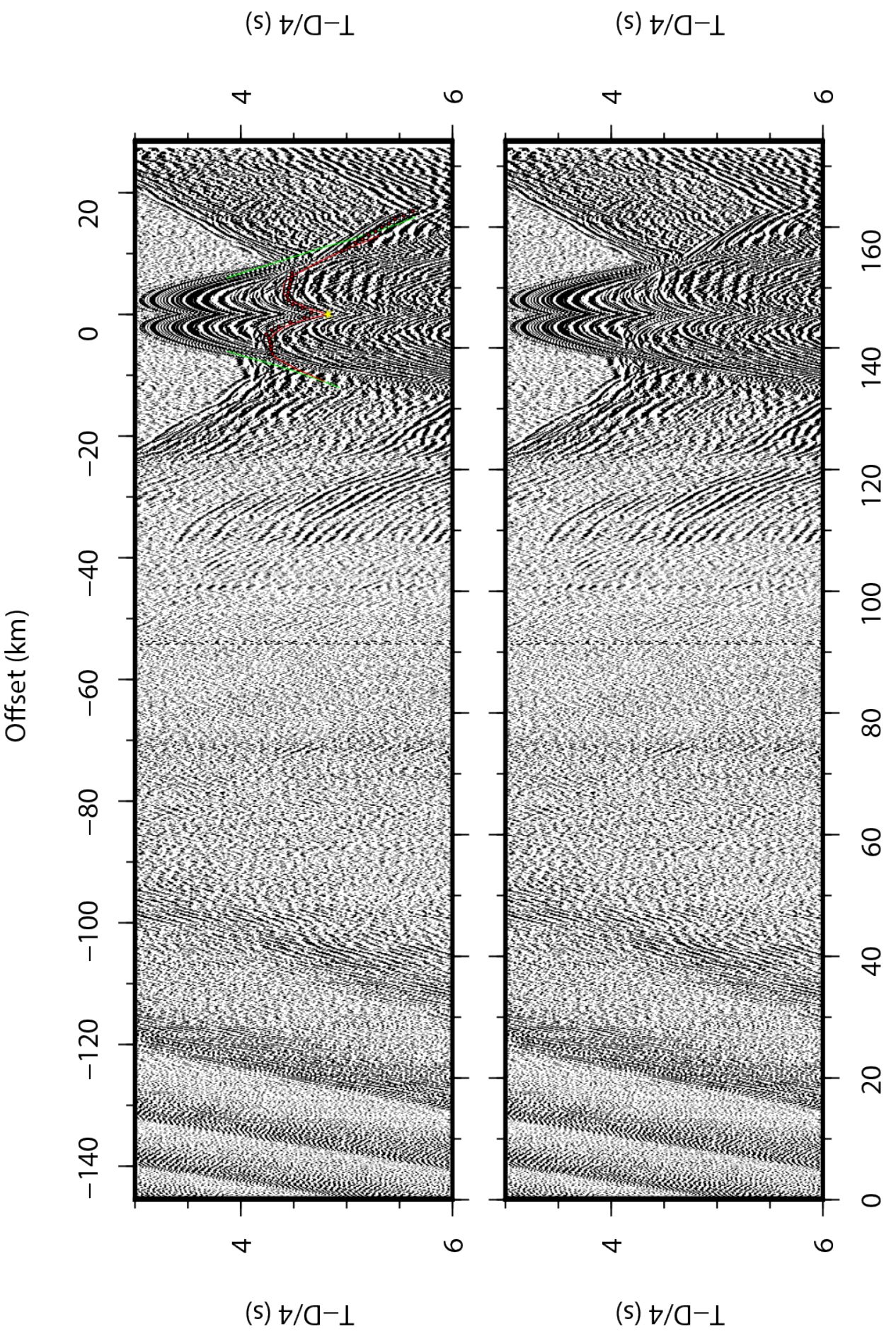


Figure C.8: Record Section: OBS9

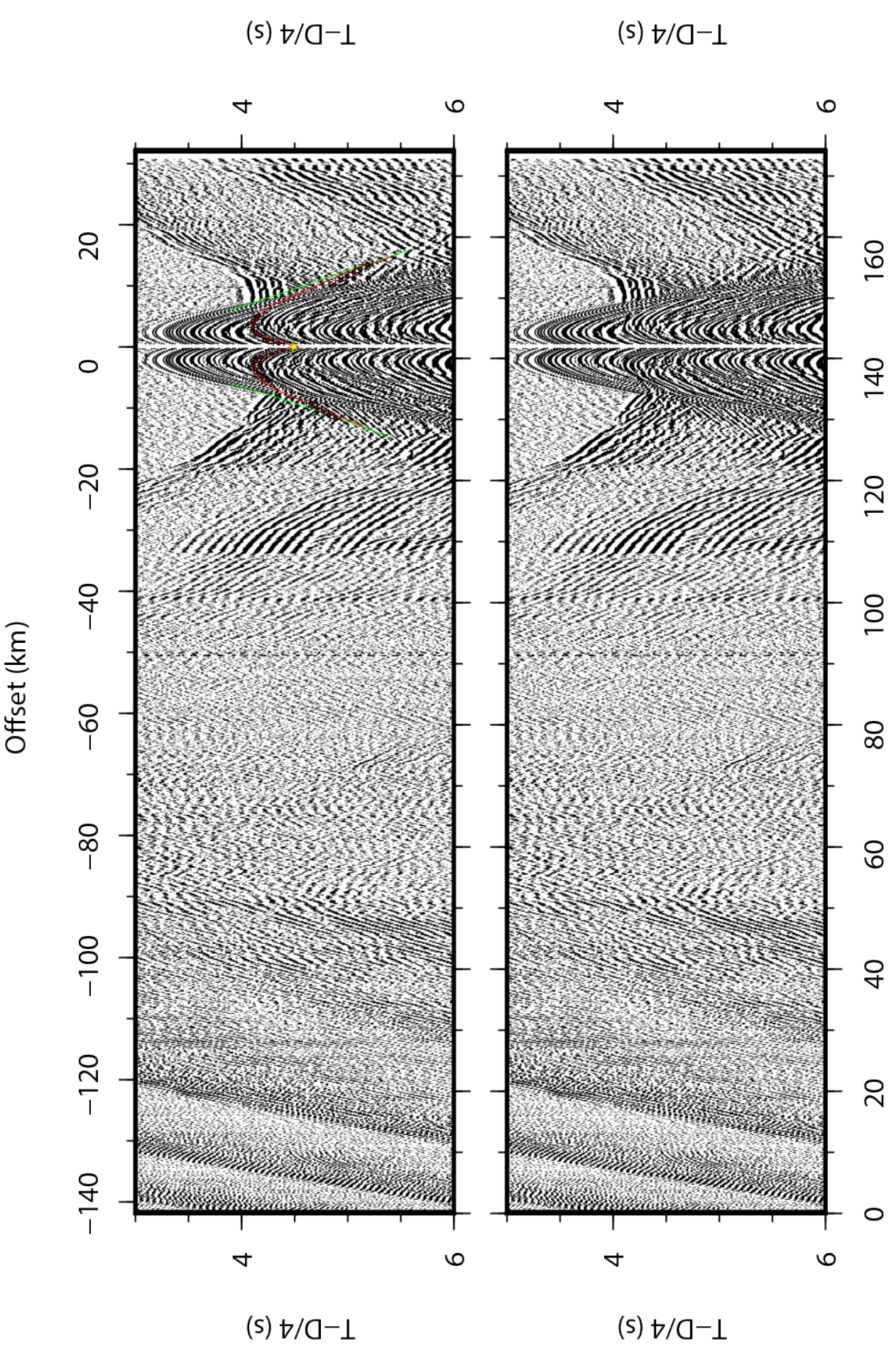


Figure C.9: Record Section: OBS10

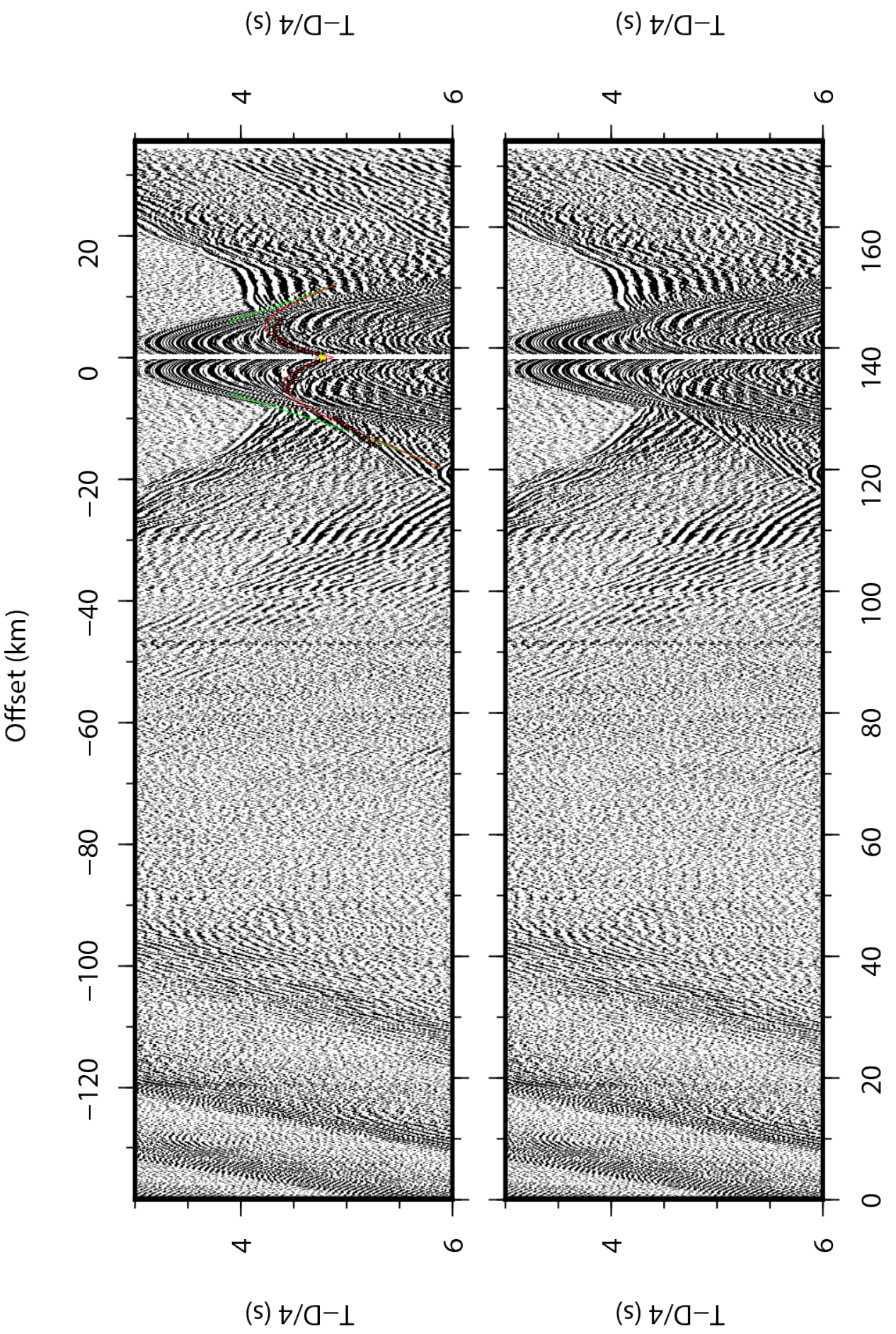


Figure C.10: Record Section: OBS11

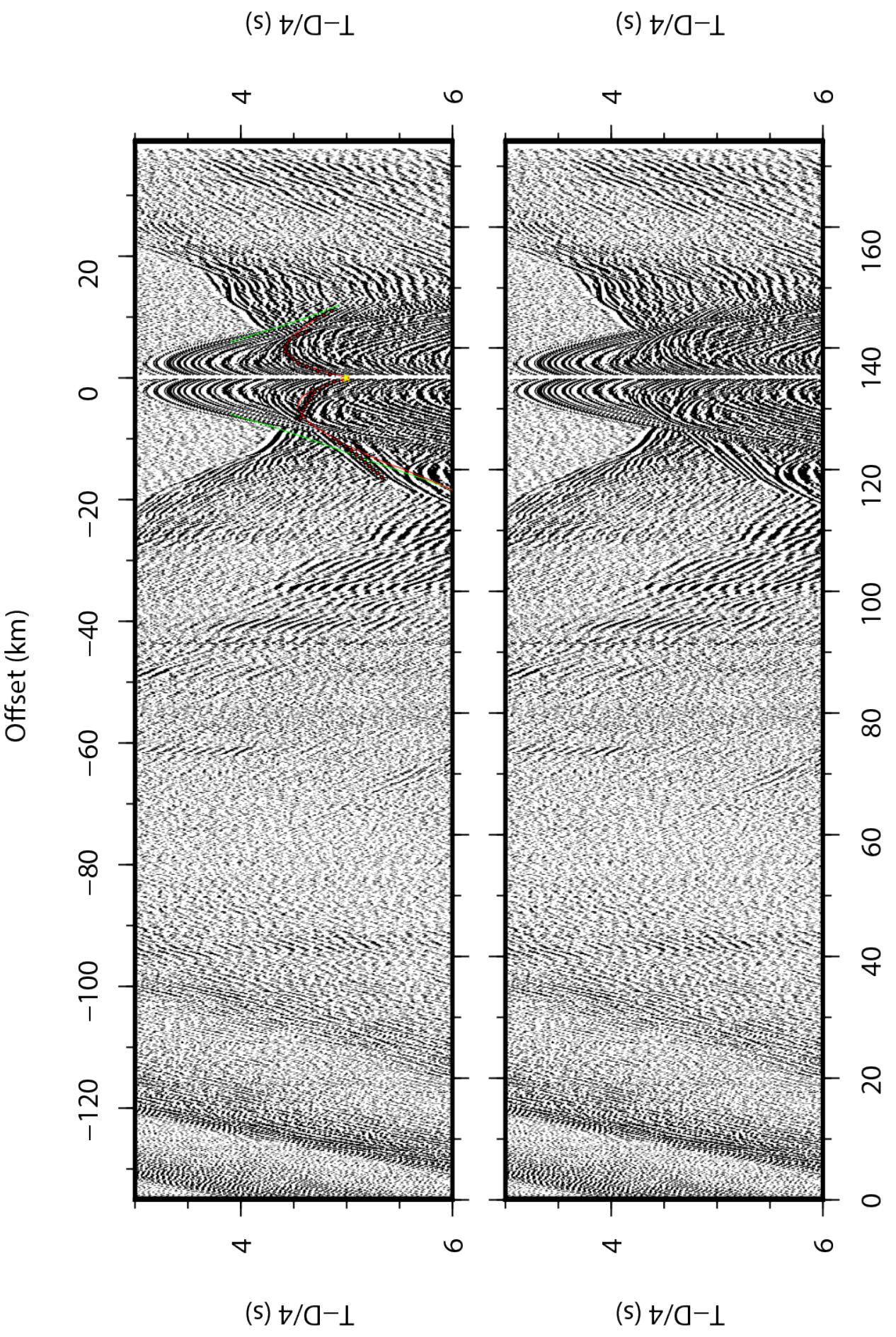


Figure C.11: Record Section: OBS12

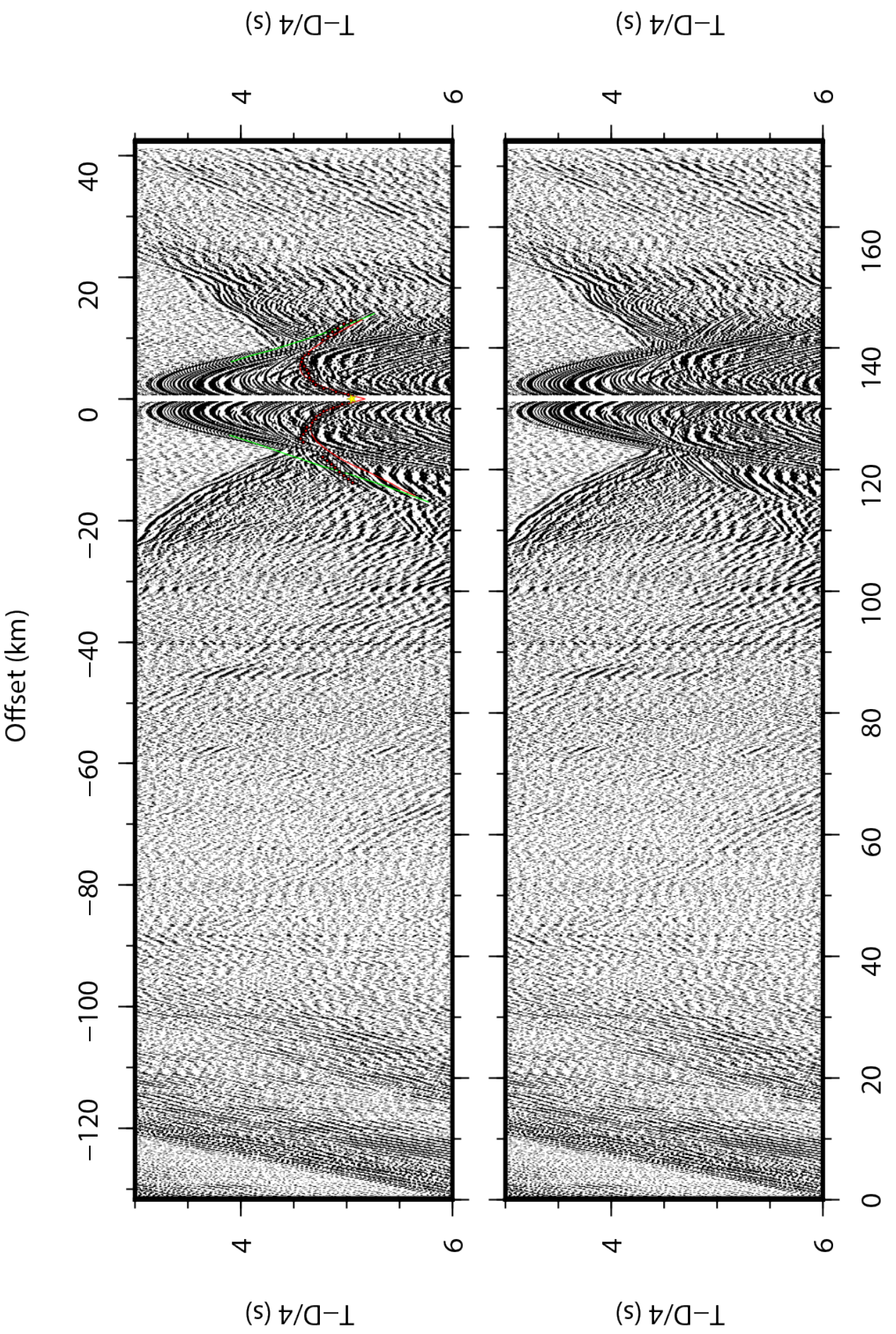


Figure C.12: Record Section: OBS13

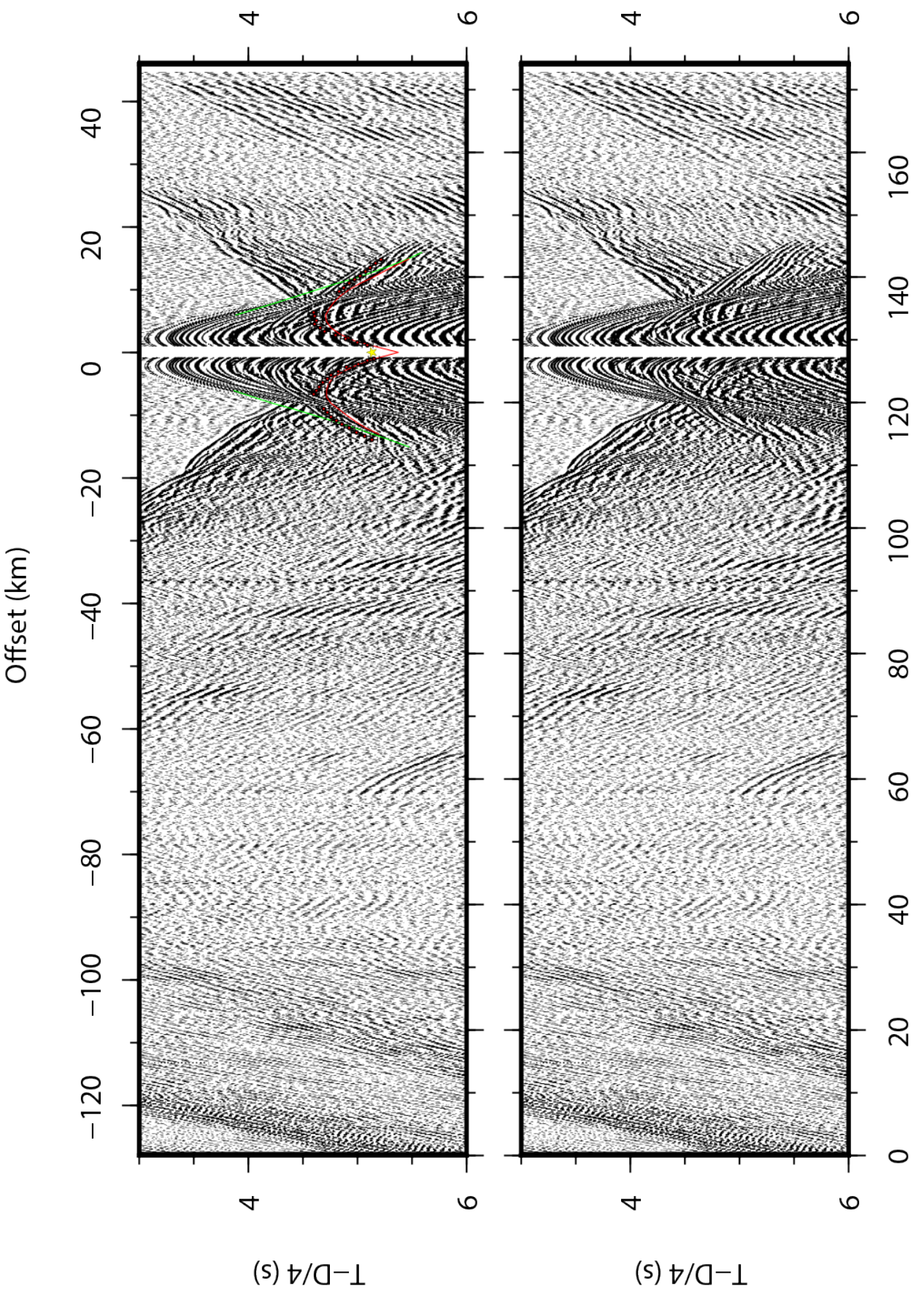


Figure C.13: Record Section: OBS14

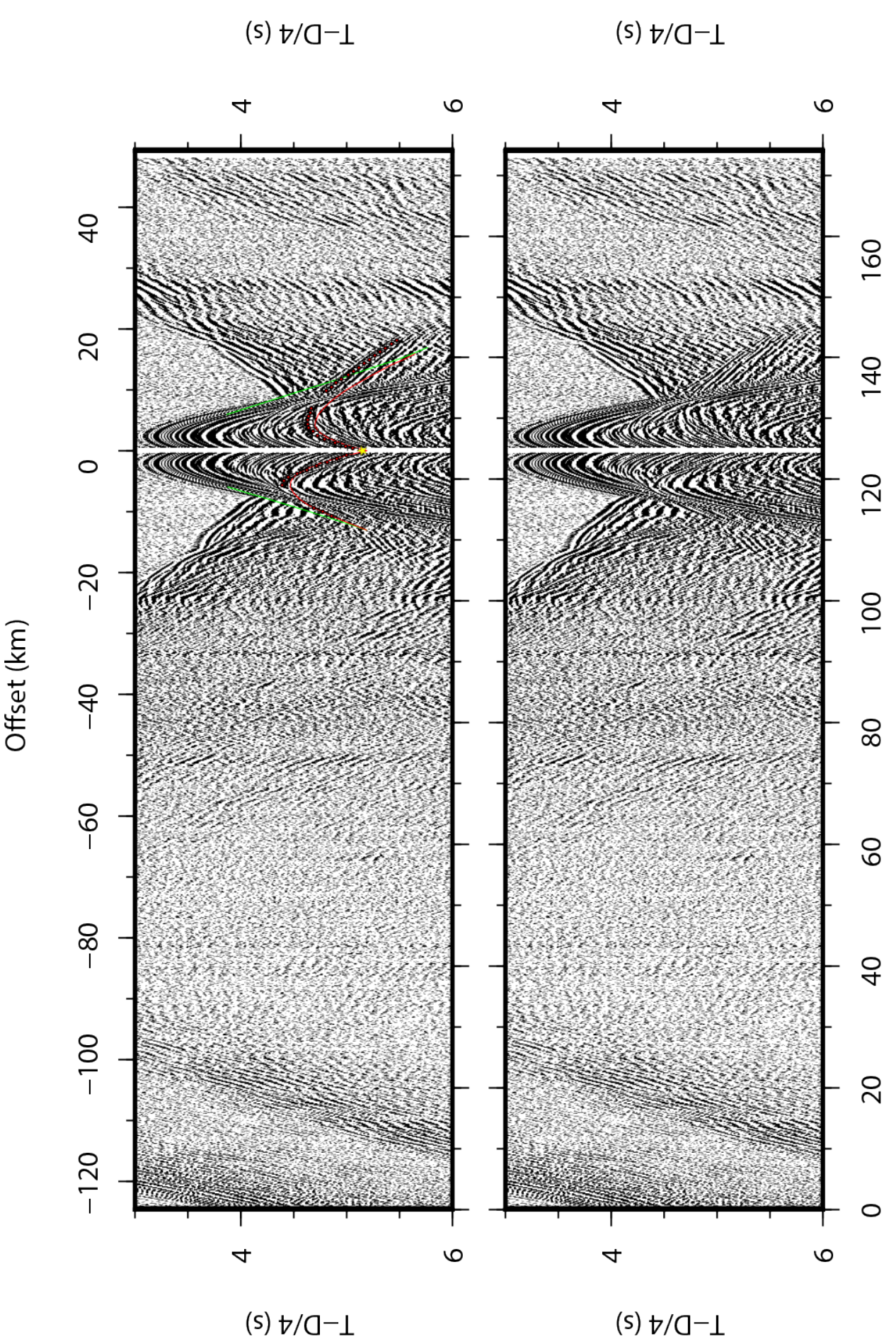


Figure C.14: Record Section: OBS15

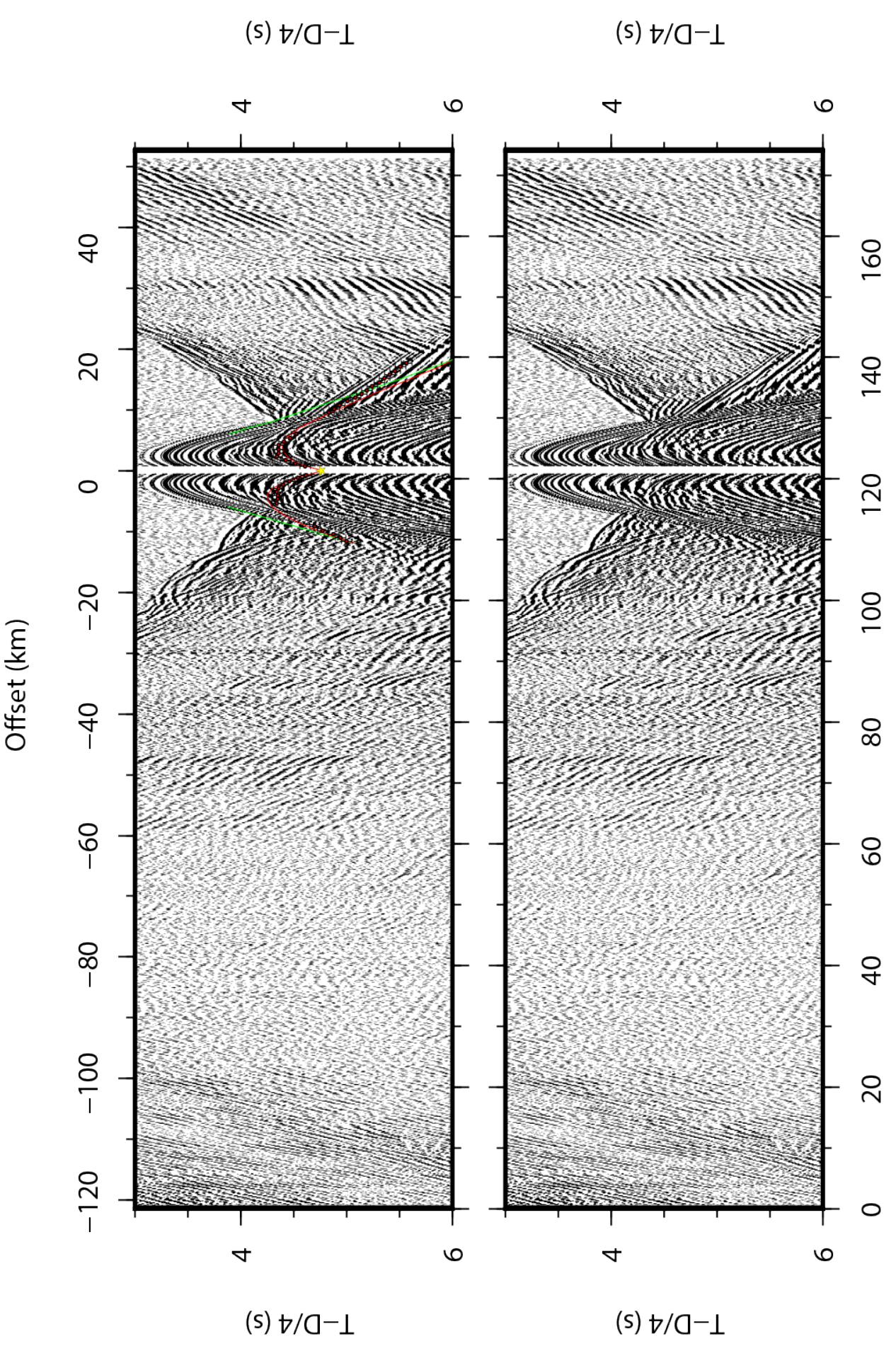


Figure C.15: Record Section: OBS16

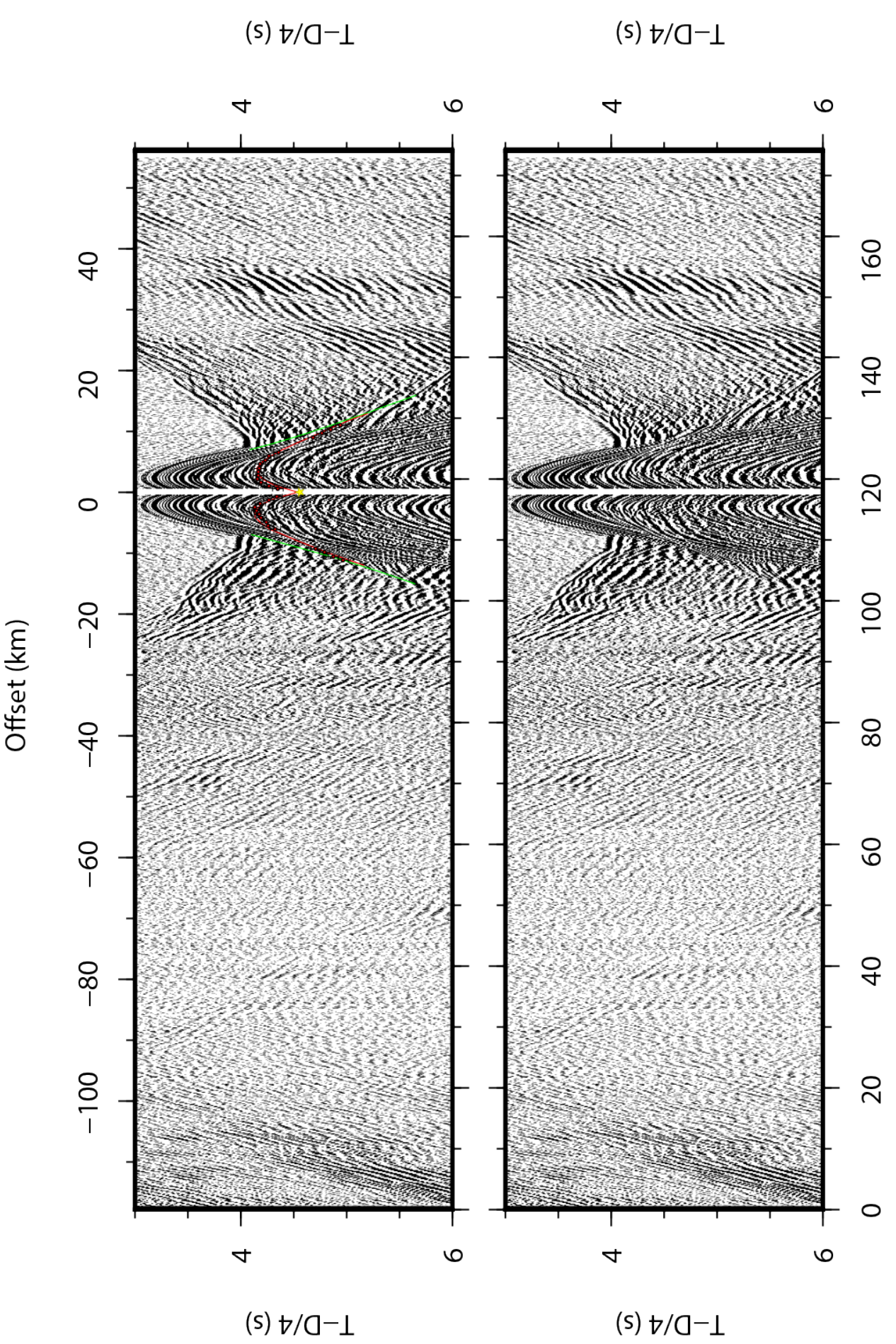


Figure C.16: Record Section: OBS17

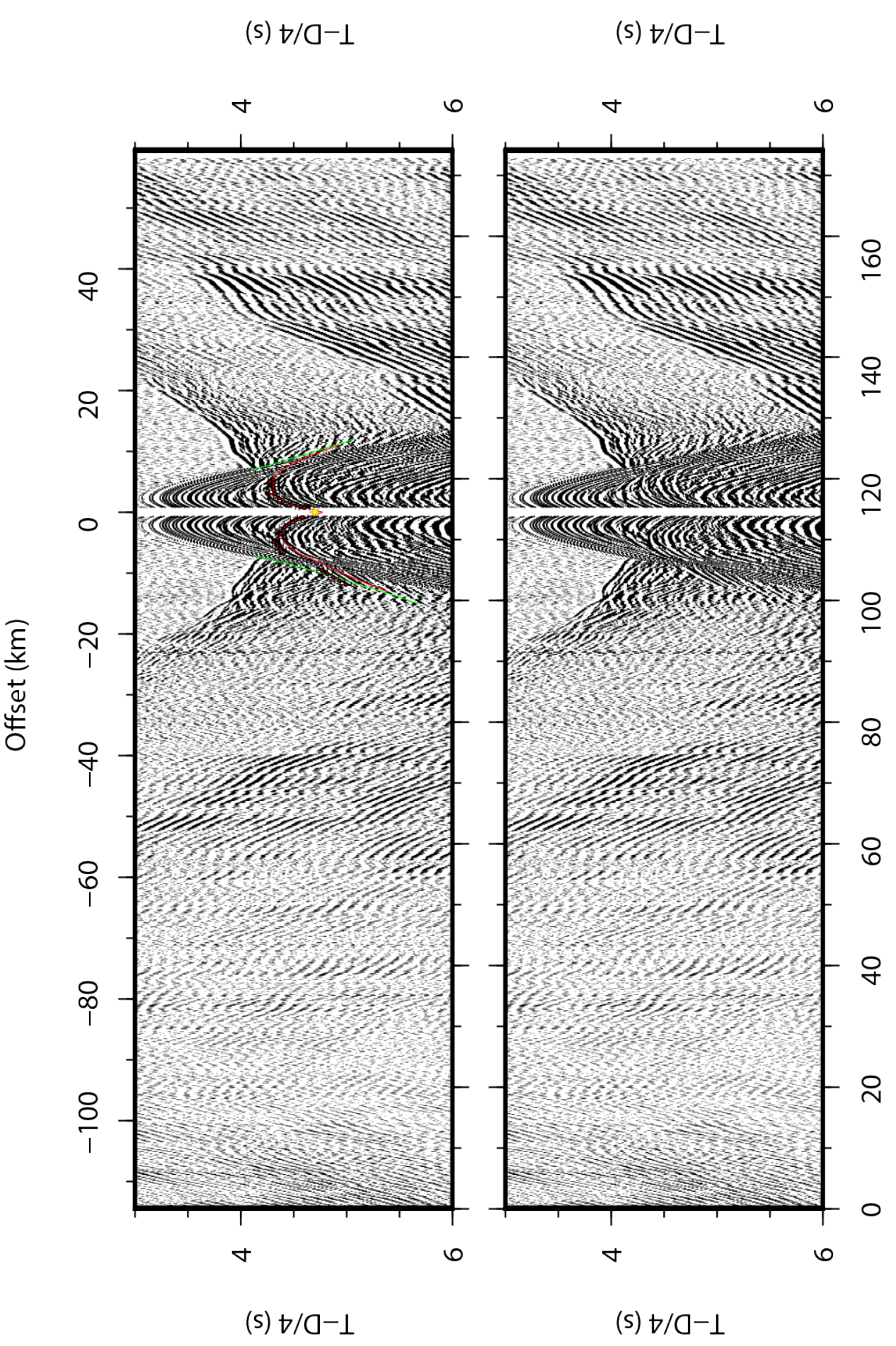


Figure C.17: Record Section: OBS18

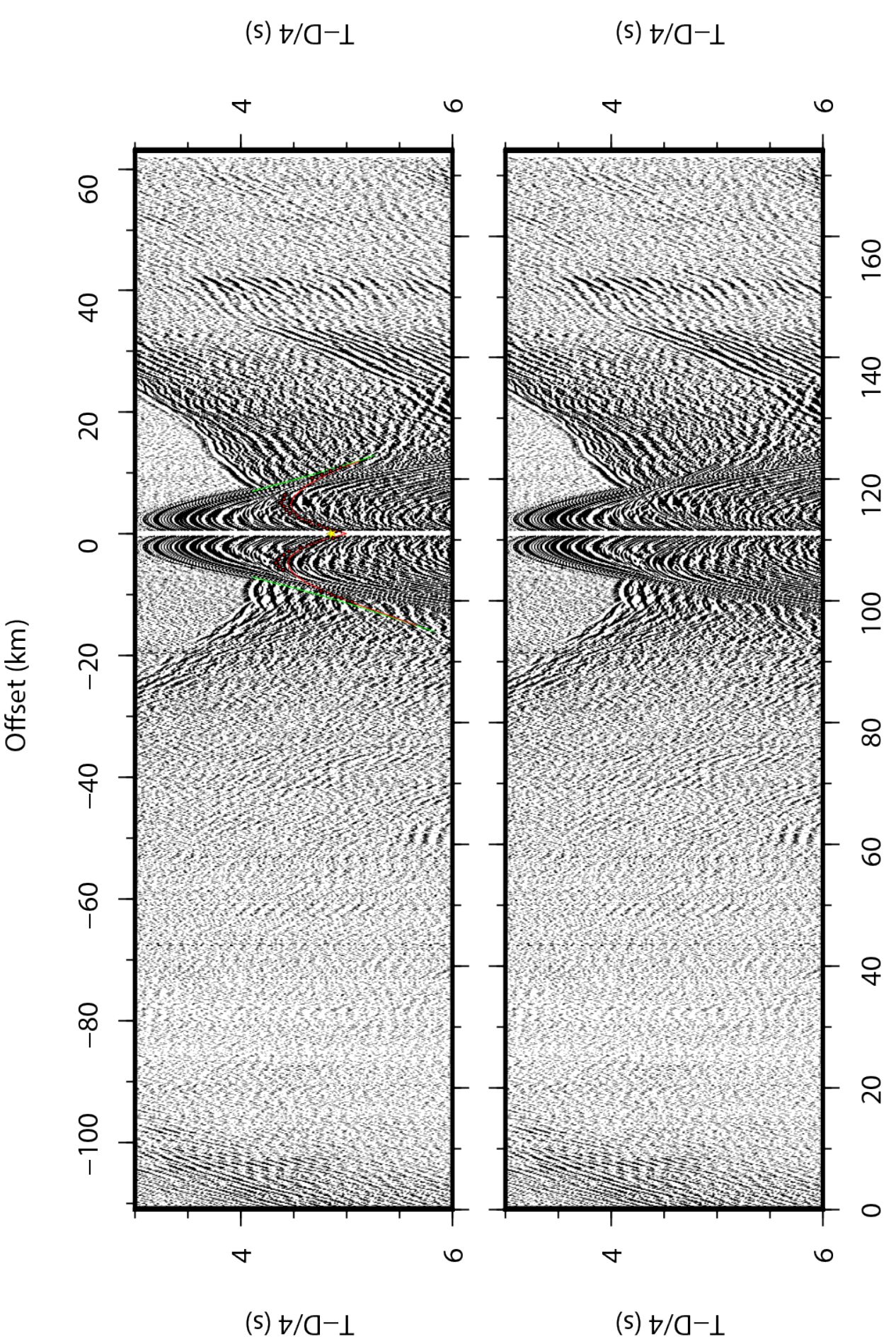


Figure C.18: Record Section: OBS19

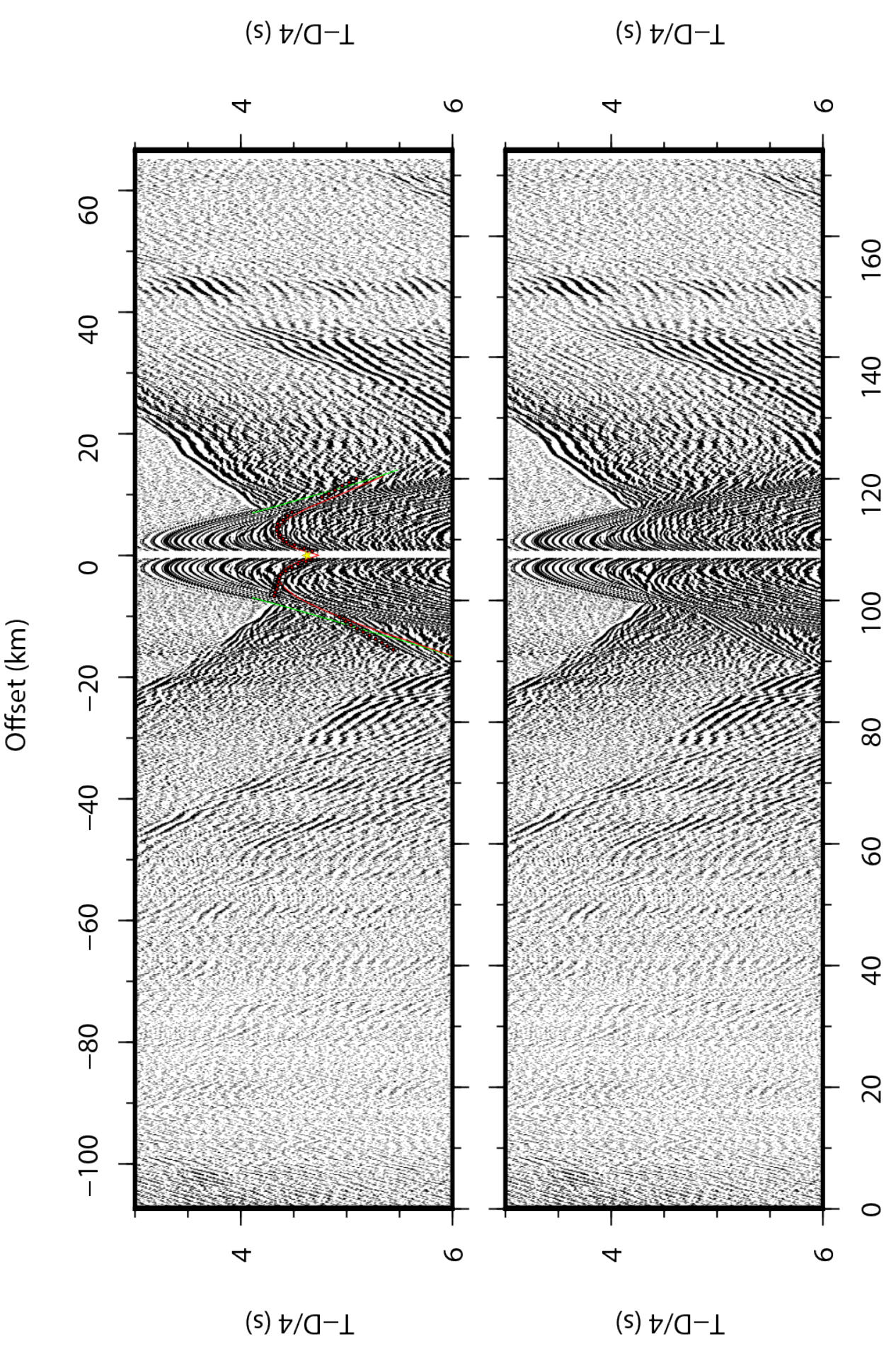


Figure C.19: Record Section: OBS20

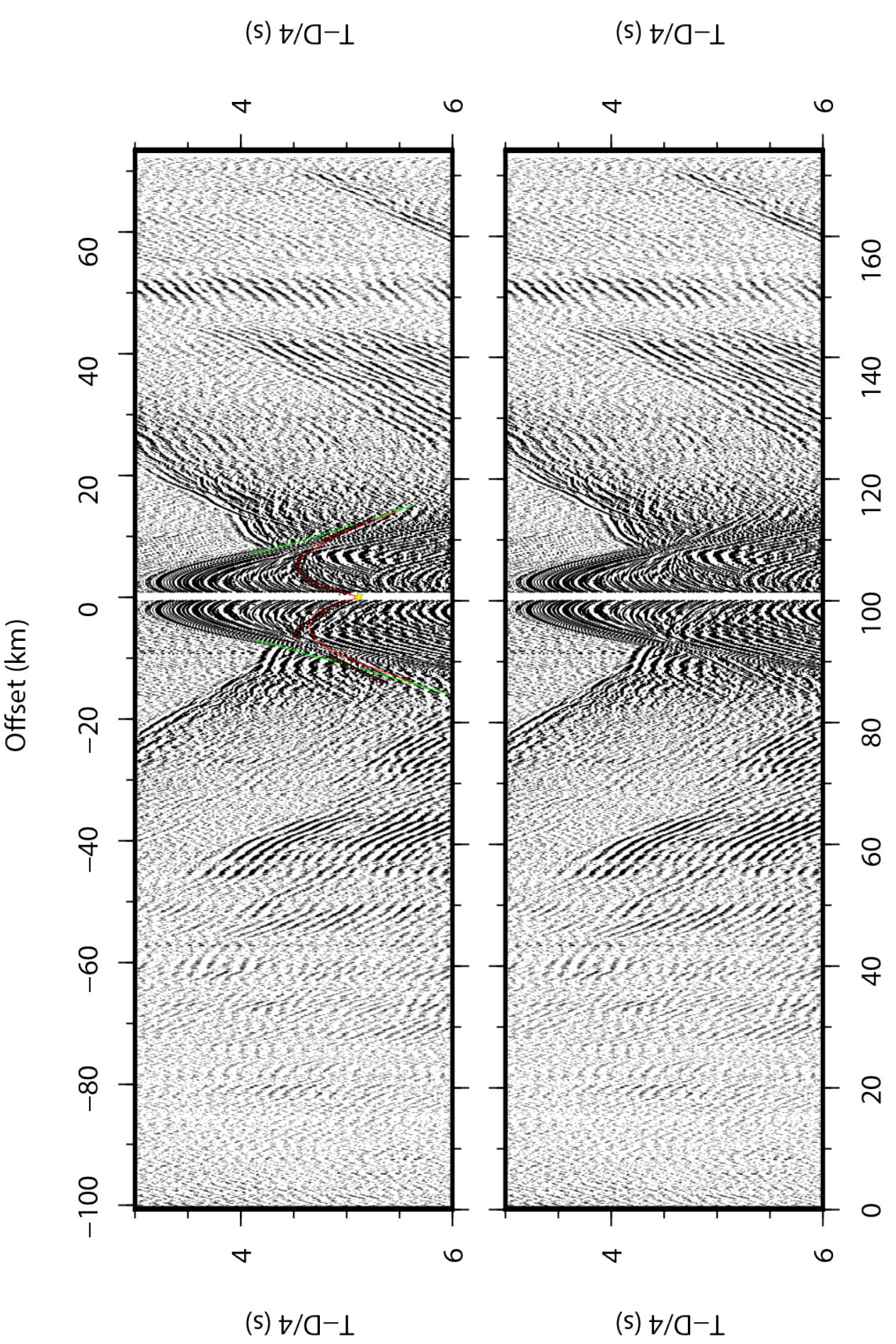


Figure C.20: Record Section: OBS21

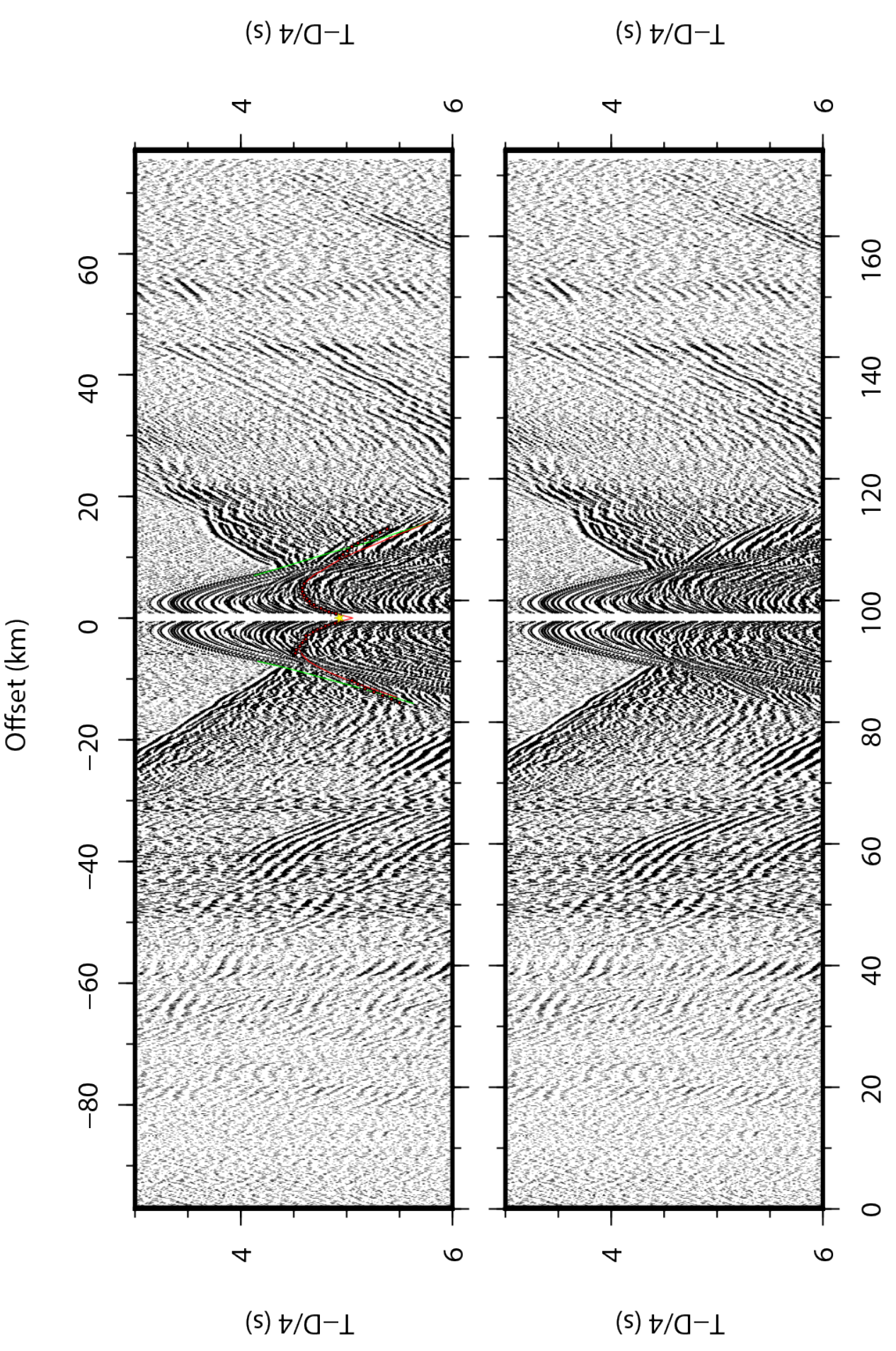


Figure C.21: Record Section: OBS22

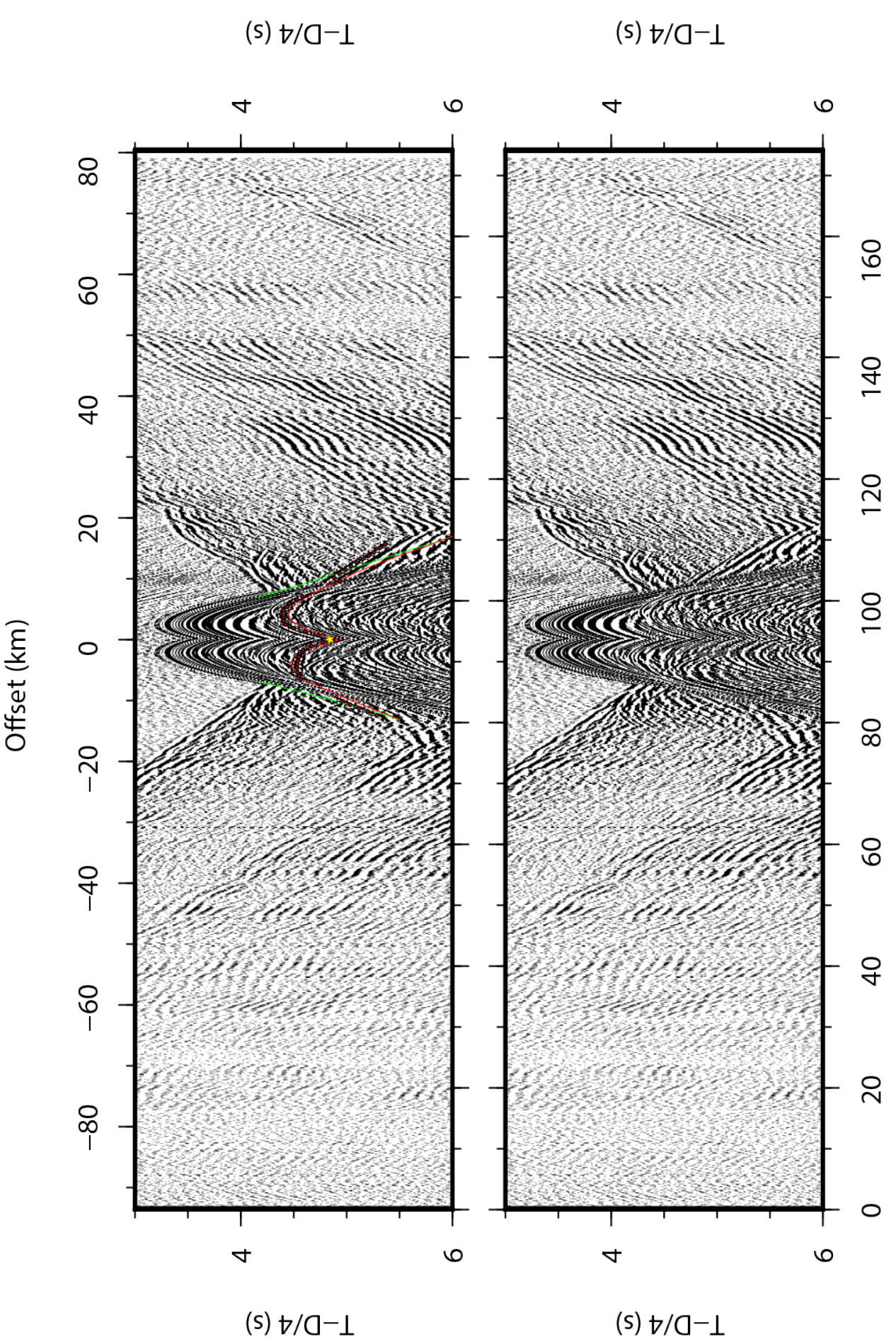


Figure C.22: Record Section: OBS23

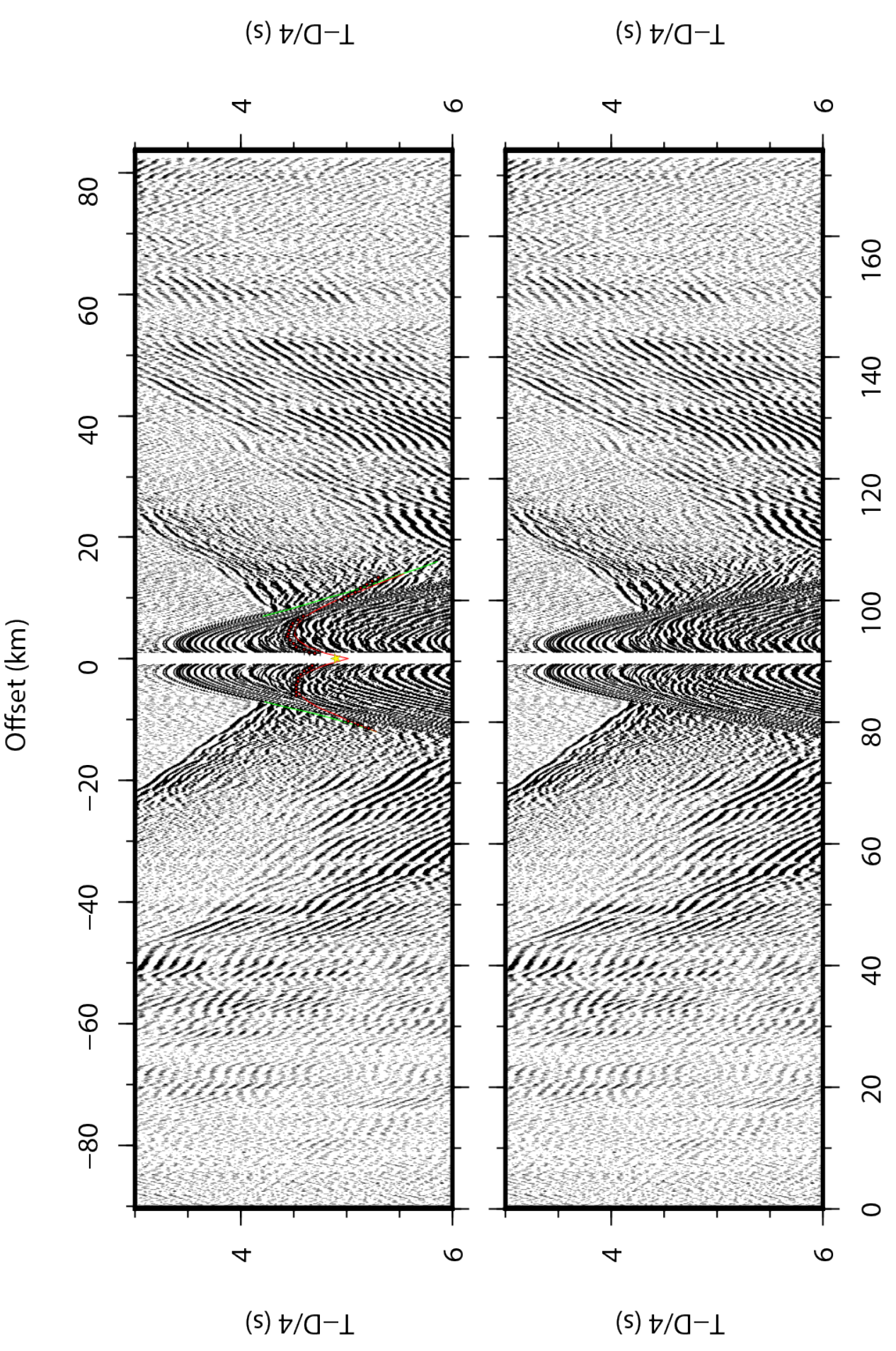


Figure C.23: Record Section: OBS24

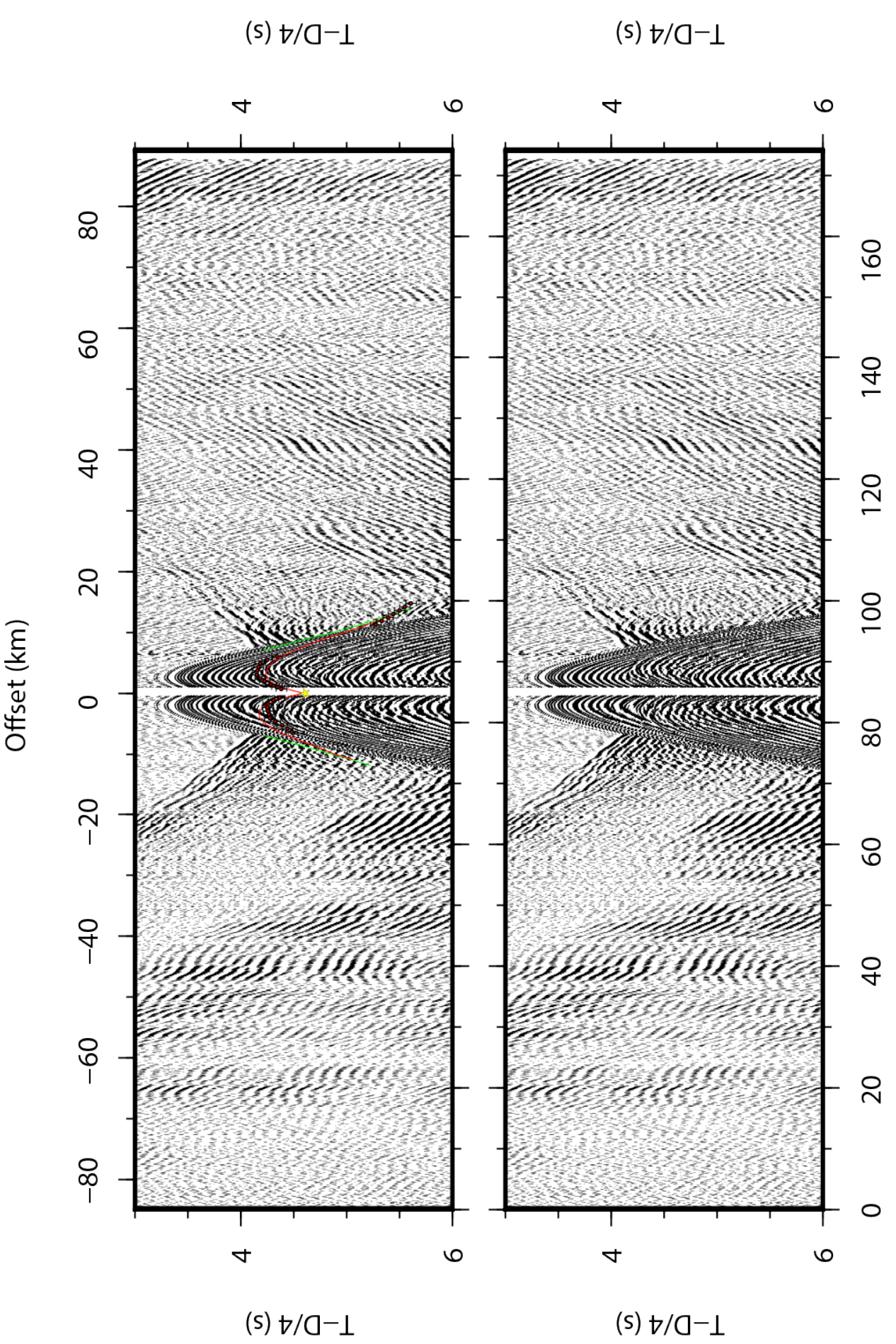


Figure C.24: Record Section: OBS26

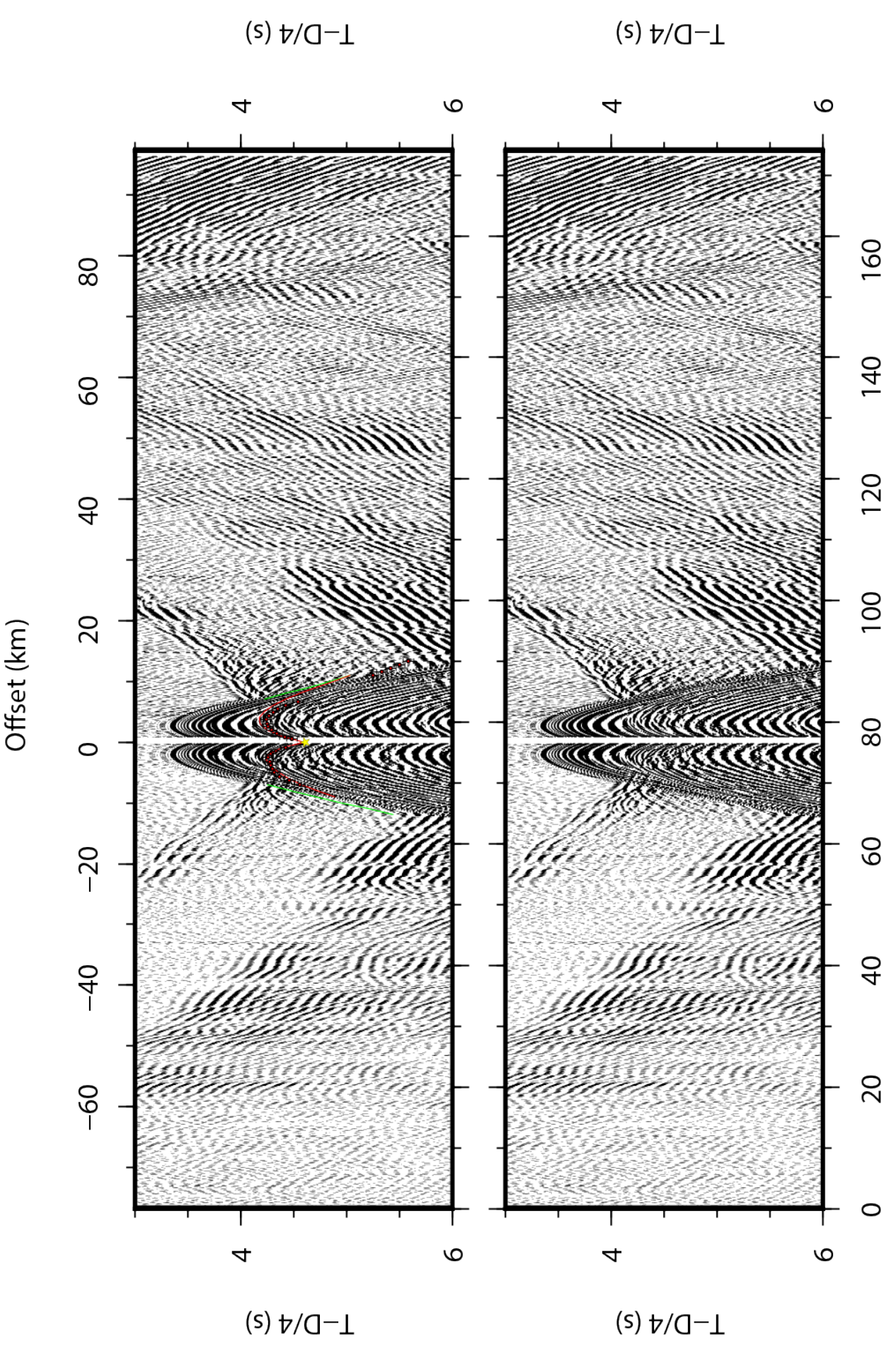


Figure C.25: Record Section: OBS27

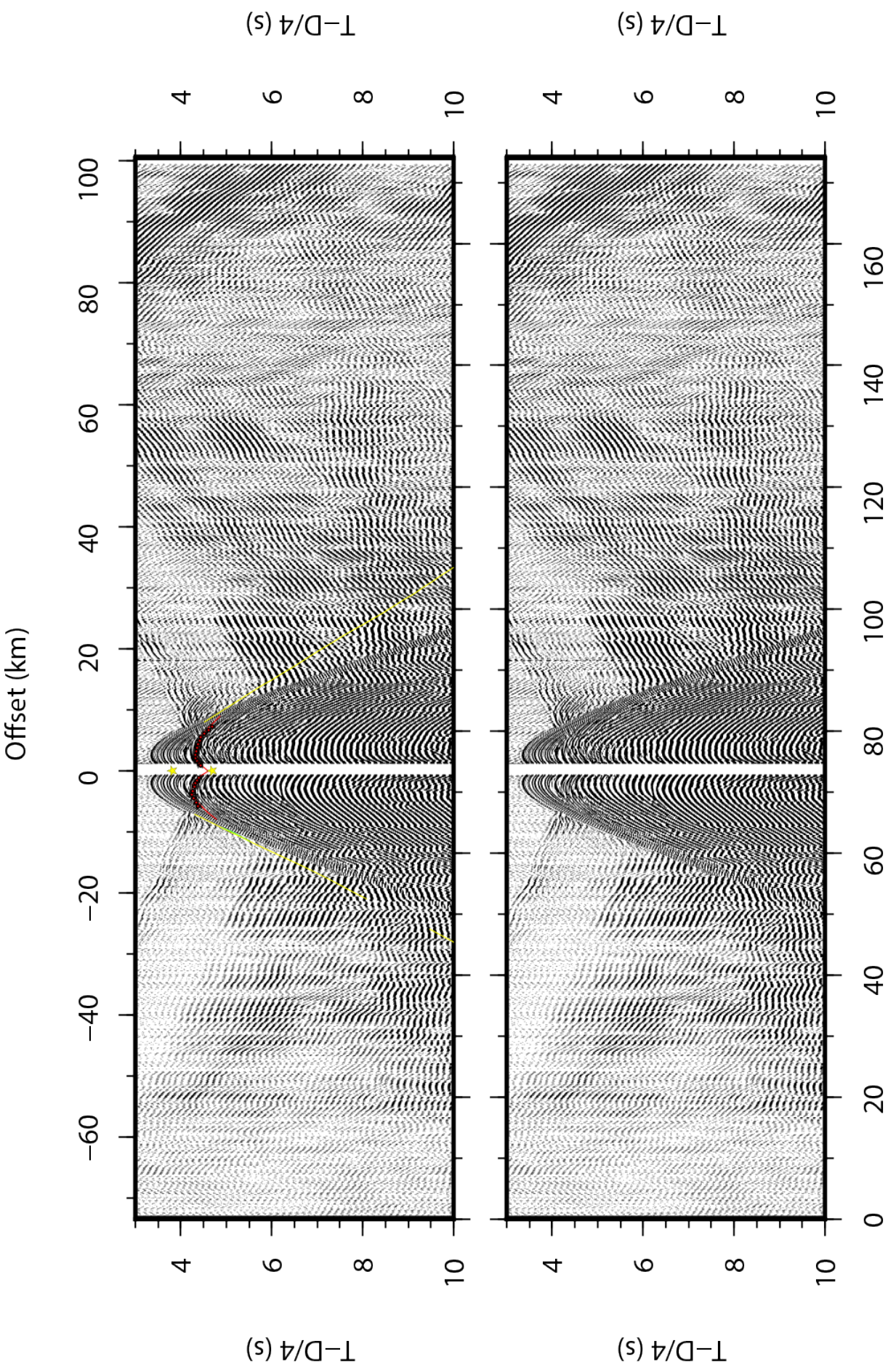


Figure C.26: Record Section: OBS28

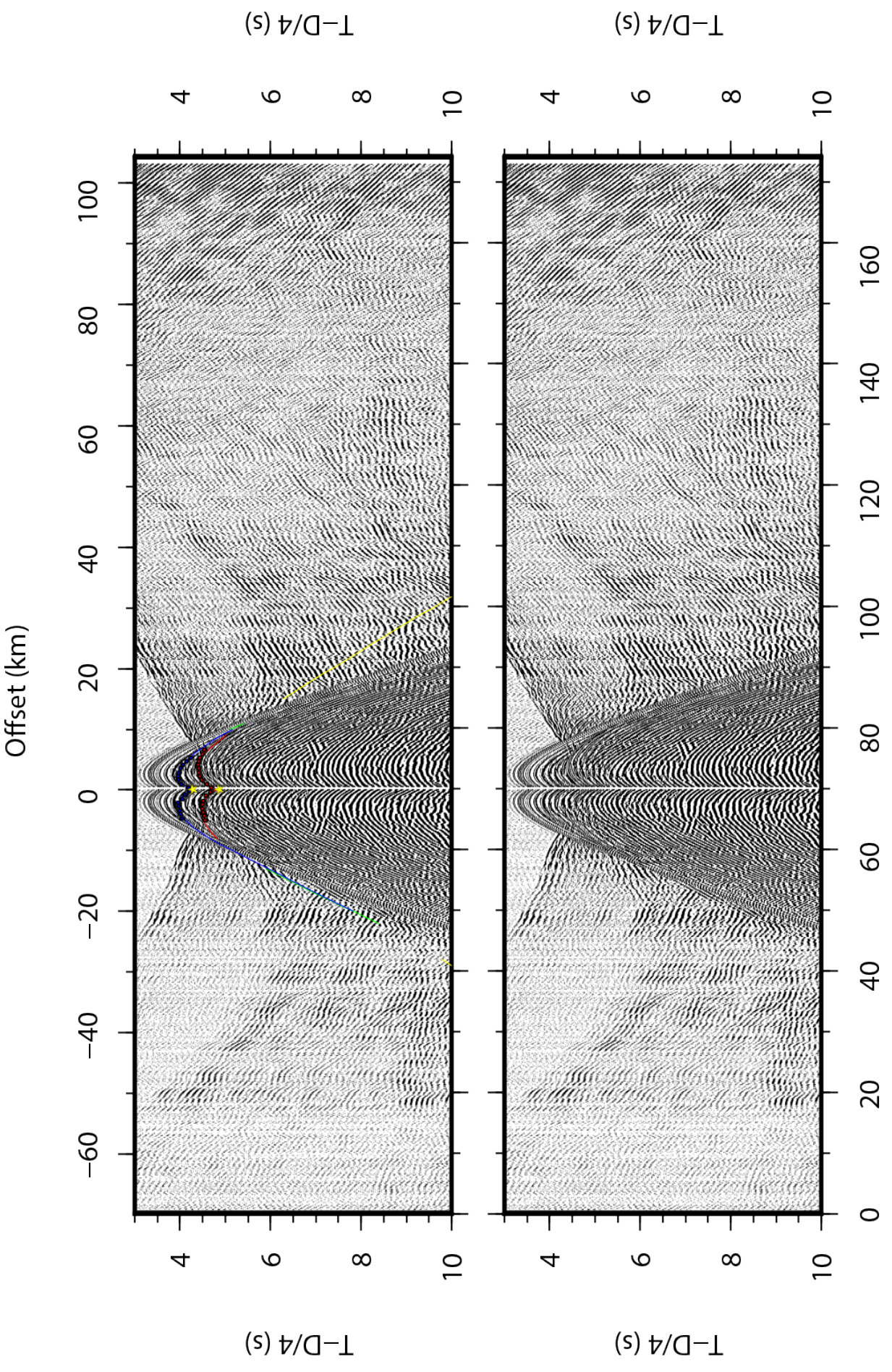


Figure C.27: Record Section: OBS29

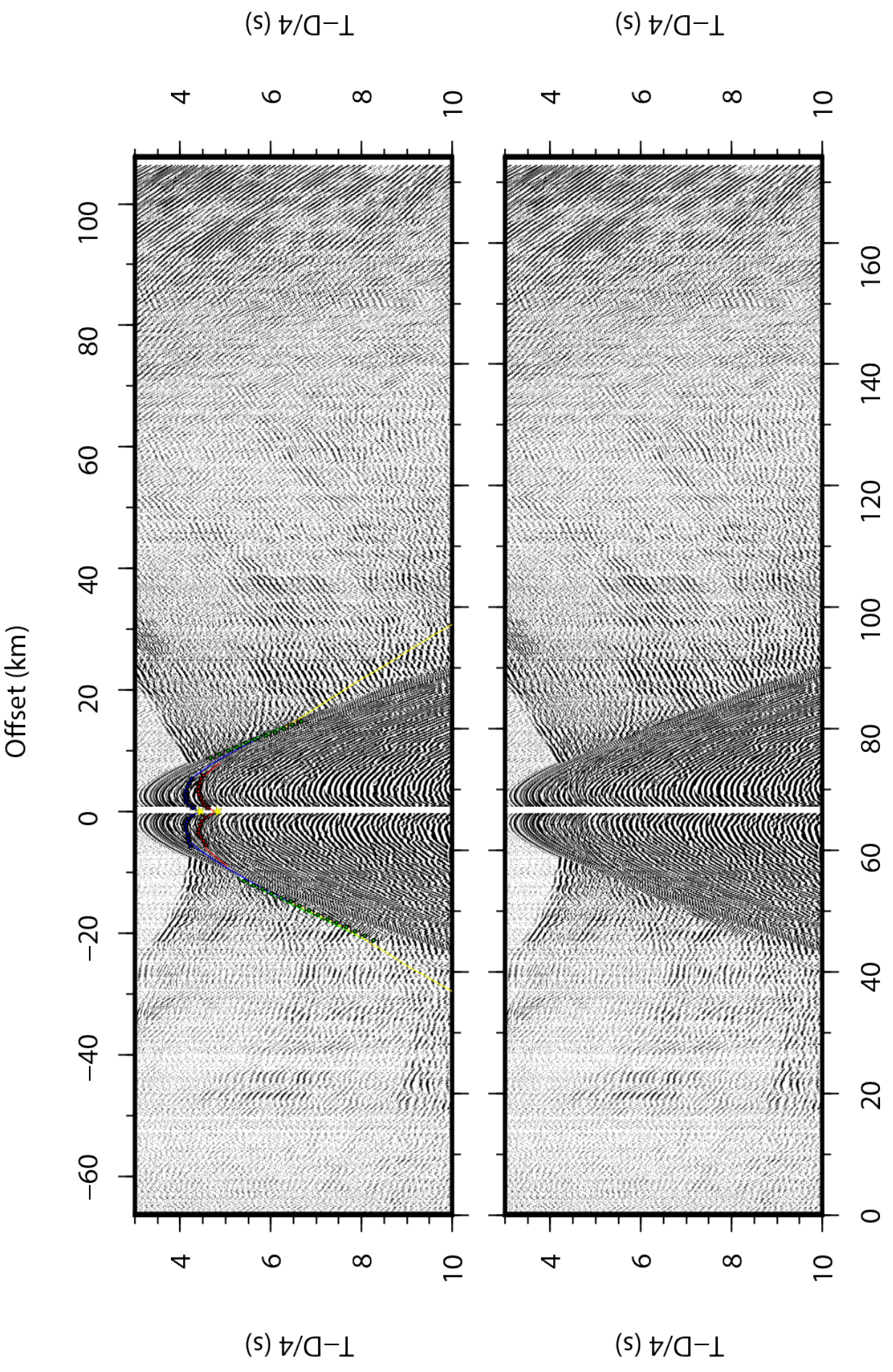


Figure C.28: Record Section: OBS30

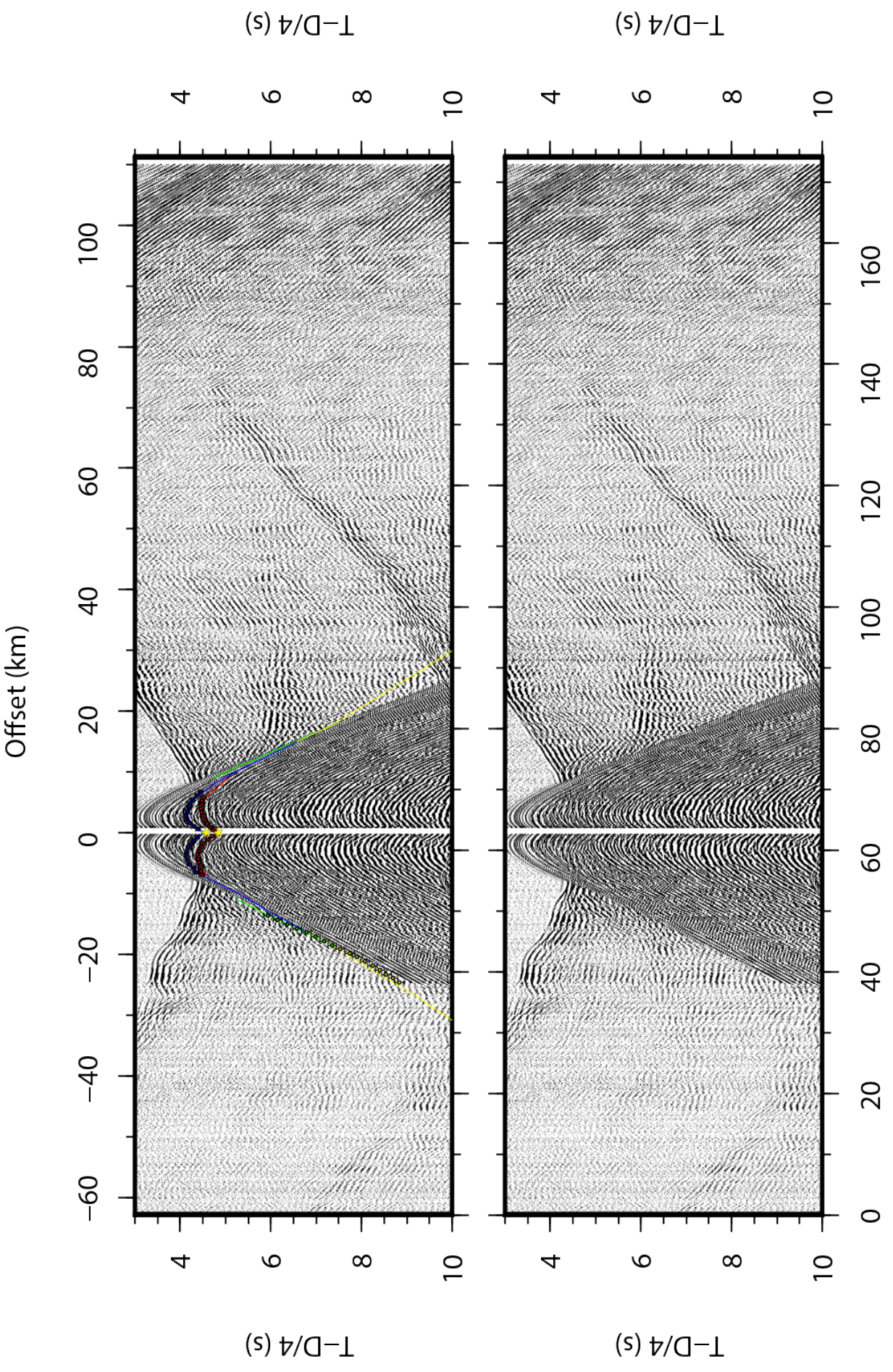


Figure C.29: Record Section: OBS31

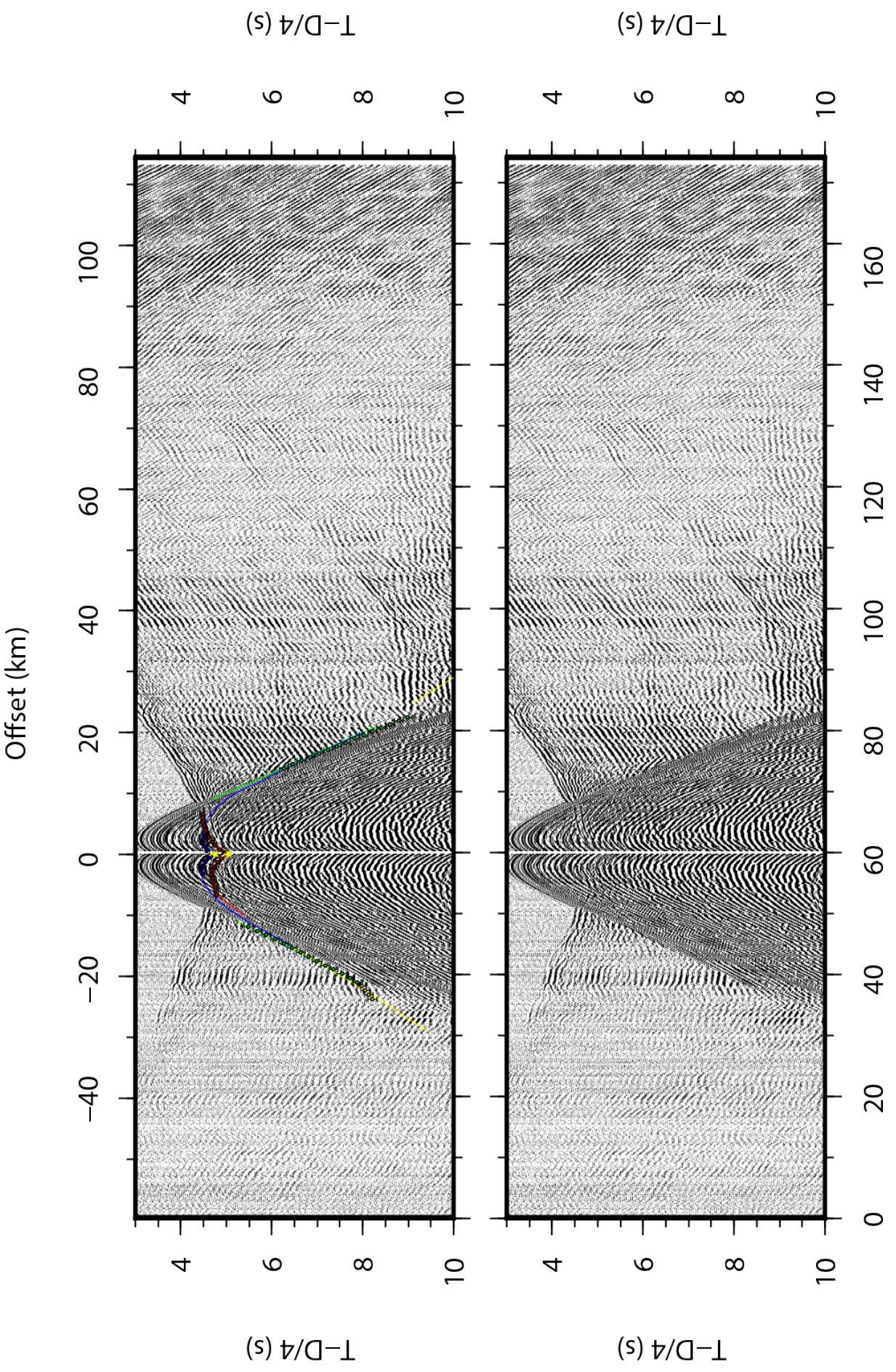


Figure C.30: Record Section: OBS32

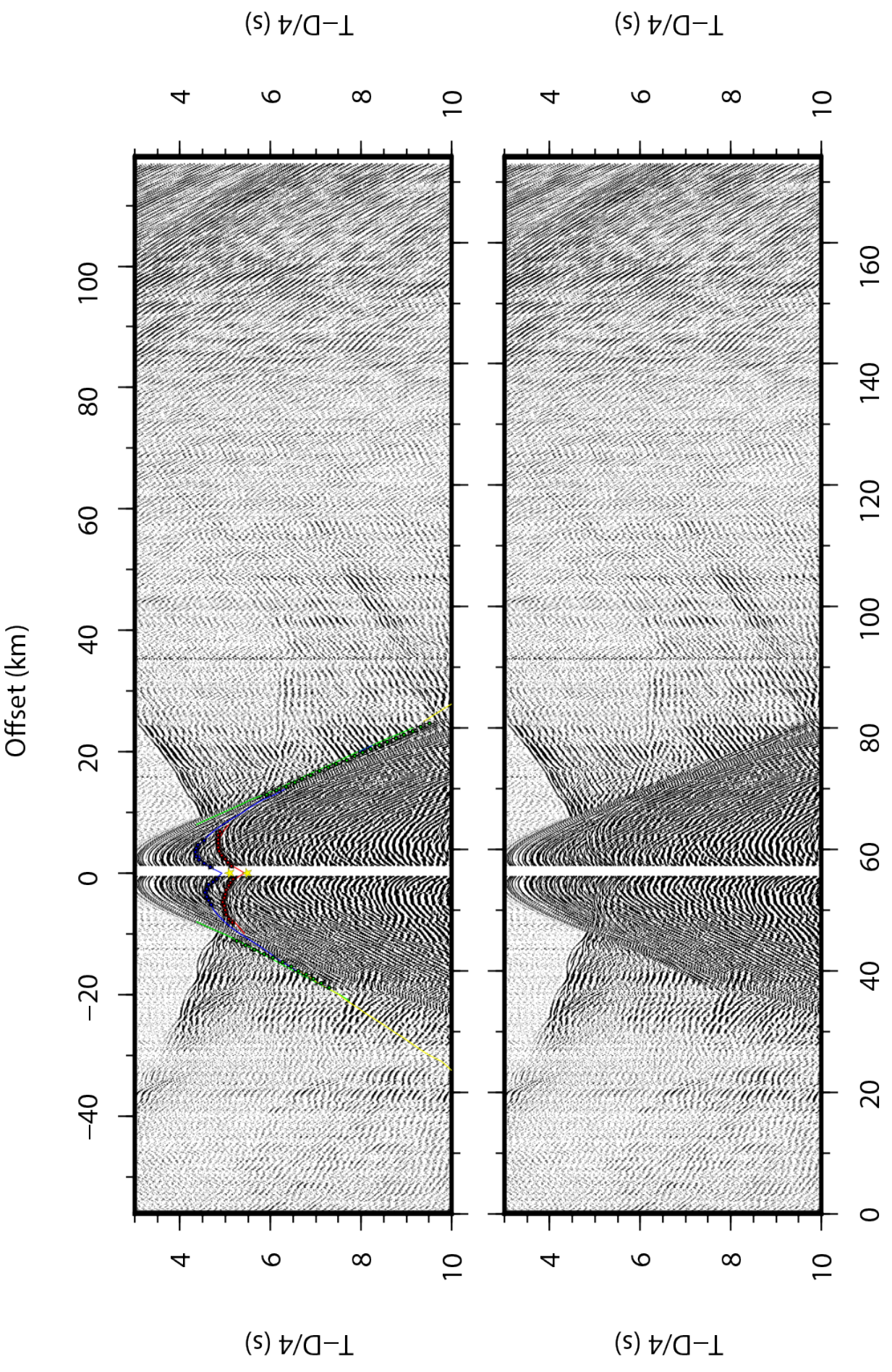


Figure C.31: Record Section: OBS33

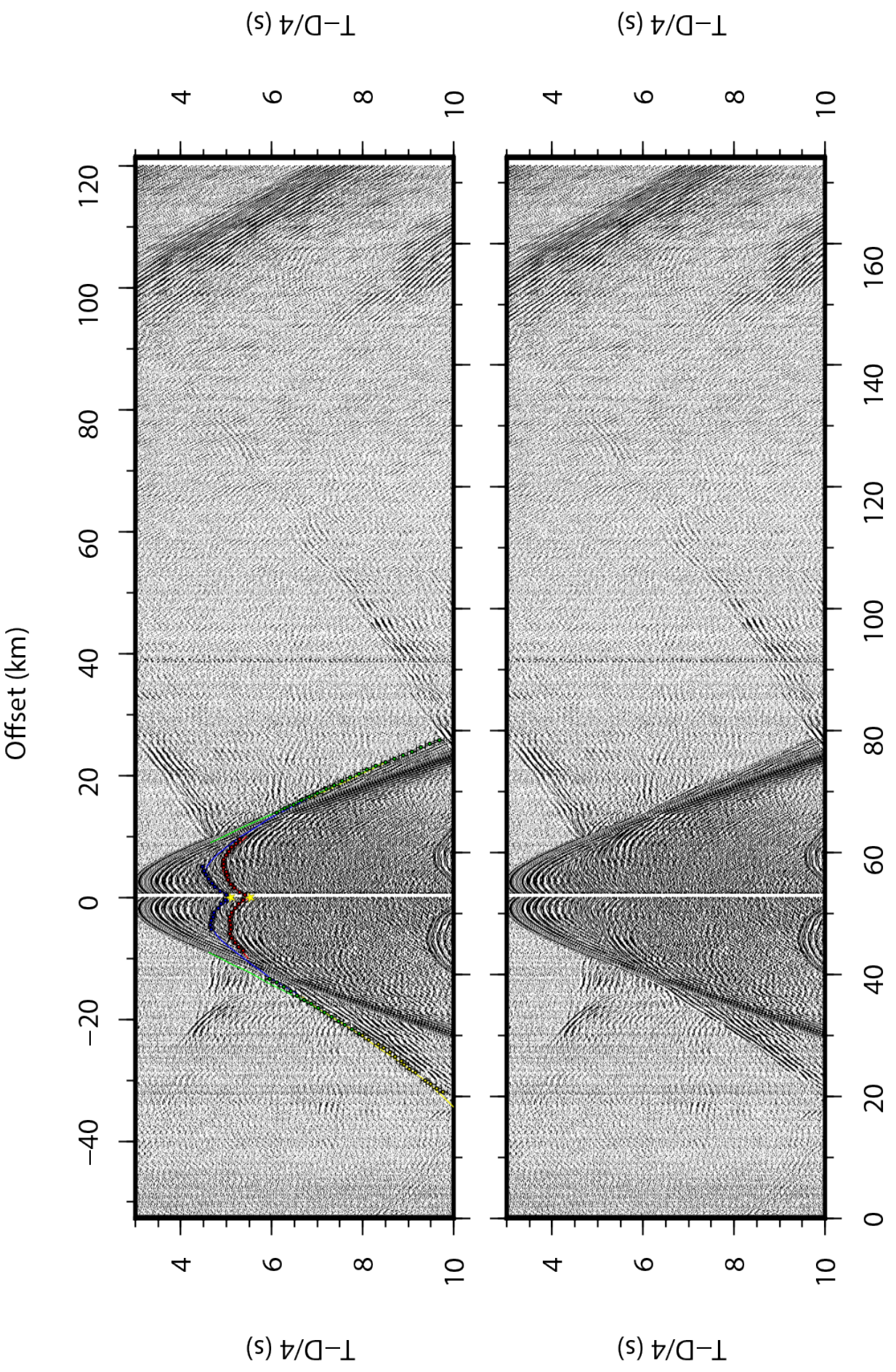


Figure C.32: Record Section: OBS34

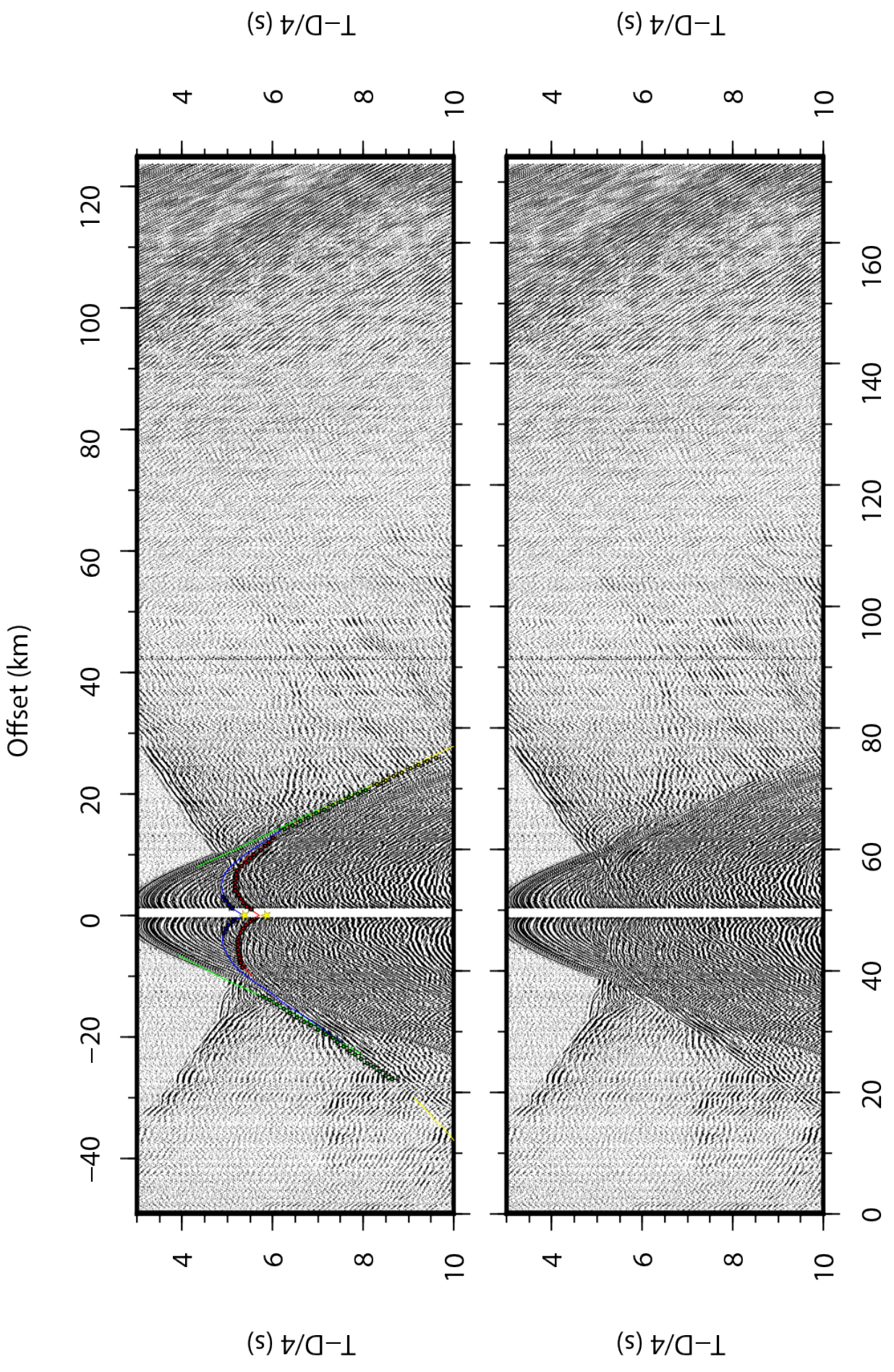


Figure C.33: Record Section: OBS35

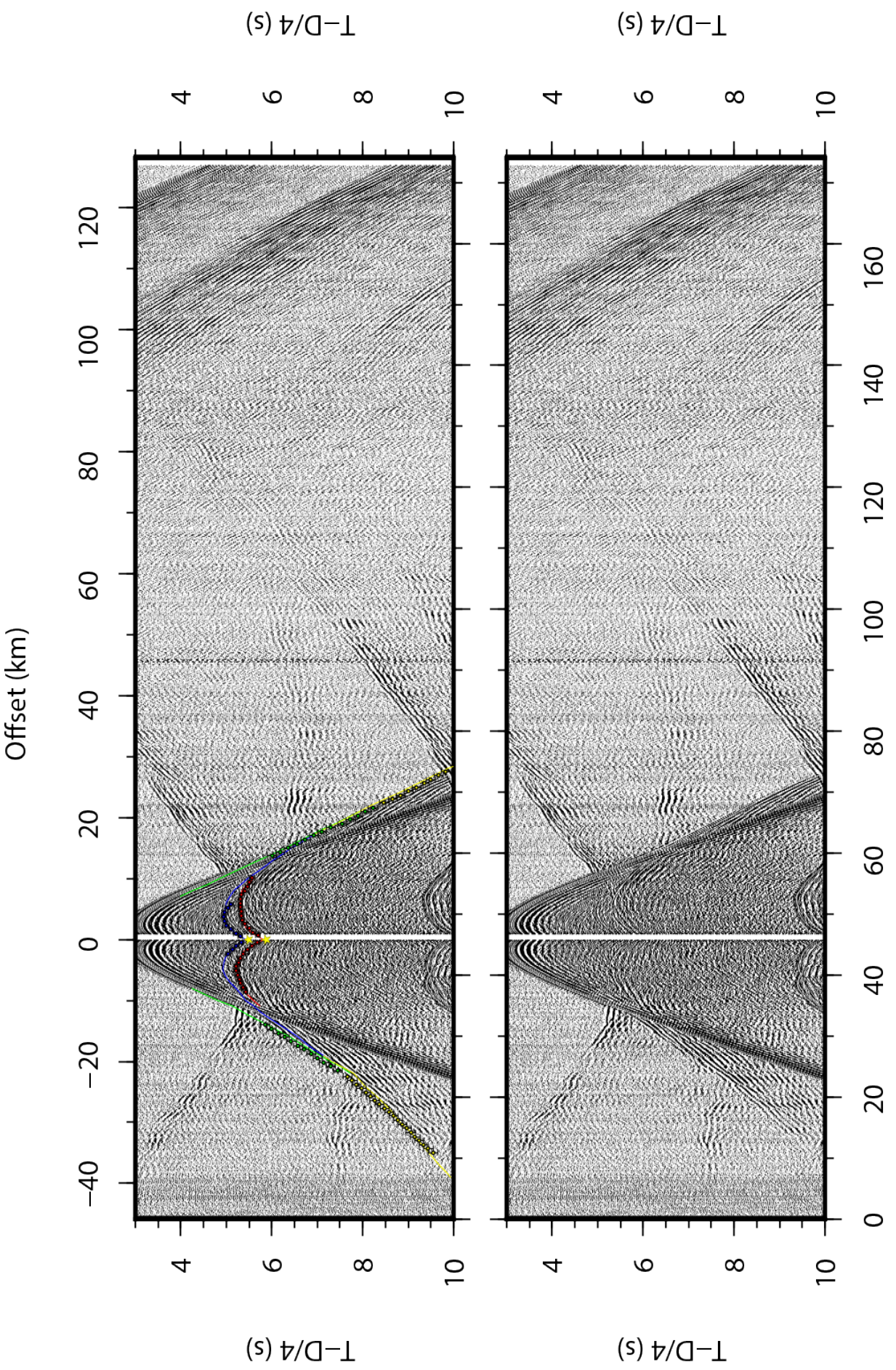


Figure C.34: Record Section: OBS36

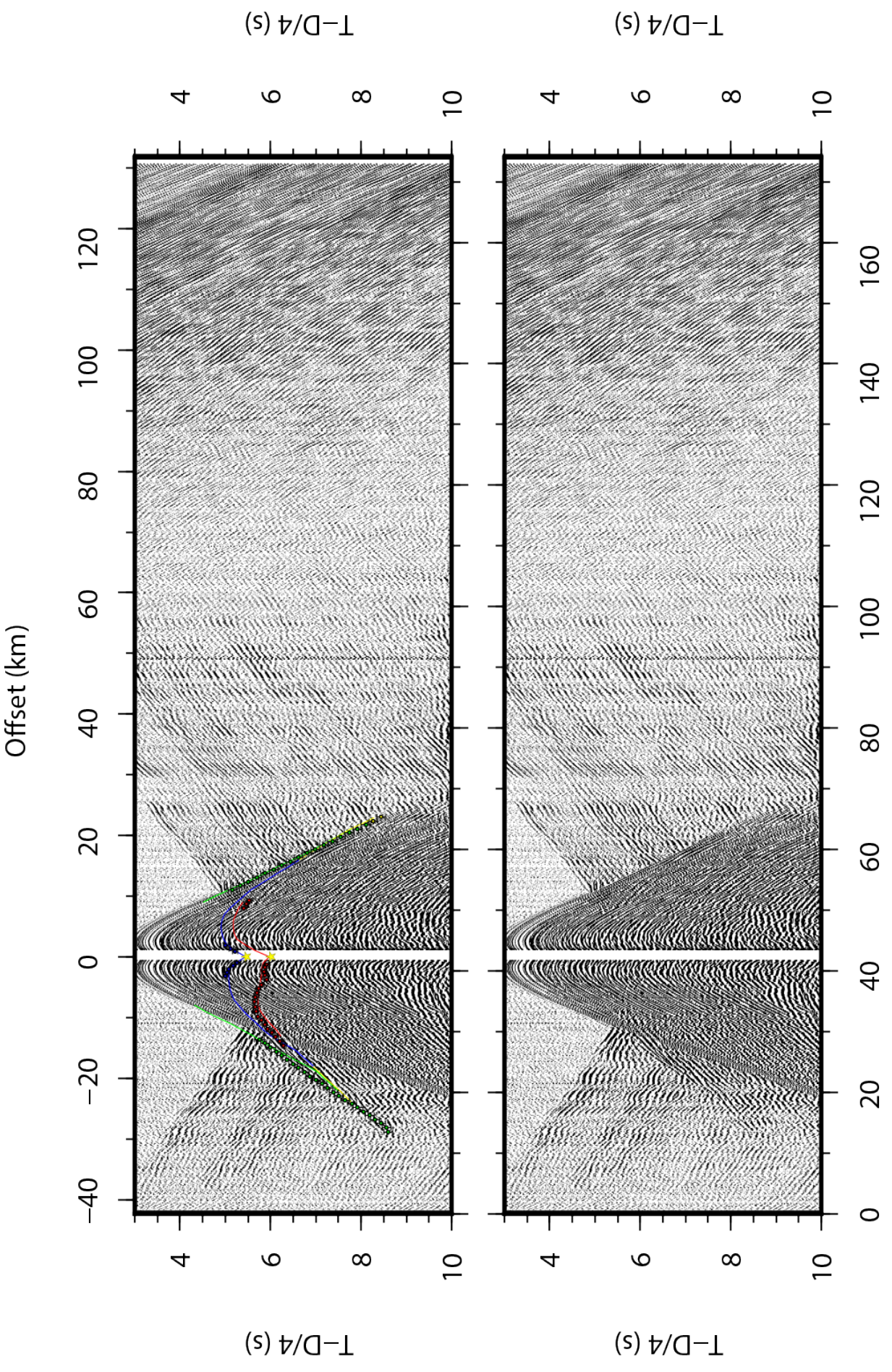


Figure C.35: Record Section: OBS37

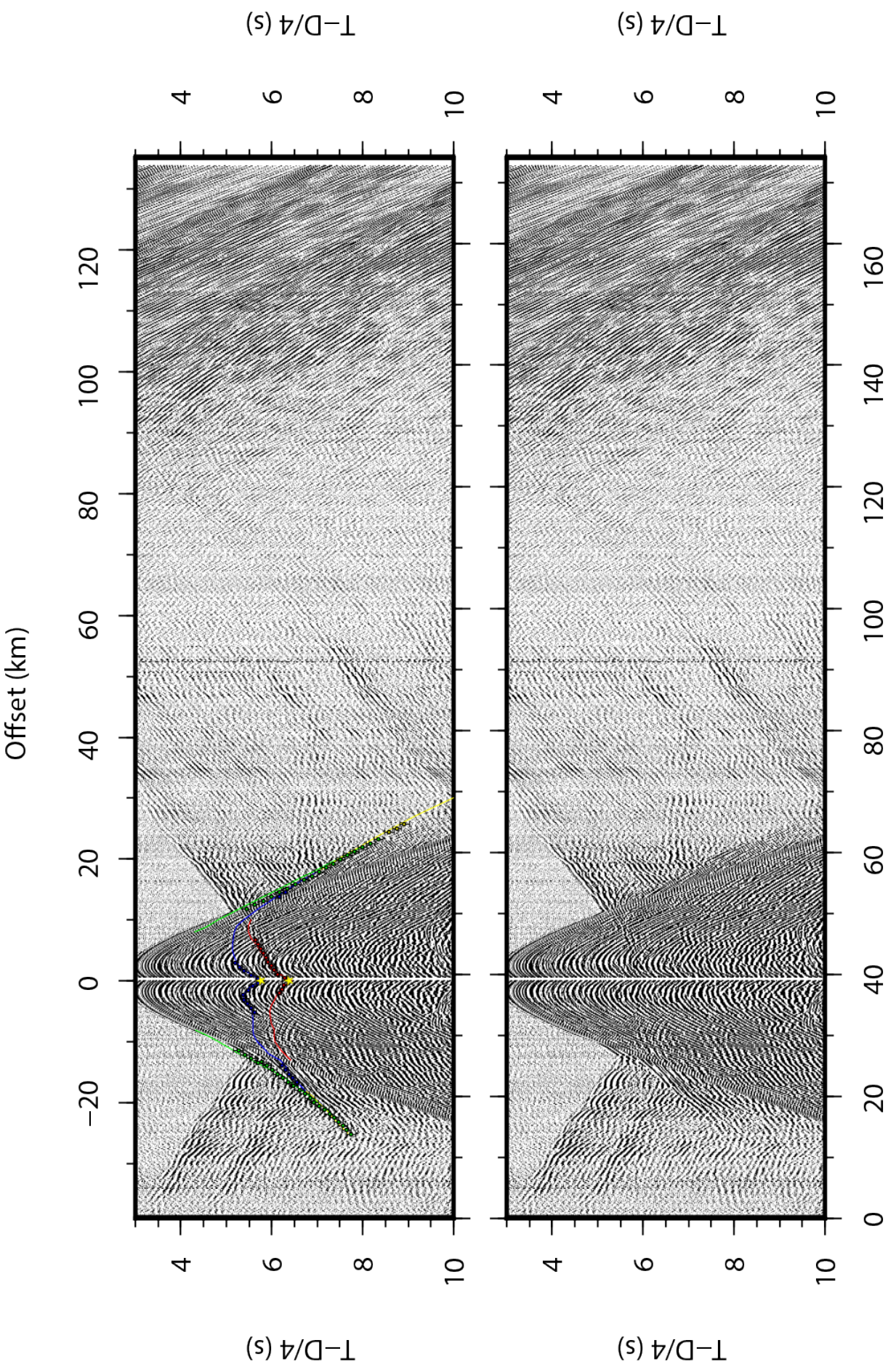


Figure C.36: Record Section: OBS38

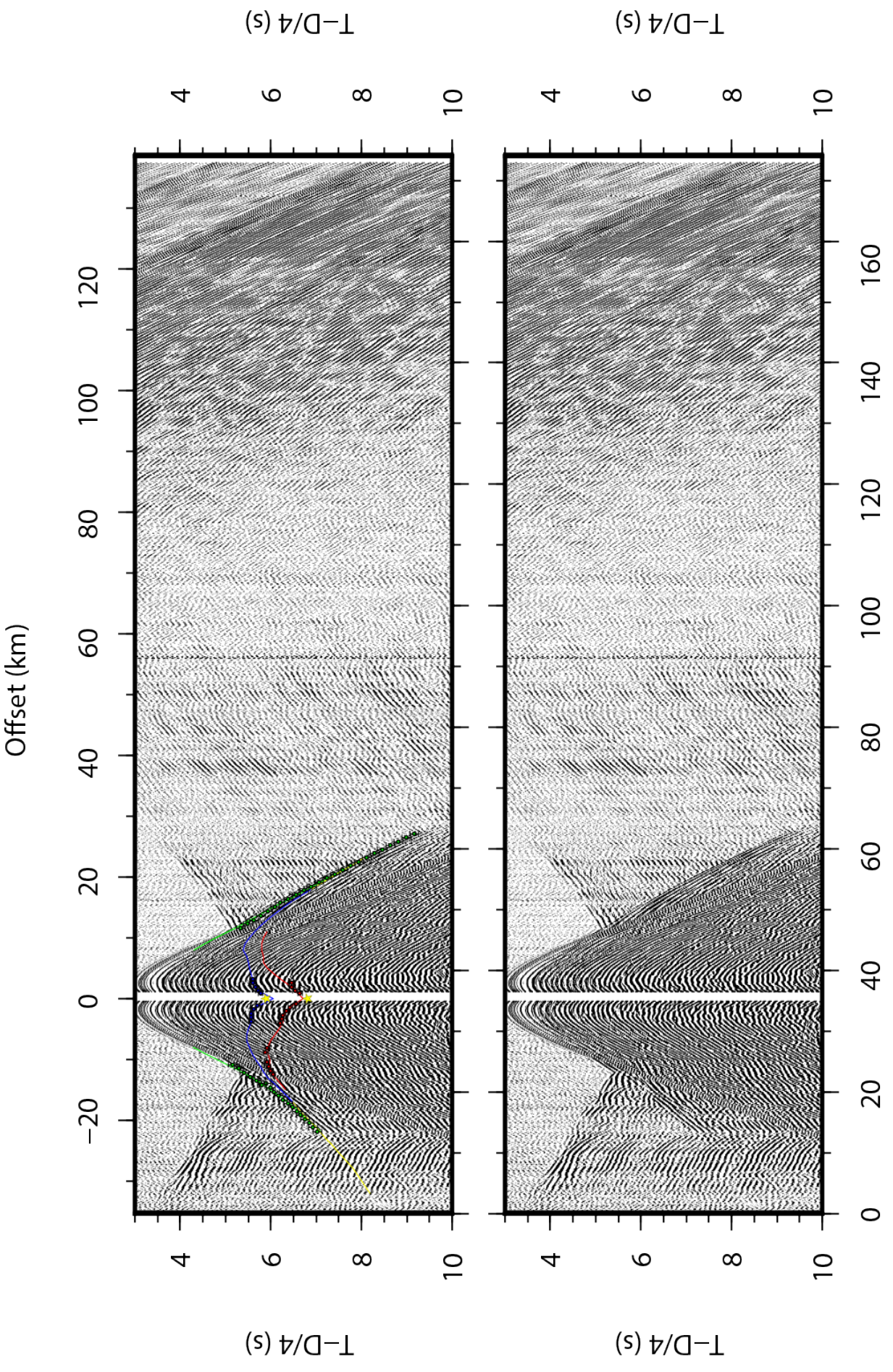


Figure C.37: Record Section: OBS39

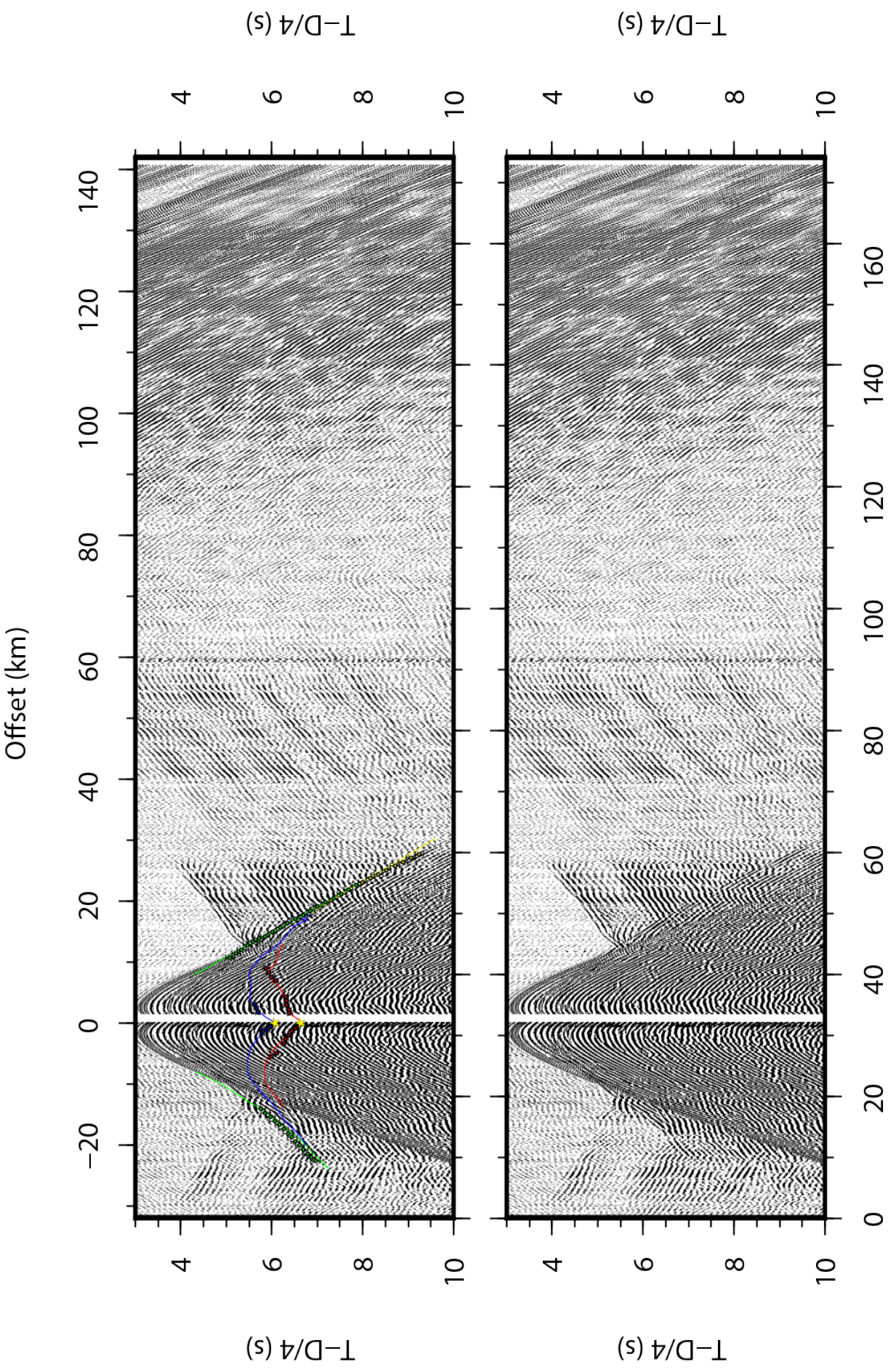


Figure C.38: Record Section: OBS40

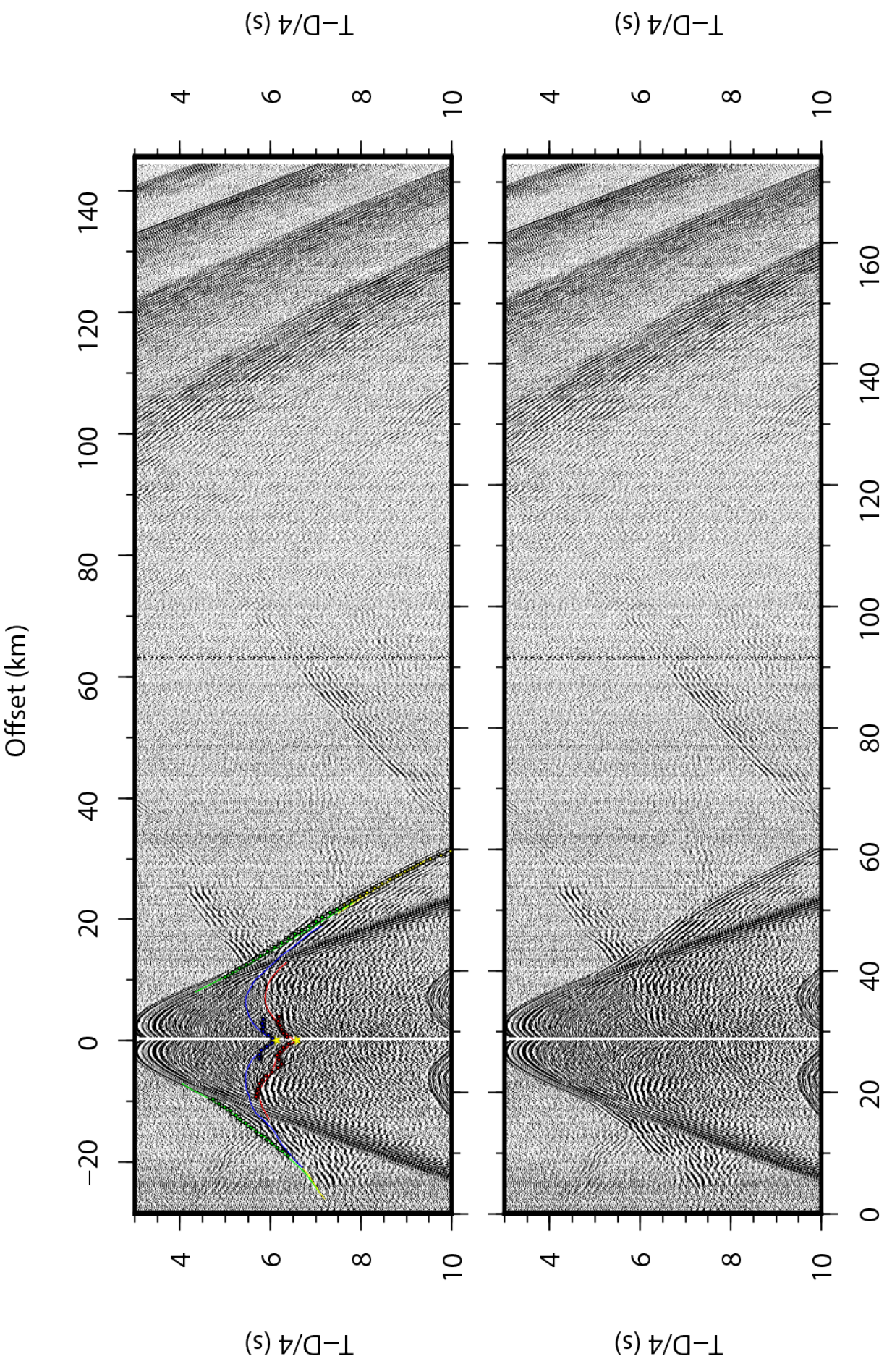


Figure C.39: Record Section: OBS41

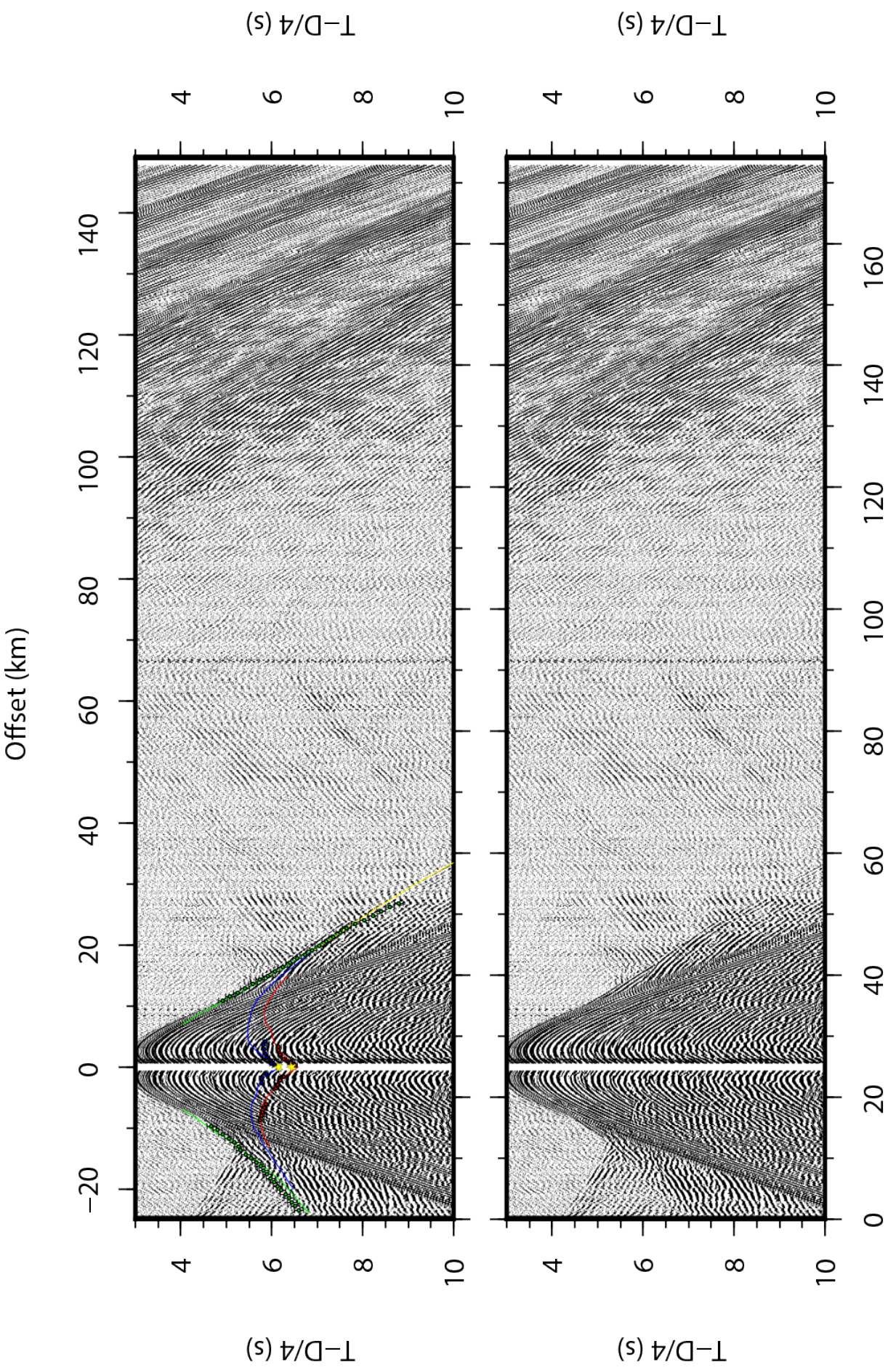


Figure C.40: Record Section: OBS42

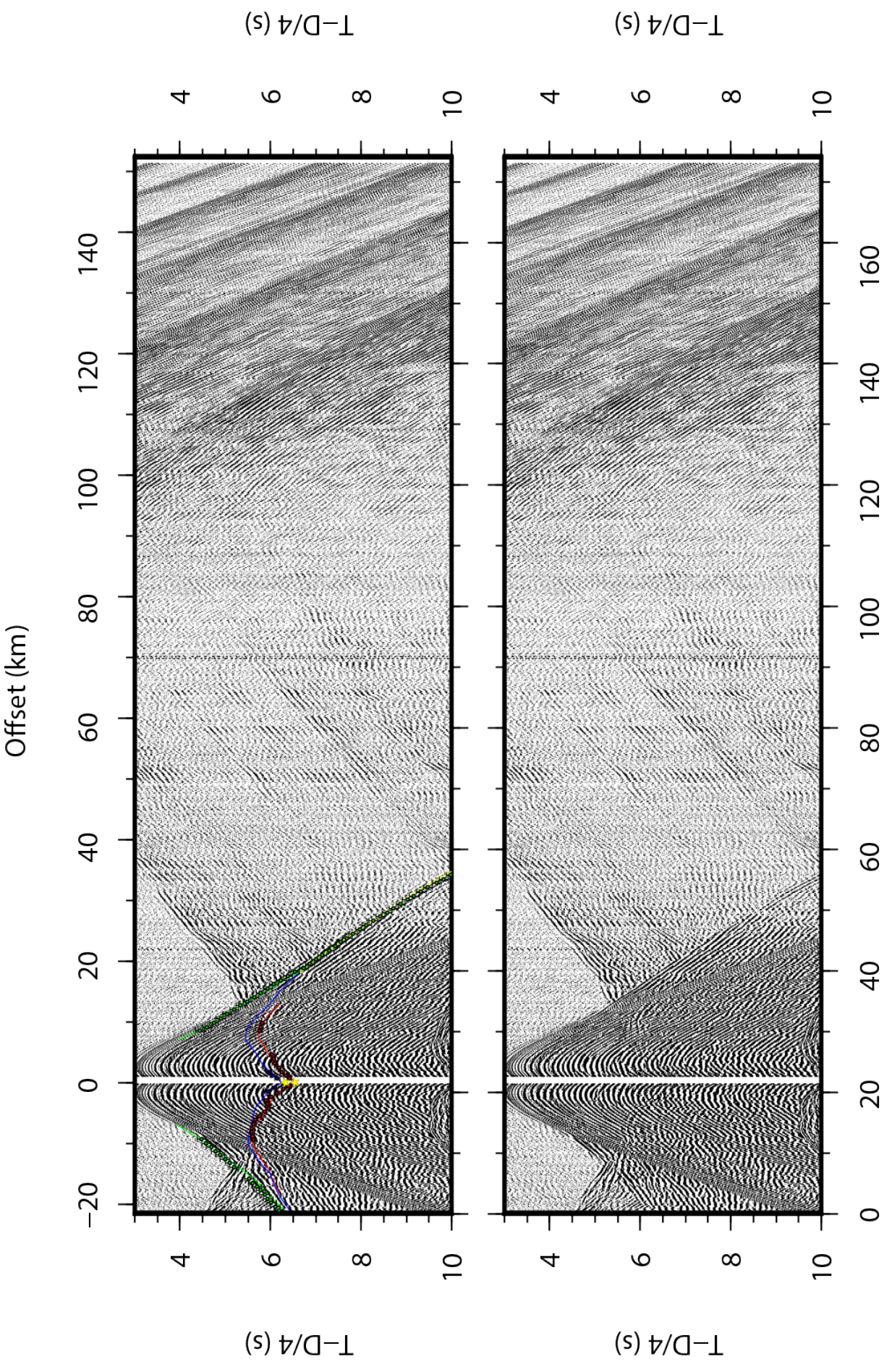


Figure C.41: Record Section: OBS43

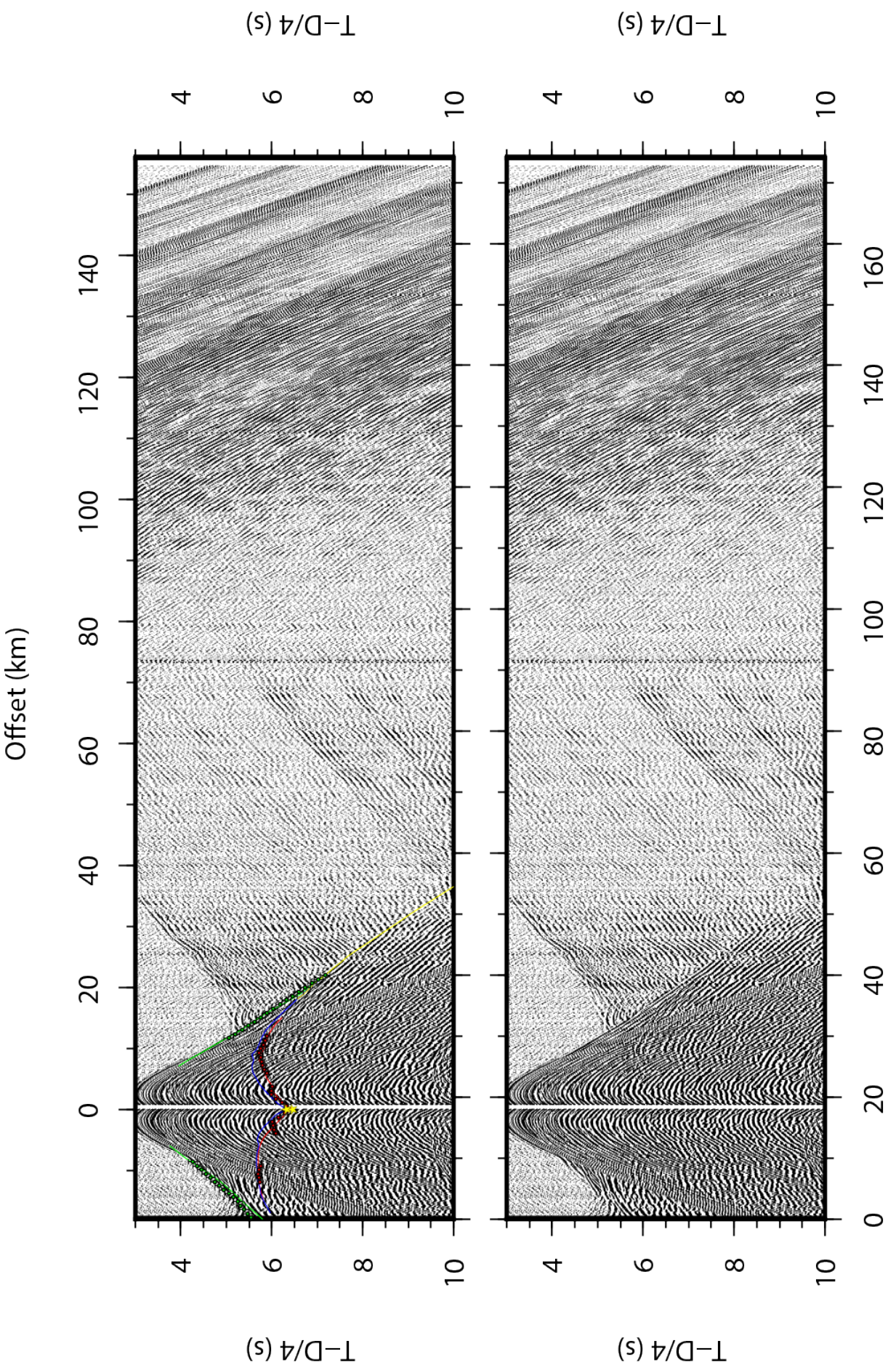


Figure C.42: Record Section: OBS44

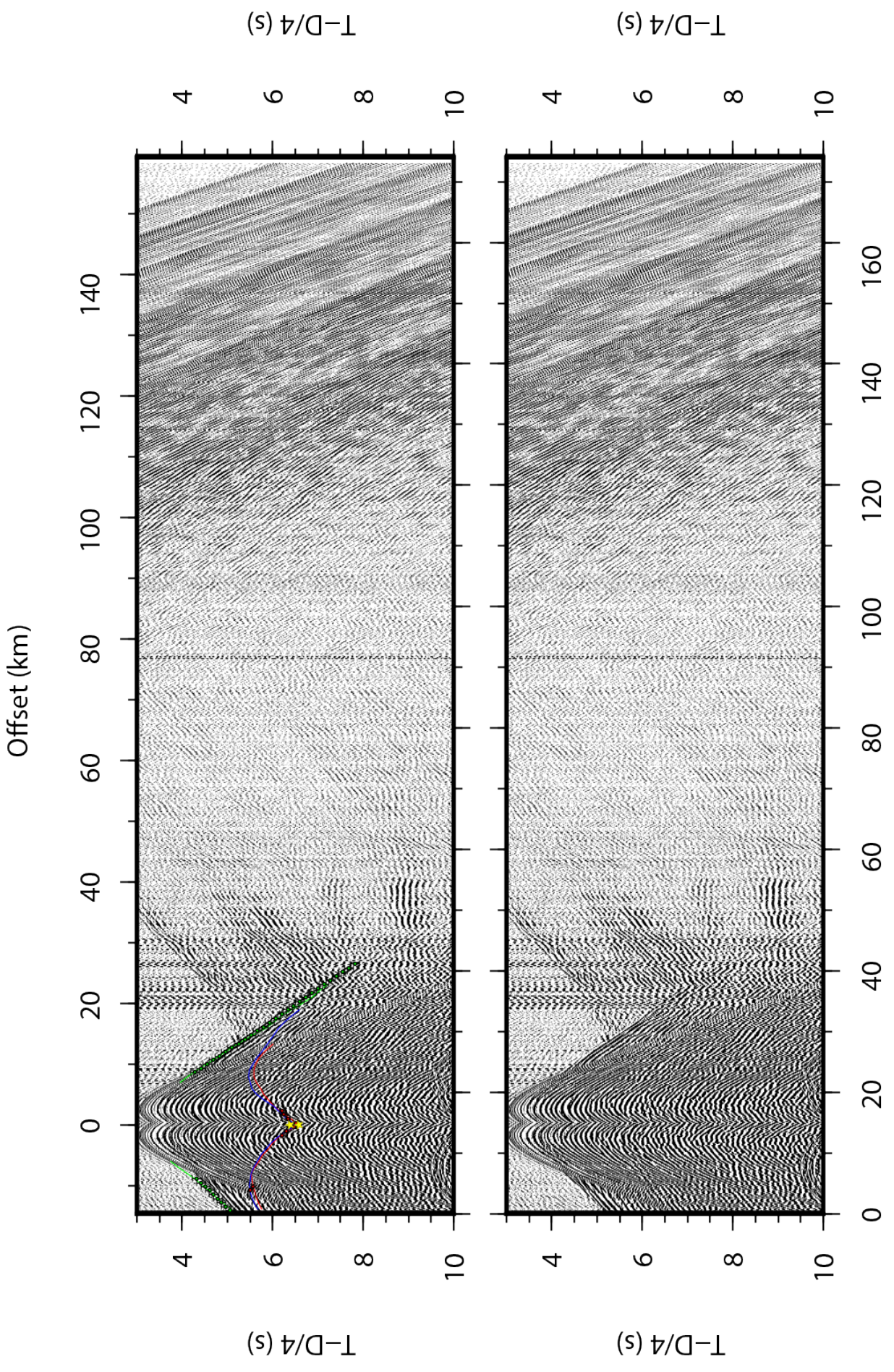


Figure C.43: Record Section: OBS45

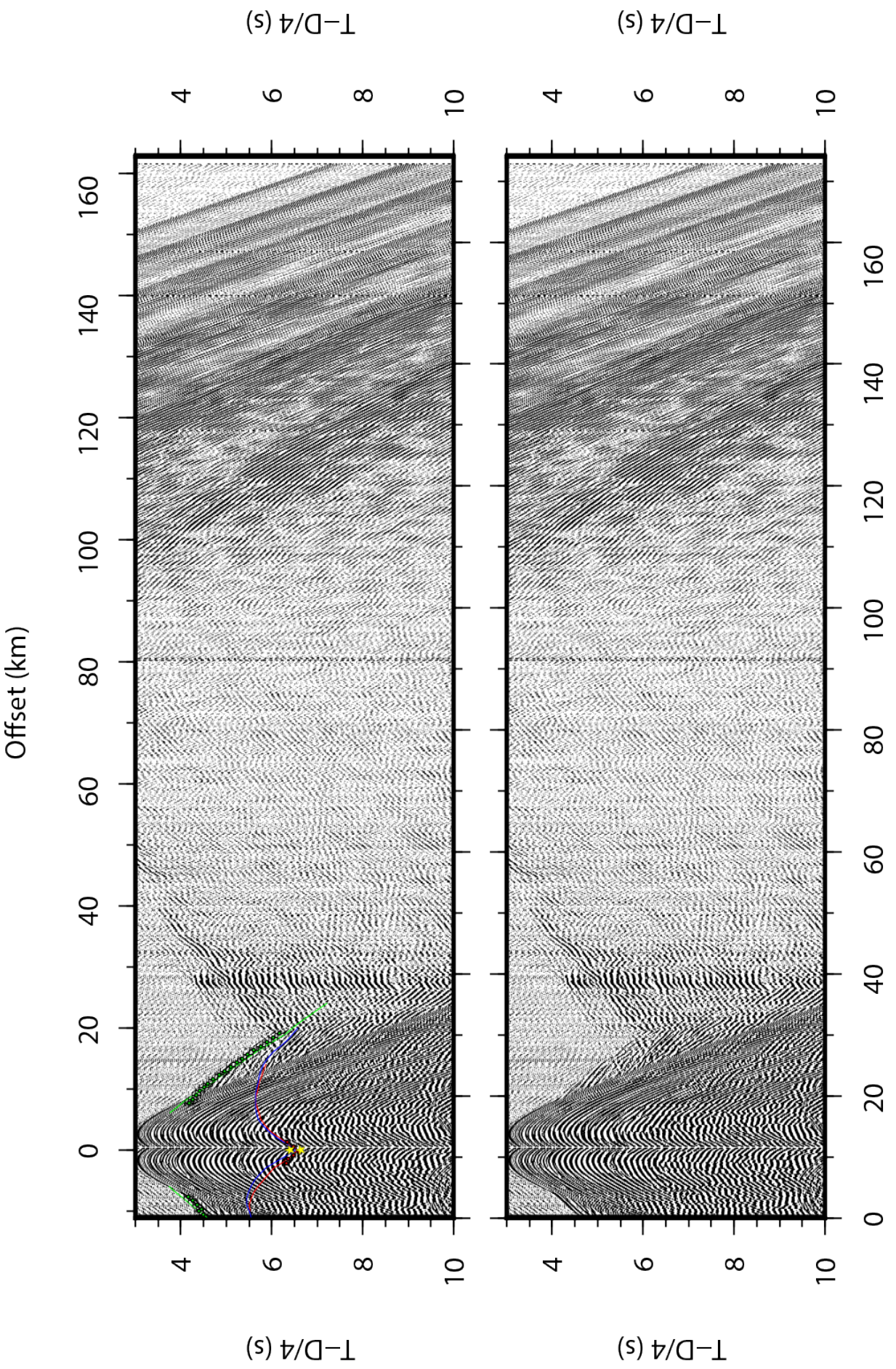


Figure C.44: Record Section: OBS46

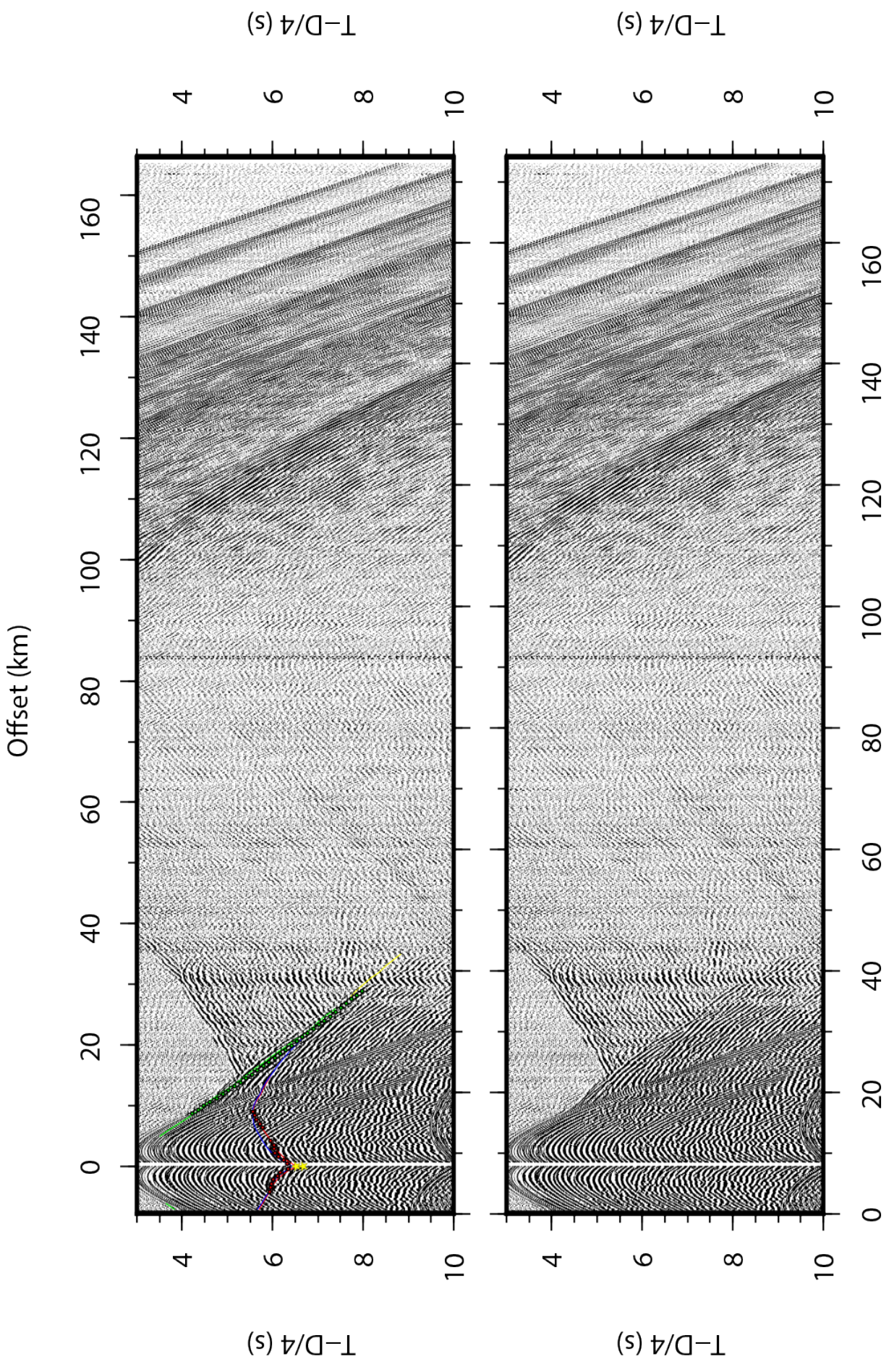


Figure C.45: Record Section: OBS47

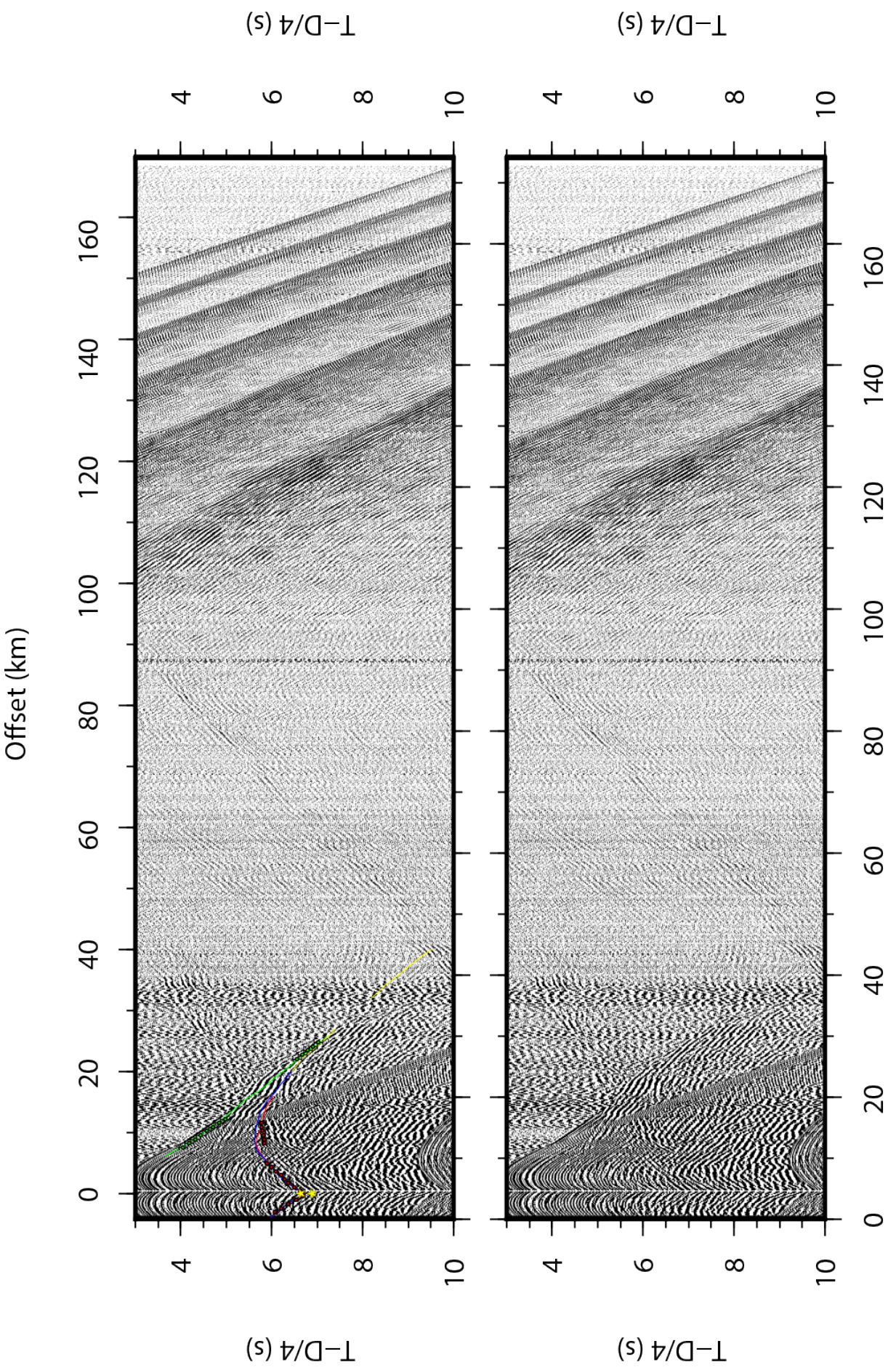


Figure C.46: Record Section: OBS48

Appendix D

Appendix: Chapter 6, OBS Record Section and Ray Trace Plots

This appendix contains a series of summary ray trace and corresponding record section plots for each of the OBS stations used in the development of the wide-angle velocity model for the structure of the crust and upper mantle along VoiLA Profile 1 in Chapter 6. See Chapter 6 for details of receiver layout and phase identification. Each plot is in 4 parts. A) Rays traced through final Monte Carlo averaged velocity model. Turning rays (Pg + Pn) are shown in black. PmP/PmP1 reflections in red. PmP2 in blue. B) Misfit by pick. Travel time misfit for each pick on the given instrument plotted against offset. Red lines mark errors of +/-0.1 s. Turning rays (Pg + Pn) shown in green, PmP/PmP1 in red, PmP2 in blue. RMS misfit also given independently for PmP/PmP1, PmP2, Pg $<$ 20 km offset (i.e. rays turning in the upper crust), Pg/Pn $>$ 20 km offset (i.e. rays turning in the lower crust and mantle). C) OBS record section with key phases labelled. First arrival picks (Pg + Pn) are shown in green, PmP/PmP1 in red and PmP2 in blue. One in five picks shown. D) As above without overlay.

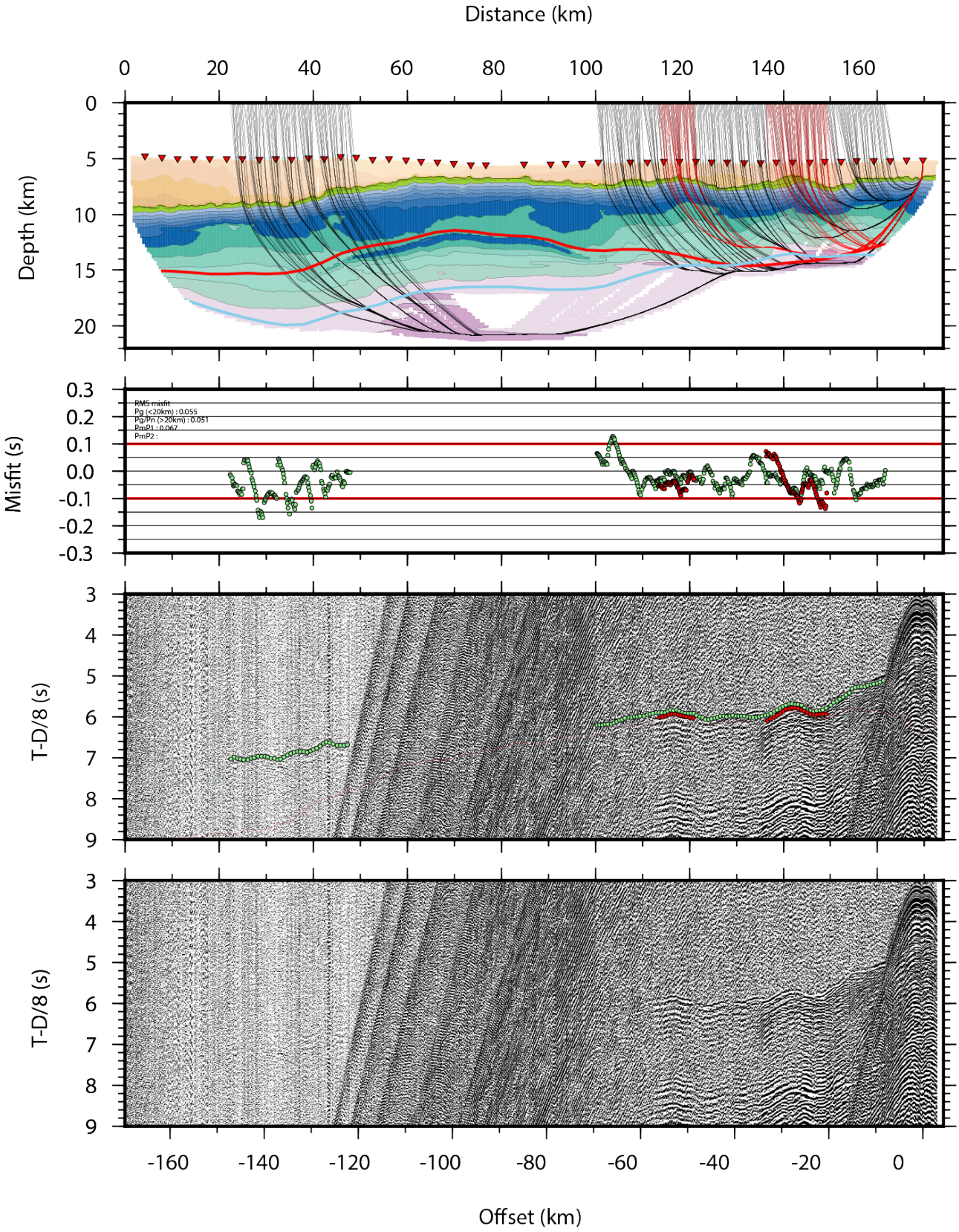


Figure D.1: Summary Plot: OBS2

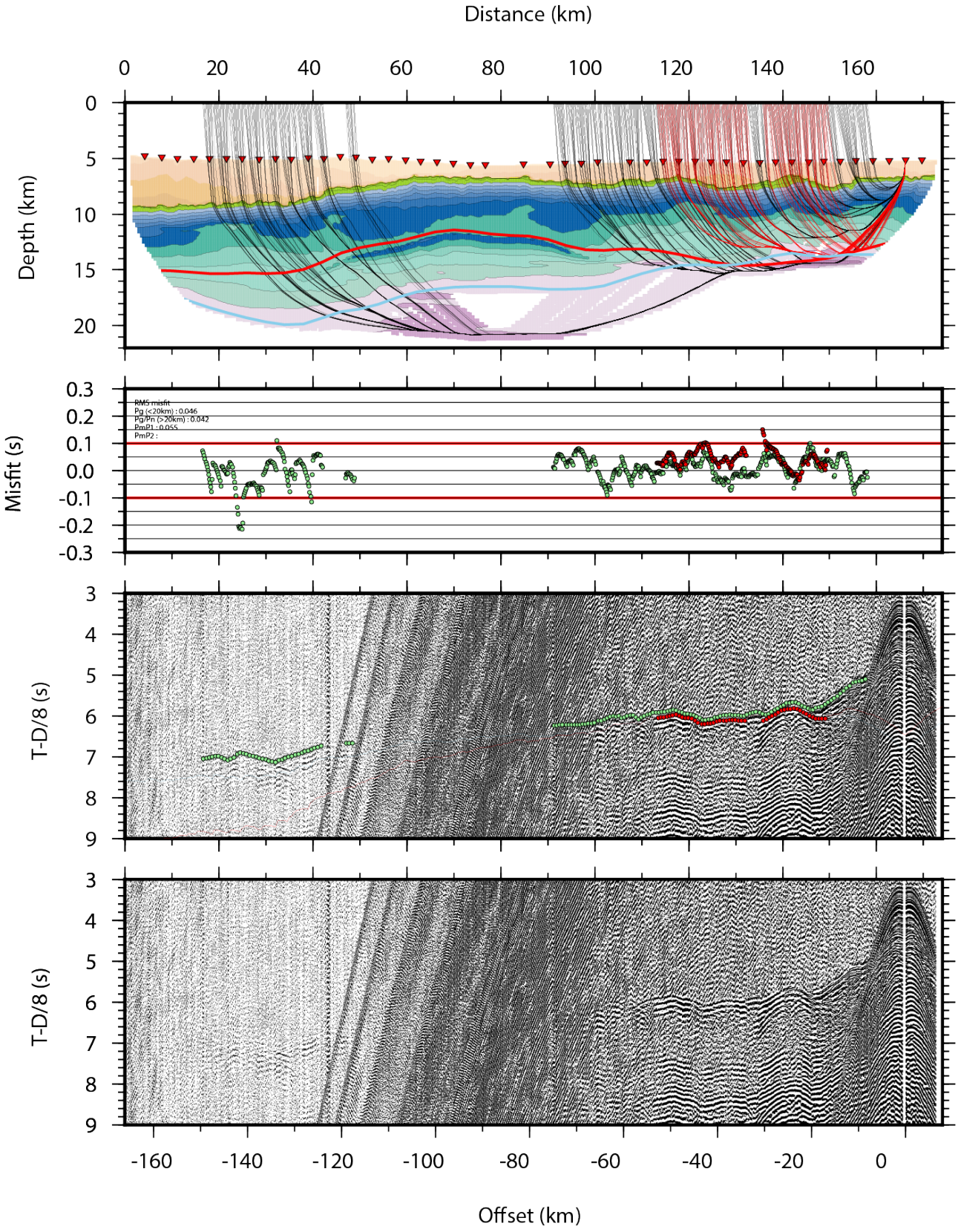


Figure D.2: Summary Plot: OBS3

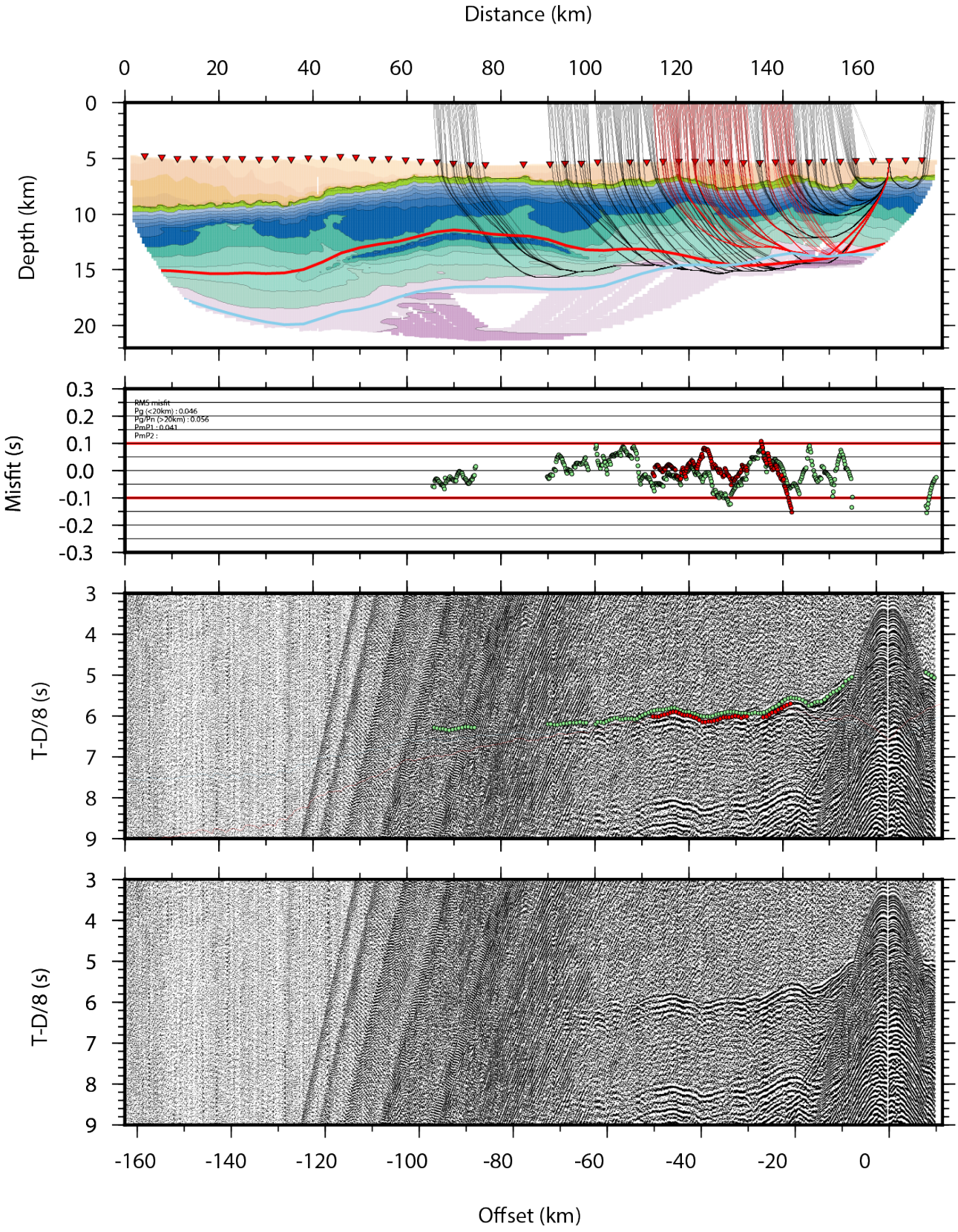


Figure D.3: Summary Plot: OBS4

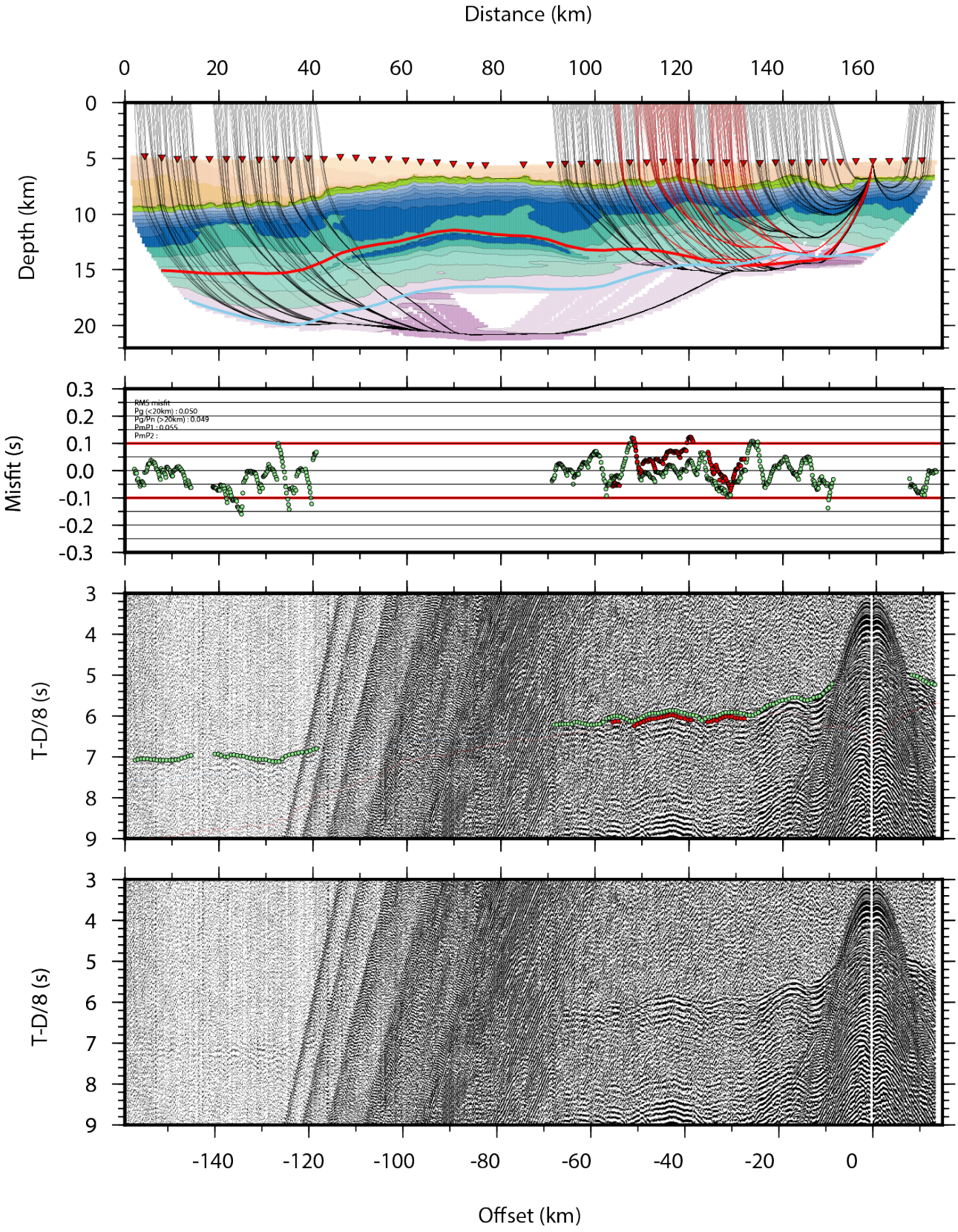


Figure D.4: Summary Plot: OBS5

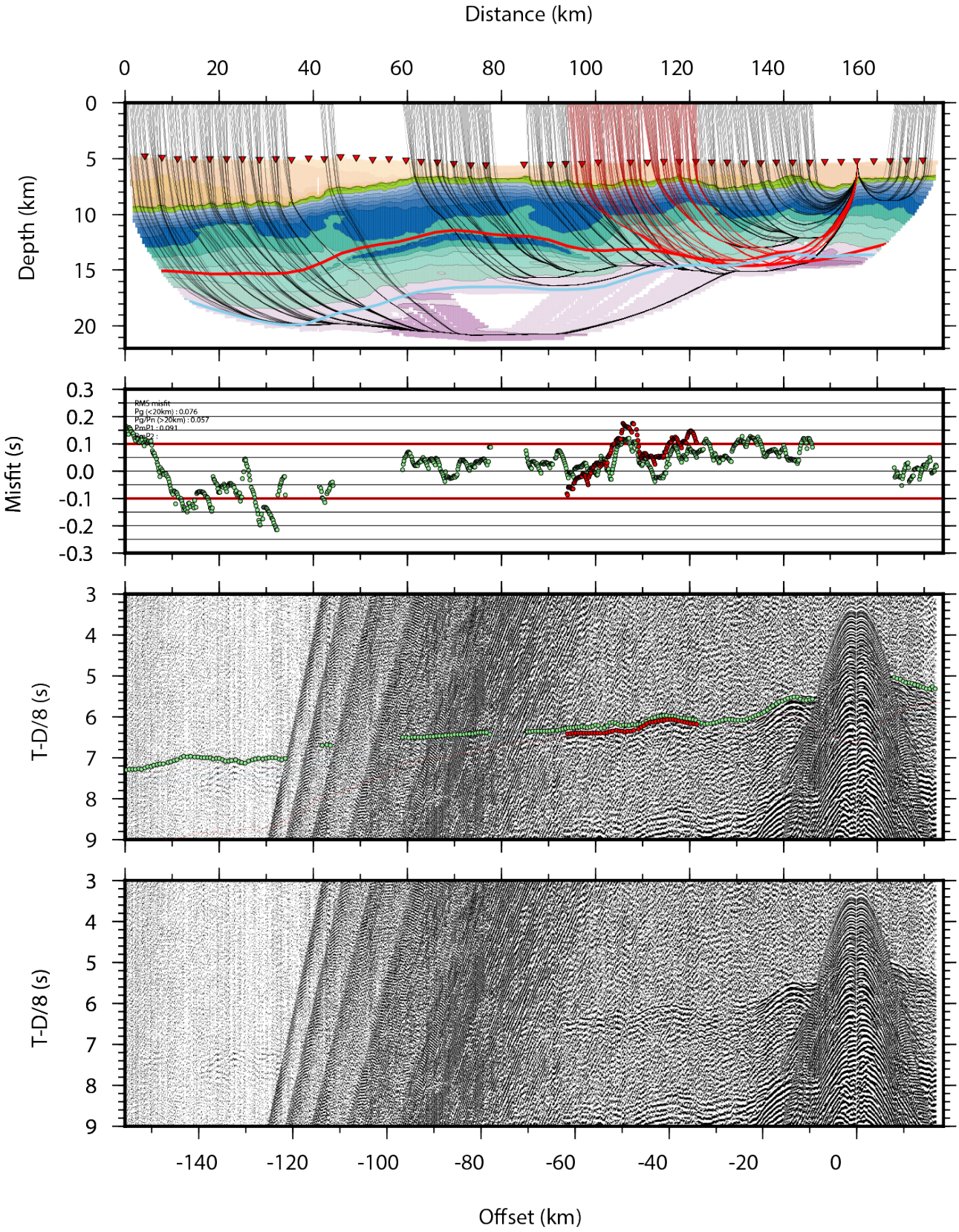


Figure D.5: Summary Plot: OBS6

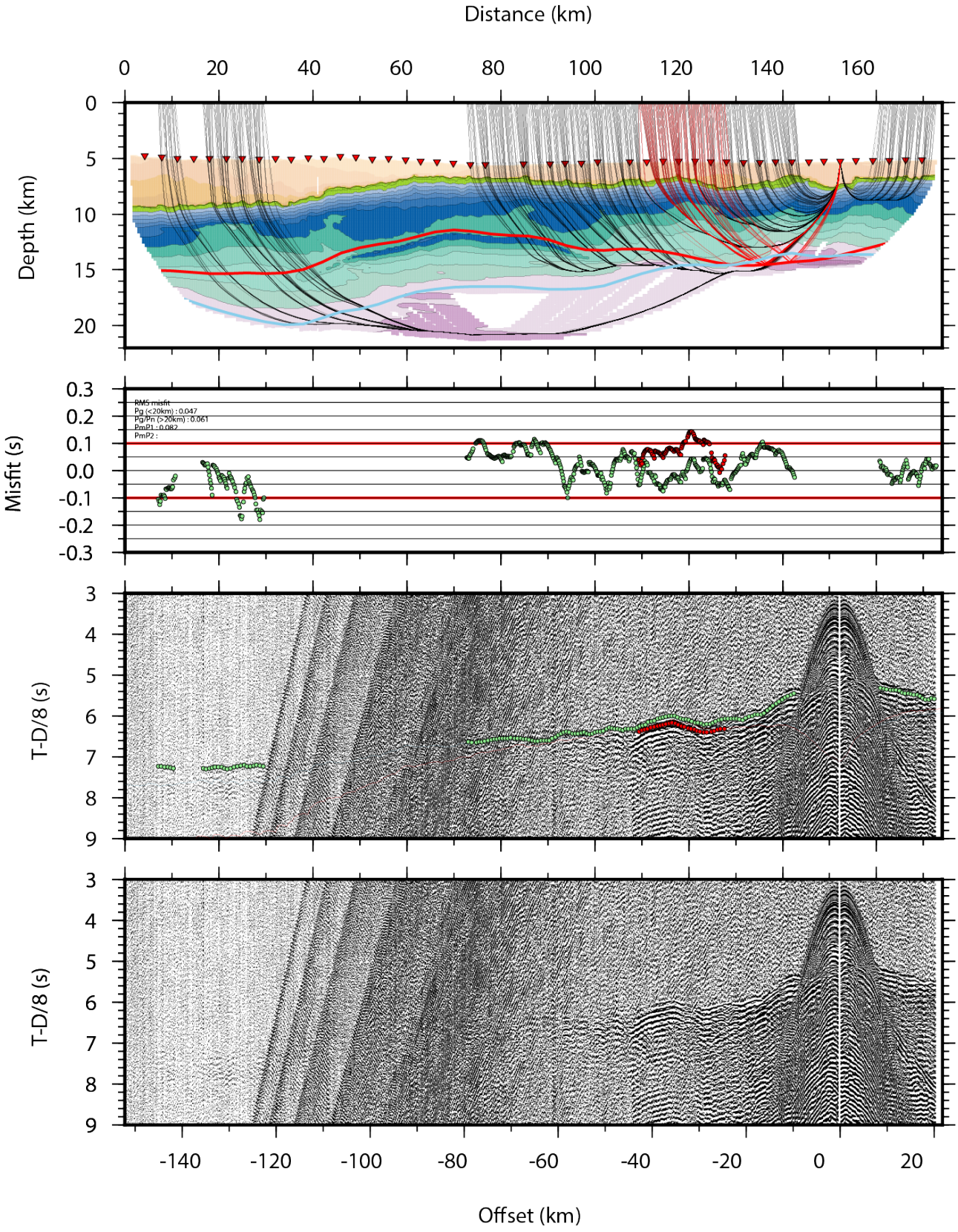


Figure D.6: Summary Plot: OBS7

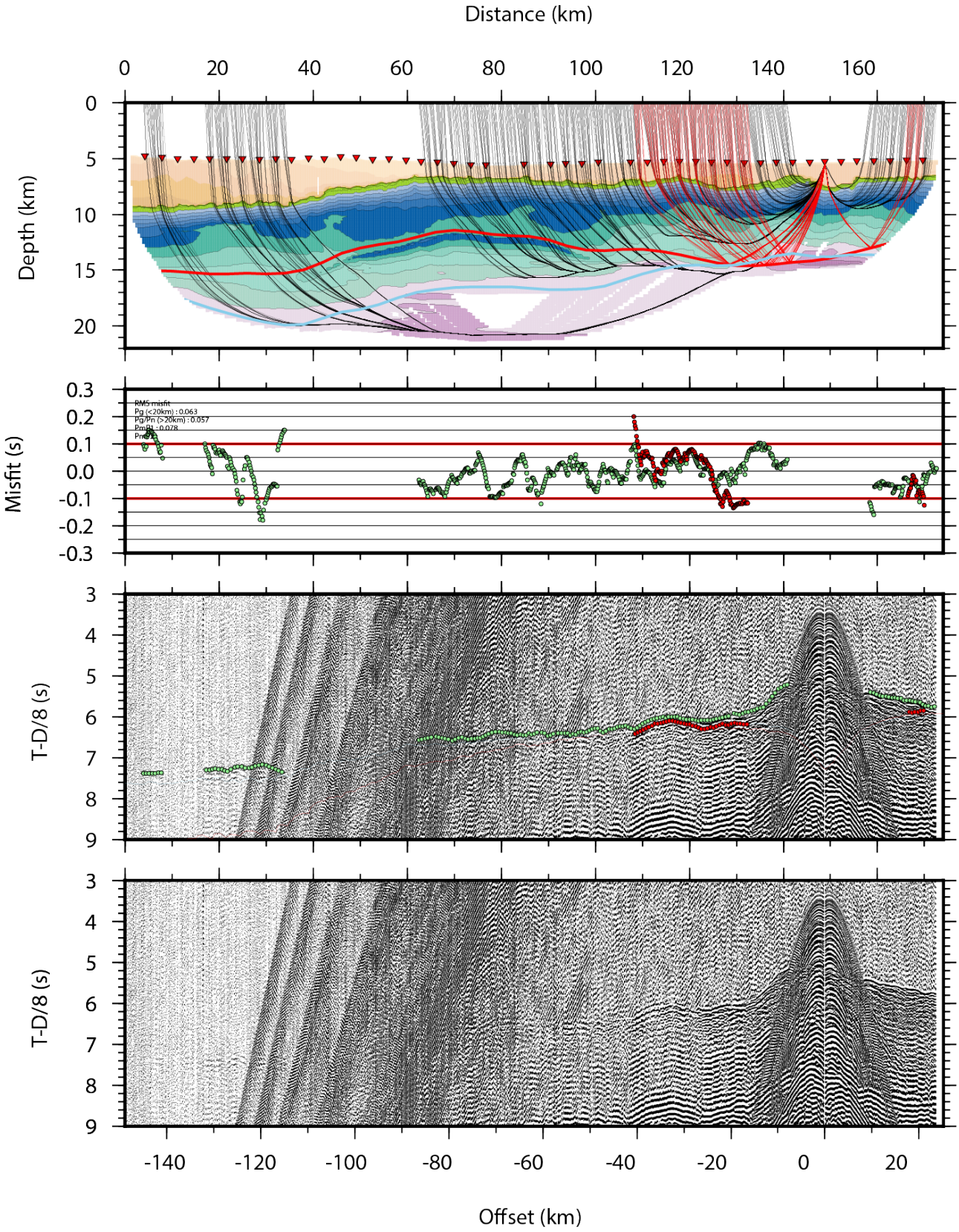


Figure D.7: Summary Plot: OBS8

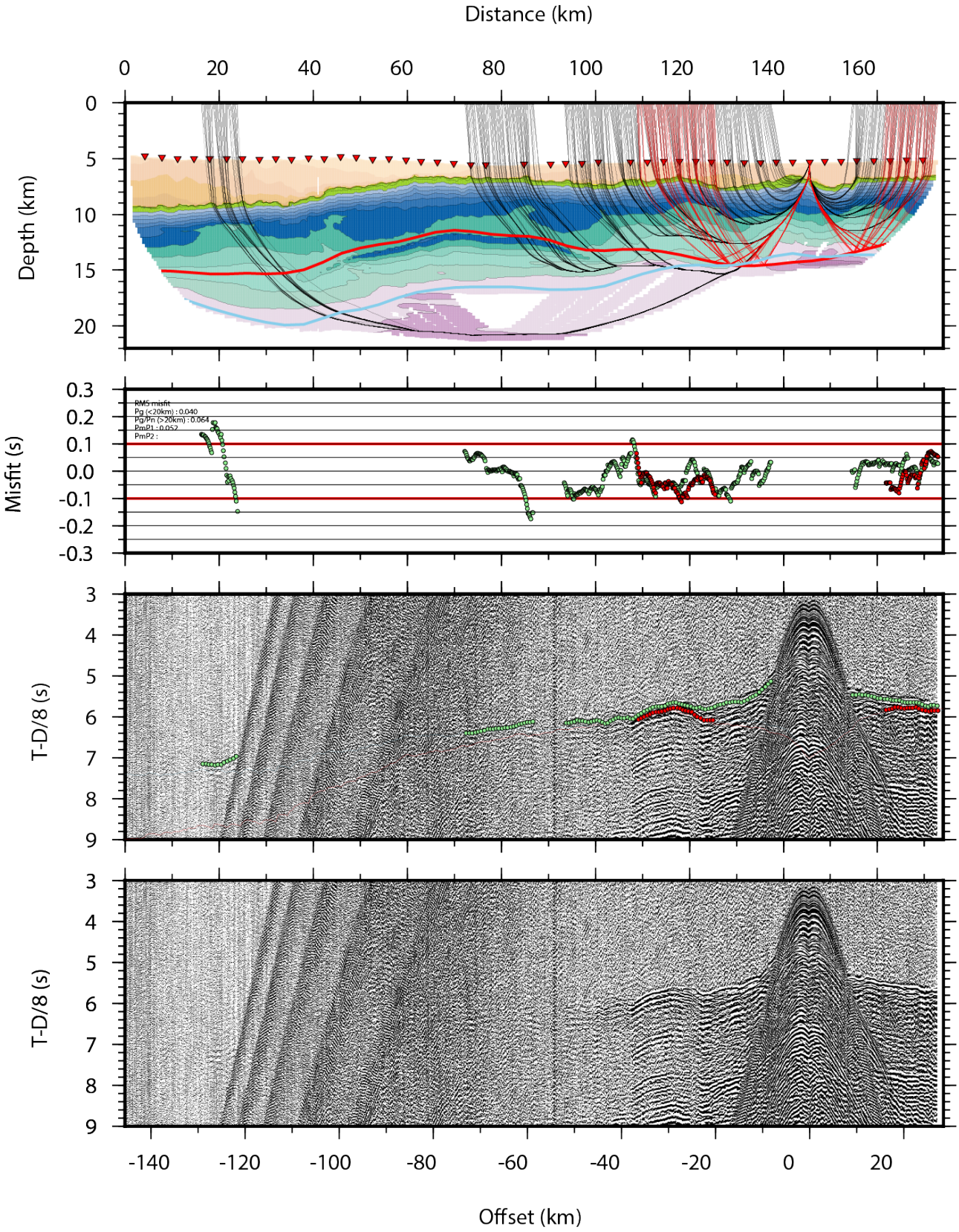


Figure D.8: Summary Plot: OBS9

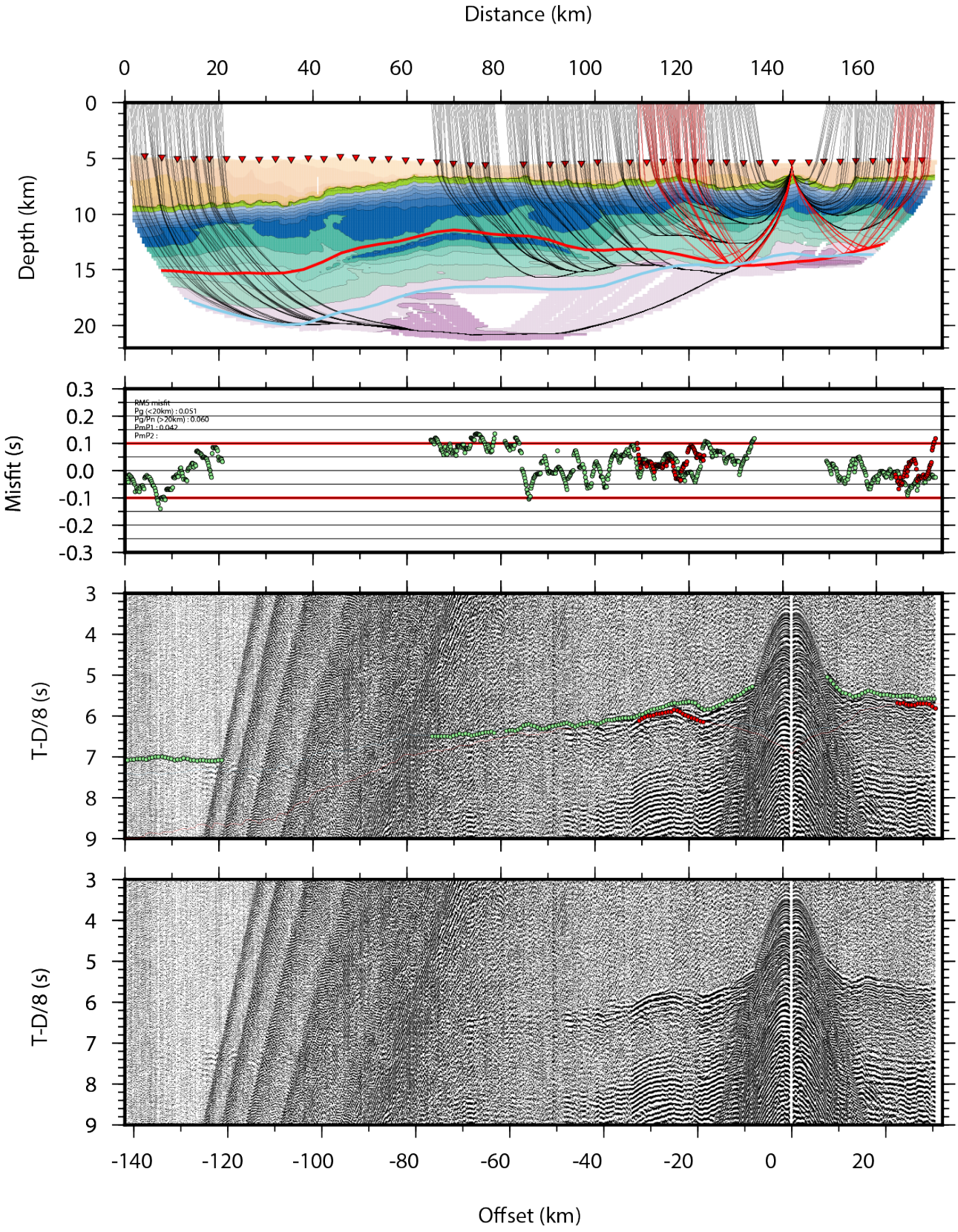


Figure D.9: Summary Plot: OBS10

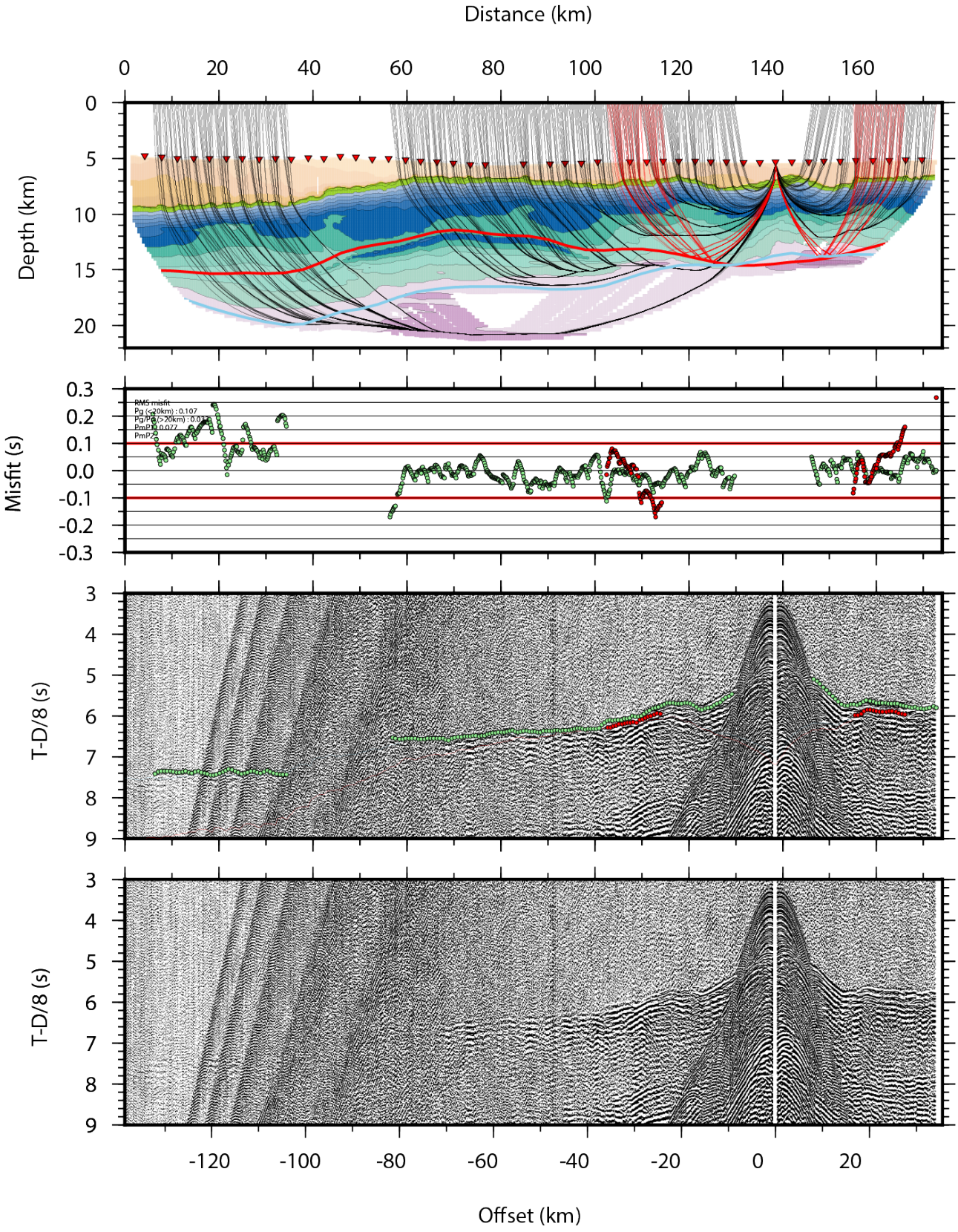


Figure D.10: Summary Plot: OBS11

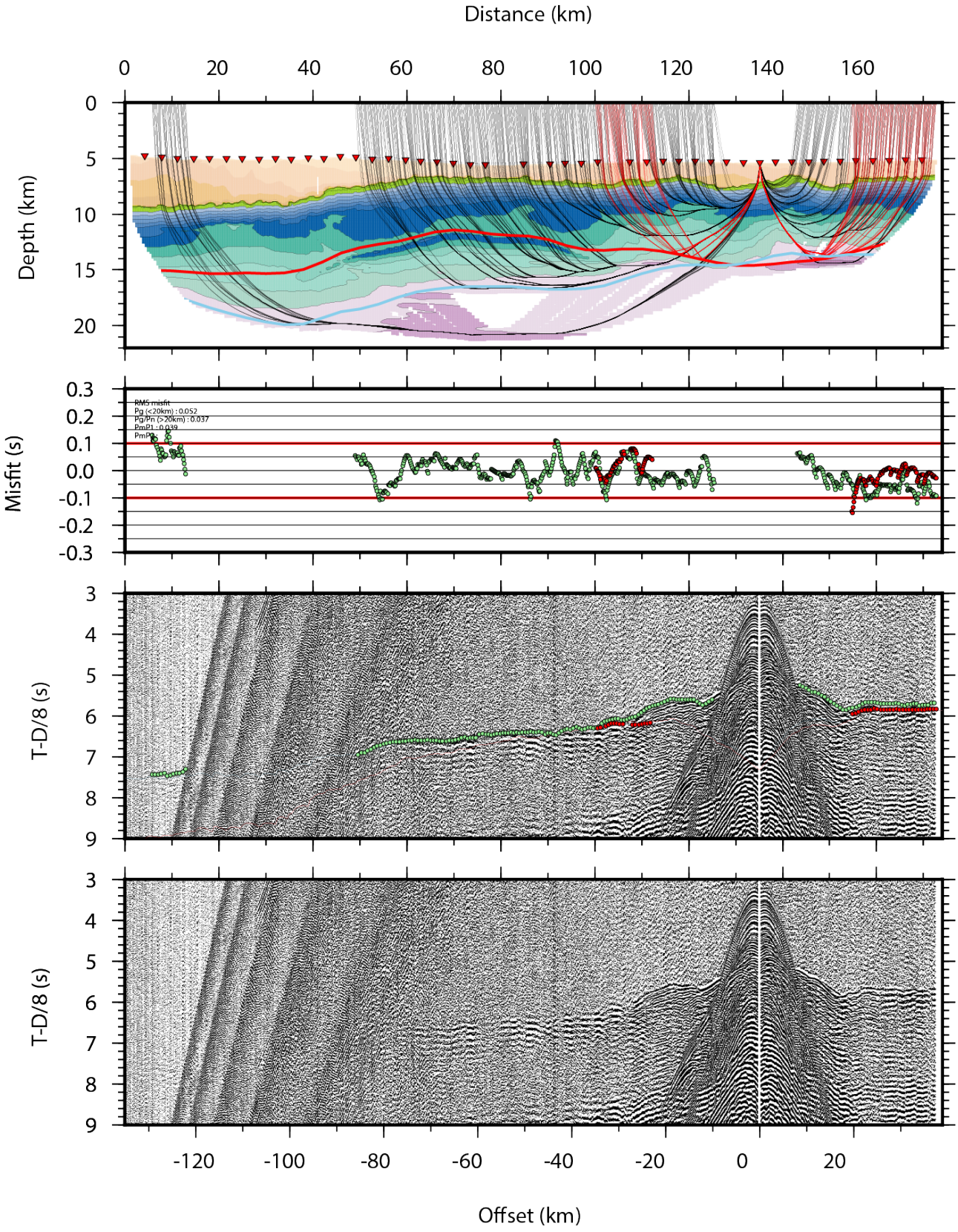


Figure D.11: Summary Plot: OBS12

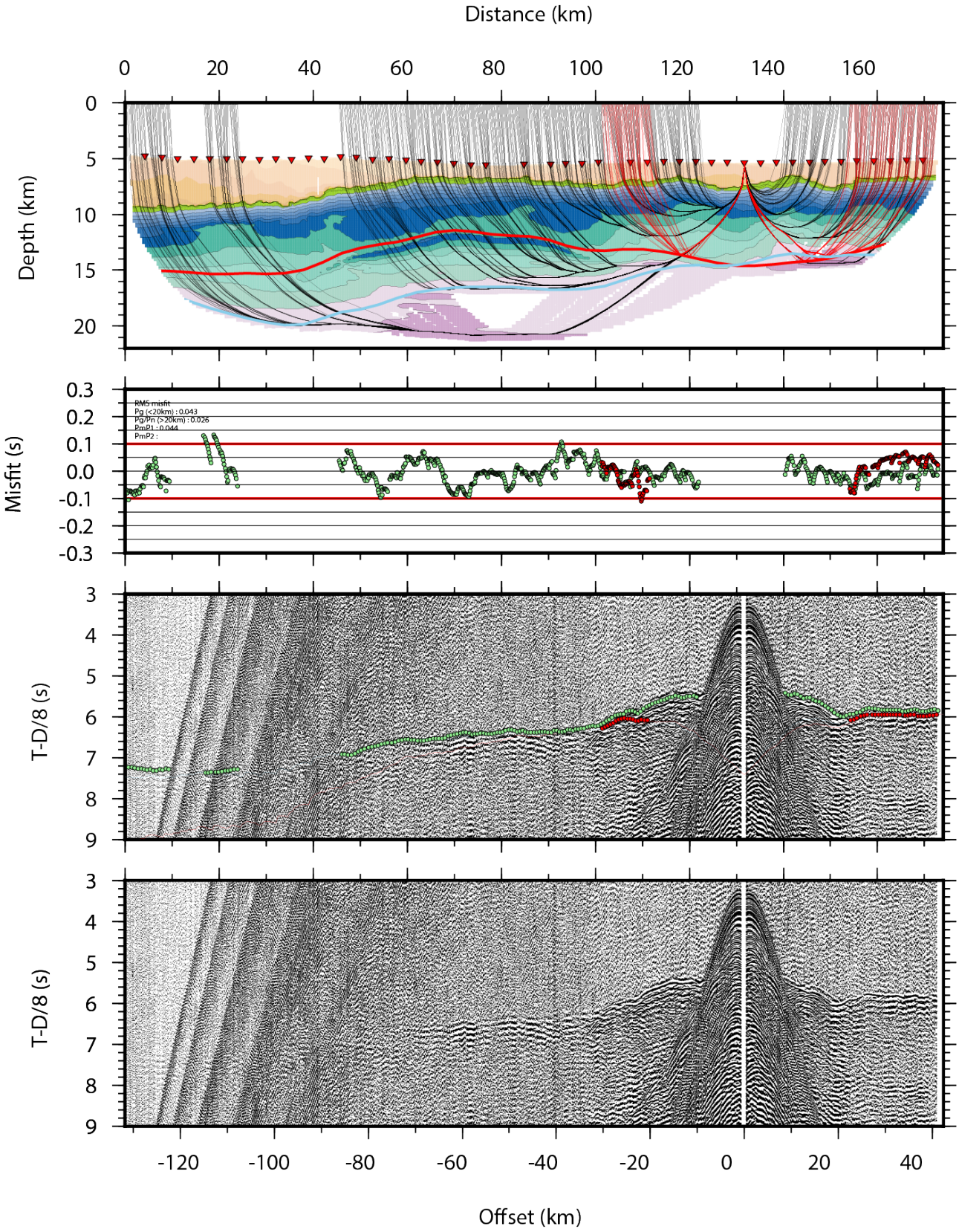


Figure D.12: Summary Plot: OBS13

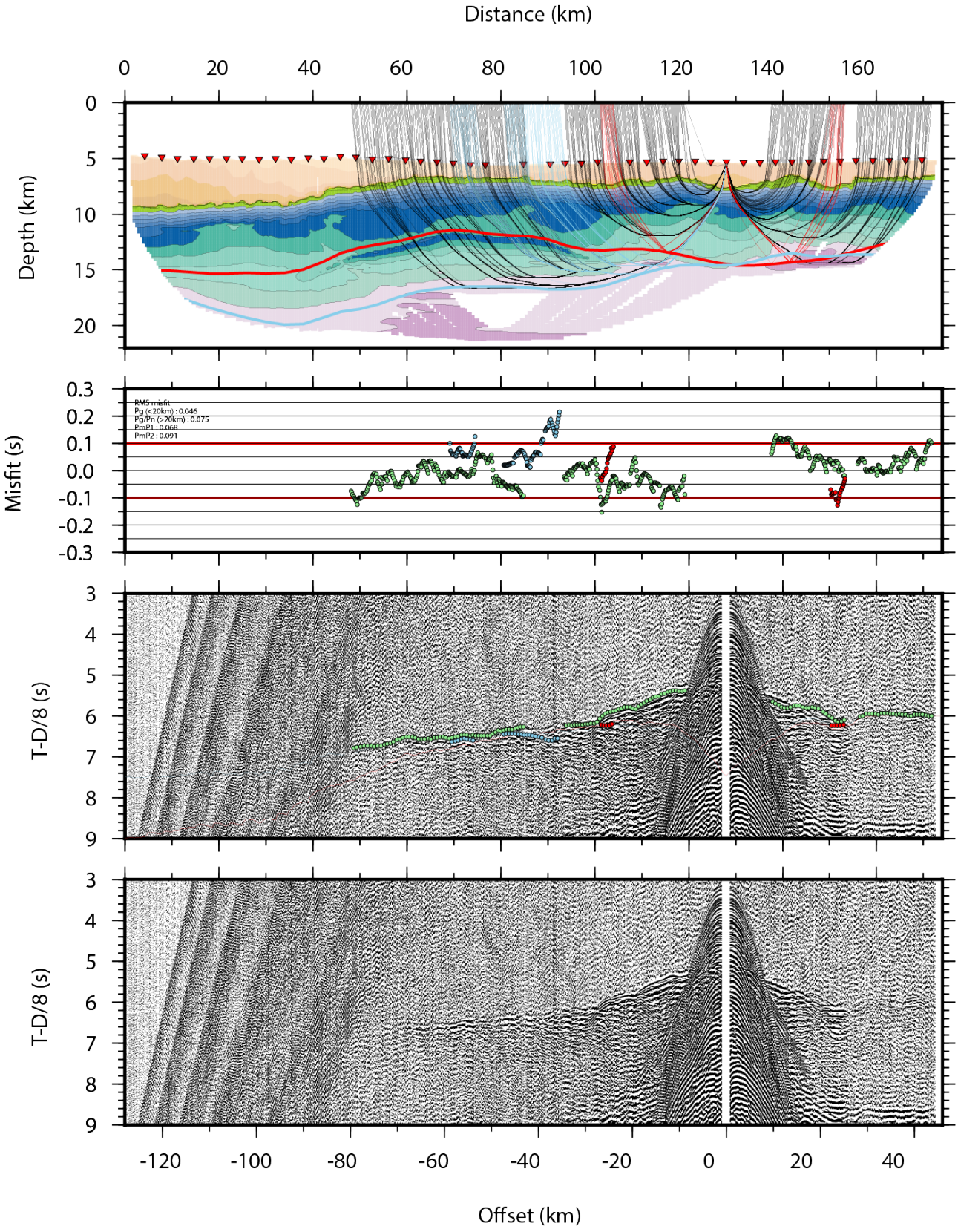


Figure D.13: Summary Plot: OBS14

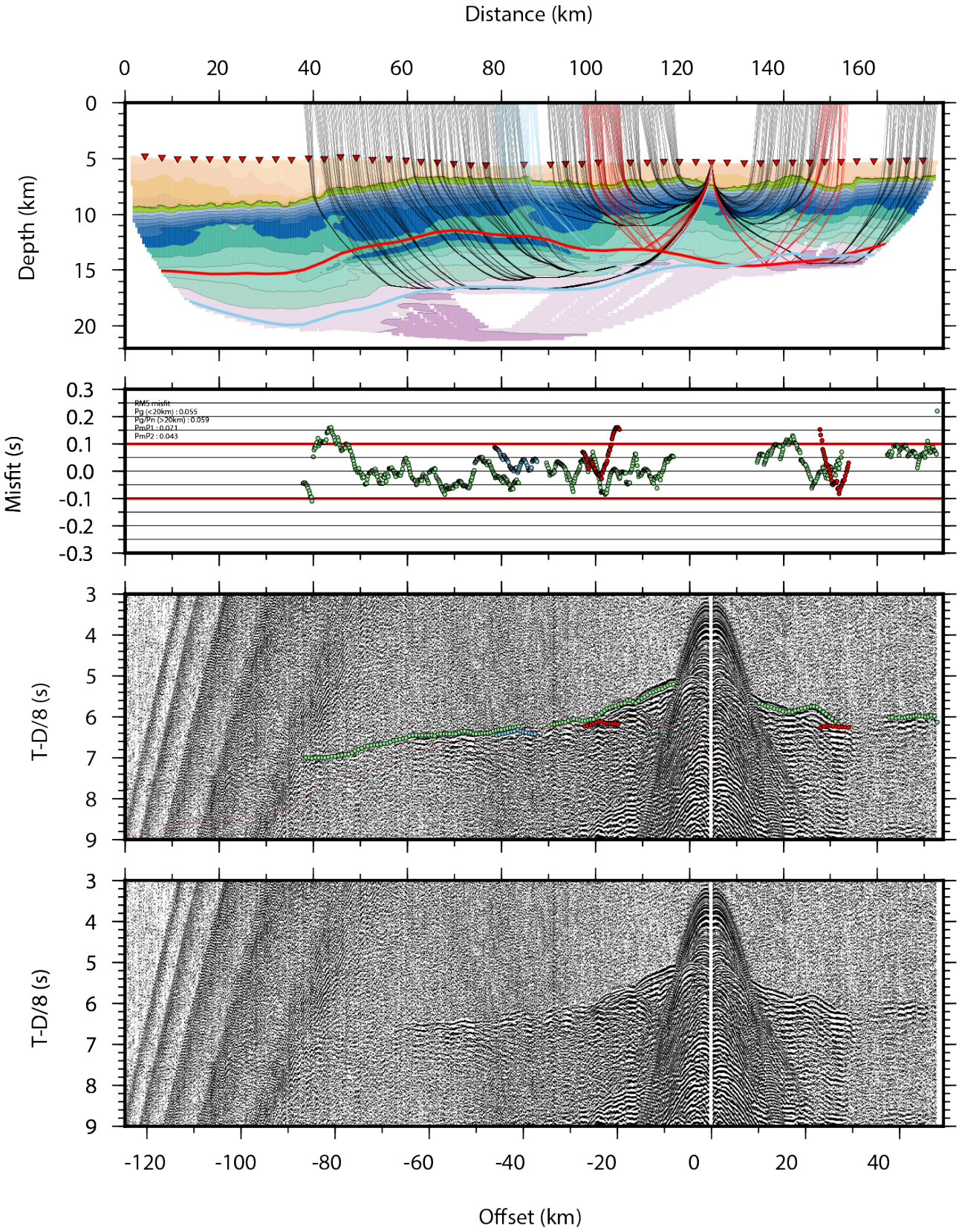


Figure D.14: Summary Plot: OBS15

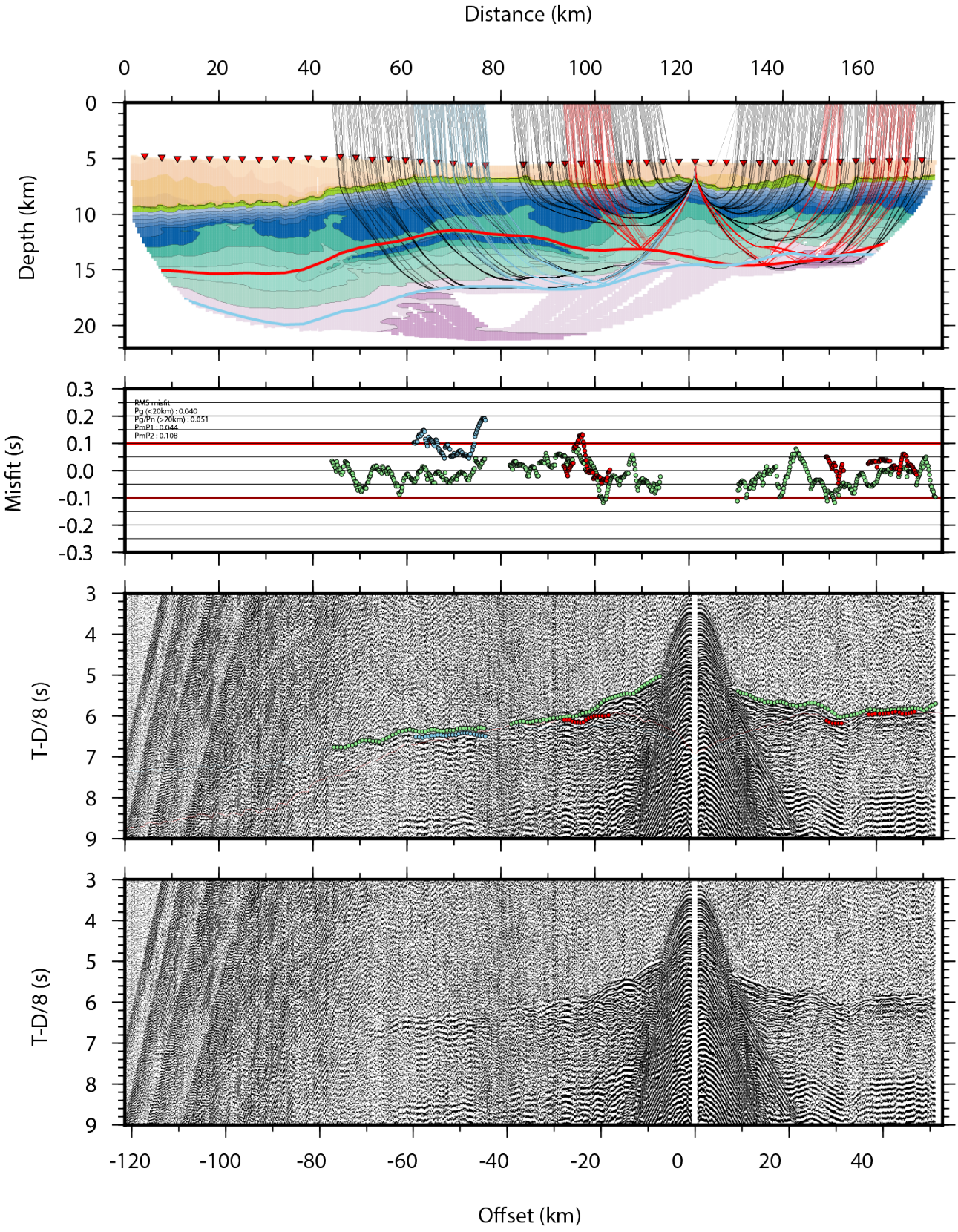


Figure D.15: Summary Plot: OBS16

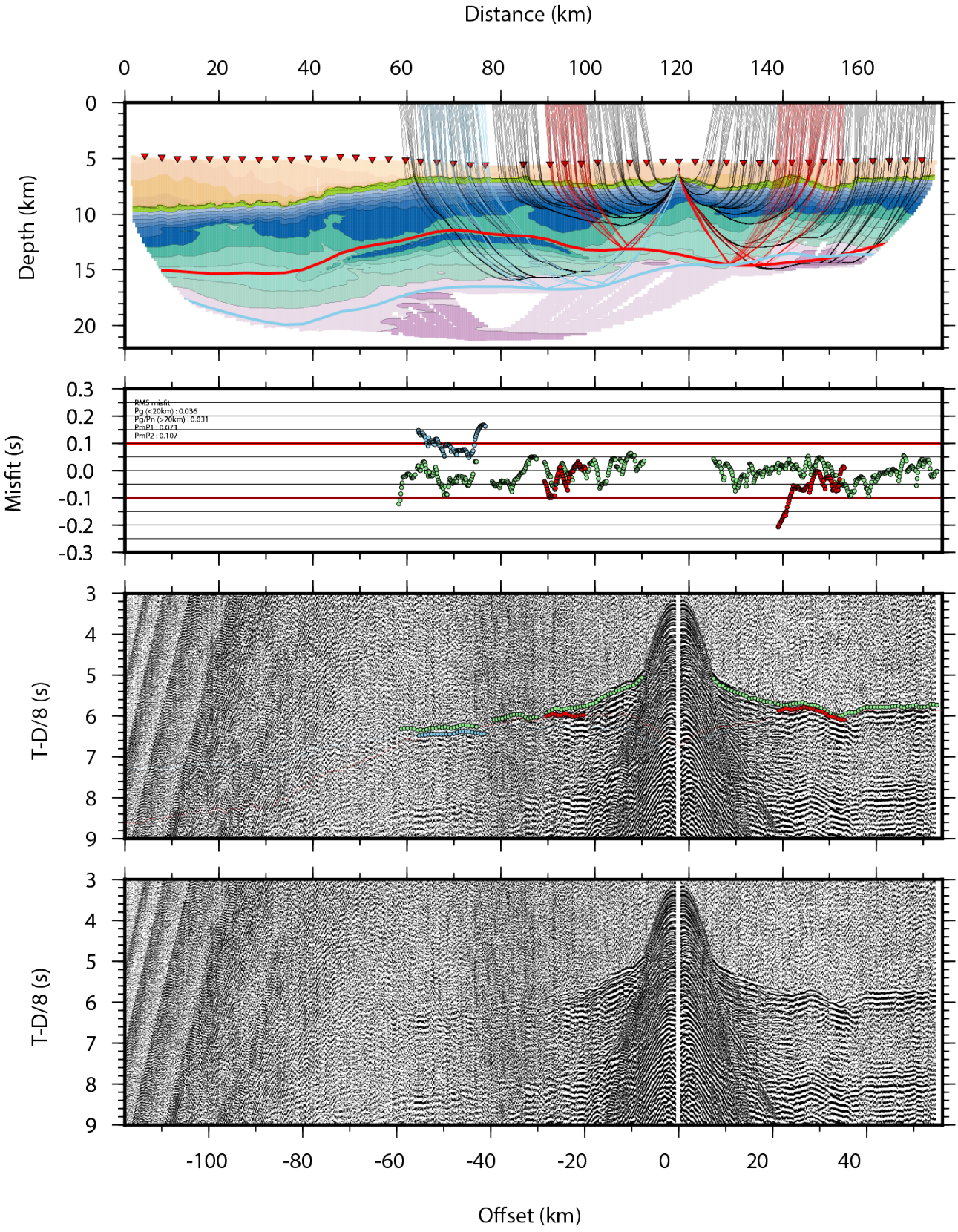


Figure D.16: Summary Plot: OBS17

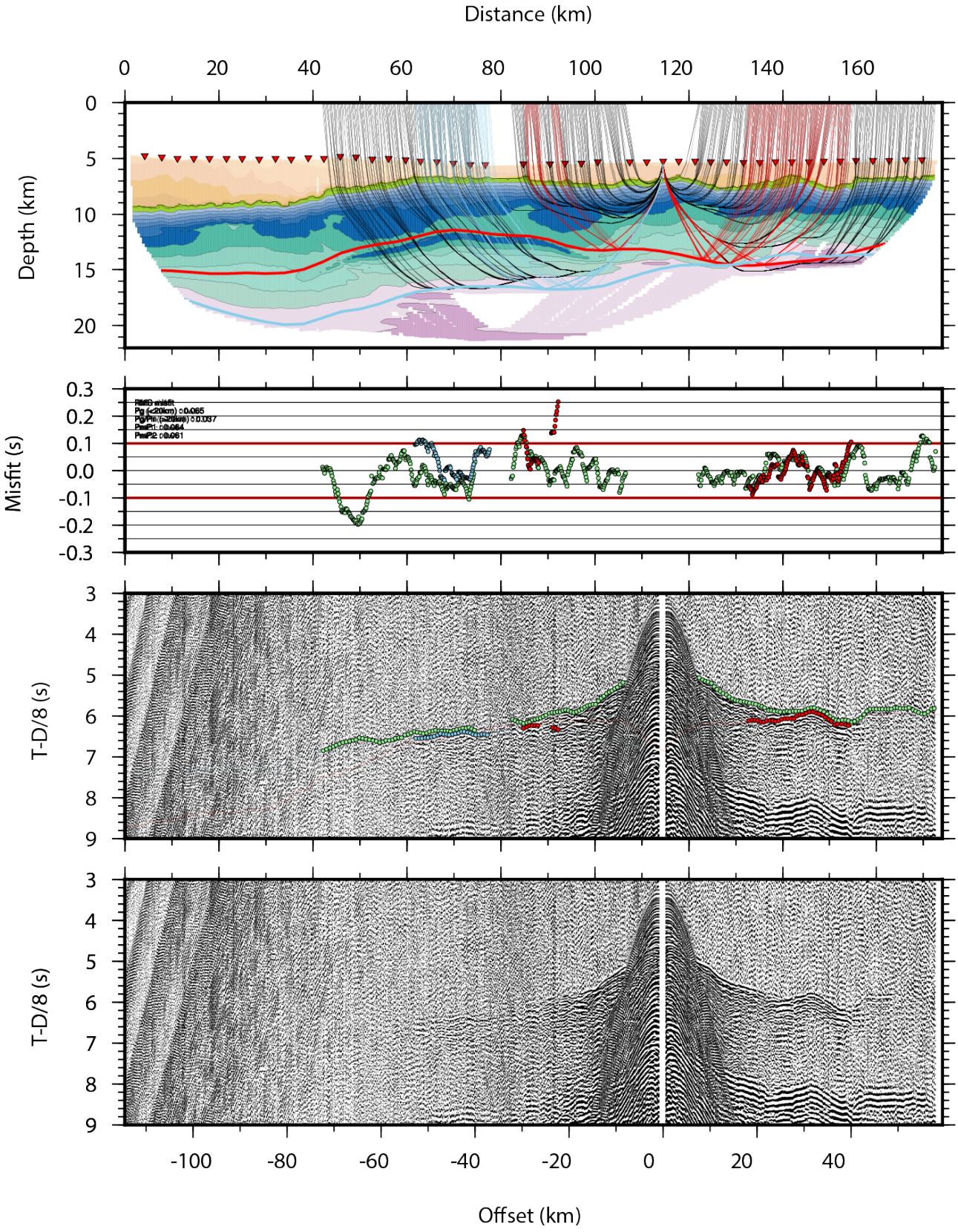


Figure D.17: Summary Plot: OBS18

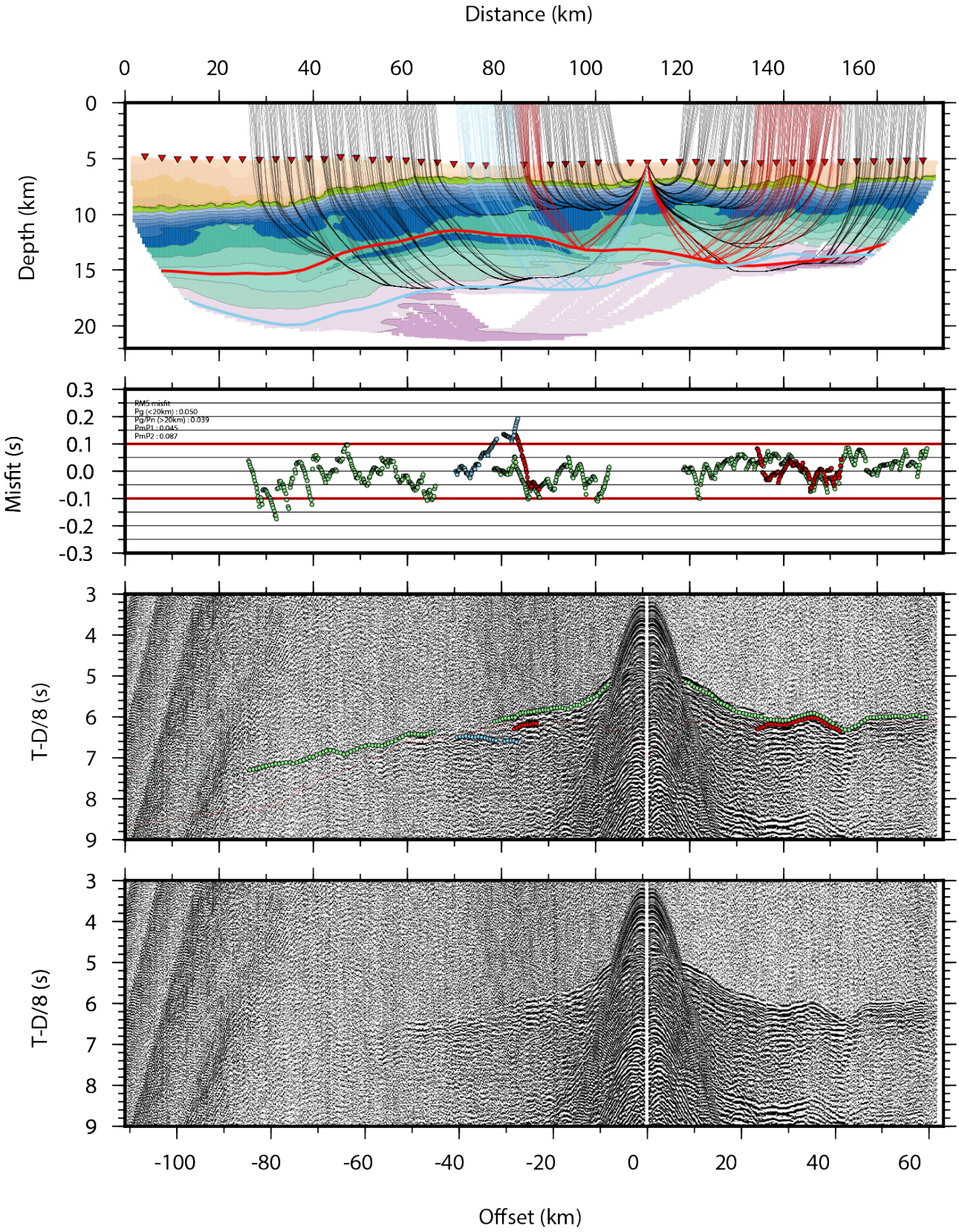


Figure D.18: Summary Plot: OBS19

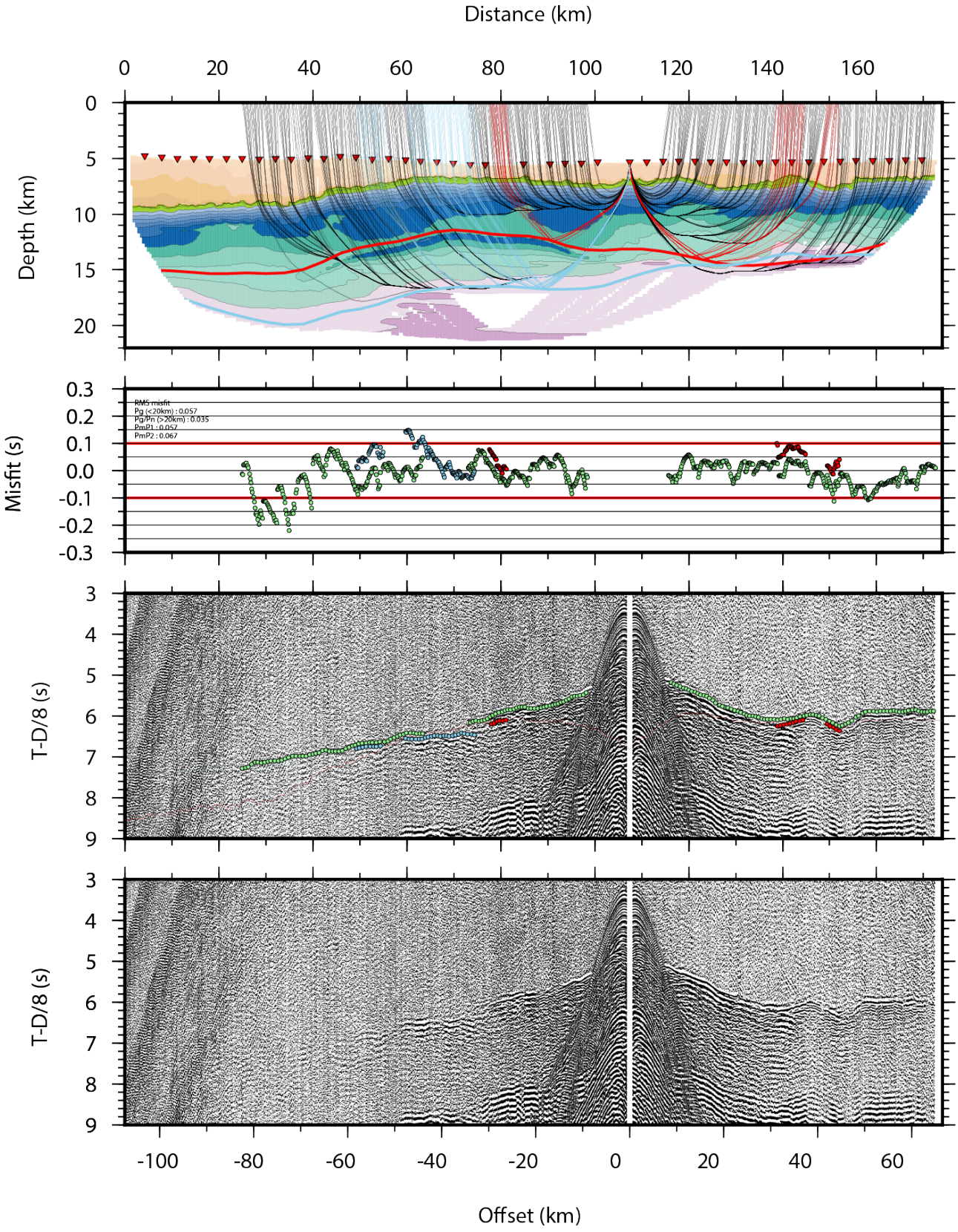


Figure D.19: Summary Plot: OBS20

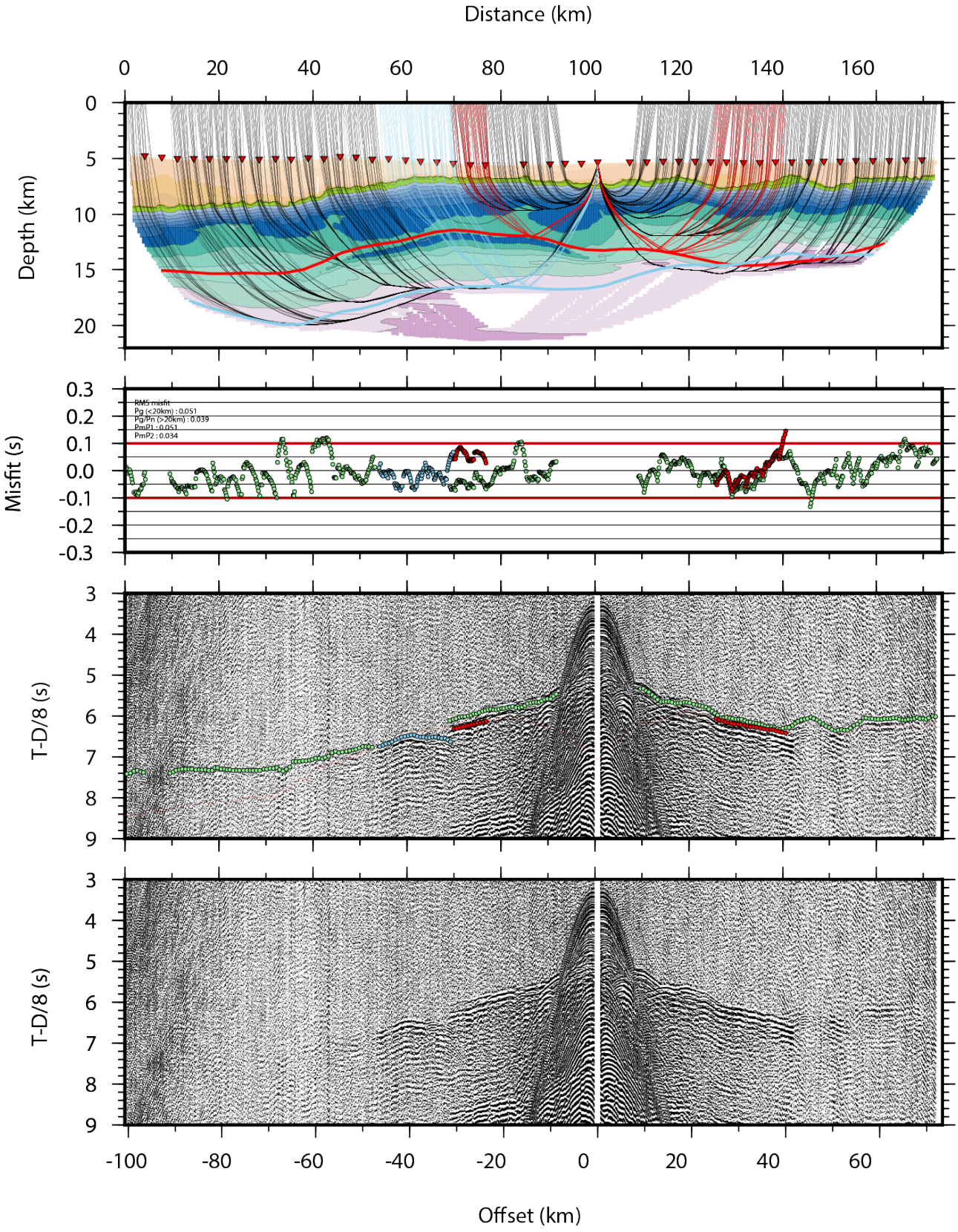


Figure D.20: Summary Plot: OBS21

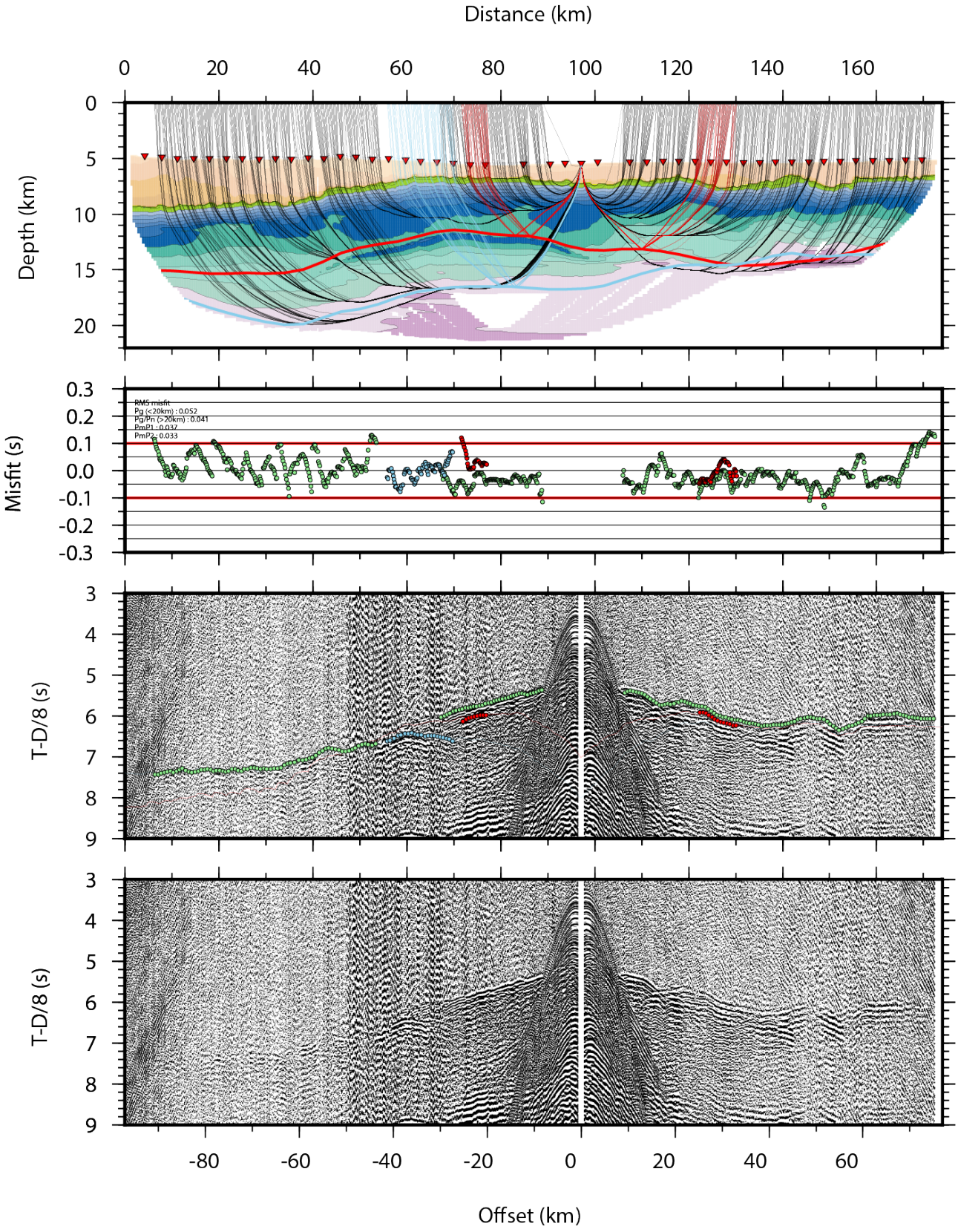


Figure D.21: Summary Plot: OBS22

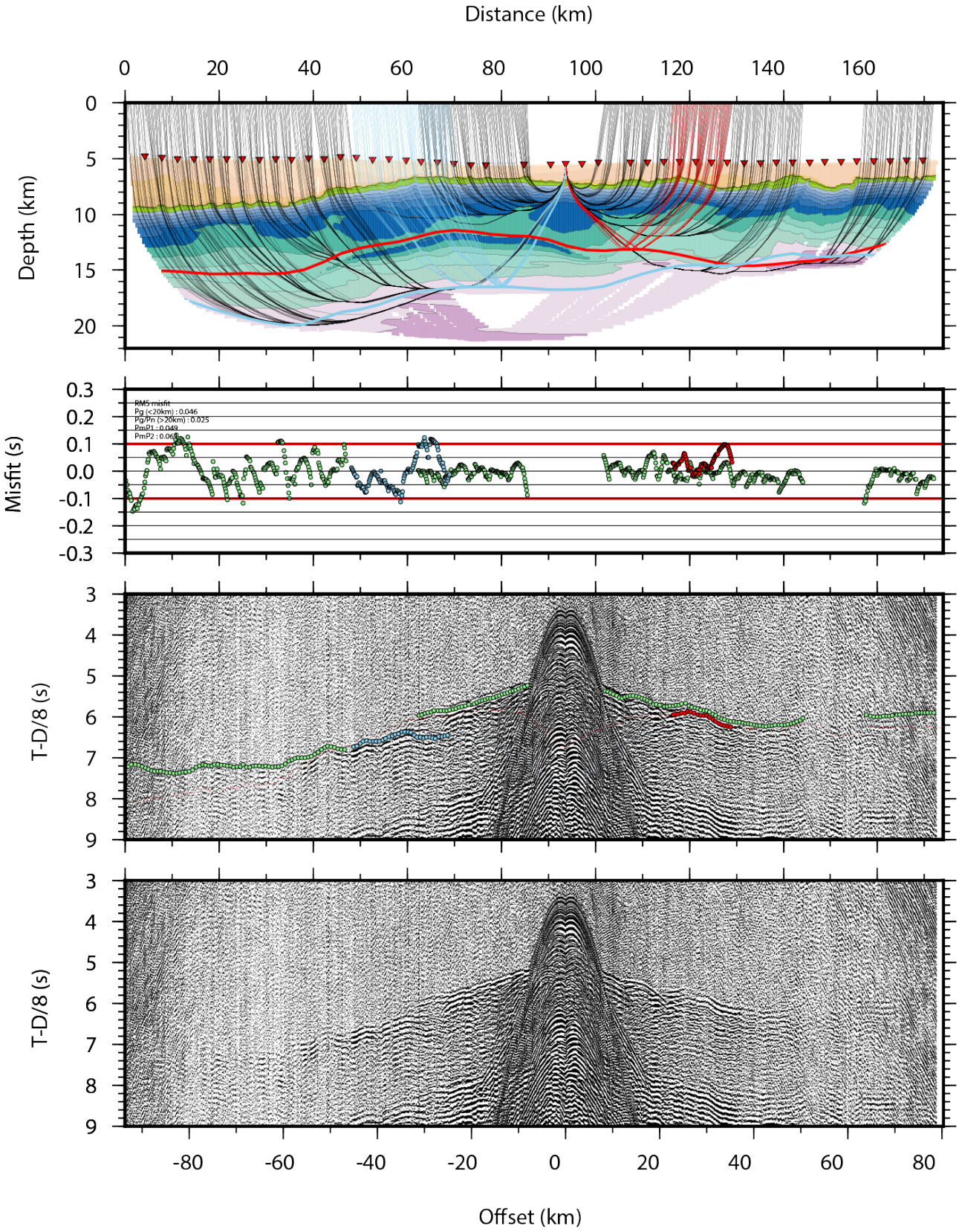


Figure D.22: Summary Plot: OBS23

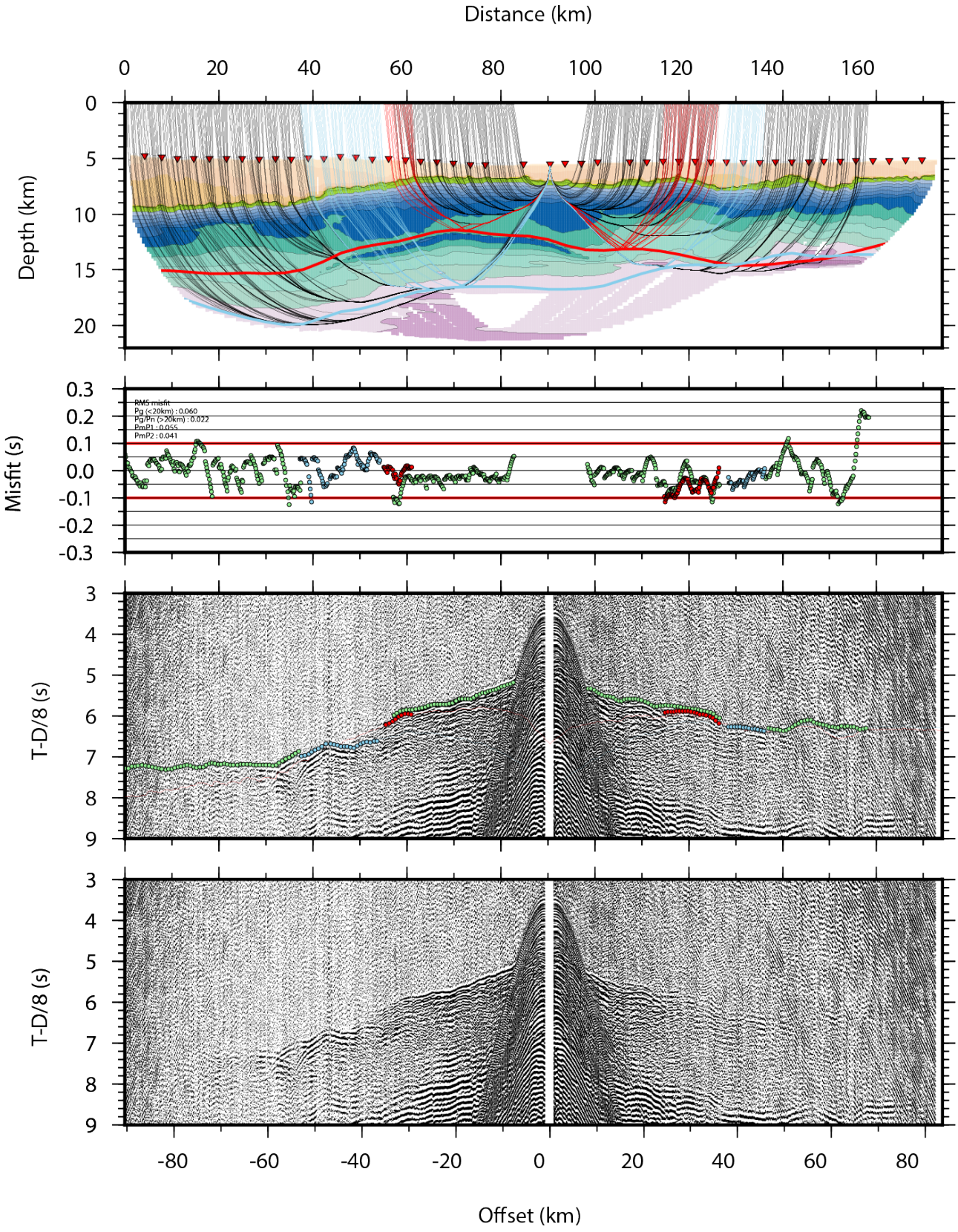


Figure D.23: Summary Plot: OBS24

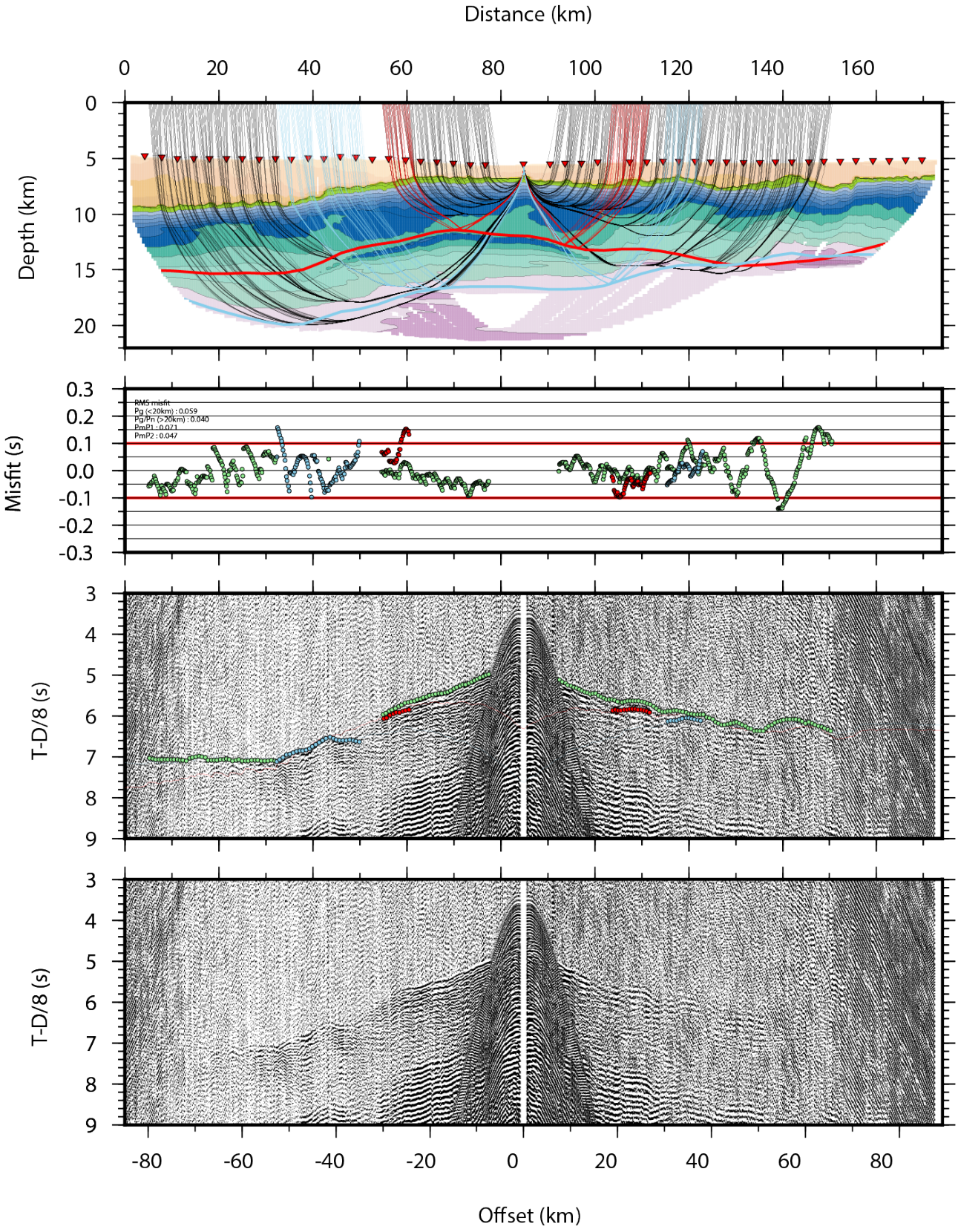


Figure D.24: Summary Plot: OBS26

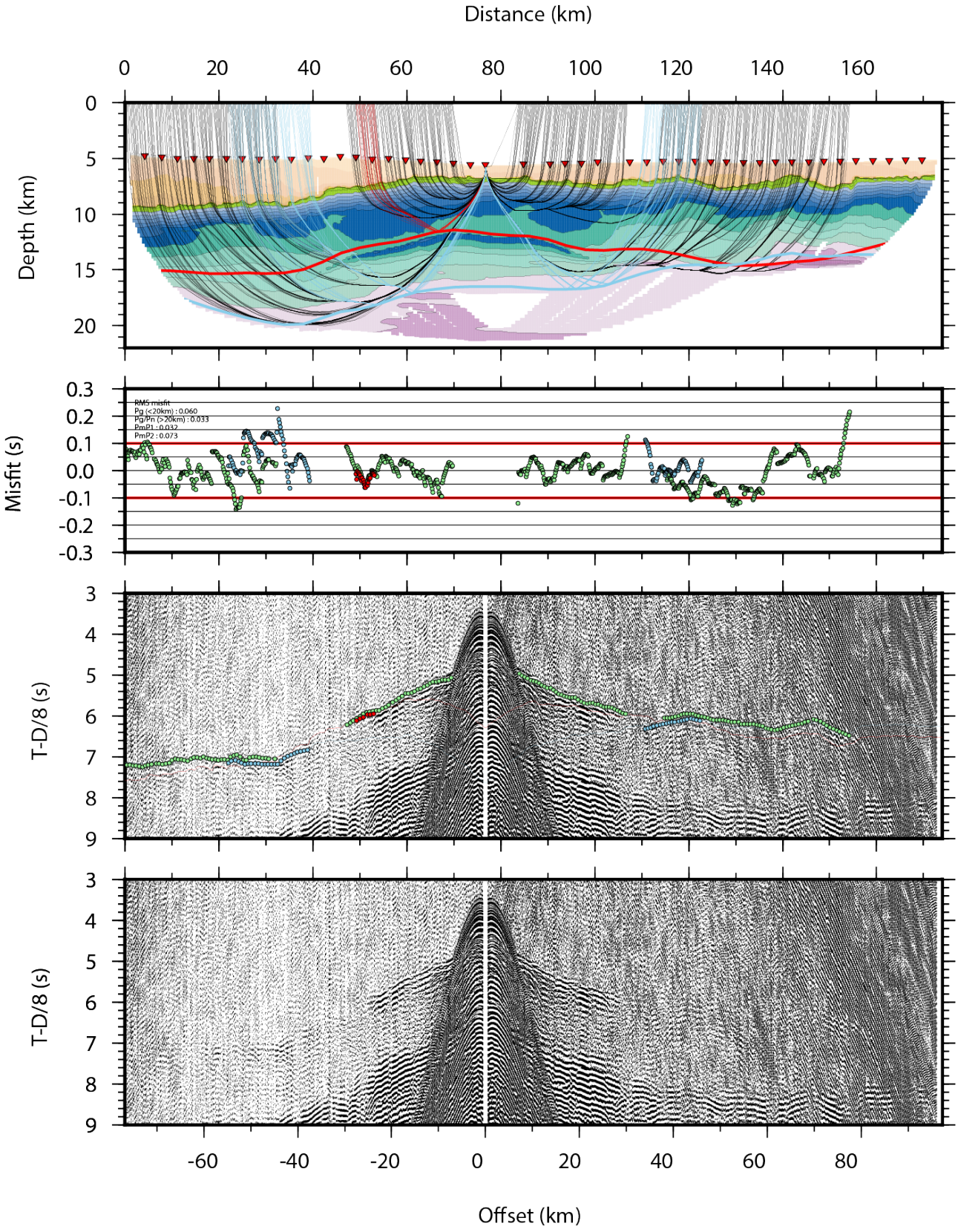


Figure D.25: Summary Plot: OBS27

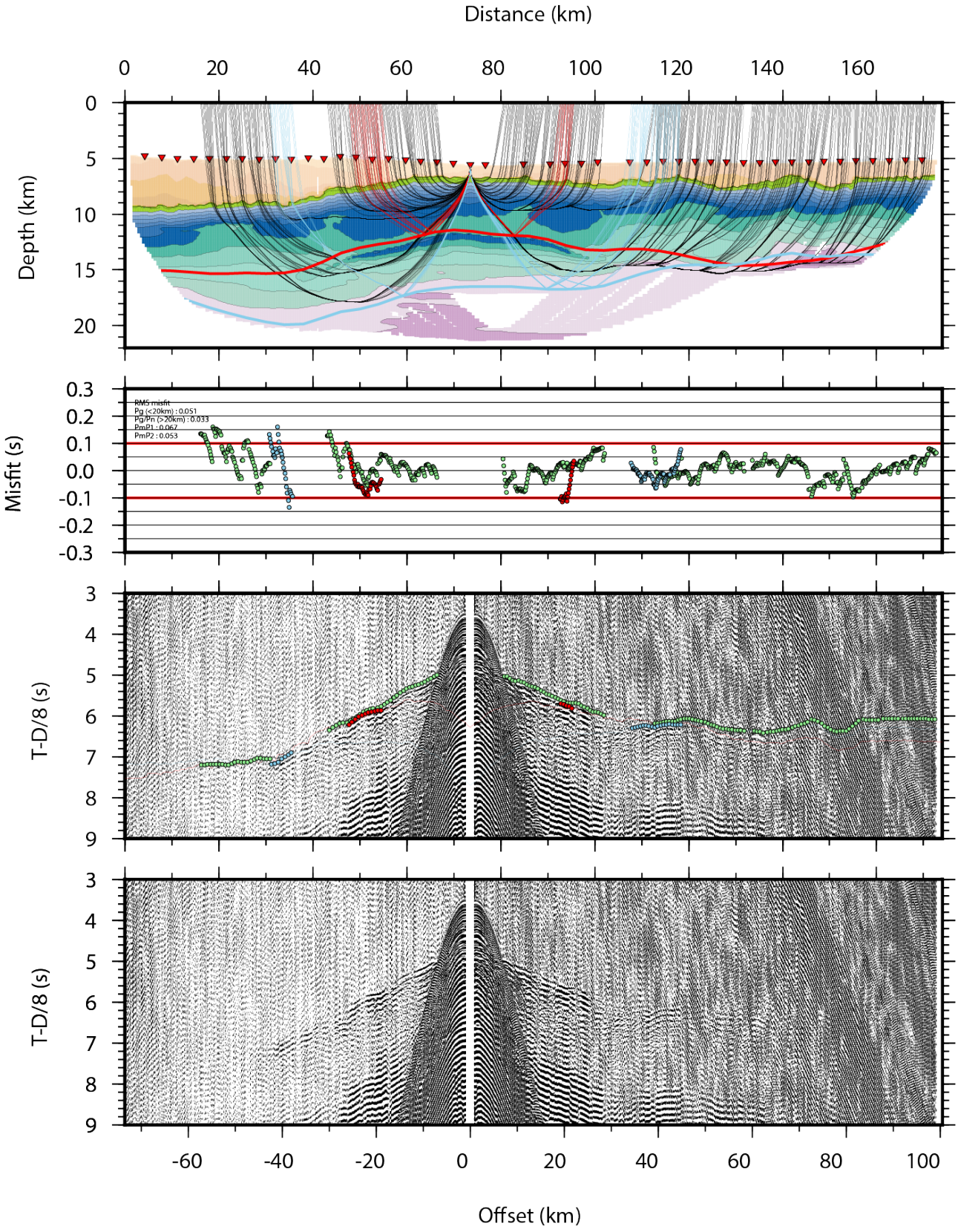


Figure D.26: Summary Plot: OBS28

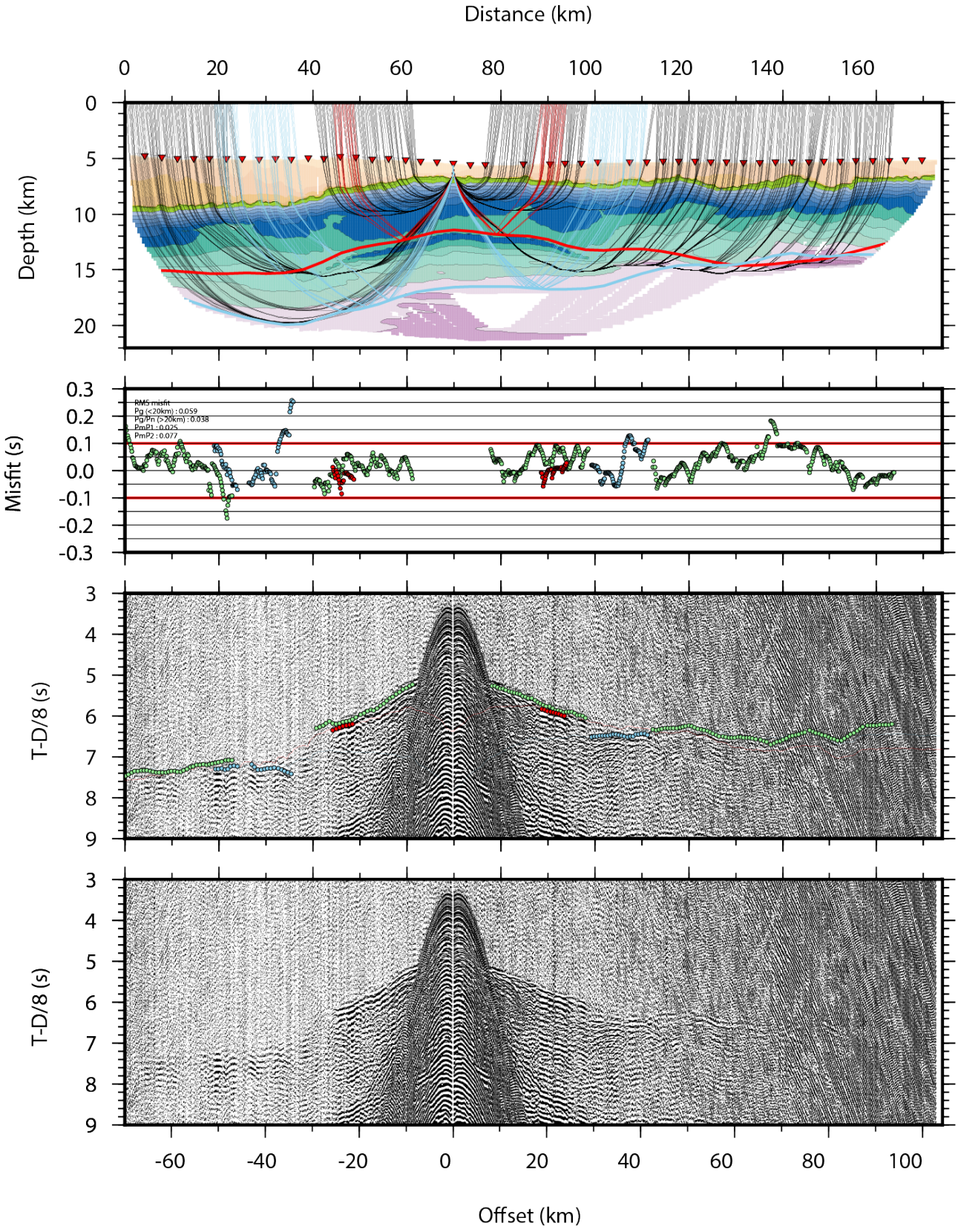


Figure D.27: Summary Plot: OBS29

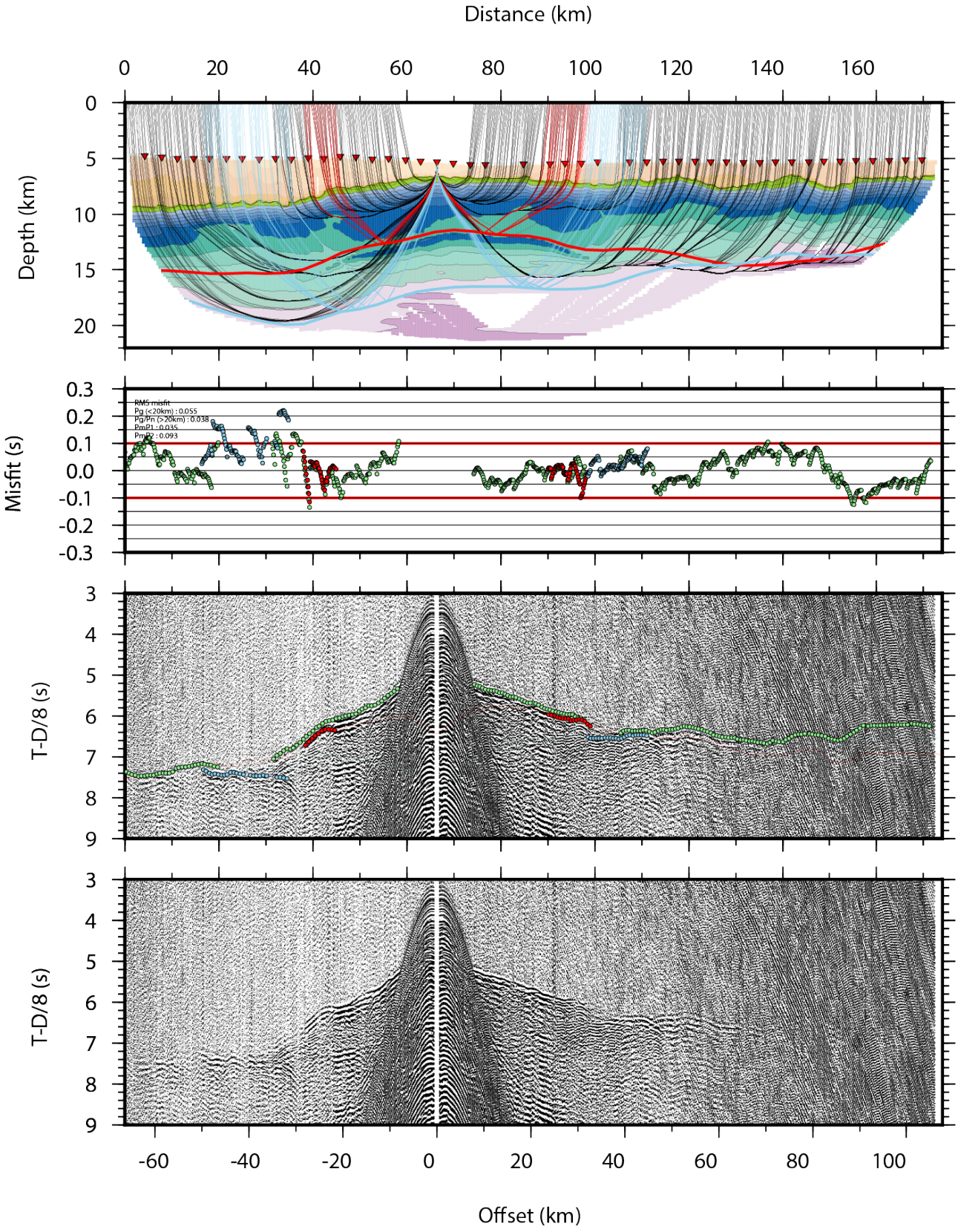


Figure D.28: Summary Plot: OBS30

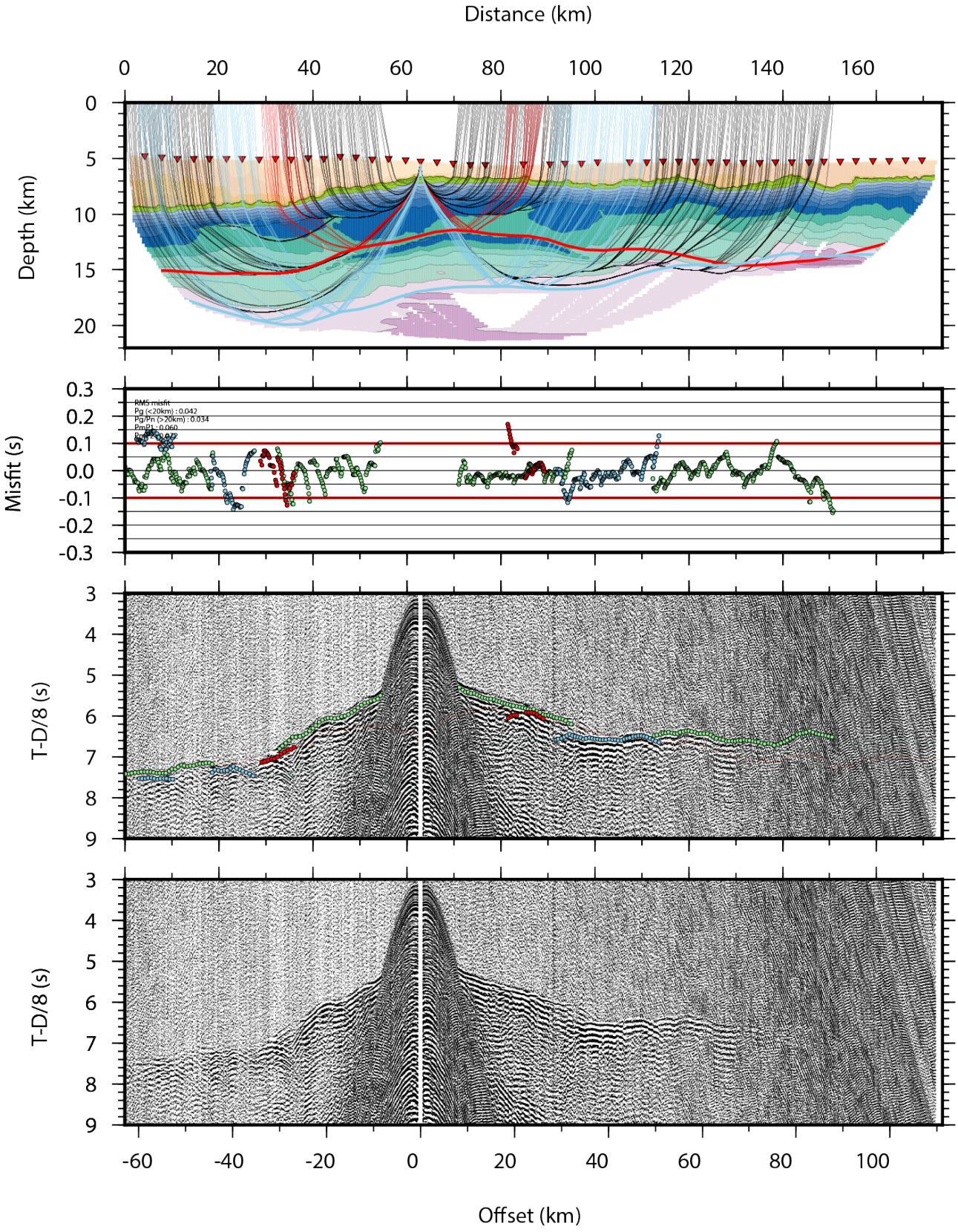


Figure D.29: Summary Plot: OBS31

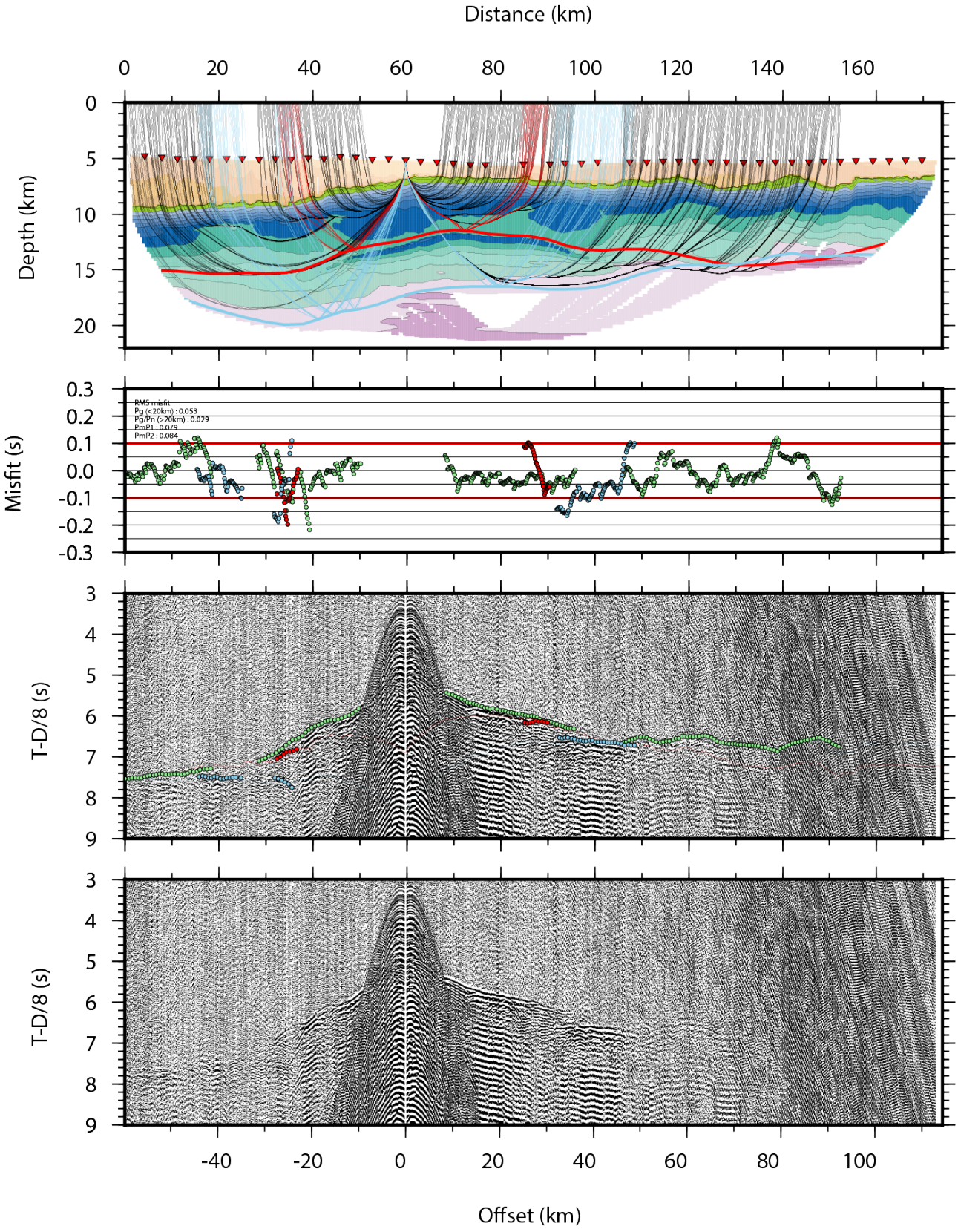


Figure D.30: Summary Plot: OBS32

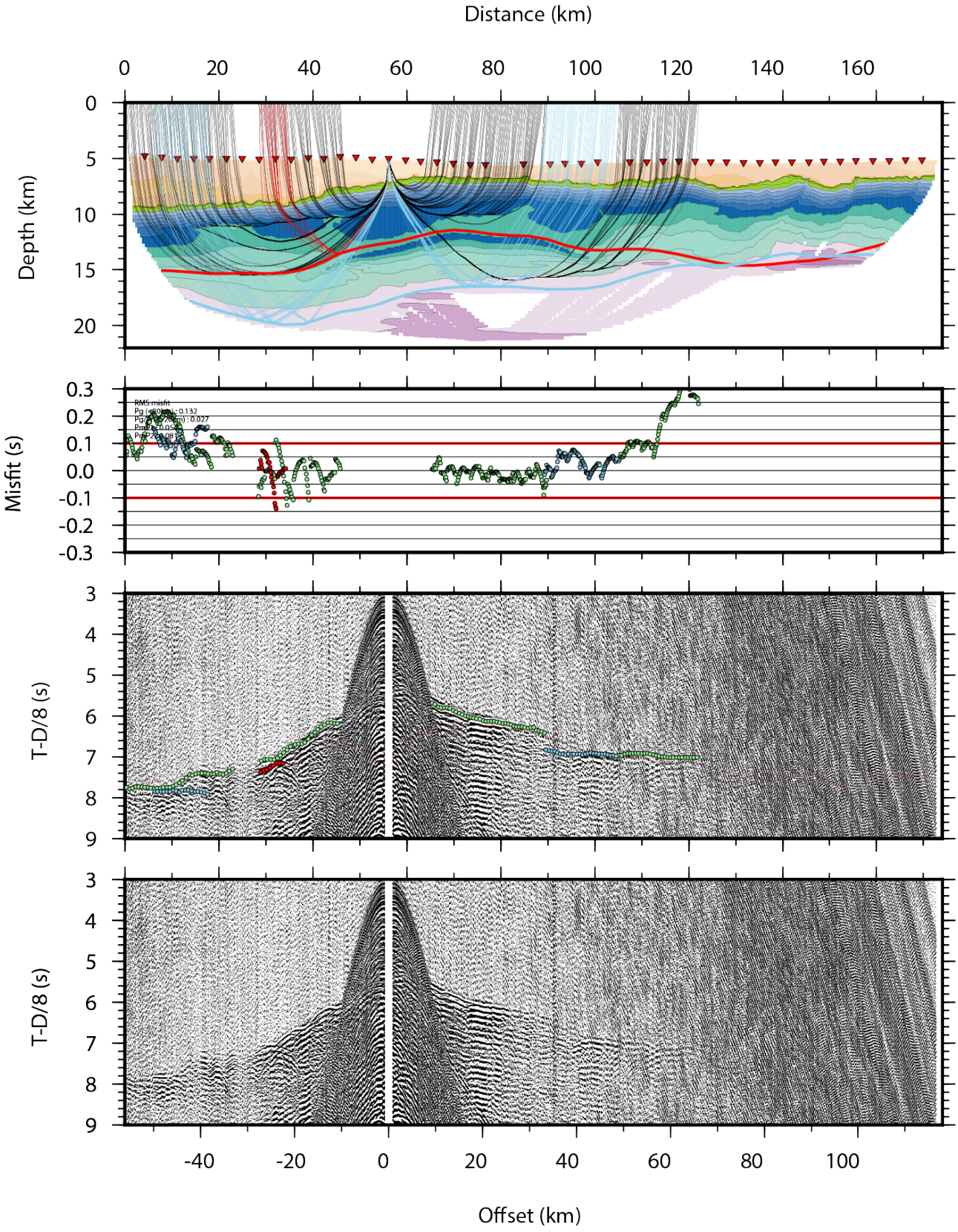


Figure D.31: Summary Plot: OBS33

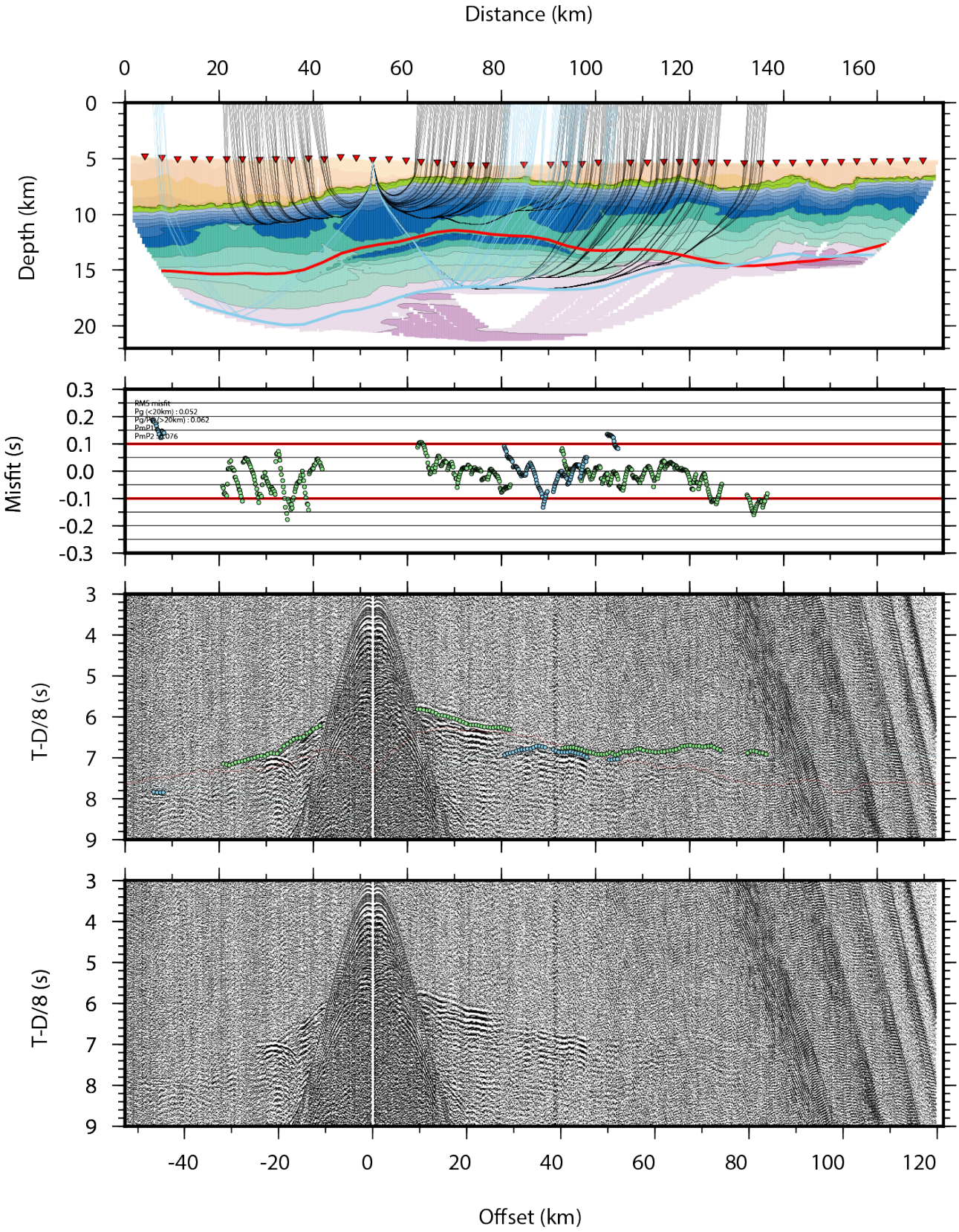


Figure D.32: Summary Plot: OBS34

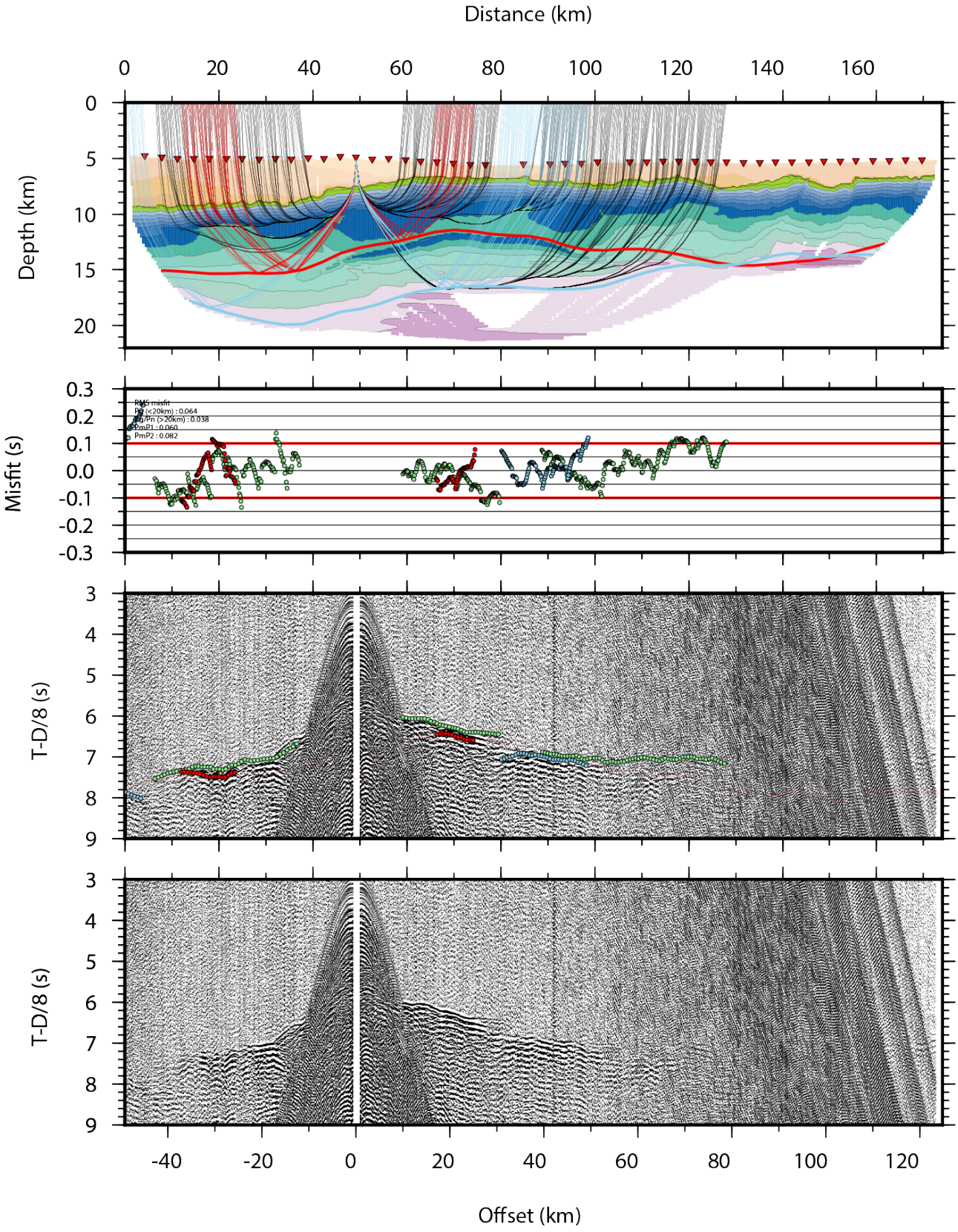


Figure D.33: Summary Plot: OBS35

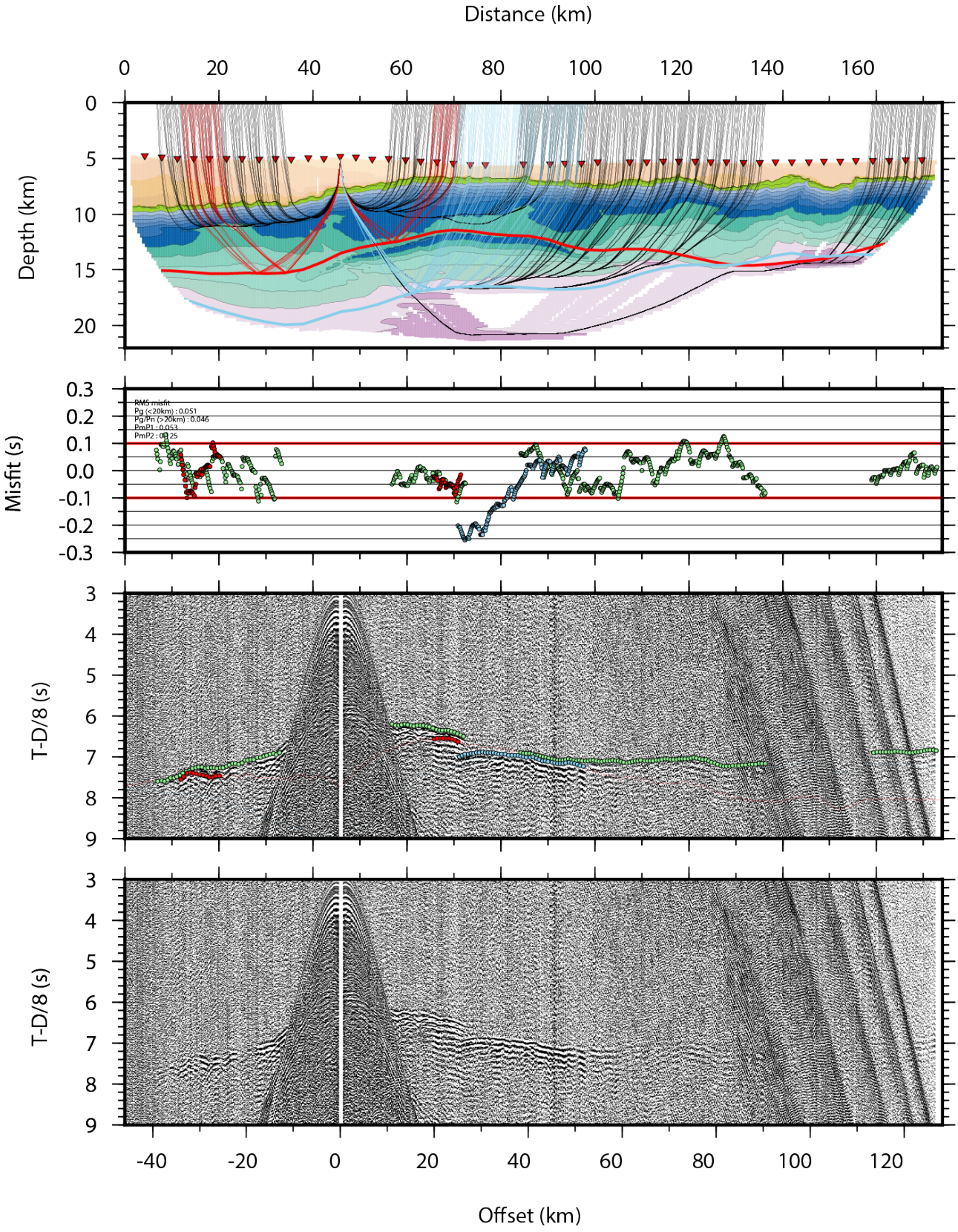


Figure D.34: Summary Plot: OBS36

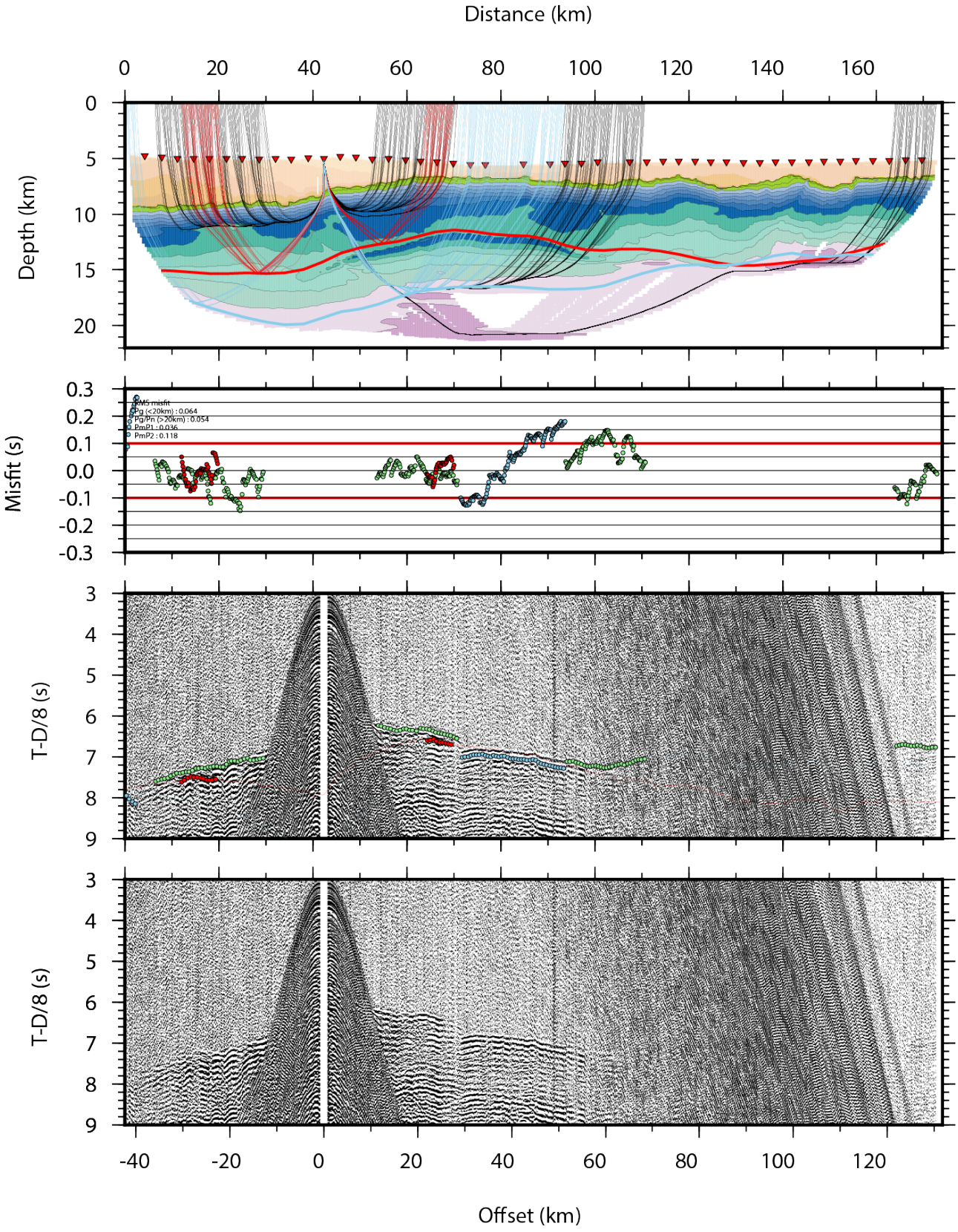


Figure D.35: Summary Plot: OBS37

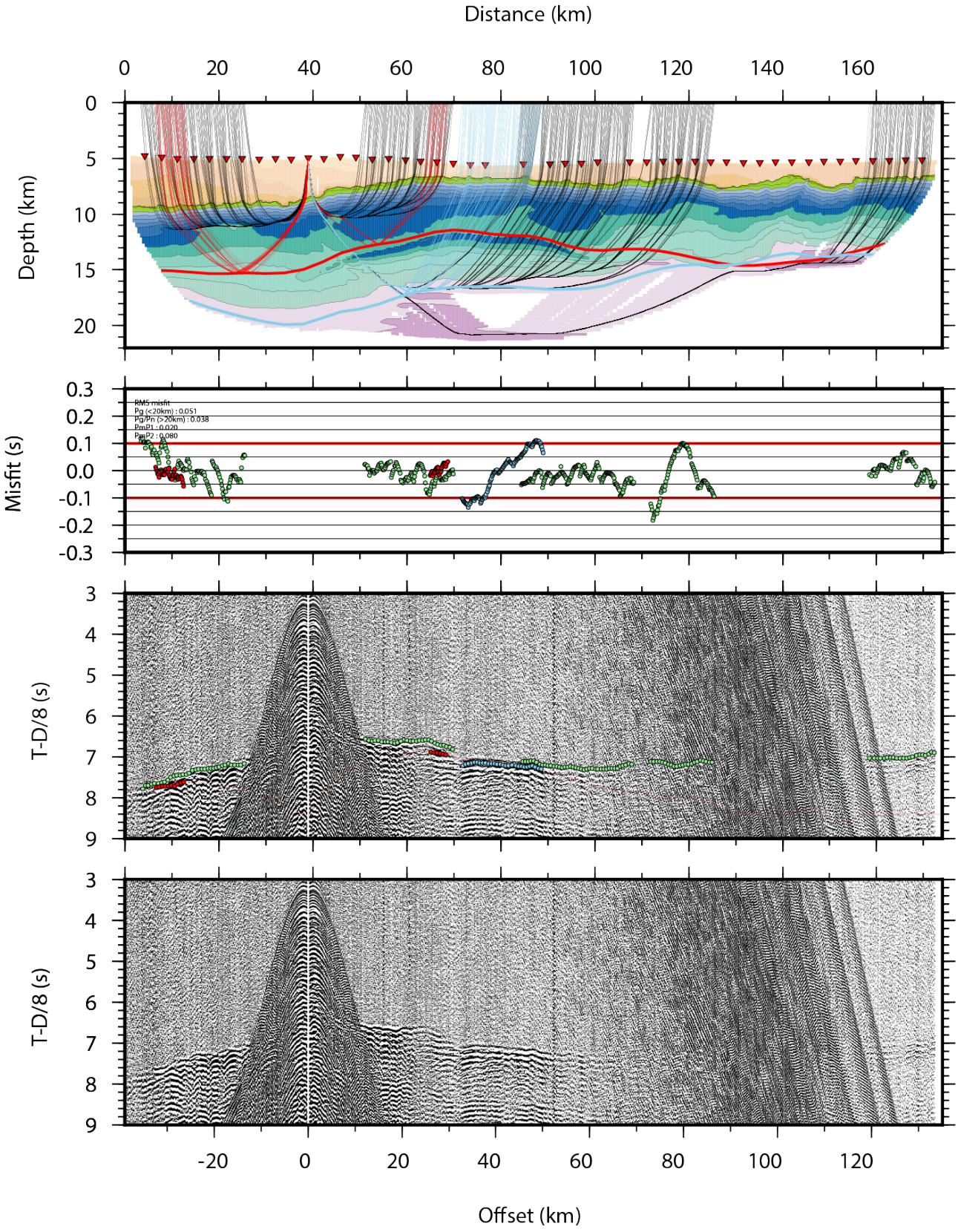


Figure D.36: Summary Plot: OBS38

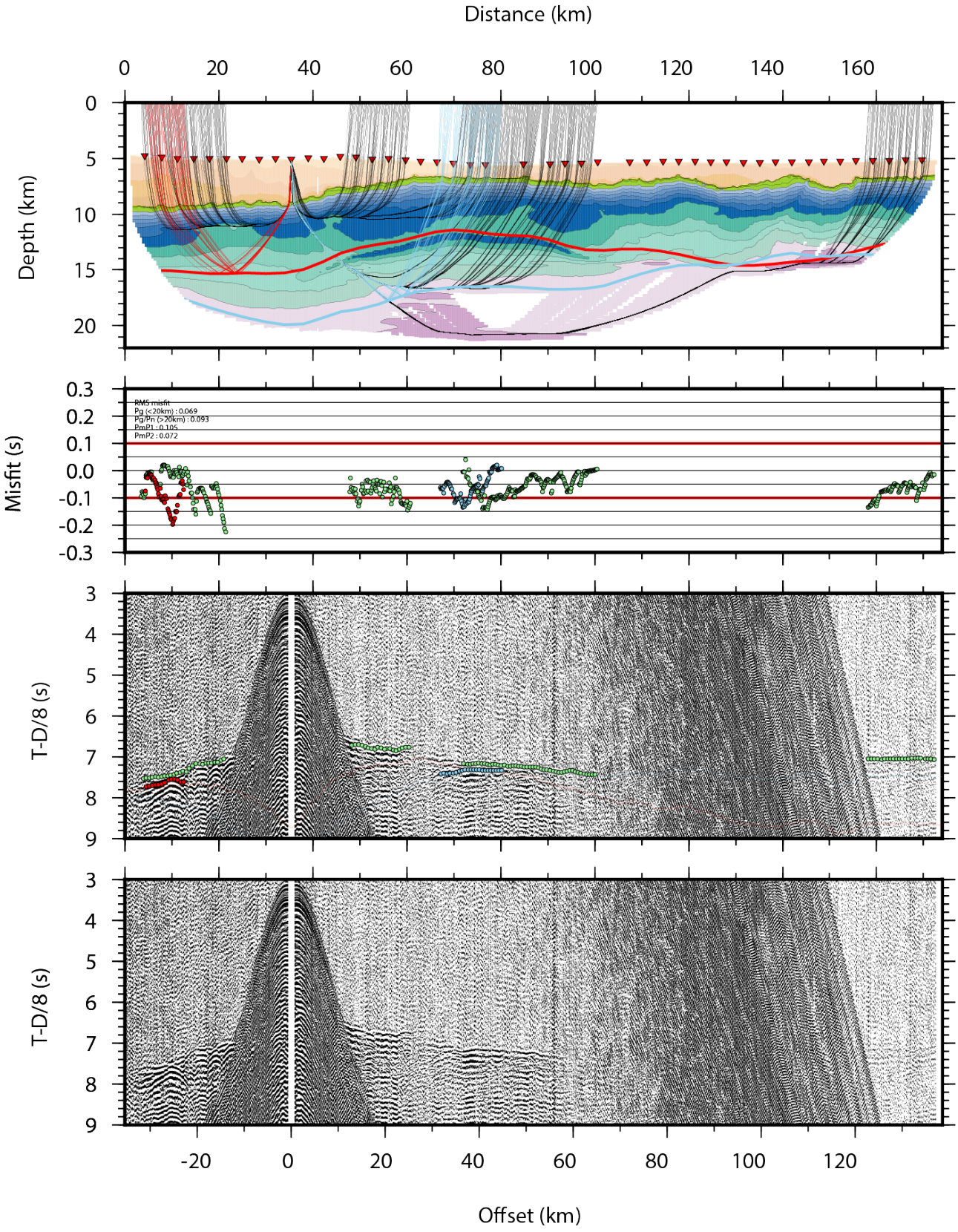


Figure D.37: Summary Plot: OBS39

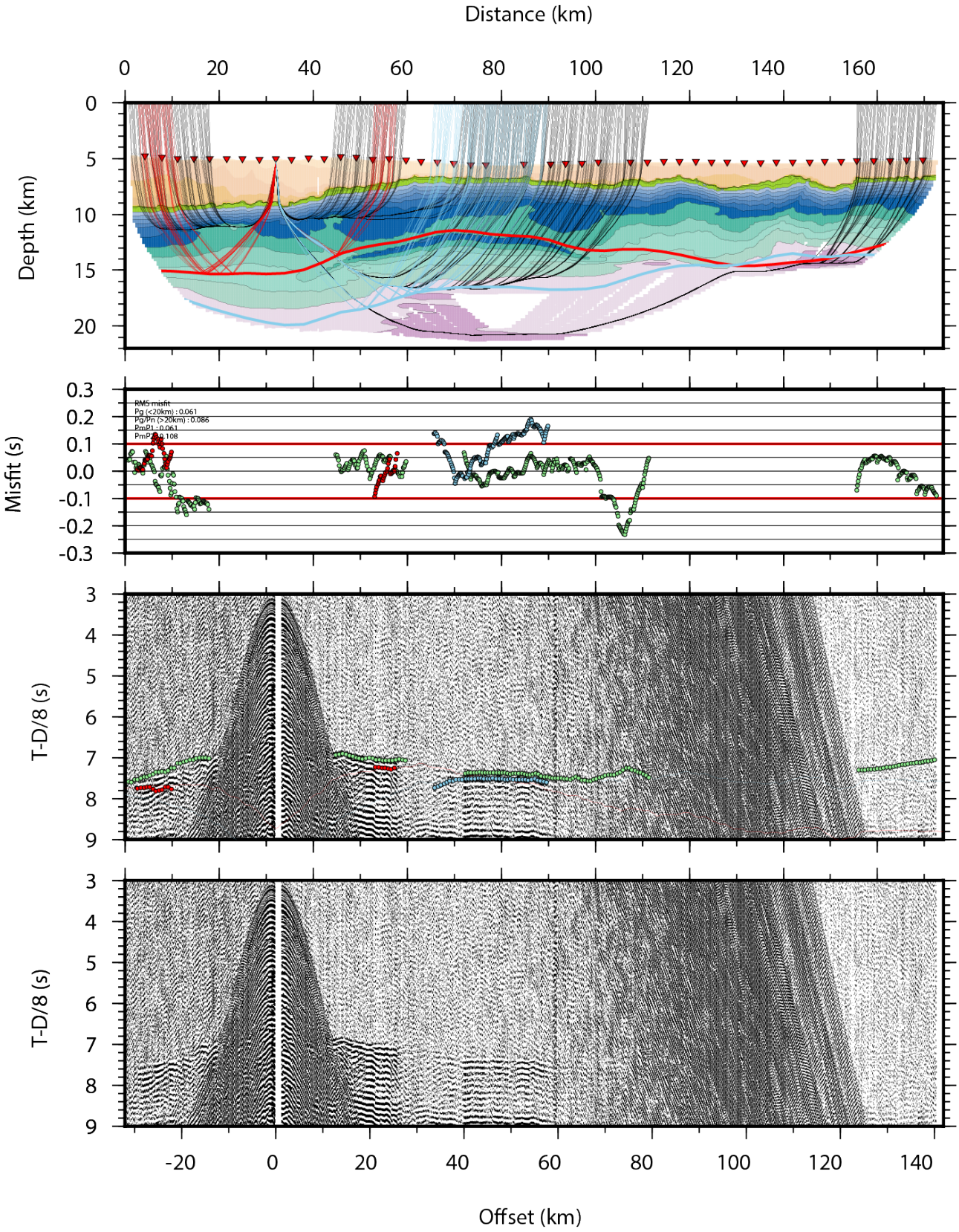


Figure D.38: Summary Plot: OBS40

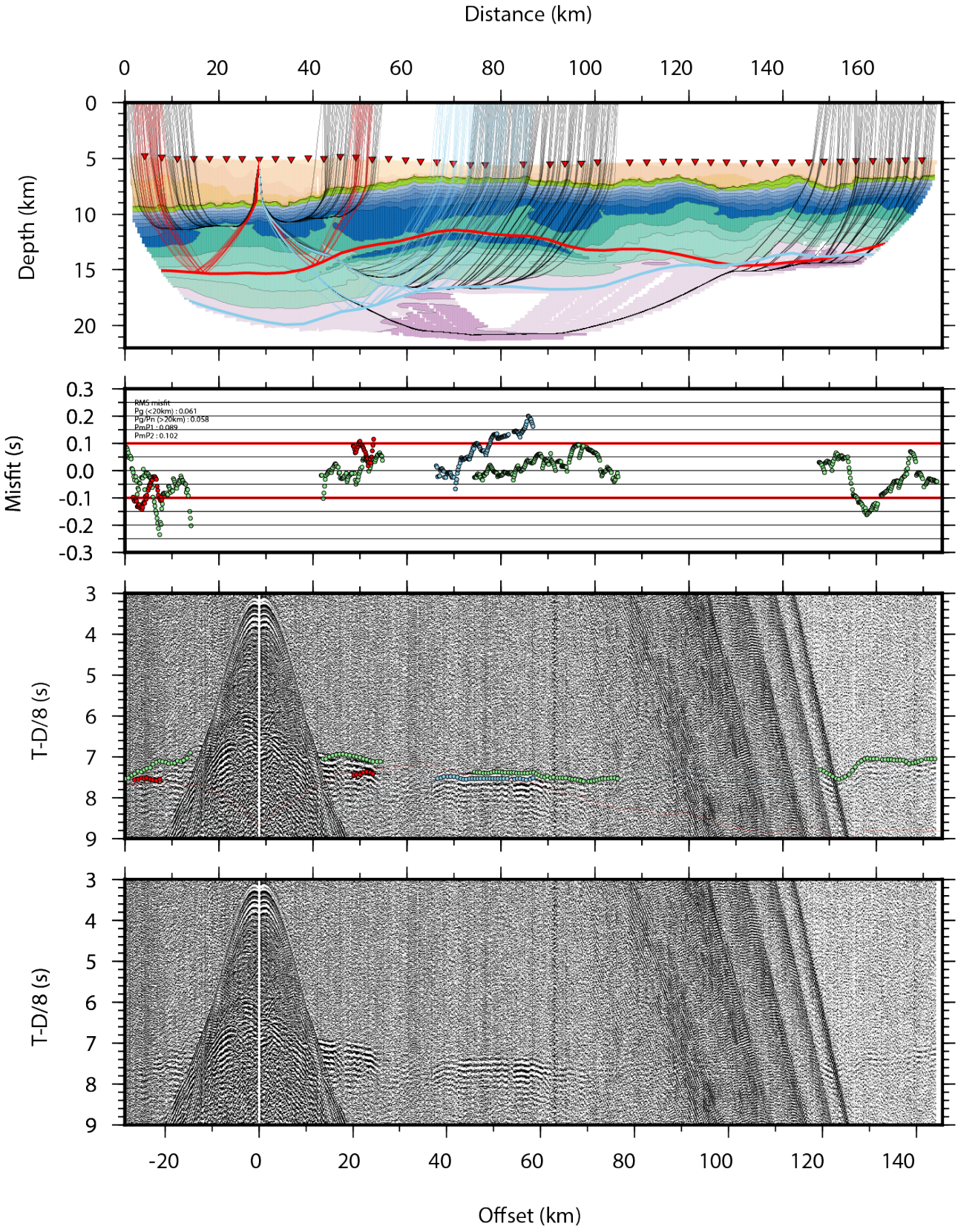


Figure D.39: Summary Plot: OBS41

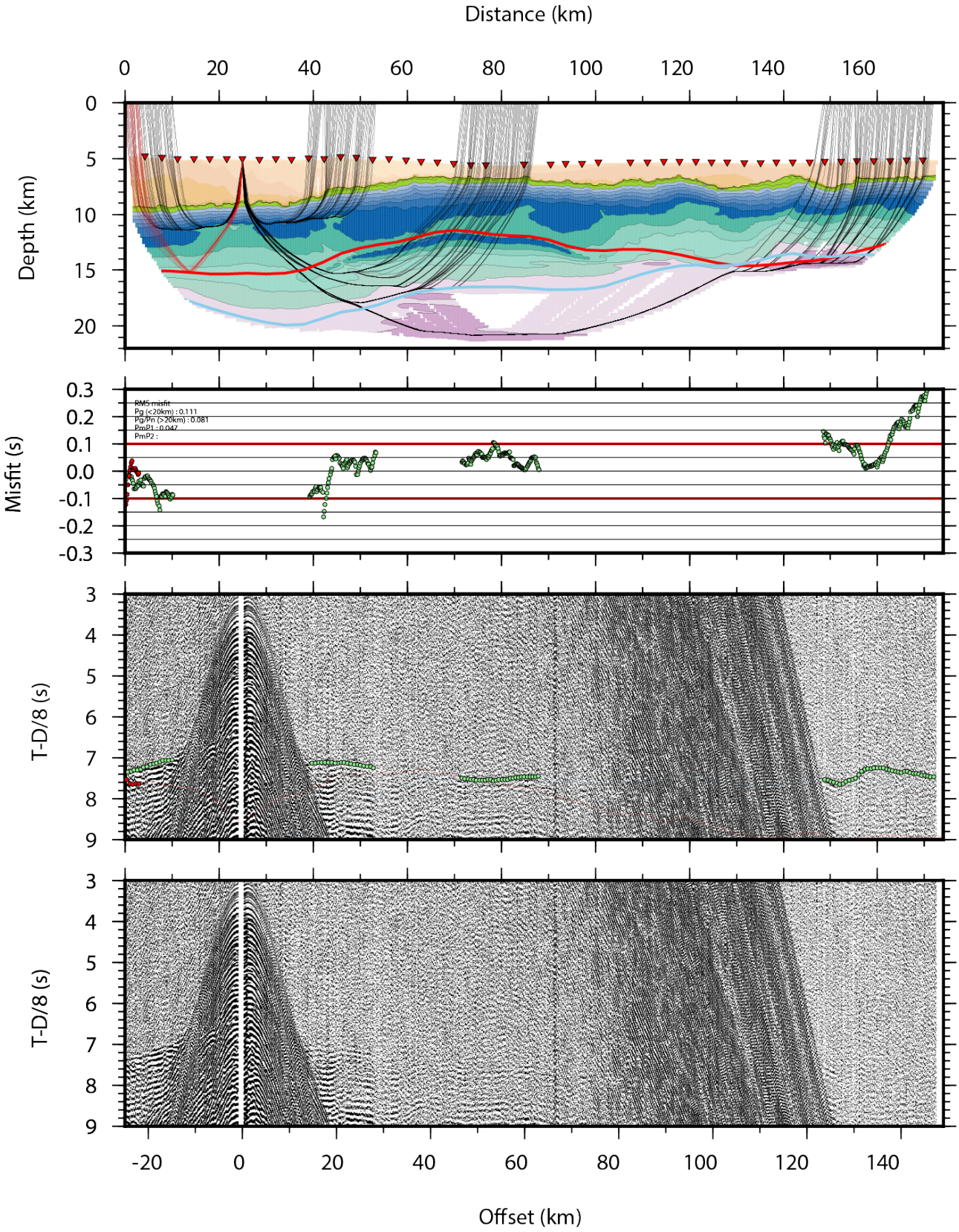


Figure D.40: Summary Plot: OBS42

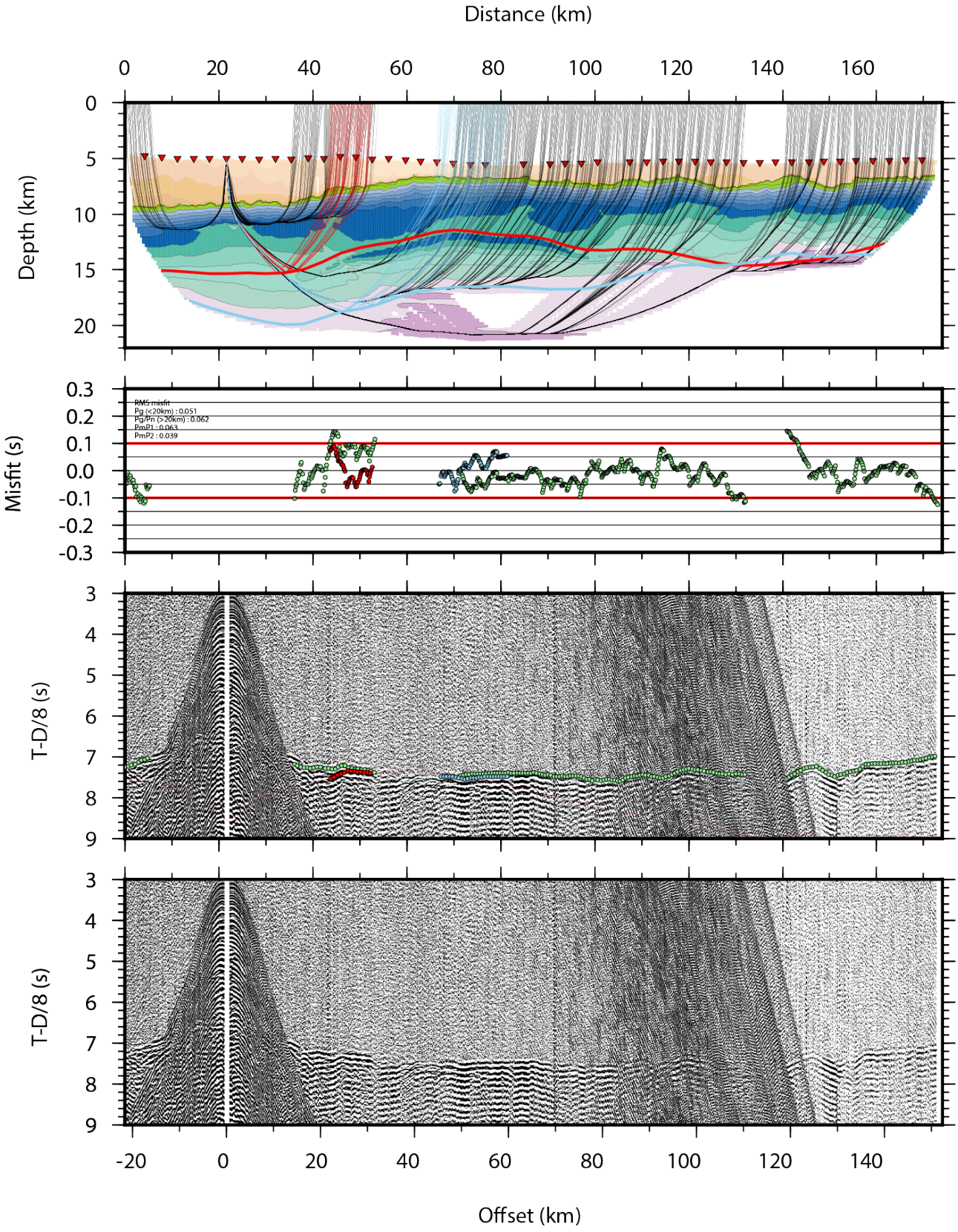


Figure D.41: Summary Plot: OBS43

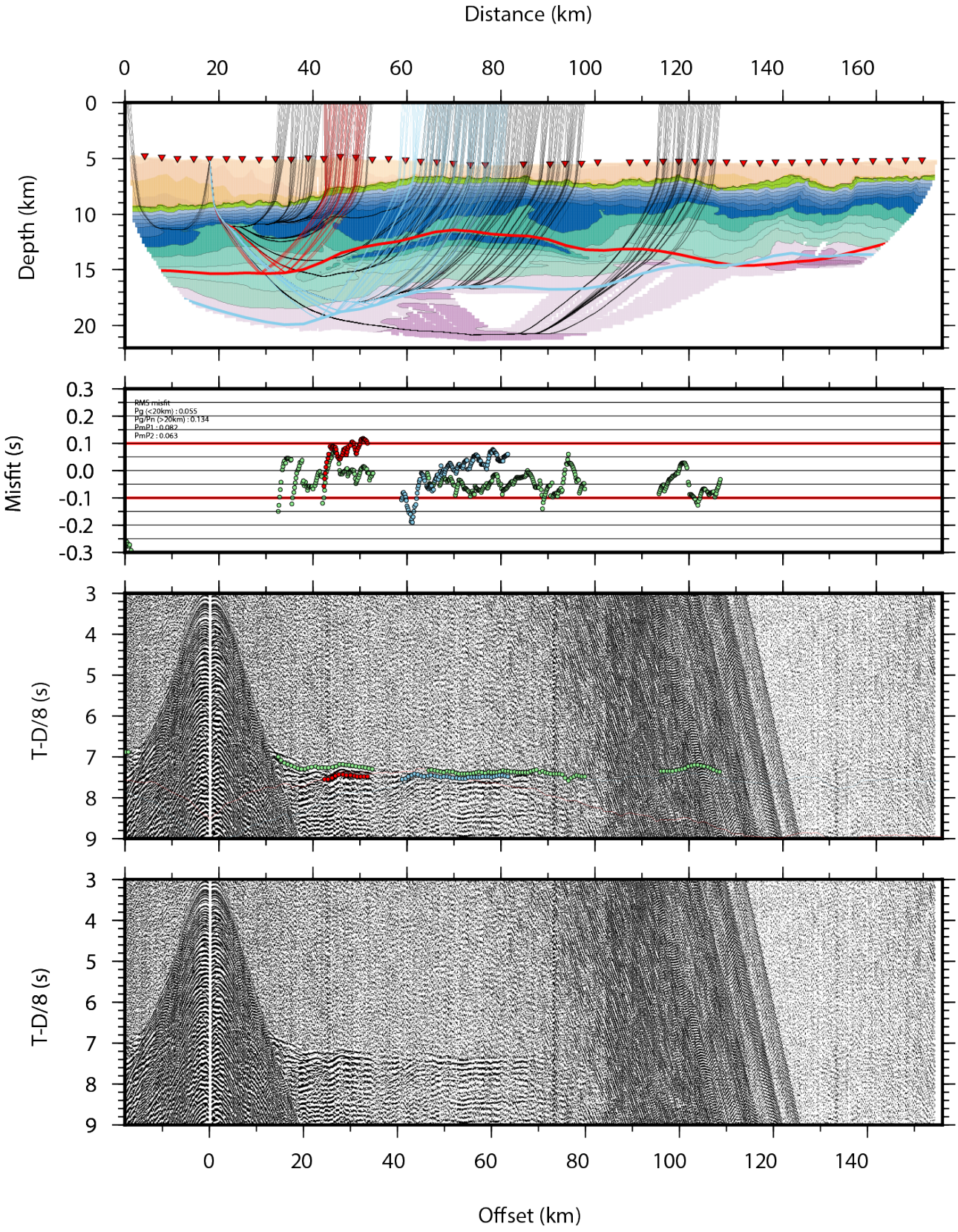


Figure D.42: Summary Plot: OBS44

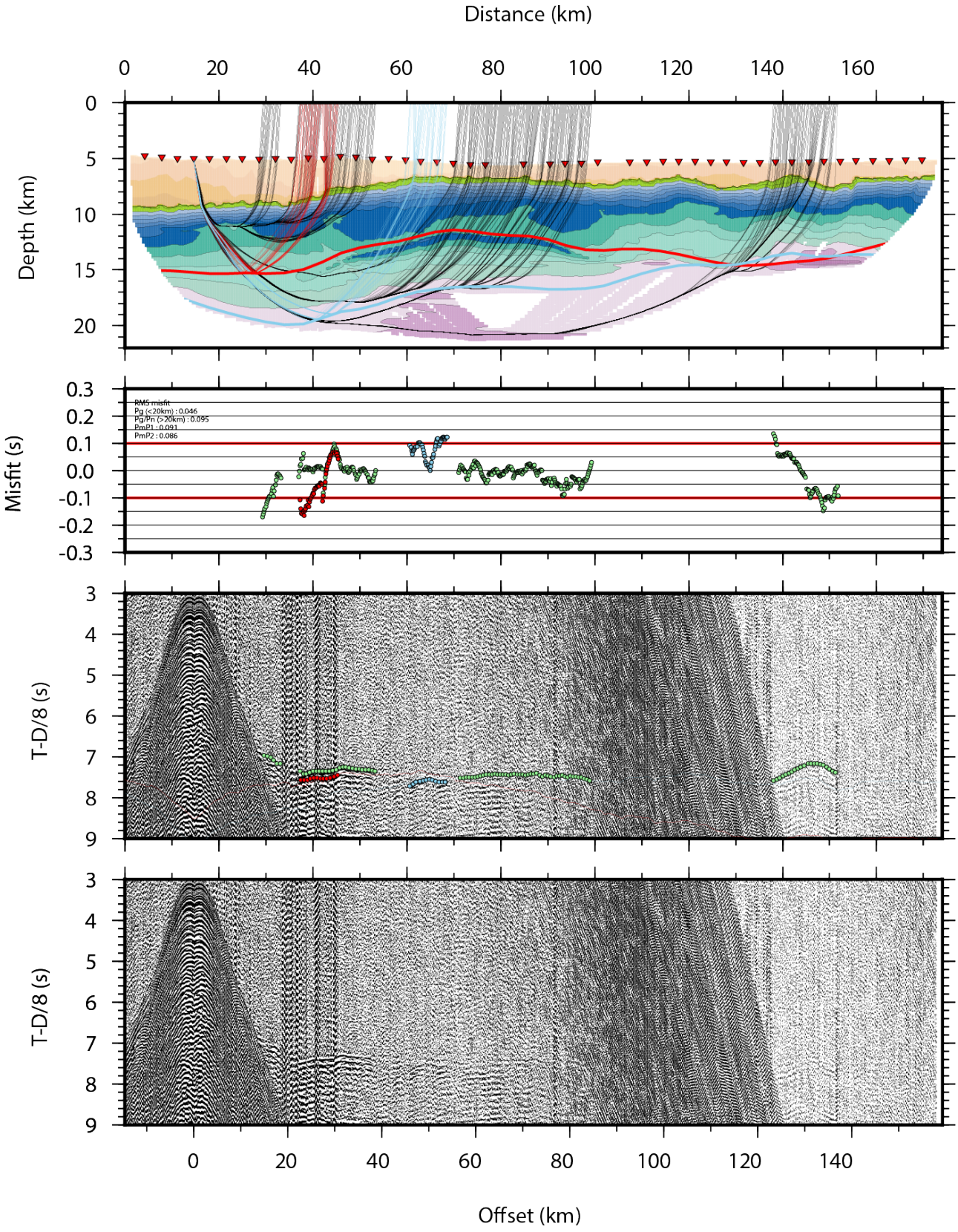


Figure D.43: Summary Plot: OBS45

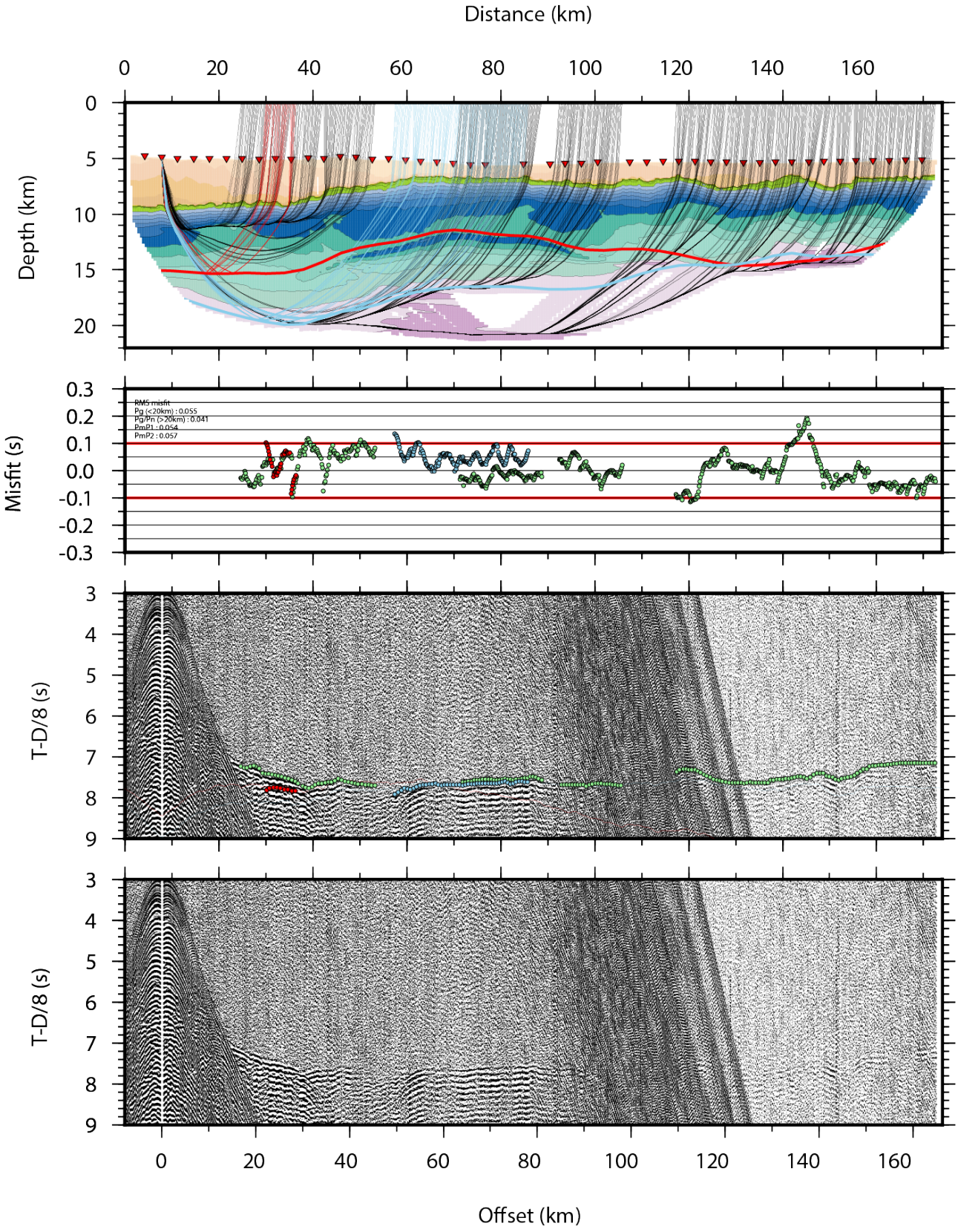


Figure D.44: Summary Plot: OBS47

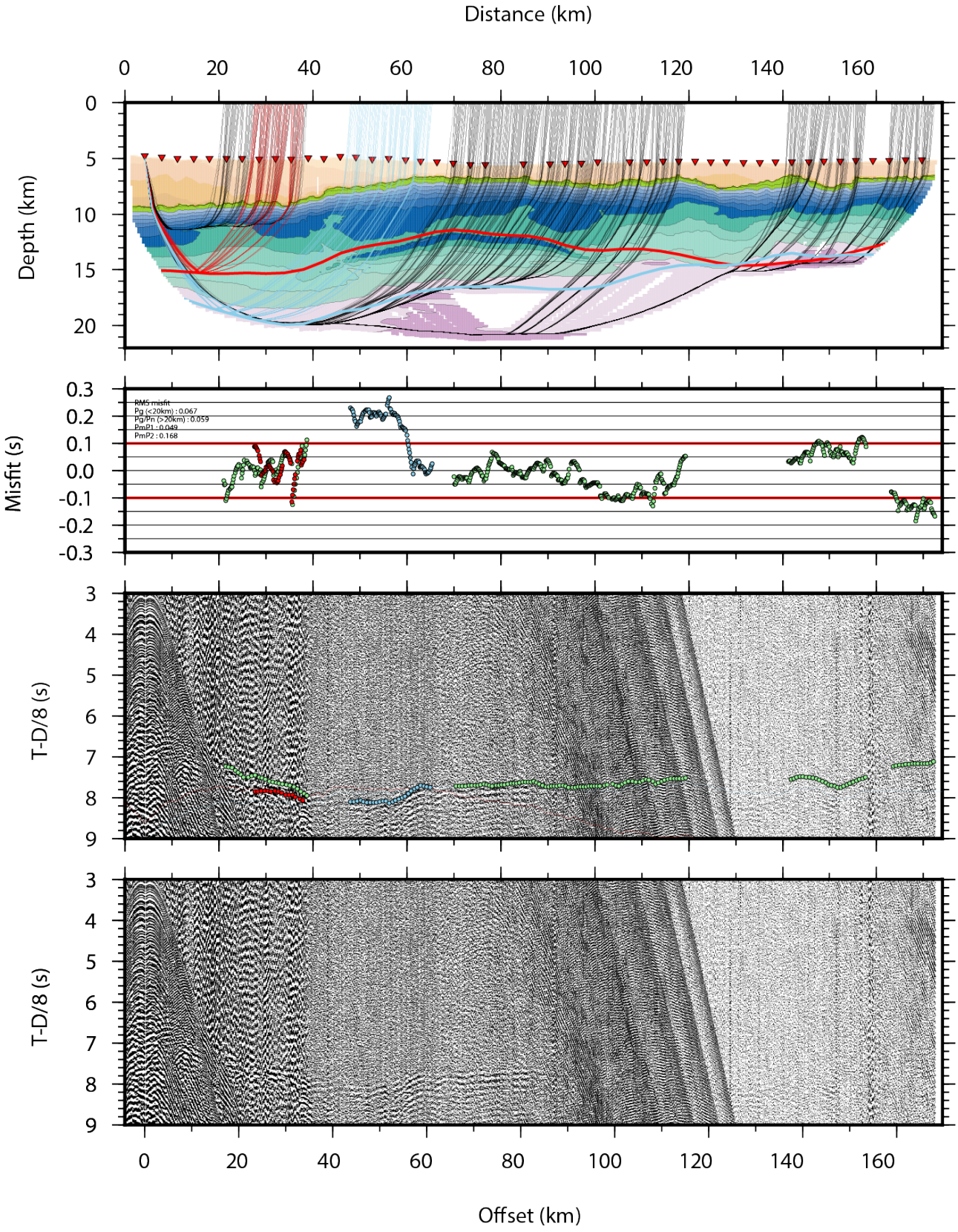


Figure D.45: Summary Plot: OBS48